Investigation and optimisation of heat storage tanks for low-flow SDHW systems

Knudsen, Søren

Publication date:
2004

Document Version
Publisher's PDF, also known as Version of record

BYG•DTU

Søren Knudsen

Investigation and optimisation of heat storage tanks for low-flow SDHW systems

DANMARKS
TEKNISKE
UNIVERSITET

Ph.D. Thesis
Rapport
BYG•DTU
R-075
2004
ISSN 1601-2917
ISBN 87-7877-138-2

I. Acknowledgements

This thesis concludes my Ph.D. work entitled 'Investigation and optimisation of heat storage tanks for low-flow SDHW systems'. The work was carried out in the period between September 2000 and January 2004 at Department of Civil Engineering at Technical University and was financed by a scholarship from Technical University of Denmark.

I would like to offer my deepest gratitude to my supervisor Associate Professor Simon Furbo. His great interest and thorough understanding of the subject has been very inspiring for my work. I really enjoyed working with and learning from Simon.

Thanks go to Professor Graham L. Morrison for letting me work in his laboratory and use the PIV equipment at University of New South Wales, Sydney. It was a great pleasure and very inspiring to work together with Professor Morrison and Professor Masud Behnia. Furthermore, from School of Mechanical and Manufacturing Engineering at University of New South Wales I would like to thank Ph.D.-student Indra Budihardjo for helping me setting up the PIV system. The stay in Australia (September 2002 – December 2002) was made possible by grants from the private funds *Larsen & Nielsen Fonden*, *Civilingeniør Poul V. Andersens Fond* and *Familien Hede Nielsens Fond*.

Special thanks are also due to my colleagues in the Solar Energy Research Group at Department of Civil Engineering for their helpful comments during my work. I acknowledge and appreciate the help and support with experiments that I was offered by Martin Dandanell and Lars Kæstel Jørgensen from the laboratory. Also thanks to Anne Rasmussen for proof reading the thesis.

Finally, I wish to express my gratitude to my girlfriend Birgitte for her admirable patience and support, and for keeping our home in a reasonable state in the last intensive month of my Ph.D. study.

Lyngby, January 14, 2004

Søren Knudsen

II. Abstract

This thesis, 'Investigation and optimisation of heat storage tanks for low-flow SDHW systems', describes a study of the heat transfer and flow structure in vertical mantle heat exchangers for low-flow Solar Domestic Hot Water (SDHW) systems. The heat storage is a key component in SDHW systems and the vertical mantle heat exchanger is one of the most promising heat storage designs for low-flow SDHW systems. The study was carried out using a combination of experimental and numerical methods.

Thermal experiments of mantle heat exchangers with different mantle inlet designs showed that the mantle inlet port with advantage can be located a distance from the top of the mantle. Consequently, the mantle heat exchangers marketed today can be improved by changing the mantle inlet position.

The heat transfer and flow structure in mantle heat exchangers are rather complex and the thermal experiments were followed by investigations by means of advanced experimental and numerical techniques such as Particle Image Velocimetry (PIV) and Computational Fluid Dynamics (CFD). Using a transparent glass mantle tank, experimental flow visualisation was carried out with a PIV system. The flow structures inside the mantle and inside the tank were visualised and then compared with the flow structures predicted by CFD-models. The investigations showed that the CFD-models were able to model the flow in the mantle and in the tank correctly. The CFD-models were also validated by means of thermal experiments with a steel mantle tank.

With the verified CFD-models, a parameter analysis was carried out for differently designed mantle heat exchangers for different typical conditions to reveal how the mantle tank parameters influence the flow structure and heat transfer in mantle heat exchangers. The heat transfer in the mantle near the mantle inlet port showed to be in the mixed convection regime, and as the distance from the inlet increased, natural convection started to dominate. The heat transfer between the tank wall and the domestic water in the tank is governed by natural convection. Dimensionless heat transfer theory was applied, and Nusselt number correlations for the heat transfer in vertical mantle heat exchangers were developed, based on the CFD-analysis.

The CFD-calculations and PIV measurements revealed that thermal stratification is built up in the inner tank above the mantle due to natural convection flow along the tank wall. Based on CFD-calculations, a method was developed for determining the heat transfer caused by the natural convection flow inside the tank. Furthermore, a method was developed for determining the mixing inside the mantle due to the mantle inlet jet.

The developed heat transfer correlations, the method for determining the heat transfer in the inner tank caused by natural convection and the method for determining the mixing in the mantle were implemented in a simulation program for SDHW systems, MantlSim. The simulation program predicts the yearly thermal performance of low-flow SDHW systems based on mantle tanks. MantlSim was verified and afterwards used as a tool for heat storage design analysis. The heat storage design analysis showed that vertical mantle heat exchangers could be designed in a better way than done today.

III. Resumé

Denne afhandling, 'Investigation and optimisation of heat storage tanks for low-flow SDHW systems', beskriver et studie af varmetransport- og strømningsforhold i kappebeholdere til low flow solvarmeanlæg. Varmelageret er en af hovedkomponenterne i et solvarmeanlæg, og kappebeholdere er en af de bedst egnede varmelagertyper til low flow solvarmeanlæg til brugsvandsopvarmning. Arbejdet har omfattet en kombination af eksperimentelle og numeriske undersøgelser.

Termiske undersøgelser af kappebeholdere med forskelligt designede kappeindløb viste, at kappeindløbet med fordel kan blive placeret et stykke fra toppen af kappen. De i dag benyttede kappebeholdere kan derfor forbedres ved at placere kappeindløbet lavere end normalt.

På grund problemernes kompleksitet blev de termiske undersøgelser fulgt op af undersøgelser ved hjælp af avancerede eksperimentelle og numeriske metoder, såsom Particle Image Velocimetry (PIV) og Computational Fluid Dynamics (CFD). Med en transparent kappebeholder af glas blev eksperimentelle strømningsvisualiseringer udført med PIV. Strømningerne i kappen og inde i tanken blev visualiseret og sammenlignet med strømningerne beregnet af CFD-modeller. CFD-modellerne viste sig i stand til at bestemme strømningsbevægelserne i kappen og inde i tanken korrekt. CFD-modellerne blev også valideret ved termiske forsøg med kappebeholdere af stål.

Med de validerede CFD-modeller er der gennemført en parameteranalyse med forskelligt udformede kappebeholdere ved typiske driftsbetingelser. I kappen viste varmetransporten sig i nærheden af indløbet at være af typen blandet konvektion, mens naturlig konvektion blev mere dominerende når afstanden fra indløbet øgedes. Inde i tanken er varmetransporten styret af naturlig konvektion. På basis af CFD-analyserne blev en række dimensionsløse Nusselt-tal korrelationer bestemt til beskrivelse af varmetransporten i kappebeholdere.

CFD-beregningerne og PIV målingerne viste at temperaturlagdelingen inde i tanken bliver opbygget på grund af vandstrømninger forårsaget af naturlig konvektion langs tankvæggen. En metode til bestemmelse af varmetransporten inde i tanken forårsaget vandstrømningerne er opstillet. Der er ydermere opstillet en metode til bestemmelse af den omrøring der finder sted i kappen ved kappeindløbet. Begge metoder er udviklet på basis af CFD-beregninger.

De opstillede varmetransportkorrelationer, metoden til bestemmelse af varmetransporten inde i tanken forårsaget af den naturlige konvektion samt metoden til bestemmelse af omrøringen i kappen blev implementeret i et simuleringsprogram for solvarmeanlæg til brugsvandsopvarmning, MantlSim. Simuleringsprogrammet kan bestemme den årlige ydelse for low flow solvarmeanlæg med kappebeholdere. MantlSim blev valideret og bagefter brugt til en analyse af, hvorledes kappebeholderens udformning påvirker ydelsen af solvarmeanlæg. Analysen viste, at der er mulighed for at udforme kappebeholdere bedre end det gøres i dag.

IV. Nomenclature

A	aspect ratio (height of annulus/gap of annulus), [-]
A	area, [m²]
c_p	specific heat of fluid, [J/kg·K]
d	diameter, [m]
dt	timestep, [s]
dz_j	height of layer j
D	diameter, [m]
DR(1)	radius of tank, [m]
DR(2)	thickness of tank wall, [m]
DR(3)	mantle gap, [m]
DR(4)	thickness of mantle wall, 8m]
e	insulation thickness, [m]
E	energy, [J]
g_i	gravity, $g_i = (g_x,g_y,g_z)$, [m/s²]
f	solar fraction, [-]
G	solar irradiance, [W/m²]
Gr_w	Grashof number based on gap of annulus, [-]
Gz	Graetz number (Re·Pr·z/(2·w)), [-]
h	convective heat transfer coefficient, [W/m²·K]
h	thermodynamic enthalpy, h = h(T,p), [J/kg]
H	height, [m]
H	total enthalpy, H = h + ½u_i^2, [J/kg]
i	section number, [-]
j	layer number, [-]
k	thermal conductivity, [W/m·K]
k	turbulence kinetic energy, [m²/s²]
L	length or height of annulus, [m]
$\dot{m}$	mass flow rate, [kg/s]
MIX	part of control volume that is mixed with incoming fluid, [-]
Nu_d	Nusselt number based on diameter, [-]
Nu_L	Nusselt number (non-dimensional heat flux) based on length, [-]
Nu_w	Nusselt number based on gap of annulus, [-]
Nu_z	local Nusselt number, [-]
p	pressure, [kg/(m·s²)]
Pe	Peclet number, [-]
Pr	Prandtl number, [-]
q	heat flux, [W/m²]
Q	rate of heat transfer, [W]
r	radius, [m]
Ra_d	Rayleigh number based on diameter, [-]
Ra_L	Rayleigh number based on length, [-]
Ra_w	Rayleigh number based on gap of annulus, [-]
Ra_z	local Rayleigh number, [-]
Re	Reynolds number, [-]
St	stratification correction parameter, [-]

Str	thermal stratification, [K/m]
t	time, [s]
T	Temperature, [K or °C]
u_i	fluid velocity, $u_i = (u,v,w)$, [m/s]
U’	overall heat transfer coefficient, [W/m²·K]
v	velocity, [m/s]
V	volume, [m³]
$\dot{V}$	volume flow rate, [m³/s]
w	gap width of annulus or mantle, [m]
x	weight percentage of propylene glycol, [%]
z	distance from bottom, [m]
z	vertical distance from mantle inlet, [-]
Z	dimensionless axial coordinate, [-]

Greek symbols

β	thermal expansion coefficient, [1/K]
ε	turbulence dissipation rate, [m²/s³]
η	collector efficiency, [-]
η	part of heat transfer at tank wall that flows up in the tank, [-]
κ	diameter ratio (r_{outer}/r_{inner}), [-]
μ	dynamic viscosity, [kg/(m·s)]
ν	kinematic viscosity, [m²/s]
θ	dimensionless temperature, [-]
ρ	density, [kg/m³]
σ	turbulent Prandtl number, [-]
τ	stress tensor, [kg/(m·s²)]
ω	specific dissipation rate, [1/s]

Subscripts

a	ambient
amb	ambient
aux	auxiliary
bot	bottom of tank
coll	collector
conv	convective
corr	correction
dhw	domestic hot water
diff	diffusive
end	end of time step
ext	external
film	film
fluid	fluid
forced	forced convection
F	forced convection
heat flow,z	heat flow at level z

i	inner
in	inlet
inlet	inlet
loss	heat loss
L	length
m	mantle
m	mean
mantle,in	inlet to mantle
mantle,out	outlet from mantle
max	maximum
min	minimum
mix	mixing
N	natural convection
net	net utilised solar energy
o	outer
out	outlet
ref	reference
start	start of time step
storage	storage
top	top of tank
T	turbulent
wall	wall
water	water
z	local
1	tank wall to domestic water
2	mantle fluid to inner mantle wall
3	mantle fluid to outer tank wall

V. Table of contents

VI. List of figures

VII. List of tables

1. Introduction

1.1 Solar Domestic Hot Water systems

In Denmark the potential for solar energy surpasses the energy demand (Danish Energy Agency, 1998). Therefore, it is relevant to develop solar energy technologies that can be a large part of the energy system in the future in order to have a sustainable society. The solar energy technology that is treated in this thesis is solar energy systems for domestic hot water supply in single-family houses – called small Solar Domestic Hot Water (SDHW) systems.

A SDHW system consists of a solar collector panel connected through pipes to the heat storage. In some parts of the world the pipes from the storage tank are connected directly to the solar collector, and water from the tank circulates through the collector to get heated. In colder climates, like for instance in Denmark, where there is a risk of the fluid freezing in the collector, an antifreeze heat transfer fluid (typically a mixture of propylene glycol and water) is used. A circulation pump pumps the heat transfer fluid through the solar collector panel, where the fluid is heated, to the heat storage where a heat exchange arrangement between the collector fluid and the water in the tank is required to transfer the heat from the heat transfer fluid to the domestic water in the tank.

The heat storage often has an auxiliary energy supply system to supply heat in periods where there is insufficient solar energy available to heat the water to the required temperature. This auxiliary energy supply system can either be an electric heating element or a heat exchanger spiral connected to an oil/gas burner.

1.1.1 Low-flow SDHW systems

Low-flow SDHW systems differ from traditional SDHW systems by having a low flow rate in the solar collector loop. In traditional pump circulated SDHW systems, the collector flow rate is around 1.2 l/(min·m² collector) while the collector flow rate in low-flow systems is around 0.2 l/(min·m² collector). The original reason for using the high flow rates was to achieve a high heat removal factor (and thereby a high efficiency) for the collector (Duffie and Beckman, 1991). van Koppen et al. (1979) introduced the low-flow principle because they considered the entire system performance instead of just the collector performance. The heat removal factor and the efficiency of the solar collector are slightly reduced by using a lower flow rate, but these effects are small compared to other benefits from the low flow rate. Low-flow operation results in a greater temperature rise across the collectors, and if the heat storage is low-flow prepared, the solar energy can be transferred to the heat storage at a higher level and give a higher degree of thermal stratification. This results in a decrease in the auxiliary energy supply, which increases the thermal performance of the system. Furthermore, with a highly stratified storage and a low flow rate, the return temperature to the solar collector will be lowered, which increases both the efficiency and the

working periods of the collector. The thereby increased energy output from the solar collector results in a higher thermal performance of the system.

Other advantages by using the low-flow operation are that smaller pipes and circulation pumps can be used, which can reduce cost, make the installation easier and further increase thermal performance (IEA, Task 14, 1996). The smaller flow rate makes it possible to use smaller pipes resulting in less material use for pipes and insulation, and less heat loss. Also smaller pumps with lower power consumption can be used.

Wuestling et al. (1985) made a numerical comparison of the thermal performance of a high-flow system with a fully mixed tank and a low-flow system with a highly stratified tank. The simulations showed that for that specific system the potential improvement in the thermal performance was up to 37% by using low-flow operation and having a highly stratified tank. However, this would not be realised in practice as real tanks are in general neither fully mixed nor fully stratified. Furbo and Mikkelsen (1987) made side-by-side measurements of a traditional high-flow SDHW system with an internal coil heat exchanger in the tank and of a low-flow SDHW system with a mantle tank. The investigation showed that the low-flow system had a thermal performance that was about 20% higher than the traditional system. A summary of the benefits of thermal stratification and low-flow operation for solar domestic hot water systems is given by Hollands and Lightstone (1989) and in IEA, Task 14 (1996) where examples on how much the performance/cost ratio can be improved country by country by applying low-flow operation are given.

1.1.2 Heat exchangers in SDHW systems

As mentioned, a heat exchanger is necessary to transfer the heat from the hot solar collector fluid to the water in the storage tank when fluid in the solar collector loop is an antifreeze solution. Several heat exchanger configurations have been employed, and the following configurations are among the most common.

- Immersed coil or immersed tubes that are the heat exchanger installed inside the storage tank (Dahm et al., 1998).
- External shell-and-tube heat exchangers with collector fluid pumped through the tubes, and the tank water (driven by natural convection) flowing through the shell (Dahl and Davidson, 1998).
- The mantle heat exchanger – in either its vertical form (Shah, 2000) or the horizontal form (Morrison et al., 1998) – consists of a narrow annular jacket around the storage tank in which the collector fluid flows.

The systems with immersed coil or immersed tubes and vertical mantle heat exchangers are mainly used in the northern part of Europe. The systems with external shell-and-tube heat exchangers are mainly used in North America and Canada. Horizontal mantle heat exchangers are used in thermosyphon systems where there is no circulation pump in the system. Thermosyphon systems with a horizontal mantle heat exchanger are mainly used in Australia and Southern Europe.

Furbo (1993) carried out side-by-side experiments with three differently designed small low-flow SDHW systems in order to compare the performance of the different heat exchangers in systems with low-flow operation. The three systems were: one system with an immersed coil heat exchanger, one system with an external heat exchanger and one system with a vertical mantle heat exchanger. The low-flow system with the vertical mantle heat exchanger outperformed the other two low-flow systems, and it also showed to have the highest performance/cost ratio.

The main reasons for the high thermal performance of systems with vertical mantle tanks are the large heat exchange surface area and a desirable solar collector fluid flow pattern in the mantle that help to prove good cooling of the collector fluid and a high degree of thermal stratification inside the tank. Furthermore, there is a smaller heat loss compared to the system with the external heat exchanger. Another advantage of the mantle tank system is the simple design due to the combination of the hot water tank and heat exchanger into one unit.

Figure 1-1 shows a typical SDHW system with a vertical mantle heat exchanger.

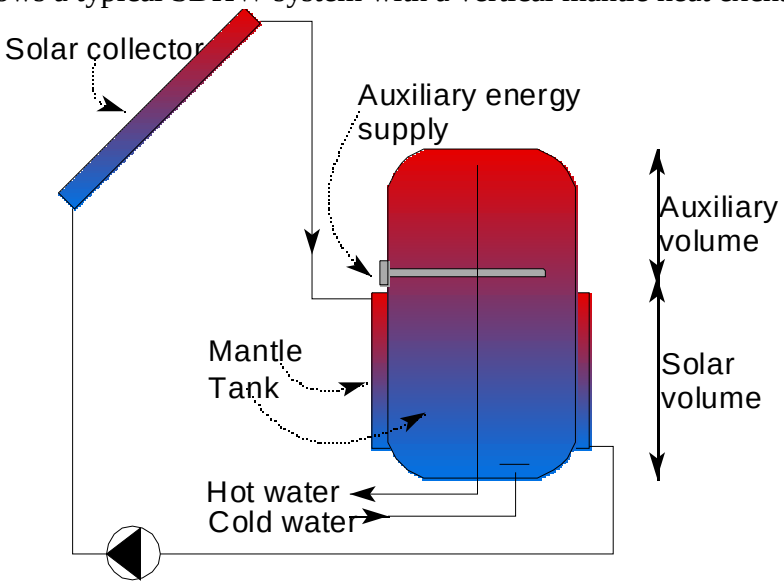

Figure 1-1: A SDHW system with a vertical mantle heat exchanger.

1.2 Scope, limitations and methods

In order to further develop and reduce the cost of heat storage tanks for SDHW systems, it is necessary to fully understand the thermal behaviour of and the fluid motion in the heat storage tanks, and it is important to have simulation tools that are able to predict the yearly thermal performance of the systems. Such a simulation tool was developed in a previous study of vertical mantle heat exchangers (Shah, 1999). However, the developed simulation tool proved to have some limitations, e.g. in calculating the thermal stratification in the upper part of the tank in the right way, and it needs, therefore, to be further developed.

The purpose of the work presented in this thesis is to investigate and analyse the heat transfer and flow structure in heat storage tanks for low-flow SDHW systems and to further develop an existing simulation tool for low-flow SDHW systems based on the results of the analysis.

It has been revealed in this chapter that the thermal performance of small SDHW systems can be improved if low-flow operation is applied to the systems, and that the vertical mantle heat exchanger is one of the most promising heat storage designs for low-flow systems. Therefore, only vertical mantle heat exchangers are investigated in this study.

The heat transfer and flow structure in mantle heat exchangers are rather complex, and in order to make the investigation and analysis it is necessary to use an advanced numerical tool such as Computational Fluid Dynamics (CFD). A CFD program solves the Navier-Stokes and energy equations, and it is therefore possible to obtain detailed information about the heat transfer and flow structure. Therefore, CFD-models are used to take the mantle heat exchangers into calculation.

The CFD-models form the basis of a large part of the results obtained in this thesis, and they need to be validated. The CFD-models are, in this thesis, validated by thermal experiments (comparing stratification in the inner tank and the outlet temperature from the mantle) and by a flow visualisation technique called Particle Image Velocimetry (comparing the flow structure and velocities in the mantle and in the inner tank).

The thermal experiments are not only used for validation of the CFD-models, they are also used for investigation of how differently designed mantle inlets influence the thermal stratification in the mantle and in the inner tank, and how they influence the thermal performance of low-flow SDHW systems.

The information obtained by the CFD-analysis is used for the further development of a simulation program (MantlSim) that predicts the yearly thermal performance of low-flow SDHW systems with vertical mantle heat exchangers as heat storage. MantlSim is used to evaluate different heat storage designs.

1.3 Structure of thesis

Chapter 2 contains a literature survey about convective heat transfer in vertical annuli and about convective heat transfer on the tank side of the wall.

The experimental and numerical techniques that are used in this study will be outlined in chapter 3.

Chapter 4 describes the thermal experiments with different mantle inlet designs. The thermal experiments consist of experiments in a heat storage test facility and side-by-side measurements of two low-flow SDHW systems.

The developed CFD-model is validated in chapter 5, by comparing the CFD-results with thermal experiments and flow visualisation experiments.

Chapter 6 contains a numerical analysis based on CFD-calculations of flow and heat transfer in vertical mantle tanks. The flow and heat transfer in both mantle and inner tank are analysed for different mantle tank designs and for different operation conditions.

The results from the analysis in chapter 6 are in chapter 7 used to develop dimensionless heat transfer correlations for convective heat transfer at the inner tank wall and at the inner and outer mantle wall. Furthermore, a model to predict the natural convection flow inside the inner tank is developed.

A method for determining the mixing inside the mantle caused by the incoming solar collector fluid is developed in chapter 8. Furthermore, the simulation program, MantlSim, is described along with the implementation of the results obtained in this thesis. MantlSim is also verified in chapter 8.

In chapter 9, MantlSim is used to perform a heat storage design analysis of vertical mantle heat exchangers.

Finally, in chapter 10, all the findings are summarised and recommendations for further work are given.

2. Background

2.1 Introduction

Mantle heat exchangers consist of two fluids separated by a cylindrical wall, where the heat transfer occurs between the fluid in the annular mantle and the fluid in the tank. In case of SDHW systems, the tank consists of domestic water. The flow of the water in the tank is driven by natural convection only, when draw-offs are not considered. The flow in the mantle is driven by a combination of forced flow due to the circulation pump in the solar collector loop (or by the thermosyphon pressure difference in a thermosyphon system), and natural convection flow from the temperature difference between the inlet stream and the fluid in the mantle and from the temperature difference between the inlet stream and the tank wall temperatures. The flow in the annular mantle is rather complex because of the combination of the low flow rates, that are often used in SDHW systems with mantle tanks, and the large temperature differences between the inlet stream and the fluid in the mantle, that sometimes occur in these systems.

It was revealed in chapter 1 that thermal stratification in the tank has a great impact on the thermal performance of SDHW systems. Thus, the performance of heat exchangers used in solar water heating systems need to be quantified in two ways. The first, as for any other heat exchanger, is the amount of heat that is transferred into the tank. The second is the vertical position in the tank where the heat is transferred. Therefore it is necessary to be able to quantify local heat transfer in the heat exchanger.

This chapter contains a literature survey of the types of heat transfer that occur in mantle heat exchangers. The emphasis will be on the annular side of the mantle heat exchanger. The survey will start with a general introduction to heat transfer in vertical annuli, as this thesis treats vertical mantle heat exchangers. Then previous studies of heat transfer in mantle heat exchangers (both vertical and horizontal) are presented. Furthermore, studies of the heat transfer at the tank side of the mantle heat exchanger will be presented.

2.2 Heat transfer in vertical annuli

Convective heat transfer in vertical annuli is a challenging engineering problem that has caused a lot of interest over the years. This literature survey of convective heat transfer in vertical annuli contains some of the most important findings and is divided into two parts, which are the types of convective heat transfer that occur in mantle heat exchangers: natural convection (often referred to as free convection) heat transfer and mixed convection heat transfer, which is combined forced and natural convection heat transfer.

2.2.1 Natural convection heat transfer

Nagendra et al. (1970) made an analytical and an experimental investigation of free convection heat transfer in vertical concentric cylindrical annuli. Heat transfer

correlations for vertical annuli were obtained by means of the approximate double boundary layer model for vertical parallel plates. The correlations were checked by experiments using annuli with an inner diameter of 0.008 m and an outer diameter and length of 0.018 m and 0.279 m, and 0.0254 m and 0.287 m, respectively. Water was used as fluid medium, and the inner cylinder was maintained at a constant high temperature and the outer cylinder at a lower constant temperature. Average Nusselt number correlations were presented as:

$$\mathrm{Nu_L} = \frac{0.48 \cdot \mathrm{Ra_L}}{6830 \cdot \left(\frac{L}{d_2}\right)^4 \cdot \left(\frac{d_1}{L}\right) + \mathrm{Ra_L}^{0.75}} \quad \text{for} \quad \left(\frac{L}{d_1} < 0.1 \cdot \mathrm{Ra_L}^{0.25}\right) \tag{2.1}$$

$$\mathrm{Nu_L} = \frac{1.19 \cdot \mathrm{Ra_L}}{16900 \cdot \left(\frac{L}{d_2}\right)^4 \cdot \left(\frac{d_1}{L}\right) + \mathrm{Ra_L}^{0.84} \cdot \left(\frac{d_1}{L}\right)^{0.36}} \quad \text{for} \quad \left(0.1 \cdot \mathrm{Ra_L}^{0.25} \le \frac{L}{d_1} \le 0.738 \cdot \mathrm{Ra_L}^{0.25}\right) \tag{2.2}$$

where L is the height of the annulus, d_1 is the outer diameter of the inner cylinder and d_2 is the inner diameter of the outer cylinder.

Kubair and Simha (1982) performed an analysis of free convection heat transfer by using the double boundary layer approach. The correlations were compared with experiments using annuli with an inner diameter in the range of 0.04 m – 0.06 m, an outer diameter of 0.1 m and a length of 0.2 m. Water and mercury were used as fluid medium. The inner cylinder was maintained at a high constant temperature and the outer cylinder at a lower constant temperature. Average Nusselt number correlations were presented as:

$$\mathrm{Nu_w} = 0.761 \cdot \left(\mathrm{Ra_w} \cdot \frac{w}{L}\right)^{0.283} \quad \text{for} \quad 10 < \mathrm{Ra_w} \cdot \frac{w}{L} < 10^3 \tag{2.3}$$

$$\mathrm{Nu_w} = 0.398 \cdot \left(\mathrm{Ra_w} \cdot \frac{w}{L}\right)^{0.284} \quad \text{for} \quad 10^3 < \mathrm{Ra_w} \cdot \frac{w}{L} < 10^5 \tag{2.4}$$

where L is the height of the annulus and w is radii gap of the annuli ($w = r_{outer} - r_{inner}$).

Keyhani et al. (1983) presented heat transfer measurements for free convection in a vertical annulus wherein the inner cylinder was at constant surface heat flux and the outer cylinder was at constant temperature. The experiments were carried out with an annulus with an inner cylinder with an outer diameter of 0.0191 m and a length of 0.876 m. The outer cylinder has an inner diameter of 0.0826 m and a length of 0.9217 m. Air and Helium were used as fluid medium, and their correlations were corrected for radiation heat transfer. Average Nusselt number correlations were presented as:

$$Nu_w = 1.406 \cdot Ra_w^{0.077} \quad \text{for} \quad 10^3 < Ra_w < 6.6 \cdot 10^3 \tag{2.5}$$

$$Nu_w = 0.163 \cdot Ra_w^{0.322} \quad \text{for} \quad 6.6 \cdot 10^3 < Ra_w < 2.3 \cdot 10^6 \tag{2.6}$$

Khan and Kumar (1989) made a numerical investigation to evaluate the effects of diameter ratio, $\kappa = r_{outer}/r_{inner}$, and aspect ratio, A = (height of annulus) / (r_{outer}-r_{inner}), in natural convection of gasses within vertical annuli. The inner cylinder was maintained at uniform heat flux and the outer cylinder at constant temperature. Results were obtained for $1 \le \kappa \le 15$ and $1 \le A \le 10$. An Average Nusselt number correlation was presented:

$$Nu_L = 0.158 \cdot Ra_L^{0.29} \cdot \kappa^{\frac{0.303}{\kappa}+0.316} \cdot A^{-0.05} \quad \text{for} \quad Ra_L < 10^6 \tag{2.7}$$

where L is the length of the annulus. They also obtained a simpler correlation for A > 5 and $\kappa > 5$ using the outer diameter of the inner cylinder as length scale:

$$Nu_{d_i} = 0.455 \cdot Ra_{d_i}^{0.202} \quad \text{for} \quad Ra_{d_i} < 10^6 \tag{2.8}$$

El-Shaarawi and Al-Nimr (1990) developed analytical solutions for fully developed natural convection in open-ended vertical concentric annuli. Four fundamental boundary conditions were investigated and corresponding fundamental solutions were obtained. The four fundamental boundary conditions were obtained by combining each of the two conditions, having one boundary maintained at uniform heat flux or at uniform wall temperature, with each of the conditions, that the opposite boundary was kept isothermal at the inlet fluid temperature or adiabatic. A Local Nusselt number correlation was obtained for each case, but due to the large amount and complexity of the findings, the results will not be described in further detail here.

Rogers and Yao (1990 and 1993) performed a study of the hydrodynamic stability of mixed convection in an annulus. The study was carried out for an annulus with a constant heat flux applied to the inner wall and the outer wall was insulated. For Rayleigh numbers between 100 and 600 they presented a Nusselt number correlation for natural convection:

$$Nu_w = 1.02 \cdot Ra_w^{0.28} \quad \text{for} \quad 100 \le Ra_w \le 600 \tag{2.9}$$

Dhimdi and Bolle (1997) made a numerical determination of heat transfer coefficients for natural convection in vertical annuli with a large Grashof number ($Gr_w = 8 \cdot 10^8$). Water was used as fluid medium and the heat transfer results were related to radius ratios and aspect radius using different uniform temperatures at the two cylindrical walls. For $Gr_w = 8 \cdot 10^8$ and for an aspect ratio of 1 (A = (height of annulus) / (r_{outer}-r_{inner})), they found the following Nusselt number correlation:

$$\log\left(Nu_w\right) = -0.17 \cdot \left(\log \kappa\right)^{1.82} + 2.573 \quad \text{for } Gr_w = 8 \times 10^8 \text{ and } A = 1 \tag{2.10}$$

where $\kappa = r_{outer}/r_{inner}$.

Except for the investigation by El-Shaarawi and Al-Nimr (1990) the temperature difference in the Rayleigh number in the above equations is defined as the difference between the hot and the cold wall for uniform wall temperatures and as the difference in mean wall temperatures in case of uniform heat flux. In the investigation by El-Shaarawi and Al-Nimr (1990) the temperature difference is defined as the difference in the temperature at the heat transfer boundary and the fluid temperature at the entrance to the annulus.

2.2.2 Mixed convection heat transfer

The combination of forced and natural convection heat transfer in vertical annuli has also caused some attention during the years, even though it is rather complex to describe. Mixed convection is when the forced convection and the buoyancy effects of the fluid are of the same magnitude and is therefore often referred to as combined forced and natural convection. In case of mixed convection, the relative direction between the buoyancy force and the externally forced flow is important. In the case where the fluid is externally forced to flow in the same direction as the buoyancy force (heated upflow or cooled downflow), the mode of heat transfer is termed assisting or aiding mixed convection. In the case where the fluid is externally forced to flow in the opposite direction to the buoyancy force (heated downflow or cooled upflow), the mode of heat transfer is termed opposing mixed convection (Gebhart et al. 1988).

El-Shaarawi and Sarhan (1980) used numerical simulations to analyse developing flow in a vertical annulus with the inner wall isothermal and outer wall insulated, for Gr/Re values ranging from –700 to 1500, and with air as fluid medium. The Grashof number and the Reynolds number were both based on the hydraulic diameter, with the characteristic temperature equal to the difference between the inlet and the isothermal wall temperatures. When the radius ratio was 0.9 it was shown that the heat transfer increased for aiding flow due to the reduction in thickness of the developing boundary layer, and vice versa for opposing flow. The results also showed that as the flow developed, the local Nusselt number converged to a value very close to that expected for fully developed forced flow between parallel plates (Nu = 4.86 (Kays and Crawford, 1993)) with one of the plates having a constant temperature, and the outer adiabatic, regardless of the value of Gr/Re.

Zenen et al. (1985) performed a numerical study of mixed convection in a vertical annulus with the inner wall insulated and the outer wall either isothermal or with a temperature varying with height. This study is one of the only ones that consider a varying wall temperature with height, even though in real situations wall temperatures are rarely isothermal. A local Nusselt number correlation was proposed:

$$Nu_w = f(Gz) \cdot g(Str) \cdot \left(\frac{\mu_{inlet}}{\mu_{wm}} \right)^{0.116} \cdot Gr_w^{\ a} \qquad (2.11)$$

where Gz is the Graetz number ($Re \cdot Pr \cdot z/(2 \cdot w)$), z is the distance from the bottom of the annulus, g(Str) is a function of the wall temperature distribution, which increases with the temperature gradient, Gr_w is the Grashof number based on the width of the annulus and on the difference between the mean wall temperature and the inlet temperature, and 'a' is a constant. The effect of the temperature dependent dynamic viscosity, μ, was taken into account by the ratio of the viscosity at the inlet, μ_{inlet}, and the mean wall temperature, μ_{wm}. The constants in the correlation were presented only for heating water when the flow was from the bottom, and the inlet temperature was less than the mean wall temperature. Other boundary conditions more relevant to mantle heat exchangers were discussed but a correlation was not given.

Iannello et al. (1988a) presented analytical solutions for fully developed vertical laminar mixed convection flows within annular and conventional rod bundle subchannel geometries. Mixed convection Nusselt number correlations (based on double annular spacing) for vertical annulus with inner cylinder heated and for aiding flow were given:

$$\ln\left(Nu_{2w}\right) = g_i \cdot \ln\left(1 + Gr_{2w}/Re_{2w}\right) \quad \text{for} \quad Gr_{2w}/Re_{2w} < 10^4 \tag{2.12}$$

where the values of g_i are presented in Table 3-14 through Table 3-17 in Iannello et al. (1988b) for α = {0.1, 0.3, 0.5, 0.7, 0.9}. α is the inner-to-outer radius ratio of the annulus (r_{inner}/r_{outer}).

El-Genk and Rao (1989) presented heat transfer data and correlations for hydrodynamically developed but thermally developing buoyancy-assisted and –opposed flows of water in vertical annuli at low Reynolds number ($Re < 10^4$). Among other things they gave data for mixed laminar flow by superimposing correlations developed for forced laminar flow and natural laminar flow on the form: $Nu_L = (Nu_{F,L}^3 + Nu_{N,L}^3)^{1/3}$, this method was first proposed by Churchill (1977) with the equation: $Nu_L = (Nu_{F,L}^c + Nu_{N,L}^c)^{1/c}$, where c is a constant. The same authors (El-Genk and Rao, 1990) used dye-injections and temperature-tracing techniques to investigate buoyancy-induced instability of developing laminar upflow and downflow of water in a vertical annulus having a diameter ratio of 2.0. The inner wall of the annulus was uniformly heated and the outer wall was insulated. They gave average Nusselt number correlations for buoyancy-assisted upflow and for buoyancy-opposed downflow:

Upflow:
$$Nu_w = 0.088 \cdot Ra_w^{0.33} \cdot Re_{inlet}^{-0.12} \quad \text{for } 500 \le Re_{inlet} \le 1700 \text{ and } 1.5 \cdot 10^6 \le Gr_w \le 5 \cdot 10^7 \tag{2.13}$$

Downflow:
$$Nu_w = 0.21 \cdot Ra_w^{0.29} \cdot Re_{inlet}^{-0.12} \quad \text{for } 125 \le Re_{inlet} \le 1200 \text{ and } 1.5 \cdot 10^5 \le Gr_w \le 2 \cdot 10^7 \tag{2.14}$$

A vertical mantle or a vertical annulus can, as an approximation, be unwrapped to form a vertical channel or vertical duct. Lin et al. (1991) performed a numerical study of laminar mixed convection in a vertical flat duct for initially developed flow between two flat plates after application of different heat fluxes to outer surface of each wall. It was found that aiding processes increased the Nusselt number while opposing processes

decreased the Nusselt number. Correlations were given for steady state aiding and opposing flows in terms of the Grashof and Reynolds numbers:

For buoyancy aiding flow

$$\frac{Nu_w}{Nu_{forced}} = \left(e^{-2X} + 0.0184 \cdot \left(\frac{Gr_w}{Re_w} \right)^{0.7463} \cdot Z^{0.5} \cdot \gamma_H^{-0.165} \right)^{1/3} \quad (2.15)$$

For buoyancy opposing flow

$$\frac{Nu_w}{Nu_{forced}} = \left(1 - 0.0012 \cdot \left(\frac{Gr_w}{Re_w} \right)^{1.2272} \cdot Z^{0.5} \cdot \gamma_H^{-0.6126} \right)^{1/3} \quad (2.16)$$

where $\gamma_H = q_1/q_2$, q_1 and q_2 are the heat flux at wall #1 and wall #2, respectively. Z is the dimensionless axial coordinate, $Z = Re_w \cdot z/w$, z is the axial distance from the inlet and w is the duct spacing. Both equations are for $Gr_w/Re_w < 1000$. Nu_{forced} is the steady local Nusselt number for pure forced convection flow, which can be calculated from the equations proposed by Shah and London (1978). These equations are given below:

$$Nu_{forced} = \begin{cases} 0.745 \cdot \xi^{-1/3} & \text{for } \xi \le 0.0002 \\ 0.745 \cdot \xi^{-1/3} - 0.2 & \text{for } 0.0002 < \xi \le 0.001 \\ 4.114 + 4.34 \cdot \left(10^3 \cdot \xi\right)^{-0.506} \cdot e^{-164\xi} & \text{for } \xi > 0.001 \end{cases} \quad (2.17)$$

where $\xi = (z/2) \cdot w \cdot Pe = (z/2) \cdot w \cdot Re \cdot Pr$.

Tsay (1994) presented a numerical study of unsteady mixed convective heat transfer in a vertical annular passage resulting from a step change in uniform wall heat flux of the inner core tube. The outer wall was kept adiabatic for the numerical study. It was found that the wall-to-fluid thermal conductivity ratio had much larger effects on the heat transfer than the ratio Gr/Re.

Thermal conductivity ratio: $K_{wf} = k_w/k_f$ (2.18)

where k is the thermal conductivity and the subscripts w and f stand for wall and fluid respectively.
For lower K_{wf} the local Nusselt number increases. This is a rather significant result as it means that the properties of the tank wall in a mantle heat exchanger may be significant in determining the heat transfer in the mantle.

2.2.3 Summary of heat transfer in vertical annuli

In this section some of the most important contributions to the description of convective heat transfer in vertical annuli were listed. Common to all the references was that the boundary conditions were very strict, because the heat transfer correlations were based on different combinations of the following boundary conditions that are commonly used

in heat transfer theory: uniform temperature, uniform heat flux and adiabatic wall. Unfortunately, these boundary conditions are non-realistic for mantle heat exchangers. The walls in a mantle heat exchanger are non-adiabatic, and the conditions in the mantle and inner tank are transient so uniform wall temperature or uniform heat flux will only occur in very rare cases and in a very short period of time. Therefore, the referenced heat transfer correlations for vertical annuli are not appropriate for calculating the heat transfer in mantle heat exchangers.

Furthermore, it can be noted that none of the correlations for mixed convective heat transfer in vertical annuli referenced in this section are based on the relationship between Ra/Re^2 or Gr/Re^2, which are the typical ways of describing mixed convective heat transfer according to a number of heat transfer text books (i.e. Arpaci and Larsen (1984), Gebhart et al. (1988), Mills (1992)).

2.3 Heat transfer in mantle heat exchangers

In this section previous studies of the heat transfer in mantle heat exchangers will be given. For completeness, studies of both vertical and horizontal mantle heat exchangers are included. Furthermore, studies of the heat transfer at the tank side of vertical storage tanks will be presented.

2.3.1 Heat transfer in vertical mantle heat exchangers

The question, when modelling the heat transfer in mantle heat exchangers, is whether the heat transfer is dominated by forced convection (circulation pump), by natural convection (temperature difference between mantle fluid and tank wall) or it is a combination of the two types of convection.

Baur et al. (1993) assumed that the heat transfer between the mantle fluid and the domestic water could be estimated by using the empirical heat transfer correlation for laminar forced flow in the entrance region between two parallel plates developed by Mercer et al. (1967):

$$Nu_{2w}(z) = 4.9 + \frac{0.0606 \cdot \left(Re_{2w} \cdot Pr \cdot \frac{2 \cdot w}{z} \right)^{1.2}}{1 + 0.0909 \cdot \left(Re_{2w} \cdot Pr \cdot \frac{2 \cdot w}{z} \right)^{0.7} \cdot Pr^{0.1}} \qquad (2.19)$$

where z is the distance from bottom of the mantle, w is the mantle gap, and thus $2 \cdot w$ is the hydraulic diameter of the annulus. The Nusselt number in equation 2.19 is the average Nusselt number from location zero to location z. The local Nusselt number at node number 'i' is obtained from:

$$Nu_i = \frac{Nu(z_i) \cdot z_i - Nu(z_{i-1}) \cdot z_{i-1}}{z_i - z_{i-1}} \qquad (2.20)$$

Baur's simulation results were compared with experimental data reported by Furbo and Berg (1990). With the mantle inlet located at the top of the mantle Baur found that a corraction factor of 1.8 had to be applied to equation 2.19 in order to obtain a match between the measured and simulated heat transfer. This model proposed by Baur has been implemented in the TRNSYS simulation package (Klein et al., 1996).

Shah and Furbo (1998) evaluated annular heat transfer in vertical mantle heat exchangers using numerical simulation of the flows in the mantle and inside the storage tank. In their case, the fluid in the annular gap was warmer than both walls, which results in heat transfer directions from the fluid to both walls (useful heat transfer to inner wall and heat loss from outer wall) instead of from one wall to another. They developed a local Nusselt number correlation in terms of the Rayleigh number, and thus based on free convection only

$$Nu_z = 0.46 \cdot \left(Ra_z \cdot \frac{z}{2 \cdot w} \right)^{0.28} \quad \text{for } w = 0.0335\,\text{m and } Ra_z \leq 10^{11} \qquad (2.21)$$

where z is the distance from the top of the annulus and is defined as the length scale. The local temperature difference between the mantle fluid and the tank wall is used as the characteristic in the local Rayleigh number.

Shah et al. (1999) used PIV and CFD to investigate the flow structure in the mantle and CFD to investigate the heat flux distribution over the mantle surface. The investigations were carried out with a mantle heat exchanger with a top inlet. They showed that for a high inlet temperature into the mantle there is a re-circulating buoyancy-driven flow in the top 20% of the mantle. With a low inlet temperature the inlet stream drops down immediately as it enters the mantle and passes along the bottom section of the mantle. This stream induces a large re-circulation zone in the top two-thirds of the mantle volume. It was concluded that both the experimental and simulation results indicate that distribution of the flow around the mantle is governed by buoyancy-driven recirculation in the mantle.

Shah (1999 and 2000) continued the 'buoyant approach' and developed a new local Nu-Ra correlation based on numerical simulation:

$$Nu_z = 0.28 \cdot \left(\frac{w}{r_i} \right)^{-0.63} \cdot \left(Ra_z \cdot \frac{z}{H} \right)^{0.28} \quad \text{for } Ra_z < 10^{10} \qquad (2.22)$$

where H is the height of the mantle and r_i is the outer radius of the inner wall of the mantle.

Equation 2.22 is valid for a wider range of geometric designs of the mantle tank than equation 2.21. Equations 2.21 and 2.22 are only valid for mantle heat exchangers with mantle inlet located at the top. The Nusselt number showed to be almost independent of the mantle flow rate, so equation 2.22 does not include a Reynolds number. Shah (1999) compared heat fluxes calculated by use of the correlation in equation 2.22 with heat fluxes calculated by using CFD, and it was found that in many cases the correlation

behaved as expected by the CFD-simulations. However, some significant differences occurred for different mantle gaps, different height diameter ratios and for increasing mantle flow rates (Shah, 1999). These inaccuracies may indicate that the heat transfer in the mantle might be of mixed convection, and thus the Nusselt number is a function of both the Rayleigh number and the Reynolds number. Especially the inaccuracies for the increasing mantle flow rate are an indication of this.

2.3.2 Heat transfer in horizontal mantle heat exchangers

Horizontal mantle heat exchangers are widely used in thermosyphon SDHW systems in Australia and Southern Europe. The flow structure and the heat transfer in the annular passageway in horizontal mantle heat exchangers have been investigated by Morrison et al. (1998, 1999) by using dye injection as flow visualisation and CFD-modelling. The flow structure was investigated for both mixed and stratified inner tank conditions and with the mantle inlet port at the bottom of the mantle. The flow structure depends on the temperature of the inlet flow relative to the thermal stratification in the inner tank, and mantle flow only rises to its thermal equilibrium level. The majority of the heat transfer showed to occur in the bottom section of the mantle rather than near the thermal equilibrium level between the inlet fluid temperature and the fluid inside the tank.

The inlet port to the mantle in horizontal mantle heat exchangers is normally located at the bottom of the mantle to avoid reverse circulation at night in the thermosyphon loop (Rosengarten et al., 1999). As a result of Morrison's findings that the bottom inlet does not provide thermal stratification, Rosengarten (2000) investigated different configurations of the mantle inlet to a horizontal mantle heat exchanger. The results were compared with the traditionally used bottom inlet with the flow direction perpendicular to the tank wall. With a side inlet at the bottom the flow moved straight towards the outlet instead of spreading out over the tank wall. The heat transfer rate was approximately 10-15% lower than with the perpendicular inlet and this is mainly due to the absence of the impinging jet region. The top inlet configuration was found to be an advantage with high inlet temperatures because the hot inlet fluid does not have to traverse the bottom region of the mantle so there is a higher heat flux in the top of the mantle. On the other hand, with inlet temperatures lower than the top tank temperatures heat was removed from the top part of the tank.

Rosengarten et al. (2001) showed that the effect of curvature on mixed convection flows and heat transfer in narrow annuli was negligible. Thus, instead of a horizontal mantle heat exchanger a rectangular cavity was used to investigate the flow structure and heat transfer in the annular passageway by using PIV and CFD. One of the walls in the cavity was adiabatic and the other wall was a heat-transfer wall with different temperature boundary conditions (isothermal and different variations where the temperature was varying with cavity height). It was found that the local heat flux (and local Nusselt number) was depending on both forced and natural convection and the heat flux was therefore in the mixed convection regime. No local Nusselt number correlation was developed. Instead, a mean Nusselt number correlation, using the difference between the inlet temperature and mean heat-transfer wall temperature and taking a stratification correction parameter into account, was developed:

$$Nu_w = Re_w \cdot Pr \cdot St \cdot \frac{w}{L} \cdot \left(1\text{-}\exp\left(\frac{-1}{Re_w \cdot Pr} \cdot \frac{363 \cdot L}{k}\right)\right) \quad (2.23)$$

where L is the length of the cavity, k is the thermal conductivity of the mantle fluid and St is the stratification correction parameter (depends on Reynolds number and stratification efficiency).

2.3.3 Heat transfer inside the storage

Inside the storage tank in vertical mantle storage tanks the flow and heat transfer are, when draw-offs are not considered, governed by natural convection.

Shah (1999, 2000) developed a local Nu-Ra correlation for the heat transfer from the tank wall to the domestic water:

$$Nu_z = \left(4.501 - \frac{3.103 \cdot D}{H}\right) \cdot \left(Ra_z \cdot \frac{z}{H}\right)^{0.19} \quad \text{for } Ra_z < 10^{11} \quad (2.24)$$

where z is the distance from the bottom of the tank, D is the diameter and H is the height. Shah (1999) compared heat fluxes calculated by use of the correlation in equation 2.24 with heat fluxes calculated by using CFD, and found that in many cases the correlation behaved as expected by the CFD-simulations. However, the heat fluxes calculated by the correlation did not perfectly match the shape of the heat fluxes predicted by CFD, and especially two tendencies should be mentioned. When the heat transfer occurs at the upper mantle level, the heat fluxes calculated by the correlation are too high at a level below the main heat transfer area. When the heat transfer occurs at the lower mantle level, the heat fluxes calculated by the correlation are too high.

Oliveski et al. (2003) made a numerical and an experimental analysis of the heat loss from a vertical storage tank submitted to natural convection. Two mean Nusselt number correlations, for volumes of 0.1 m³ and 0.2 m³, respectively, were presented:

$$Nu \cdot \left(\frac{H}{D}\right)^{-0.3}_{V=0.1} = \left(9.40739 \cdot U'^{0.288329}\right) \cdot \left(1000 \cdot \left(\overline{T}\text{-}T_{amb}\right)^{-1} \text{-}20\right)^{(0.00988842 \cdot U' - 0.189428)} \quad (2.25)$$

$$Nu \cdot \left(\frac{H}{D}\right)^{-0.3}_{V=0.2} = \left(10.6039 \cdot U'^{0.310719}\right) \cdot \left(1000 \cdot \left(\overline{T}\text{-}T_{amb}\right)^{-1} \text{-}20\right)^{(0.013052 \cdot U' - 0.224677)} \quad (2.26)$$

where $\overline{T}$ is the average fluid temperature and U' is the global heat transfer coefficient defined as:

$$U' = \frac{1}{\frac{e}{k} + \frac{1}{h_{ext}}} \tag{2.27}$$

where e is the insulation thickness, k is the thermal conductivity of the insulation material and h_{ext} is external convection of the tank.

Equations 2.25 and 2.26 are valid for height/diameter ratios between 1 and 2.5, and they are limited to predict the heat loss and therefore they cannot be used to predict the heat transfer from the mantle fluid. Equation 2.24 developed by Shah (1999, 2000) can be used both to predict the heat loss and to predict the heat transfer from the mantle fluid.

2.4 Summary

A literature survey of the types of heat transfer that occur in mantle heat exchangers was given in this chapter. First general studies of natural and mixed convection heat transfer in vertical annuli were presented. Common for the presented studies was that the boundary conditions were very strict and, unfortunately, these boundary conditions are non-realistic for mantle heat exchangers.

Previous studies of the heat transfer in vertical and horizontal mantle heat exchangers were also presented. The investigations of the heat transfer in horizontal mantle heat exchangers showed that the local heat transfer was in the mixed convection regime, but a local Nusselt number correlation was not given. Instead, a mean Nusselt number correlation, where the Nusselt number was a function of the Reynolds number, was developed (Rosengarten et al., 2001). The presented studies of the heat transfer in vertical mantle heat exchangers indicated that the buoyancy forces are dominating the flow and heat transfer in the mantle, and therefore a local Nu-Ra correlation was developed (Shah, 1999 and 2000). However, when heat fluxes calculated by use of the correlation were compared to heat fluxes calculated by use of CFD, some differences occurred for increasing mantle flow rates, different mantle gaps and different height diameter ratios (Shah, 1999). Theses inaccuracies may indicate that the heat transfer in the mantle is in mixed convection regime. Therefore, one of the goals in this thesis is, based on the findings by Shah and Rosengarten, to develop a mixed convection local Nusselt number correlation for the heat transfer in the mantle.

Finally, previous studies of the natural convection heat transfer on the tank side of the mantle heat exchanger were presented.

3. Experimental and numerical techniques

3.1 Introduction

In this chapter the methods used to obtain all the data presented in this thesis are explained. Three different experimental techniques are used; which are transient thermal measurements in a heat storage test facility, system tests in a side-by-side laboratory test facility, and flow visualisation by means of particle image velocimetry (PIV). The rest of the data were obtained from numerical simulations using a commercial computational fluid dynamics (CFD) code and by using the solar simulation program MantlSim to simulate the yearly thermal performance of SDHW systems.

3.2 Thermal experiments in a heat storage test facility

Prototypes of vertical mantle heat exchangers were tested in a heat storage test facility. In the heat storage test facility it was possible to control the flow rate in the mantle and the mantle inlet temperature in a closed loop to simulate the solar loop. Water was used as mantle fluid and the mantle fluid was heated by electric heating elements. During the experiments the following parameters were measured: the mantle flow rate, the mantle inlet temperature, the mantle outlet temperature, the temperature of the domestic water in the inner tank at seven points inside the tank, the temperature at five points on the outside of the mantle wall (where the temperature is close to the temperature of the fluid inside the mantle), and the ambient temperature.

Figure 3-1: Experimental set-up in the heat storage test facility.

The temperatures were measured by means of copper/constantan thermocouples (Type TT). The differences of temperatures at the mantle inlet and the mantle outlet were measured by means of thermopiles (copper/constantan), each with 5 thermocouples. Hereby a better measuring accuracy was obtained. The temperature measuring in the

inner tank was carried out with copper/constantan thermocouples placed in a glass tube that is placed in the tank through the bottom. The measuring accuracy of the thermocouples is estimated at about ± 0.5 K and for the thermopiles about ± 0.03 K (Ellehauge, 1993). The mantle flow rate was measured by an Aqua Metro (Type VZTH 8-G) flow meter. By the manufacturer the volume flow rate measuring accuracy is estimated at about ± 2.5% at a volume flow rate of 0.5 l/min. The data logging is controlled on PC (using the software: IMPVIEW) using two Schlumberger IMP measuring cards (Type 35951C and Type 35952A). Figure 3-1 shows the experimental set-up in the heat storage test facility. A more detailed description of the test facility can be found in (Furbo, 1984).

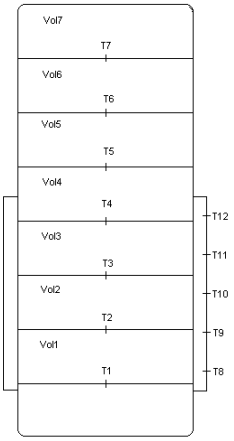

Figure 3-2: Thermal measuring points.

Figure 3-2 shows the measuring points for the temperature measurements inside the inner tank and on the outside of the mantle wall. The temperature on the outside of the mantle wall was measured half-way between the mantle inlet and the mantle outlet.

The tests of the heat storages were carried out for two different initial conditions of the temperatures inside the storage. The initial conditions were that the tank was either mixed at around 20ºC or stratified with temperatures at 20ºC in the bottom and 55ºC in the top. The initial stratification was created in the following way. All the water in the inner tank was overnight heated to 55ºC by having an inlet temperature of 60ºC to the mantle, and then approximately half of the volume of the inner tank was changed with cold water. The cold water was entering at the bottom with a flow rate of 1 l/min and the hot water was leaving from the top with the same flow rate. Stable conditions were reached in the tank approximately 1 hour after the draw-off and the experiments were ready to begin.

The tests were carried out with a heating period with a high mantle inlet temperature of 70ºC as a start. The heating period was followed by a period where the system was resting. When a stable condition in the heat storage was reached, the test was conducted with a period where the mantle inlet temperature was lower than the temperature in the top of the mantle. This test is similar to a day with heavy overcast in the morning, sunshine at noon and then heavy overcast before some sunshine in the late afternoon. The inlet temperature to the mantle in the last period of the test was different from test to test due to the different temperature levels in the heat storage during the tests. The mantle inlet temperature in the last period of the tests was at the same level as the temperature in the middle of the mantle.

3.3 Side-by-side laboratory test

Two systems with different mantle inlet position were tested side-by-side under realistic conditions in a test facility for SDHW systems in a period of 8 months. The test facility

is built at the test area of Department of Civil Engineering. The test facility consists of a rack for the mounting of solar collectors and a hall in which the storage tanks and measuring tools are placed. The rack with solar collectors is shown in Figure 3-3.

Figure 3-3: The SDHW test facility. A building with heat storages and control systems is located behind the rack.

The tanks were placed inside the hall, which is located behind the rack (Figure 3-3). Each tank was placed in a box with inlet and outlet for domestic water. Electric heating elements were used as auxiliary heating for the tanks. The tapping and auxiliary heating were computer controlled. The solar collectors were mounted on the rack (Figure 3-3). The rack is tilted 45º from horizontal and facing south. The length of the tubes from the rack to the hall was about 13-15 m (each way). Of this about 10-12 m were outside.

The temperatures were measured by means of copper/constantan thermocouples (Type TT). The differences of temperatures in the solar collector loop and drawing loop were measured by means of thermopiles (copper/constantan), each with 5 thermocouples. Hereby a better measuring accuracy was obtained. The temperature measuring in the inner tank was carried out with copper/constantan thermocouples placed in a glass tube that is placed in the tank through the bottom. Thermocouples and thermopiles have been connected to the data logger system that is placed in a separate office in the building. The voltage of thermocouples was measured in 5 Fluke Hydra data loggers. The measuring accuracy of the thermocouples was estimated at about ± 0.5 K and for the thermopiles about ± 0.03 K (Ellehauge, 1993).

The flow in the solar collector loop and drawing loop was measured using a Clorius Combimeter 1.5 EPD energy and flow meter. The meters emitted pulses that were counted by the data logger system. In the drawing loops the meters emitted 1 pulse for

each 0.1 litre. In the solar collector loops the meters emitted 1 pulse for each litre. The flow meters have an accuracy of ± 2-3% (Ellehauge, 1993).

The energy quantities were formed in the data logger system from the flow measurements, the differences of temperatures over the respective thermopiles and from functions of thermal capacity and density of the fluid. The thermal capacity and the density of the solar collector fluid are dependent on the glycol percentage and the temperature. Measurements from the thermopiles and flow measurements form part of the energy calculations. The largest uncertainties with regard to the energy calculations are errors of measurement as a result of the thermal capacity of the sensor tubes, the thermal conduction to the surroundings and the time step between each scanning (20 sec.). The energy quantities are, however, expected to balance within about 5% (Ellehauge, 1993).

Total and diffuse solar radiation on the solar collector rack were measured on the plane of the solar collectors (45º tilt, south). The solar radiation was measured with Kipp & Zonen solarimeters Type CM5. The diffuse solar radiation was measured by means of a solarimeter with a shadow ring with a diameter of 45 cm and a width of 7 cm. The solarimeters have an accuracy of ± 2-3% (Ellehauge, 1993).

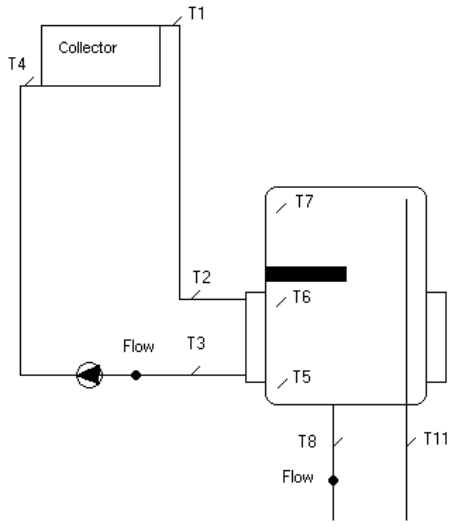

Figure 3-4: System sketch with measuring points.

Figure 3-4 shows a system sketch that illustrates the principles and measuring points of both the tested systems.

The solar heating systems were tested with 3 draw-offs per day at 7:00, 12:00 and 19:00. The drawing off was made in three equal energy quantities, corresponding to a total of 100 l/day heated from 10ºC to 50ºC = 4.575 kWh/day. The temperatures at the top of the storage tanks were kept at 50.5ºC by means of an electric heating element. As surroundings, draw-off times and the thermostat set point for the storage temperature at the top of the tanks were identical for both systems, these were tested under identical conditions.

3.4 Flow visualisation

The flow visualisation experiments were carried out at School of Mechanical and Manufacturing Engineering, University of New South Wales, Sydney, Australia. The experimental set-up for the flow visualisation experiments consisted of two parts: the heat storage control facility and the Particle Image Velocimetry system.

3.4.1 Heat storage control facility

A vertical mantle heat exchanger was constructed of glass for flow visualisation and velocity measurements with an optical PIV system. To allow the velocity measurements in the narrow mantle gap the glass model mantle tank was constructed as a square tank. The glass model tank is like a standard vertical mantle heat exchanger used in Denmark for small low-flow SDHW systems. The mantle and the inner tank volume, as well as the ratio between the solar volume and the volume above the mantle, are similar to commercial solar water heater tanks used in Denmark. Figure 3-5 shows a photograph of the glass model tank. The glass model tank was un-insulated during the experiments.

Figure 3-5: Glass model of the mantle tank.

During the experiments the mantle was supplied with a constant inlet temperature and flow rate. To obtain heat transfer data for the mantle the following variables were measured: Mantle inlet temperature, mantle outlet temperature, volume flow rate in the mantle, temperatures in the inner tank (T1-T5) and ambient temperature. Figure 3-6 shows the measuring points in the glass model tank.

Temperatures were measured using copper/constantan thermocouples Type TT. The thermocouples were placed directly in the fluid in order to get fast reaction time. A data logger (Model 328121 Hybrid Recorder, Yokogawa Electric Corporation) was used to control the data sampling and the temperatures were stored on a PC. The mantle flow rate was measured by a turbine flow meter (Farnell Electronics) and logged manually from a frequency counter (HP 5315A Universal Counter).

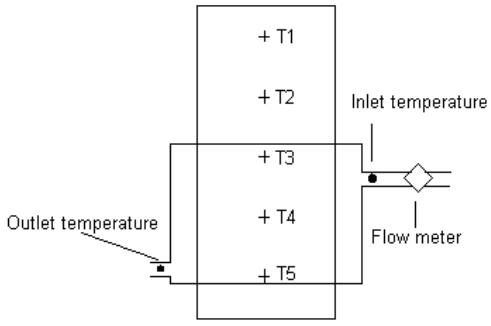

Figure 3-6: Measuring points in the heat storage test facility.

The measuring accuracy of the thermocouples was estimated at about ± 0.5 K. The mantle flow rate was measured by reading the time for one round of the turbine flow meter. The reading of the time for one round of the turbine flow meter was inverted into a frequency and the frequency was then recalculated into a volume flow rate [l/min]. Figure 3-7 shows the flow meter calibration curve valid for fluid temperatures between 30ºC and 50ºC. The inaccuracies were below 4%.

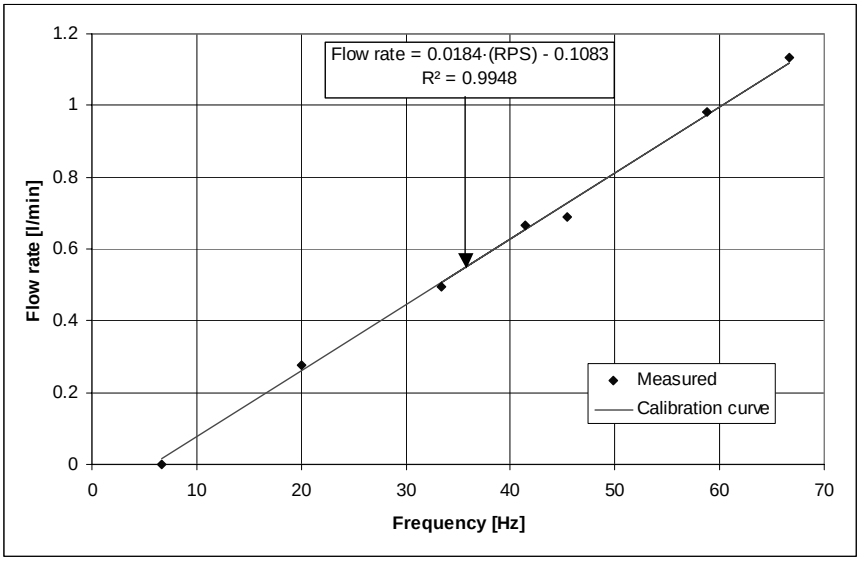

Figure 3-7: Flow meter calibration curve valid for temperatures between 30ºC and 50ºC.

Like the thermal experiments described in section 3.2, the PIV tests of the heat storages were carried out for two different initial conditions of the temperatures inside the storage. The initial conditions were that the tank was either mixed at around 20ºC or stratified with temperatures at 20ºC in the bottom and 40ºC in the top. The initial stratification was created in the following way. First, about 75 litres of water at a temperature of 40ºC were delivered to the empty tank and then the rest of the tank was filled with cold water entering slowly at the bottom of the tank. The cold water had a temperature of approximately 20ºC.

Three heating situations were studied; Case 1 is for an initially mixed inner tank (~20ºC) with the mantle supplied with a constant flow rate of 0.45 l/min and an inlet temperature of 50ºC. Case 2 is for an initially stratified inner tank (20ºC at the bottom and 40ºC at the top) with the mantle supplied with a constant flow rate 0.45 l/min and an inlet temperature of 50ºC. Case 3 is for an initially stratified inner tank (20ºC at the bottom and 40ºC at the top) with the mantle supplied with a constant flow rate of 0.45 l/min and an inlet temperature of 35ºC. The three cases correspond to typical operation conditions for a vertical mantle heat exchanger in a low-flow SDHW system. The three cases are quite similar to the thermal experiments described in section 3.2. However, the difference is that the maximum thermal difference over the glass plates was limited to 30 K to avoid thermal stress of the glass and therefore the initial temperatures at the top of the tank had a lower value.

3.4.2 Particle Image Velocimetry system

Particle Image Velocimetry is a non-intrusive optical measurement technique that enables the mapping of instantaneous velocity distributions within planar cross-sections of a flow field. The basic principle of PIV is to determine fluid flow velocity indirectly by analysing the motion of seed particles in the flow. Small neutral density particles were used, so the velocity of each seed particle could be considered to be the same as the fluid velocity. The PIV system is based on continuous recording of the position of particles in a slice of the flow illuminated with laser light sheet using a digital CCD (Charge Couple Device) camera.

A PIV system from ILA Intelligent Laser Applications GmbH, was used in these tests. The PIV system consisted of a double-cavity Nd:YAG 120 mJ laser with a wavelength of 532 nm, a 12 bit cooled imaging SensiCam (CCD camera) with a 35 mm focal length lens, a synchronizer and a processor. The synchronizer is the timing unit for the whole PIV system, coordinating the laser flash lamps and Q-switches as well as the image capture by the camera. The recorded data were processed by the VidPIV 3.0 program from Optical Flow Systems (Optical Flow systems, 1999).

Double-frame images of particles in the flow can be captured by the CCD camera at a rate of 4 exposures per second. The required separation time between the two laser pulses depends on the fluid velocity to be measured. If the velocities are high, a short time interval between the two lasers is needed, and if the velocities are small, a longer time interval is needed. A laser pulse separation of 12 ms at a frequency of 4 Hz was used for the current experiments. The displacement of particles in the flow between laser pulses is analysed to determine the velocity field over the section of flow in view of the camera. Water in the vertical mantle heat exchanger was seeded with Polyamid Seeding Particles (PSP-5) with a diameter of 5 μm to provide illuminated points for the optical flow measurement.

The camera had a resolution of 1280 x 1024 pixels. In order to get sufficient resolution with the PIV system, the mantle and the inner tank were divided into smaller sections, and images of particle tracks from each section were assembled to get the full flow field in the area of interest. The half of the mantle was divided into 12 sections (Figure 3-8) and the flow was measured in the centre plane of the mantle gap. In the inner tank the fluid velocity was measured above the mantle near the tank walls in a plane 2.5 cm from the centre plane through the inlet and outlet to and from the mantle. The measurement area in the inner tank was divided into 6 sections (Figure 3-9). Figure 3-10 shows a particle image near the mantle inlet captured by the CCD camera. The CCD camera was damaged in the right side, so the part of the image that is right to the vertical white line in Figure 3-10 could not be used.

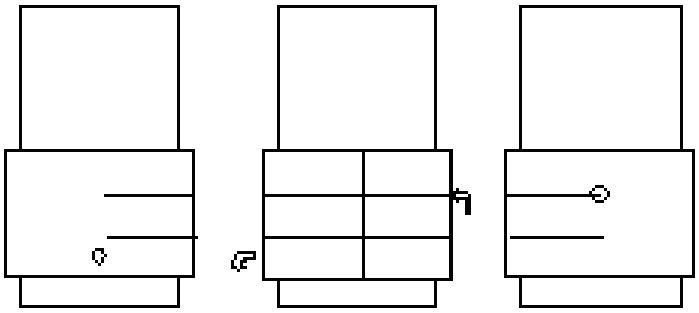

Figure 3-8: The mantle was divided into 12 sections.

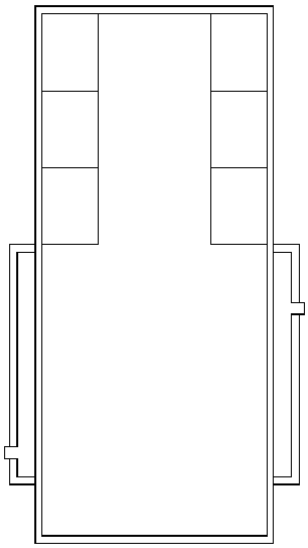

Figure 3-9: The measurement area in the inner tank was divided into 6 sections.

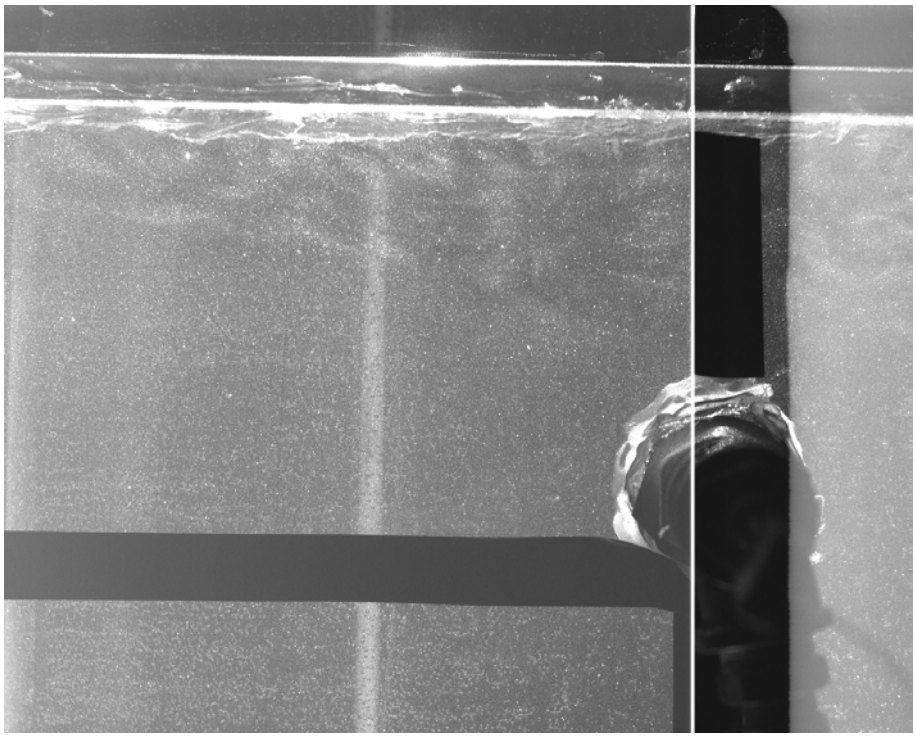

Figure 3-10: A particle image near the mantle inlet captured by the CCD camera.

The distance from the camera to the measurement plane depended on the area of the measurement plane; the distance was varying between 800-1200 mm. When the cross-correlation analysis of the particle image positions was applied, the flow domain was divided into smaller sub-areas, typically 32x32 pixels in size; the flow field was averaged over 30 pairs of images. Figure 3-11 shows the PIV set-up and Figure 3-12 illustrates the steps involved in PIV measurements.

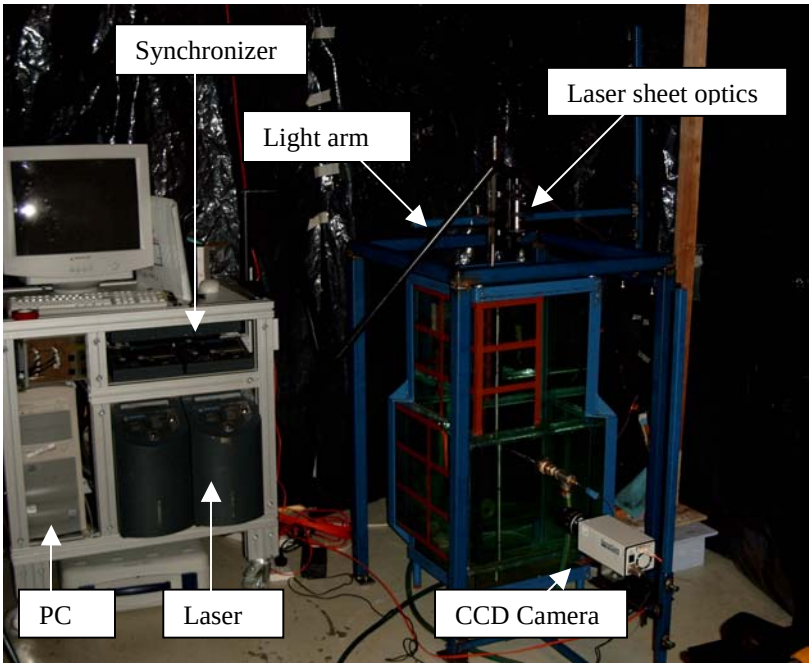

Figure 3-11: The PIV set-up and the glass model tank.

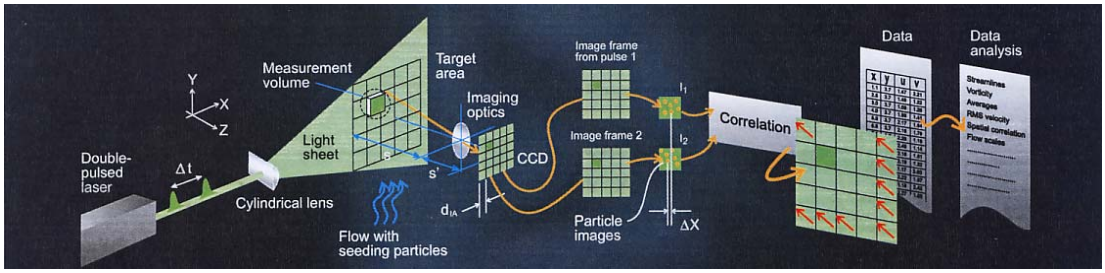

Figure 3-12: Steps involved in PIV measurements (graph: Dantec Dynamics).

The accuracy of the measurements is influenced by the inadequacy of the statistical method for cross-correlation and the measurement uncertainty induced by background noise of the CCD recording, particle diffraction patterns, lens aberrations, the density gap between particles and fluid, the number of particles within the volume of interest, etc. (Raffel et al., 1998). It is guaranteed from ILA that the PIV system is capable of measuring velocities from below 1 mm/s up to transonic (ILA, 2002).

3.5 Computational Fluid Dynamics

The commercial computational fluid dynamics code FLUENT 6.0 (FLUENT, 2001) was used for the theoretical investigations of the convective heat transfer and the flow structures in the mantle heat exchangers.

Computational Fluid Dynamics (CFD) is the science of predicting fluid flow, heat transfer and related phenomena by solving mathematical equations that represent physical laws, using a numerical process. The solution is through space or time and the goal is to obtain a numerical description of the complex flow field of interest. CFD models are used, because in many cases it is possible to obtain more detailed information about flow structure and heat transfer than by experimental investigations. Furthermore, results can often be obtained more cost effective and faster than by experiments.

The following sections summarise the basic theory behind CFD and describe the solution algorithms used in this project; the descriptions follow very much the description in FLUENT (2001).

3.5.1 Governing equations

The governing equations for laminar fluid flow and heat transfer are summarised in this section. They are called Navier-Stokes equations.

The basic set of equations necessary for solving laminar fluid flow and heat transfer includes the continuity equation, the momentum equation and the energy equation. The equations are given in tensor notation where x_i (i=1,2,3) or (x,y,z) are the Cartesian coordinates and u_i or (u_x, u_y, u_z) are the Cartesian components of the velocity vector $\boldsymbol{v}$. Repeated indices in a term of an equation imply summation of the term over the three

values of *k* (summation convention). The Kronecker delta is $\delta_{ij} = 0$, $i \neq j$, and $\delta_{ij} = 1$, $i = j$.

The continuity equation:

$$\frac{\partial \rho}{\partial t} + \frac{\partial}{\partial x_i}(\rho u_i) = 0 \tag{3.1}$$

The momentum equation:

$$\frac{\partial}{\partial t}(\rho u_i) + \frac{\partial}{\partial x_j}(\rho u_j u_i) = -\frac{\partial p}{\partial x_i} + \frac{\partial \tau_{ij}}{\partial x_j} + \rho g_i \tag{3.2}$$

where τ_{ij} is the stress tensor:

$$\tau_{ij} = \mu\left[\left(\frac{\partial u_i}{\partial x_j} + \frac{\partial u_j}{\partial x_i}\right) - \left(\frac{2}{3}\frac{\partial u_k}{\partial x_k}\right)\delta_{ij}\right] \tag{3.3}$$

The energy equation:

$$\frac{\partial}{\partial t}(\rho H) + \frac{\partial}{\partial x_i}(\rho u_i H) = \frac{\partial}{\partial x_j}\left(k\frac{\partial T}{\partial x_j}\right) + \frac{\partial p}{\partial t} \tag{3.4}$$

where

g_i	is the gravity, $g_i = (g_x, g_y, g_z)$, [m/s²]
H	is the total enthalpy, $H = h + \frac{1}{2}u_i^2$, [J/kg]
h	is the thermodynamic enthalpy, h = h(T,p), [J/kg]
k	is the thermal conductivity, [W/(m·K)]
p	is the pressure, [kg/(m·s²)]
T	is the temperature, [K]
t	is the time, [s]
u_i	is the fluid velocity, $u_i = (u,v,w)$, [m/s]
μ	is the dynamic viscosity, [kg/(m·s)]
ρ	is the density, [kg/m³]

3.5.2 Using the Boussinesq approximation

Natural convection plays an important role in the heat transfer and fluid flow in mantle heat exchangers. Simulations of natural convection flows often have convergence problems, as the buoyancy terms leads to the energy and momentum equations become highly coupled through the temperature dependent density. Instead of using temperature dependent density the Boussinesq approximation was applied in order to get faster convergence.

The Boussinesq approximation treats density as a constant value in all solved equations, except for the buoyancy term in the momentum equation (the last term in equation 3.2):

$$(\rho - \rho_0)\, g_i \approx -\rho_0 \beta (\mathrm{T}-\mathrm{T}_0)\, g_i \tag{3.5}$$

$$\Downarrow$$

$$\rho = \rho_0 \left(1 - \beta (\mathrm{T}-\mathrm{T}_0)\right) \tag{3.6}$$

where

T	is the actual temperature of the flow, [K]
T_0	is the operating temperature of the flow, [K]
β	is the thermal expansion coefficient, [1/K]
ρ	is the variable density, [kg/m³]
ρ_0	is the (constant) density at the operating temperature, T_0, [kg/m³]

Equation 3.6 can be used to eliminate ρ from the buoyancy term in the momentum equation. This approximation is accurate as long as the changes in actual density are small; specifically the Boussinesq approximation is valid when $\beta(T - T_0) << 1$.

3.5.3 Turbulence modelling

Turbulent flows are characterised by fluctuating velocity fields. These fluctuations mix transported quantities such as momentum and energy. Since these fluctuations can be of small scale and high frequency, they are too computationally expensive to simulate directly. Instead, the instantaneous (exact) governing equations can be time-averaged to remove the small scales, resulting in a modified set of equations that are computationally less expensive to solve. However, the modified equations contain additional unknown variables, and turbulence models are needed to determine these variables in terms of known quantities.

With Reynolds Averaging Method, the solution variables in the instantaneous (exact) Navier-Stokes equations are decomposed into a time-averaged value and a fluctuating component. The velocity component in the x-direction can be written as:

$$u = \bar{u} + u' \tag{3.7}$$

where

$$\bar{u} = \frac{1}{Time} \int_0^{Time} u\,dt \tag{3.8}$$

and

$$\overline{u'} = \frac{1}{\Delta t} \int_{t_0}^{t_0+\Delta t} u'\,dt \equiv 0 \tag{3.9}$$

Likewise for other parameters like velocity in y- and z-direction, pressure, temperature and enthalpy:

$$\phi = \bar{\phi} + \phi' \tag{3.10}$$

where ϕ denotes a parameter like *v*, *w*, p, T and H. Figure 3-13 shows the relationship between $u, \bar{u}$ and u'.

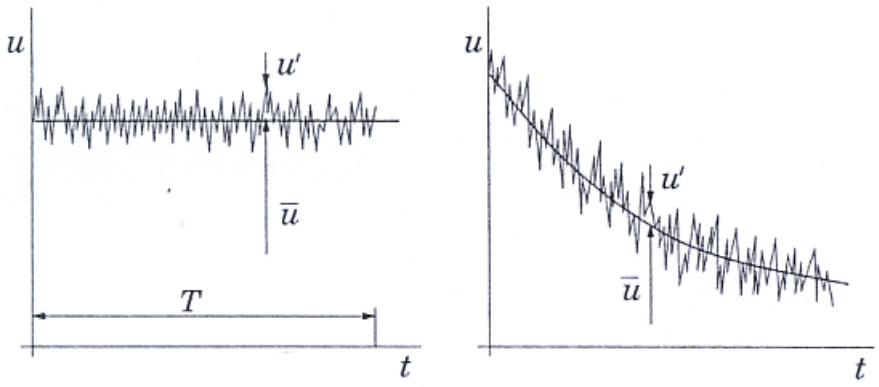

Figure 3-13: Relations between $u, \bar{u}$ and u' for steady flow (left) and unsteady flow (right).

The Reynolds averaged values can be substituted into the Navier-Stokes equations:
Continuity:

$$\frac{\partial \rho}{\partial \mathrm{t}} = \frac{\partial}{\partial x_i}\left(\rho \overline{u_i}\right) = 0 \tag{3.11}$$

Momentum:

$$\frac{\partial}{\partial \mathrm{t}}\left(\rho \overline{u_i}\right) + \frac{\partial}{\partial x_j}\left(\rho \overline{u_i}\,\overline{u_j}\right) = -\frac{\partial \mathrm{p}}{\partial \mathrm{x_i}} + \frac{\partial}{\partial x_j}\left(\tau_{ij} - \rho \overline{u_i' u_j'}\right) + \rho g_i \tag{3.12}$$

Energy:

$$\frac{\partial}{\partial \mathrm{t}}\left(\rho \overline{\mathrm{H}}\right) + \frac{\partial}{\partial x_i}\left(\rho \overline{u_i}\,\overline{\mathrm{H}}\right) = \frac{\partial}{\partial x_j}\left(\mathrm{k_{eff}}\,\frac{\partial \overline{\mathrm{T}}}{\partial \mathrm{x_j}}\right) + \frac{\partial \overline{\mathrm{p}}}{\partial \mathrm{t}} \tag{3.13}$$

Equations 3.11-3.13 are called Reynolds-averaged Navier-Stokes (RANS) equations. Additional terms now appear that represent the effects of turbulence. That is $-\rho \overline{u_i' u_j'}$, which is called Reynolds stress, and it has to be modelled to solve equation 3.12. In equation 3.13 $\mathrm{k_{eff}}$ is the effective thermal conductivity and depends on the used turbulence model:

$$\mathrm{k_{eff}} = \mathrm{k} + \mathrm{k}_T = \mathrm{k} + \frac{c_p \mu_T}{\mathrm{Pr}_T} \tag{3.14}$$

where Pr_T is the turbulent energy Prandtl number (Pr_T = 0.85), and μ_T is the turbulent viscosity (it will be defined in equation 3.18).

The mean total enthalpy is given by:

$$\overline{\mathrm{H}} = \overline{\mathrm{h}} + \frac{1}{2}\overline{\mathbf{U}}^2 + \frac{1}{2}\overline{\mathbf{u}'^2} \tag{3.15}$$

where the last term is called turbulence kinetic energy, *k*.

Reynolds stresses describe the influence of the fluctuations on the mean flow distribution, and the purpose of the turbulence models is to obtain a description of Reynolds stresses. In this project the standard *k*-ω-model is used.

The *k*-ω-model used by FLUENT is developed by Wilcox (1998). The *k*-ω-model is an empirical model based on model transport equations for the turbulence kinetic energy (*k*) and the specific dissipation rate (ω), which can also be thought of as the ratio of ε to *k*. ε is the dissipation rate.

The turbulence kinetic energy, *k*, and the specific dissipation rate, ω, are obtained from the following transport equations:

$$\frac{\partial}{\partial \mathrm{t}}(\rho k) + \frac{\partial}{\partial x_i}\left(\rho k \overline{u_i}\right) = \frac{\partial}{\partial x_j}\left(\left(\mu + \frac{\mu_T}{\sigma_k}\right)\frac{\partial k}{\partial x_j}\right) + 2\mu_T S_{ij} S_{ij} - \rho\beta^* f_{\beta^*} k\omega \tag{3.16}$$

$$\frac{\partial}{\partial \mathrm{t}}(\rho \omega) + \frac{\partial}{\partial x_i}\left(\rho \omega \overline{u_i}\right) = \frac{\partial}{\partial x_j}\left(\left(\mu + \frac{\mu_T}{\sigma_\omega}\right)\frac{\partial \omega}{\partial x_j}\right) + \alpha\frac{\omega}{k} 2\mu_T S_{ij} S_{ij} - \rho\beta f_\beta \omega^2 \tag{3.17}$$

In these equations, the last term represent the dissipation of *k* and ω due to turbulence, and the second last term represent the generation of turbulence kinetic energy due to mean velocity gradients (equation 3.16) and the generation of ω (equation 3.17). σ_k and σ_ω are the turbulent Prandtl numbers for *k* and ω, respectively ($\sigma_k = \sigma_\omega = 2.0$). The *k*-ω-model introduces the turbulent viscosity, μ_T, to model the turbulent mean flow:

$$\mu_T = \frac{\rho k}{\omega} \tag{3.18}$$

To close equations 3.16 and 3.17 the following coefficients have to be defined:

$$\alpha = \frac{13}{25}, \quad \beta = \frac{9}{125}, \quad \beta^* = \frac{9}{100} \tag{3.19}$$

$$f_\beta = \frac{1+70\chi_\omega}{1+80\chi_\omega}, \quad \chi_\omega \equiv \left|\frac{\Omega_{ij}\Omega_{jk}S_{ki}}{\left(\beta^*\omega\right)^3}\right| \tag{3.20}$$

$$f_{\beta^*} = \begin{cases} 1, & \chi_k \le 0 \\ \dfrac{1+680\chi_k^2}{1+400\chi_k^2}, & \chi_k > 0 \end{cases}, \quad \chi_k \equiv \frac{1}{\omega^3}\frac{\partial k}{\partial x_j}\frac{\partial \omega}{\partial x_j} \tag{3.21}$$

$$\Omega_{ij} = \frac{1}{2}\left(\frac{\partial \overline{u_i}}{\partial x_j} - \frac{\partial \overline{u_j}}{\partial x_i}\right), \quad S_{ij} = \frac{1}{2}\left(\frac{\partial \overline{u_i}}{\partial x_j} + \frac{\partial \overline{u_j}}{\partial x_i}\right) \tag{3.22}$$

The *k*-ω-model is explained in more detail in FLUENT (2001) and Wilcox (1998).

By solving equations 3.16 and 3.17 for *k* and ω and computing μ_T as a function of *k* and ω the Reynolds stresses can be calculated by employing the Boussinesq hypothesis that relates the Reynolds stresses to the mean velocity gradient:

$$-\rho\overline{u_i' u_j'} = \mu_T\left(\frac{\partial \overline{u_i}}{\partial x_j} + \frac{\partial \overline{u_j}}{\partial x_i}\right) - \frac{2}{3}\left(\rho k + \mu_T \frac{\partial u_i}{\partial x_i}\right)\delta_{ij} \tag{3.23}$$

The *k*-ω-model was chosen as turbulence model instead of the better-known *k*-ε-model, where an equation for the dissipation rate (ε) is solved instead of the equation for the specific dissipation rate (ω) as in the *k*-ω-model. The *k*-ε-model is primarily valid for turbulent core flows (i.e., the flow in the regions somewhat far from walls), and on the other hand the *k*-ω-model is designed to be applied throughout the boundary layer, provided that the near-wall mesh resolution is sufficient (FLUENT, 2001 and Wilcox, 1998). The flow in the inner tank is very dependent on the natural convection flow near the tank wall and therefore the *k*-ω-model was chosen.

3.5.4 Discretisation and solution algorithms

Within numerical calculations, different discretisation methods are used. FLUENT uses a control-volume-based technique to convert the governing equations to algebraic equations that can be solved numerically. This involves, firstly, integrating the equations over a control volume so that values of the dependent variable are located at the control volume boundaries or faces. The variables are then interpolated to obtain finite difference equations at the node values. A second-order upwind scheme was used for the interpolation. A fully implicit procedure was used for the time stepping discretisation in the transient simulations.

The methods used for updating pressure and for correcting velocity components is the PISO algorithm (PISO = Pressure-Implicit with Splitting of Operators), which is part of the SIMPLE family of algorithms (Patankar, 1980).

3.5.5 Discussion

This section has summarised the basic theory behind CFD and described the solution algorithms used in this project. The theory and the solution strategy are not described in

full details, as it is very comprehensive. Further details about CFD-theory and the used procedures can be found in either the FLUENT manual (FLUENT, 2001) or in other existing literature i.e. Ferziger and Perić (2002), Versteeg and Malalasekear (1995), Wilcox (1998) and Patankar (1980).

3.6 SDHW simulation model

The low flow SDHW simulation program MantlSim was used to simulate the yearly thermal performance of low flow SDHW systems. MantlSim was originally developed and validated by Furbo and Berg (1990) and later modified by Shah and Furbo (1996) and Shah (1999, 2000).

MantlSim will in this thesis be further developed. Improved heat transfer correlations to describe the heat transfer between the mantle fluid and the inner and outer mantle wall as well as improved heat transfer correlations to describe the heat transfer between the tank wall and the domestic water in the tank will be implemented in MantlSim. Furthermore, correlations to calculate the natural convection building up thermal stratification in the hot water tank, both at and above the mantle level of the tank will be implemented. Finally, MantlSim will be developed to include the possibility to place the mantle inlet at different levels of the mantle and take the mixing inside the mantle caused by the incoming solar collector fluid into account. The development of MantlSim will be described in chapter 8.

3.7 Summary

In this chapter the experimental and numerical techniques of the thesis were outlined. Two types of thermal experiments were described: thermal experiments in heat storage test facility and side-by-side laboratory tests of wholes systems. Particles Image Velocimetry, a flow visualisation technique, was outlined as well as the Computational Fluid Dynamics technique, which is a numerical method to simulate fluid flow and heat transfer. Finally, the low flow SDHW simulation program, MantlSim, was introduced.

4. Thermal experiments of mantle inlet designs

4.1 Introduction

Thermal experiments were carried out to investigate how different mantle inlet designs influence the thermal stratification and the thermal performance of the mantle tanks. The first part of this chapter describes the thermal experiments carried out in the heat storage test facility where different designs of the mantle inlet port were investigated. The last part of the chapter describes the side-by-side laboratory test of two SDHW systems. The two SDHW systems are identical except for the position of the mantle inlet port.

Simulations of 15 different (see Table 4-1) low-flow SDHW systems with a vertical mantle heat exchanger were carried out with the simulation program MantlSim (Shah, 1999) to see how often the mantle inlet temperature is lower than the temperature in the top of the mantle. When the inlet temperature to the mantle is lower than the mantle top temperature there is a risk that the thermal stratification in the mantle and in the inner tank is destroyed. The mantle tanks in the simulations had the inlet to the mantle at the top of the mantle. The Danish Test Reference Year (Statens Byggeforskningsinstitut, 1982) was used as weather data. Figure 4-1 shows the relationship between the part of the operation time where the inlet temperature to the mantle is lower than the mantle top temperature as a function of the solar fraction. For a system with a solar fraction of 40% (a typical solar fraction for a Danish system) the inlet temperature to the mantle is lower than the mantle top temperature in approximately 60% of the operation time of the circulation pump in the solar collector loop.

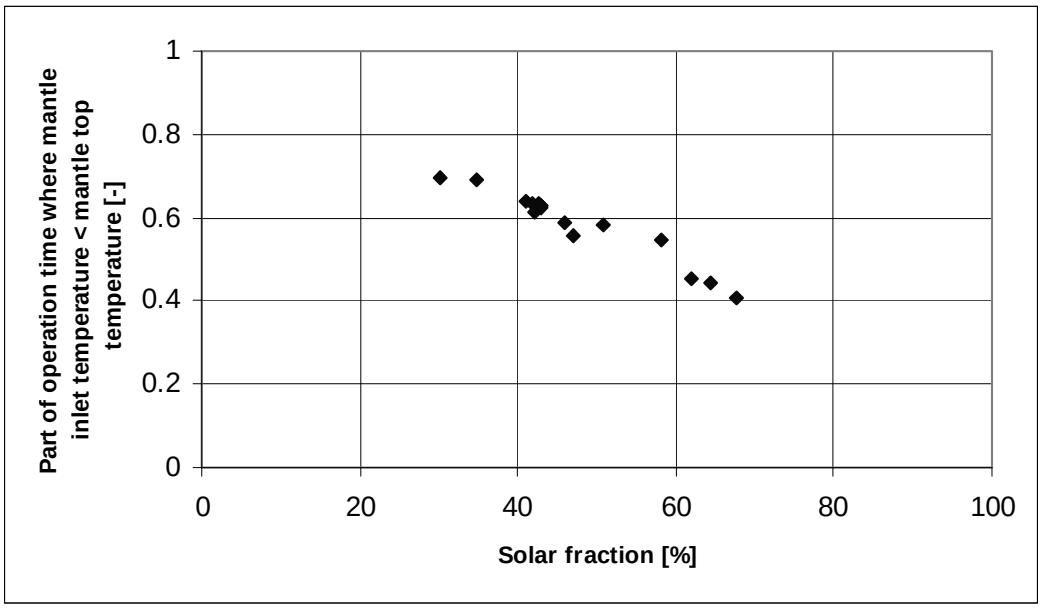

Figure 4-1: Part of the operation time where the inlet temperature is lower than the mantle top temperature as a function of the solar fraction for 15 different SDHW systems with vertical mantle heat exchanger.

System #	Tank size (m^3)	Auxiliary volume (m^3)	Solar volume (m^3)	Mantle gap (m)	Collector area (m^2)	Collector flow rate ($l/min/m^2$)	Hot water consumption (m^3/day)
1	0.175	0.070	0.105	0.013	2.19	0.2	0.050
2	0.175	0.070	0.105	0.013	2.19	0.2	0.100
3	0.175	0.070	0.105	0.013	2.19	0.2	0.160
4	0.175	0.070	0.105	0.013	2.19	0.2	0.200
5	0.175	0.070	0.105	0.013	4.38	0.2	0.050
6	0.175	0.070	0.105	0.013	4.38	0.2	0.100
7	0.175	0.070	0.105	0.013	4.38	0.2	0.160
8	0.175	0.070	0.105	0.013	4.38	0.2	0.200
9	0.175	0.070	0.105	0.013	6.57	0.2	0.160
10	0.175	0.070	0.105	0.013	6.57	0.2	0.200
11	0.100	0.040	0.060	0.013	2.19	0.2	0.100
12	0.150	0.060	0.090	0.013	2.19	0.2	0.100
13	0.200	0.080	0.120	0.013	2.19	0.2	0.100
14	0.250	0.100	0.150	0.013	2.19	0.2	0.100
15	0.300	0.120	0.180	0.013	2.19	0.2	0.100

Table 4-1: Data for the 15 different SDHW systems taken into calculation.

This is the background for an investigation of different designs of mantle inlet to a vertical mantle tank. Different sizes of the inlet were investigated. With a larger inlet the mean inlet velocity is smaller for the same flow rate and with a smaller mean inlet velocity less mixing near the inlet might occur. Different positions of the inlet were investigated as well. The mantle inlet is normally located at the top of the mantle, but in cases with a low inlet temperature there is a risk of mixing near the inlet. Therefore a lower inlet position was investigated.

4.2 Thermal experiments in heat storage test facility

As described in section 3.2, prototypes of vertical mantle heat exchangers were tested in a heat storage test facility. The same mantle tank is used for all the experiments, but the size and the location of the inlet to the mantle were changed from experiment to experiment. The data of the mantle tank are given in Table 4-2. Figure 4-3 shows the mantle tank.

Hot-water tank volume (m^3)	0.175
Volume in inner tank above mantle (m^3)	0.081
Mantle volume (m^3)	0.0319
Tank height (m)	1.449
Inner diameter of tank (m)	0.394
Material thickness (m)	0.003
Mantle height (m)	0.7
Mantle gap (m)	0.0335
Insulation material	Mineral wool
Insulation top (m)	0.26
Insulation sides (m)	0.06
Insulation bottom (m)	0

Table 4-2: Data for the tested mantle tank.

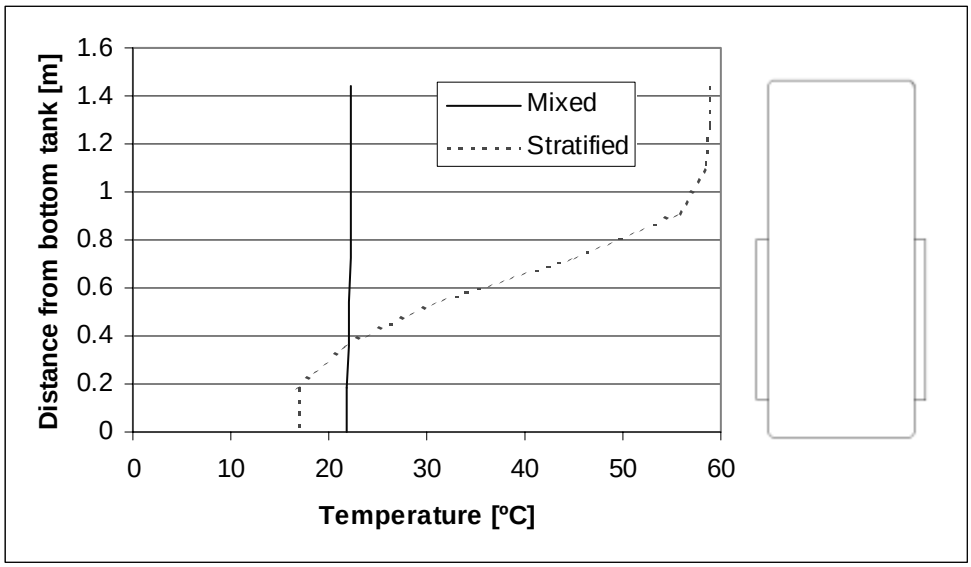

Figure 4-2: Illustration of initial temperatures in the thermal experiments.

Tests were carried out with a low mantle flow rate of 0.4 l/min and with a relatively high mantle flow rate of 0.8 l/min. Furthermore tests were carried out for two different initial conditions of the temperatures inside the storage. The initial conditions were that the tank was either mixed at around 20-25ºC or stratified with temperatures at 16-22ºC in the bottom and 55-60ºC in the top. The initial temperatures are illustrated in Figure 4-2.

As described in section 3.2, the tests were carried out with a heating period with a high mantle inlet temperature of 70ºC. The heating period was followed by a period where the system was resting. When a stable condition in the heat storage was reached, the test was continued with a period where the mantle inlet temperature was lower than the temperature in the top of the mantle. This test is similar to a day with heavy overcast in the morning, sunshine at noon and then heavy overcast before some sunshine in the late afternoon. The inlet temperature to the mantle in the last period of the test was different from test to test due to the different temperature levels in the heat storage during the tests. The mantle inlet temperature in the last period of the tests was at the same level as the temperature in the middle of the mantle. The duration of the tests was a bit different for the two mantle flow rates and the two initial temperature profiles in the storage. The mantle inlet temperature during

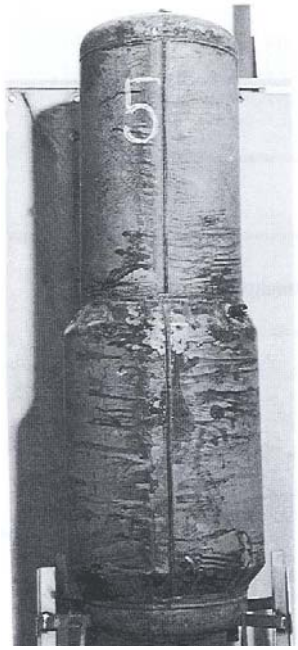

Figure 4-3: The mantle tank used in the thermal experiments.

the tests is illustrated in Figure 4-4 where a mantle inlet temperature of 0ºC corresponds to the resting period without flow in the mantle.

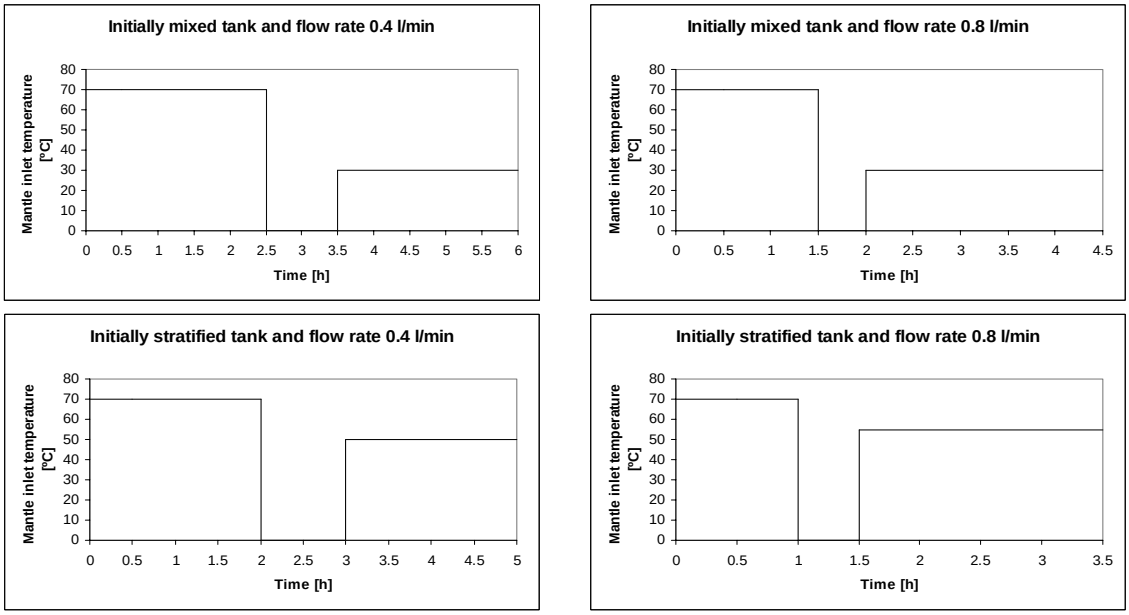

Figure 4-4: The mantle inlet temperatures during the tests.

The description of the results of the experiments in the heat storage test facility is divided into two sections. That is, one section (4.2.2) with the results of the experiments with the different mantle inlet sizes and a section (4.2.3) with the results of the experiments with different locations of the mantle inlet port. The tests are described in Table 4-3.

Experiment #	Mantle flow rate [l/min]	Position of mantle inlet	Mantle inlet size	Initial temperatures
1a	0.4	Top of mantle	½”	Mixed
1b	0.4	Top of mantle	1”	Mixed
2a	0.8	Top of mantle	½”	Mixed
2b	0.8	Top of mantle	1”	Mixed
3a	0.4	Top of mantle	½”	Stratified
3b	0.4	Top of mantle	1”	Stratified
3c	0.4	Top of mantle	2”	Stratified
4a	0.8	Top of mantle	½”	Stratified
4b	0.8	Top of mantle	1”	Stratified
4c	0.8	Top of mantle	2”	Stratified
5a	0.4	0.175 m from top	1”	Mixed
6a	0.8	0.175 m from top	1”	Mixed
7a	0.4	0.175 m from top	1”	Stratified
8a	0.8	0.175 m from top	1”	Stratified

Table 4-3: Description of the 14 tests.

4.2.1 Methods of analysing results

The temperature of the domestic water in the inner tank was measured at seven points inside the tank. The temperature was measured at five points on the outside of the mantle wall halfway between the mantle inlet and the mantle outlet where the temperature is close to the temperature of the fluid inside the mantle. Furthermore, the ambient temperature and the mantle inlet and outlet temperatures were measured along with the mantle flow rate. The seven measuring points inside the tank were distributed with equal distance so the tank can be divided into seven equal volumes, V. The measuring points and divisions into volumes can be seen in Figure 4-5. Vol1 denotes the volume between T1 and T2, Vol2 denotes the volume between T2 and T3 etc. The volume below T1 is not taken into account because the main part of the volume is below the mantle. Table 4-4 shows the position of the measuring points in the tank and on the outside of the mantle.

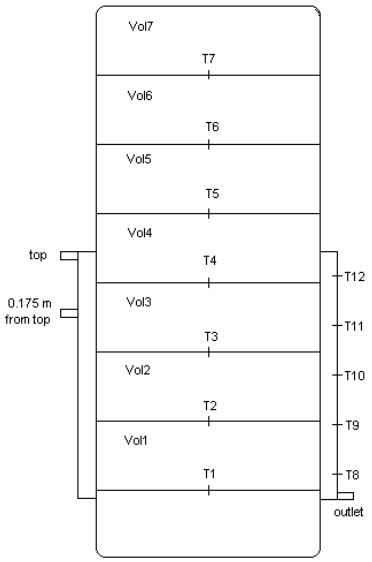

Figure 4-5: Measuring points and divisions into volumes.

In inner tank	Distance from bottom of tank [m]	On the outside mantle wall	Distance from bottom of mantle [m]
T1	0.181	T8	0.07
T2	0.362	T9	0.21
T3	0.543	T10	0.35
T4	0.724	T11	0.49
T5	0.905	T12	0.63
T6	1.086		
T7	1.267		

Table 4-4: Positions of measuring points in inner tank and on outside of mantle wall.

Different sizes of mantle inlet port:

The results of the experiments with the different sizes of the mantle inlet port were analysed by comparing the rate of heat transfer to each of the volumes in the inner tank.

The rate of heat transfer to each volume in the inner tank can approximately be calculated by the equation:

$$Q_{vol(i)} = \frac{V \cdot \rho \cdot c_p \cdot \Delta T_{vol(i)}}{\Delta t} \qquad (4.1)$$

The measured data was stored every fourth minute (Δt) and $\Delta T_{vol(i)}$ is the change in temperature (T(i)) of volume number "i" over the four-minute period. ρ is the density of water and c_p is the heat capacity of water. ρ and c_p are considered to be constant as an approximation. V = 21.875 l for each volume.

Furthermore the thermal stratification in the inner tank was compared. The temperatures from each experiment were made dimensionless to neglect the influence from small differences in the initial temperatures:

$$\theta = \frac{T\text{-}T_{min}}{T_{max}\text{-}T_{min}} \tag{4.2}$$

Different locations of mantle inlet port:

The differences in the results from the experiments with the different locations of the mantle inlet port were best illustrated by comparing the energy delivered to the top and to the bottom part as a function of the energy supply to the heat storage during the tests.

Energy delivered to the top part is defined as energy delivered to Vol4, Vol5, Vol6 and Vol7 while energy delivered to the bottom part is defined as energy delivered to Vol1, Vol2 andVol3. The energy delivered to the top part (E_{top}) and to the bottom part (E_{bot}) of the tank can approximately be calculated by the following equations:

$$E_{top} = V \cdot \rho \cdot c_p \cdot \sum_{i=4}^{7} \Delta T_{vol(i)} \tag{4.3}$$

$$E_{bot} = V \cdot \rho \cdot c_p \cdot \sum_{i=1}^{3} \Delta T_{vol(i)} \tag{4.4}$$

Again, the measured data was stored every fourth minute and $\Delta T_{vol(i)}$ is the change in temperature (T(i)) of volume number "i" over the four-minute period. ρ is the density of water and c_p is the heat capacity of water. ρ and c_p are considered to be constant as an approximation. V = 21.875 l for each volume.

The energy supply to the heat storage during the tests can be calculated by:

$$E_{storage} = \int_{t_{start}}^{t_{end}} \dot{m} \cdot c_p \cdot \left(T_{mantle,in} - T_{mantle,out} \right) \cdot dt \tag{4.5}$$

Where t is the time, $\dot{m}$ is the mantle flow rate, $T_{mantle,in}$ is the mantle inlet temperature and $T_{mantle,out}$ is the mantle outlet temperature.

4.2.2 Size of mantle inlet port

With the mantle inlet port located at the top of the mantle, tests with three different mantle inlet sizes were carried out; ½" (ID = 0.0189 m), 1" (ID = 0.0306 m) and 2" (ID = 0.0570 m). For a constant mantle flow rate, the mean inlet velocity depends on the mantle inlet size. The mean inlet velocity and the inlet Reynolds number for different mantle inlet sizes are shown in Figure 4-6. The mean inlet velocity at a mantle flow rate of 0.4 l/min decreases from 0.0238 m/s with a ½" inlet to 0.0026 m/s with a 2" inlet. However, the flow at the inlet is in the laminar flow regime for pipe flow due to the low mantle flow rate.

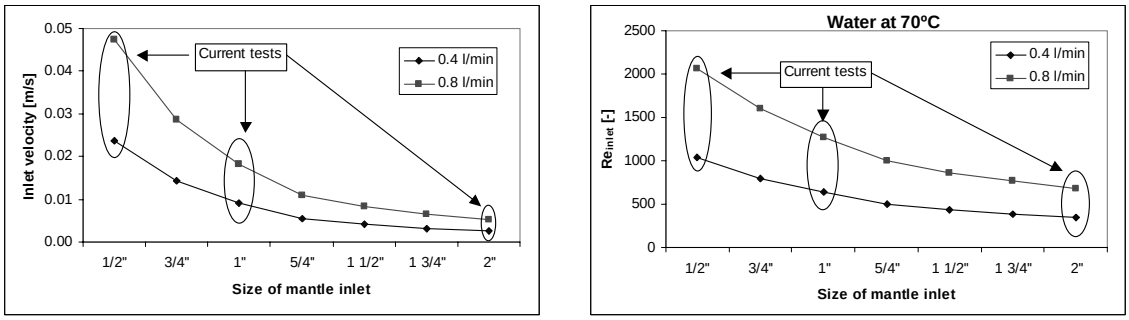

Figure 4-6: Mean inlet velocity (left) and Reynolds number (right) at the mantle inlet as a function of inlet size.

Experiment 1a-1b (Initially mixed, 0.4 l/min, Top inlet (sizes: ½" and 1")):
The measured temperatures for experiment 1a (½" inlet) and experiment 1b (1" inlet) are shown in Figure 4-7 and Figure 4-8. The mantle inlet temperature and the ambient temperature were close to identical in the experiments while the initial temperatures were 3-4 K higher in experiment 1a than in experiment 1b. The mantle flow rate was a little higher in experiment 1b than in experiment 1a. In the first part of the experiments, when the mantle inlet temperature is high, the thermal stratification is built up in both experiments. In the last part, when the inlet temperature is low, T5-T7 (above mantle) remains more or less constant, while T3 and T4 decrease and T1 and T2 increase.

The rate of heat transfer to each volume in the inner tank during the two experiments is shown in Figure 4-9. In the first part of the experiments the heat is first supplied to the volumes in the top of the tank and then later to the volumes in the bottom. This is desirable because the thermal stratification is built up this way. The rate of heat transfer to the inner tank is a little higher for experiment 1b (peaks at 275 W) than for experiment 1a (peaks at 250 W). This difference might be due to the small differences in flow rate and initial temperatures because these small differences are in favour of higher heat transfer rates for experiment 1b. In the last part of the experiments, the heat is supplied to volume 1 and volume 2 and there is an unwanted negative rate of heat transfer to volume 4.

The thermal stratification at the start and at the end for both experiments is shown in Figure 4-10 and minor differences are observed.

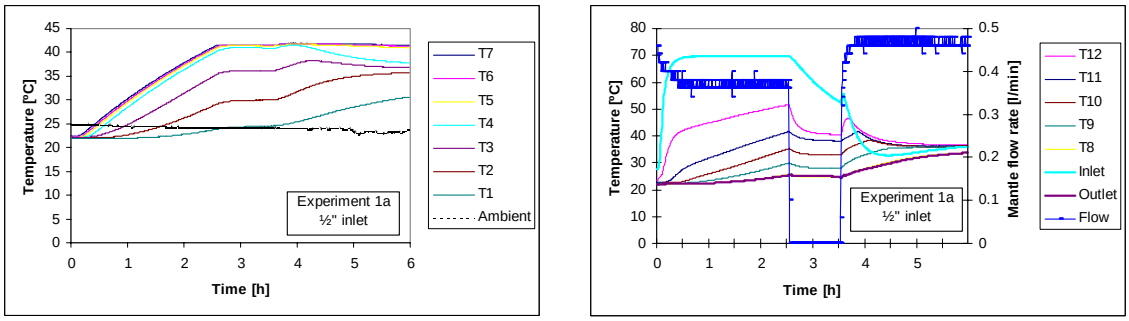

Figure 4-7: Measured temperatures and flow rate for experiment 1a (½" inlet).

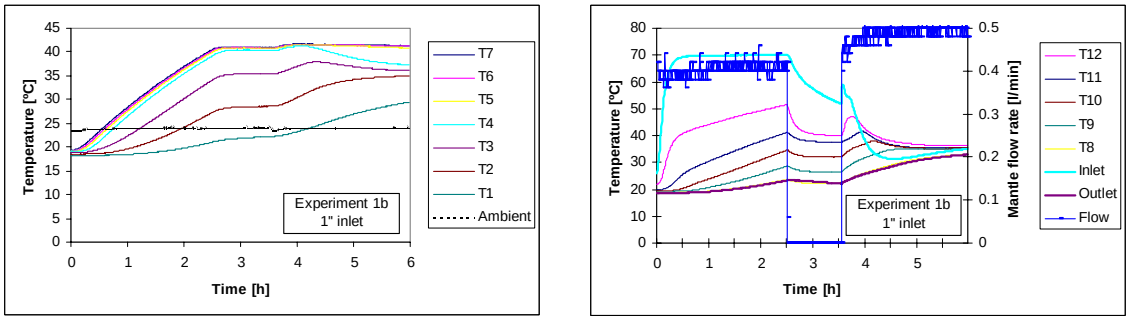

Figure 4-8: Measured temperatures and flow rate for experiment 1b (1" inlet).

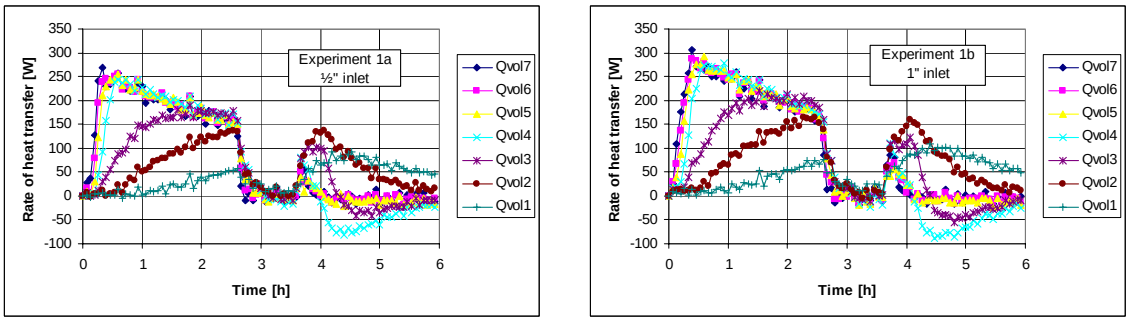

Figure 4-9: Rate of heat transfer to each volume in inner tank in experiment 1a and experiment 1b.

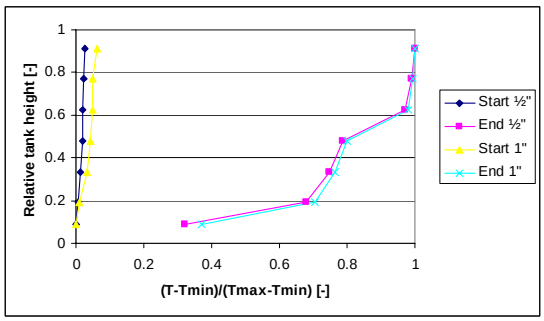

Figure 4-10: Thermal stratification in experiment 1a and experiment 1b.

Experiment 2a-2b (Initially mixed, 0.8 l/min, Top inlet (sizes: ½" and 1")):

The measured temperatures for experiment 2a (½" inlet) and experiment 2b (1" inlet) are shown in Figure 4-11 and Figure 4-12. The mantle inlet temperature and the ambient temperature were close to identical in the experiments. The mantle flow rate was a little higher in experiment 2b than in experiment 2a. In the first part of the experiments, when the mantle inlet temperature is high, the thermal stratification is built up in both experiments. In the last part when the inlet temperature is low, T5-T7 (above mantle) remains more or less constant, while T3 and T4 decrease and T1 and T2 increase.

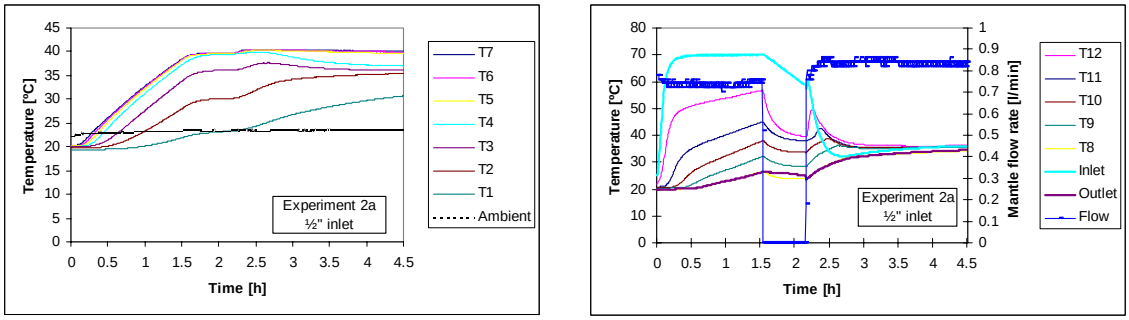

Figure 4-11: Measured temperatures and flow rate for experiment 2a (½" inlet).

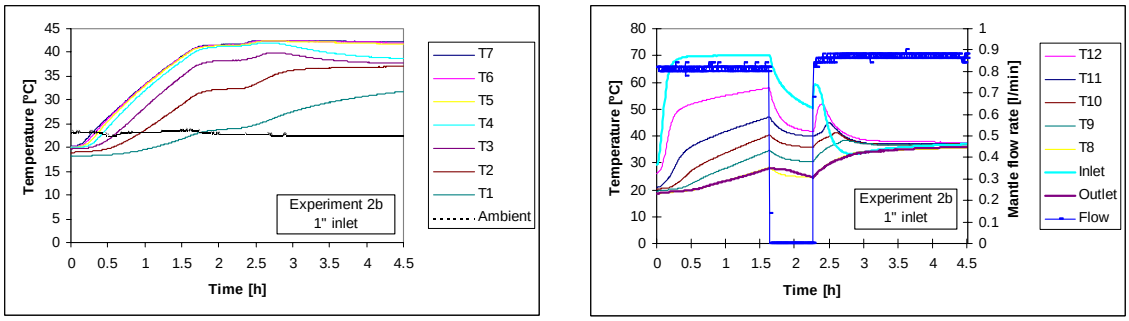

Figure 4-12: Measured temperatures and flow rate for experiment 2b (1" inlet).

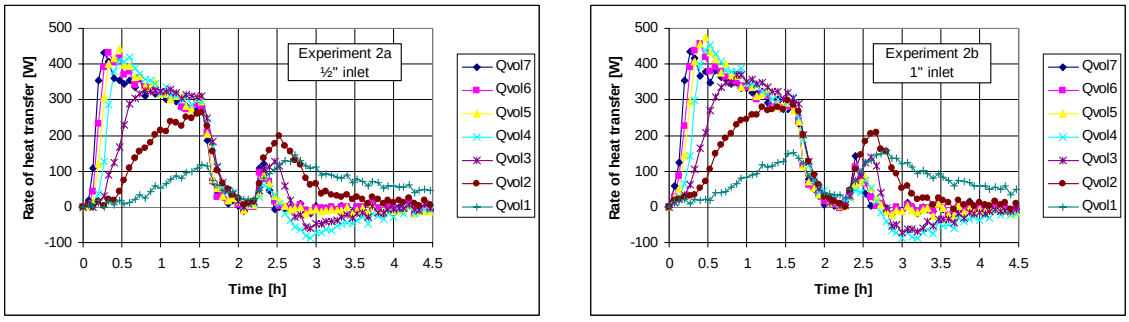

Figure 4-13: Rate of heat transfer to each volume in inner tank in experiments 2a and 2b.

The rate of heat transfer to each volume in the inner tank during the two experiments is shown in Figure 4-13. The rate of heat transfer to the inner tank shows the same tendency as for the experiments with the mantle flow rate of 0.4 l/min, but the rates are higher due to the higher flow rate. The rate of heat transfer to the inner tank is a little

higher for experiment 2b (peaks at 470 W) than for experiment 2a (peaks at 430 W). This difference might be due to the small differences in the flow rate.

The thermal stratification at the start and at the end for both experiments is shown in Figure 4-14, and minor differences are observed.

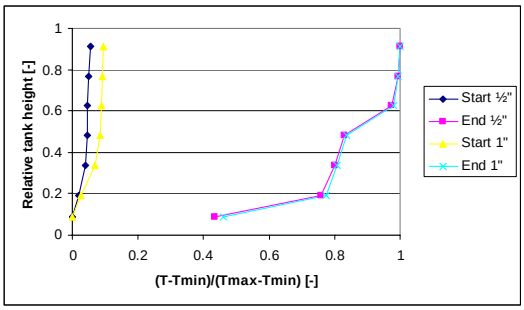

Figure 4-14: Thermal stratification in experiment 2a and experiment 2b.

Experiment 3a-3c (Initially stratified, 0.4 l/min, Top inlet (sizes: ½", 1" and 2")):

The measured temperatures for experiment 3a (½" inlet), experiment 3b (1" inlet) and experiment 3c (2" inlet) are shown in Figure 4-15, Figure 4-16 and Figure 4-17. The mantle inlet temperature and the ambient temperature were close to identical in the experiments. The mantle flow rate was also close to identical in the three experiments. In the first part of the experiments, when the mantle inlet temperature is high, the temperatures T5-T7 (above mantle) increase 1-2 K, while T3-T4 (level at top of mantle) increase 10-15 K and the temperatures at the bottom (T1-T2) also increase. In the last part when the inlet temperature is low, T5-T7 (above mantle) remains more or less constant (decrease less than 1 K) while T3 and T4 decrease 3-5 K and T1 and T2 increase 8-12 K.

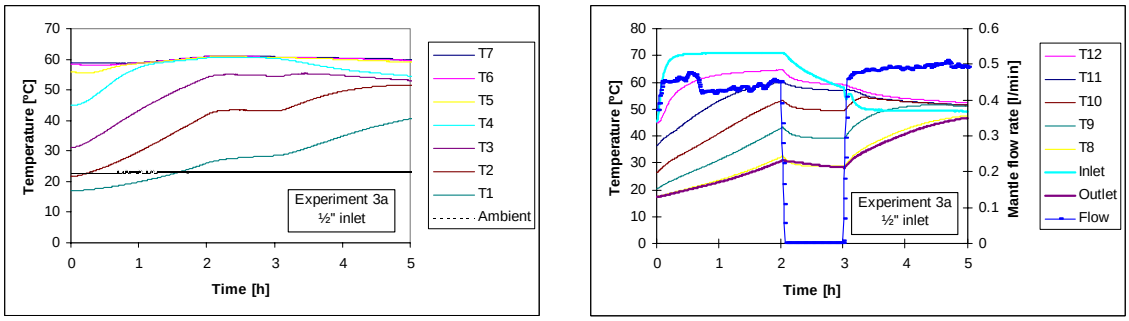

Figure 4-15: Measured temperatures and flow rate for experiment 3a (½" inlet).

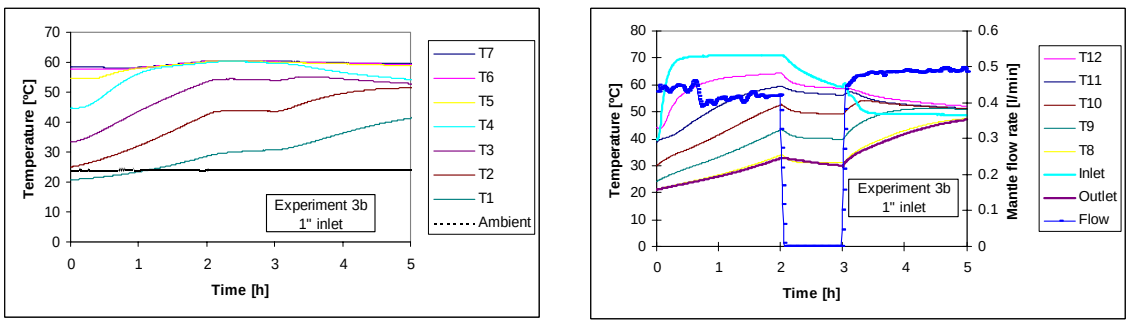

Figure 4-16: Measured temperatures and flow rate for experiment 3b (1" inlet).

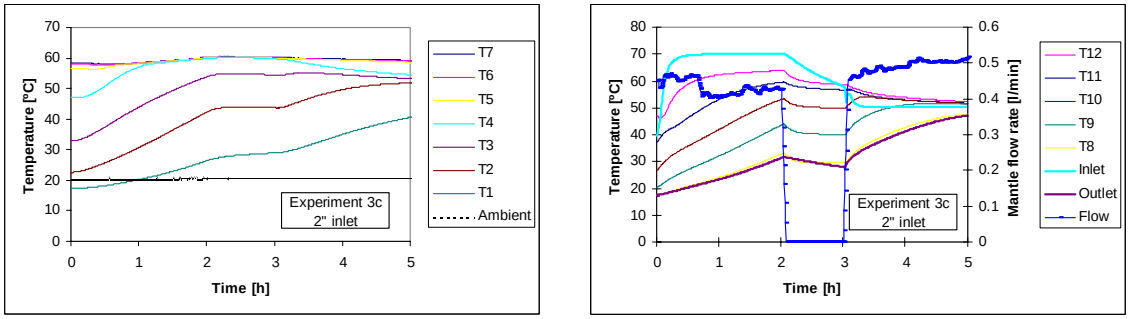

Figure 4-17: Measured temperatures and flow rate for experiment 3c (2" inlet).

The rate of heat transfer to each volume in the inner tank during the three experiments is shown in Figure 4-18. In the first part of the experiments the heat is mainly supplied to volume 2 to volume 4, with peaks at 450 W for experiment 3a and 3b, and at 400 W for experiment 3c. The small difference might be due to a small difference in the initial temperature of volume 4, it is about 3 K higher in experiment 3c than in experiment 3a and 3b. In the last part of the experiments the heat is supplied to volume 1 and volume 2 and there is an unwanted negative rate of heat transfer to volume 4.

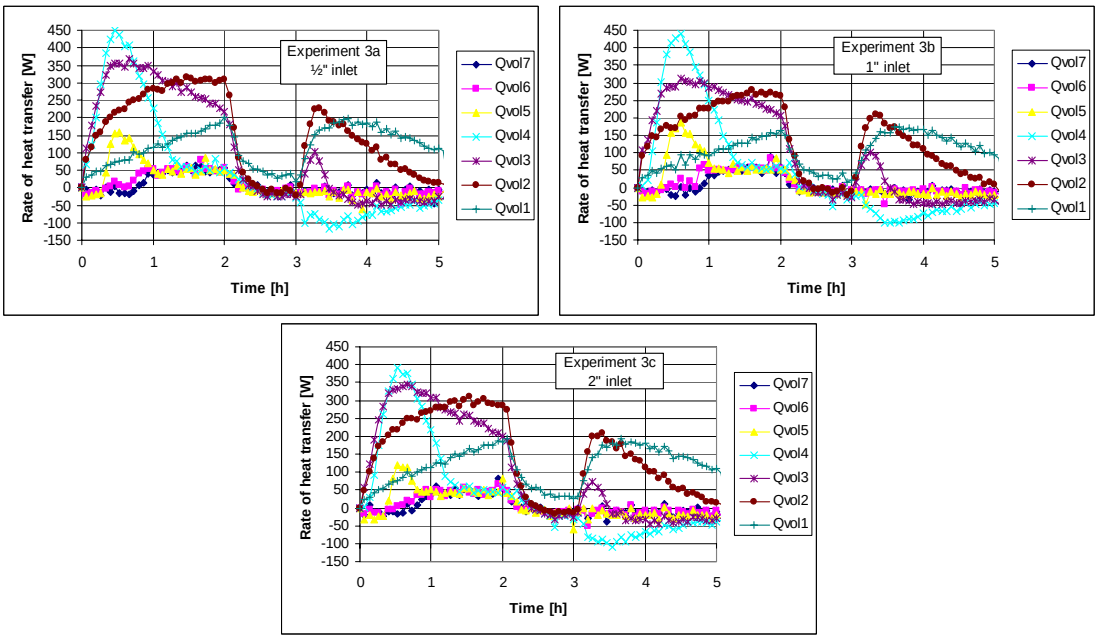

Figure 4-18: Rate of heat transfer to each volume in inner tank in experiments 3a, 3b and 3c.

The thermal stratification at the start and at the end for the three experiments is shown in Figure 4-19 and minor differences are observed.

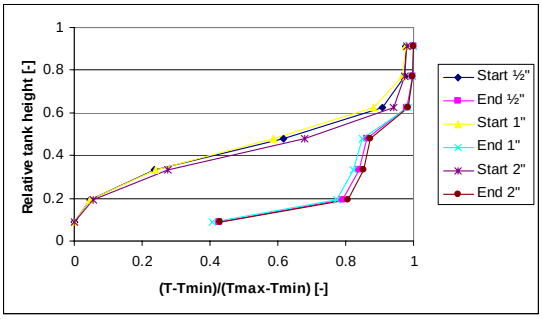

Figure 4-19: Thermal stratification in experiment 3a, experiment 3b and experiment 3c.

Experiment 4a-4c (Initially stratified, 0.8 l/min, Top inlet (sizes: ½", 1" and 2")):
The measured temperatures for experiment 4a (½" inlet), experiment 4b (1" inlet) and experiment 4c (2" inlet) are shown in Figure 4-20, Figure 4-21 and Figure 4-22. The mantle inlet temperature and the ambient temperature were close to identical in the experiments. The mantle flow rate was a little higher in experiment 4b than in the other two experiments. In the first part of the experiments, when the mantle inlet temperature is high, the temperatures T5-T7 (above mantle) increase 1-2 K, while T3-T4 (level at top of mantle) increase 15-18 K and the temperatures at the bottom (T1-T2) also increase. In the last part when the inlet temperature is low; T5-T7 (above mantle) remains more or less constant (decrease less than 1 K), T4 decreases about 5 K, T3 remains constant, and T1 and T2 increase 10-18 K.

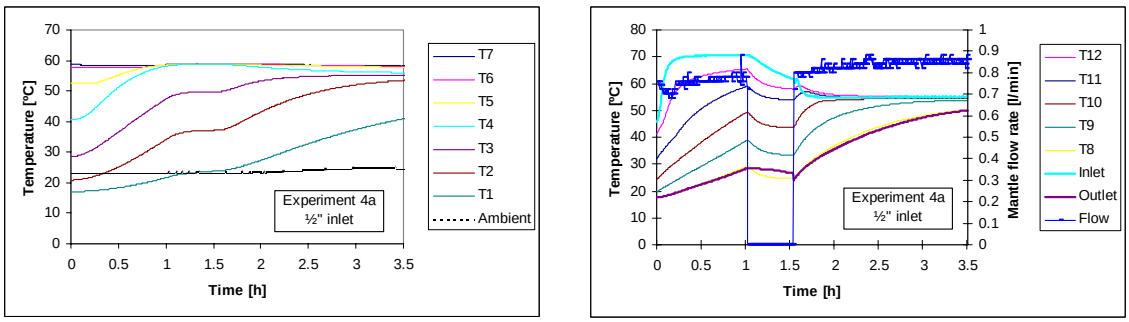

Figure 4-20: Measured temperatures and flow rate for experiment 4a (½" inlet).

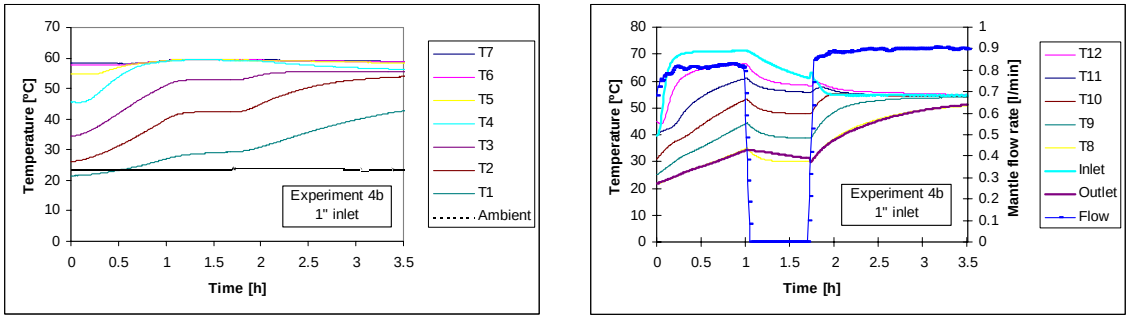

Figure 4-21: Measured temperatures and flow rate for experiment 4b (½" inlet).

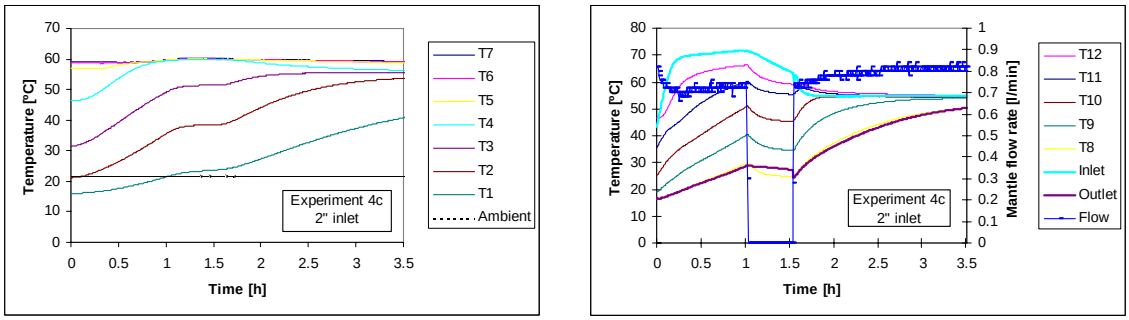

Figure 4-22: Measured temperatures and flow rate for experiment 4c (2" inlet).

The rate of heat transfer to each volume in the inner tank during the three experiments is shown in Figure 4-23. The rate of heat transfer to the inner tank show the same tendency as for the experiments with the mantle flow rate of 0.4 l/min, but the rates are higher due to the higher flow rate. When the mantle inlet temperature is high, the rate of heat transfer to the inner tank is highest for experiment 4a (peak at 750 W), then for experiment 4b (peak at 670 W) and lowest for experiment 4c (peak at 570 W). This difference could be due to the different sizes of the mantle inlet port, but it is more likely due to the differences in the initial temperatures.

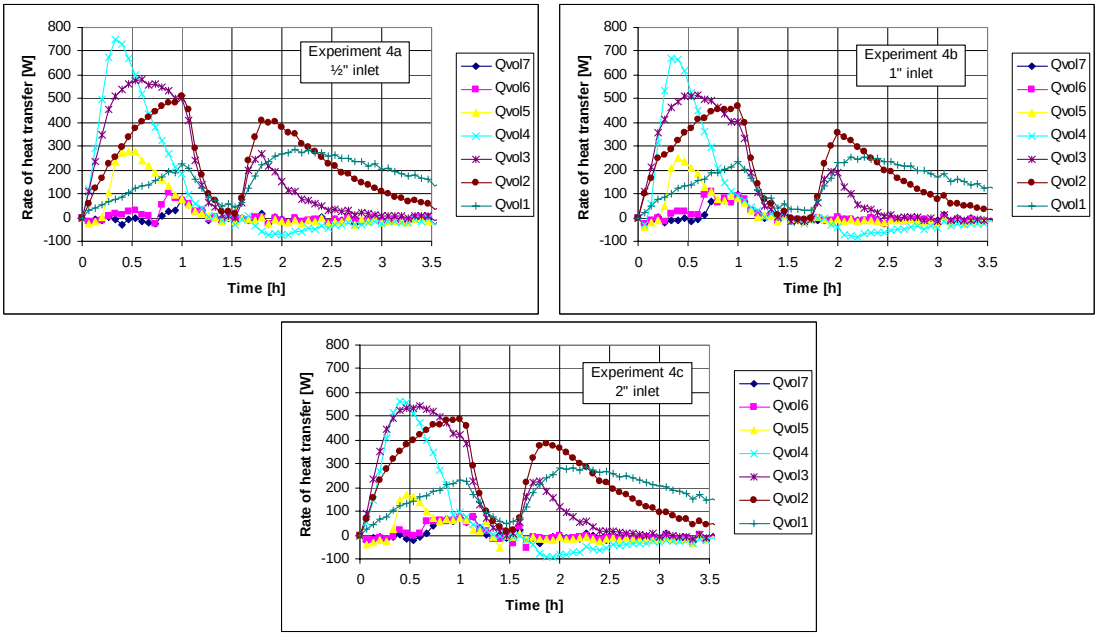

Figure 4-23: Rate of heat transfer to each volume in inner tank in experiments 4a, 4b and 4c.

The thermal stratification at the start and at the end for the three experiments is shown in Figure 4-24 and minor differences are observed.

Summary of experiments with different mantle inlet sizes:

The experiments described in this section showed that the size of the mantle inlet port has a minor effect on the thermal stratification. In some cases small differences were observed, but the differences could be explained by small differences in either the initial conditions or in the test conditions. The small Re_{inlet} and the small inlet velocities showed in Figure 4-6 are most likely the explanation for the minor effect on the thermal

stratification. For larger flow rates than considered in this thesis, the mantle inlet size might have an influence.

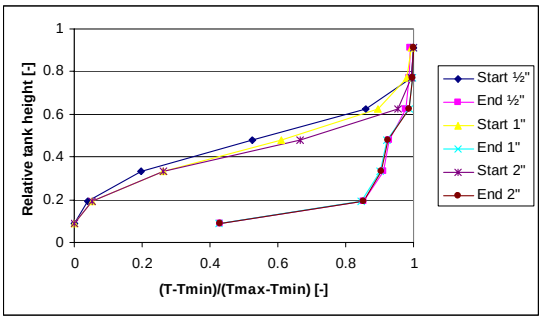

Figure 4-24: Thermal stratification in experiment 4a, experiment 4b and experiment 4c.

4.2.3 Position of mantle inlet port

With a mantle inlet size of 1" (ID = 0.0306 m) tests with two different locations of the mantle inlet port were carried out; that is top inlet position and lower inlet position. The lower inlet position was 0.175 m (one fourth of the total mantle height) from the top.

Experiments 1b and 5a (Initially mixed, 0.4 l/min, 1" inlet (Position: top and lower)):
The measured temperatures for experiment 1b (Top inlet) and experiment 5a (lower inlet) are shown in Figure 4-25 and Figure 4-26. The mantle inlet temperature and the ambient temperature were close to identical in the experiments. The mantle flow rate was a little higher in experiment 1b than in experiment 5a and also the initial temperatures were a little higher in experiment 1b than in experiment 5a.

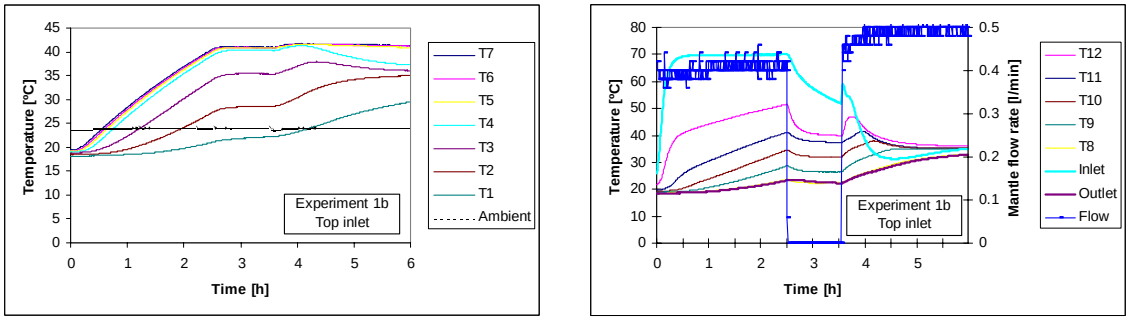

Figure 4-25: Measured temperatures and flow rate for experiment 1b (Top inlet).

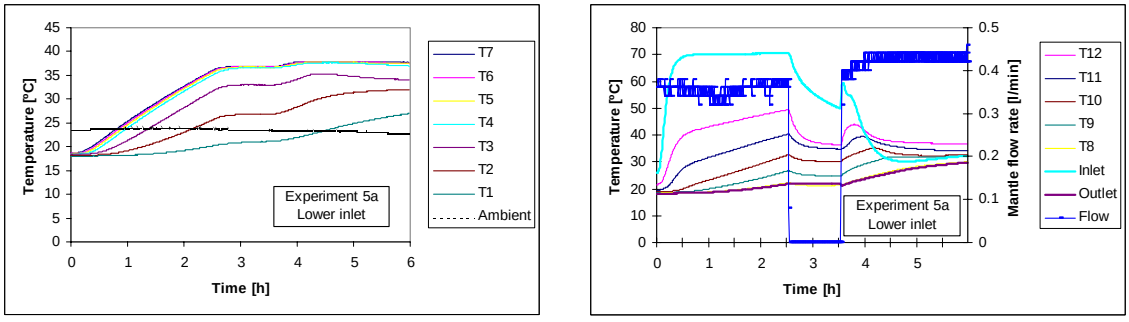

Figure 4-26: Measured temperatures and flow rate for experiment 5a (Lower inlet).

The rate of heat transfer to each volume in the inner tank during the two experiments is shown in Figure 4-27. In the first part of the experiments, where there was a high inlet temperature to the mantle, the rate of heat transfer to the upper part of the tank was highest in experiment 1b where the mantle inlet port is located at the top. The peaks of the rate of heat transfer to the volumes in the upper part were around 250-300 W in experiment 1b, while it was around 200-250 W in experiment 5a. In the last part of the experiment, where the mantle inlet temperature was low, the major difference is that the rate of heat transfer to volume 4 was below 0 W in experiment 1b, while it was about 0 W in experiment 5a. Thus, when the mantle inlet port is located at the top, heat is removed from the tank at the level of the mantle top in the last part of the experiment.

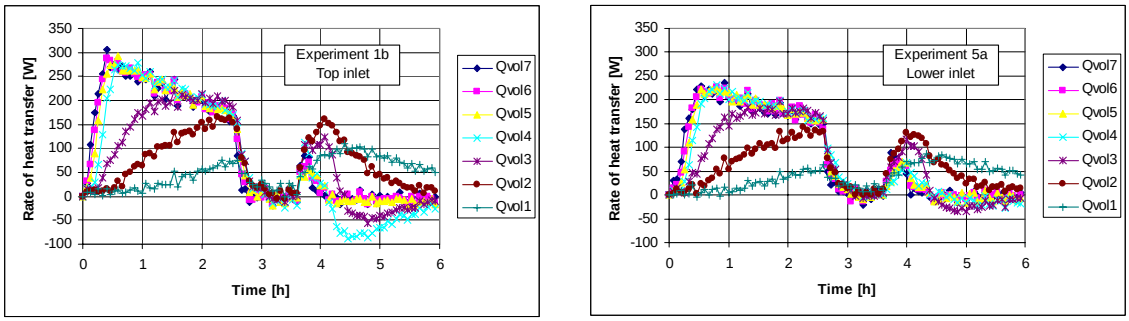

Figure 4-27: Rate of heat transfer to each volume in inner tank in experiments 1b and 5a.

The thermal stratification at start and at the end for both experiments is shown in Figure 4-28. The dimensionless temperature in the middle of the tank was, at the end, lower in experiment 1b than in experiment 5a.

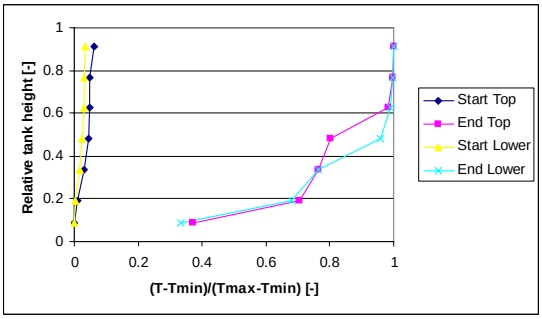

Figure 4-28: Thermal stratification in experiment 1b and experiment 5a.

<u>Experiments 2b and 6a (Initially mixed, 0.8 l/min, 1" inlet (Position: top and lower)):</u>
The measured temperatures for experiment 2b (Top inlet) and experiment 6a (lower inlet) are shown in Figure 4-29 and Figure 4-30. The mantle inlet temperature and the ambient temperature were close to identical in the experiments. The mantle flow rate was a little higher in experiment 2b than in experiment 6a.

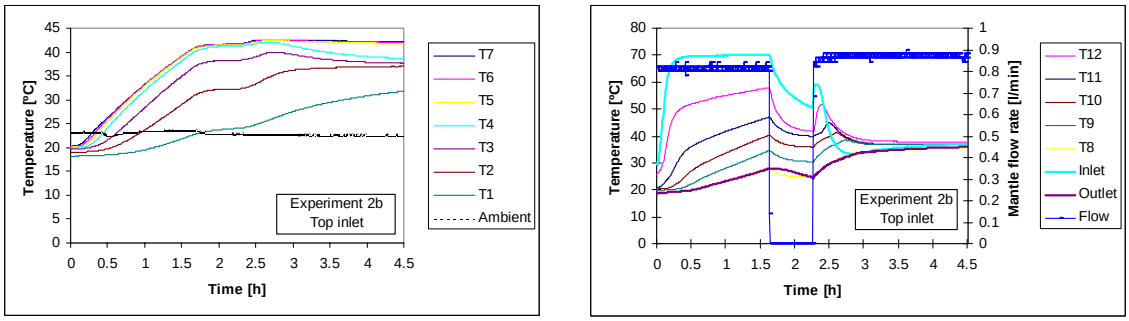

Figure 4-29: Measured temperatures and flow rate for experiment 2b (Top inlet).

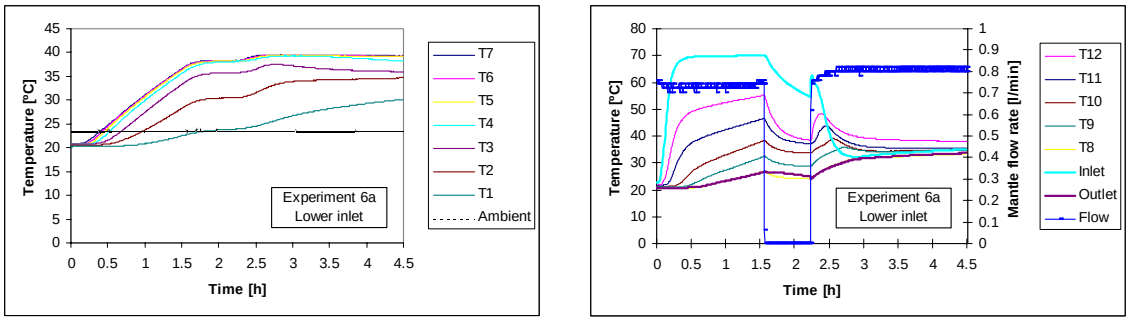

Figure 4-30: Measured temperatures and flow rate for experiment 6a (Lower inlet).

The rate of heat transfer to each volume in the inner tank during the two experiments is shown in Figure 4-31. In the first part of the experiments, where there was a high inlet temperature to the mantle, the rate of heat transfer to the upper part of the tank was highest in experiment 2b where the mantle inlet port is located at the top. The peaks of the rate of heat transfer to the volumes in the upper part were around 400-475 W in experiment 2b, while it was around 300-400 W in experiment 6a. In the last part of the experiment, where the mantle inlet temperature was low, the major difference is that the rate of heat transfer to volume 4 was below 0 W in experiment 2b while it was about 0 W in experiment 6a. Thus, when the mantle inlet port is located at the top, heat is removed from the tank at the level of the mantle top in the last part of the experiment.
The thermal stratification at the start and at the end for both experiments is shown in Figure 4-32. The dimensionless temperature in the middle of the tank was at the end lower in experiment 2b than in experiment 6a.

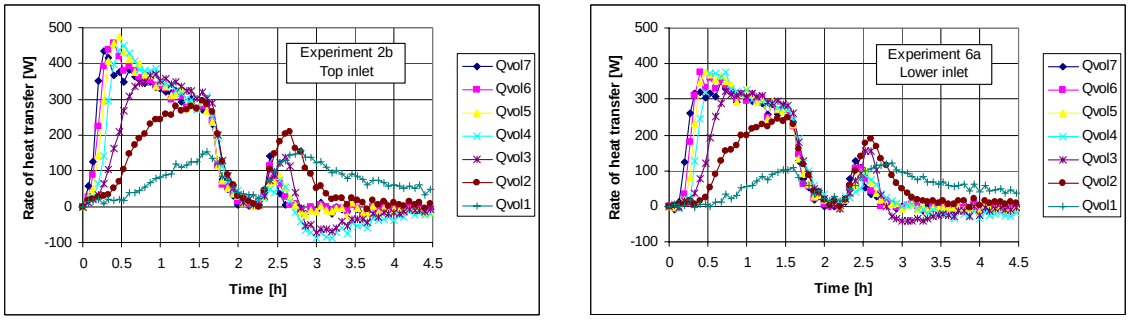

Figure 4-31: Rate of heat transfer to each volume in inner tank in experiments 2b and 6a.

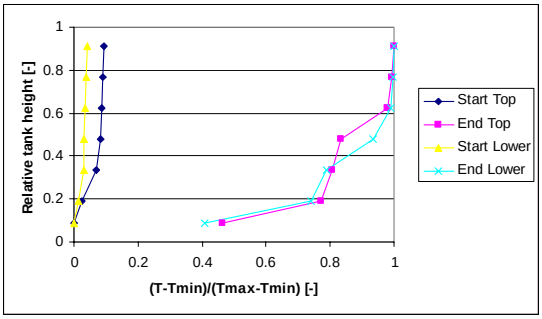

Figure 4-32: Thermal stratification in experiment 2b and experiment 6a.

Experiments 3b and 7a (Initially stratified, 0.4 l/min, 1" inlet (Position: top and lower)):
The measured temperatures for experiment 3b (Top inlet) and experiment 7a (lower inlet) are shown in Figure 4-33 and Figure 4-34. The mantle inlet temperature and the ambient temperature were close to identical in the experiments. The mantle flow rate was a little higher in experiment 3b than in experiment 7a.

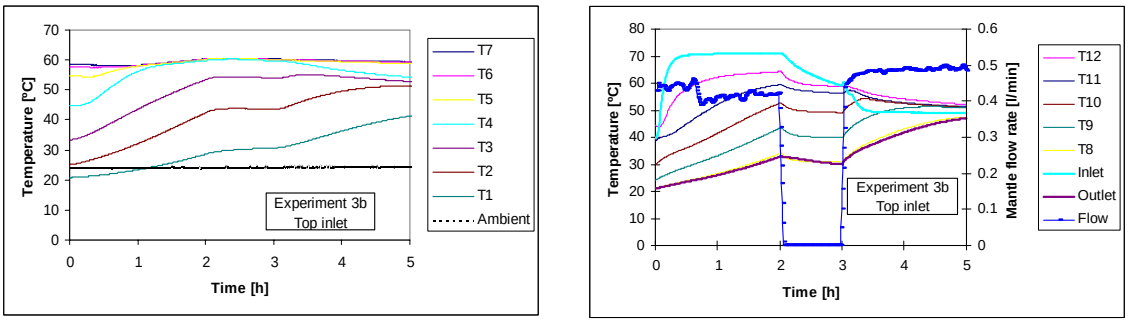

Figure 4-33: Measured temperatures and flow rate for experiment 3b (Top inlet).

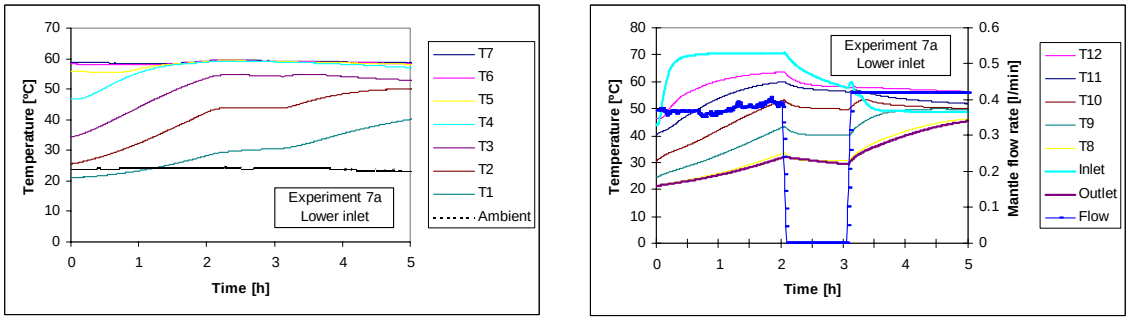

Figure 4-34: Measured temperatures and flow rate for experiment 7a (Lower inlet).

The rate of heat transfer to each volume in the inner tank during the two experiments is shown in Figure 4-35. In the first part of the experiment the rate of heat transfer to the tank was highest in experiment 3b with a peak value of 450 W compared to a peak value of 300 W in experiment 7a. The tank was in both experiments initially stratified so most of the heat transfer goes to volume 1 – volume 4. In the last part of the experiment, where the mantle inlet temperature was low, the major difference is that the rate of heat transfer to volume 4 was below 0 W in experiment 3b, while it was about 0

W in experiment 7a. Thus, when the mantle inlet port is located at the top, heat is removed from the tank at the level of the mantle top in the last part of the experiment.

The thermal stratification at the start and at the end for both experiments is shown in Figure 4-36. The dimensionless temperature in the middle of the tank was at the end lower in experiment 3b than in experiment 7a.

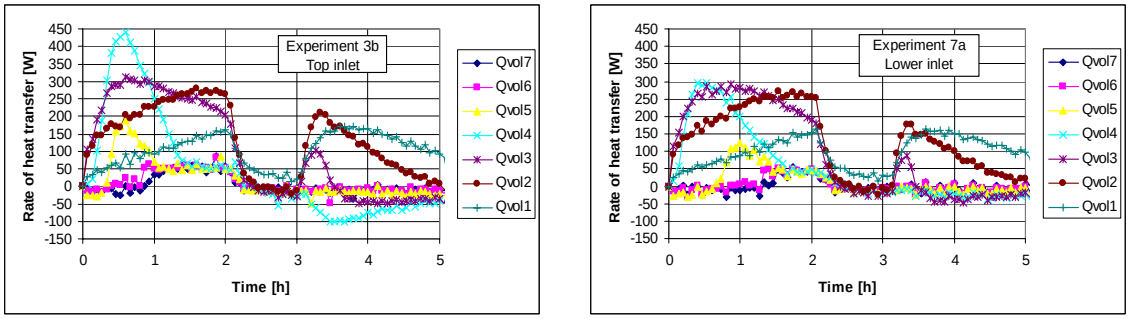

Figure 4-35: Rate of heat transfer to each volume in inner tank in experiments 3b and 7a.

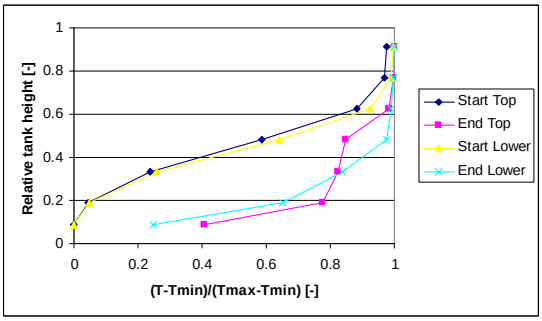

Figure 4-36: Thermal stratification in experiment 3b and experiment 7a.

Experiments 4b and 8a (Initially stratified, 0.8 l/min, 1" inlet (Position: top and lower)):
The measured temperatures for experiment 4b (Top inlet) and experiment 8a (lower inlet) are shown in Figure 4-37 and Figure 4-38. The mantle inlet temperature, the mantle flow rate and the ambient temperature were close to identical in the experiments.

The rate of heat transfer to each volume in the inner tank during the two experiments is shown in Figure 4-39. In the first part of the experiment the rate of heat transfer to the tank was highest in experiment 4b with a peak value of 670 W compared to a peak value of 575 W in experiment 8a. The tank was in both experiments initially stratified so most of the heat transfer goes to volume 1 – volume 4. In the last part of the experiment, where the mantle inlet temperature was low, the major difference is that the rate of heat transfer to volume 4 was below 0 W in experiment 4b, while it was about 0 W in experiment 8a. Thus, when the mantle inlet port is located at the top, heat is removed from the tank at the level of the mantle top in the last part of the experiment.

The thermal stratification at the start and at the end for both experiments is shown in Figure 4-40. The dimensionless temperature in the middle of the tank was at the end lower in experiment 4b than in experiment 8a.

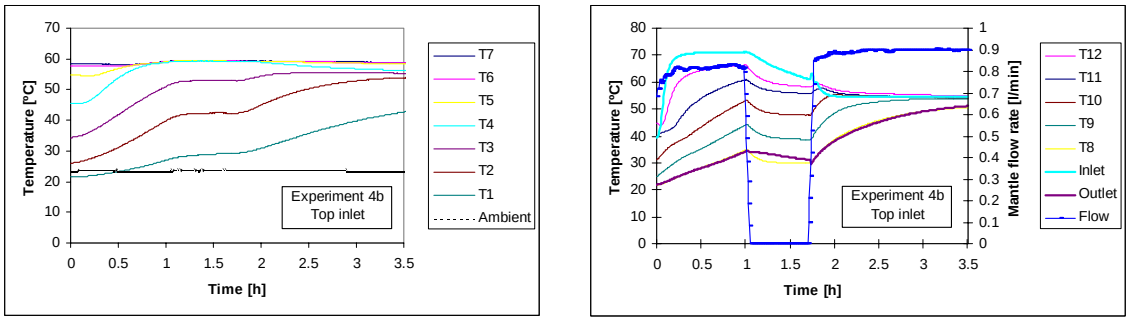

Figure 4-37: Measured temperatures and flow rate for experiment 4b (Top inlet).

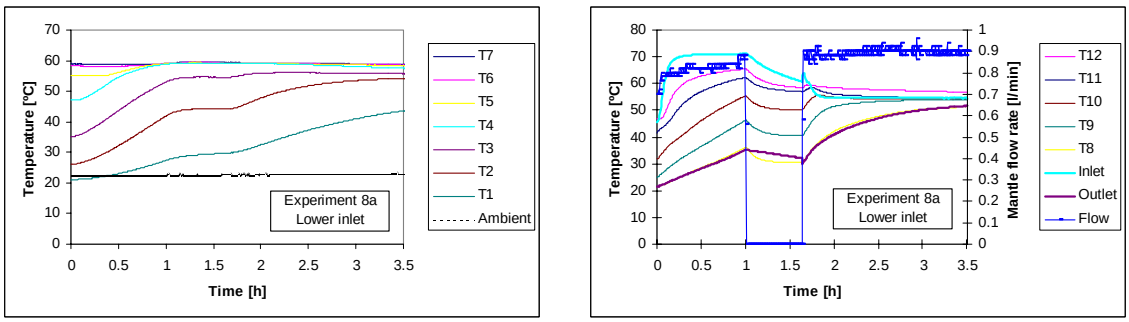

Figure 4-38: Measured temperatures and flow rate for experiment 8a (Lower inlet).

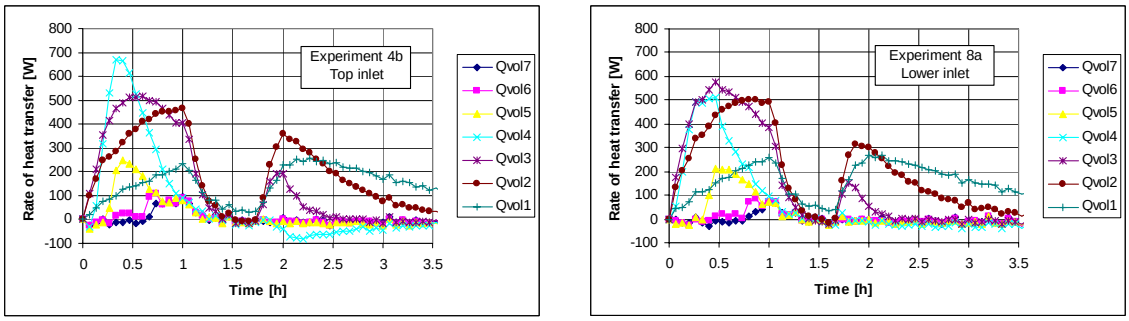

Figure 4-39: Rate of heat transfer to each volume in inner tank in experiments 4b and 8a.

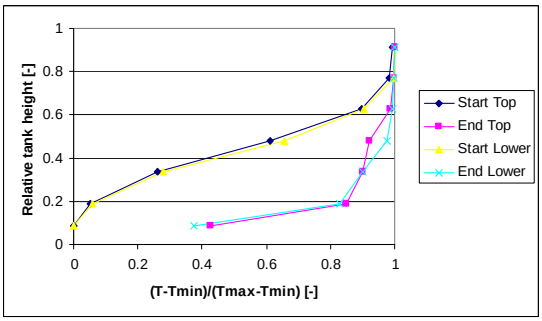

Figure 4-40: Thermal stratification in experiment 4b and experiment 8a.

Energy delivery to top and bottom of tank:

Thermal stratification is important to achieve a high thermal performance. Therefore it is of interest to quantify the amount of energy delivered to the top part and the bottom part of the tank during the experiments. Basically it is preferable if most of the energy is delivered to the top to achieve a high degree of thermal stratification.

In order to see the effect from the different mantle inlet locations and the initial tank conditions, the energy delivery to the top part and the bottom part was calculated according to equations 4.3 and 4.4 for experiments 1b, 3b, 5a and 7a.

Figure 4-41 shows the accumulated energy delivered to either the top part or the bottom part of the tank for the first part of experiments 1b and 5a where the mantle inlet temperature was 70ºC. Figure 4-42 shows the accumulated energy delivered to either the top part or the bottom part of the tank for the last part of experiments 1b and 5a where the mantle inlet temperature was 30-35ºC.

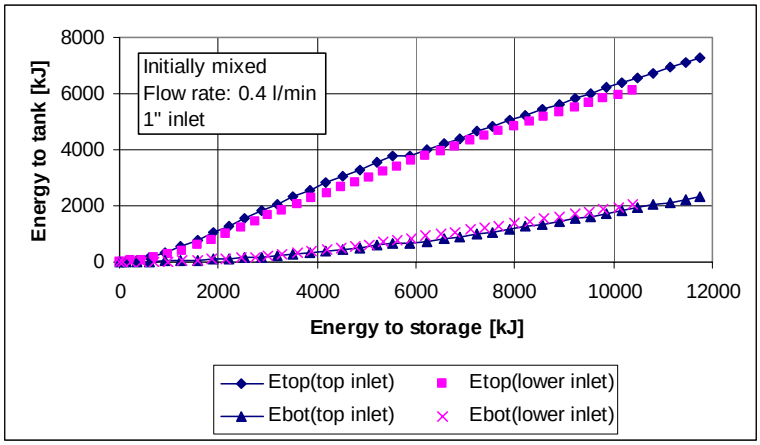

Figure 4-41: Accumulated energy delivered to the top (Etop) and bottom (Ebot) of the tank as a function of the accumulated energy delivered to the storage by the mantle fluid in the first part of experiments 1b and 5a where the mantle inlet temperature was 70ºC.

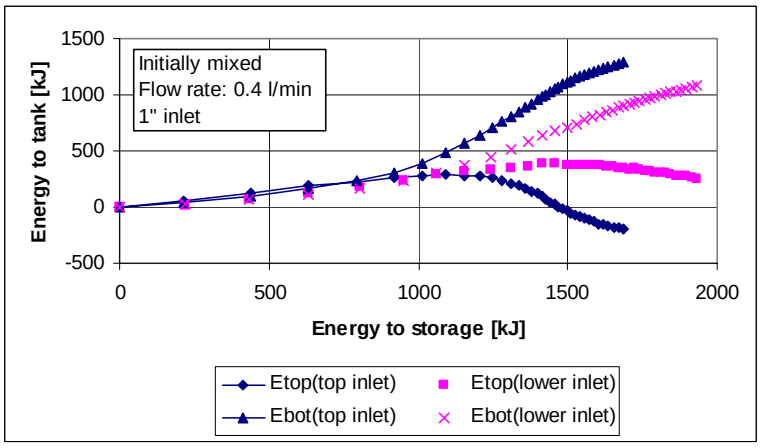

Figure 4-42: Accumulated energy delivered to the top (Etop) and bottom (Ebot) of the tank as a function of the accumulated energy delivered to the storage by the mantle fluid in the last part of experiments 1b and 5a where the mantle inlet temperature was 30-35ºC.

The results in Figure 4-41 show that when the mantle inlet temperature is high (70ºC) and the tank is initially mixed at a temperature of 20ºC, more energy was delivered to the top part than to the bottom part, and more energy was delivered to the top part when the mantle inlet was located at the top. Figure 4-42 shows, on the other hand, that when the mantle inlet temperature was low (30-35ºC), more energy was delivered to the bottom part than to the top part of the tank. More energy was delivered to the top part when the mantle inlet was moved down than when the mantle inlet was located at the top. There was a decrease in the energy content at the top part of the tank with the mantle inlet located at the top.

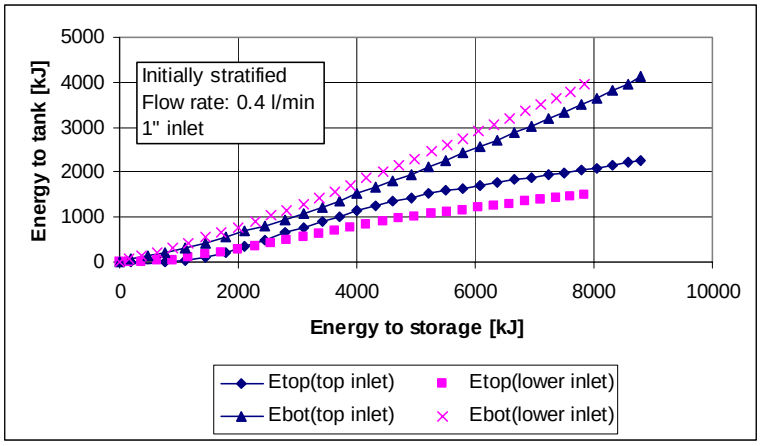

Figure 4-43: Accumulated energy delivered to the top (Etop) and bottom (Ebot) of the tank as a function of the accumulated energy delivered to the storage by the mantle fluid in the first part of experiments 3b and 7a where the mantle inlet temperature was 70ºC.

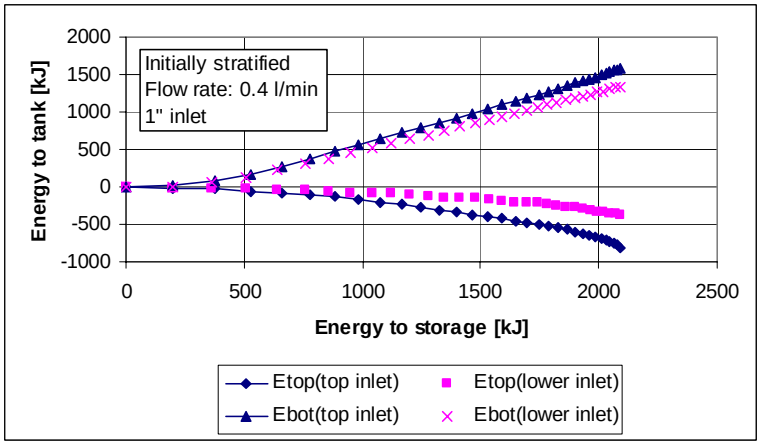

Figure 4-44: Accumulated energy delivered to the top (Etop) and bottom (Ebot) of the tank as a function of the accumulated energy delivered to the storage by the mantle fluid in the last part of experiments 3b and 7a where the mantle inlet temperature was 50ºC.

Figure 4-43 shows the accumulated energy delivered to either the top part or the bottom part of the tank for the first part of experiments 3b and 7a where the mantle inlet temperature was 70ºC. Figure 4-44 shows the accumulated energy delivered to either the top part or the bottom part of the tank for the last part of experiments 3b and 7a where the mantle inlet temperature was 50ºC.

The results in Figure 4-43 and Figure 4-44 show that when the tank is initially stratified, more energy was delivered to the bottom part than to the top part for both high and low inlet temperatures. With a high mantle inlet temperature more energy was delivered to the top part of the tank with the mantle inlet at the top than to the tank with the mantle inlet moved down. With a low mantle inlet temperature, there was a decrease in the energy content in the top part of the tank and the decrease was smallest for the tank with the mantle inlet moved down.

Consequently, under some conditions it is preferable to have the mantle inlet located at the top, under other conditions it is preferable to have the mantle inlet located at a lower position.

4.3 Side-by-side laboratory test

Two small low-flow solar domestic hot-water systems with mantle tanks as heat storage were tested under the same realistic conditions side-by-side in the laboratory test facility described in section 3.3. The systems are identical, with exception of the mantle tanks. One of the mantle tanks has the mantle inlet port located at the top of the mantle and the other mantle tank has the mantle inlet port moved 0.175 m down from the top of the mantle; the two inlet positions are showed in Figure 4-5. Both of the two mantle tanks make use of electric heating elements as auxiliary energy supply systems, and the electric heating elements heat up the top volume to 51ºC during all hours.

The solar collector in each system is identical and of the type ST-NA (Nielsen, 2000) with an area of 2.51 m². They consist of a cover of 4 mm low iron content glass with a Teflon foil on the inside and an absorber based on Sunstrips.

The solar collector loop in both systems is equipped with a Grundfos circulation pump (type UPS 25-40), which has been running at stage 2 to secure a flow rate of about 0.5 l/min throughout the measuring period. The circulation pump is controlled by a differential thermostat, which measures the temperature difference between the outlet from the solar collector and the bottom of the mantle. The differential thermostat has a start/stop set point at 10/2 K.

The two solar heating systems were tested with the same daily hot-water consumption of 0.100 m³. An energy quantity of 1.525 kWh, corresponding to 0.033 m³ of hot water heated from 10ºC to 50ºC, was tapped from each system three times each day: at 7 am, 12 am and 7 pm.

The test period was from the beginning of March to the middle of November 2003 with duration of 252 days.

The data for the two SDHW systems are given in Table 4-5. The solar collector in each of the two systems is shown in Figure 4-45, and Figure 4-46 shows the heat storage in each of the two systems.

Tank design	
Inner tank	
Hot-water tank volume, [m³]	0.175
Inner height [m]	1.45
Inner diameter, [m]	0.394
Tank wall thickness, [m]	0.003
Auxiliary volume, [m³]	0.063
Power of auxiliary energy supply, [W]	1200
Mantle	
Mantle volume, [m³]	0.0319
Mantle height, [m]	0.7
Mantle gap, [m]	0.0335
Position of mantle inlet	Top/0.175 m from top
Inside diameter of mantle inlet, [m]	0.0189
Insulation	
Material	Mineral wool
Insulation top, [m]	0.13
Insulation side above/below mantle, [m]	0.06
Insulation side mantle, [m]	0.06
Insulation bottom, [m]	0.0
Solar collector	
Area, [m²]	2.51
Start efficiency, [-]	0.801
1st order heat loss coefficient, [W/m²·K]	3.21
2nd order heat loss coefficient, [W/m²·K²]	0.013
Incident angle modifier (tangens equation)	a = 3.6
Heat capacity, [J/m²·K]	5339
Tilt, [°]	45
Orientation	South
Solar collector loop	
Pipe material	Copper
Outer diameter, [m]	0.010
Inner diameter, [m]	0.008
Insulation thickness (PUR foam), [m]	0.01
Length of pipe from storage to collector, indoor, [m]	4.6
Length of pipe from storage to collector, outdoor, [m]	13.3
Length of pipe from collector to storage, indoor, [m]	5.1
Length of pipe from collector to storage, outdoor, [m]	10.0
Solar collector fluid (propylene glycol / water mixture), [%]	40
Power of circulation pump, [W]	50

Table 4-5: Data for the two SDHW systems in the side-by-side laboratory test.

4.3.1 Measured collector efficiency

The efficiency of the solar collector in the two tested systems were compared in order to make sure that the collectors have the same efficiency. The efficiency was compared on days with a clear sky and the following days in 2003 were chosen: 30/7, 31/7, 6/8, 9/8, 10/8, 13/10, 14/10, 15/10 and 16/10. The efficiency was measured when the total solar irradiance on the solar collectors was higher than 800 W/m² and when the inlet temperature to the collector was changing less than 0.7 K and the outlet temperature was changing less than 0.7 K in the sampling period of 15 minutes. The temperature limit of 0.7 K on the inlet temperature to the solar collector is larger than the limit of

±0.1 K given in ISO/DIS 9806 (ISO, 1992) for measuring thermal performance tests for solar collectors. However, the limit could not be reduced without a considerable loss of data points and for the purpose of comparing the solar collectors the limits are considered to be reasonable. The minimum limit of 800 W/m² on the solar irradiance caused that the efficiency was measured at the middle of the day and the incident angle was below 25º in all measurements.

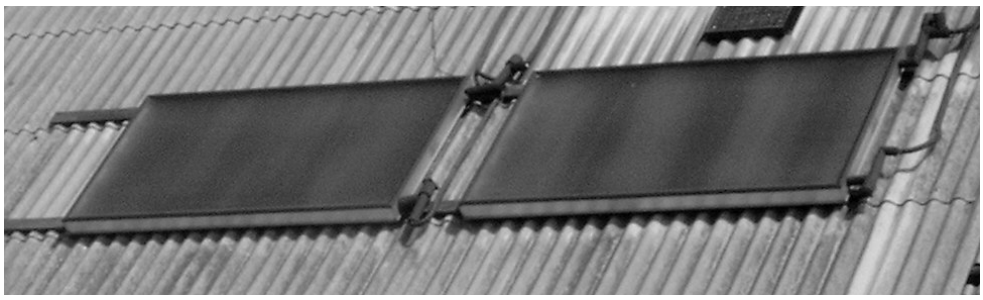

Figure 4-45: The solar collector in each of the two systems.

Figure 4-46: Left: Heat storage in system with lower mantle inlet. Right: Heat storage in system with top mantle inlet.

The collector efficiency is given by:

$$\eta = \frac{Q_{coll}}{Q_{rad}} = \frac{\dot{V} \cdot \rho \cdot c_p \cdot \left(T_{coll,out} - T_{coll,in}\right)}{A \cdot G} \tag{4.6}$$

where

A	is the area of the collector, [m²]
c_p	is the specific heat of the collector fluid, [J/kg·K]
G	is the solar irradiance, [W/m²]
Q_{coll}	is the useful power extracted from the collector, [W]
Q_{rad}	is the total irradiance on the collector, [W]
$T_{coll,in}$	is the inlet temperature to the collector, [ºC]
$T_{coll,out}$	is the outlet temperature from the collector, [ºC]
$\dot{V}$	is the volume flow rate in the collector, [m³/s]
η	is the instantaneous collector efficiency, [-]
ρ	is the collector fluid density, [kg/m³]

The mean collector fluid temperature, T_m, is, as a rough assumption, given by:

$$T_m = \frac{T_{coll,in} + T_{coll,out}}{2} \tag{4.7}$$

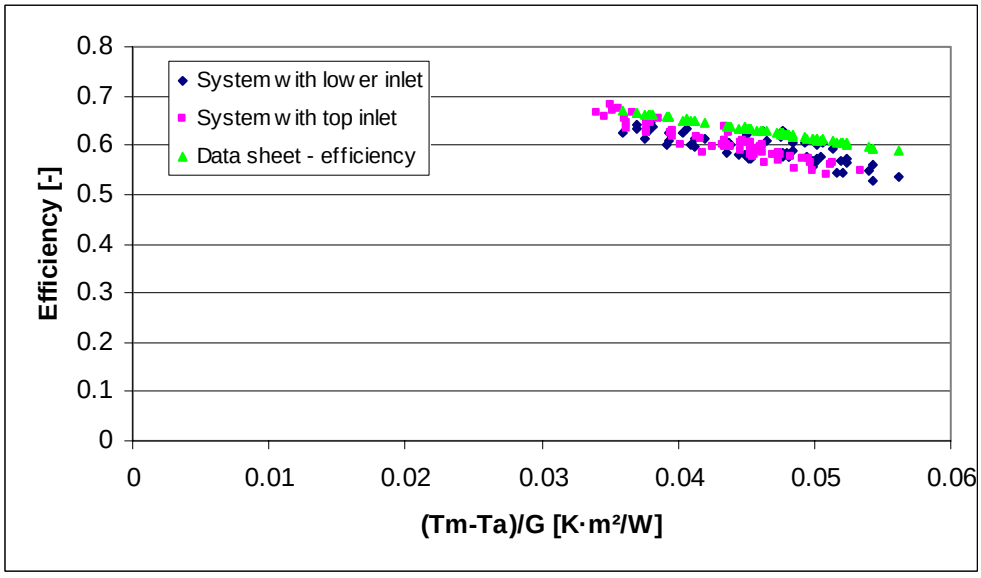

Figure 4-47: Solar collector efficiency for the collector in each system and from data sheet of ST-NA collector, (Nielsen, 2000).

Figure 4-47 shows the measured efficiency as a function the difference between mean collector fluid temperature and ambient temperature divided by the solar irradiance. It is seen that there is minor differences in the instantaneous efficiency for the two solar collectors. Furthermore, it is seen that the measured efficiency for the two collectors are below the efficiency curve from the data sheet of the collector (Nielsen, J.E. 2000). Based on Figure 4-47 it is concluded that the efficiency of the two collectors is the same

and they can be used in the comparison of the thermal performance of the two systems with different mantle inlet position.

4.3.2 Thermal performance of systems

The thermal performance of the two systems is compared by the net utilised solar energy and the solar fraction of the systems. The net utilised solar energy, E_{net}, and the solar fraction, *f*, are defined by:

$$E_{net} = E_{dhw} - E_{aux} \tag{4.8}$$

$$f = \frac{E_{net}}{E_{dhw}} \tag{4.9}$$

where

E_{aux}	is the measured auxiliary energy supply, [kWh]
E_{dhw}	is the measured domestic hot-water load, [kWh]
E_{net}	is the net utilised solar energy, [kWh]
f	is the solar fraction, [-]

The measured energy quantities for the two systems are shown in Table 4-6. From Table 4-6, it is seen that the two systems had a relatively high solar fraction (0.66-0.68) in the period and that the thermal performance for the system with the lower mantle inlet was higher than the thermal performance of the system with top inlet; the increase in net utilised solar energy is 2%.

Energy quantity	SDHW system with top mantle inlet	SDHW system with lower mantle inlet
E_{dhw}, [kWh]	1158	1158
E_{aux}, [kWh]	395	377
E_{net}, [kWh]	763	781
f, [-]	0.66	0.68

Table 4-6: Measured energy quantities for the two SDHW systems in the period 3/3 2003 –10/11 2003.

At high solar fractions, large periods with high inlet temperatures to the mantle are expected and when the system with the lower mantle inlet has a higher thermal performance at high solar fractions, the relative improvement by moving the inlet down is expected to be higher for smaller solar fractions where lower inlet temperatures are expected. The 252 days measuring period have been divided into 36 periods of 7 days. The performance ratio as a function of the solar fraction for the system with top inlet for the 36 periods is shown in Figure 4-48. The performance ratio is defined as:

$$\text{Performance ratio} = \frac{E_{net,lower\ inlet}}{E_{net,top\ inlet}} \tag{4.10}$$

Figure 4-48 shows the expected tendency that the performance ratio increases for lower solar fractions. However, the performance ratio drops below 1 for two 7-day periods at

solar fractions of 0.65-0.70, which can be explained by the distribution of the solar irradiance in these two 7-day periods. Each of the two 7-day periods have 4 days with a clear sky and 3 days more or less overcast, while the other 7-day periods, where the solar fraction is around 0.6-0.7 and the performance ratio is above unity, have clouds every day, which result in lower inlet temperatures to the mantle than on the days with a clear sky. Based on the tendency that the performance ratio increases for lower solar fractions and that the solar fraction was relatively high in most of the measuring period it can be concluded that these measurements show that the thermal performance of this SDHW system can be increased by moving the mantle inlet down.

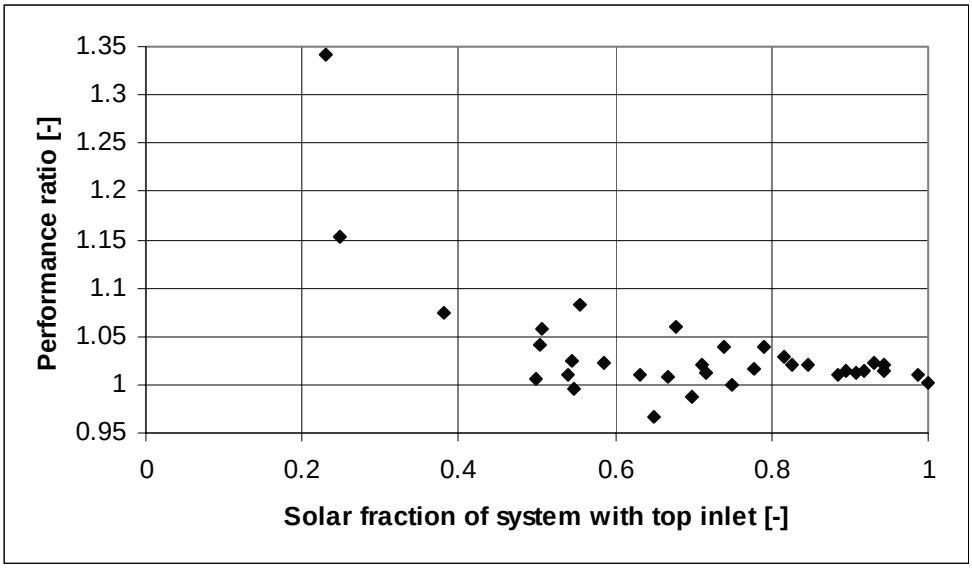

Figure 4-48: Performance ratio as a function of the solar fraction for the system with the mantle inlet located at the top.

4.4 Summary

In this chapter it was investigated how different mantle inlet designs influence the thermal stratification and the performance of mantle tanks. A wide range of thermal experiments of mantle tanks with different designs of the mantle inlet port was carried out in a heat storage test facility. The experiments showed that the size of the mantle inlet port has a minor effect on the thermal stratification in mantle tanks; this is mainly due to the low flow rates and thereby small inlet velocities that are typical in low flow systems. For larger flow rates than considered in this thesis, the mantle inlet size might have an influence. On the other hand, the thermal experiments showed that the vertical position of the mantle inlet port has an influence on the thermal stratification in mantle heat exchangers. In cases with a mantle inlet temperature higher than the mantle top temperature, it is preferable to have the mantle inlet located at the top. In cases with a mantle inlet temperature lower than the mantle top temperature, it is preferable to have the mantle inlet located at a lower position. Furthermore, the experiments showed that for an initially stratified tank and with the mantle inlet temperature either 10 K higher or 10 K lower than the tank top temperature, more energy is delivered to the bottom part of the tanks than to the top part.

Side-by-side laboratory tests were carried out with SDHW systems with different mantle inlet positions. The solar fraction of the two SDHW systems was relatively high (0.66-0.68) during the period of the measurements. The SDHW system with the lower mantle inlet had, in the period of measurements, a 2% higher thermal performance than the SDHW system with the mantle inlet located at the top of the mantle. In periods with a lower solar fraction, the inlet temperature to the mantle will be lower and the experiments in this chapter show that the system with the mantle inlet moved down will have the best thermal performance in these periods. Consequently, the investigations in this chapter show that moving the mantle inlet down can increase the thermal performance of this SDHW system.

5. Validation of CFD-model

5.1 Introduction

The results presented in the coming chapters are from numerical simulations of mantle heat exchangers performed by the CFD-program FLUENT (FLUENT, 2001). The results from the numerical simulations must be validated through a comparison with experimental results. The basic results from the CFD calculations include temperature distribution and flow structures. Therefore, experiments of the following type were necessary for the validation:

Thermal experiments:
With a steel mantle tank, different transient thermal experiments were carried out in the heat storage test facility. The results were used to evaluate the calculated temperature distribution and the mantle outlet temperature. The experiments were carried out in the heat storage test facility at Department of Civil Engineering, Technical University of Denmark.

Flow visualisation:
With a transparent glass mantle tank, flow visualisation experiments that illustrate the flow structure in the mantle and in the inner tank were carried out with a PIV system. These results were used to evaluate the calculated flow structures. The experiments were carried out at School of Mechanical and Manufacturing Engineering, University of New South Wales, Sydney, Australia.

Besides the thermal validation and the validation of the calculated flow field, the following calculations were carried out with the CFD-model to make a further validation of the model. With the CFD-model of the glass mantle tank, investigations of the influence of using a turbulence model instead of a laminar model on the calculated temperatures as well as a test of the grid dependence and the time dependence of the flow were carried out.

5.2 Thermal experiments

The thermal experiments were carried out in the heat storage test facility described in section 3.2. A steel tank was used for the thermal experiments. The tank is a prototype and is like a standard Danish mantle tank used for small low-flow solar domestic hot water systems. The mantle and the inner tank volume, as well as the ratio between the solar volume and the volume above the mantle, are similar to commercial solar water heater tanks used in Denmark. The data of the mantle tank is given in Table 5-1. The mantle tank is shown in Figure 4-3.
The mantle tank was tested by two different heating sequences:

Hot inlet condition:
For an initially stratified inner tank with temperatures of 16-20ºC in the bottom and 60ºC in the top, a 2-hour period with a hot inlet condition of 70ºC was carried out. The

mantle flow rate was 0.44 l/min. This operation condition could be a typical situation for a SDHW system at noon on a day where the sun shines and heats up the collector fluid resulting in a high mantle inlet temperature. Hot means a mantle inlet temperature higher than the core tank temperature at the top of the mantle.

Warm inlet condition:
For an initially stratified inner tank with temperatures of 28-30ºC in the bottom and 60ºC in the top, a 2-hour period with a warm inlet condition of 50ºC was carried out. The mantle flow rate was 0.49 l/min. This operation condition could be a typical situation for a SDHW system in the late afternoon on a day where the sun shines and heats up the collector fluid, but the mantle inlet temperature is lower than earlier in the day. Warm means a mantle inlet temperature between the core tank temperature at the top and bottom of the mantle.

Hot water tank volume [m³]	0.175
Volume in inner tank above mantle [m³]	0.081
Tank height [m]	1.44
Inner diameter of tank [m]	0.394
Material thickness [m]	0.003
Mantle height [m]	0.7
Mantle gap width [m]	0.0335
Mantle inlet position	0.175 m from top of mantle
Mantle inlet size	½" (ID = 0.0189 m)
Steel material properties	
Specific heat [J/kg·K]	460
Density [kg/m³]	7820
Thermal conductivity [W/m·K]	60
Insulation material	Mineral wool
Thermal conductivity of insulation material [W/m·K]	0.045
Insulation top [m]	0.13
Insulation sides [m]	0.03
Insulation bottom [m]	0

Table 5-1: Data for the mantle tank used in the thermal experiments.

5.2.1 CFD-model of steel mantle tank

A three-dimensional grid model of the steel mantle tank was developed. Only half a tank was modelled as symmetry was assumed in the centre plane through the inlet and outlet to and from the mantle. The model was simplified by modelling the top and the bottom of the tank with horizontal walls instead of the dome-shaped walls. Also the top and bottom mantle walls were modelled with horizontal walls instead of sloping walls.

Figure 5-1 shows the vertical grid distribution and Figure 5-2 shows the horizontal grid distribution of the model. The mesh was concentrated in high gradient regions near the walls. The computational domain consists of the inner tank and the mantle with the inlet and the outlet, and Table 5-2 shows the number of cells in the different parts of the model.

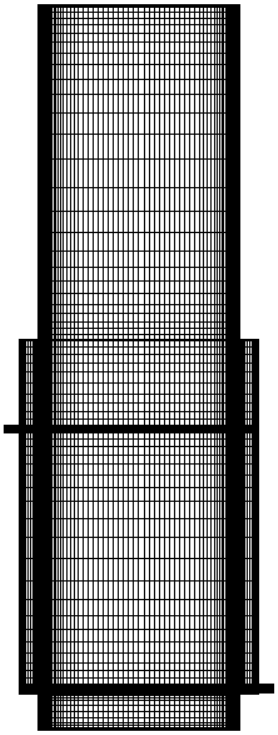

Figure 5-1: Vertical grid distribution of the CFD-model of the steel mantle tank.

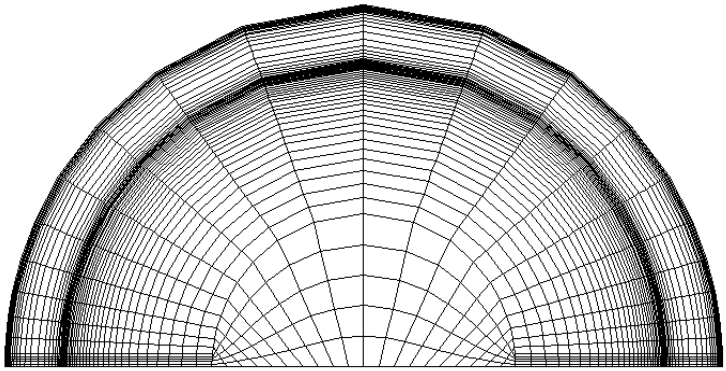

Figure 5-2: Horizontal grid distribution of the CFD-model of the steel mantle tank.

Water in inner tank	75650
Tank wall	23350
Mantle fluid	20500
Mantle wall	12250
Total	131750

Table 5-2: Number of computational cells in the CFD-model.

The model was supplied with physical properties for water, tank material (steel) and the mantle fluid (water). The mantle inlet temperature, the ambient temperature, and the

mantle fluid flow rate were specified to match the test conditions. The heat loss from the tank was modelled using outside convective heat transfer coefficients on the outside surfaces, and the thermal resistance of the insulation was included in the convective heat transfer coefficient.

The time step in the transient simulations was 0.5 s and turbulence was modelled with the *k*-ω-model. The commercial CFD-code FLUENT 6.0 was used and the background for the CFD-calculations is described in section 3.5.

5.2.2 Results: Hot inlet condition

A transient simulation of the experiment with the hot inlet condition was carried out with the CFD-model of the steel mantle tank. The model predictions were compared with measured temperatures T1-T7 (see Figure 3-2) in the inner tank and the outlet temperature from the mantle. If good agreement between these measured and calculated temperatures were achieved, both the temperature stratification in the inner tank and the cooling of the mantle fluid were modelled correctly and indicating that the heat exchange between mantle fluid and water in the inner tank also was modelled correctly.

Figure 5-3 shows the test conditions and the boundary conditions for the simulation model. There were small differences between the measured test conditions and the model boundary conditions, as the measured test conditions were not directly read into the model. However, the differences are relatively minor and should not have a significant influence on the results.

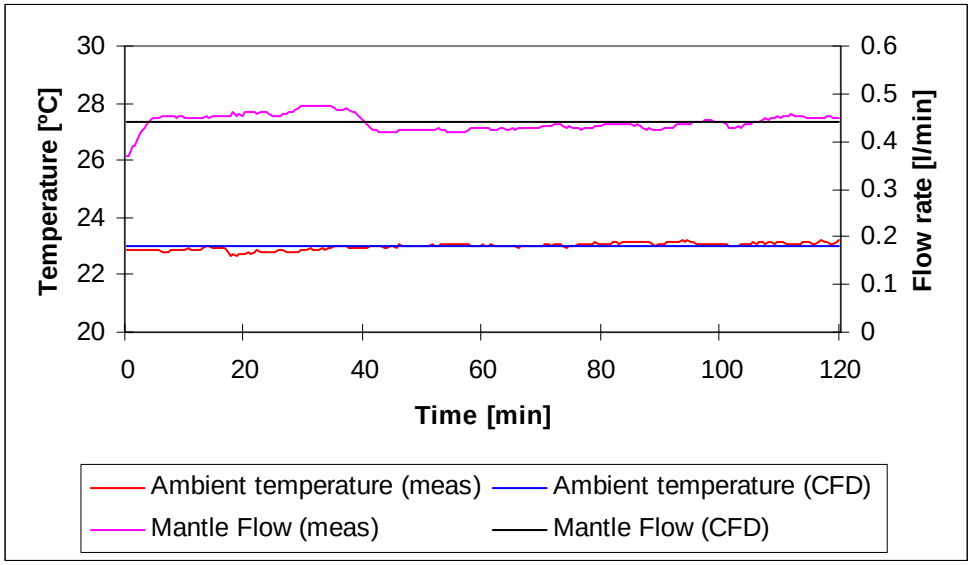

Figure 5-3: Test conditions and boundary conditions for simulation model for the hot inlet condition.

Figure 5-4 compares measured inner tank temperatures and CFD-predicted inner tank temperatures. Figure 5-5 compares the measured mantle inlet and mantle outlet temperatures with the values predicted by the CFD-model. The mantle inlet temperature was a boundary value in the CFD-model. There is a good agreement between measured and calculated temperatures in Figure 5-4 and Figure 5-5.

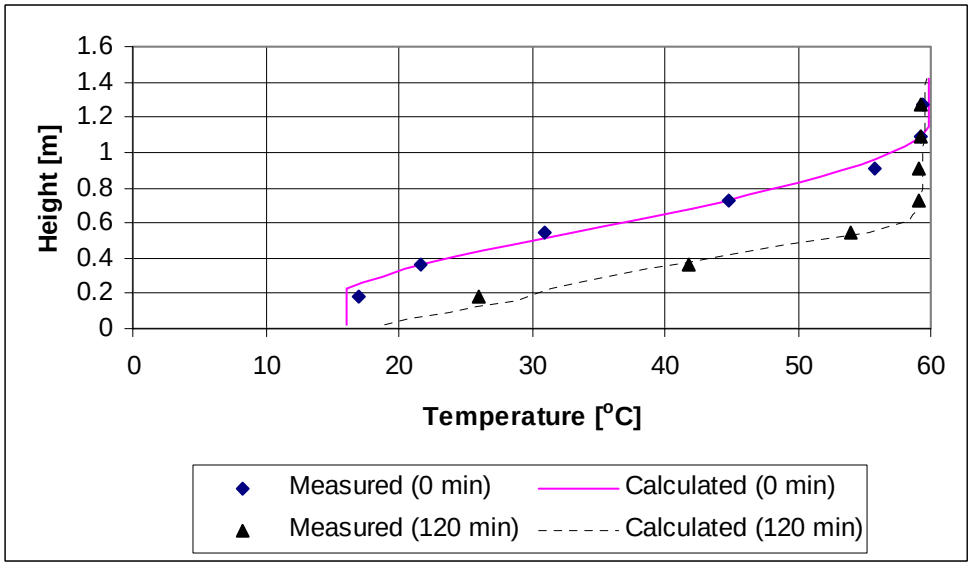

Figure 5-4: Measured and calculated inner tank temperatures for hot inlet condition.

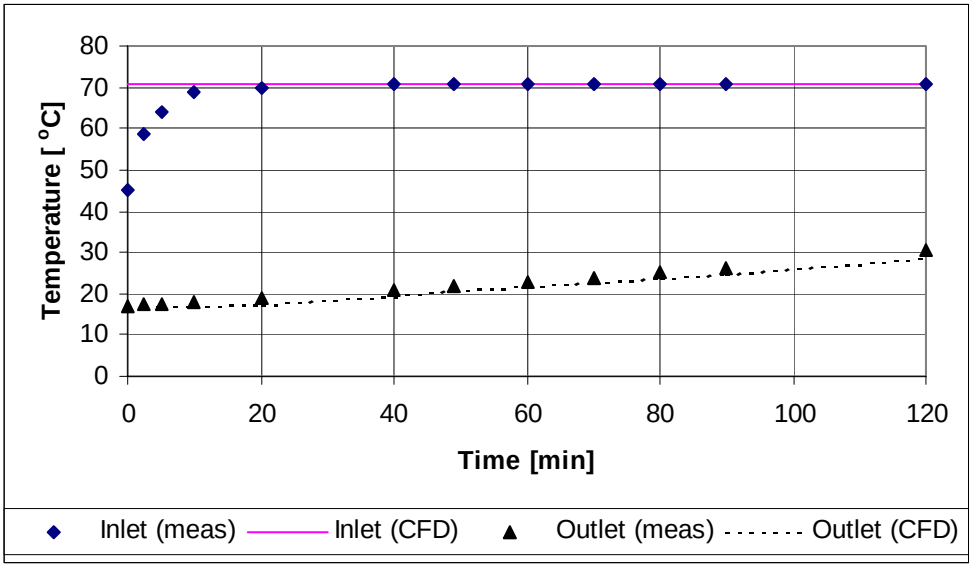

Figure 5-5: Measured and calculated mantle inlet and outlet temperatures for hot inlet condition.

5.2.3 Results: Warm inlet condition

A transient simulation of the experiment with the warm inlet condition was carried out with the CFD-model of the steel mantle tank. The model predictions were compared with measured temperatures T1-T7 (see Figure 3-2) in the inner tank and the outlet temperature from the mantle. If good agreement between these measured and calculated temperatures was achieved, both the temperature stratification in the inner tank and the cooling of the mantle fluid were modelled correctly and indicating that the heat exchange between mantle fluid and water in the inner tank was also modelled correctly.

Figure 5-6 shows the test conditions and the boundary conditions for the simulation model. There were small differences between the measured test conditions and the model boundary conditions, as the measured test conditions were not directly read into the model. However, the differences are relatively minor and should not have a significant influence on the results.

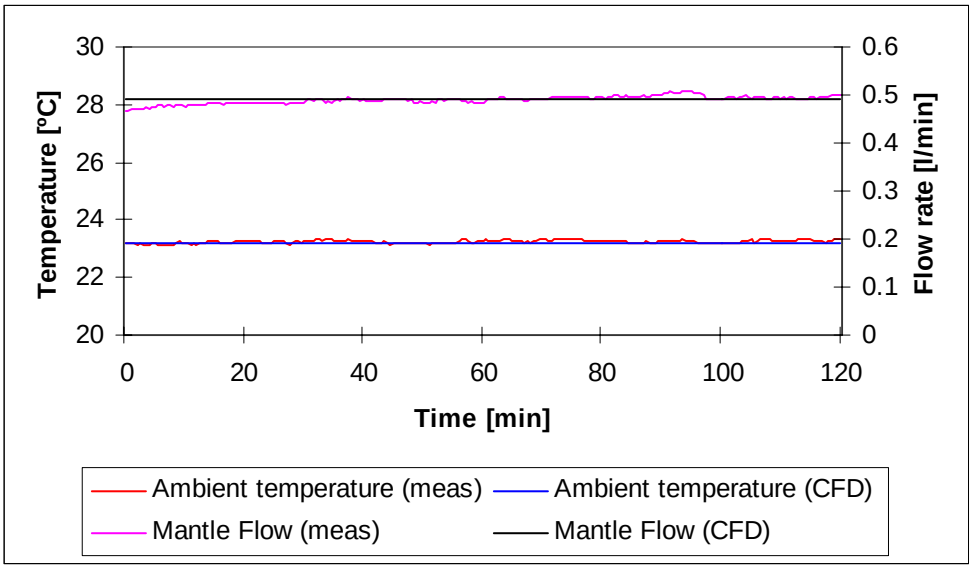

Figure 5-6: Test conditions and boundary conditions for simulation model for the warm inlet condition.

Figure 5-7 compares measured inner tank temperatures and CFD-predicted inner tank temperatures. Figure 5-8 compares the measured mantle inlet and mantle outlet temperatures with the values predicted by the CFD-model. The mantle inlet temperature was a boundary value in the CFD-model. There is a good agreement between measured and calculated temperatures in Figure 5-7 and Figure 5-8.

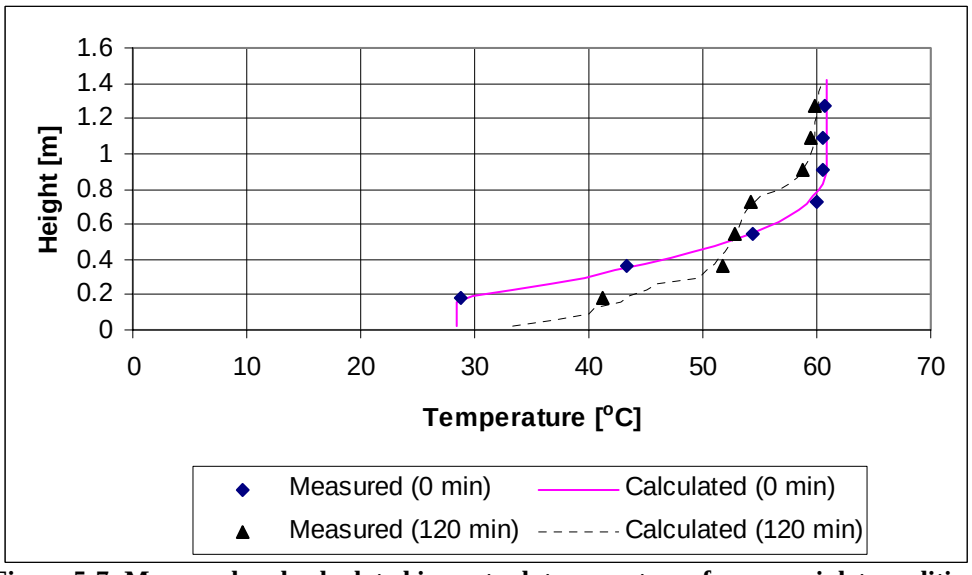

Figure 5-7: Measured and calculated inner tank temperatures for warm inlet condition.

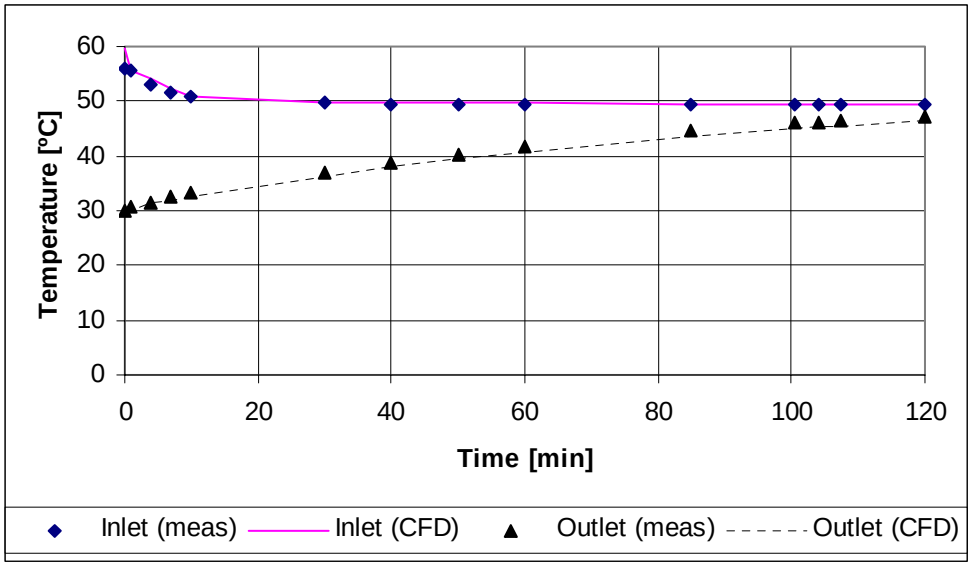

Figure 5-8: Measured and calculated mantle inlet and outlet temperatures for warm inlet condition.

5.3 Flow visualisation

The flow visualisation experiments were carried out using the heat storage control facility and PIV system described in section 3.4. A vertical glass mantle tank was designed for flow visualisation and velocity measurements. To allow the velocity measurements in the narrow mantle gap the glass model mantle tank was constructed as a square tank. The glass model tank is like a standard vertical mantle heat exchanger used in Denmark for small low-flow SDHW systems. The mantle and the inner tank volume, as well as the ratio between the solar volume and the volume above the mantle, are similar to commercial solar water heater tanks used in Denmark. Figure 5-9 shows a photograph of the glass model tank. The glass model tank was un-insulated during the experiments. The data of the mantle tank is given in Table 5-3. As described in section 3.4 the temperature of the water in the inner tank was measured at five points. Table 5-4 shows the position of the measuring points in Figure 3-6.

Figure 5-9: Glass model of mantle tank.

Inner tank volume [m³]	0.1255
Mantle volume [m³]	0.0194
Inner tank volume above mantle [m³]	0.0565
Inner tank volume inside mantle [m³]	0.0565
Inner tank volume under mantle [m³]	0.0125
Total height of inner tank [m]	0.9
Total height of mantle [m]	0.4
Tank wall thickness [m]	0.012
Mantle wall thickness [m]	0.012
Mantle gap width	0.033
Heat transfer area between mantle and tank [m²]	0.64
Mantle inlet position	0.094 m from top of mantle
Mantle inlet size	¾" (ID = 0.0244 m)
Glass material properties	
Specific heat [J/kg·K]	2250
Density [kg/m³]	840
Thermal conductivity [W/m·K]	1

Table 5-3: Data for the glass mantle tank.

Measuring point	Distance from bottom of inner tank, [m]
T1	0.80
T2	0.63
T3	0.46
T4	0.29
T5	0.12

Table 5-4: Position of the measuring points in the inner tank.

Three heating situations were studied:

Case 1:
Case 1 is for an initially mixed inner tank (~20ºC) with the mantle supplied with a constant flow rate of 0.45 l/min and an inlet temperature of 50ºC (hot inlet condition).

Case 2:
Case 2 is for an initially stratified inner tank (20ºC at the bottom and 40ºC at the top) with the mantle supplied with a constant flow rate of 0.45 l/min and an inlet temperature of 50ºC (hot inlet condition).

Case 3:
Case 3 is for an initially stratified inner tank (20ºC at the bottom and 40ºC at the top) with the mantle supplied with a constant flow rate of 0.45 l/min and an inlet temperature of 35ºC (warm inlet condition).

Case 1 could resemble a typical situation in a preheating tank for a SDHW system: After a large draw-off from the heat storage, the sun shines and heats up the collector fluid resulting in a high mantle inlet temperature that heats up the cold tank. Case 2 is similar to the hot inlet condition and case 3 is similar to the warm inlet condition for the thermal experiments with the steel mantle tank explained in section 5.2. However, the difference is that the maximum thermal difference over the glass plates was limited to

30 K to avoid thermal stress of the glass, and therefore the initial temperatures at the top of the tank had a lower value in the glass tank. The flow distribution in the inner tank was measured for case 1 and case 2 while the flow distribution in the mantle gap was measured for all three cases.

Half of the mantle was divided into 12 sections (see Figure 3-8) and the measurement area in the inner tank was divided into 6 sections (see Figure 3-9) in order to get sufficient resolution with the PIV system as described in section 3.4. The measured and calculated flow structure for the three cases were compared at the 12 sections in the mantle and at the 6 sections in the inner tank. Furthermore, measured and calculated horizontal velocities in the mantle were compared at a vertical line through the centre of the front side of the mantle, and measured and calculated vertical velocities in the inner tank were compared at three levels in the inner tank between the top of the mantle and the top of the tank in a plane 2.5 cm from the centre plane through the inlet and outlet to and from the mantle. The position of the vertical line for comparison in the mantle is shown in Figure 5-10 and the levels for comparison in the inner tank are shown in Figure 5-11.

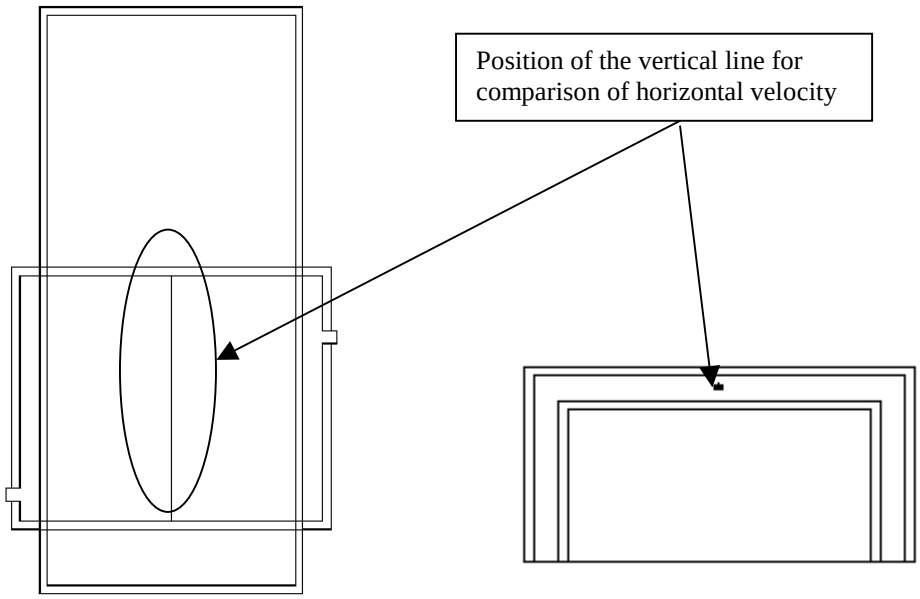

Figure 5-10: The position of the vertical line for comparison of horizontal velocity in mantle shown in a vertical outline (left) and in a horizontal outline (right) of the mantle heat exchanger.

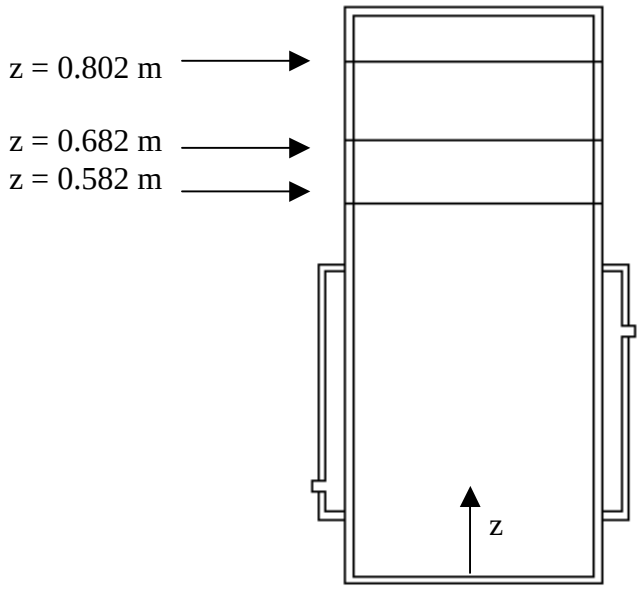

Figure 5-11: Three levels for comparison of vertical velocity in inner tank.

5.3.1 CFD-model of glass mantle tank

A three-dimensional grid model of the glass mantle tank was developed. Only half the tank was modelled as symmetry was assumed in the centre plane through the inlet and outlet to and from the mantle.

Figure 5-12 shows the vertical grid distribution and Figure 5-13 shows the horizontal grid distribution of the model. The mesh was concentrated in high gradient regions near the walls. The computational domain consists of the inner tank, the walls and the mantle with the inlet and the outlet and Table 5-5 shows the number of cells in the different parts of the model.

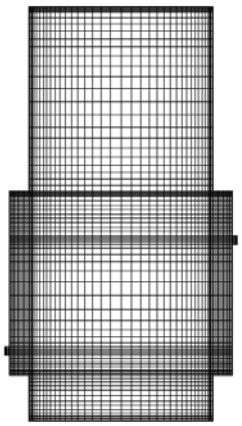

Figure 5-12: Vertical grid distribution of the CFD-model of the glass model tank.

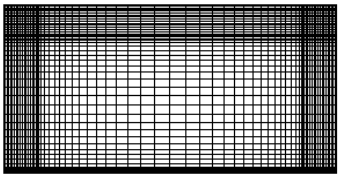

Figure 5-13: Horizontal grid distribution of the CFD-model of the glass model tank.

The model was supplied with physical properties for water, tank material (glass) and mantle fluid (water). The mantle inlet temperature, the ambient temperature, and the mantle fluid flow rate were specified to match the test conditions. Heat loss from the tank was modelled with an outside convective heat transfer coefficient of 5 $W/m^2 \cdot K$ on the outside surfaces.

Water in inner tank	57000
Tank wall	46200
Mantle fluid	43700
Mantle wall	46250
Total	193150

Table 5-5: Number of computational cells in the CFD-model of the glass model tank.

The time step in the transient simulations was 0.5 s and a laminar flow model was used. The commercial CFD-code FLUENT 6.0 was used and the background for the CFD-calculations is described in section 3.5.

5.3.2 Results: Flow distribution in the mantle gap

The flow distribution in the mantle gap was measured for all three cases and compared to the CFD-predictions.

Case 1:

Figure 5-14 shows the measured flow field in the centre plane of the mantle for case 1 after 40-120 minutes. The measured flow field shows that the inlet stream initially flows from the inlet to the top before it flows around the top of the mantle, and the flow then reverses and flows back towards the inlet at a level below the main inlet stream. During this reverse motion the fluid is cooled and hereafter the fluid drops slowly down, and then develops a return stream along the bottom of the mantle towards the outlet port. This flow structure is the same as was observed by Shah et al. (1999) with the top inlet configuration. Figure 5-15 shows the flow field after 40 minutes predicted by the CFD-model, and the calculated flow pattern is similar to the measured flow pattern. There is the same reverse flow, dead centre zone and suction from the outlet port.

Figure 5-16 shows the measured and calculated horizontal velocity profile at a vertical line (Figure 5-10) through the centre of the front side of the mantle for case 1 after 40 minutes. A negative horizontal velocity in Figure 5-16 means that the flow is towards the outlet side. The horizontal velocity profile illustrates the reverse flow at the top, dead zone in the middle and suction towards the outlet in the bottom as shown in Figure 5-14 and Figure 5-15. The CFD-simulations slightly under-predict the inlet flow around the mantle and the reverse flow compared to the PIV measurements, while the suction towards the outlet at the bottom is slightly over-predicted by the CFD-simulations.

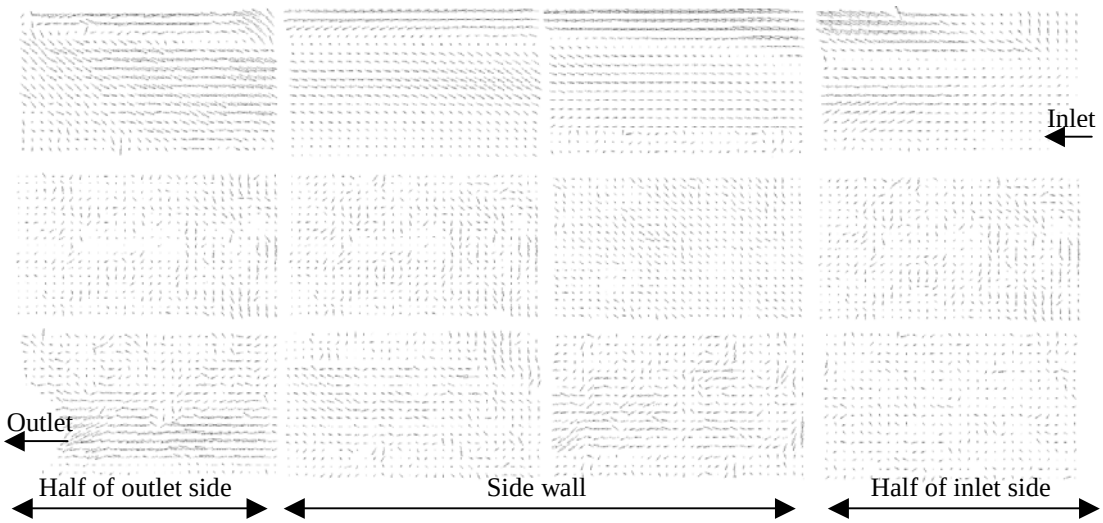

Figure 5-14: Measured flow field over one half of the mantle circumference in the mantle centre plane for case 1.

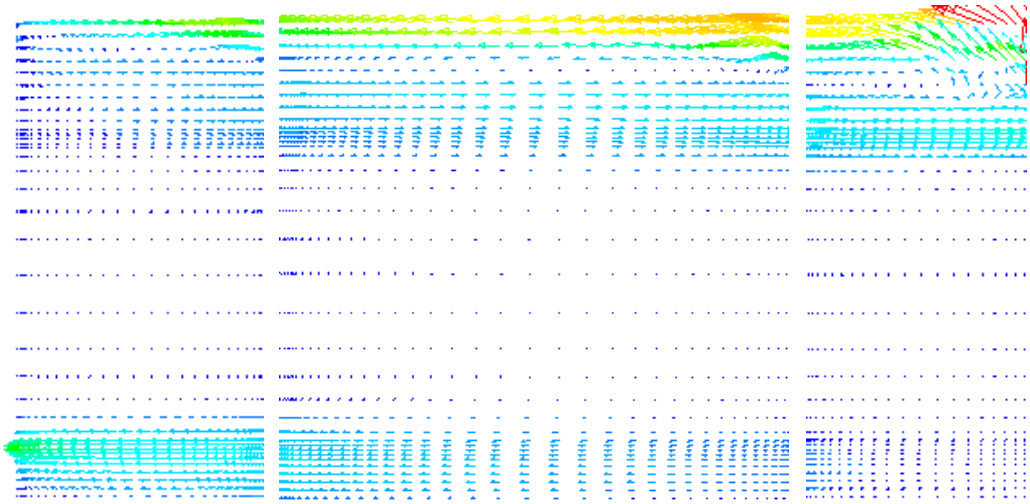

Figure 5-15: Calculated flow field over one half of the mantle circumference in the mantle centre plane for case 1.

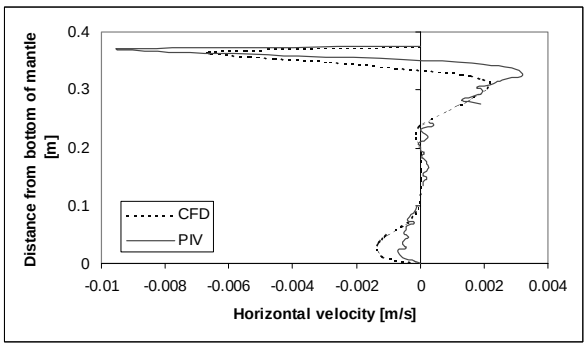

Figure 5-16: Measured (PIV) and calculated (CFD) horizontal velocity profiles in the centre plane of the mantle for case 1.

Case 2:

Figure 5-17 shows the measured flow field in the centre plane of the mantle for case 2 after 40-120 minutes. The measured flow field shows that the inlet stream initially flows from the inlet to the top before it flows around the top of the mantle, and the flow then reverses and flows back towards the inlet at a level below the main inlet stream. During this reverse motion the fluid is cooled and hereafter the fluid drops slowly down, and then develops a return stream along the bottom of the mantle towards the outlet port. This flow structure is very similar to the flow structure observed for case 1. The small difference is that some of the inlet stream cools faster and reverses earlier than in case 1. Figure 5-18 shows the flow field after 40 minutes predicted by the CFD-model, and the calculated flow pattern is similar to the measured flow pattern.

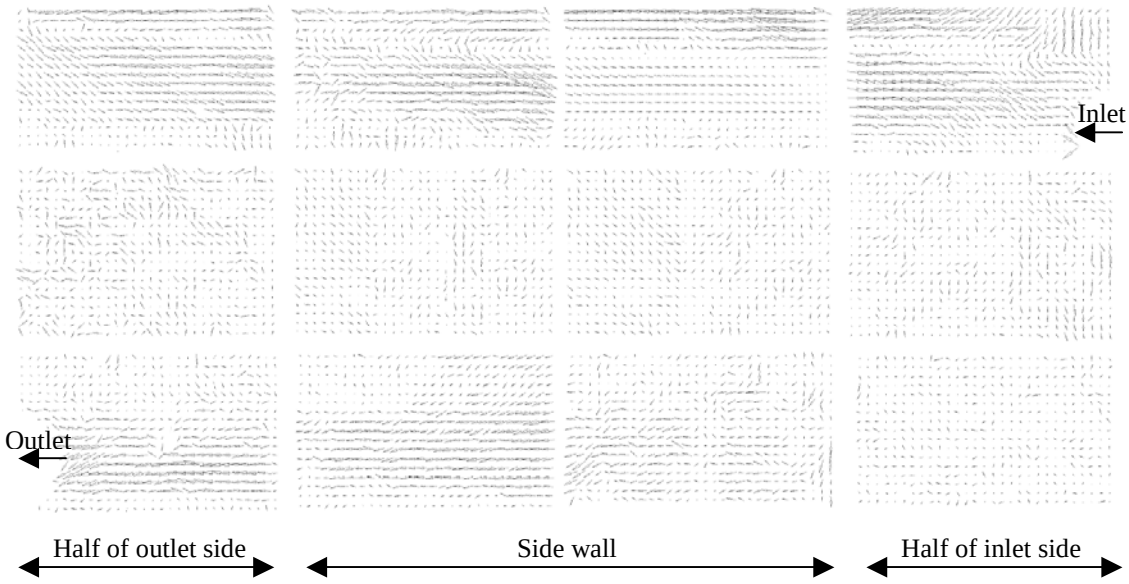

Figure 5-17: Measured flow field over one half of the mantle circumference in the mantle centre plane for case 2.

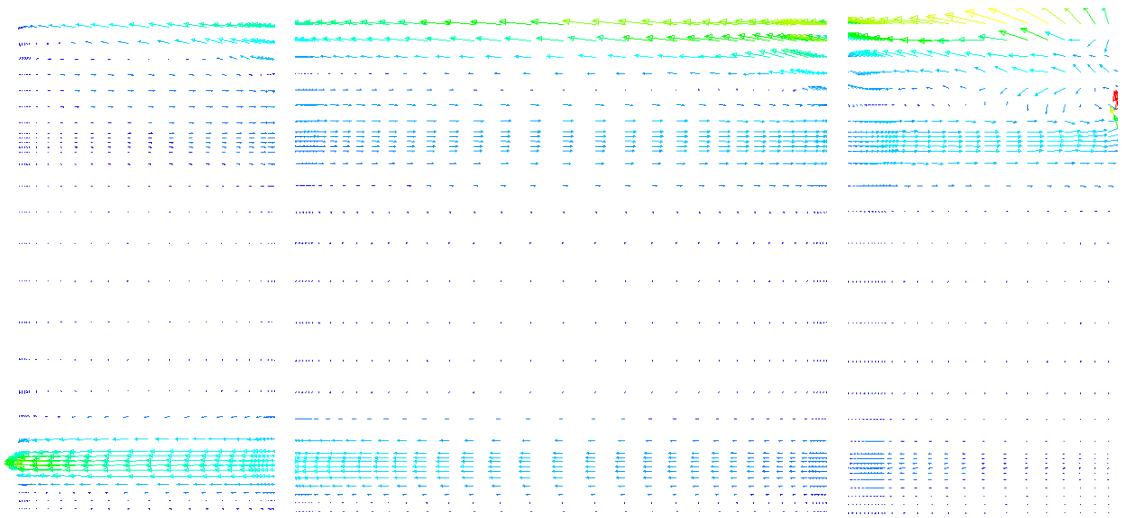

Figure 5-18: Calculated flow field over one half of the mantle circumference in the mantle centre plane for case 2.

Figure 5-19 shows the measured and calculated horizontal velocity profile at a vertical line (Figure 5-10) through the centre of the front side of the mantle for case 2 after 40 minutes. The horizontal velocity profile illustrates the reverse flow at the top, the dead zone in the middle and suction towards the outlet in the bottom as shown in Figure 5-17 and Figure 5-18. The horizontal velocities are smaller compared to the horizontal velocities for case 1 in Figure 5-16. The flow in the top of the mantle for case 2 is over-predicted by the CFD-calculation.

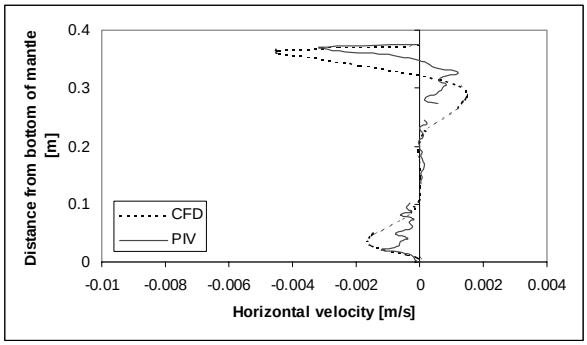

Figure 5-19: Measured (PIV) and calculated (CFD) horizontal velocity profiles in the centre plane of the mantle for case 2.

Case 3:

Figure 5-20 shows the measured flow field in the centre plane of the mantle for case 3 after 40-120 minutes. The measured flow field is different from the flow field for case 1 and case 2. The mantle inlet temperature is lower than the mantle top temperature so the inlet stream drops down and passes around the middle part of the mantle. This stream induces a reverse flow in the top of the mantle. For this case there is still suction towards the outlet at the bottom. This flow pattern is somewhat similar to what was observed by Shah et al. (1999). Figure 5-21 shows the flow field after 40 minutes predicted by the CFD-model and the calculated flow pattern is similar to the measured flow pattern.

Figure 5-22 shows the measured and calculated horizontal velocity profile at a vertical line (Figure 5-10) through the centre of the front side of the mantle for case 3 after 40 minutes. The horizontal velocity profile illustrates the reverse flow at the top and suction towards the outlet in the bottom as shown in Figure 5-20 and Figure 5-21. The horizontal velocities are predicted well by the CFD-calculation.

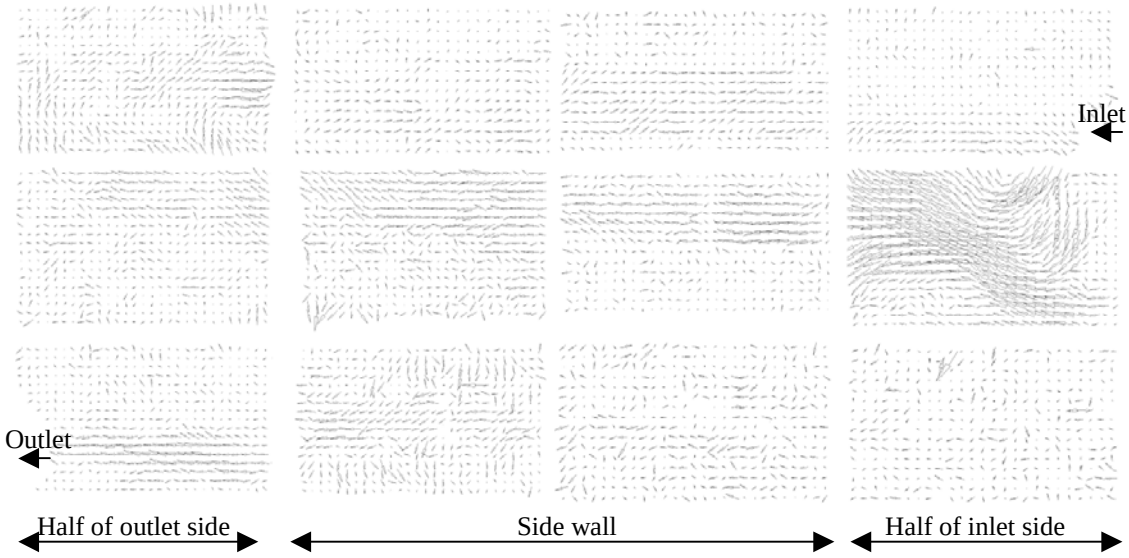

Figure 5-20: Measured flow field over one half of the mantle circumference in the mantle centre plane for case 3.

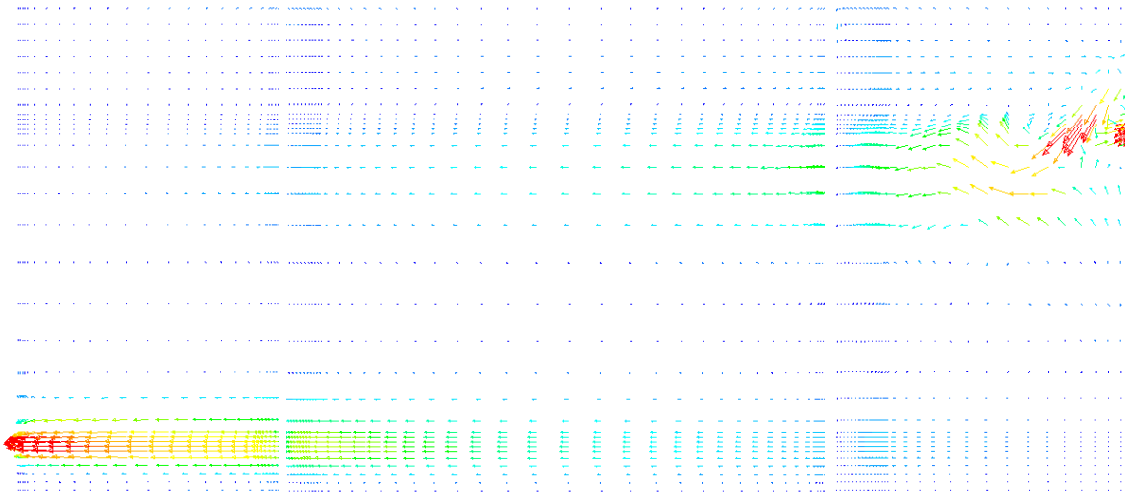

Figure 5-21: Calculated flow field over one half of the mantle circumference in the mantle centre plane for case 3.

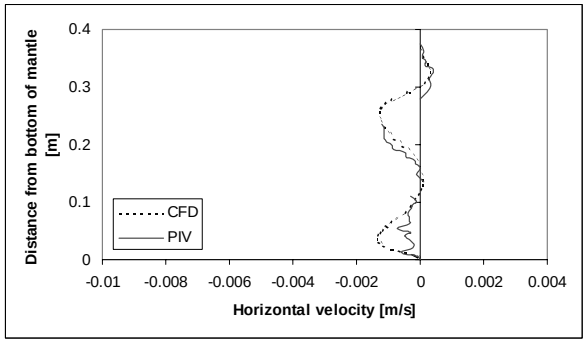

Figure 5-22: Measured (PIV) and calculated (CFD) horizontal velocity profiles in the centre plane of the mantle for case 3.

5.3.3 Results: Flow distribution in inner tank

The flow distribution in the inner tank was measured for case 1 and case 2 and compared to the CFD-predictions.

Case 1:

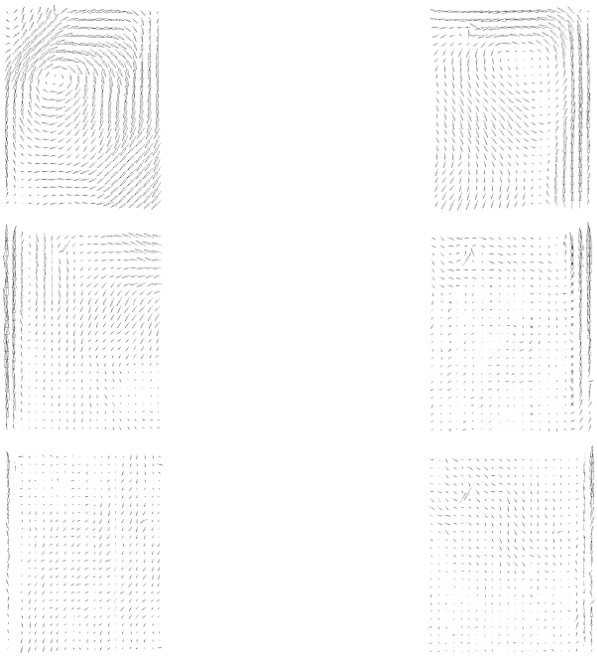

Figure 5-23: Measured flow field above the mantle in the inner tank for case 1 after 40-100 minutes.

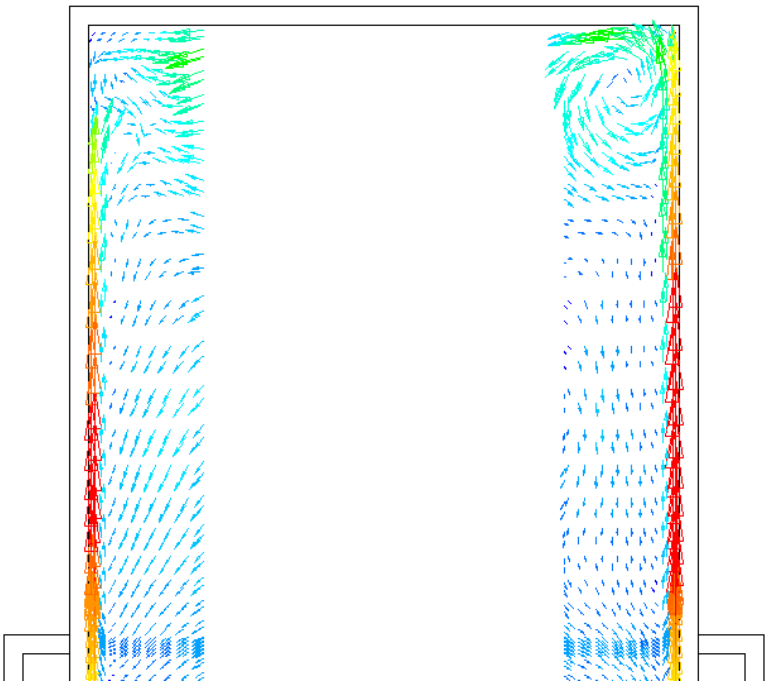

Figure 5-24: Calculated flow field above the mantle in the inner tank for case 1 after 40 minutes.

Figure 5-23 shows the measured flow field in the tank above the mantle for case 1 after 40-100 minutes. The heat exchange from the hot fluid in the mantle induces an upward flow near the tank wall. The upward flow accelerates on the way to the top of the tank before it decelerates when it gets close to the top wall where a re-circulation zone is created. In the core of the tank the flow passes down to the bottom of the tank before rising up near the mantle heat transfer surface. The re-circulation zone in upper left corner (outlet side) is stronger than in upper right (inlet side). It was expected to be the other way round and can be explained by the time delay of up to 60 minutes in the measurements. The measurements started in the inlet side and ended in the upper corner in the outlet side. Figure 5-24 shows the calculated flow field in the tank above the mantle for case 1 after 40 minutes. There is good agreement between PIV and CFD results, except for the upper left corner where a re-circulation zone is observed in the measurement that is not observed in the CFD-results.

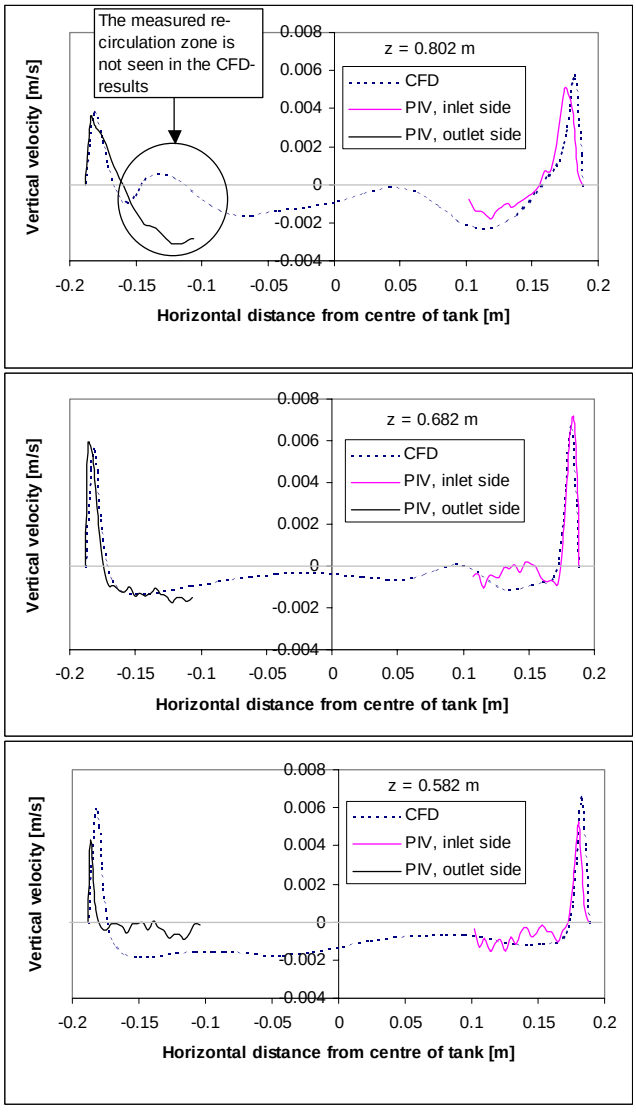

Figure 5-25: Measured (PIV) and calculated (CFD) vertical velocities in the inner tank at distances of 0.582 m, 0.682 m and 0.802 m from bottom of tank for case 1 after 40 minutes.

The measured and calculated vertical velocities at the three levels in the tank (shown in Figure 5-11) are compared in Figure 5-25. Figure 5-25 shows the same tendency as Figure 5-23 and Figure 5-24 that in a heating situation like case 1 there is an upward flow near the walls and a slow downward flow in the centre of the tank that continues down to the bottom of the tank. The vertical velocities are very small with 0.007 m/s as the largest vertical velocity for case 1. These small vertical velocities along the tank wall are one of the reasons why mantle heat exchangers are good at promoting thermal stratification in the upper part of the tank. It is seen that the upward velocity at the inlet side of the tank is somewhat higher than the upward velocity at the outlet side of the tank. It is also seen that there is good agreement between the PIV and CFD results. The difference at the outlet side at z = 0.802 corresponds to the upper left corner in Figure 5-23 and Figure 5-24 where the measured re-circulation zone is not seen in the CFD-results. The CFD-results were evaluated after 40 minutes while the PIV measurements in the upper left corner were taken at approximately 90-100 minutes, so the time difference might be the reason for the differences.

Case 2:

Figure 5-26 shows the measured flow field in the tank above the mantle for case 2 after 40-100 minutes. Case 2 is a heating situation where the mantle inlet temperature is 50ºC, and the tank is initially stratified with 20ºC at the bottom and 40ºC at the top. However, the tank is un-insulated so the natural convection from the heat loss is stronger than the natural convection from the heat exchange with the hot mantle fluid, and a downward flow near the walls above the mantle is created. Small re-circulation zones are observed near the wall just above the mantle. It is where the downward flow meets the upward flow due to the heat exchange from the mantle. The calculated flow field in the tank above the mantle is shown in Figure 5-27 and there is good agreement between the measured and calculated flow field.

The measured and calculated vertical velocities at the three levels in the tank (shown in Figure 5-11) are compared in Figure 5-28. Figure 5-28 shows the same tendency as Figure 5-26 and Figure 5-27 with the downward flow near the walls, and in the centre of the tank a slow upward flow is observed. The vertical velocities are smaller than for case 1 and there is good agreement between the PIV and CFD results.

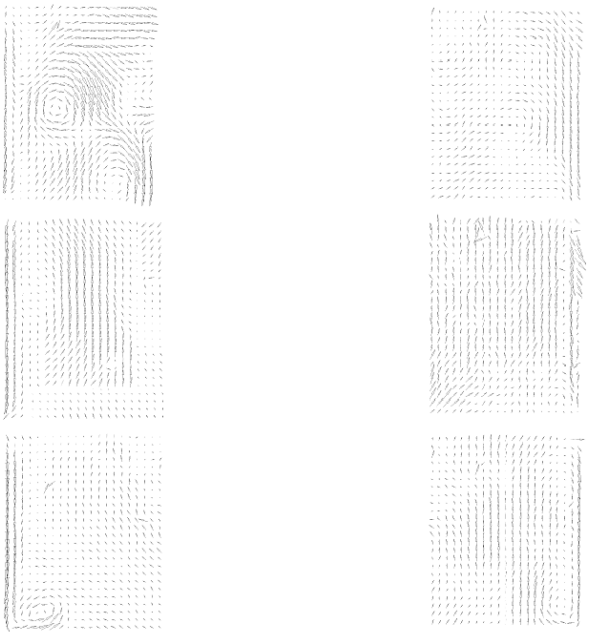

Figure 5-26: Measured flow field above the mantle in the inner tank for case 2 after 40-100 minutes.

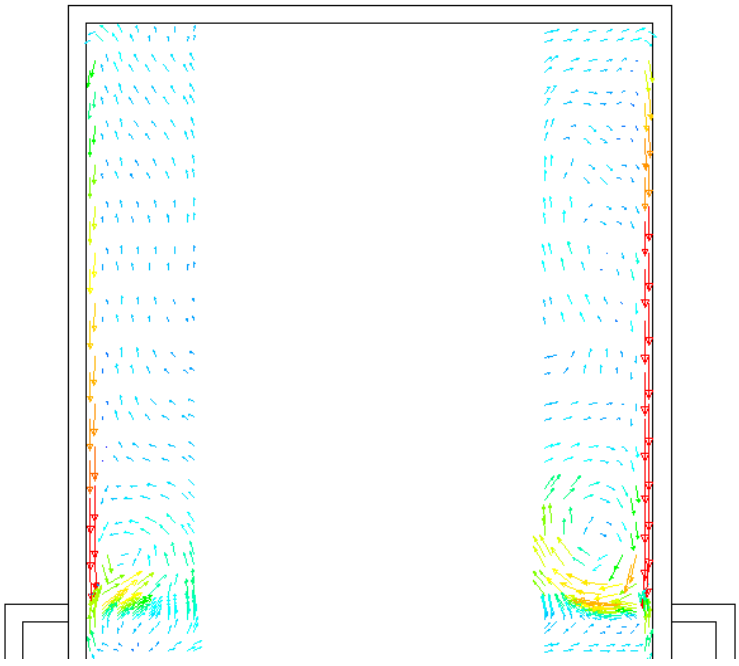

Figure 5-27: Calculated flow field above the mantle in the inner tank for case 2 after 40 minutes.

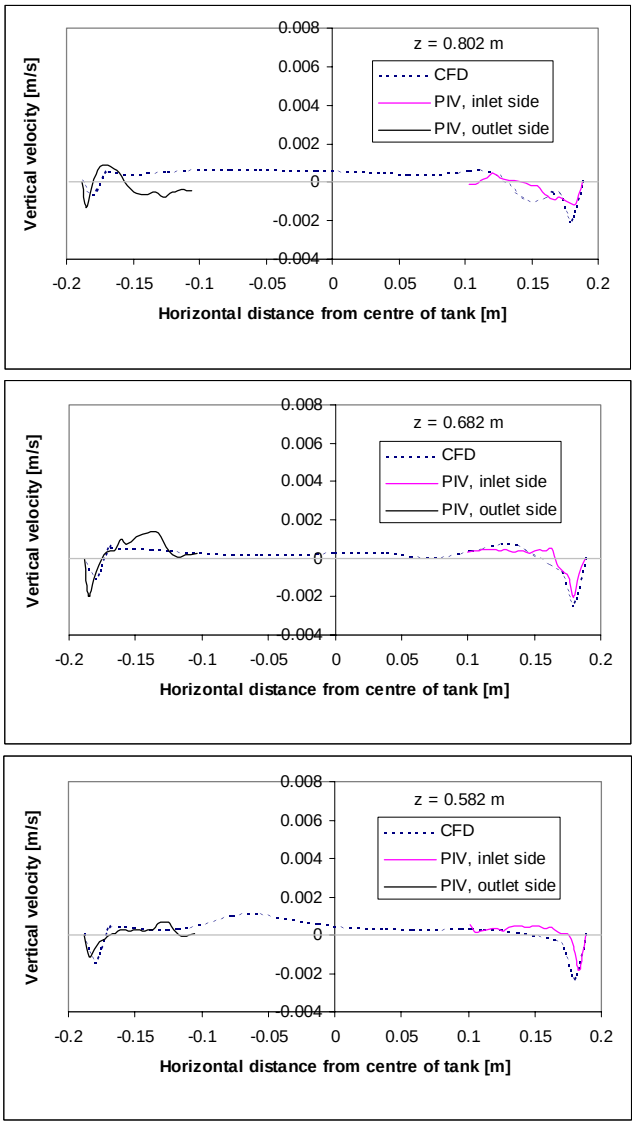

Figure 5-28: Measured (PIV) and calculated (CFD) vertical velocities in the inner tank at distances of 0.582 m, 0.682 m and 0.802 m from bottom of tank for case 2 after 40 minutes.

Case 2 and case 3 with insulation:

The PIV experiments described above were carried out with an un-insulated tank to allow the flow visualisation. In almost any cases in practice a hot-water tank will be insulated, therefore two extra CFD-calculations were carried out for case 2 and case 3 with an insulated glass mantle tank to illustrate the flow structure under realistic operation conditions. In case 2 and case 3 the inner tank is initially stratified and case 2 is the hot inlet condition and case 3 is the warm inlet condition. Figure 5-29 shows the flow field in the inner tank after 40 minutes.

In case 2 there is an upward flow near the walls due to the heat exchange from the hot mantle fluid. The upward flow accelerates on the way to the top of the tank before it decelerates when it gets close to the top wall where a re-circulation zone is created. In

the core of the tank the flow passes down towards the bottom of the tank before rising up near the mantle heat transfer surface. The upward flow is strongest at the inlet side and therefore the upward flow at the outlet side is not going all the way to the top of the tank.

The mantle inlet temperature in case 3 is lower than the top tank temperature and the flow above the mantle is governed by the heat loss at the walls, and a downward flow near the walls above the mantle is created. There is an upward flow in the centre of the tank above the mantle. At the level between the mantle top and the mantle inlet there is very little movement of the fluid in the tank. At the level below the mantle inlet there is an upward flow near the walls due to the heat exchange from the mantle fluid and there is a slow downward flow in the central part of the tank.

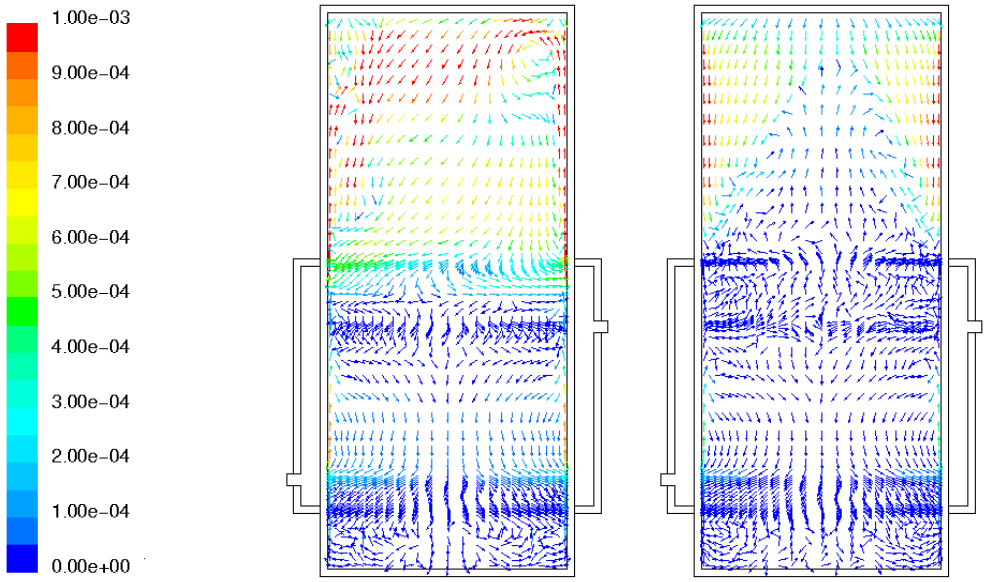

Figure 5-29: Calculated flow field in inner tank for case 2 (left) and case 3 (right) with an insulated glass tank. The velocity is in m/s in the colour scale.

5.4 Effect of turbulence in the CFD-models

In order to see the effect of turbulence in the CFD-models, a CFD-calculation of case 1 was carried out with the *k*-ω-model modelling the turbulence.

5.4.1 Velocities in the mantle gap

To compare the laminar and the turbulent flow model, the flow in the mantle gap was compared at a vertical line (Figure 5-10) through the centre of the front side of the mantle for case 1 after 40 minutes. Figure 5-30 shows the horizontal velocity profiles at the vertical line for the laminar and the turbulent model. Minor differences are observed in Figure 5-30.

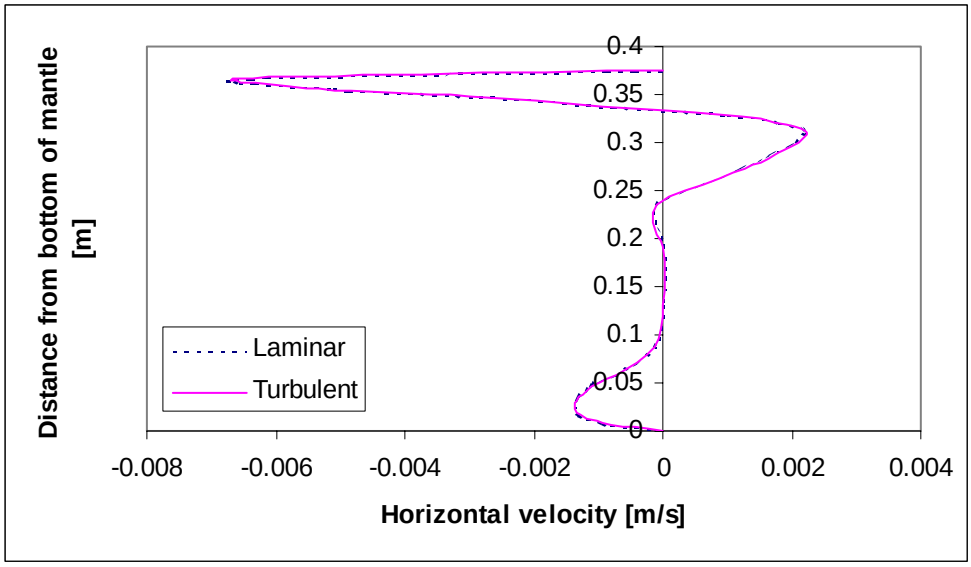

Figure 5-30: Horizontal velocity profiles in the centre plane of the mantle for the laminar and the turbulent model of case 1.

5.4.2 Velocities in the inner tank

To compare the laminar and the turbulent flow model, the flow in the inner tank was compared at three levels in the tank (Figure 5-11) for case 1 after 40 minutes. Figure 5-31 shows the vertical velocity profiles at the three levels in the tank for the laminar and the turbulent model. The boundary layer near the walls is a bit wider in the turbulent model than in the laminar model. However, minor differences are observed.

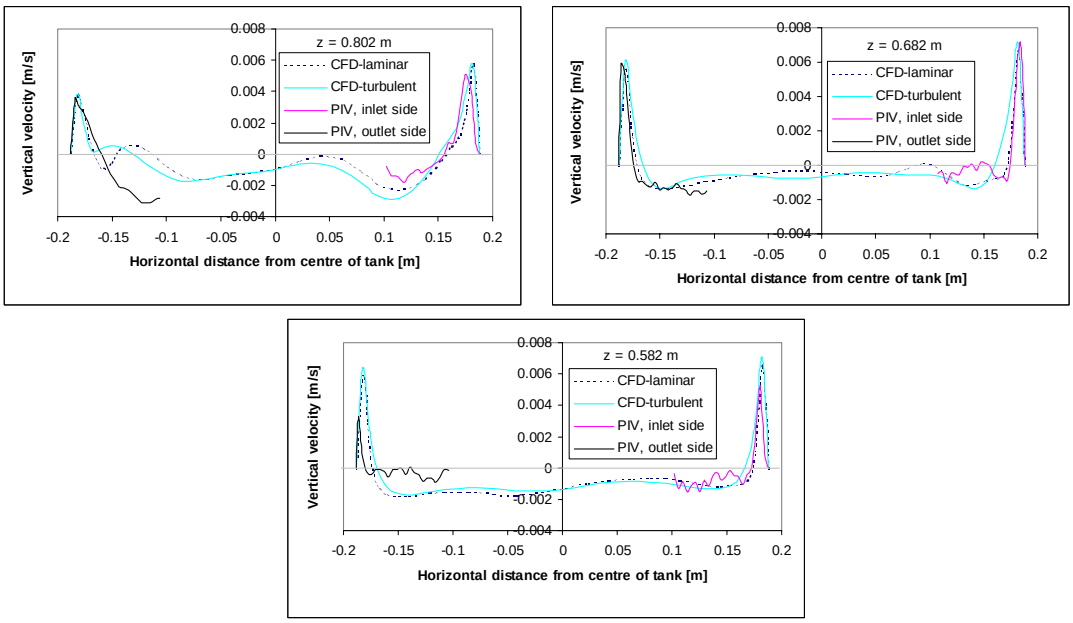

Figure 5-31: Vertical velocity profiles in the inner tank at distances of 0.582 m, 0.682 m and 0.802 m from bottom of tank for laminar and turbulent model of case 1 after 40 minutes.

5.4.3 Heat flux at mantle wall and tank wall

The heat flux from the mantle fluid to the inner mantle wall is averaged around the wall at different levels in the mantle. The heat flux profiles at the mantle wall for case 1 after 40 minutes are shown in Figure 5-32. The heat flux in the top of the mantle is a little higher in the turbulent model than in the laminar model.

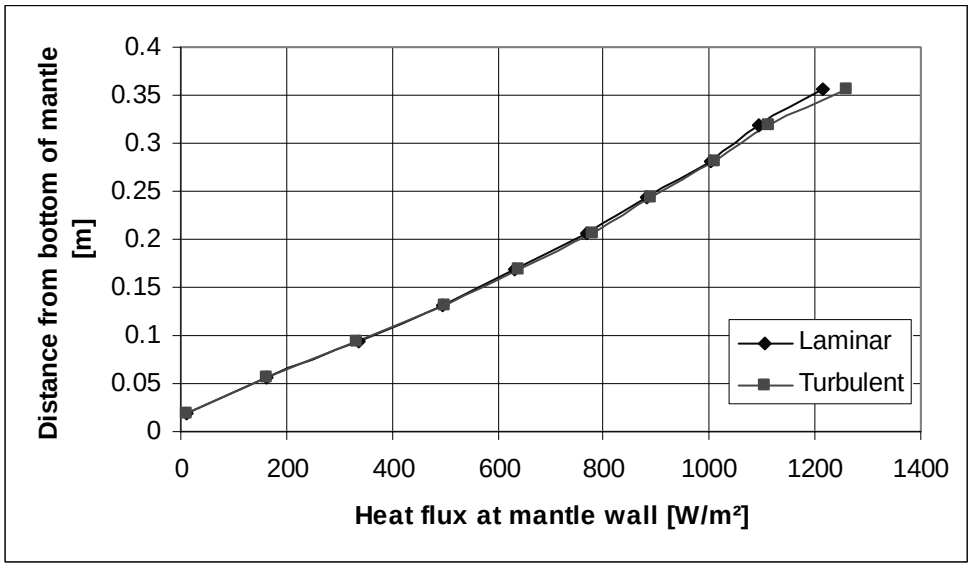

Figure 5-32: Calculated heat flux profiles at the mantle wall for the laminar and the turbulent model for case 1 after 40 minutes.

The heat flux from the tank wall to the water in the tank is averaged around the wall at different levels in the tank. The heat flux profiles at the tank wall for case 1 after 40 minutes are shown in Figure 5-33. The heat flux at the level of the mantle top is a little higher in the turbulent model than in the laminar model.

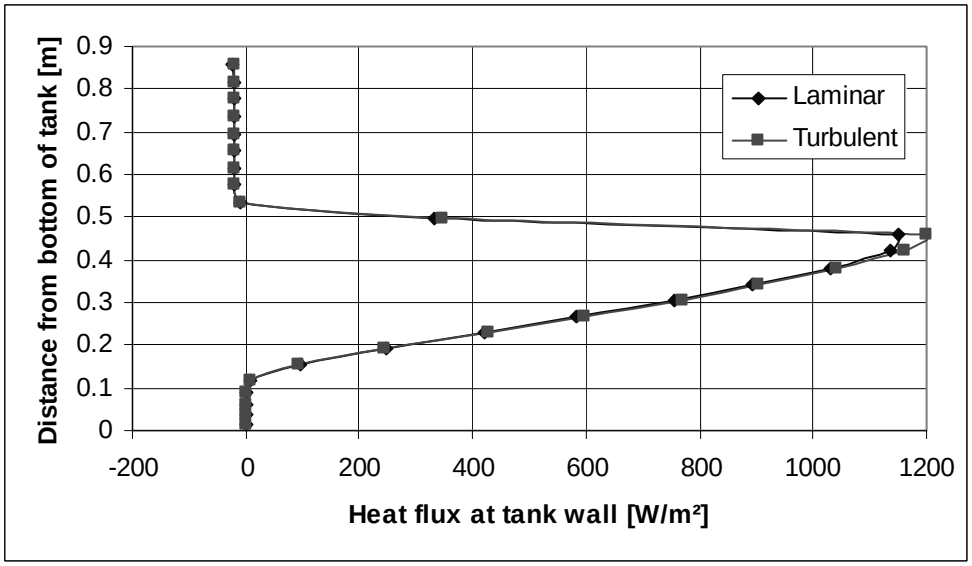

Figure 5-33: Calculated heat flux profiles at the tank wall for the laminar and the turbulent model for case 1 after 40 minutes.

The heat flux profiles in Figure 5-32 and Figure 5-33 indicates that there might be some turbulence near the mantle inlet due to the impinging jet, but the difference between the heat flux profiles predicted by the turbulent model and the heat flux profiles predicted by the laminar model is small because the heat flux is averaged all around the wall in the respective levels. The differences between the results from the turbulent model and the laminar model are so small that it can be concluded that a laminar flow model can model the vertical mantle heat exchangers. However, the results that will be presented in the coming chapters are based on CFD-calculations using the *k*-ω-model.

5.5 Grid dependence of CFD-models

An important aspect of CFD-modelling or numerical modelling in general is the way the equations are discretised. The governing equations are solved only on a discrete grid of points called the "mesh" or the "grid". In order to produce a good model the results must be independent of the grid. The number of grid points should be as low as possible to reduce the computational time and computer memory requirements while keeping the numerical errors below some acceptable value. The numerical modelling in this thesis used a structured grid, which consisted of a structured array of node points.

Three different grids of the glass mantle tank were produced. The three grids were: a coarse grid with 78658 (model A) computational cells, a detailed model with 138325 (model B) computational cells and a more detailed model with 193150 (model C) computational cells. Figure 5-34 shows the vertical grid for the three models and Table 5-6 shows the number of computational cells in each model.

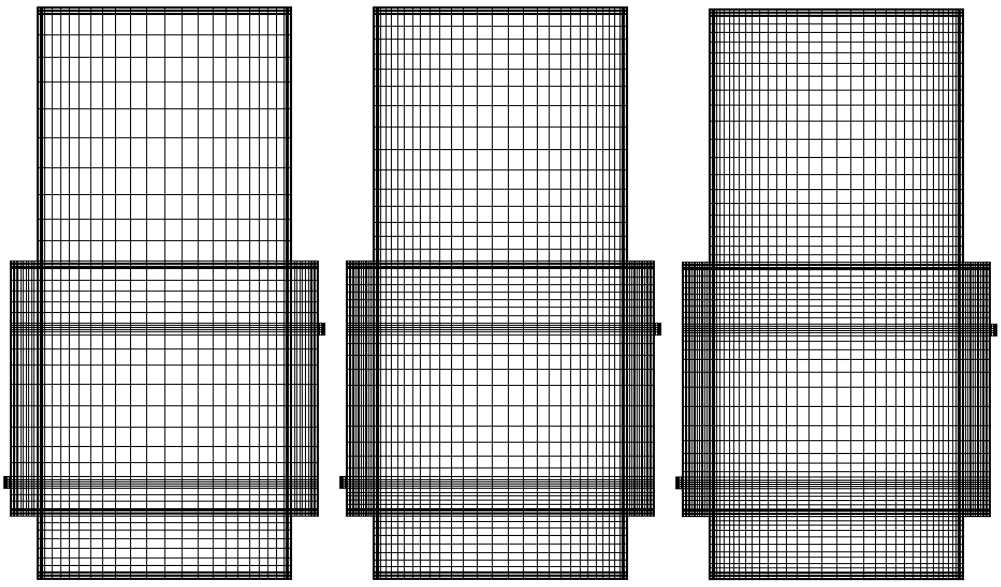

Figure 5-34: Vertical grid of the CFD-models. Model A (left), model B (centre) and model C (right).

Part of model	Model A	Model B	Model C
Water in inner tank	15900	32500	57000
Tank wall	21900	33125	46200
Mantle fluid	15788	34100	43700
Mantle wall	25070	38600	46250
Total	78658	138325	193150

Table 5-6: Number of computational cells in the three models.

5.5.1 Mantle outlet temperature

Figure 5-35 shows the calculated mantle outlet temperature in the three CFD-models compared with the measured mantle outlet temperature for case 1 after 40 minutes. As the CFD-calculations are time–consuming, the calculations were started prior to the measurements and this is the reason why the measured mantle outlet temperature at 0 min. was higher than in the CFD-calculations. There is good agreement between the measured mantle outlet temperature and the calculated mantle outlet temperatures for model B and model C while there is bad agreement with model A. Thus, it is concluded that model A is not sufficient to model the flow and heat transfer in the glass mantle tank and model A will not be considered in the following comparisons.

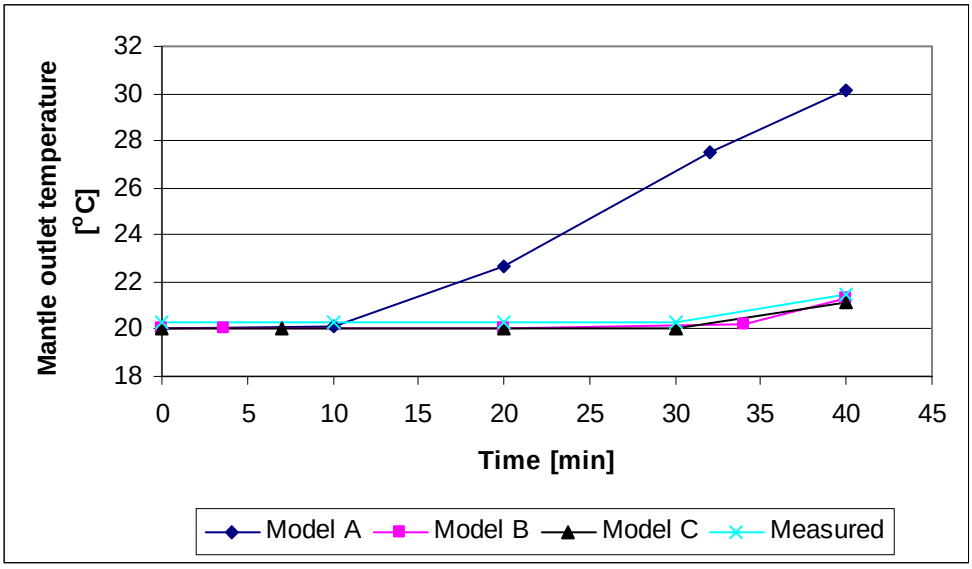

Figure 5-35: Mantle outlet temperature measured and calculated by the three CFD-models for case 1 after 40 minutes.

5.5.2 Heat flux at mantle wall and tank wall

The calculated heat flux profiles at the mantle wall for case 1 after 40 minutes are shown in Figure 5-36. Model C calculates a higher heat flux at the mantle wall than model B, but the differences are very small. The calculated heat flux profiles at the tank wall after 40 minutes are shown in Figure 5-37. Model C calculates a higher heat flux at the mantle level than model B, but as in Figure 5-36 the differences are very small.

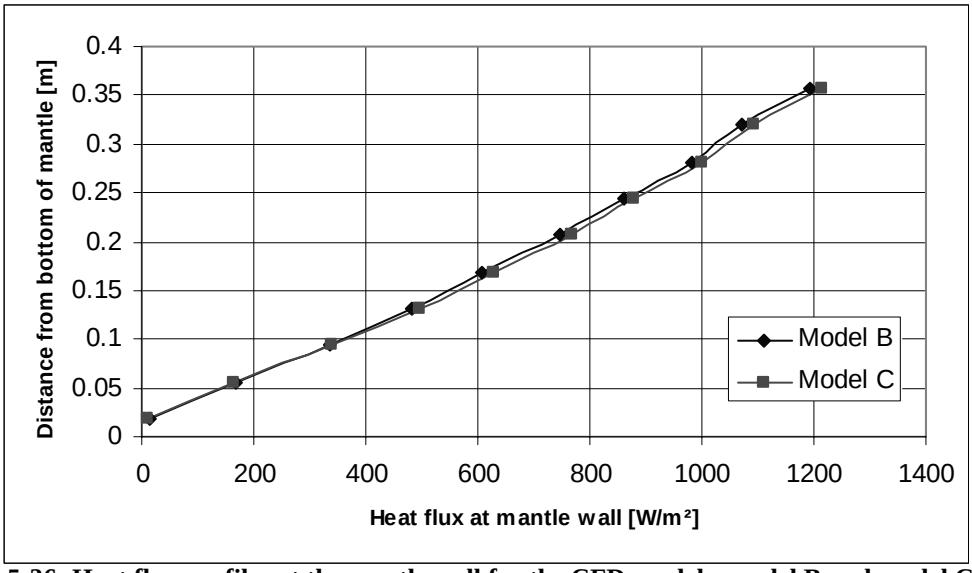

Figure 5-36: Heat flux profiles at the mantle wall for the CFD-models, model B and model C for case 1 after 40 minutes.

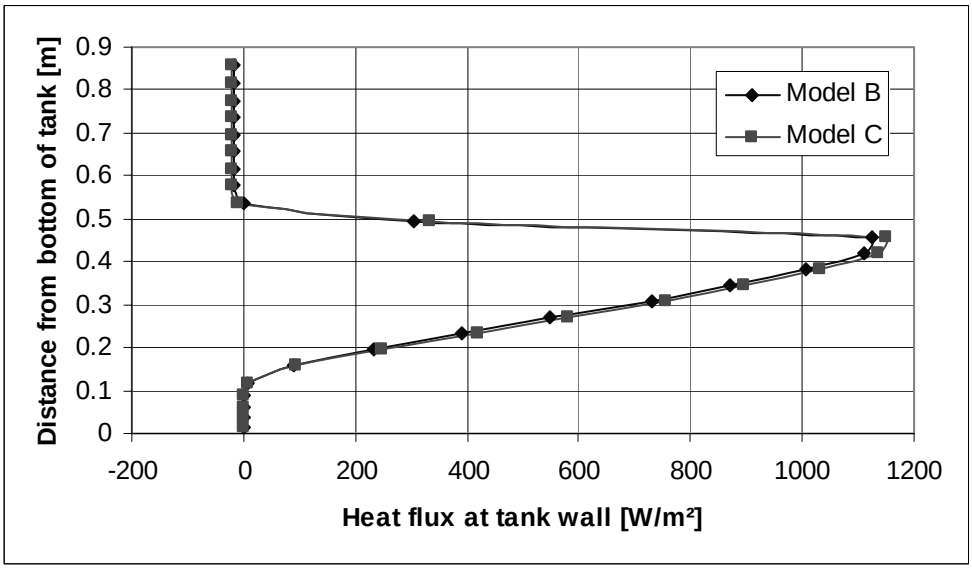

Figure 5-37: Heat flux profiles at the tank wall for the CFD-models, model B and model C for case 1 after 40 minutes.

5.5.3 Bulk flow in inner tank

The third component that will be compared between the two models is the flow in the inner tank. The capability of the models of modelling the uprising bulk flow near the walls and the downward flow in the centre of the tank is compared at a horizontal slice in the tank at a level just at the top of the mantle. Table 5-7 shows the calculated upward flow and downward flow in the tank for both models for case 1 after 40 minutes. The upward and downward flow in Table 5-7 are calculated manually by multiplying the vertical velocity at face number 'i' in the horizontal grid with the area of the same face number 'i', and then make a sum of all the positive (upward) and negative (downward) values on the horizontal slice, respectively.

	Upward flow [m³/s]	Downward flow [m³/s]	Difference between upward and downward flow in each model [%]
Model B	4.05E-05	4.14E-05	2
Model C	4.02E-05	4.08E-05	1
Difference between each model, [%]	1	1	

Table 5-7: Upward and downward flow in the inner tank in model B and model C at a level just at the top of the mantle.

The results in Table 5-7 show that the two models are very close in modelling the bulk flow in the inner tank. Model C was used for the comparison with the PIV results in section 5.3, but it can be concluded based on the comparison in this section that model B is also capable of modelling the flow and heat transfer in the glass mantle tank. In the coming chapters the presented results are based on CFD-calculations with a model of the steel mantle tank with around 130.000-140.000 computational cells for a volume of 175 l.

5.6 Time dependence of flow in inner tank in CFD-models

Only 40 minutes of case 1, 2 and 3 (described in section 5.3) were modelled with CFD due to the computational cost in CFD-modelling. The PIV measurements of the flow fields of interest, on the other hand, could not be made at one time, but they had to be done over an interval of time because the CCD camera and the laser sheet optics had to be moved during the experiments to capture the entire flow field. The PIV measurements shown in section 5.3 were all captured approximately 40-120 minutes after the start of the experiment. In this section the flow in the inner tank for case 1 is evaluated after 20, 30 and 40 minutes based on the CFD-results to see the development of the flow field.

Figure 5-38 shows the vertical velocity profiles at three levels (Figure 5-11) in the tank for case 1 after 20, 30 and 40 minutes. The velocity profiles show that the flow field is relatively stable, but there are some small fluctuations in the central part of the tank. Near the walls is the upward peak velocity from 20 minutes to 40 minutes increasing by 10-11% at the inlet side (right) and 6-8% at the outlet side (left) at z = 0.582m and z = 0.682m. At z = 0.802 the upward peak velocity from 20 minutes to 40 minutes is increasing by 1% at the inlet side and decreasing by 2% at the outlet side. The flow is strongest in the inlet side and therefore this flow influences the flow in the top of the outlet side leading to a decrease in the peak velocity there. If the calculations were continued the flow would probably still develop slowly, but the general trend of the flow field will not change radically. However, the heat flux distribution around the mantle wall at the mantle top will, with time, have a smaller difference between the inlet side and the outlet side, and this can result in the re-circulation zone in the upper left corner that were observed in the PIV measurements because there will be a smaller difference between the flow at the inlet side and at the outlet side.

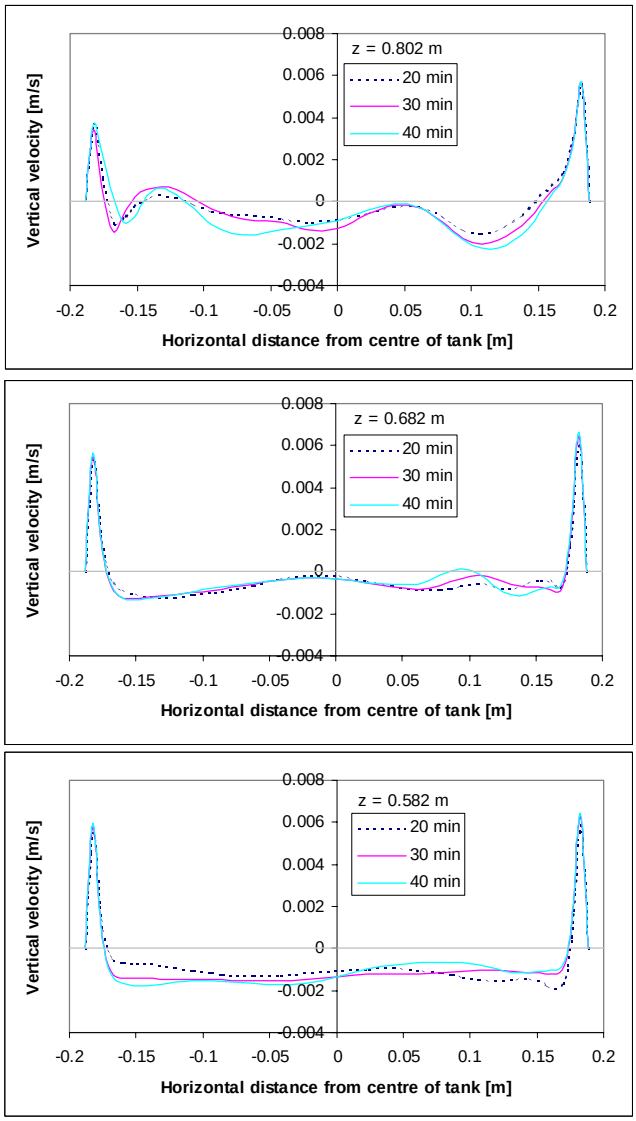

Figure 5-38: Calculated vertical velocity profiles in the inner tank after 20, 30 and 40 minutes.

5.7 Discussion and conclusion

The purpose with this chapter was to evaluate the CFD-model with respect to temperatures, heat transfer and flow distribution in the mantle and flow distribution in the inner tank.

The CFD-model predicted results in good agreement with both the thermal experiments and the PIV measurements. The flow visualisation illustrated the flow structure in both the mantle and in the inner tank at different operation conditions and the small vertical velocities in the inner tank revealed why vertical mantle heat exchangers are able to promote thermal stratification.

The effect of using a turbulence model in the CFD-calculations was investigated. The results showed that turbulence had a minor effect on the results and it was concluded

that a laminar flow model could be used. The grid dependence of the CFD-model of the glass mantle tank was investigated. A coarse grid of 78658 computational cells showed not to be capable of modelling the flow and heat transfer while two more detailed grids of 138325 and 193150 computational cells, respectively, showed to be sufficient. Furthermore, the time dependence of the flow in the inner tank was investigated. The flow showed to be developing slowly.

Based on the investigations in this chapter it can be concluded that the CFD-models developed are able to simulate the flow and heat transfer in vertical mantle heat exchangers. In the following chapters the CFD-model of the steel mantle tank will be used to investigate the effect on thermal stratification, heat transfer and flow structure from different geometrical designs (chapter 6). The results will be used to derive general correlations for heat transfer at the inner and outer mantle wall and at the tank wall, and a general way to describe the heat flow in the inner tank will also be derived (chapter 7).

6. Numerical analysis of flow and heat transfer in vertical mantle tanks

6.1 Introduction

It was established in chapter 5 that the CFD-model is able to model flow and heat transfer in vertical mantle heat exchangers. In this chapter the flow in the mantle, the flow in the inner tank and the heat transfer at the mantle wall and at the tank wall are analysed for a number of different mantle designs and different operation conditions.

The model used for the parameter variations is the same model as described in section 5.2.1. The standard tank used in the model and standard boundary conditions are given in Table 6-1.

Hot water tank volume [m³]	0.175
Volume in inner tank above mantle [m³]	0.081
Tank height [m]	1.44
Inner diameter of tank [m]	0.394
Mantle height [m]	0.7
Mantle top (distance from bottom of tank) [m]	0.773
Mantle bottom (distance from bottom of tank) [m]	0.073
Heat transfer area [m²]	0.880
Mantle gap width [m]	0.0335
Wall thickness [m]	0.003
Mantle inlet position	0.175 m from top of mantle
Mantle inlet size	½" (ID = 0.0189 m)
Steel material properties	
Specific heat [J/kg·K]	460
Density [kg/m³]	7820
Thermal conductivity [W/m·K]	60
Heat loss	
Top [W/m²·K]	0.4
Sides (above and below mantle) [W/m²·K]	1.4
Mantle side [W/m²·K]	1.3
Bottom [W/m²·K]	8.9
Other	
Initial tank conditions	Stratified 60ºC at top and 15ºC at bottom (see Figure 6-14)
Mantle fluid	Water
Mantle flow rate [l/min]	0.4
Ambient temperature [ºC]	21

Table 6-1: Standard tank and standard boundary conditions for the CFD-simulation.

The insulation is not included directly in the computational domain but it is indirectly taken into account by applying U-values as boundary condition to the steel tank. The insulation and the outer thermal resistance are included in the U-values. The U-values in Table 6-1 are calculated with the insulation data given in Table 5-1, and all the CFD-models in this chapter have the insulation material and thickness given in Table 5-1.

Two heating situations were studied; a hot inlet condition with a mantle inlet temperature of 70ºC, which was 10 K higher than the mantle top temperature, and a warm inlet condition with a mantle inlet temperature of 50ºC, which was 10 K lower than the mantle top temperature. The results for both heating situations were evaluated after 40 minutes. The two heating situations correspond to the two heating situations described in section 5.2.

The parameter variations are described in Table 6-2 and Table 6-3. One parameter is varied at a time, and hereby the influence of the specific parameter is directly determined. The mantle tank with the lower mantle inlet described in Table 6-1 is used as the reference tank and the change in each model is highlighted in Table 6-2 and Table 6-3. For the initially cold tank only the hot inlet condition with a mantle inlet temperature of 70ºC was studied. The mantle inlet port in the models with High mantle, Small H/D ratio and Large H/D ratio is located at a distance of ¼ of the total mantle height from the top.

Model	Reference Lower inlet	Mantle inlet position	Initially cold tank	Mantle inlet size	Small mantle gap	High flow rate
Inner tank volume, [m³]	0.175	0.175	0.175	0.175	0.175	0.175
Inner tank height, [m]	1.440	1.440	1.440	1.440	1.440	1.440
Inner tank diameter, [m]	0.394	0.394	0.394	0.394	0.394	0.394
Tank material	Steel	Steel	Steel	Steel	Steel	Steel
Inner mantle height, [m]	0.700	0.700	0.700	0.700	0.700	0.700
Heat transfer area, [m²]	0.880	0.880	0.880	0.880	0.880	0.880
Mantle gap, [m]	0.0335	0.0335	0.0335	0.0335	0.0105	0.0335
Mantle volume, [m³]	0.0319	0.0319	0.0319	0.0319	0.0095	0.0319
Mantle flow rate, [l/min]	0.4	0.4	0.4	0.4	0.4	0.8
Position of mantle inlet	0.175 m down	Top	0.175 m down	0.175 m down	0.175 m down	0.175 m down
Size of mantle inlet (ID), [m]	0.0189 (½")	0.0189	0.0189	0.0306 (1")	0.0189	0.0189
Initial thermal conditions	Stratified	Stratified	Mixed 20ºC	Stratified	Stratified	Stratified
Mantle inlet temperature, [ºC]	70/50	70/50	70	70/50	70/50	70/50
Mantle fluid	Water	Water	Water	Water	Water	Water

Table 6-2: Description of the parameter variations. The grey sections describe the reference tank and the changed parameters with respect to the reference tank.

Model	Reference Lower inlet	Tank material	High mantle	Mantle fluid (40% glycol)	Small H/D ratio	Large H/D ratio
Inner tank volume, [m³]	0.175	0.175	0.175	0.175	0.175	0.175
Inner tank height, [m]	1.440	1.440	1.440	1.440	0.959	1.778
Inner tank diameter, [m]	0.394	0.394	0.394	0.394	0.482	0.354
Tank material	Steel	Stainless steel	Steel	Steel	Steel	Steel
Inner mantle height, [m]	0.700	0.700	1.440	0.700	0.468	0.864
Heat transfer area, [m²]	0.880	0.880	1.810	0.880	0.717	0.948
Mantle gap, [m]	0.0335	0.0335	0.0335	0.0335	0.0355	0.0335
Mantle volume, [m³]	0.0319	0.0319	0.0657	0.0319	0.0257	0.0358
Mantle flow rate, [l/min]	0.4	0.4	0.4	0.4	0.4	0.4
Position of mantle inlet	0.175 m down	0.175 m down	0.36 m down	0.175 m down	0.117 m down	0.216 m down
Size of mantle inlet (ID), [m]	0.0189 (½")	0.0189	0.0189	0.0189	0.0189	0.0189
Initial thermal conditions	Stratified	Stratified	Stratified	Stratified	Stratified	Stratified
Mantle inlet temperature, [°C]	70/50	70/50	70/50	70/50	70	70
Mantle fluid	Water	Water	Water	40% propylene glycol/water mixture	Water	Water

Table 6-3: Description of the parameter variations. The grey sections describe the reference tank and the changed parameters with respect to the reference tank.

Figure 6-1 shows an outline of the different tank configurations considered in this chapter. The results of the parameter variations will be shown with a section for each parameter variation where the results are compared with results for the reference tank configuration. At the end of the chapter a summary with all the results will be given.

6.2 Method of analysing results

The output from a single CFD-simulation is numerous. For each control volume temperature, three velocity components, enthalpy, viscosity, turbulence, heat flux at surfaces etc. are indicated. Furthermore, it is possible to create virtual surface within the domain of the model and then either visualise the results at that surface or write selected results for the surface to a file for further analysis.

In this chapter absolute values of heat flux at mantle wall and at tank wall are analysed along with the vertical velocity at certain levels in the inner tank and the tangential velocity at the centre of the mantle. In chapter 7 the heat transfer results are analysed by means of dimensionless heat transfer theory.

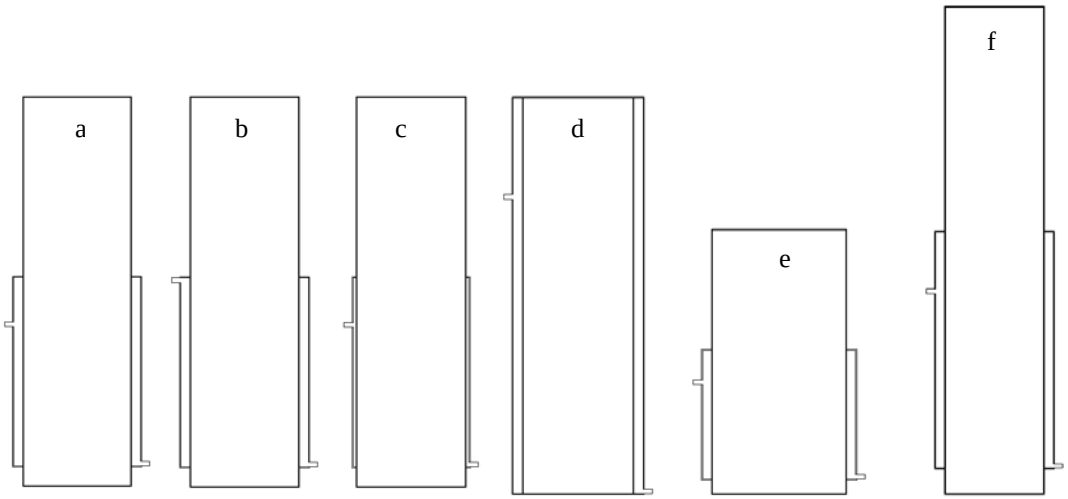

Figure 6-1: Outline of the different tank configurations considered in this chapter. a) Reference tank with lower inlet, b) Top inlet, c) Small mantle gap, d) High mantle, e) Small H/D ratio and f) Large H/D ratio.

6.2.1 Heat flux

In this chapter the heat flux at the mantle wall is defined as the heat flux from the mantle fluid to the inner tank wall and the heat flux at the tank wall is defined as the heat flux from the tank wall to the domestic water in the tank. Figure 6-2 illustrates the heat flux at the mantle wall and at the tank wall. The heat flux from the mantle fluid to the outer mantle wall will not be treated in this chapter, but it will be treated on a dimensionless basis in section 7.4.

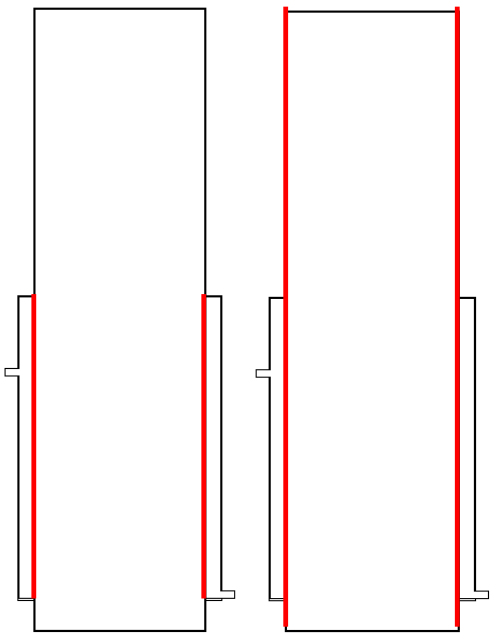

Figure 6-2: Heat flux at the mantle wall (left) and at the tank wall (right).

In order to evaluate the heat flux at different levels at the mantle wall and at the tank wall, the walls were divided into smaller pieces at different levels as shown in Figure 6-3. The average heat flux for each of the smaller pieces at either the mantle wall or the tank wall was calculated by calculating an area-weighted average of the heat flux. The calculation of the area-weighted average heat flux was performed within the CFD-programme (Fluent, 2001) by the equation given below:

$$q = \frac{1}{A_w} \sum_{i=1}^{n} q_i \cdot A_{w,i} \qquad (6.1)$$

where

A_w	is the total area of the piece of the wall, [m²]
$A_{w,i}$	is the area of face number 'i' on the surface, [m²]
n	is the total number of faces on the piece of the wall, [-]
q	is the area-weighted average of the heat flux, [W/m²]
q_i	is the heat flux at face number 'i', [W/m²]

The average temperature at different horizontal levels are calculated in the same way:

$$T = \frac{1}{A_h} \sum_{j=1}^{m} T_j \cdot A_{h,j} \qquad (6.2)$$

where

A_h	is the total area of the horizontal virtual surface, [m²]
$A_{h,j}$	is the area of face number 'j' on the surface, [m²]
m	is the total number of faces on the horizontal virtual surface, [-]
T	is the area-weighted average of the temperature, [K]
T_j	is the temperature of face number 'j', [K]

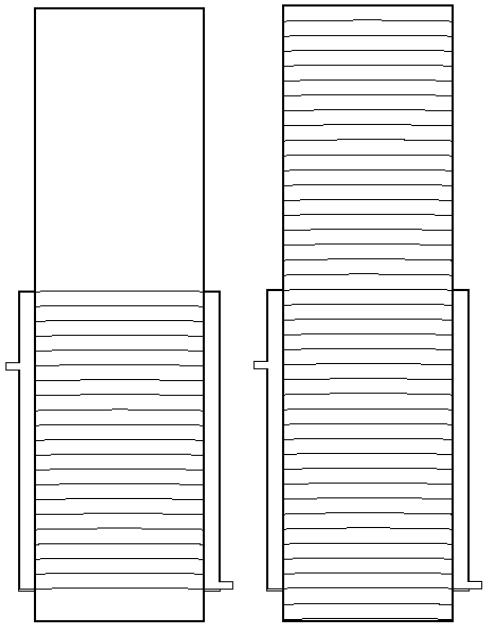

Figure 6-3: Mantle wall (left) and tank wall (right) are divided into smaller pieces for the analysis of local heat transfer.

6.2.2 Velocity

The flow in the mantle was compared by comparing the tangential velocity in the mantle at a vertical line through the centre plane of the mantle, midway between the mantle inlet and the mantle outlet as shown in Figure 6-4. The tangential velocity is defined to be positive towards the outlet. The flow in the inner tank was compared by comparing the vertical velocity at two levels in the inner tank in the symmetry plane through inlet and outlet. The two levels in the inner tank are shown in Figure 6-5.

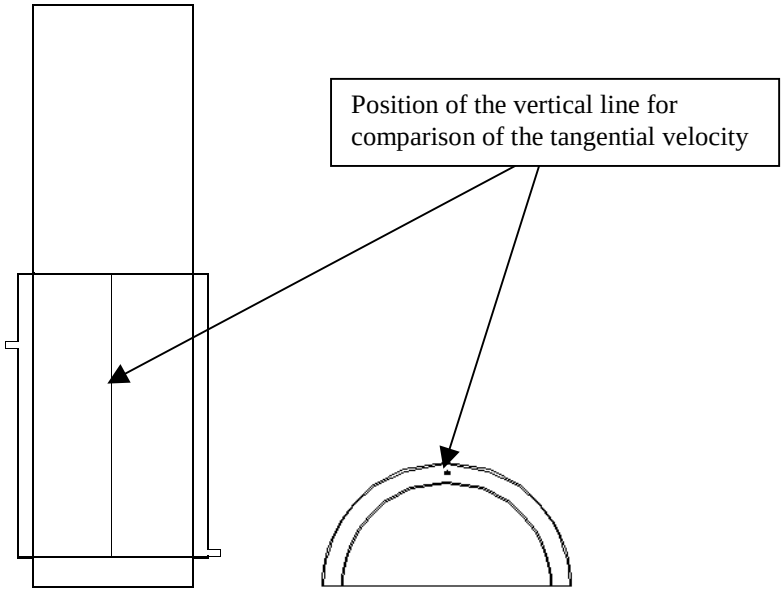

Figure 6-4: The position of the vertical line for comparison of the tangential velocity in the mantle shown in a vertical outline (left) and in a horizontal outline (right) of the mantle heat exchanger.

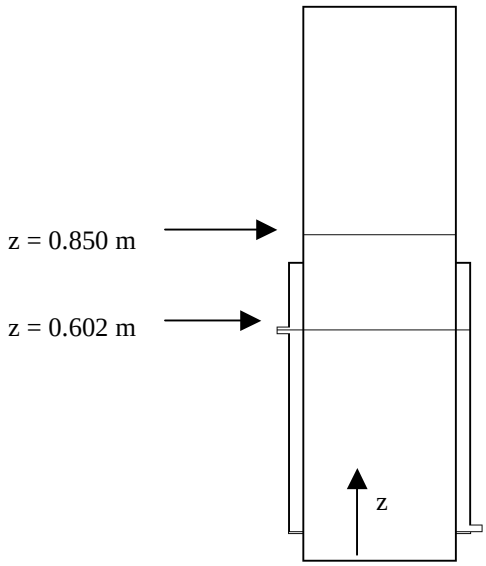

Figure 6-5: Two levels for comparison of the vertical velocity in the inner tank.

6.3 Effect of mantle inlet port position

Two different positions of the mantle inlet port were investigated. That is, the top inlet position and the inlet moved 0.175 m down (reference tank). This is the two mantle inlet configurations that were investigated experimentally in chapter 4.

6.3.1 Heat flux

Figure 6-6 shows the simulated heat flux profiles at the mantle wall after 40 minutes. The heat flux is highest at the top of the mantle for the hot inlet condition (70ºC), while the heat flux is concentrated at the bottom part (up to 0.4 m) of the mantle for the warm inlet condition (50ºC).

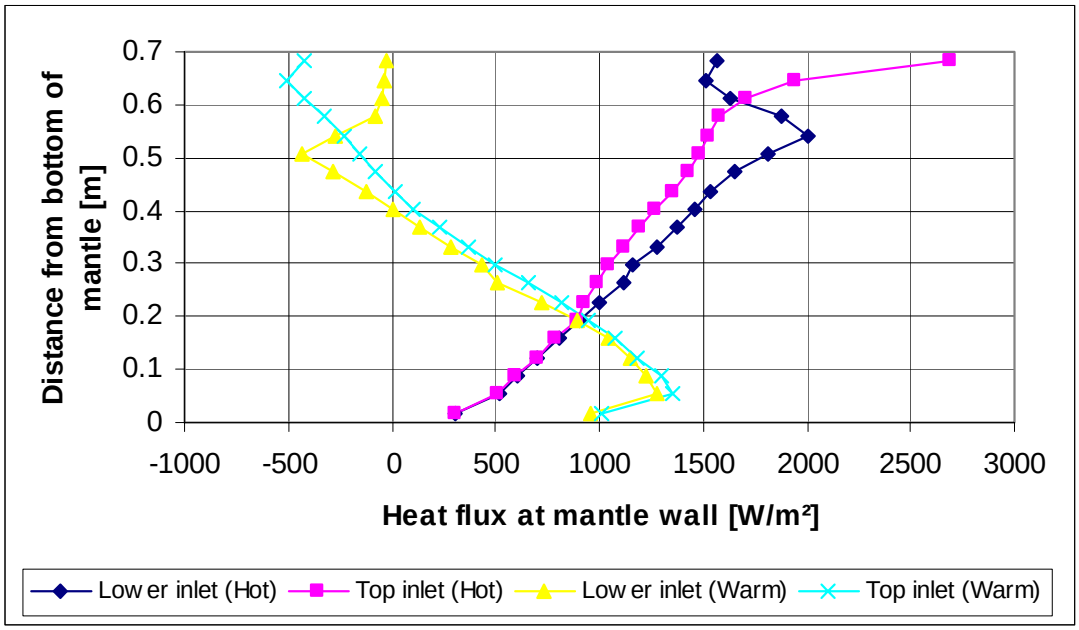

Figure 6-6: Heat flux at the mantle wall after 40 minutes for the reference tank and for the tank with top inlet to the mantle.

The influence of the different positions of the mantle inlet port is clearly seen from Figure 6-6.

Hot inlet condition: The mantle tank with the mantle inlet port at the top has the highest heat transfer at the very top of the mantle, while the mantle tank with the mantle inlet port moved down has the highest heat transfer at a distance of about 0.5 m from the bottom of the mantle. For the hot inlet condition it is preferable to have the heat flux concentrated as high as possible in the mantle to promote stratification in the tank.

Warm inlet condition: Very little difference at a distance from 0-0.4 m from the bottom of the mantle. The heat transfer is for both mantle tanks negative in the upper part of the mantle, but the negative heat transfer is reduced when the mantle inlet is moved down. For the warm inlet condition it is preferable to have the negative heat flux located as low as possible in the mantle in order to minimise the de-stratification in the tank.

Figure 6-7 shows the simulated heat flux profiles at the tank wall after 40 minutes. At a distance of 0-0.8 m from the bottom of the tank the heat flux profiles for the tank wall are very similar to the heat flux profiles for the mantle wall. From 0.12 m above the mantle and to the tank top the heat flux is below 0 W/m² in all the studied cases because of the heat loss at the tank wall above the mantle.

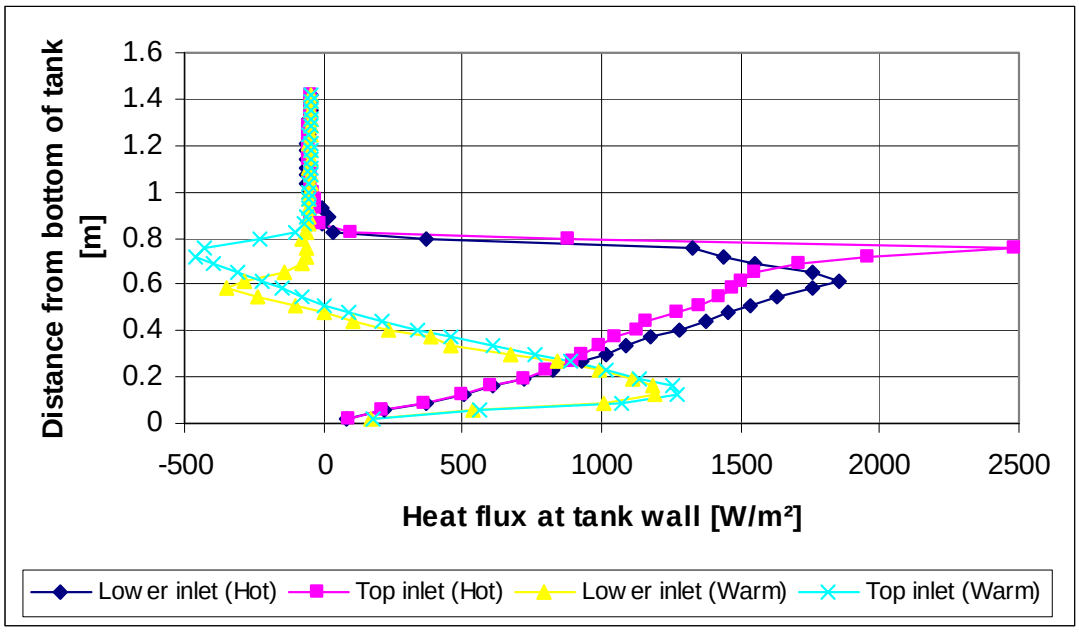

Figure 6-7: Heat flux at the tank wall after 40 minutes for the reference tank and for the tank with top inlet to the mantle.

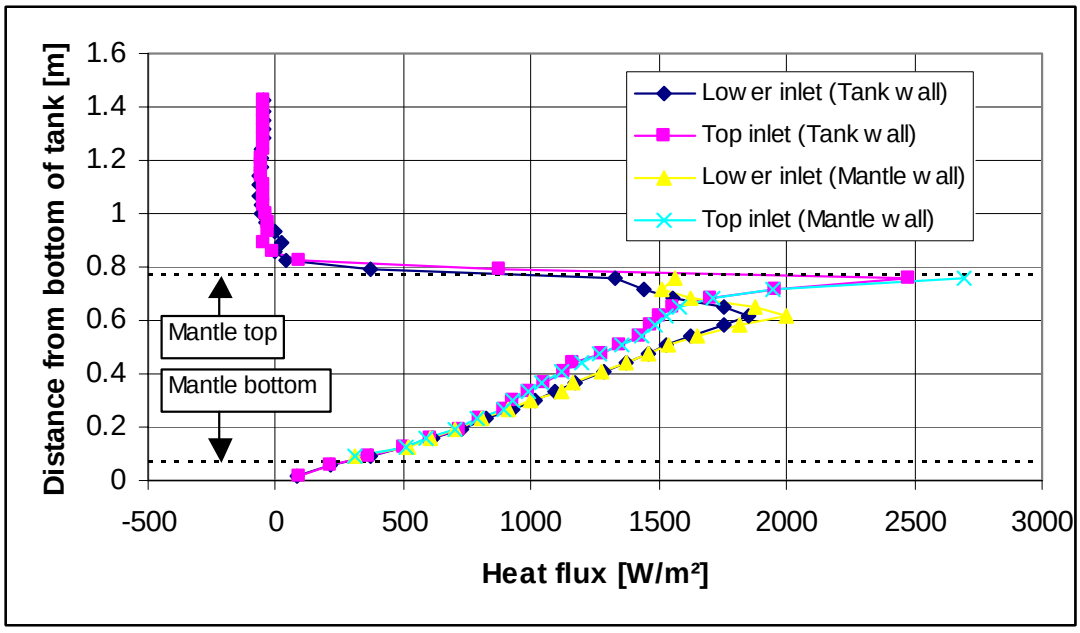

Figure 6-8: Comparison of heat flux at mantle and at tank wall after 40 minutes for hot inlet condition for the reference tank and for the tank with top inlet to the mantle.

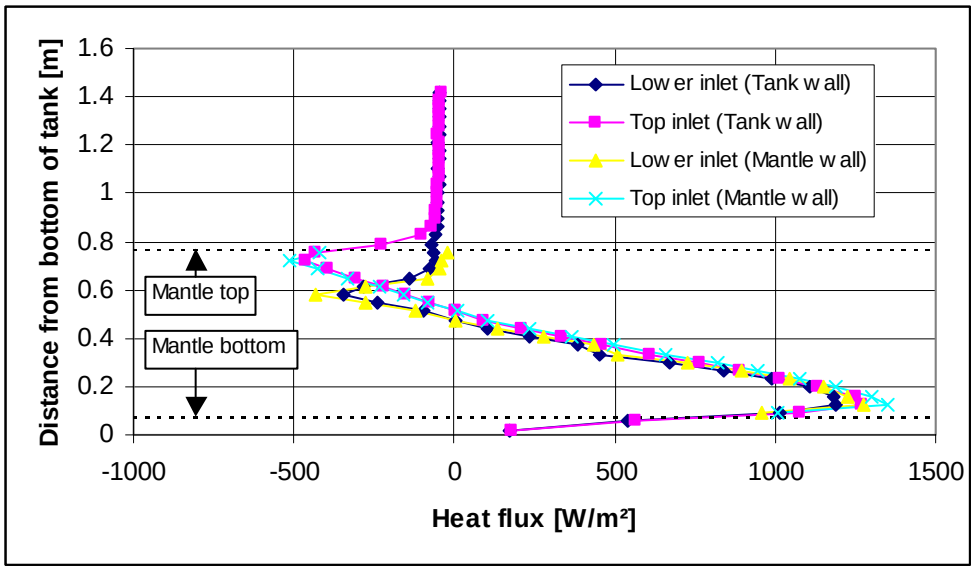

Figure 6-9: Comparison of heat flux at mantle and at tank wall after 40 minutes for warm inlet condition for the reference tank and for the tank with top inlet to the mantle.

Figure 6-8 shows a comparison of the heat flux at the mantle wall and at the tank wall after 40 minutes for hot inlet condition. The heat flux at the level of the mantle is slightly lower at the tank side because of vertical heat conduction in the wall. Figure 6-9 shows a comparison of the heat flux at the mantle wall and at the tank wall after 40 minutes for warm inlet condition. It is seen that at the level of the bottom part of the mantle the heat flux is smaller at the tank side, and at the level of the upper part of the mantle the peak heat flux is less negative at the tank side. In both cases it is due to the vertical heat conduction in the wall.

6.3.2 Velocity

Figure 6-10 shows the tangential velocity profile after 40 minutes at a vertical line (Figure 6-4) through the centre plane of the mantle, midway between the mantle inlet and the mantle outlet for the hot inlet condition. The main incoming stream and the reverse flow in the top of the mantle is for the top inlet concentrated to the very top while the reverse flow for the lower inlet is located lower in the mantle. The high concentration of the flow in the top of the mantle for the top inlet results in the high heat flux as shown in Figure 6-6. In the bottom the suction towards the outlet is of the same size for both inlet configurations.

Figure 6-11 shows the tangential velocity profile after 40 minutes at a vertical line (Figure 6-4) through the centre plane of the mantle, midway between the mantle inlet and the mantle outlet for the warm inlet condition. The reverse flow in the top of the mantle with the top inlet is located at 0.6-0.7 m from the bottom and has a peak velocity at around –0.002 m/s. The reverse flow in the mantle with lower inlet is moved down to 0.5-0.6 m from the bottom and the peak velocity is around –0.001 m/s. Furthermore, the fluid above the reverse flow in the mantle with lower inlet is almost undisturbed. So the lower inlet results in a reverse flow, which occurs in a lower part of the mantle, and it also covers a smaller part of the mantle. This is desirable because it results in negative

heat flux at a lower level in the mantle as shown in Figure 6-6. In the bottom the suction towards the outlet is of the same size for both inlet configurations.

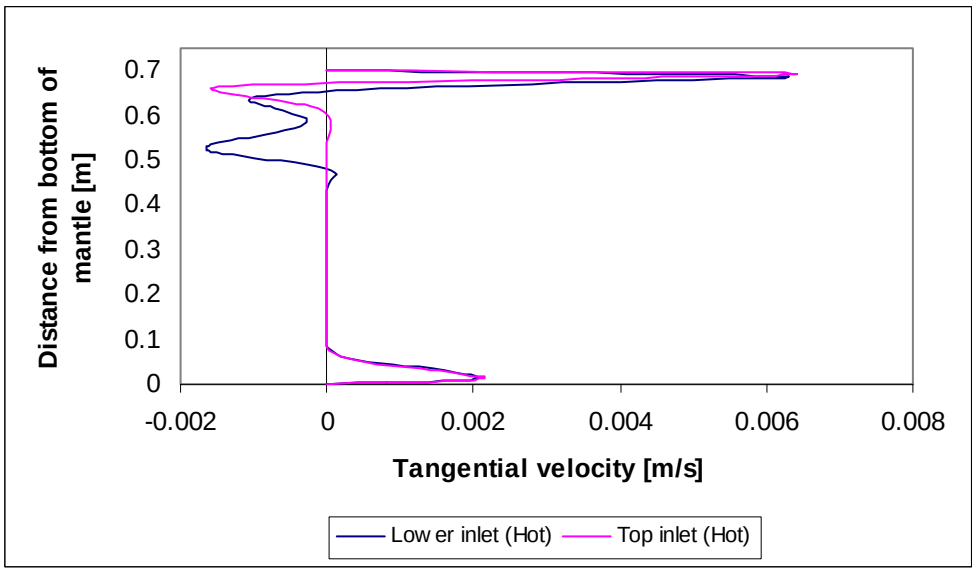

Figure 6-10: Tangential velocity profile in the mantle after 40 minutes in the reference tank and in the tank with top inlet to the mantle (Hot inlet condition).

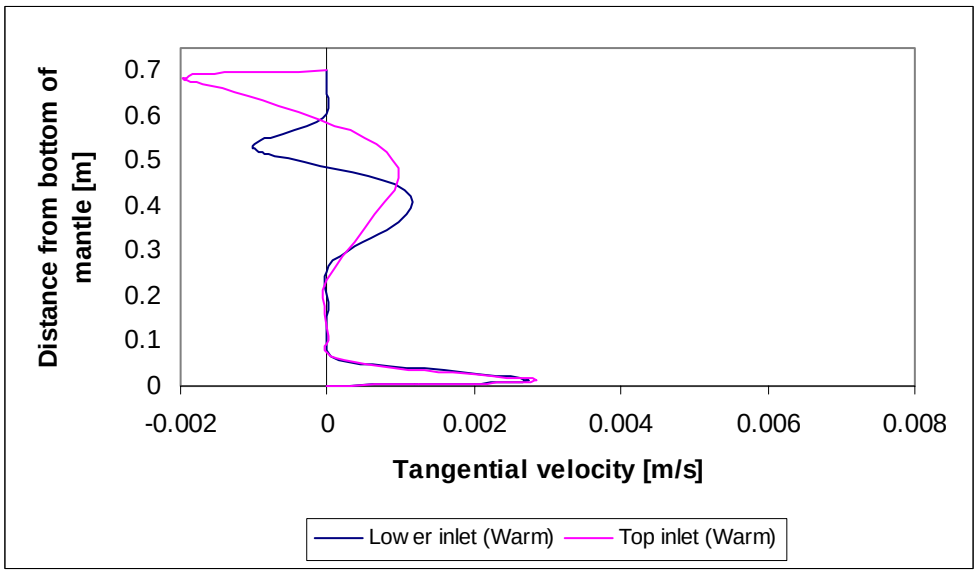

Figure 6-11: Tangential velocity profile in the mantle after 40 minutes in the reference tank and in the tank with top inlet to the mantle (Warm inlet condition).

Figure 6-12 (hot inlet) and Figure 6-13 (warm inlet) show the vertical velocities after 40 minutes at two levels in the inner tank (Figure 6-5). In Figure 6-12a and Figure 6-12b, which are for hot inlet condition, there are an upward flow near the walls and a slow downward flow in the centre of the tank. In Figure 6-12a the peak velocity is highest in the tank with lower inlet because the comparison is made at the level of the lower inlet, and at that level, the heat flux from the tank wall is highest for the lower inlet. In Figure

6-12b the peak velocity is highest in the tank with top inlet because the heat flux at the tank wall is concentrated at mantle top level for the top inlet and from there the flow is accelerated to the level just above the mantle.

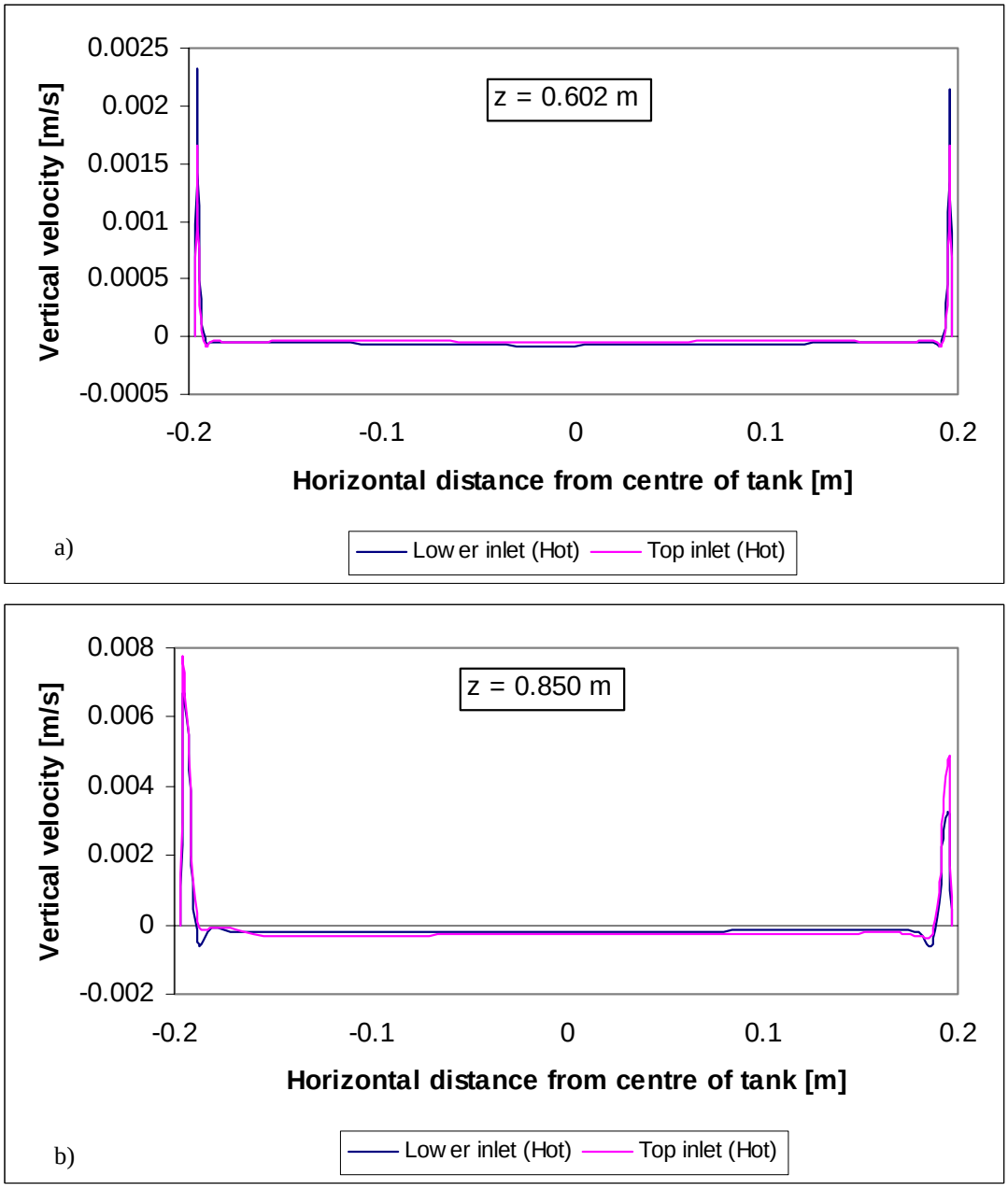

Figure 6-12: Vertical velocity profiles after 40 minutes in the tank in the reference tank and in the tank with top inlet to the mantle. Hot inlet condition. The mantle inlet is in the negative side and the mantle outlet is in the positive side of the horizontal axis.

In Figure 6-13a and Figure 6-13b, which are for warm inlet condition, there are a downward flow near the walls and a very slow upward flow in the centre of the tank. The downward flow is highest at the inlet side and highest in the tank with top inlet, and this is mainly due to the high negative heat flux at the mantle top level for the top inlet. Furthermore, it is seen that the downward flow is highest at z = 0.602 m (at the level of the mantle inlet) because the flow is driven by the cooling due to the negative heat flux at the tank wall at this level. At z = 0.850 m (above the mantle) the flow is driven by the cooling due to the heat loss, which is smaller than the negative heat flux at z = 0.602 m.

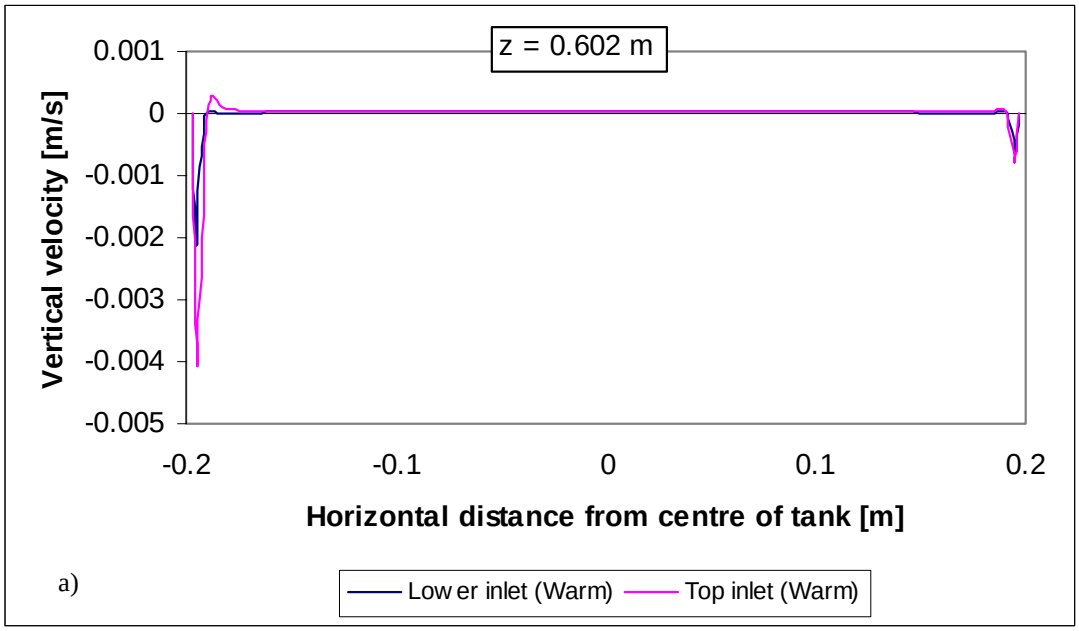

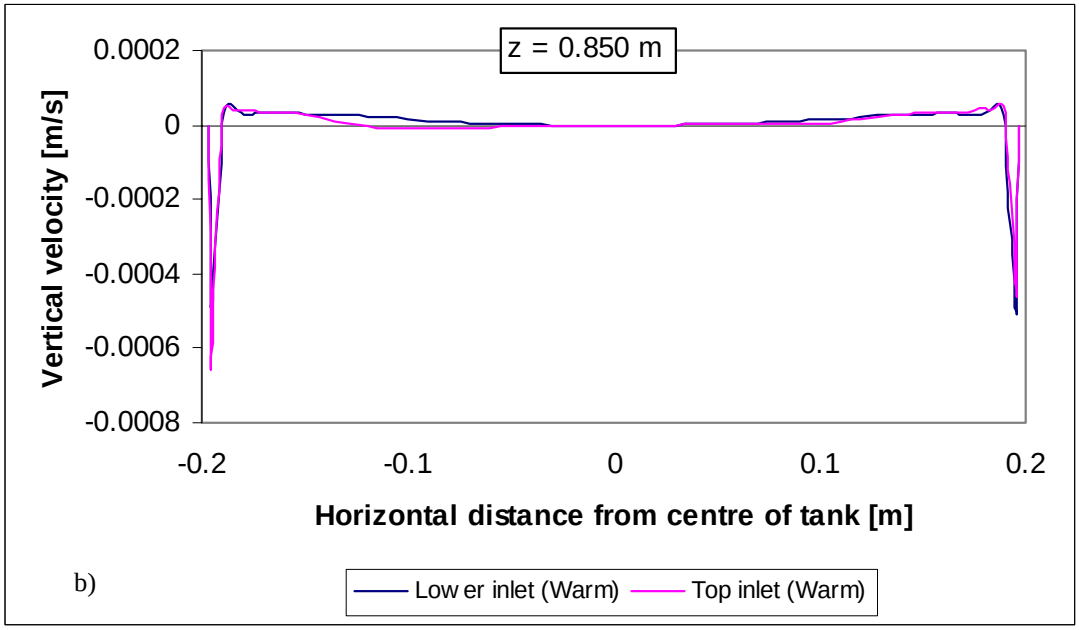

Figure 6-13: Vertical velocity profiles after 40 minutes in the tank in the reference tank and in the tank with top inlet to the mantle. Warm inlet condition. The mantle inlet is in the negative side and the mantle outlet is in the positive side of the horizontal axis.

6.4 Effect of initial thermal conditions

In this section it is investigated how the heat flux and velocities are affected by the initial thermal conditions in the mantle heat exchanger. Two different initial conditions were investigated for the reference tank with the lower inlet: Initially stratified tank (called 'Lower inlet') with temperatures of 60ºC in top of tank and 15ºC in bottom of tank and initially mixed tank (called 'Ini. cold tank') with temperatures of 20ºC. The initially stratified case could resemble a typical situation in a mantle heat exchanger with an auxiliary energy supply, and the initially mixed case could resemble a typical situation after a large draw-off in a mantle heat exchanger used in a preheating system. The temperature profiles for both inner tank and mantle are shown in Figure 6-14.

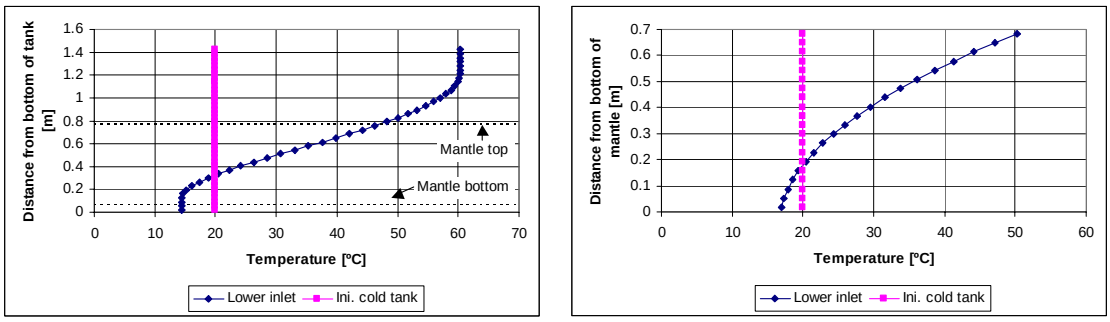

Figure 6-14: The initial temperature profiles of the water in the inner tank (left) and of the mantle fluid in the mantle (right) for the initially stratified (Lower inlet) case and for the initially mixed (Ini. cold tank) case.

6.4.1 Heat flux

Figure 6-15 shows the simulated heat flux profiles at the mantle wall after 40 minutes. The heat flux is highest at the top of the mantle for both the studied cases. However, the heat flux is much higher in the upper part for the initially mixed case due to the large temperature difference between the incoming jet (70ºC) and the mantle wall (~20ºC).

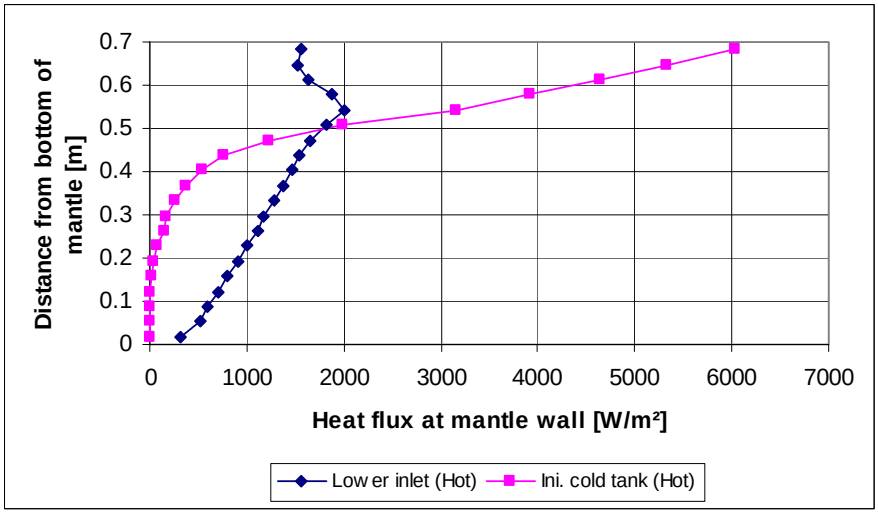

Figure 6-15: Heat flux at mantle wall after 40 minutes for the initially stratified (Lower inlet) case and for the initially mixed (Ini. cold tank) case.

Figure 6-16 shows the simulated heat flux profiles at the tank wall after 40 minutes. At a distance of 0-0.8 m from the bottom of the tank, the heat flux profiles for the tank wall are very similar to the heat flux profiles for the mantle wall. From 0.12 m above the mantle and to the tank top the heat flux is below 0 W/m² in both of the studied cases because of the heat loss at the tank wall above the mantle. The negative heat flux above the mantle is a little smaller in the initially mixed case due to the lower temperature in the top of the tank compared to the initially stratified case.

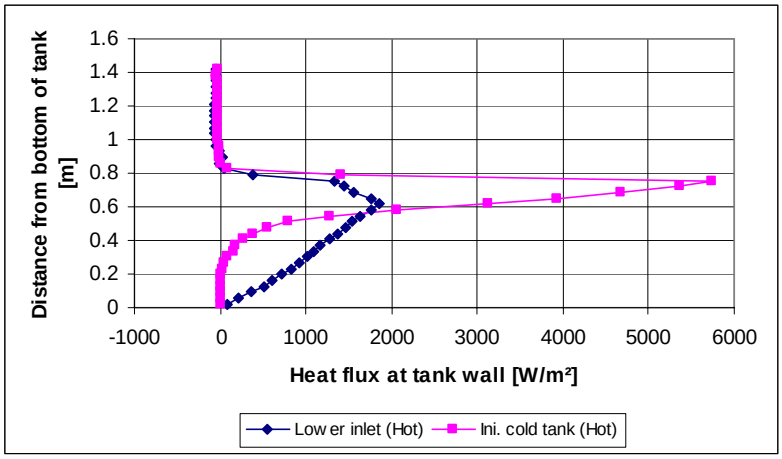

Figure 6-16: Heat flux at tank wall after 40 minutes for the initially stratified (Lower inlet) case and for the initially mixed (Ini. cold tank) case.

6.4.2 Velocity

Figure 6-17 shows the tangential velocity profile after 40 minutes at a vertical line (Figure 6-4) through the centre plane of the mantle, midway between the mantle inlet and the mantle outlet for the two studied cases. The main incoming stream and the reverse flow in the top of the mantle cover the same part of the mantle in the two cases, but the velocities in the initially mixed case have approximately the double size compared to the initially stratified cases. The high velocities in the initially mixed case are due to high buoyancy forces because of the larger temperature difference between the incoming jet and the mantle fluid in the top of the mantle. In the bottom the suction towards the outlet covers a larger part of the mantle, but has lower velocities for the initially mixed case than for the initially stratified case because of the differences in the stratification in the two cases. In the initially stratified case the heavy water at the bottom is forced to the outlet by the suction, while in the initially mixed case the internal forces in the water are much smaller and the suction will cover a larger part of the bottom, but with lower velocities, as the outflow is the same in the two cases.

Figure 6-18 shows the vertical velocities after 40 minutes at two levels in the inner tank (Figure 6-5) for the two studied cases. In Figure 6-18 there are an upward flow near the walls and a slow downward flow in the centre of the tank. The upward velocities are higher in the initially mixed cases at both levels, and this is due to the higher heat flux at the tank wall as shown in Figure 6-16. It is also seen from Figure 6-18 that the upward flow accelerates from z = 0.602 m to z = 0.850 m.

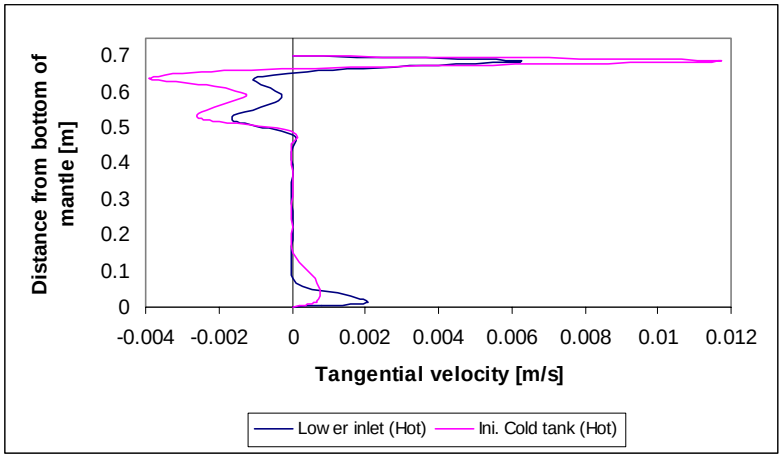

Figure 6-17: Tangential velocity profile in the mantle after 40 minutes for the initially stratified (Lower inlet) case and for the initially mixed (Ini. cold tank) case.

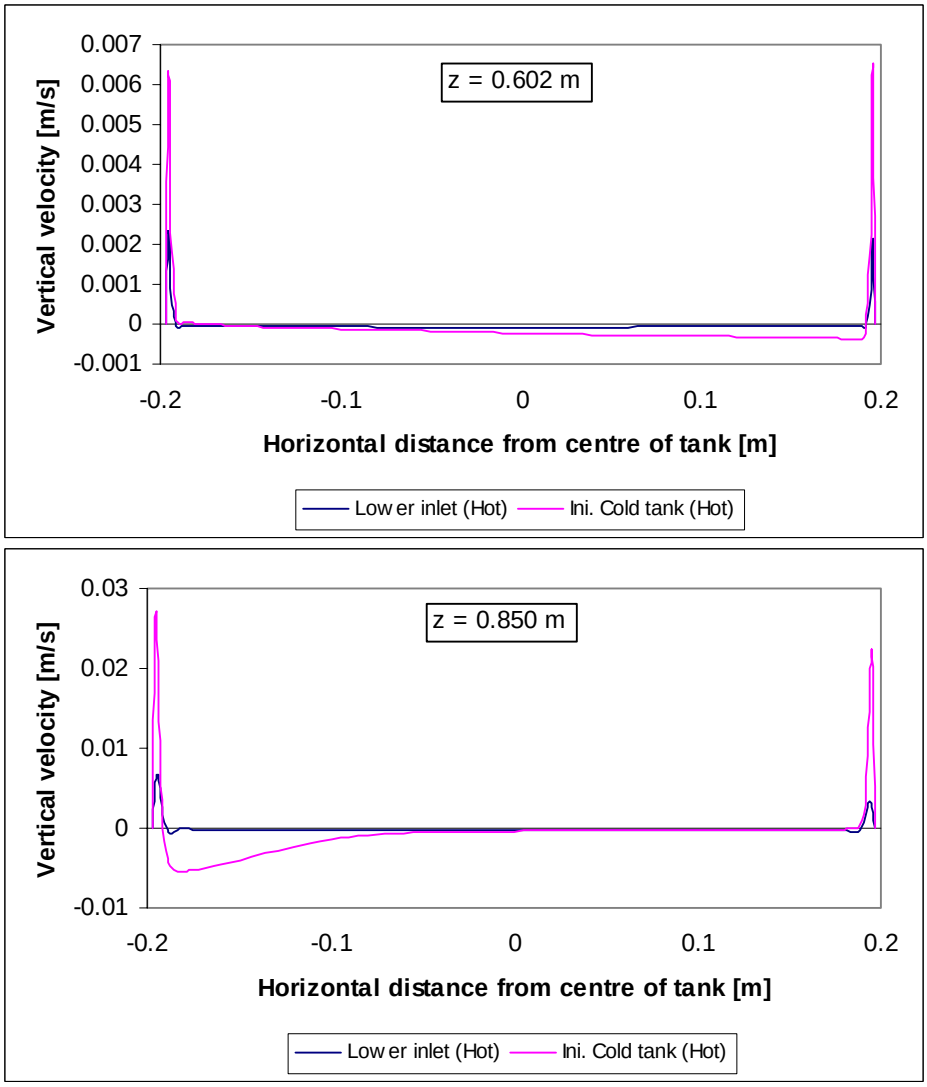

Figure 6-18: Vertical velocity profiles after 40 minutes in the tank for the initially stratified (Lower inlet) case and for the initially mixed (Ini. cold tank) case.

6.4.3 Thermal stratification

Figure 6-19 shows the temperature profiles of the water in the inner tank in the initially mixed case. Figure 6-16 showed that there was a negative heat flux at the tank wall above the mantle, but despite that, Figure 6-19 shows that the water is heated and thermal stratification is built up in the tank above the mantle. This is due to the upward flow near the tank wall as shown in Figure 6-18.

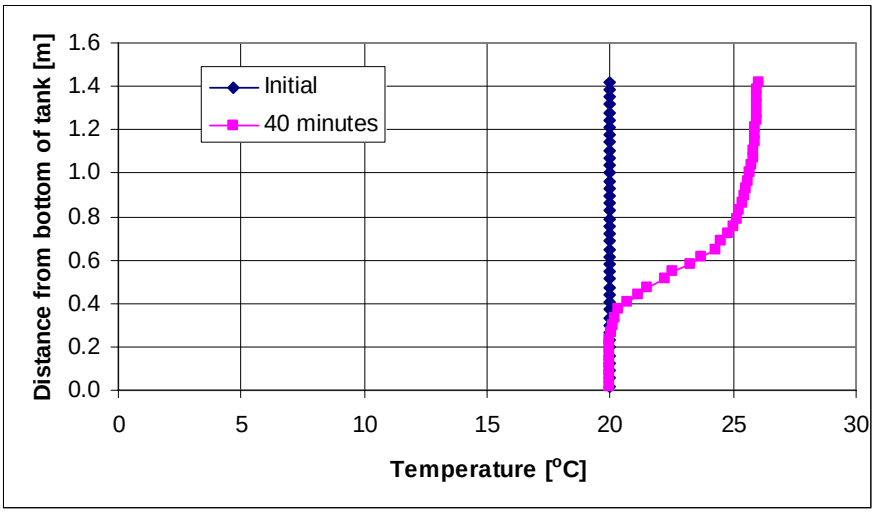

Figure 6-19: The temperature profiles of the water in the inner tank in the initially mixed case.

6.5 Effect of size of mantle inlet port

In this section it is investigated how the heat flux and velocities are affected by the size of the mantle inlet port. Two different sizes were investigated for the reference tank with the lower inlet: ½" inlet (called Lower inlet) and 1" inlet (called 1" inlet). The experiments in section 4.2 showed that the size of the mantle inlet port had minimal effect on the thermal stratification in the tank. However, the two different sizes are investigated in this section to see if there is any effect on the heat flux and on the velocities in the mantle. The mean inlet velocity was 0.025 m/s for the ½" inlet and 0.010 m/s for the 1" inlet to obtain a mantle flow rate of 0.4 l/min in both cases.

6.5.1 Heat flux

Figure 6-20 shows the simulated heat flux profiles at the mantle wall after 40 minutes.
Hot inlet condition: At the level of the mantle inlet (0.525 m from bottom of mantle) the heat flux is highest for the ½" inlet due to higher mean inlet velocity. At the very top of the mantle the heat flux is highest for the 1" inlet. This is unexpected because of the lower inlet velocity. However, in the ½" inlet case mixing occurs near the inlet when the impinging jet hits the mantle wall, this reduces the velocity of the fluid going to the top of the mantle and results in lower heat flux at the top compared to the 1" inlet case.
Warm inlet condition: At the level of the mantle inlet the heat flux is less negative for the 1" case due to the lower inlet velocity.

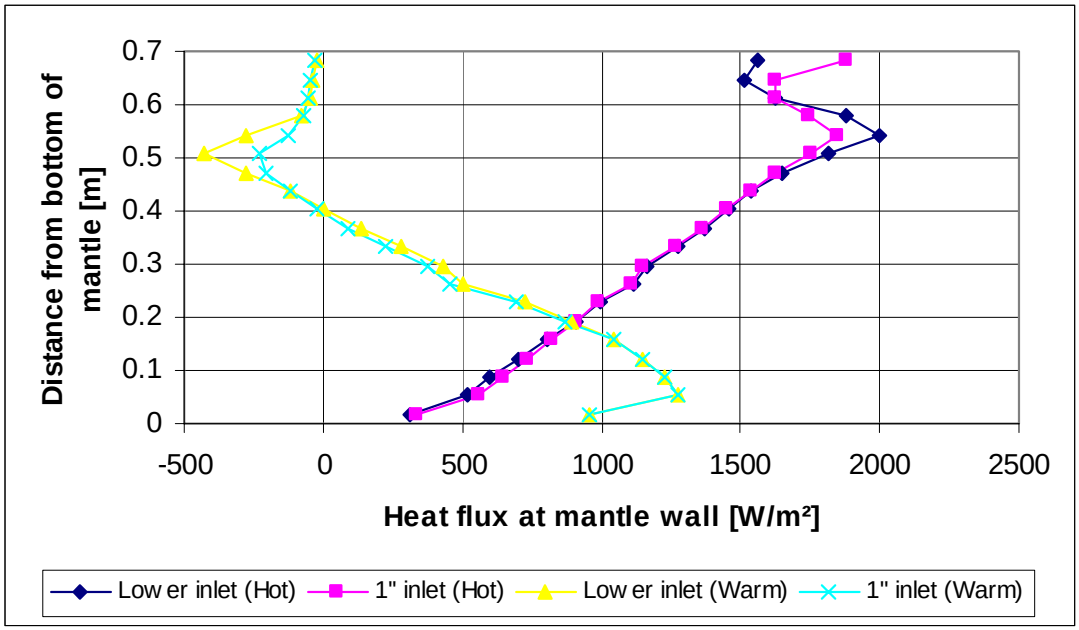

Figure 6-20: Heat flux at mantle wall after 40 minutes for the reference tank with ½" inlet (Lower inlet) and for the 1" inlet (1" inlet) case.

Figure 6-21 shows the simulated heat flux profiles at the tank wall after 40 minutes. At a distance of 0-0.8 m from the bottom of the tank the heat flux profiles for the tank wall are very similar to the heat flux profiles for the mantle wall. From 0.12 m above the mantle and to the tank top, the heat flux is below 0 W/m² in all the studied cases because of the heat loss at the tank wall above the mantle.

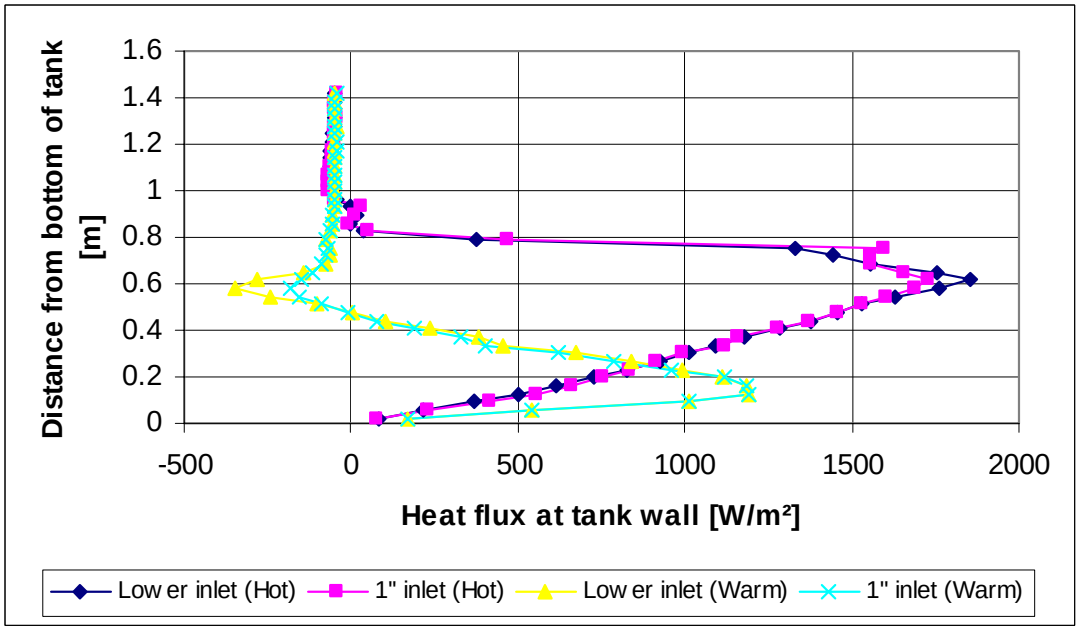

Figure 6-21: Heat flux at tank wall after 40 minutes for the reference tank with ½" inlet (Lower inlet) and for the 1" inlet (1" inlet) case.

6.5.2 Velocity

Figure 6-22 shows the tangential velocity profile after 40 minutes at a vertical line (Figure 6-4) through the centre plane of the mantle, midway between the mantle inlet and the mantle outlet for all the studied cases.

Hot inlet condition: The main incoming stream and the reverse flow in the top of the mantle cover the same part of the mantle for the two mantle inlet sizes, but the velocities at the top is a little higher for the 1" inlet because of the mixing near the inlet in the ½" inlet case as explained in the previous section.

Warm inlet condition: For both cases the reverse flow is located 0.5-0.6 m from the bottom, but the velocity is higher for the ½" inlet, and this results in the higher negative heat flux at this level as shown in Figure 6-20.

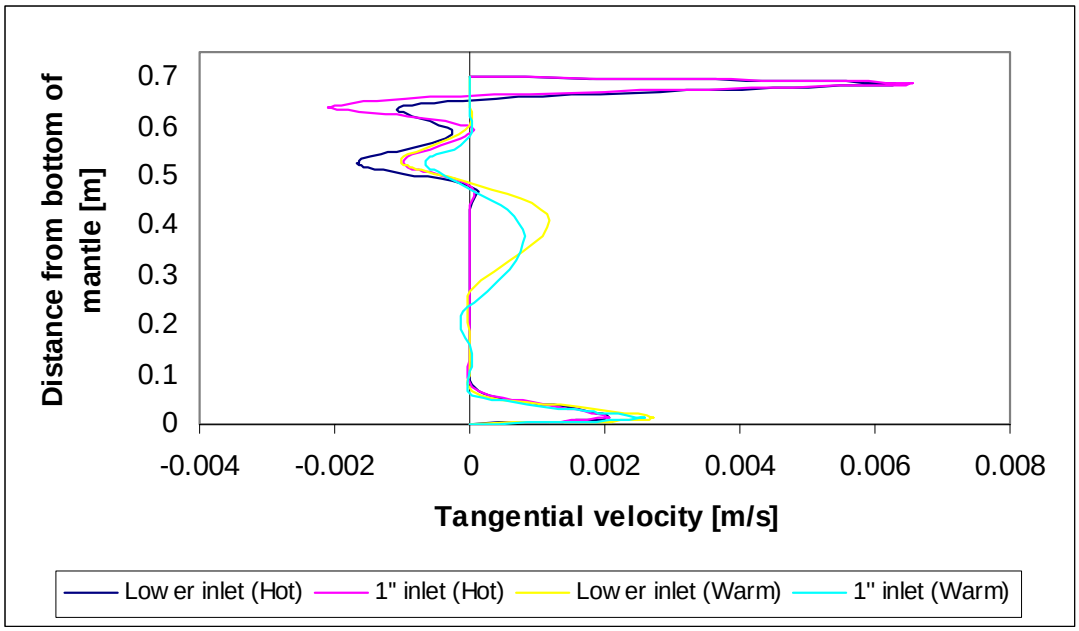

Figure 6-22: Tangential velocity profile in the mantle after 40 minutes for the reference tank with ½" inlet (Lower inlet) and for the 1" inlet (1" inlet) case.

6.5.3 Effect of re-circulation at mantle inlet

When the first CFD-model of the mantle tank with the 1" inlet was developed, it was observed that according to the simulations re-circulation would occur at the inlet. This means that the inlet was too large compared with the incoming flow and then re-circulation can occur at the inlet. The calculated re-circulation is shown in Figure 6-23a for a hot inlet condition. Re-circulation at the inlet can occur also in 'real life' but the results in section 6.5.1 and 6.5.2 are for a 1" inlet without re-circulation in order to find the effect of only the different inlet size. The flow field near the inlet for the 1" inlet without re-circulation is shown in Figure 6-23b, where the inlet pipe is shortened to avoid the re-circulation. It is seen from Figure 6-23a that the re-circulation makes the inlet smaller and this accelerates the incoming jet and results in high inlet velocity that hits the mantle wall before the fluid seeks to the mantle top. In Figure 6-23b there is no re-circulation and the inlet velocity is low, and just after the entrance to the mantle the incoming fluid seeks towards the top due to buoyancy forces.

As the re-circulation is a possibility in 'real life' the numerical results with and without re-circulation are compared in this section, and they are furthermore compared with the results for the ½" inlet.

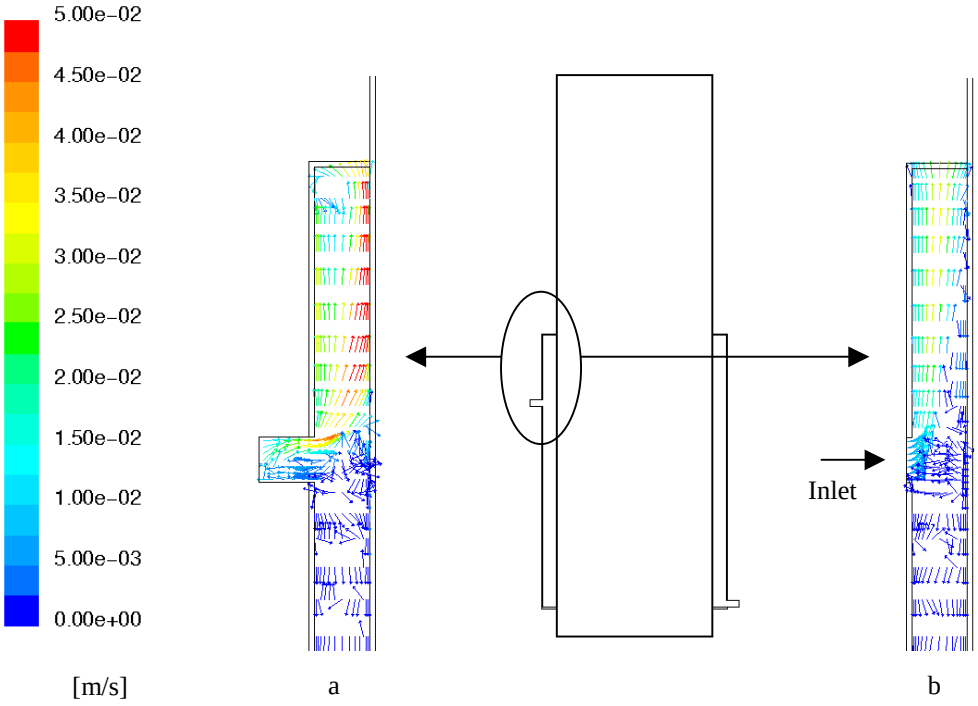

Figure 6-23: The flow field near the mantle inlet (1") for a hot inlet condition with re-circulation (a) and without re-circulation (b).

Heat flux at mantle wall:

Figure 6-24 shows the heat flux profiles at the mantle wall after 40 minutes for all the studied cases. For the hot inlet condition it is seen that that re-circulation results in higher heat flux at the inlet level and this is due to the accelerated inlet velocity shown in Figure 6-23a. For the warm inlet condition the negative heat flux at the level of the inlet is higher for the 1" inlet with re-circulation than for the 1" inlet without re-circulation, but a little lower than the ½" inlet. The positive heat flux is at a distance of 0.15-0.35 m from the bottom highest for the 1" inlet with re-circulation, because the re-circulation at the warm inlet condition forces the inlet jet down in the mantle before it hits the mantle wall and by this increases the heat flux.

Velocity in mantle:

Figure 6-25 shows the tangential velocity profile after 40 minutes at a vertical line (Figure 6-4) through the centre plane of the mantle, midway between the mantle inlet and the mantle outlet for all the studied cases. From Figure 6-25a it is seen that the high velocities of the incoming jet created by the re-circulation result in higher velocities in the upper part of the mantle for the hot inlet condition. Figure 6-25b shows that, for the warm inlet condition, the re-circulation results in higher velocities in the reverse flow than for the 1" inlet without re-circulation. It is not known whether there was re-circulation or not in the experiments with 1" and 2" inlets in chapter 4.

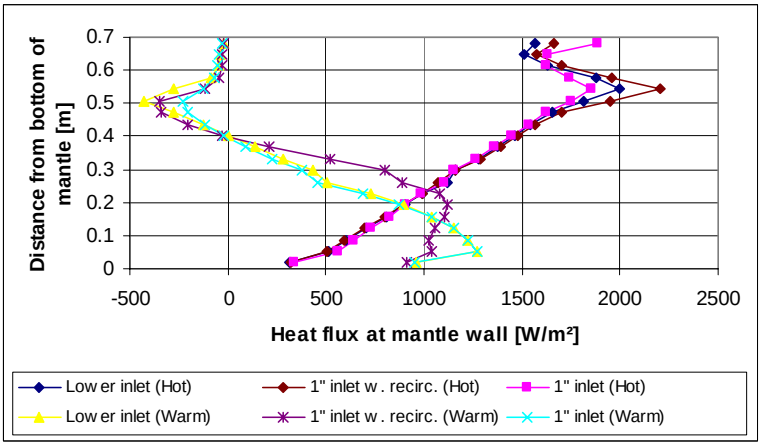

Figure 6-24: Heat flux at the mantle wall after 40 minutes for the ½" inlet (Lower inlet), 1" inlet with re-circulation (1" inlet w. recirc.) and 1" inlet (1" inlet).

a)

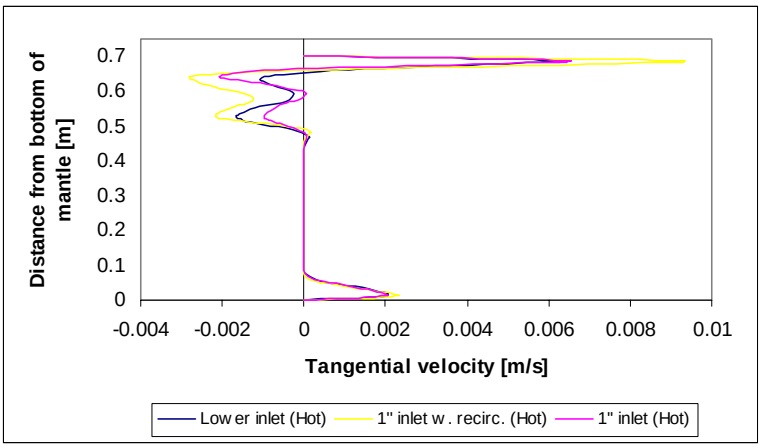

b)

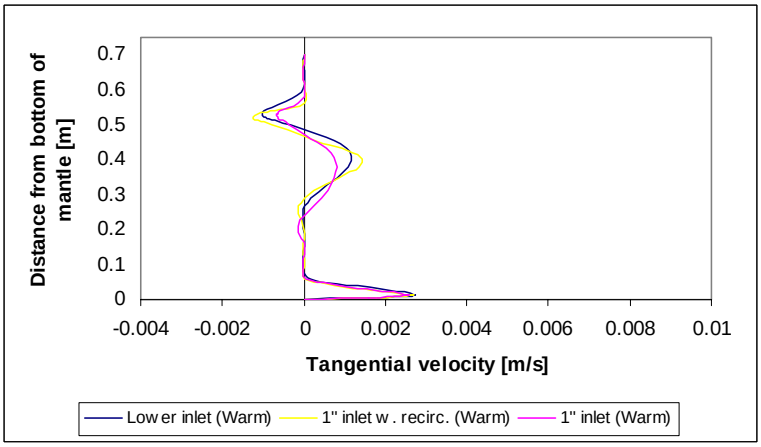

Figure 6-25: Tangential velocity in the mantle after 40 minutes for hot inlet condition (a) and warm inlet condition (b). The velocity profiles is for the ½" inlet (Lower inlet), 1" inlet with re-circulation (1" inlet w. recirc.) and 1" inlet (1" inlet).

6.6 Effect of mantle gap

In this section it is investigated how the heat flux and velocities are affected by the size of the mantle gap. Two different mantle gaps were investigated for the reference tank with the lower inlet: A large mantle gap (called Lower inlet) of 0.0335 m and a small mantle gap (called Small mantle gap) of 0.0105 m. The different mantle gaps result in different mantle volumes and at a flow rate of 0.4 l/min it takes 80 minutes to change all the fluid in the mantle with a mantle gap of 0.0335 m while it takes 24 minutes to change all the fluid in the mantle with a mantle gap of 0.0105 m.

6.6.1 Heat flux

Figure 6-26 shows the simulated heat flux profiles at the mantle wall after 40 minutes.
Hot inlet condition: At the level of the mantle inlet (0.525 m from bottom of mantle) and at the very top of the mantle, the heat flux is slightly higher for the small mantle gap. From 0.5 m and down to the bottom of the mantle the heat flux is highest for the small mantle gap. This is mainly due to the smaller mantle volume where the mantle fluid is changed faster and the temperature in the bottom part of the mantle is therefore higher, and this results in the higher heat flux.
Warm inlet condition: At the level of the mantle inlet the heat flux is less negative for the small mantle gap, this is unexpected, but it will be discussed in section 6.13. At the bottom of the mantle the positive heat flux is highest for the small mantle gap because of the faster change of the fluid in the mantle.

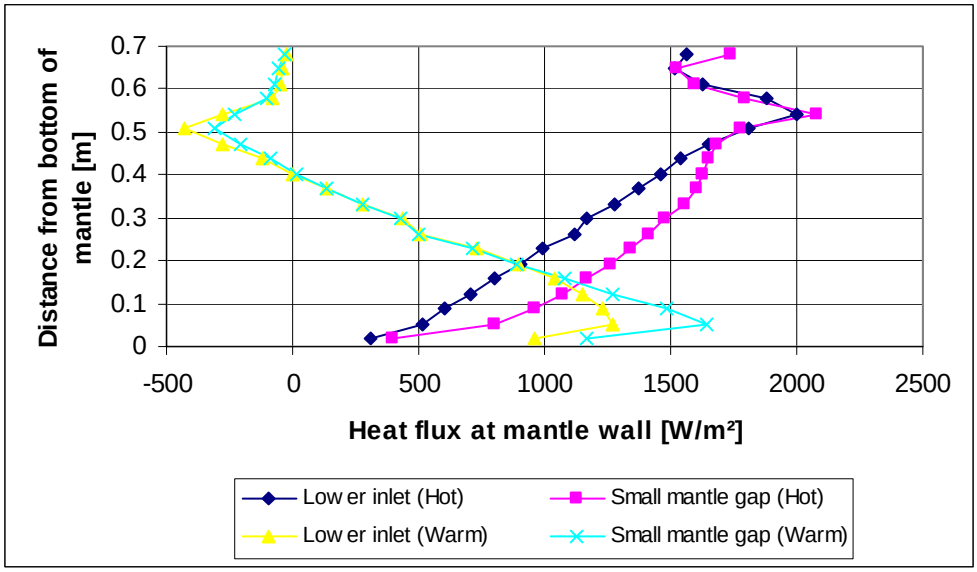

Figure 6-26: Heat flux at mantle wall after 40 minutes for the reference tank with large mantle gap (Lower inlet) and for the tank with small mantle gap (Small mantle gap).

Figure 6-27 shows the simulated heat flux profiles at the tank wall after 40 minutes. At a distance of 0-0.8 m from the bottom of the tank, the heat flux profiles for the tank wall are very similar to the heat flux profiles for the mantle wall. From 0.12 m above the mantle and to the tank top, the heat flux is below 0 W/m² in all the studied cases because of the heat loss at the tank wall above the mantle.

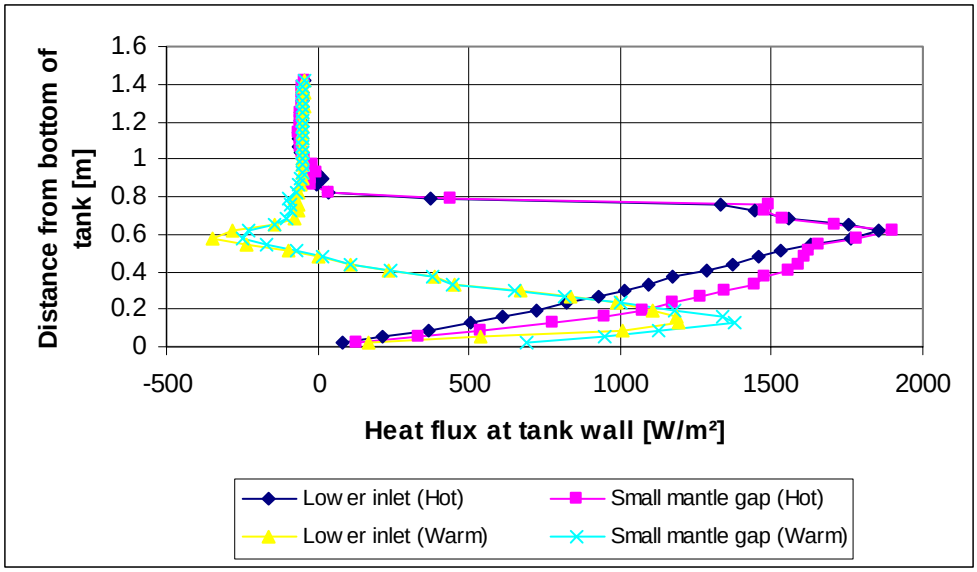

Figure 6-27: Heat flux at the tank wall after 40 minutes for the reference tank with large mantle gap (Lower inlet) and for the tank with small mantle gap (Small mantle gap).

6.6.2 Velocity

Figure 6-28 shows the tangential velocity profile after 40 minutes at a vertical line (Figure 6-4) through the centre plane of the mantle, midway between the mantle inlet and the mantle outlet for all the studied cases.

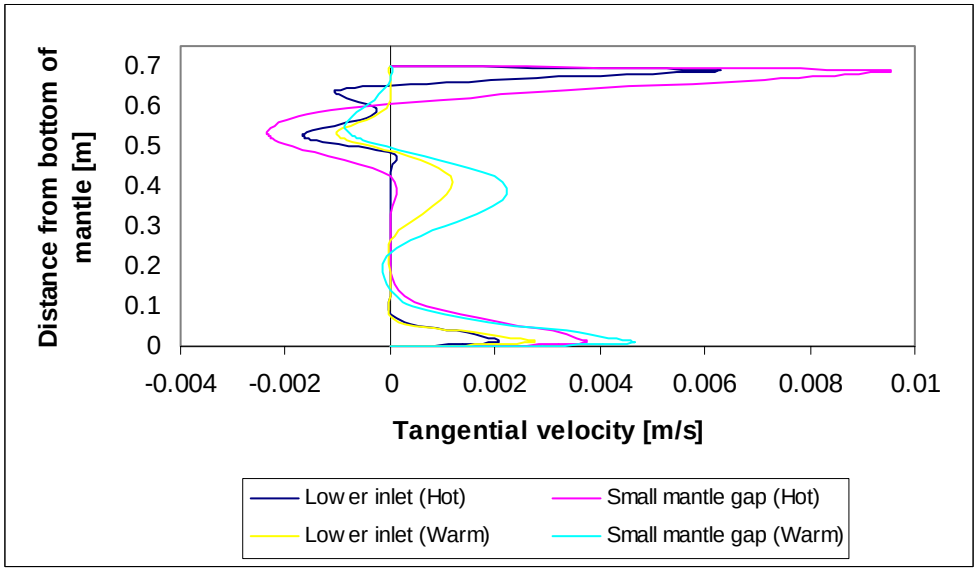

Figure 6-28: Tangential velocity profile in the mantle after 40 minutes for the reference tank with large mantle gap (Lower inlet) and for the tank with small mantle gap (Small mantle gap).

Hot inlet condition: The main incoming stream and the reverse flow in the top of the mantle cover a larger part of the upper mantle for the small mantle gap. The velocities in the upper part and in the bottom are higher for the small mantle gap.
Warm inlet condition: The reverse flow is in the large mantle gap located 0.5-0.6 m from the bottom and 0.5-0.66 m from the bottom in the small mantle gap, so a larger part in the upper mantle is disturbed by the reverse flow in the small mantle gap. In the bottom half the velocities are higher in the small mantle gap.

6.7 Effect of mantle flow rate

In this section it is investigated how the heat flux and velocities are affected by the mantle flow rate. Two different flow rates were investigated for the reference tank with the lower inlet: A flow rate of 0.4 l/min (called Lower inlet) and 0.8 l/min (called High flow rate). The mean inlet velocity is 0.025 m/s for the flow rate of 0.4 l/min and 0.05 m/s for the flow rate of 0.8 l/min.

6.7.1 Heat flux

Figure 6-29 shows the simulated heat flux profiles at the mantle wall after 40 minutes.
Hot inlet condition: The heat flux is highest for the high flow rate and especially from the level of the mantle inlet and down to the bottom. This was expected because the high flow rate results in higher velocities and also higher temperatures in the lower part of the mantle. It is seen for the high flow rate that the heat flux is not concentrated at the top, but instead it is even distributed over the mantle wall from the inlet and down to the bottom.
Warm inlet condition: The high flow rate results in a higher negative heat flux in the upper part of the mantle and at the bottom the there is a high positive heat flux due to higher velocities and higher temperatures.

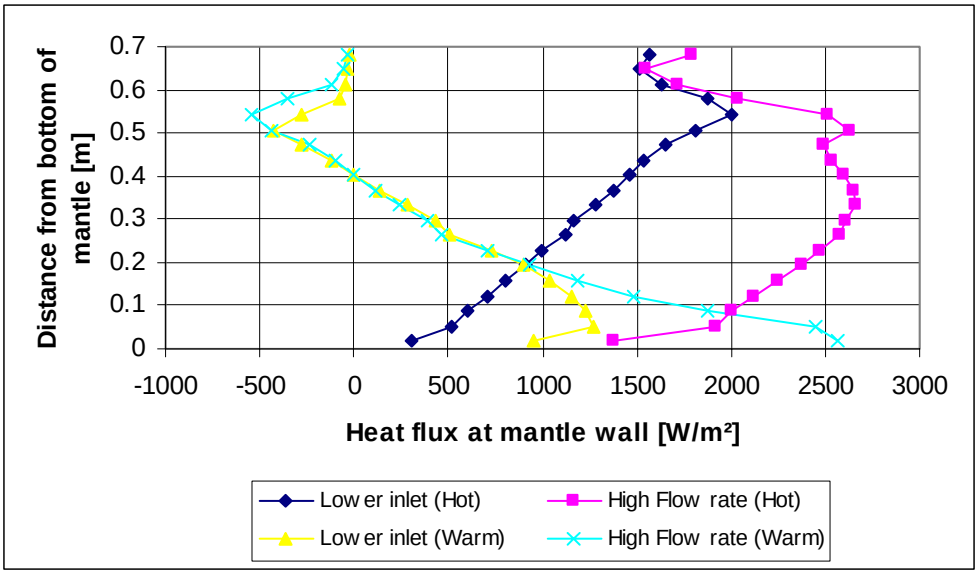

Figure 6-29: Heat flux at the mantle wall after 40 minutes for the tank with a flow rate of 0.4 l/min (Lower inlet) and for the tank with a high flow rate of 0.8 l/min (High flow rate).

Figure 6-30 shows the simulated heat flux profiles at the tank wall after 40 minutes. At a distance of 0-0.8 m from the bottom of the tank, the heat flux profiles for the tank wall are very similar to the heat flux profiles for the mantle wall. From 0.12 m above the mantle and to the tank top, the heat flux is below 0 W/m² in all the studied cases because of the heat loss at the tank wall above the mantle.

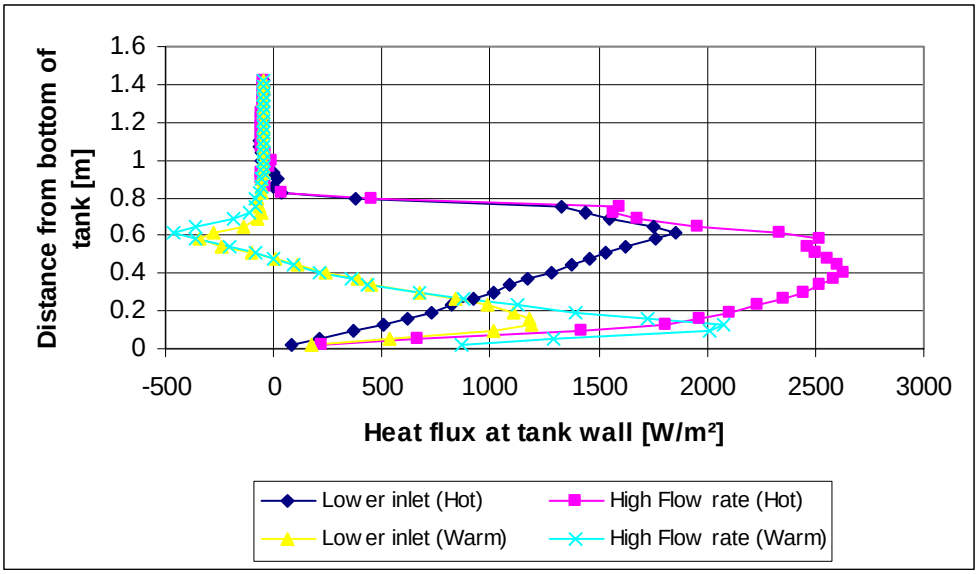

Figure 6-30: Heat flux at tank wall after 40 minutes for the tank with a flow rate of 0.4 l/min (Lower inlet) and for the tank with a high flow rate of 0.8 l/min (High flow rate).

6.7.2 Velocity

Figure 6-31 shows the tangential velocity profile after 40 minutes at a vertical line (Figure 6-4) through the centre plane of the mantle, midway between the mantle inlet and the mantle outlet for all the studied cases.

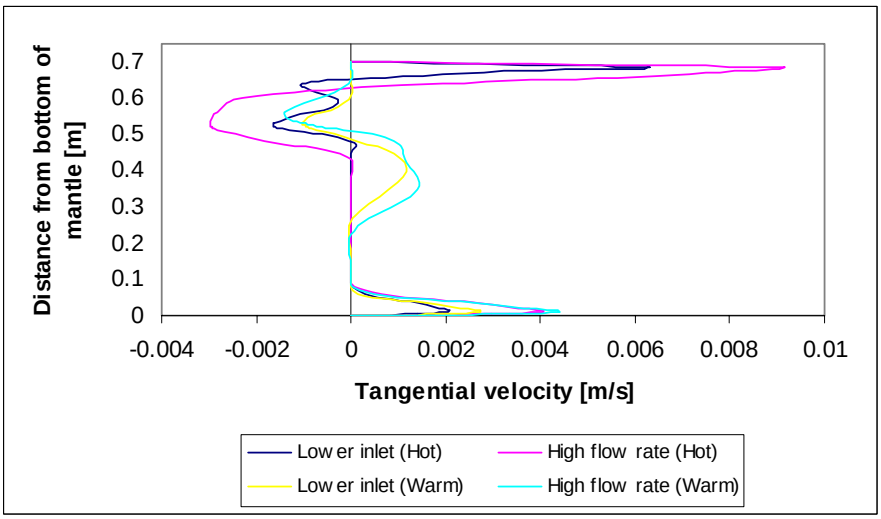

Figure 6-31: Tangential velocity profiles in the mantle after 40 minutes for the tank with a flow rate of 0.4 l/min (Lower inlet) and for the tank with a high flow rate of 0.8 l/min (High flow rate).

Hot inlet condition: The main incoming stream and the reverse flow in the top of the mantle cover a larger part of the upper mantle for the high flow rate. The velocities in the upper part and in the bottom are higher for the high flow rate.
Warm inlet condition: The reverse flow is, for the flow rate of 0.4 l/min, located 0.5-0.6 m from the bottom and 0.5-0.66 m from the bottom for the high flow rate, and the velocities are higher for the high flow rate. Thus a larger part in the upper mantle is disturbed by the reverse flow when the flow rate is high, and this results in the higher negative heat flux in the upper part of the mantle. In the bottom the velocities are higher for the high flow rate.

6.8 Effect of tank material

In this section it is investigated how the tank material affects the heat flux and velocities. Two different materials were investigated for the reference tank with the lower inlet: Steel St-37 (called Lower inlet) and stainless steel (called Stainless steel). Table 6-4 shows the properties used in the CFD-simulations for the different materials. It is seen that the major difference in properties for the two materials is the thermal conductivity, and the lower thermal conductivity for stainless steel results in lower vertical heat flux in the tank walls. It is preferable to reduce the downward vertical flux in the tank wall that moves the heat from the top down to the bottom. A wall thickness of 2 mm is normally used in storage tanks made of stainless steel, but in this simulation a wall thickness of 3 mm is used.

Property	Steel St-37	Stainless steel
Density, [kg/m³]	7820	8000
Specific heat, [J/kg·K]	460	480
Thermal conductivity, [W/m·K]	60	15

Table 6-4: Properties for the two tank materials.

6.8.1 Heat flux

Figure 6-32 shows the simulated heat flux profiles at the mantle wall after 40 minutes.
Hot inlet condition: There are minor differences in the heat flux profiles, but the heat flux is slightly higher in the upper part of the mantle for stainless steel and slightly lower in the bottom part of the mantle. So the inability of stainless steel to distribute the heat over the mantle wall results in a slightly higher flux in the upper part of the mantle where the inlet jet hits the wall.
Warm inlet condition: Minor differences on the heat flux profiles are observed at the warm inlet condition.

Figure 6-33 shows the simulated heat flux profiles at the tank wall after 40 minutes. At a distance of 0-0.8 m from the bottom of the tank, the heat flux profiles for the tank wall are very similar to the heat flux profiles for the mantle wall. From 0.12 m above the mantle and to the tank top, the heat flux is below 0 W/m² in all the studied cases because of the heat loss at the tank wall above the mantle. The differences between the heat flux at the mantle wall and at the tank wall are larger for the reference tank than for the tank with stainless steel, because of the lower thermal conductivity of stainless steel.

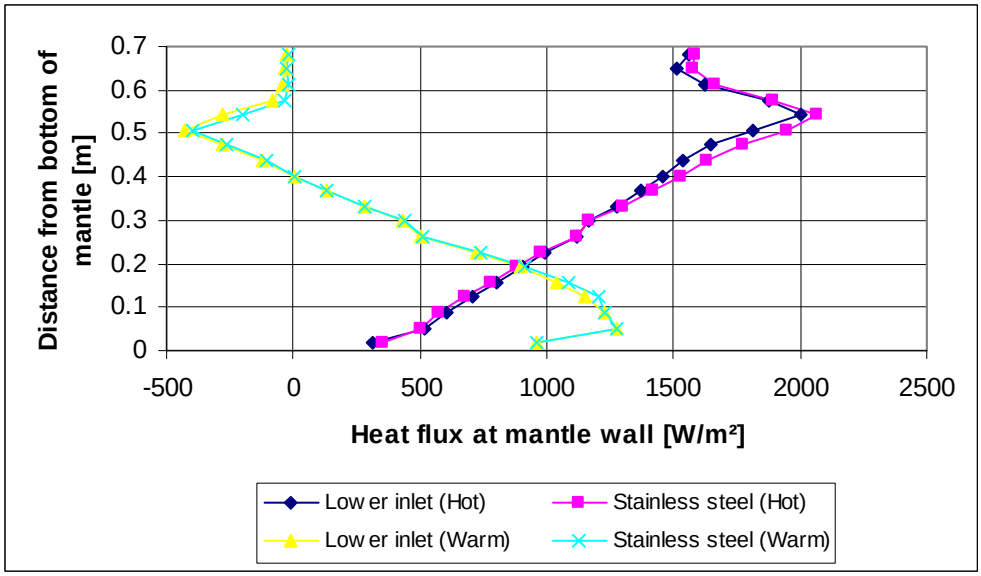

Figure 6-32: Heat flux at the mantle wall after 40 minutes for the reference tank of steel st-37 (Lower inlet) and for the tank of stainless steel (Stainless steel).

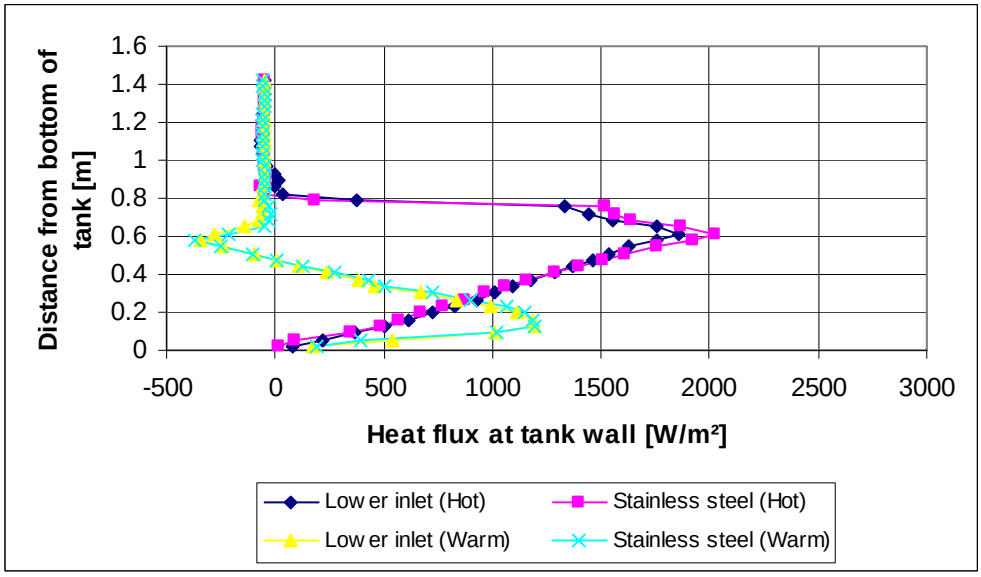

Figure 6-33: Heat flux at tank wall after 40 minutes for the reference tank of steel st-37 (Lower inlet) and for the tank of stainless steel (Stainless steel).

6.8.2 Velocity

Figure 6-34 shows the tangential velocity profile after 40 minutes at a vertical line (Figure 6-4) through the centre plane of the mantle, midway between the mantle inlet and the mantle outlet for all the studied cases.

Hot inlet condition: There are minor differences in the velocity profiles. However, the velocities at the top of the mantle are slightly higher for Steel St-37.

Warm inlet condition: Again minor differences in the velocity profiles are observed, but the velocities in the reverse flow are slightly higher for Steel St-37.

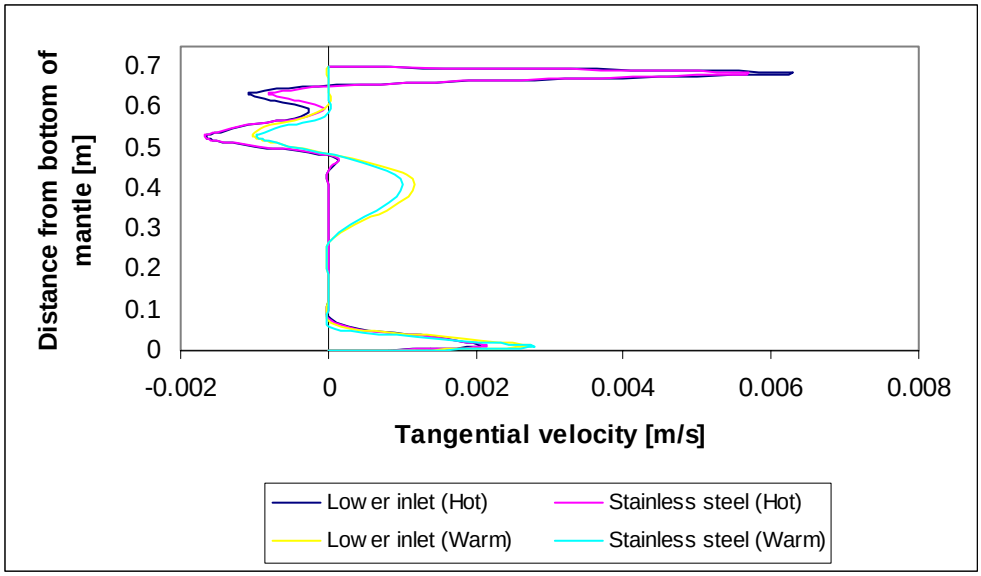

Figure 6-34: Tangential velocity profiles in the mantle after 40 minutes for the reference tank of steel st-37 (Lower inlet) and for the tank of stainless steel (Stainless steel).

6.9 Effect of mantle height

In this section it is investigated how the heat flux and velocities are affected by the height of the mantle. Two different mantle heights were investigated for the reference tank with the lower inlet: A height of 0.7 m (called Lower inlet) covering approximately the low half of the tank height, and a height of 1.44 m (called High mantle) covering all the tank height. If the tank has an auxiliary volume the top of the mantle is usually situated below the level of the auxiliary volume to avoid using auxiliary energy to heat up some of the mantle fluid. In a mantle heat exchanger used as a preheating tank, the mantle will usually cover all the tank height. The mantle inlet is located 0.36 m from the top in the high mantle, which is one fourth of the total mantle height. See Table 6-3 for more details of the tank with the high mantle. The initial temperatures of the domestic water inside the inner tank are the same in the two cases and are shown in Figure 6-14 (Lower inlet). The initial temperatures of the mantle fluid are shown in Figure 6-35. The initial temperatures of the mantle fluid in the high mantle are chosen to be 1.5 K higher than the temperature of the domestic water at the same level in the tank.

6.9.1 Heat flux

Figure 6-37 shows the simulated heat flux profiles at the mantle wall after 40 minutes.
Hot inlet condition: The heat flux profile is quite different for the high mantle. The main heat flux occurs at a relative mantle height of 0.1-0.6 and not at the top of the mantle. The reason for this is that when the mantle is covering all the tank height, the temperature difference between the mantle fluid and the water is lower in the top of the mantle compared to the temperature difference when the mantle covers the bottom half of the tank, because the temperature of the water in the tank is higher at the top than at the middle of the tank. The temperature difference is shown in Figure 6-36.
Warm inlet condition: The peak of the negative heat flux also occurs at the level of the mantle inlet for the high mantle. The negative heat flux below the inlet covers a larger

part of the mantle for the high mantle and this is also explained by the higher temperatures of the water in the inner tank compared to the temperatures of the water at the same relative mantle height levels when the mantle covers the bottom half of the tank.

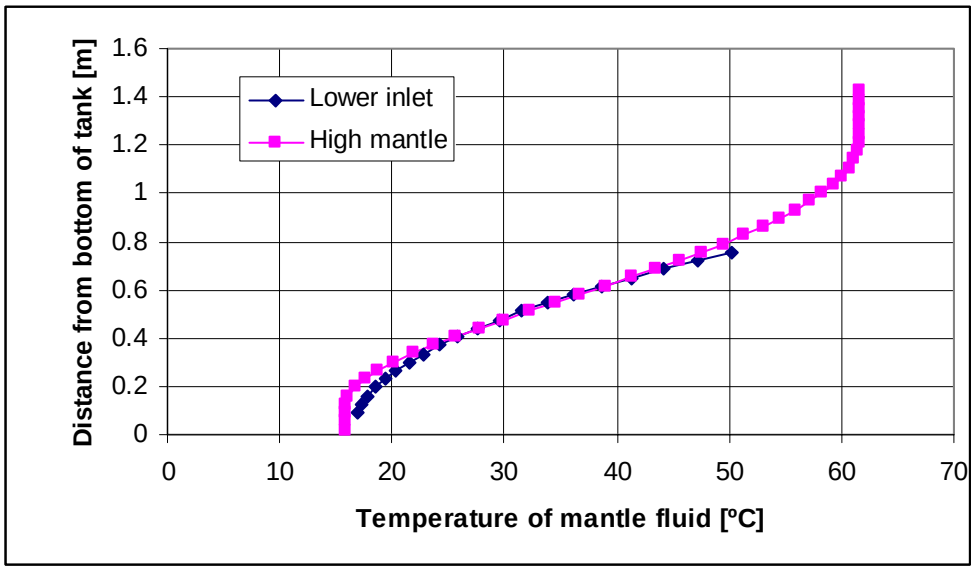

Figure 6-35: Initial temperatures of the mantle fluid in the two cases.

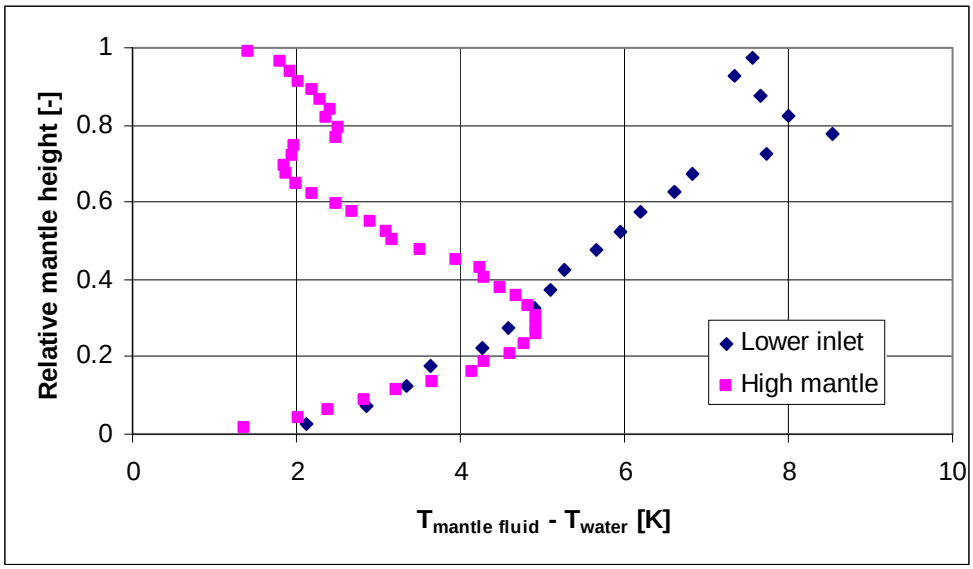

Figure 6-36: Temperature difference between the mantle fluid and the domestic water in the inner tank after 40 minutes with the hot inlet condition.

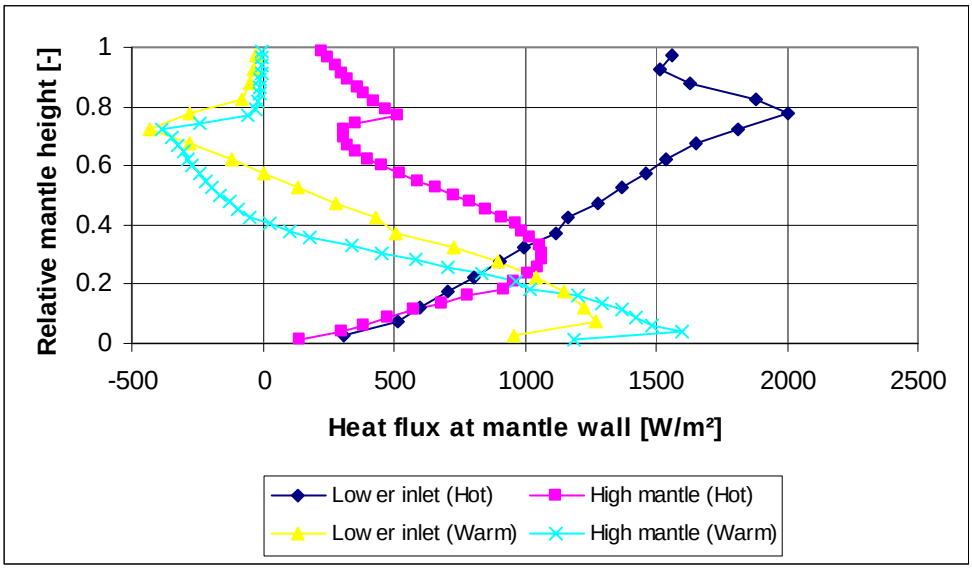

Figure 6-37: Heat flux at the mantle wall after 40 minutes for the reference tank with the mantle covering the bottom half of the tank (Lower inlet) and the tank with the high mantle (High mantle).

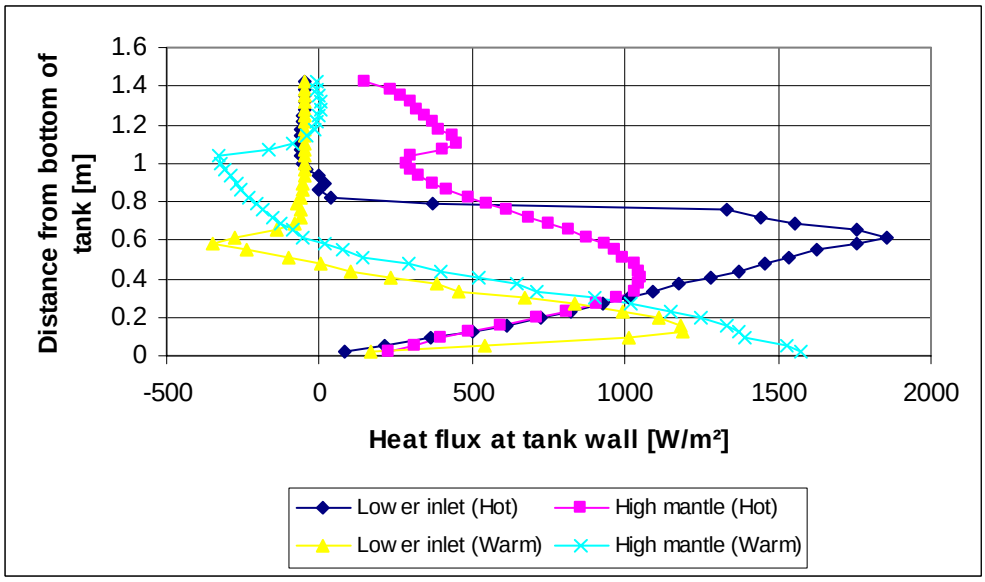

Figure 6-38: Heat flux at the tank wall after 40 minutes for the reference tank with the mantle covering the bottom half of the tank (Lower inlet) and the tank with the high mantle (High mantle).

Figure 6-38 shows the simulated heat flux profiles at the tank wall after 40 minutes.
Hot inlet condition: The main heat flux for the high mantle occurs at a lower level and with a lower heat flux than when the mantle covers the bottom half of the tank. On the other hand there is positive heat flux at the upper half of the tank wall in the high mantle case, but in the upper part of the tank the solar energy will have to compete with a possible auxiliary energy supply system.

Warm inlet condition: The negative heat flux at the tank wall occurs at a higher level in the high mantle case and thus taking heat out of the tank at a higher level. In a tank heated by means of both auxiliary energy and solar energy the heat taken out will be supplied again by the auxiliary energy supply system.
Figure 6-38 illustrates very well why it is not recommended to let the mantle cover all the tank height if the tank is heated by means of both auxiliary energy and solar energy. In a preheating tank the temperatures of the domestic water will typically be lower than the temperatures considered in this case and there it would be an advantage to let the mantle cover all the tank height.

6.9.2 Velocity

Figure 6-39 shows the tangential velocity profile after 40 minutes at a vertical line (Figure 6-4) through the centre plane of the mantle, midway between the mantle inlet and the mantle outlet for all the studied cases.
Hot inlet condition: The velocity profiles look similar except that the tangential velocities are higher in the mantle covering the bottom half of the tank, this is probably due to the difference in mantle volume in the two cases.
Warm inlet condition: Also here the tangential velocity profiles are quite similar except that the incoming fluid in the high mantle seeks a lower relative level because the thermal equilibrium is at a lower relative level.

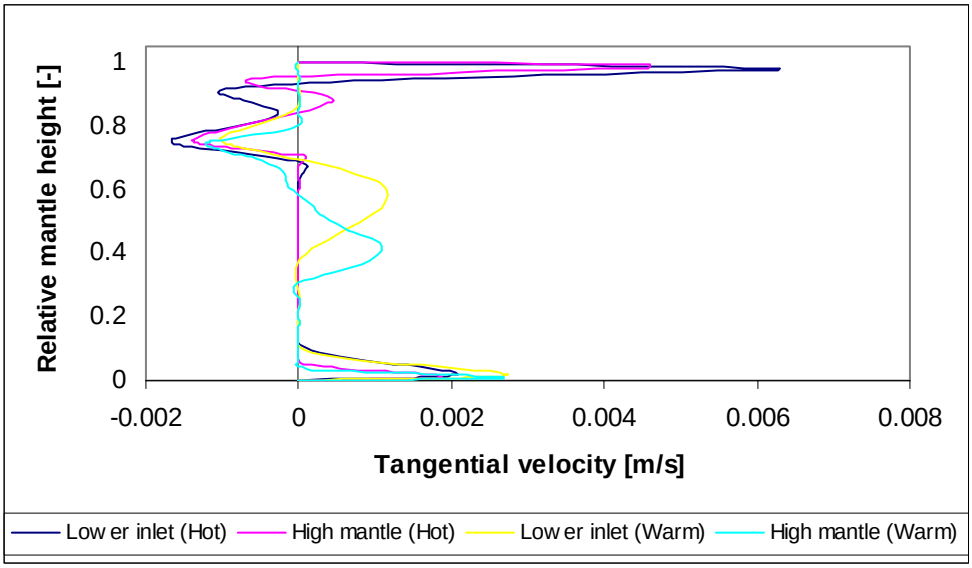

Figure 6-39: Tangential velocity profiles in the mantle after 40 minutes for the reference tank with the mantle covering the bottom half of the tank (Lower inlet) and the tank with the high mantle (High mantle).

Figure 6-40 shows the vertical velocities after 40 minutes at a level of z = 0.850 m in the inner tank (Figure 6-5) for both hot and warm inlet conditions. The comparison level in the tank is just above the mantle for the case where the mantle covers the bottom half of the tank while it is below the level of the mantle inlet in the high mantle case. Therefore higher velocities near the tank wall are observed for the hot inlet condition (Figure 6-40a) in the case where the mantle covers the bottom half of the tank. For the

warm inlet condition (Figure 6-40b) higher downward velocities are observed near the tank wall in the high mantle case because there is a high negative heat flux at the tank wall at this level.

a)

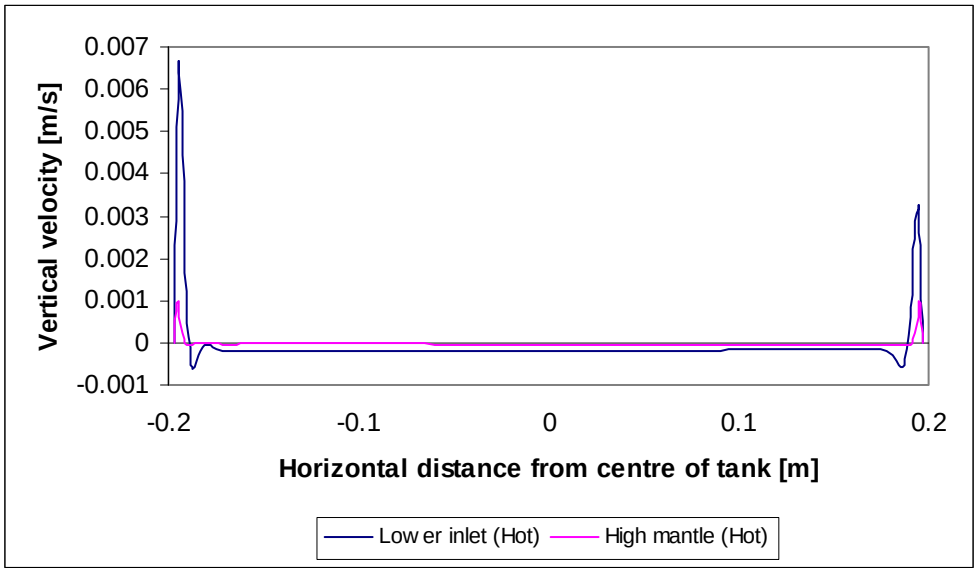

b)

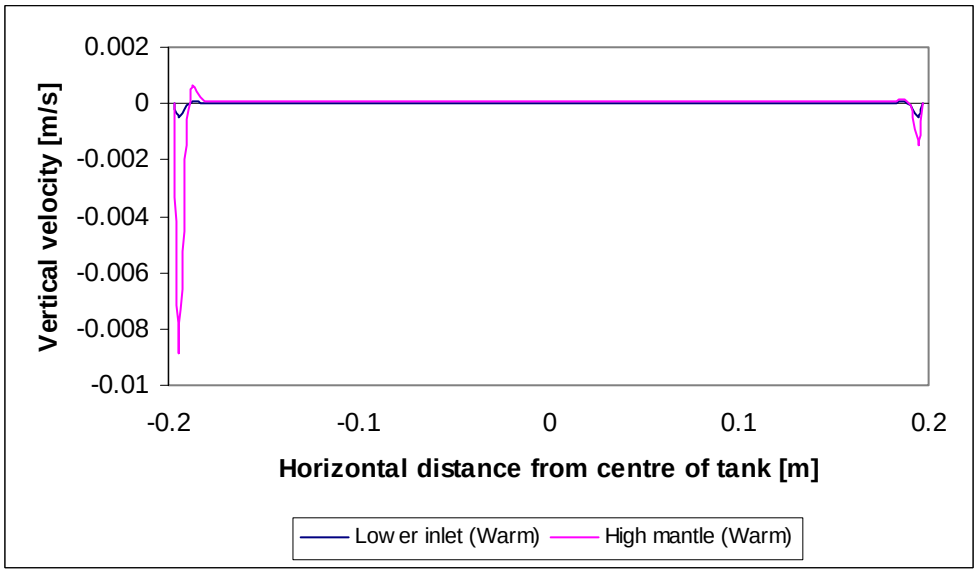

Figure 6-40: Vertical velocity profiles in the tank (at z = 0.850 m) after 40 minutes for the reference tank with the mantle covering the bottom half of the tank (Lower inlet) and the tank with the high mantle (High mantle). a) is for the hot inlet condition and b) is for the warm inlet condition. The mantle inlet is in the negative side of the horizontal axis.

6.10 Effect of mantle fluid

In this section it is investigated how the mantle fluid affects the heat flux and velocities. Two different mantle fluids were investigated for the reference tank with the lower inlet: Water (called Lower inlet) and 40% propylene glycol/water mixture (called 40% Glycol). Table 6-5 shows the thermal properties used in the CFD-simulations for the two mantle fluids. All the properties except density are kept constant in the simulations. The densities in Table 6-5 are the reference values used in the Boussinesq

approximation as explained in section 3.5. It is seen that water is a better heat transfer media than the 40% propylene glycol/water mixture due to the higher heat capacity and thermal conductivity.

Property	Water	40% propylene glycol/water mixture
Density, [kg/m³]	990	1017
Specific heat, [J/kg·K]	4178	3815
Thermal conductivity, [W/m·K]	0.623	0.428
Viscosity, [kg/m·s]	$6.66 \cdot 10^{-4}$	$2.39 \cdot 10^{-3}$
Thermal expansion coefficient, [1/K]	0.000422	0.000628

Table 6-5: Thermal properties at 45ºC for the two mantle fluids used in the CFD-simulations.

6.10.1 Heat flux

Figure 6-41 shows the simulated heat flux profiles at the mantle wall after 40 minutes.
Hot inlet condition: The higher specific heat and thermal conductivity for water results in a higher heat flux than for the 40% glycol.
Warm inlet condition: At the level of the mantle inlet water has a higher negative heat flux due to the higher specific heat and thermal conductivity. In the rest of the mantle there is minor difference in the heat flux.

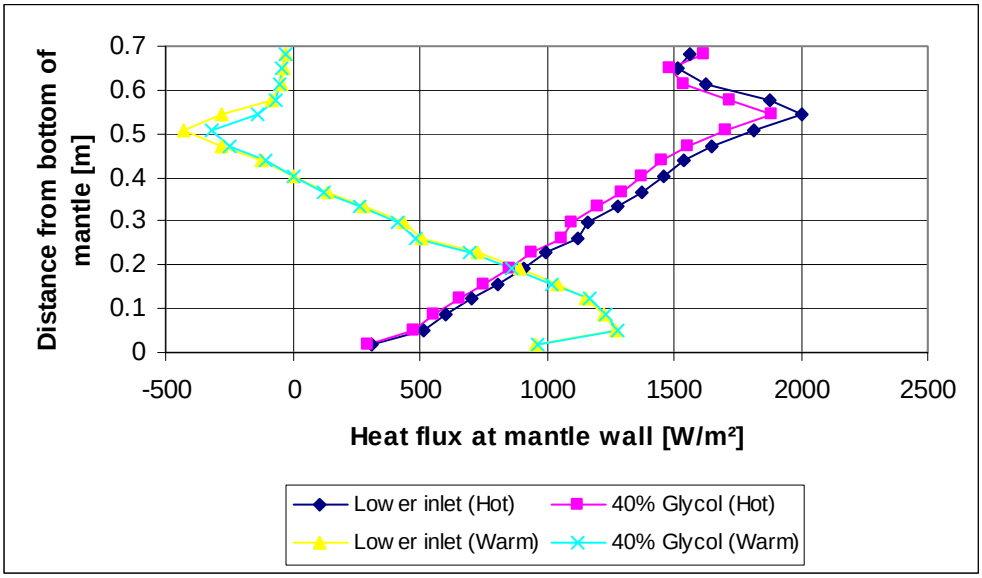

Figure 6-41: Heat flux at the mantle wall after 40 minutes for the reference tank with water as mantle fluid (Lower inlet) and for the tank using 40% propylene glycol/water mixture as mantle fluid (40% Glycol).

Figure 6-42 shows the simulated heat flux profiles at the tank wall after 40 minutes. At a distance of 0-0.8 m from the bottom of the tank the heat flux profiles for the tank wall are very similar to the heat flux profiles for the mantle wall. From 0.12 m above the mantle and to the tank top the heat flux is below 0 W/m² in all the studied cases because of the heat loss at the tank wall above the mantle.

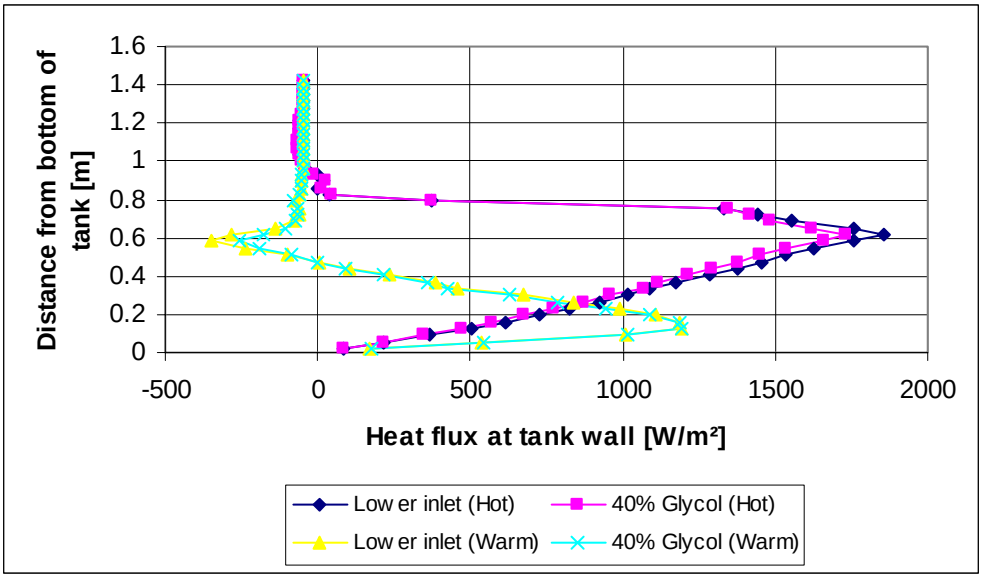

Figure 6-42: Heat flux at the tank wall after 40 minutes for the reference tank with water as mantle fluid (Lower inlet) and for the tank using 40% propylene glycol/water mixture as mantle fluid (40% Glycol).

6.10.2 Velocity

Figure 6-43 shows the tangential velocity profile after 40 minutes at a vertical line (Figure 6-4) through the centre plane of the mantle, midway between the mantle inlet and the mantle outlet for all the studied cases.

Minor differences are observed in the tangential velocity profiles for both hot and warm inlet conditions.

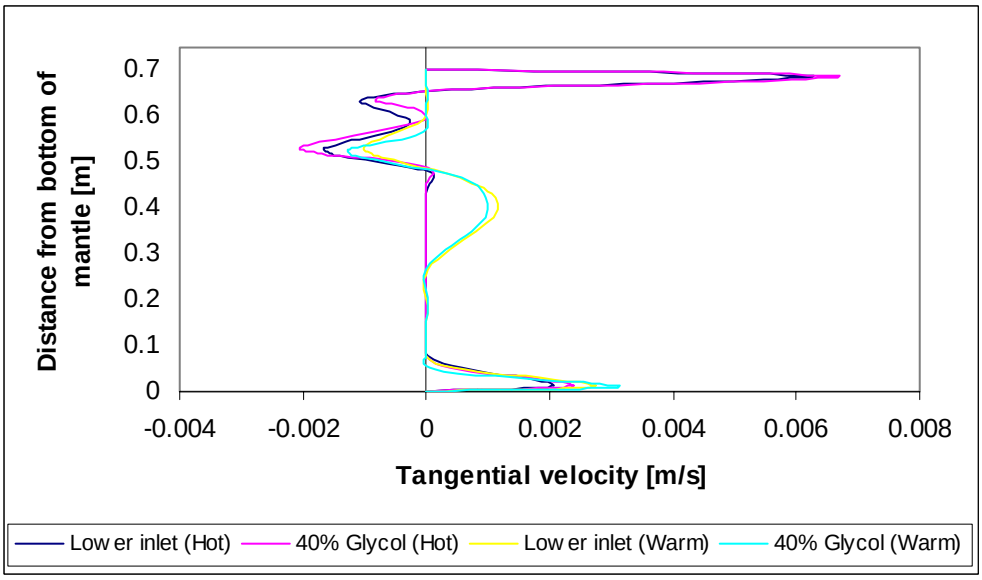

Figure 6-43: Tangential velocity profiles in the mantle after 40 minutes for the reference tank with water as mantle fluid (Lower inlet) and for the tank using 40% propylene glycol/water mixture as mantle fluid (40% Glycol).

6.11 Effect of small H/D ratio

In this section it is investigated how the heat flux and velocities are affected by a small H/D ratio of the inner tank. Two different H/D ratios were investigated: The reference tank with a H/D ratio of 3.7 (called Lower inlet) and a small H/D ratio of 2 (called Small HD). The reference tank with a H/D ratio of 3.7 has a mantle volume of 31.9 l while the tank with a H/D ratio of 2 has a mantle volume of 25.7 l. The case of the small H/D ratio is only simulated for the hot inlet condition.

6.11.1 Heat flux

Figure 6-44 shows the simulated heat flux profiles at the mantle wall after 40 minutes. The heat flux is higher in the case of the small H/D ratio. The heat transfer area and the mantle volume are smaller in the case of the small H/D ratio and this result in the higher heat flux. The reasons for the higher heat flux are that the smaller mantle volume and the smaller heat transfer area result in higher mantle fluid temperatures.

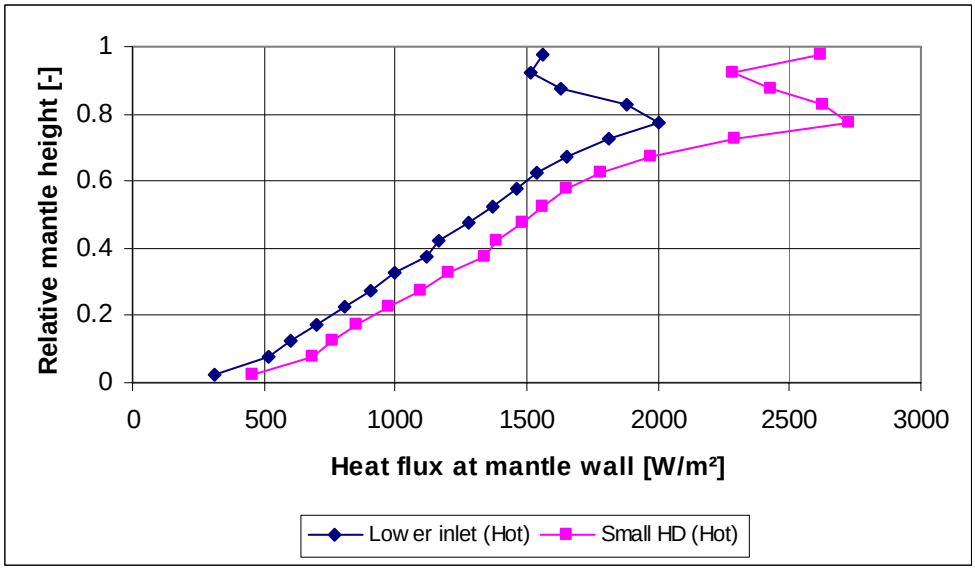

Figure 6-44: Heat flux at the mantle wall after 40 minutes for the reference tank with a H/D ratio of 3.7 (Lower inlet) and for the tank with a small H/D ratio of 2 (Small HD).

Figure 6-45 shows the simulated heat flux profiles at the tank wall after 40 minutes. At a relative distance of 0-0.52 from the bottom of the tank, the heat flux profiles for the tank wall are very similar to the heat flux profiles for the mantle wall. From a relative distance of 0.1 above the mantle and to the tank top, the heat flux is below 0 W/m² in the two studied cases because of the heat loss at the tank wall above the mantle.

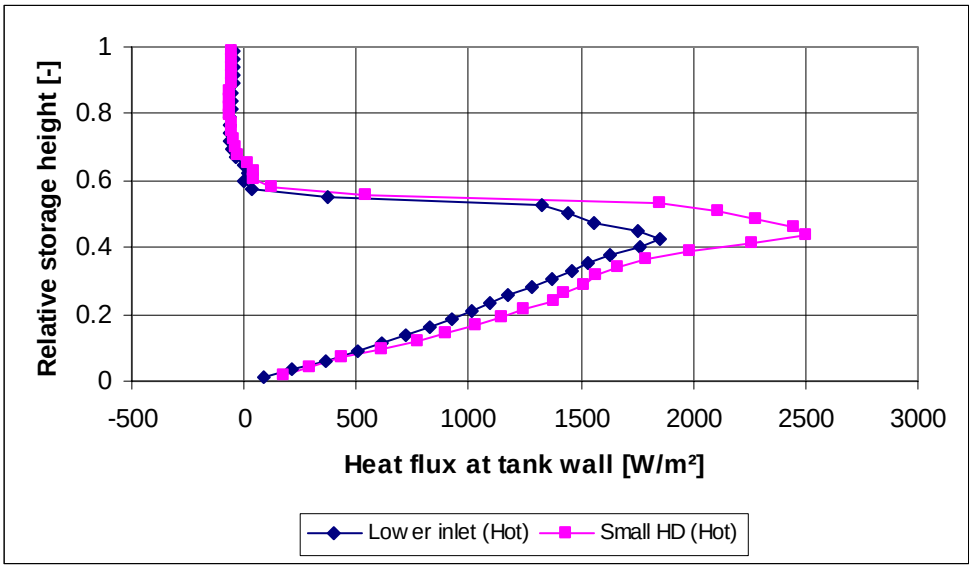

Figure 6-45: Heat flux at tank wall after 40 minutes for the reference tank with a H/D ratio of 3.7 (Lower inlet) and for the tank with a small H/D ratio of 2 (Small HD).

6.11.2 Velocity

Figure 6-46 shows the tangential velocity profile after 40 minutes at a vertical line (Figure 6-4) through the centre plane of the mantle, midway between the mantle inlet and the mantle outlet for the two studied cases. The shapes of the velocity profiles are quite similar, but the smaller mantle volume causes a higher velocity of the incoming stream at the top of the mantle in the case of the small H/D ratio.

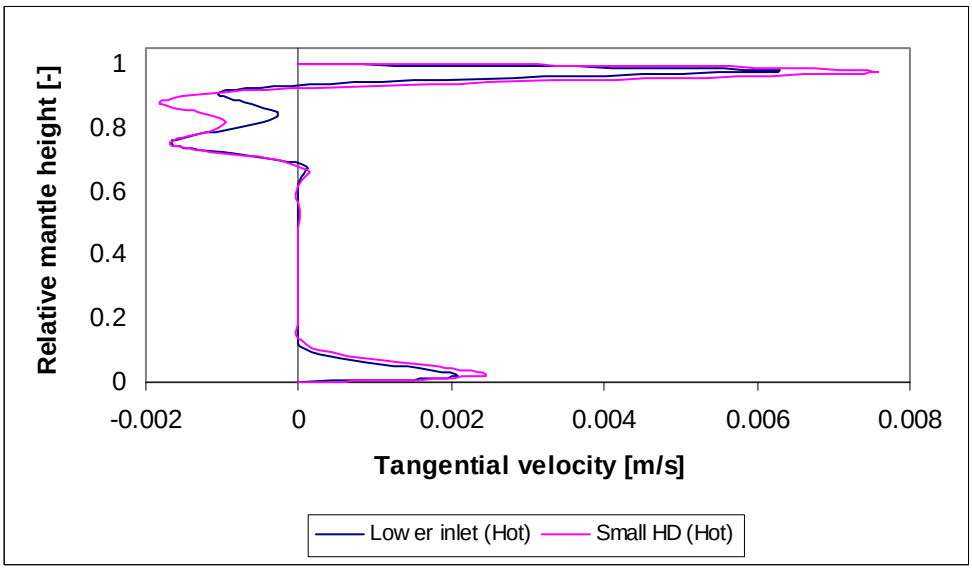

Figure 6-46: Tangential velocity profiles in the mantle after 40 minutes for the reference tank with a H/D ratio of 3.7 (Lower inlet) and for the tank with a small H/D ratio of 2 (Small HD).

Figure 6-47 shows the vertical velocities after 40 minutes at a relative height of 0.59 in the inner tank (corresponding to z = 0.850 m in Figure 6-5). There is an upward flow near the walls and a slow downward flow in the centre of the tank in both cases. The diameter of the tank is different in the two cases, and therefore the upward flow is at different distances from the centre of the tank. Higher upward velocities occur in the tank with the small H/D ratio and this is probably related to the higher heat flux at the tank wall at the level of the top of the mantle, as shown in Figure 6-45.

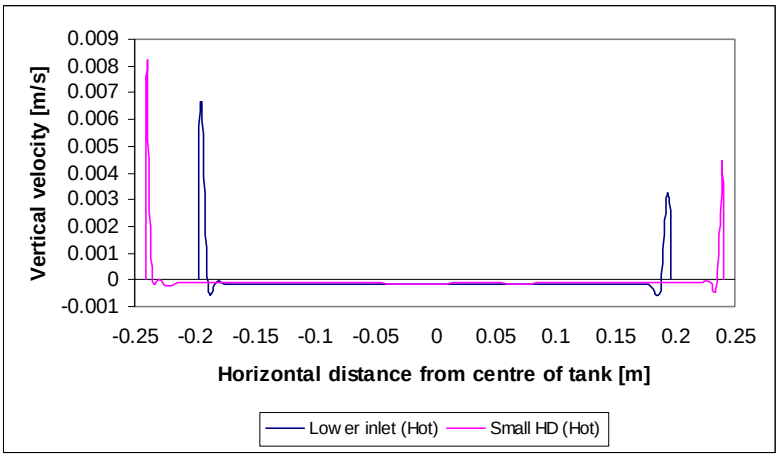

Figure 6-47: Vertical velocity profiles in the tank at a relative height of 0.59 after 40 minutes for the reference tank with a H/D ratio of 3.7 (Lower inlet) and for the tank with a small H/D ratio of 2 (Small HD). The tank with H/D ratio of 3.7 has a radius of 0.197 m and the tank with H/D ratio of 2 has a radius of 0.241 m.

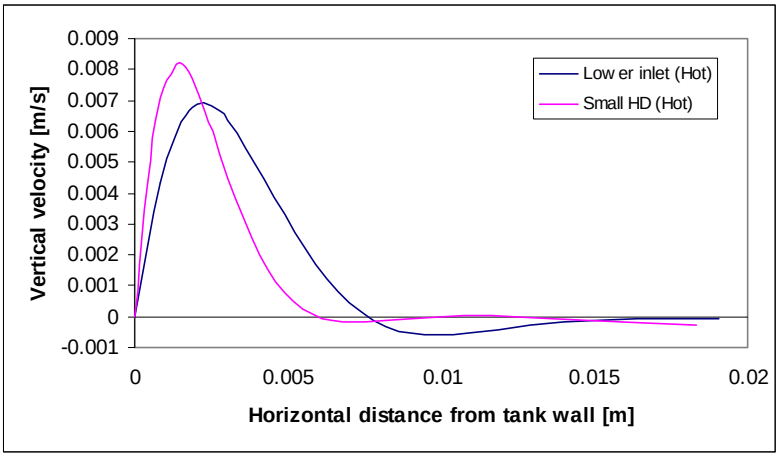

Figure 6-48: Vertical velocity near the tank wall at the inlet side at a relative height of 0.59 after 40 minutes for the reference tank with a H/D ratio of 3.7 (Lower inlet) and for the tank with a small H/D ratio of 2 (Small HD).

Figure 6-48 shows the vertical velocities after 40 minutes near the tank wall in the mantle inlet side at the same level in the tank as in Figure 6-47 for the two studied cases. It is seen that there is some difference in the boundary layer near the tank wall. In the case of small H/D ratio the upward velocity is higher (as seen in Figure 6-47) but the

boundary layer thickness is smaller. The higher velocity and the thinner boundary layer for the small H/D ratio are both related to the different H/D ratio, but also to the different conditions at the tank wall where there is different heat flux. These differences will be discussed further in section 6.12 and section 6.13 where the results for the tank with the large H/D ratio of 5 will also be included.

6.12 Effect of large H/D ratio

In this section it is investigated how the heat flux and velocities are affected by a large H/D ratio of the inner tank. Two different H/D ratios were investigated: The reference tank with a H/D ratio of 3.7 (called Lower inlet) and a large H/D ratio of 5 (called Large HD). The reference tank with a H/D ratio of 3.7 has a mantle volume of 31.9 l while the tank with a H/D ratio of 5 has a mantle volume of 35.8 l. The case of the large H/D ratio is only simulated for the hot inlet condition.

6.12.1 Heat flux

Figure 6-49 shows the simulated heat flux profiles at the mantle wall after 40 minutes. There is small difference in the heat flux above the mantle inlet port. The heat flux is lowest for the large H/D ratio below the mantle inlet port. The reason for this is mainly that the tank with large H/D ratio has a larger heat transfer area and this results in a better cooling of the mantle fluid and therefore lower temperatures in the lower part of the mantle.

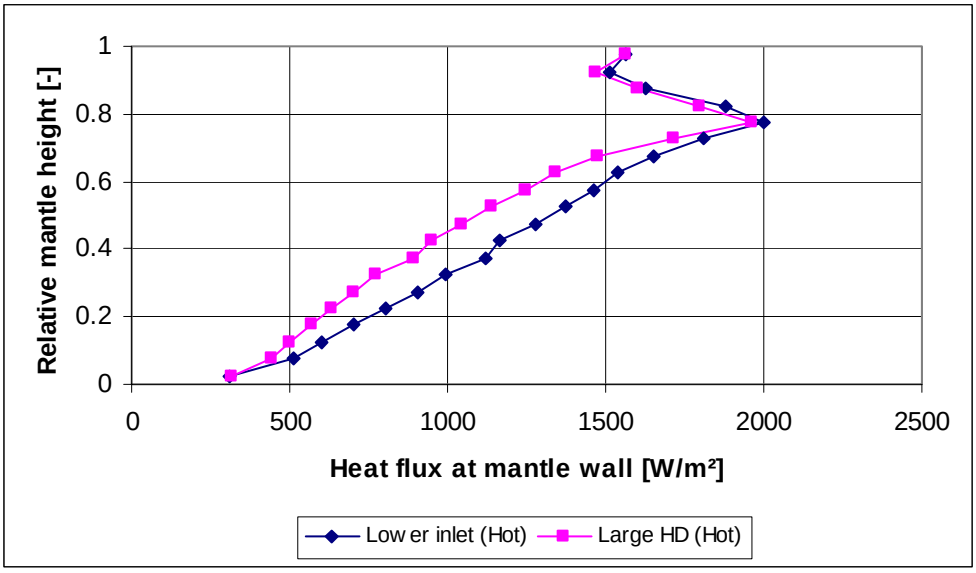

Figure 6-49: Heat flux at the mantle wall after 40 minutes for the reference tank with a H/D ratio of 3.7 (Lower inlet) and for the tank with a large H/D ratio of 5 (Large HD).

Figure 6-50 shows the simulated heat flux profiles at the tank wall after 40 minutes. At a relative distance of 0-0.52 from the bottom of the tank, the heat flux profiles for the tank wall are very similar to the heat flux profiles for the mantle wall. From a relative

distance of 0.1 above the mantle and to the tank top, the heat flux is below 0 W/m² in the two studied cases because of the heat loss at the tank wall above the mantle.

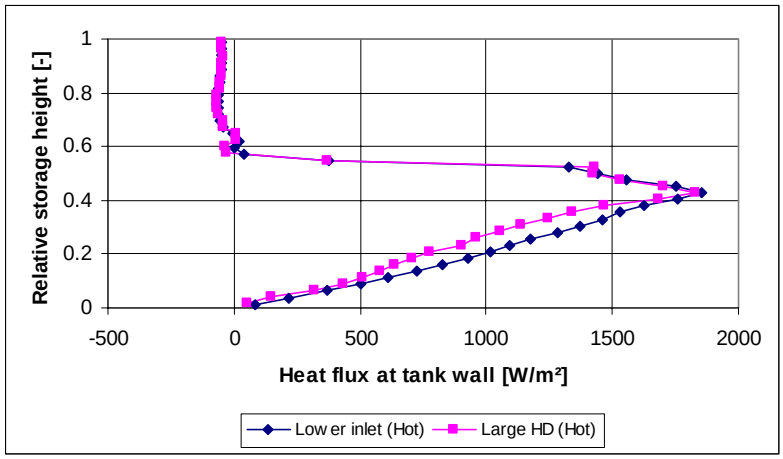

Figure 6-50: Heat flux at tank wall after 40 minutes for the reference tank with a H/D ratio of 3.7 (Lower inlet) and for the tank with a large H/D ratio of 5 (Large HD).

6.12.2 Velocity

Figure 6-51 shows the tangential velocity profile after 40 minutes at a vertical line (Figure 6-4) through the centre plane of the mantle, midway between the mantle inlet and the mantle outlet for the two studied cases. The shapes of the velocity profiles are quite similar, but higher tangential velocities occur in the upper part of the mantle in the case of the large H/D ratio. There is not found a specific reason for this, but in section 6.13 the results for the different H/D ratios will be compared and the differences will be discussed.

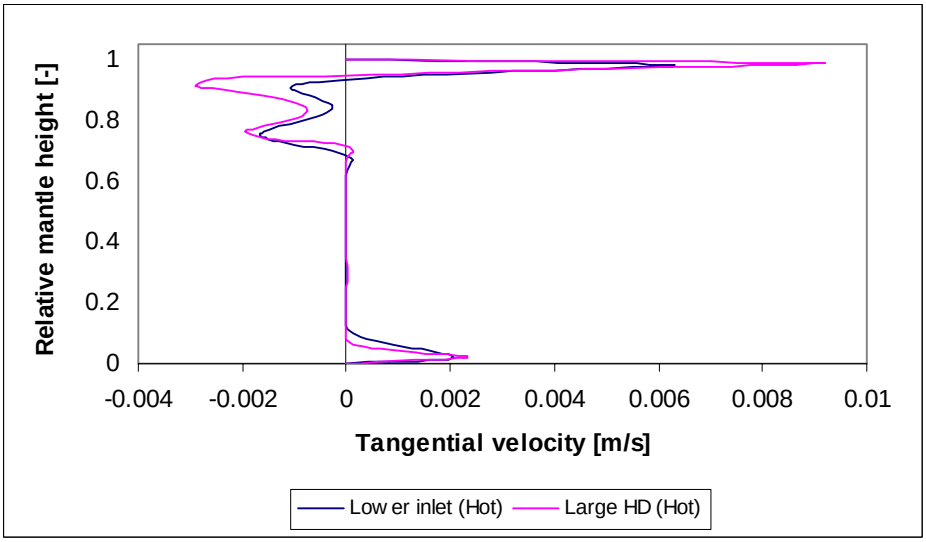

Figure 6-51: Tangential velocity profiles in the mantle after 40 minutes for the reference tank with a H/D ratio of 3.7 (Lower inlet) and for the tank with a large H/D ratio of 5 (Large HD).

Figure 6-52 shows the vertical velocities after 40 minutes at a relative height of 0.59 in the inner tank (corresponding to z = 0.850 m in Figure 6-5). There is an upward flow near the walls and a slow downward flow in the centre of the tank in both cases. The diameter of the tank is different in the two cases, and therefore the upward flow is at different distances from the centre of the tank. Higher upward velocities occur in the tank with the large H/D ratio and this is probably related to the differences in the height of the mantle in the two cases. In the case of the large H/D ratio the upward flow is accelerated along a higher mantle.

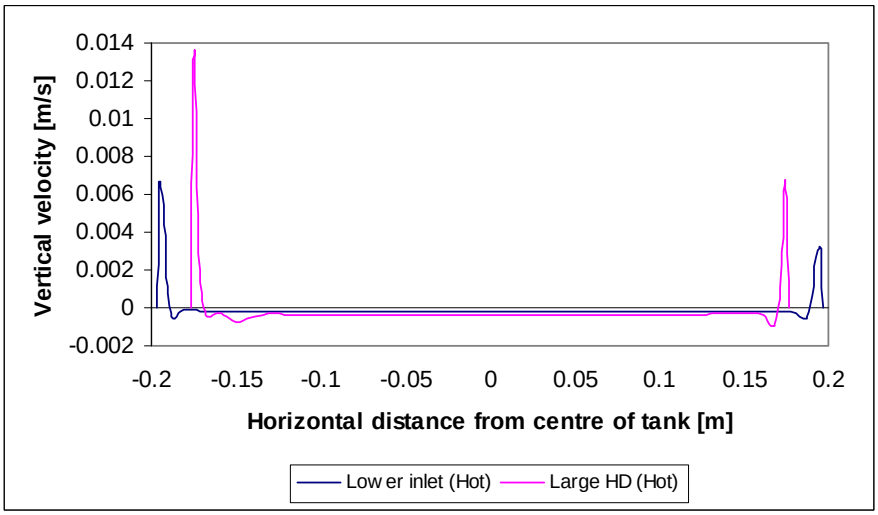

Figure 6-52: Vertical velocity profiles in the tank at a relative height of 0.9 after 40 minutes for the reference tank with a H/D ratio of 3.7 (Lower inlet) and for the tank with a large H/D ratio of 5 (Large HD). The tank with the H/D ratio of 3.7 has a radius of 0.197 m and the tank with H/D ratio of 5 has a radius of 0.177 m. The mantle inlet is in the negative side and the mantle outlet is in the positive side of the horizontal axis.

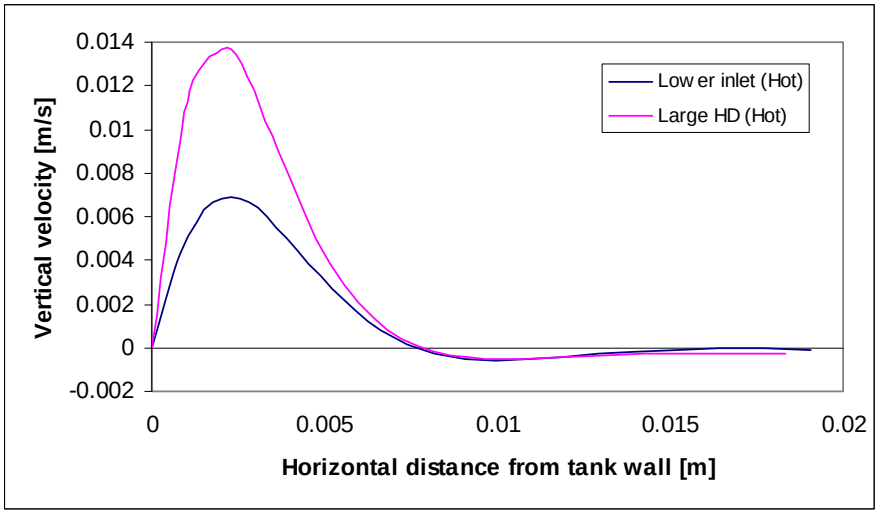

Figure 6-53: Vertical velocity near the tank wall at the inlet side at a relative height of 0.59 after 40 minutes for the reference tank with a H/D ratio of 3.7 (Lower inlet) and for the tank with a large H/D ratio of 5 (Large HD).

Figure 6-53 shows the vertical velocities after 40 minutes near the tank wall in the mantle inlet side at the same level in the tank as in Figure 6-52 for the two studied cases. It is seen that the thickness of the boundary layer near the tank wall is the same in the two cases, but, as shown in Figure 6-52, the upward velocity is higher in the case of the large H/D ratio.

6.13 Summary and discussion

In this chapter a number of CFD-simulations were carried out to analyse the flow in the mantle, the flow in the inner tank and the heat transfer at the mantle wall and the tank wall for different mantle designs and different operation conditions. One parameter at a time was varied so the influence of the specific parameter was directly determined by comparing the results with the results of the reference tank with lower inlet. In this section some of the results for the different mantle designs and different operation conditions will be compared. The results for the initially mixed case and for the high mantle case will not be included in the comparison (see sections 6.4 and 6.9 for results for these two cases). Furthermore, the results for the different H/D-ratios will be compared separately.

Figure 6-54 shows the simulated heat flux profiles at the mantle wall after 40 minutes for the hot inlet condition. It is seen that there is a relatively small difference in the shape of the heat flux profile for Lower inlet, 1” inlet, Stainless steel and 40% Glycol, only at the mantle inlet level the peak heat flux is different. At that level the Stainless steel has the highest heat flux and the 1” inlet has the smallest heat flux of the four designs. The Top inlet, the Small mantle gap and the High Flow rate have a rather different heat flux profile. The Top inlet has the heat flux concentrated at the top of the mantle, the High Flow rate has the main heat flux at a distance of 0.1-0.6 m from the bottom, while the Small mantle gap has the same shape at the top as the four previously mentioned, but a higher heat flux at the bottom half of the mantle.

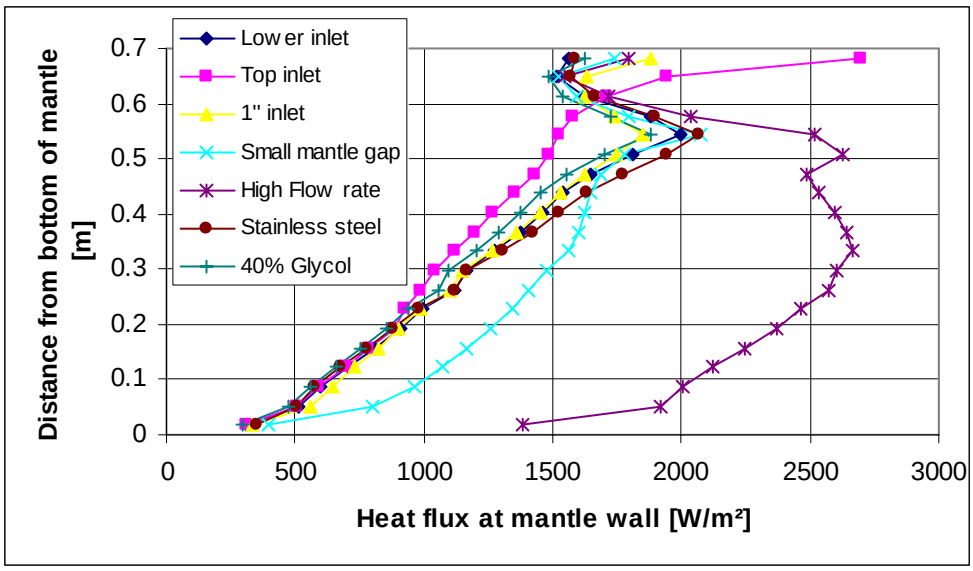

Figure 6-54: Heat flux at the mantle wall after 40 minutes for hot inlet condition.

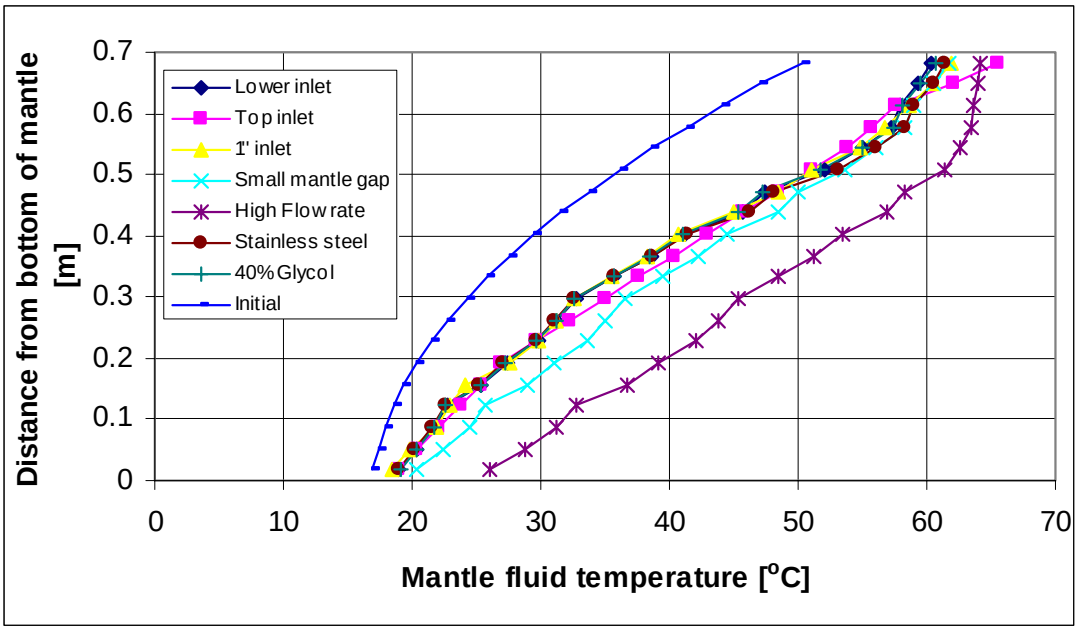

Figure 6-55: Mantle fluid temperatures for hot inlet condition – initial and after 40 minutes.

Figure 6-55 shows the mantle fluid temperatures for the hot inlet condition – initial and after 40 minutes. It appears that the high flow rate results in high temperatures of the mantle fluid, the small mantle gap results in higher temperatures in the bottom, the Top inlet results in high temperatures at the very top, and minor differences are observed for the other cases. Figure 6-56 shows the temperatures of the water in the inner tank for the hot inlet condition – initial and after 40 minutes. It is seen that the same tendencies as in Figure 6-55 occur at the level of the mantle (0-0.8 m), and just above the mantle the same temperatures are observed for Top inlet and High Flow rate. Besides these differences there are minor differences between the different cases.

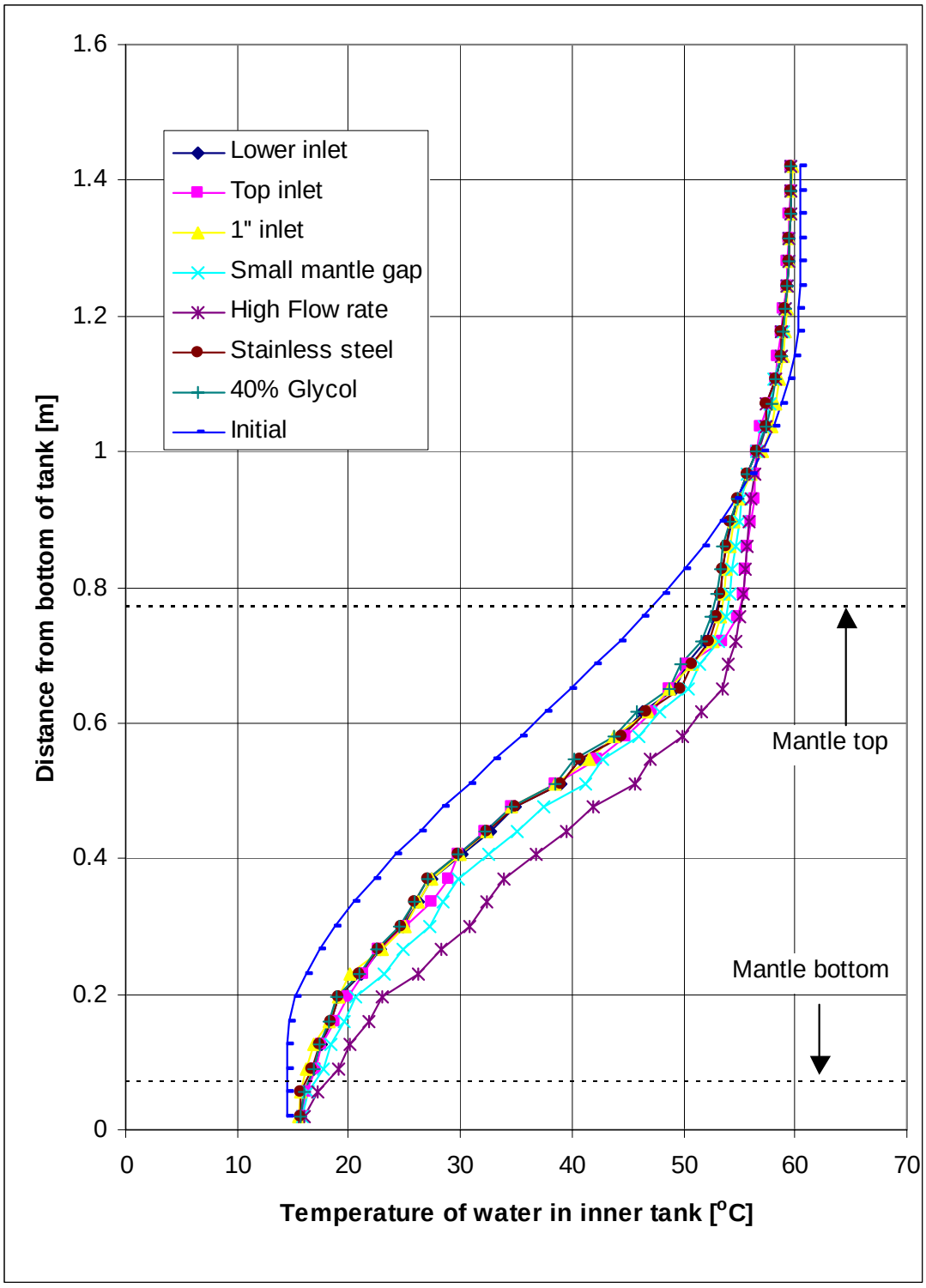

Figure 6-56: Inner tank temperatures for hot inlet condition – initial and after 40 minutes.

Figure 6-57 shows the simulated heat flux profiles at the mantle wall after 40 minutes for the warm inlet condition. There is also very little difference in the heat flux profile for the warm inlet condition for Lower inlet, 1" inlet, Stainless steel and 40% Glycol. They all have the peak negative heat flux at a distance of 0.5 m from the bottom of the mantle. Top inlet has the negative heat flux at a higher level and Small mantle gap has a higher heat flux at the bottom of the mantle. High flow rate has the negative heat flux at 0.55 m from the bottom, and then a higher heat flux at the bottom of the mantle.

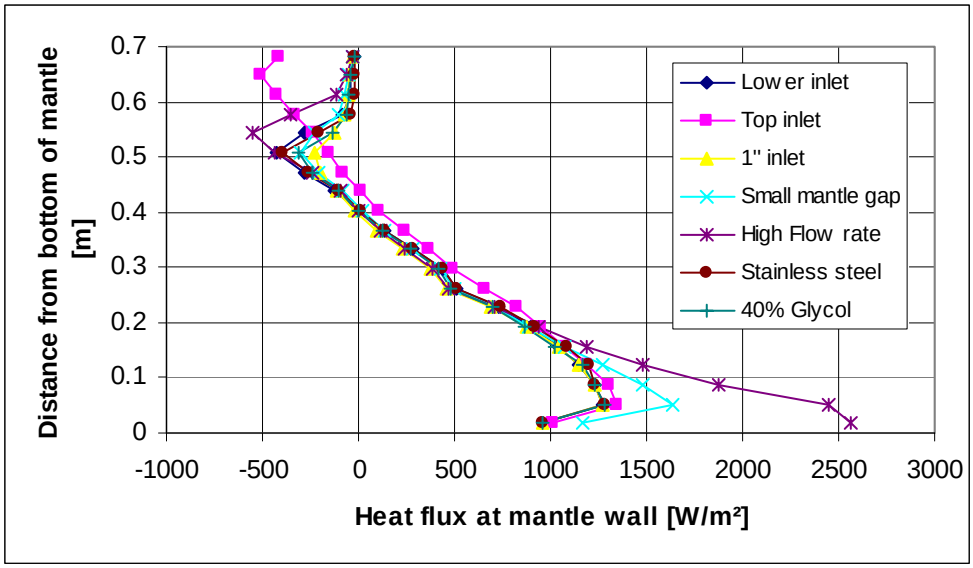

Figure 6-57: Heat flux at the mantle wall after 40 minutes for warm inlet condition.

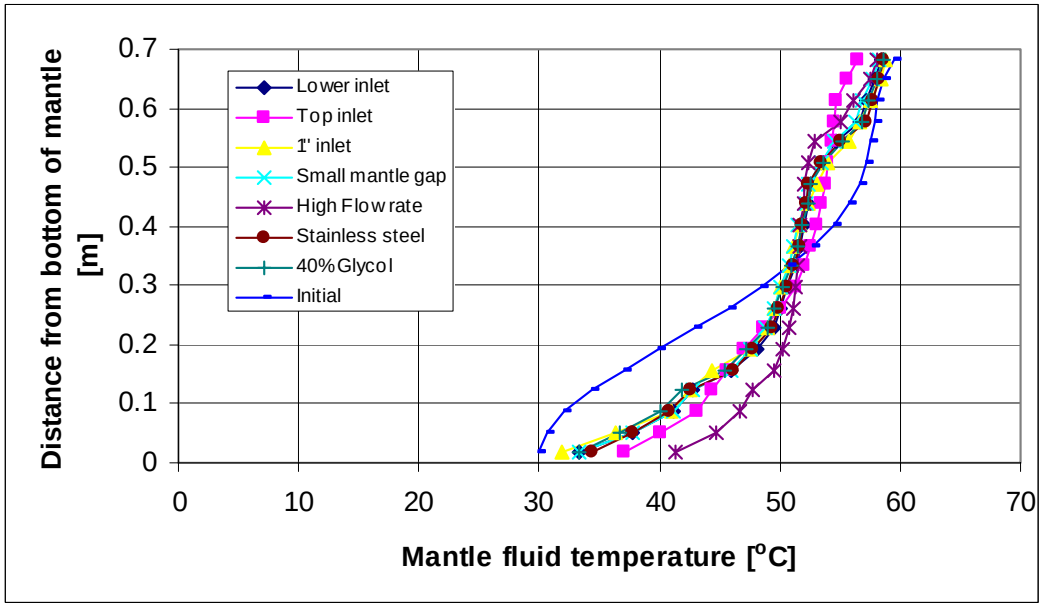

Figure 6-58: Mantle fluid temperatures for warm inlet condition – initial and after 40 minutes.

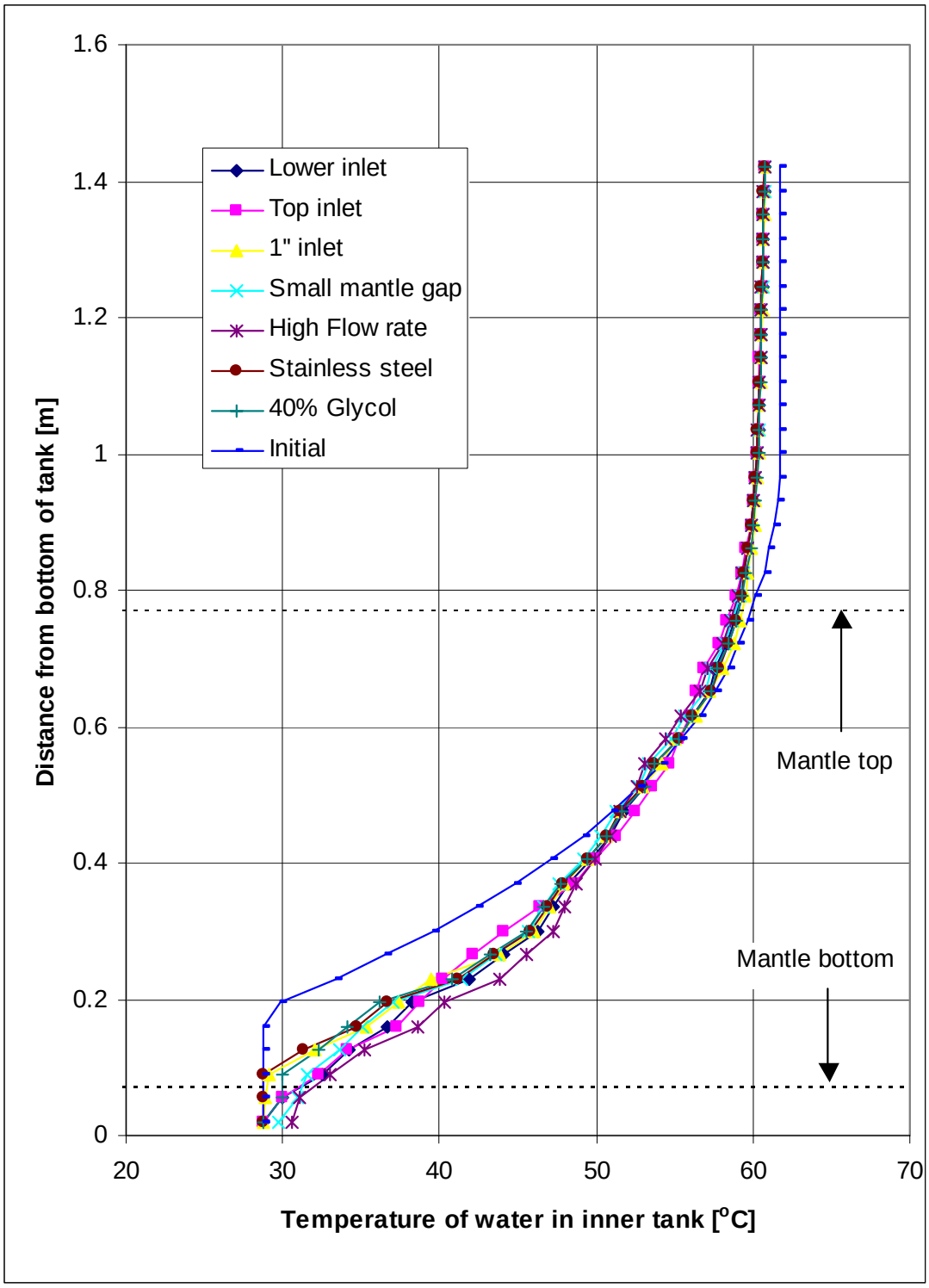

Figure 6-59: Inner tank temperatures for warm inlet condition – initial and after 40 minutes.

Figure 6-58 shows the mantle fluid temperatures for the warm inlet condition – initial and after 40 minutes. It appears that the high flow rate results in higher temperatures in the bottom part of the mantle and lower temperatures at the level of the inlet. The Top inlet results in lower temperatures at the very top. Except from these differences minor differences are observed for the other cases. Figure 6-59 shows the temperatures of the water in the inner tank for the warm inlet condition – initial and after 40 minutes. It is seen that the same tendencies as in Figure 6-58 occur at the level of the mantle (0-0.8 m), and except from that small differences are observed. In section 6.6.1 it was observed for the warm inlet condition that the heat flux at the level of the mantle inlet was less negative for the small mantle gap than for the lower inlet case. The reason for this can be explained by the temperatures of the domestic water in the inner tank at the level of the mantle inlet. During the 40 minutes with warm inlet condition the temperature of the domestic water at the mantle inlet level is approximately 0.5 K lower in the small mantle gap case than in the lower inlet case (this is hardly seen on Figure 6-59), and the lower temperature results in a smaller temperature difference between the domestic water and the mantle fluid at the same level. Figure 6-60 shows the temperature difference between the mantle fluid and the domestic water after 40 minutes for warm inlet condition, and it is seen that the difference is less negative for the small mantle gap at the level of the mantle inlet. If the comparison of the heat flux had been made after 5 minutes with the warm inlet condition, the small mantle gap would have had a more negative heat flux at the level of the mantle inlet.

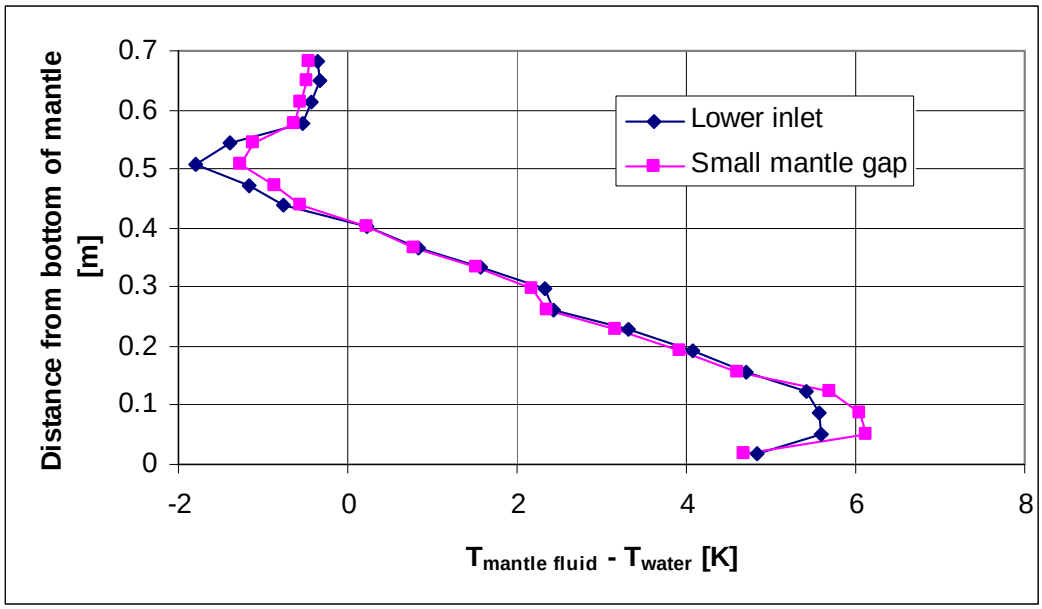

Figure 6-60: Temperature difference between the mantle fluid and the domestic water in the inner tank after 40 minutes with the warm inlet condition for 'Lower inlet' and 'Small mantle gap'.

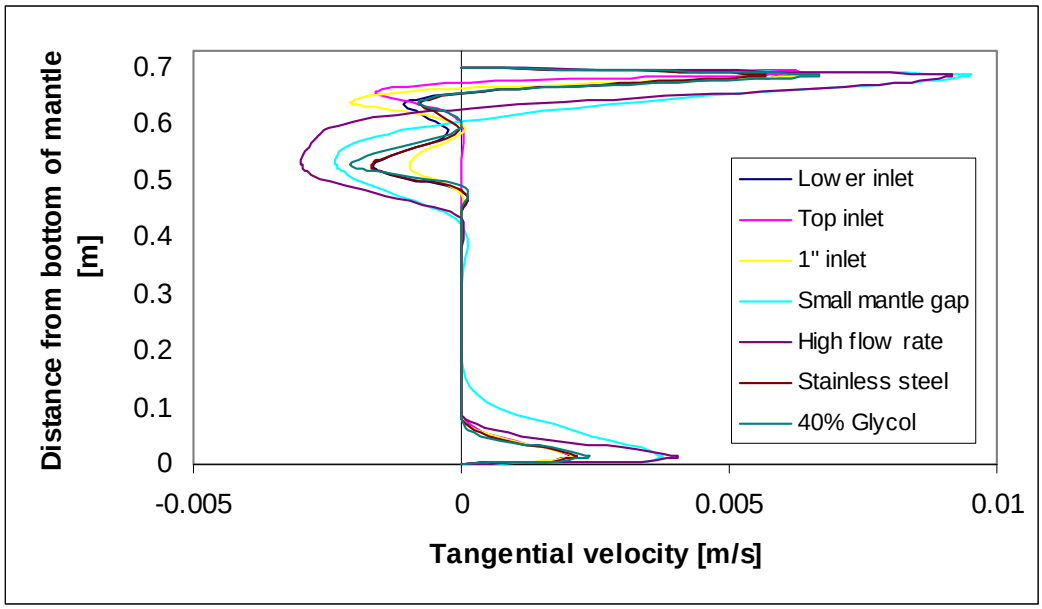

Figure 6-61: Tangential velocity profiles in the mantle after 40 minutes for the hot inlet condition.

Figure 6-61 shows a comparison of the tangential velocity profile after 40 minutes for the hot inlet condition. It is seen that the highest velocities occur in the Small mantle gap and with the high flow rate.

Figure 6-62 shows a comparison of the tangential velocity profile after 40 minutes for the warm inlet condition. The tangential velocity profile for the Top inlet differs from the others by having the reverse flow at the very top and a higher velocity. At the bottom, the highest velocities occur in the Small mantle gap and with the high flow rate.

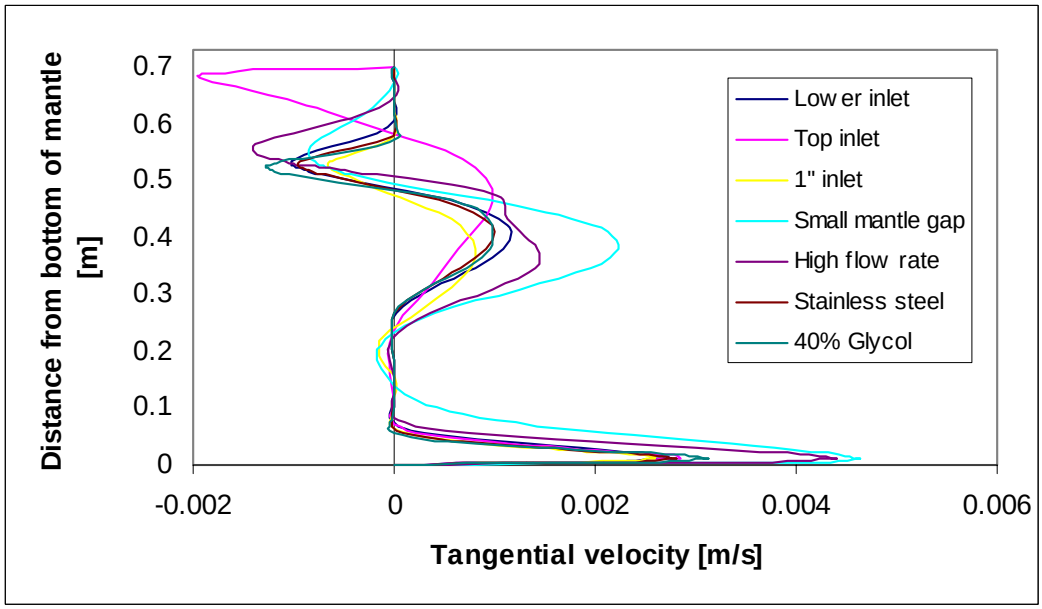

Figure 6-62: Tangential velocity profiles in the mantle after 40 minutes for the warm inlet condition.

The vertical velocities near the tank wall in the mantle inlet side at z = 0.850 m (Figure 6-5) in the tank are shown in Figure 6-63. The velocities are for the hot inlet condition after 40 minutes. The momentum boundary layer thickness for free-convection flows is defined as the distance from the wall to where the vertical velocity is 0 m/s (Kays and Crawford, 1993). There is a small difference in the thickness of the boundary layer near the tank wall; Top inlet has the largest boundary layer with 0.0088 m and 40% Glycol has the smallest boundary layer with 0.0076 m, which gives an absolute difference of 0.0012 m (1.2 mm). There is a larger difference in the peak vertical velocities that are induced by the heat flux at the tank wall. The highest vertical velocity is induced in the case of the high mantle flow rate (peak of 0.0094 m/s) because of the constant high heat flux over a large part of the mantle wall (see Figure 6-54) and at the tank wall. Then comes Stainless steel (peak velocity of 0.0082 m/s) because of the inability of Stainless steel to distribute the heat flux over the mantle wall and the tank wall, and this results in a high flux near the mantle inlet and induces the relatively high vertical velocity in the tank. After stainless steel come the Top inlet (0.0077 m/s) and the Small mantle gap (0.0077 m/s). The high velocity for the Top inlet is due to the high concentration of the heat flux at the level of the top of the mantle, and for the Small mantle gap it is induced by the relatively higher heat flux at the level of the bottom part of the mantle (see Figure 6-54). Lower inlet has a vertical peak velocity of 0.0067 m/s. The lowest vertical velocities have 1” inlet (0.0053 m/s) and 40% glycol (0.0052 m/s), and in both cases is it due to the lower peak heat flux at the level of the mantle inlet (see Figure 6-54).

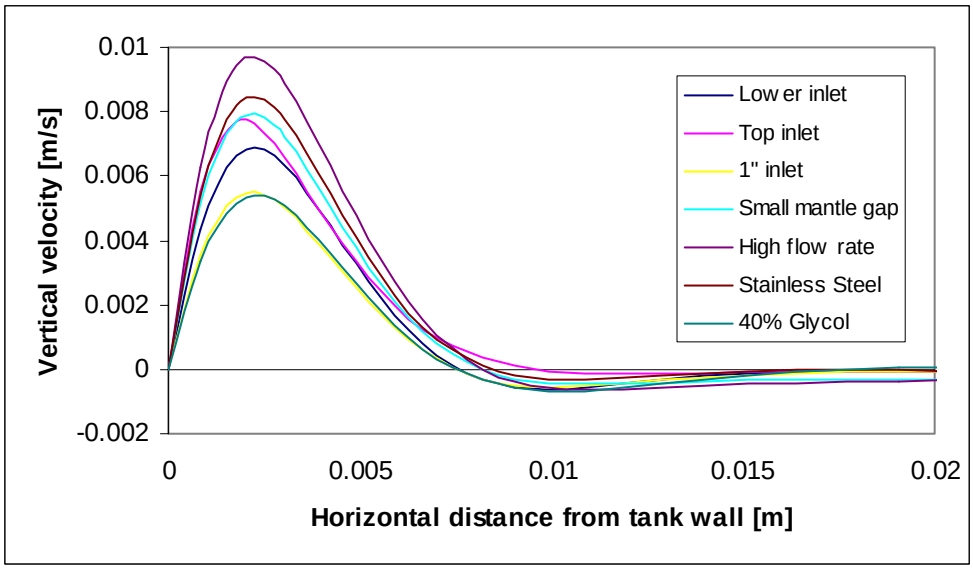

Figure 6-63: Vertical velocity near the tank wall at the inlet side at z = 0.850 m after 40 minutes for the hot inlet condition.

The simulated heat flux profiles at the mantle wall after 40 minutes for the different H/D ratios are shown in Figure 6-64. The heat flux is highest in the case of the small H/D ratio. There are small differences in the heat flux above the mantle inlet for Lower inlet and Large HD, but below the mantle inlet the heat flux is lowest for the large H/D ratio. The differences in the heat flux profiles are mainly due to the differences in the mantle volume and the heat transfer area. With the small H/D ratio the tank has a small

mantle volume and heat transfer area, this results in higher mantle fluid temperatures and in a higher heat flux. With the large H/D ratio the tank has a larger mantle volume and heat transfer area, this results in a better cooling of the mantle fluid and therefore lower mantle fluid temperatures and lower heat flux in the lower part of the mantle.

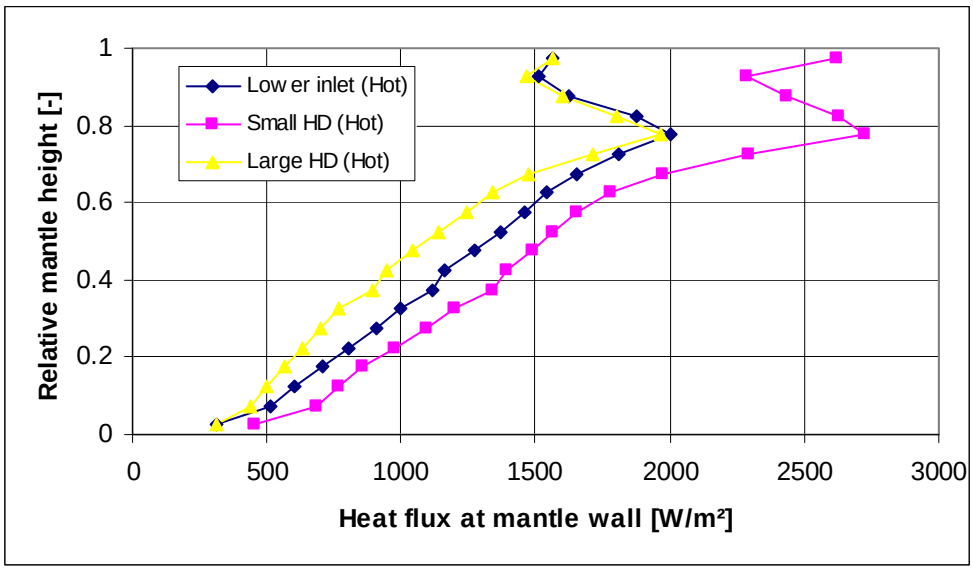

Figure 6-64: Heat flux at the mantle wall after 40 minutes for the reference tank with a H/D ratio of 3.7 (Lower inlet), small H/D ratio of 2 (Small HD) and large H/D ratio of 5 (Large HD).

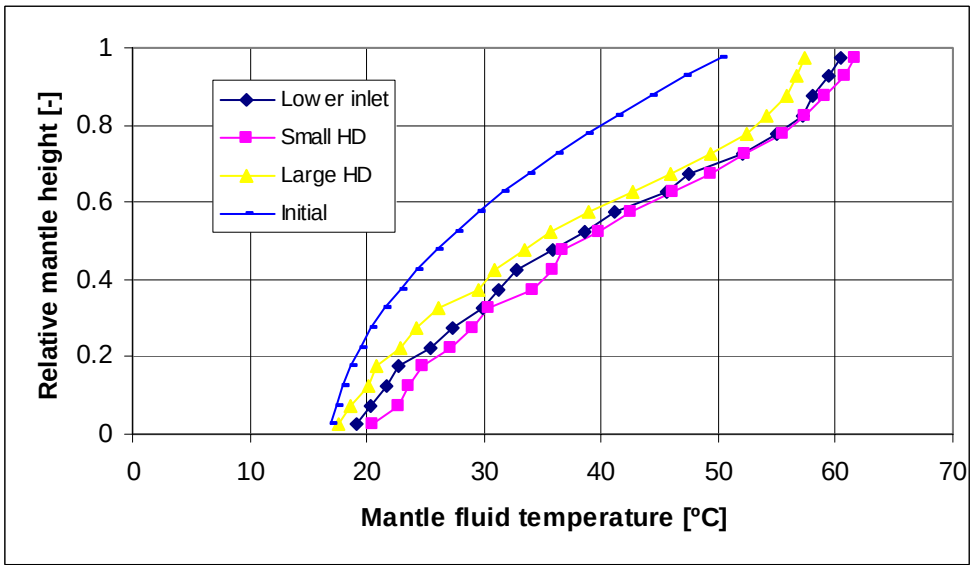

Figure 6-65: Mantle fluid temperatures after 40 minutes with hot inlet condition for the reference tank with a H/D ratio of 3.7 (Lower inlet), small H/D ratio of 2 (Small HD) and large H/D ratio of 5 (Large HD).

Figure 6-65 shows the mantle fluid temperatures after 40 minutes for the three different H/D ratios. The temperatures of the mantle fluid are lowest in the case of the large H/D ratio because of the larger mantle volume. Figure 6-66 shows the temperatures of the

water in the inner tank for the hot inlet condition – initial and after 40 minutes. It is seen that there are relatively small differences in the temperatures at the level of the mantle. The temperatures are highest for the small H/D ratio (and lowest for the large H/D ratio) just above the mantle, but further up in the tank it changes, and the highest temperatures occur in the tank with large H/D ratio while the lowest temperatures occur in the tank with the small H/D ratio.

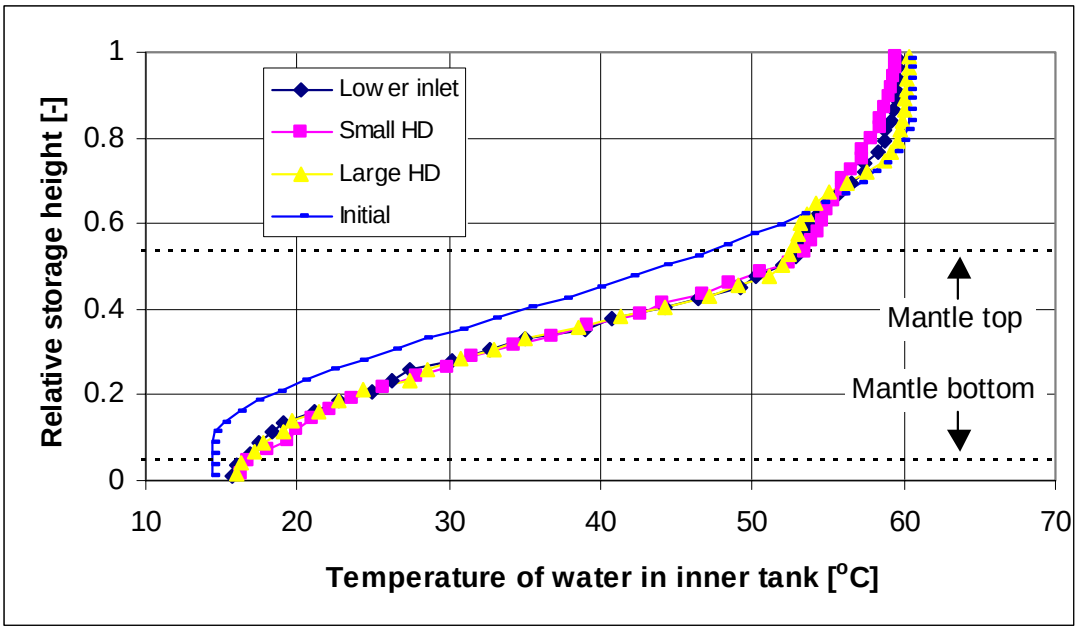

Figure 6-66: Inner tank temperatures for hot inlet condition – initial and after 40 minutes.

Figure 6-67 shows a comparison of the tangential velocity profile after 40 minutes for the different H/D ratios. The shapes of the velocity profiles are quite similar, but there are differences in the magnitude of the velocity in the upper part of the mantle. The largest velocities occur in the Large HD, then comes Small HD and the smallest velocities occur in the Lower inlet. It was expected that the largest tangential velocities would occur in the mantle with the smallest mantle volume, and this can explain the differences between Lower inlet and Small HD. The reason why Large HD has the largest tangential velocities in the upper part of the mantle might be explained by the thermal conditions in the mantle above the mantle inlet. Figure 6-65 showed that the temperatures of the mantle fluid above the mantle inlet are lowest in the case of the large H/D ratio, and due to the lower temperatures in the top of the mantle there is a larger temperature difference between the incoming fluid and the fluid in the upper part of the mantle and this results in increased buoyancy forces and higher velocities in the upper part of the mantle. This effect seems to overshadow the fact that there is a larger mantle volume in the tank with the large H/D ratio. Furthermore, the distance from the mantle inlet to the middle of the mantle gets smaller for large H/D ratios, and therefore there is less resistance. The high tangential velocities in the upper part of the mantle increase the convective heat transfer coefficient at the mantle wall, and this explains why the heat flux in the upper part of the mantle is of the same magnitude for Lower inlet and Large HD (see Figure 6-64), despite that the temperatures of the mantle fluid are lower in the case of the large H/D ratio.

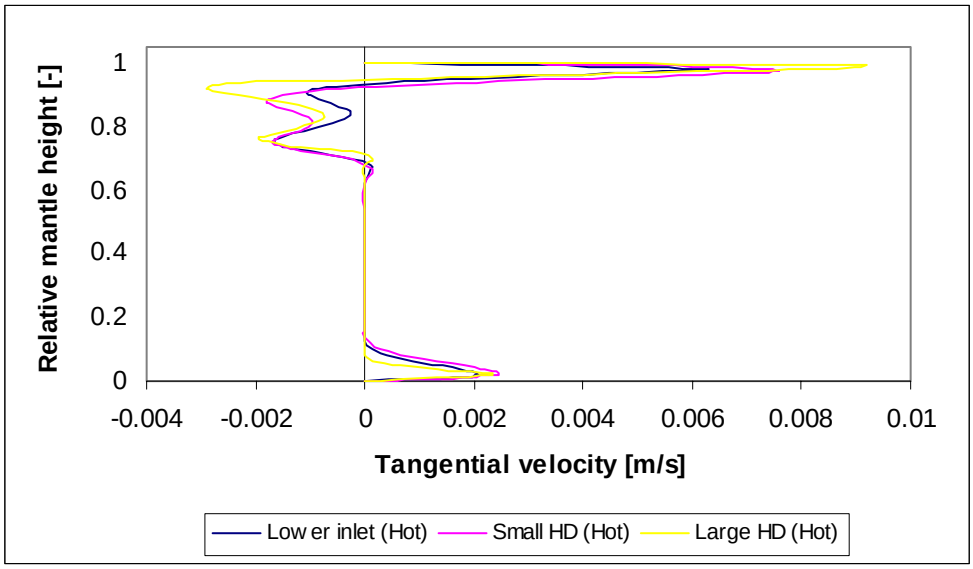

Figure 6-67: Tangential velocity profiles in the mantle after 40 minutes for the reference tank with a H/D ratio of 3.7 (Lower inlet), small H/D ratio of 2 (Small HD) and large H/D ratio of 5 (Large HD).

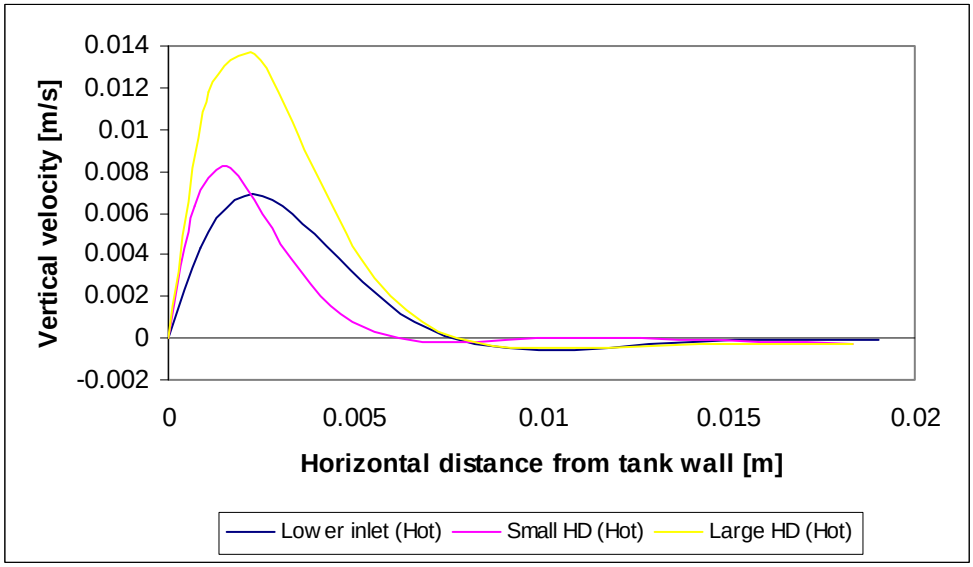

Figure 6-68: Vertical velocity near the tank wall at the mantle inlet side at a relative height of 0.59 after 40 minutes for the reference tank with a H/D ratio of 3.7 (Lower inlet), small H/D ratio of 2 (Small HD) and large H/D ratio of 5 (Large HD).

The vertical velocities near the tank wall in the mantle inlet side at a relative storage height of 0.59 (corresponding to z = 0.850 m in Figure 6-5) are shown in Figure 6-68 for the different H/D ratios. The velocities are after 40 minutes. It appears that the highest vertical velocities occur in the tank with large H/D ratio, then comes the small H/D ratio and the smallest vertical velocities occur in the Lower inlet case. Normally it would be expected that for the same heat flux at the tank wall the vertical velocities

would increase for a larger H/D ratio because the upward flow is accelerated over a longer distance. This can explain why the highest vertical velocities occur in the tank with large H/D ratio. In the cases of the small H/D ratio and the Lower inlet the conditions at the tank wall are not the same, so the differences in the vertical velocities are not only related to the difference in the H/D ratio. The higher heat flux at the tank wall (see Figure 6-45) in the tank with the small H/D ratio induces the higher vertical velocities. The high vertical velocities and the large boundary layer in the tank with large H/D ratio result in higher temperatures in the top of the tank than in the tanks with a smaller H/D ratio (see Figure 6-66).

In this chapter the results from a number of CFD-simulations were analysed to investigate how the heat flux and flow patterns react under different typical operation conditions and for different mantle designs. In the next chapter the results from the CFD-simulations will be analysed by means of dimensionless heat transfer theory in order to obtain heat transfer correlations for the heat transfer at the mantle wall and at the tank wall.

7. Heat transfer correlations and stratification model

7.1 Introduction

In the previous chapter the convective heat transfer at the mantle wall and at the tank wall based on absolute values was investigated for a number of different mantle tank designs and different operation conditions. In this chapter the convective heat transfer in the mantle and in the inner tank, for the same mantle tank designs and operation conditions as in chapter 6, will be analysed by means of dimensionless heat transfer theory in order to obtain dimensionless heat transfer correlations for vertical mantle heat exchangers.

It was also revealed in chapter 6 that the flow structure inside the inner tank helps to heat up the part of the tank situated above the mantle, and increase the degree of stratification although there might be a negative heat flux at the tank wall above the mantle. Therefore, it is not enough only to be able to predict the heat transfer at the mantle wall and at the tank wall to model the thermal stratification in the inner tank, it is also necessary to know which level the heat transfer goes to due to the heat flows inside the inner tank. Thus, a model to predict the heat flows inside the inner tank will be developed in the end of this chapter.

The mantle tank designs that are taken into consideration in this chapter are the mantle tank designs described in Table 6-1, Table 6-2 and Table 6-3. Two heating situations were studied; a hot inlet condition with a mantle inlet temperature of 70ºC, which was 10 K higher than the mantle top temperature, and a warm inlet condition with a mantle inlet temperature of 50ºC, which was 10 K lower than the mantle top temperature. The results for both heating situations were evaluated after 40 minutes. The two heating situations are the same as the two described in section 6.1.

7.2 Dimensionless analysis

The dimensionless heat transfer theory was applied to generalise the results from chapter 6. In the following a brief review of the method of analysis is given for the heat transfer from the mantle fluid to the inner mantle wall. The principles of the method were also used to identify the convective heat transfer from the mantle fluid to the outer mantle wall and from the tank wall to the domestic water in the inner tank.

When considering the modelling of vertical mantle heat exchangers, it is important to be able to calculate the thermal stratification of the water in the inner tank as the thermal stratification has an important role in the thermal performance of a SDHW system. Therefore the local heat transfer was analysed (instead of the average heat transfer of the whole mantle wall), and the mantle wall and the tank was divided into smaller pieces as shown in Figure 6-3.

The required determination is the local convective heat transfer coefficient, h_z, from the mantle fluid to the inner mantle wall at any height in the mantle. The local convective heat transfer coefficient can be determined by the equation below:

$$h_z = \frac{q_z}{T_{\text{mantle fluid,z}} - T_{\text{mantle wall,z}}} \tag{7.1}$$

where

h_z	is the local convective heat transfer coefficient, [W/m²·K]
q_z	is the local heat flux from mantle fluid to mantle wall, [W/m²]
T	is the temperature (of mantle fluid and mantle wall), [K]
z	is the vertical distance from the mantle inlet, [m]

It appears from equation 7.1 that the convective heat transfer coefficient was analysed as a function of the z-direction. This means that the differences in the tangential direction were not taken into account.

Values of q_z and T were determined from the results of the CFD-calculation as the mantle heat exchanger was modelled by a number of control volumes (see Figure 5-1 and Figure 5-2) where these quantities were calculated. The heat flux at the mantle wall was given directly in the CFD-results, and the local heat flux for each of the smaller pieces in Figure 6-3 was calculated by surface integration (area-weighted average) within the CFD-programme by the equation given below:

$$q_z = \frac{1}{A_z}\int q_z dA_z = \frac{1}{A_z}\sum_{i=1}^{n} q_{i,z} \cdot A_{i,z} \tag{7.2}$$

where

A_z	is the total area of the piece of the wall at level z, [m²]
$A_{i,z}$	is the area of face number ‘i’ on the surface at level z, [m²]
n	is the total number of faces on the piece of the wall, [-]
q_z	is the local heat flux at level z, [W/m²]
$q_{i,z}$	is the heat flux at face number ‘i’ at level z, [W/m²]
z	is the distance from the mantle inlet, [m]

The mean temperature of the mantle fluid and the mantle wall were calculated by volume integration (volume-weighted average) for each layer corresponding to the smaller pieces in Figure 6-3. The volume integration was performed within the CFD-programme by the equation given below:

$$T_{\text{mantle fluid,z}} = \frac{1}{V_z}\int T_z dV_z = \frac{1}{V_z}\sum_{i=1}^{m} T_{i,z} \cdot V_{i,z} \tag{7.3}$$

where

m	is the total number of control volumes in the layer at level z, [-]
$T_{i,z}$	is the temperature of control volume number ‘i’ at level z, [K]
$T_{\text{mantle fluid,z}}$	is the mean temperature of the mantle fluid at level z, [K]

$V_{i,z}$ is the volume of control volume number 'i' at level z, [m³]
V_z is the total volume of the layer at level z, [m³]
z is the distance from the mantle inlet, [m]

In order to generalise the results, the dimensionless heat transfer theory is now introduced. The local convective heat transfer coefficient, h_z, is rewritten to the dimensionless local Nusselt number, Nu_z:

$$Nu_z = \frac{h_z \cdot z}{k_z} \tag{7.4}$$

where
h_z is the local convective heat transfer coefficient, [W/m²·K]
k_z is the thermal conductivity of the mantle fluid, [W/m·K]
Nu_z is the local Nusselt number, [-]
z is the distance from the mantle inlet, [m]

In the upper part of the mantle, the heat flow is driven by both the temperature difference between the mantle fluid and the mantle wall, and by the impinging jet at the inlet. The temperature difference was rewritten to the dimensionless local Rayleigh number, Ra_z:

$$Ra_z = \frac{g \cdot \beta_z \cdot \left(T_{\text{mantle fluid,z}} - T_{\text{mantle wall,z}}\right) \cdot z^3}{\nu_z^2} \cdot Pr_z \tag{7.5}$$

where
g is the gravity, [m/s²]
Pr_z is the local Prandtl number of the mantle fluid, [-]
Ra_z is the local Rayleigh number, [-]
T is the temperature, [K]
z is the distance from the mantle inlet, [m]
β_z is the local thermal volume expansion coefficient, [1/K]
ν_z is the local kinematic viscosity of the mantle fluid, [m²/s]

The influence of the impinging jet at the mantle inlet was rewritten to the Reynolds number for mantle inlet, Re_{inlet}:

$$Re_{inlet} = \frac{v_{inlet} \cdot D_{inlet}}{\nu} \tag{7.6}$$

where
D_{inlet} is the diameter of the mantle inlet port, [m]
Re_{inlet} is the inlet Reynolds number, [-]
v_{inlet} is the average inlet velocity, [m/s]
ν is the kinematic viscosity of the incoming fluid, [m²/s]

In the lower part of the mantle the characteristic length was changed from the distance from the mantle inlet, z, to the mantle gap, w, in order to avoid the z^3 to be to dominant in the local Rayleigh number, where the driving force should be the temperature difference between the mantle fluid and the mantle wall.

The local Nusselt number, Nu_w, based on the mantle gap is given by:

$$Nu_{w,z} = \frac{h_z \cdot w}{k_z} \tag{7.7}$$

where

h_z	is the local convective heat transfer coefficient, [W/m²·K]
k_z	is the thermal conductivity of the mantle fluid, [W/m·K]
$Nu_{w,z}$	is the local Nusselt number based on the mantle gap, [-]
w	is the mantle gap, [m]

In the lower part of the mantle, the heat flow is driven by the temperature difference between the mantle fluid and the mantle wall, and the local Rayleigh number based on the mantle gap is given by:

$$Ra_{w,z} = \frac{g \cdot \beta_z \cdot \left(T_{\text{mantle fluid,z}} - T_{\text{mantle wall,z}}\right) \cdot w^3}{\nu_z^2} \cdot Pr_z \tag{7.8}$$

where

g	is the gravity, [m/s²]
Pr_z	is the local Prandtl number of the mantle fluid, [-]
$Ra_{w,z}$	is the local Rayleigh number based on the mantle gap, [-]
T	is the temperature, [K]
w	is the mantle gap, [m]
β_z	is the local thermal volume expansion coefficient, [1/K]
ν_z	is the local kinematic viscosity of the mantle fluid, [m²/s]

Fluid properties in equations 7.4 - 7.8 should be evaluated at the film temperature:

$$T_{\text{film,z}} = \frac{T_{\text{fluid,z}} + T_{\text{wall,z}}}{2} \tag{7.9}$$

Thus, by means of these rewritings, it is the goal, for a given tank and with a given mantle fluid, to determine the local Nusselt number as a function of the local Rayleigh number and the inlet Reynolds number (upper part of the mantle), and for the lower part of the mantle to determine the local Nusselt number as a function of the local Rayleigh number:

Upper part: $$Nu_z = f\left(Ra_z, Re_{\text{inlet}}\right) \tag{7.10}$$

Lower part: $$Nu_{w,z} = f\left(Ra_{w,z}\right) \tag{7.11}$$

7.3 Heat transfer from mantle fluid to inner mantle wall

The theory described in section 7.2 assumes that the heat transfer in the upper part of the mantle is governed by mixed convection and that natural convection dominates in the lower part of the mantle far away from the inlet. The heat transfer is in the mixed convection regime if Ra_z/Re_{inlet}^2 is in the order of 1, on the other hand if $Ra_z/Re_{inlet}^2 << 1$ then forced convection dominates the heat transfer and if $Ra_z/Re_{inlet}^2 >> 1$ then natural convection dominates the heat transfer.

Figure 7-1 shows the ratio between the local Rayleigh number and the squared inlet Reynolds number as a function of the vertical distance from the mantle inlet port, for the different tank designs and operation conditions. It appears that in the upper part of the mantle near the mantle inlet port, the heat transfer is in the mixed convection regime and in the bottom part of the mantle far away from the mantle inlet, natural convection dominates the flow behaviour. Therefore, a mixed convection solution, where the local Nusselt number is a function of the ratio between the local Rayleigh number to the squared inlet Reynolds number, will be searched in the upper half of the mantle. In the lower half of the mantle a natural convection solution where the local Nusselt number is a function of the local Rayleigh number will be searched. The decision to divide the mantle in an upper and a lower half at the middle of the mantle was made at an early stage of the analysis after simulation with the tank with lower inlet where the middle of the mantle is at a distance of 0.175 m from the mantle inlet. A more correct way would have been to let the level for the transition between mixed and natural convection depend on Ra_z/Re_{inlet}^2, as it is seen that in some cases there is natural convection in the upper half of the mantle. The criteria for saying when only natural convection occurs could then have been: $Ra_z/Re_{inlet}^2 > 100$.

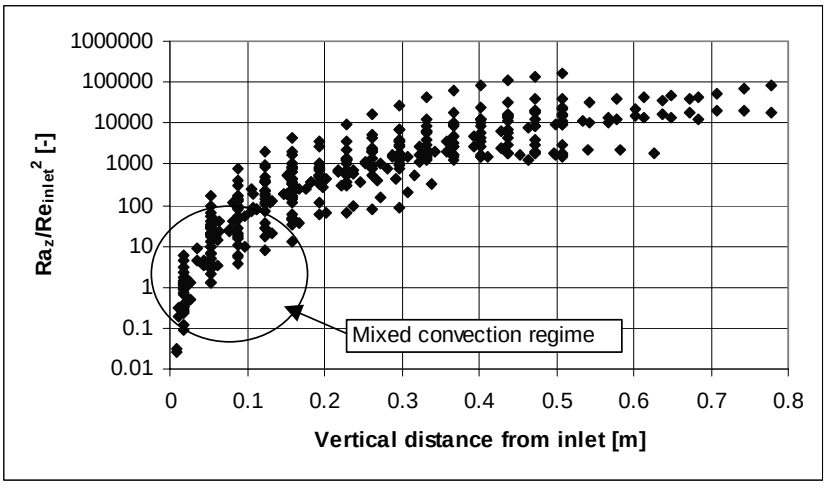

Figure 7-1: Ratio between the local Rayleigh number to the squared inlet Reynolds number as a function of the vertical distance from the mantle inlet port.

Upper half of the mantle:

Figure 7-2 shows the local Nusselt number as a function of the ratio between the local Rayleigh number and the squared inlet Reynolds number, for the different tank designs and operation conditions. It appears that there is no significant difference in the way the data correlate for the different mantle tank designs and operation conditions. If a

correlation based on the least squared fit through all the points in Figure 7-2 were made, then an R^2-value of 0.89 would have been obtained.

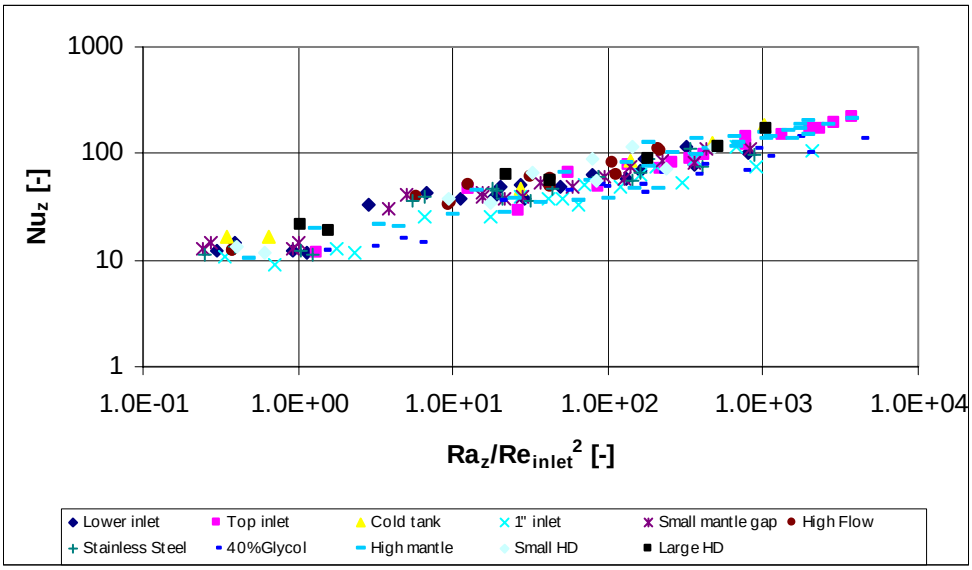

Figure 7-2: Local Nusselt number as a function of the ratio between the local Rayleigh number and the squared inlet Reynolds number for the different tank designs and operation conditions.

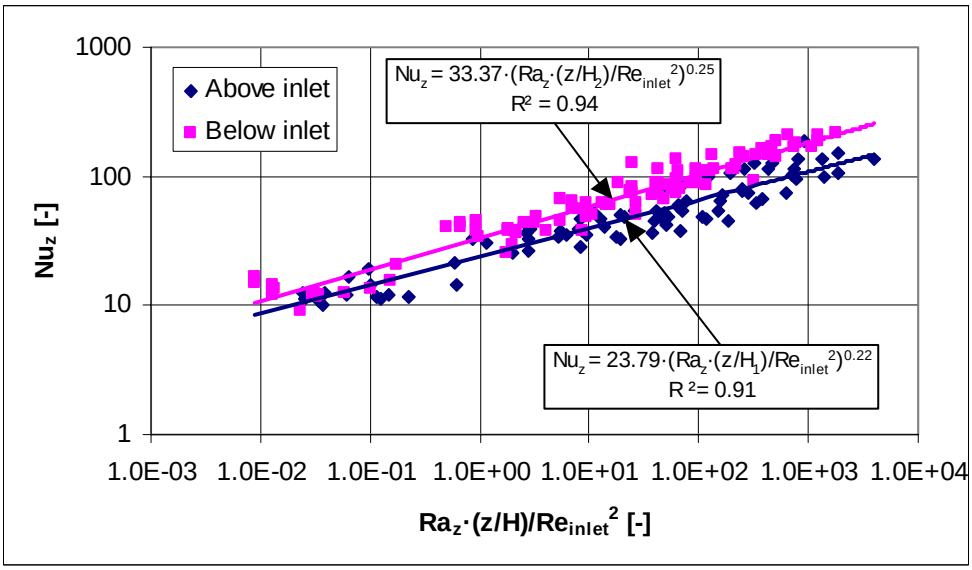

Figure 7-3: The local Nusselt number as a function of the ratio between the local Rayleigh number and the squared inlet Reynolds number multiplied by the dimensionless vertical distance from mantle inlet for the different tank designs and operation conditions. A correlation is given for the part above the mantle inlet and for the part below the mantle inlet.

In order to get a better correlation of the data, the local Nusselt number is now plotted as a function of the ratio between the local Rayleigh number and the squared inlet Reynolds number multiplied by the dimensionless vertical distance from the mantle

inlet, for the different tank designs and operation conditions. This is shown in Figure 7-3 where the value of H has different values for above and below inlet. Above the mantle inlet H is equal to the distance from the inlet to the top of the mantle, and below the mantle inlet H is equal to the distance from the inlet to the bottom of the mantle. It appears from Figure 7-3 that there is a significant difference in the way the data correlate for the part above the mantle inlet and for the part below the mantle inlet. Therefore two different correlations are needed for the upper half of the mantle: one for the part above the mantle inlet and one for the part below the mantle inlet. The correlations are calculated by the least squared fit through the points using the equation $Nu_z=C_1\cdot(Ra_z\cdot(z/H)/Re_{inlet}^2)^{C2}$ where C_1 and C_2 are constants.
Thus, the correlations become:

Above mantle inlet:
$$Nu_z = 23.79 \cdot \left(\frac{Ra_z \cdot \frac{z}{H_1}}{Re_{inlet}^2} \right)^{0.22} \tag{7.12}$$

Below mantle inlet:
$$Nu_z = 33.37 \cdot \left(\frac{Ra_z \cdot \frac{z}{H_2}}{Re_{inlet}^2} \right)^{0.25} \tag{7.13}$$

where

H_1	is the distance from mantle inlet to top of mantle, [m]
H_2	is the distance from mantle inlet to bottom of mantle, [m]
z	is the vertical distance from the mantle inlet, [m]

The definition of H_1, H_2 and z is shown in Figure 7-4.

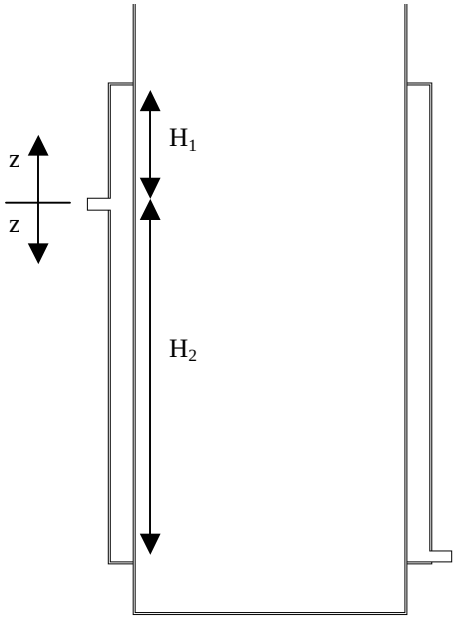

Figure 7-4: Definitions of H_1, H_2 and z.

Lower half of the mantle:

Figure 7-5 shows the local Nusselt number as a function of the local Rayleigh number, for the different tank designs and operation conditions. As explained in section 7.2, a correlation where the local Nusselt number is a function of the local Rayleigh number was expected. However, Figure 7-5 shows that the local Nusselt number based on the mantle gap width is independent of the local Rayleigh number based on the mantle gap width. Furthermore, it is seen from Figure 7-5 that the differences in the local Nusselt number are related to differences in the geometry of the mantle heat exchangers. The reference tank with a H/D ratio of 3.7, the tank with small mantle gap, the tank with the high mantle, the tank with a small H/D ratio and the tank with a large H/D ratio have all different local Nusselt numbers, but the local Nusselt number is relatively constant for each of the different geometries. Therefore a new geometrical parameter for mantle heat exchangers was introduced. That is the ratio between the horizontal flow area of the mantle gap and the heat transfer area at the inner mantle wall:

$$\frac{A_{flow}}{A_{heat\,transfer}} = \frac{\pi \cdot \left(r_o^2 - r_i^2\right)}{2 \cdot \pi \cdot r_i \cdot H} = \frac{\left(r_o^2 - r_i^2\right)}{2 \cdot r_i \cdot H} \qquad (7.14)$$

where

A_{flow}	is the horizontal flow area of the mantle gap, [m²]
$A_{heat\,transfer}$	is the heat transfer area at the inner mantle wall, [m²]
H	is the height of the mantle, [m]
r_i	is the inner annuli radius (see Figure 7-6), [m]
r_o	is the outer annuli radius (see Figure 7-6), [m]

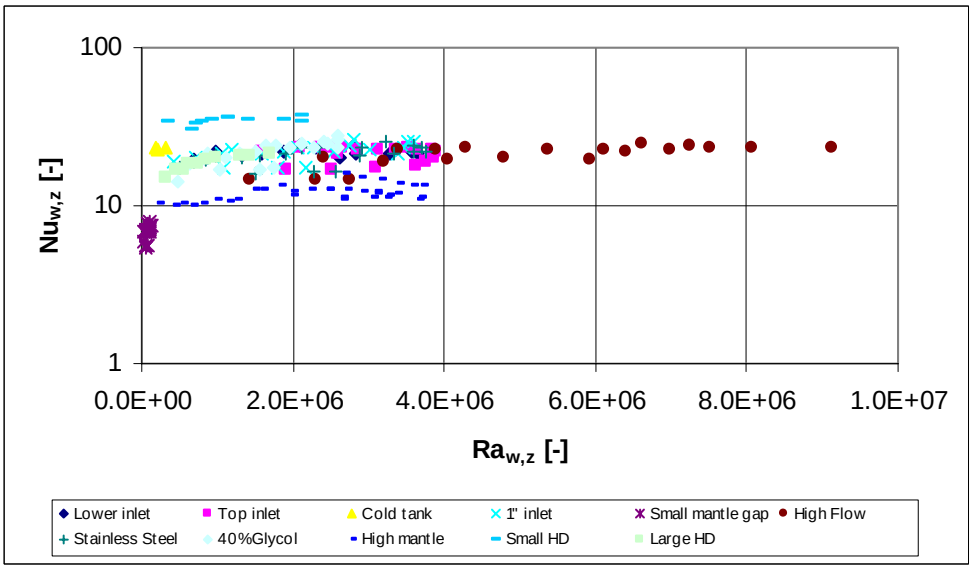

Figure 7-5: Local Nusselt number as a function of local Rayleigh number for the different tank designs and operation conditions. Characteristic length is the mantle gap width, w.

All the points from Figure 7-5 are now plotted in Figure 7-7, where the local Nusselt number is shown as a function of the ratio between the horizontal flow area of the mantle gap and the heat transfer area at the inner mantle wall. The correlation in Figure 7-7 is calculated by the least squared fit through the points using the equation $Nu_{w,z} = C_3 \cdot (A_{flow}/A_{heat\ transfer}) + C_4$ where C_3 and C_4 are constants.

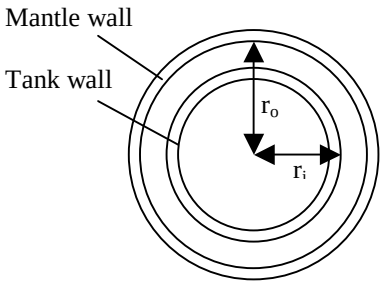

Figure 7-6: Definition of r_i and r_o.

Thus, the correlation becomes:

$$Nu_{w,z} = 403.9 \cdot \left(\frac{A_{flow}}{A_{heat\ transfer}} \right) + 0.98 \qquad (7.15)$$

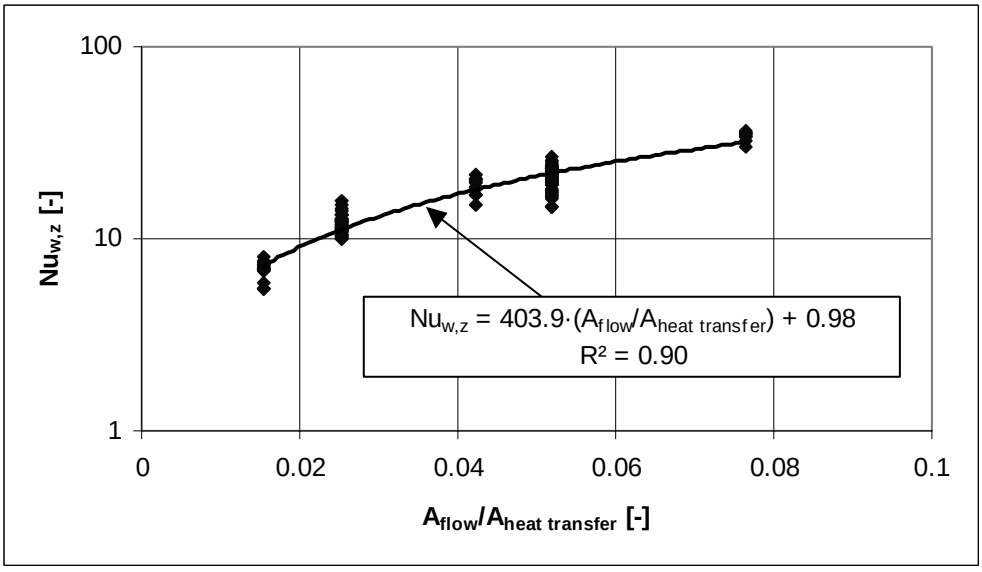

Figure 7-7: Local Nusselt number as a function of the ratio between the horizontal flow area of the mantle gap and the heat transfer area at the inner mantle wall.

7.3.1 Comparison of calculated heat flux at inner mantle wall

The heat fluxes calculated by use of the correlations (equations 7.12, 7.13 and 7.15) are compared to the heat fluxes calculated by CFD to make sure that the correlations behave as expected. If a good agreement is achieved, the correlations are suitable for calculating heat fluxes from the mantle fluid to the inner mantle wall. Table 7-1 gives an overview of the comparisons.

Model	Tank volume [m³]	Inner tank height [m]	Inner diameter [m]	Inner mantle height [m]	Mantle gap [m]	Mantle flow rate [l/min]	Heat fluxes illustrated in:
Ref. tank Lower inlet	0.175	1.440	0.394	0.700	0.0335	0.4	Figure 7-8 – Figure 7-9
Top inlet	0.175	1.440	0.394	0.700	0.0335	0.4	Figure 7-10 – Figure 7-11
Ini. cold tank	0.175	1.440	0.394	0.700	0.0335	0.4	Figure 7-12
1" inlet	0.175	1.440	0.394	0.700	0.0335	0.4	Figure 7-13 – Figure 7-14
Small mantle gap	0.175	1.440	0.394	0.700	0.0105	0.4	Figure 7-15 – Figure 7-16
High flow rate	0.175	1.440	0.394	0.700	0.0335	0.8	Figure 7-17 – Figure 7-18
Stainless steel	0.175	1.440	0.394	0.700	0.0335	0.4	Figure 7-19 – Figure 7-20
40% Glycol	0.175	1.440	0.394	0.700	0.0335	0.4	Figure 7-21 – Figure 7-22
High mantle	0.175	1.440	0.394	1.440	0.0335	0.4	Figure 7-23 – Figure 7-24
Small H/D ratio	0.175	0.959	0.482	0.468	0.0335	0.4	Figure 7-25
Large H/D ratio	0.175	1.778	0.354	0.864	0.0335	0.4	Figure 7-26

Table 7-1: Overview of the comparisons of the heat fluxes from the mantle fluid to the inner mantle wall.

Figure 7-8 – Figure 7-26 show heat fluxes from the mantle fluid to the inner mantle wall calculated by CFD, with the correlations developed in this thesis (equations 7.12, 7.13 and 7.15) and with the correlation (equation 2.22) developed by Shah (1999, 2000). The temperatures used in the correlations are extracted from the CFD results and all the results are presented after 40 minutes with either the hot or the warm inlet condition. It should be noted that equation 2.22, the correlation developed by Shah (1999, 2000) is developed for mantle heat exchangers with mantle inlet port located at the top of the mantle, and most of the mantle heat exchangers in this comparison have the mantle inlet port at a lower position.

The overall conclusions from the figures are that the correlations developed in this thesis give heat fluxes in good agreement with CFD for both hot and warm inlet conditions. However, in some cases the heat flux is slightly over-predicted near the mantle inlet for the hot inlet condition. It is also seen that the correlations give a better prediction of the heat flux than the correlation developed by Shah (1999, 2000), but, as stated above, the comparison is not fair, because Shah's correlation was developed for top inlet only and mainly for larger temperature differences than occur in the cases shown in Figure 7-8 – Figure 7-26. The case where Shah's correlation gives the best prediction is actually the case with the initially cold tank where large temperature differences occur.

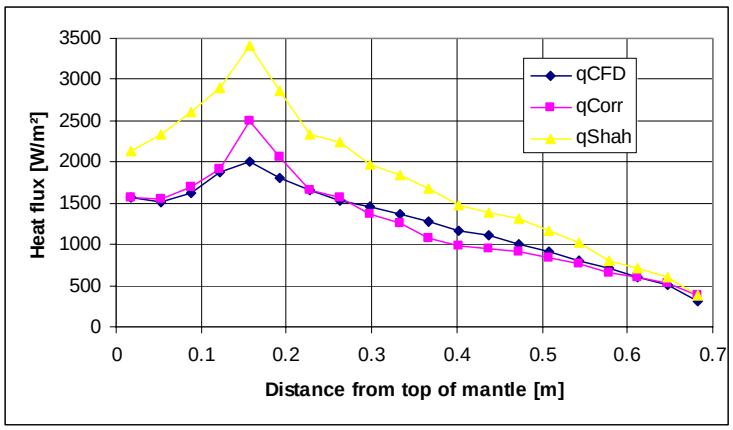

Figure 7-8: Lower inlet configuration (hot inlet condition): Comparison of heat flux from mantle fluid to inner mantle wall after 40 minutes predicted by CFD (qCFD), the correlations developed in this thesis (qCorr) and Shah's correlation (qShah), respectively.

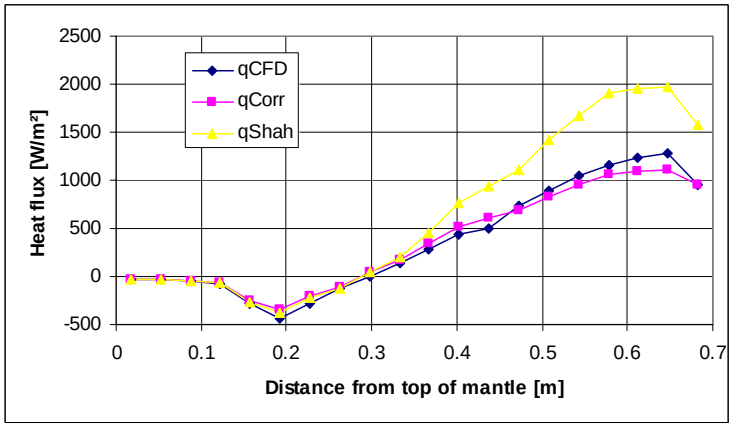

Figure 7-9: Lower inlet configuration (warm inlet condition): Comparison of heat flux from mantle fluid to inner mantle wall after 40 minutes predicted by CFD (qCFD), the correlations developed in this thesis (qCorr) and Shah's correlation (qShah), respectively.

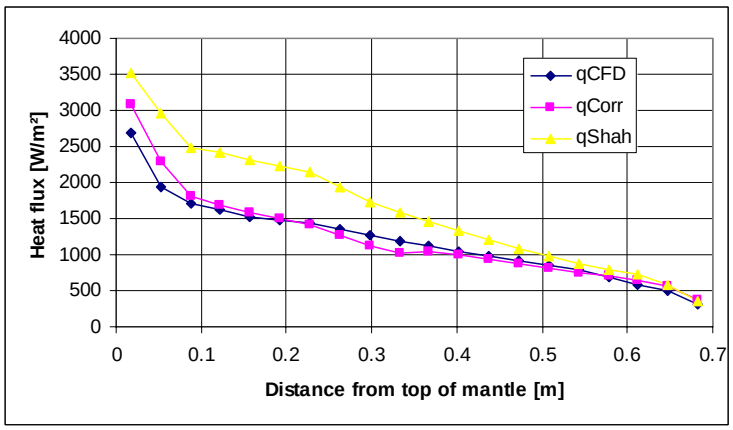

Figure 7-10: Top inlet configuration (hot inlet condition): Comparison of heat flux from mantle fluid to inner mantle wall after 40 minutes predicted by CFD (qCFD), the correlations developed in this thesis (qCorr) and Shah's correlation (qShah), respectively.

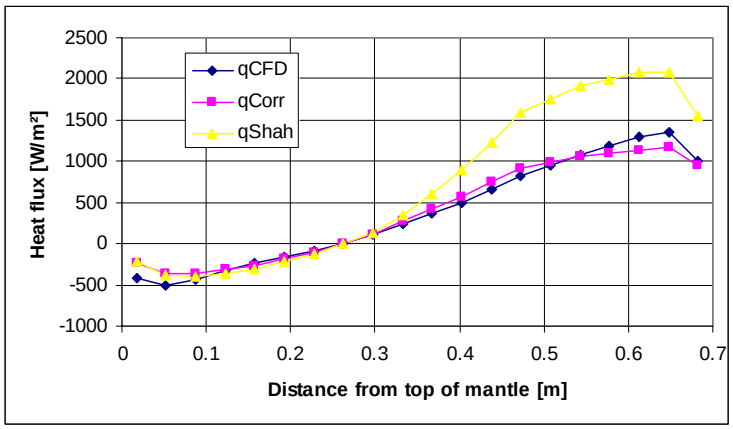

Figure 7-11: Top inlet configuration (warm inlet condition): Comparison of heat flux from mantle fluid to inner mantle wall after 40 minutes predicted by CFD (qCFD), the correlations developed in this thesis (qCorr) and Shah's correlation (qShah), respectively.

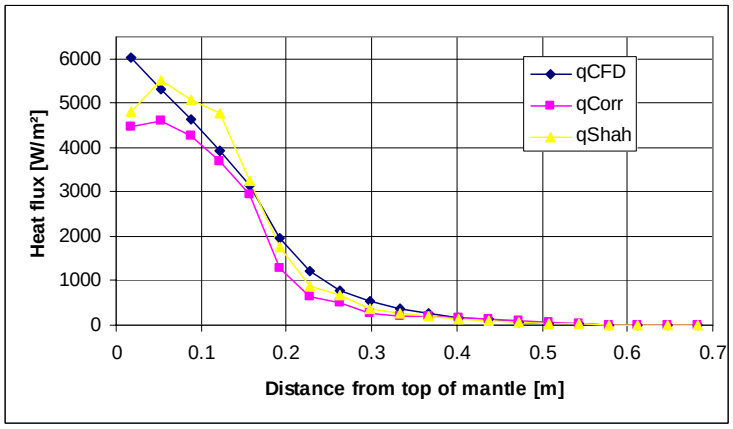

Figure 7-12: Initially cold tank (hot inlet condition): Comparison of heat flux from mantle fluid to inner mantle wall after 40 minutes predicted by CFD (qCFD), the correlations developed in this thesis (qCorr) and Shah's correlation (qShah), respectively.

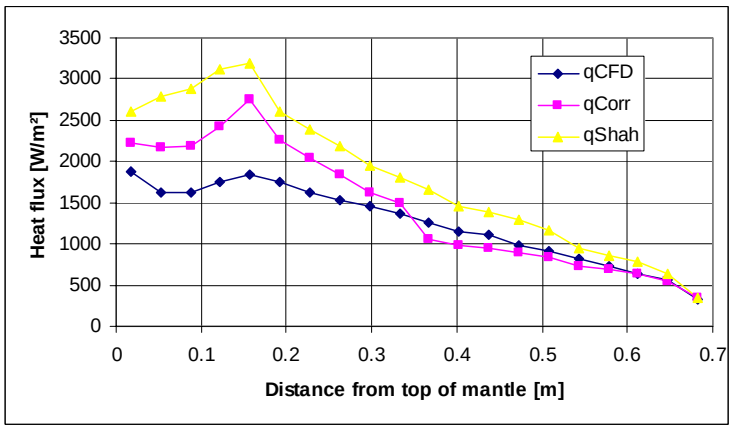

Figure 7-13: 1" inlet configuration (hot inlet condition): Comparison of heat flux from mantle fluid to inner mantle wall after 40 minutes predicted by CFD (qCFD), the correlations developed in this thesis (qCorr) and Shah's correlation (qShah), respectively.

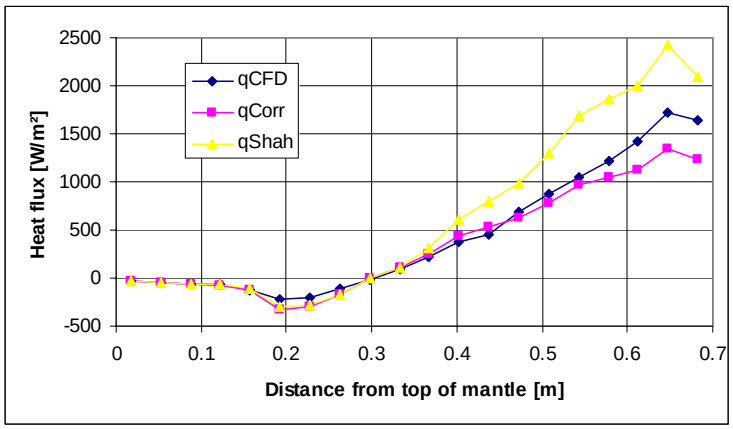

Figure 7-14: 1" inlet configuration (warm inlet condition): Comparison of heat flux from mantle fluid to inner mantle wall after 40 minutes predicted by CFD (qCFD), the correlations developed in this thesis (qCorr) and Shah's correlation (qShah), respectively.

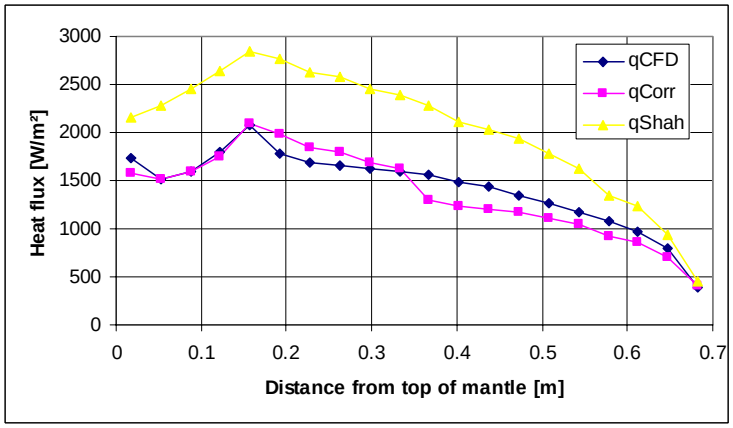

Figure 7-15: Small mantle gap configuration (hot inlet condition): Comparison of heat flux from mantle fluid to inner mantle wall after 40 minutes predicted by CFD (qCFD), the correlations developed in this thesis (qCorr) and Shah's correlation (qShah), respectively.

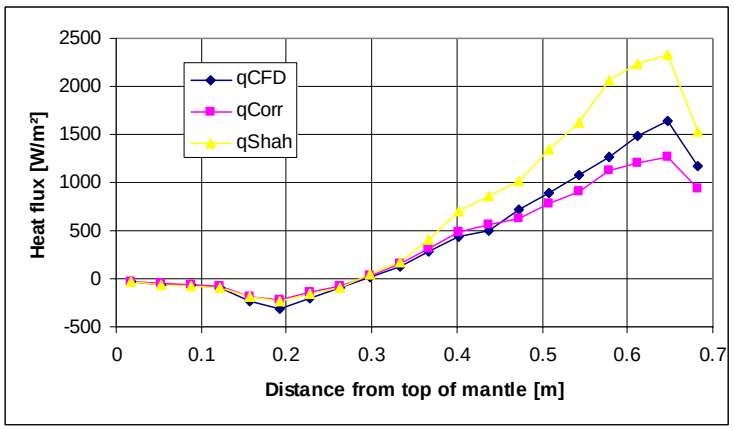

Figure 7-16: Small mantle gap configuration (warm inlet condition): Comparison of heat flux from mantle fluid to inner mantle wall after 40 minutes predicted by CFD (qCFD), the correlations developed in this thesis (qCorr) and Shah's correlation (qShah), respectively.

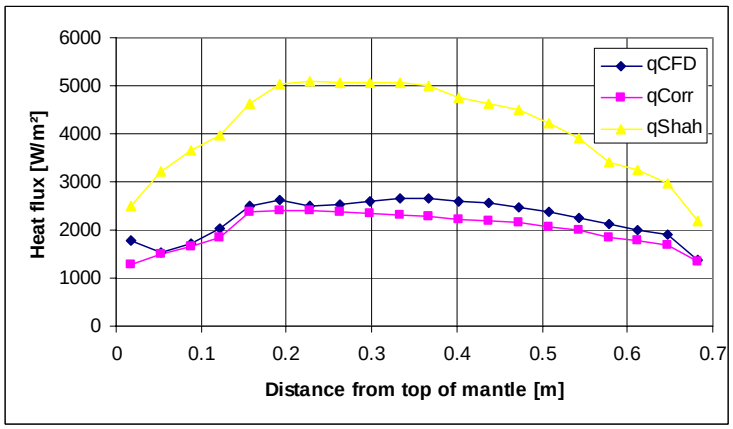

Figure 7-17: High flow rate (hot inlet condition): Comparison of heat flux from mantle fluid to inner mantle wall after 40 minutes predicted by CFD (qCFD), the correlations developed in this thesis (qCorr) and Shah's correlation (qShah), respectively.

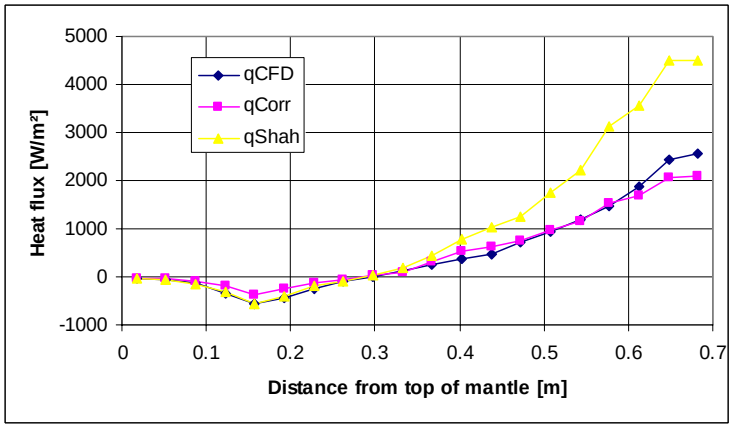

Figure 7-18: High flow rate (warm inlet condition): Comparison of heat flux from mantle fluid to inner mantle wall after 40 minutes predicted by CFD (qCFD), the correlations developed in this thesis (qCorr) and Shah's correlation (qShah), respectively.

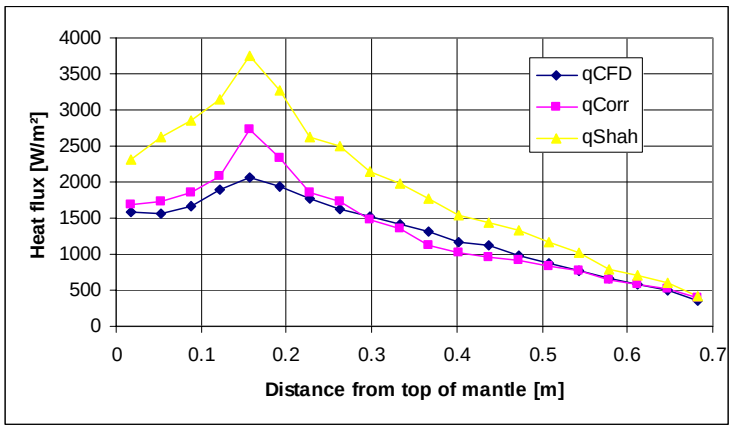

Figure 7-19: Stainless steel tank configuration (hot inlet condition): Comparison of heat flux from mantle fluid to inner mantle wall after 40 minutes predicted by CFD (qCFD), the correlations developed in this thesis (qCorr) and Shah's correlation (qShah), respectively.

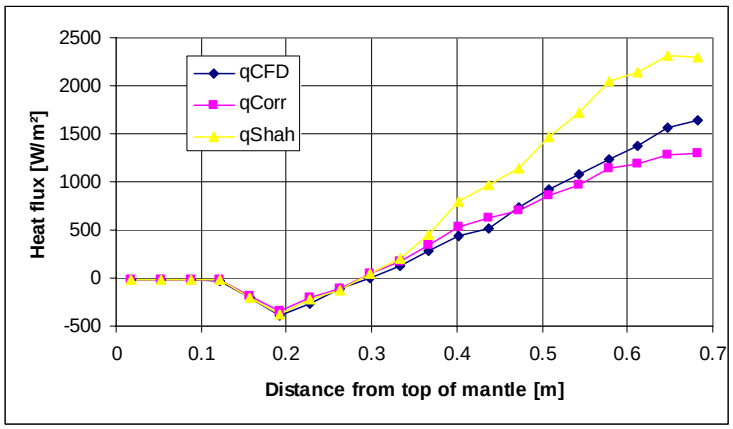

Figure 7-20: Stainless steel tank configuration (warm inlet condition): Comparison of heat flux from mantle fluid to inner mantle wall after 40 minutes predicted by CFD (qCFD), the correlations developed in this thesis (qCorr) and Shah's correlation (qShah), respectively.

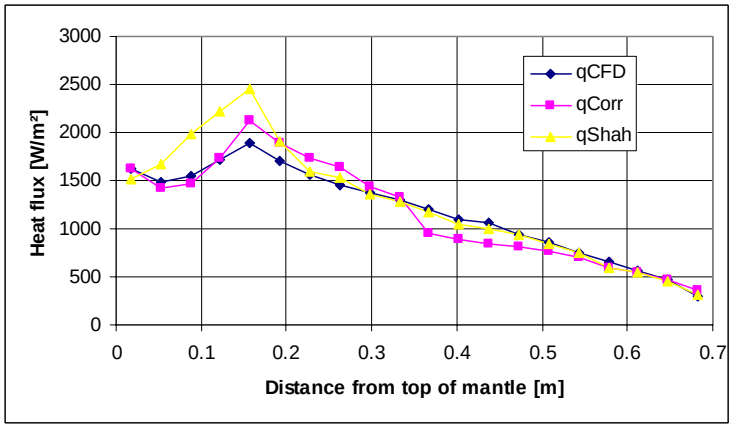

Figure 7-21: 40% Glycol (hot inlet condition): Comparison of heat flux from mantle fluid to inner mantle wall after 40 minutes predicted by CFD (qCFD), the correlations developed in this thesis (qCorr) and Shah's correlation (qShah), respectively.

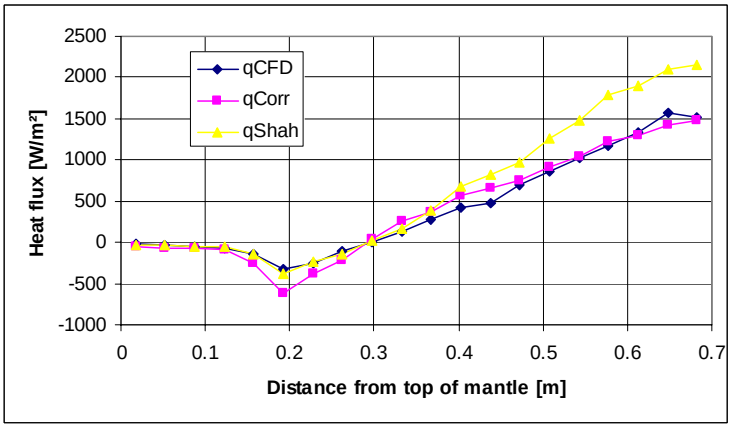

Figure 7-22: 40% Glycol (warm inlet condition): Comparison of heat flux from mantle fluid to inner mantle wall after 40 minutes predicted by CFD (qCFD), the correlations developed in this thesis (qCorr) and Shah's correlation (qShah), respectively.

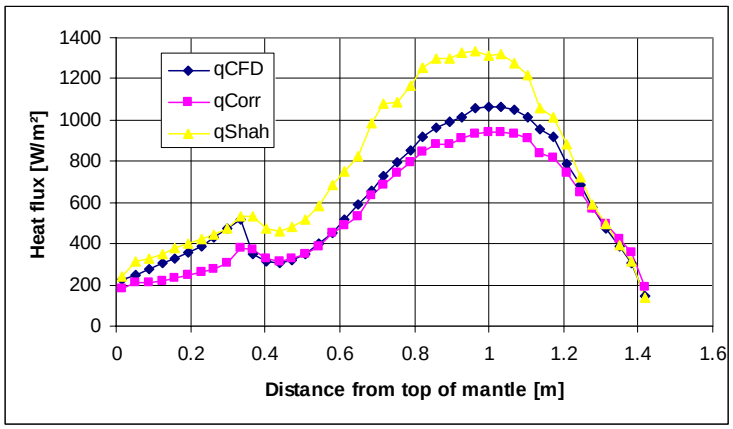

Figure 7-23: High mantle configuration (hot inlet condition): Comparison of heat flux from mantle fluid to inner mantle wall after 40 minutes predicted by CFD (qCFD), the correlations developed in this thesis (qCorr) and Shah's correlation (qShah), respectively.

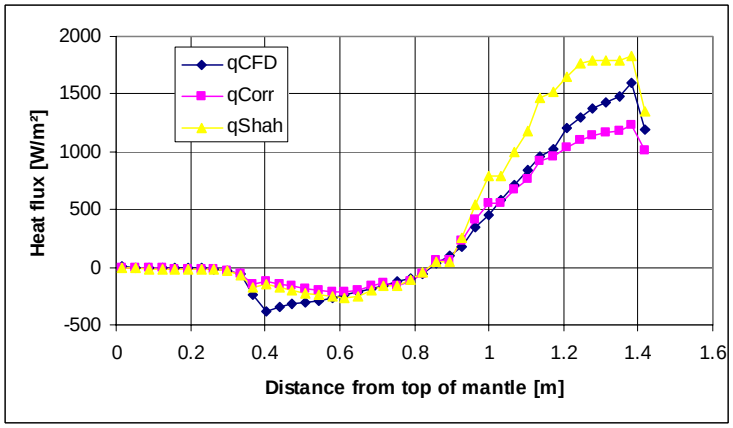

Figure 7-24: High mantle configuration (warm inlet condition): Comparison of heat flux from mantle fluid to inner mantle wall after 40 minutes predicted by CFD (qCFD), the correlations developed in this thesis (qCorr) and Shah's correlation (qShah), respectively.

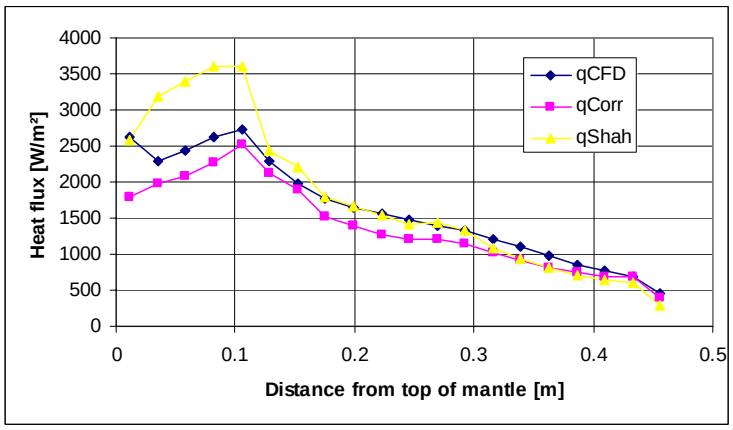

Figure 7-25: Small H/D ratio tank configuration (hot inlet condition): Comparison of heat flux from mantle fluid to inner mantle wall after 40 minutes predicted by CFD (qCFD), the correlations developed in this thesis (qCorr) and Shah's correlation (qShah), respectively.

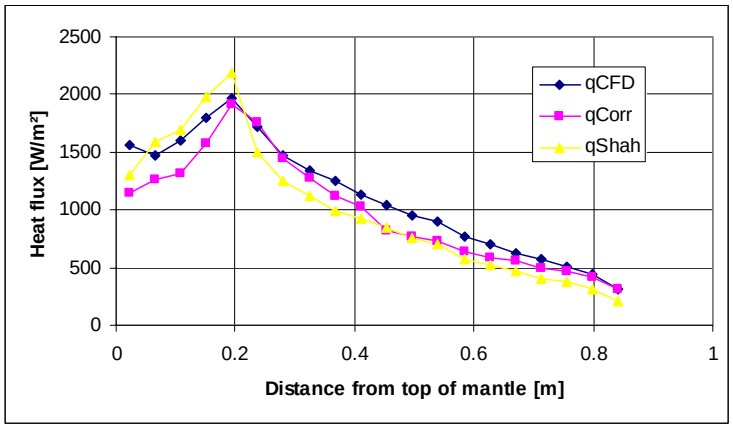

Figure 7-26: Large H/D ratio tank configuration (hot inlet condition): Comparison of heat flux from mantle fluid to inner mantle wall after 40 minutes predicted by CFD (qCFD), the correlations developed in this thesis (qCorr) and Shah's correlation (qShah), respectively.

7.4 Heat transfer from mantle fluid to outer mantle wall

The analysis of heat transfer from mantle fluid to outer mantle wall is, as it was for the heat transfer from mantle fluid to inner mantle wall, divided into two parts; the upper half of the mantle and the lower half of the mantle. Figure 7-27 illustrates the heat flux at the outer mantle wall.

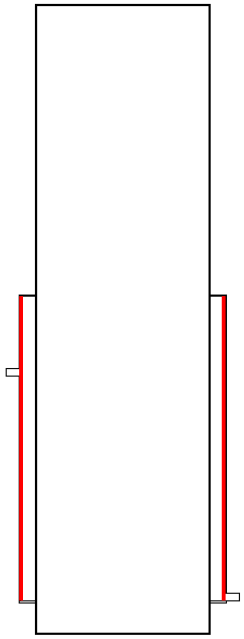

Figure 7-27: Heat flux at outer mantle wall.

Upper half of the mantle:

Figure 7-28 shows the local Nusselt number plotted as a function of the ratio between the local Rayleigh number and the squared inlet Reynolds number multiplied by the dimensionless vertical distance from the mantle inlet, for the different tank designs and operation conditions. As for the heat transfer from mantle fluid to inner mantle wall, there is a difference in the way the data correlate for the part above the mantle inlet and for the part below the mantle inlet. The correlations in Figure 7-28 are calculated by the least squared fit through the points using the equation $Nu_z=C_5\cdot(Ra_z\cdot(z/H)/Re_{inlet}^{2})^{C6}$ where C_5 and C_6 are constants.

Thus, the correlations become:

Above mantle inlet:
$$Nu_z = 31.51 \cdot \left(\frac{Ra_z \cdot \frac{z}{H_1}}{Re_{inlet}^{\ 2}} \right)^{0.18} \quad (7.16)$$

Below mantle inlet:
$$Nu_z = 56.24 \cdot \left(\frac{Ra_z \cdot \frac{z}{H_2}}{Re_{inlet}^{\ 2}} \right)^{0.22} \quad (7.17)$$

where

H_1	is the distance from mantle inlet to top of mantle, [m]
H_2	is the distance from mantle inlet to bottom of mantle, [m]
z	is the vertical distance from the mantle inlet, [m]

The definition of H_1, H_2 and z is shown in Figure 7-4.

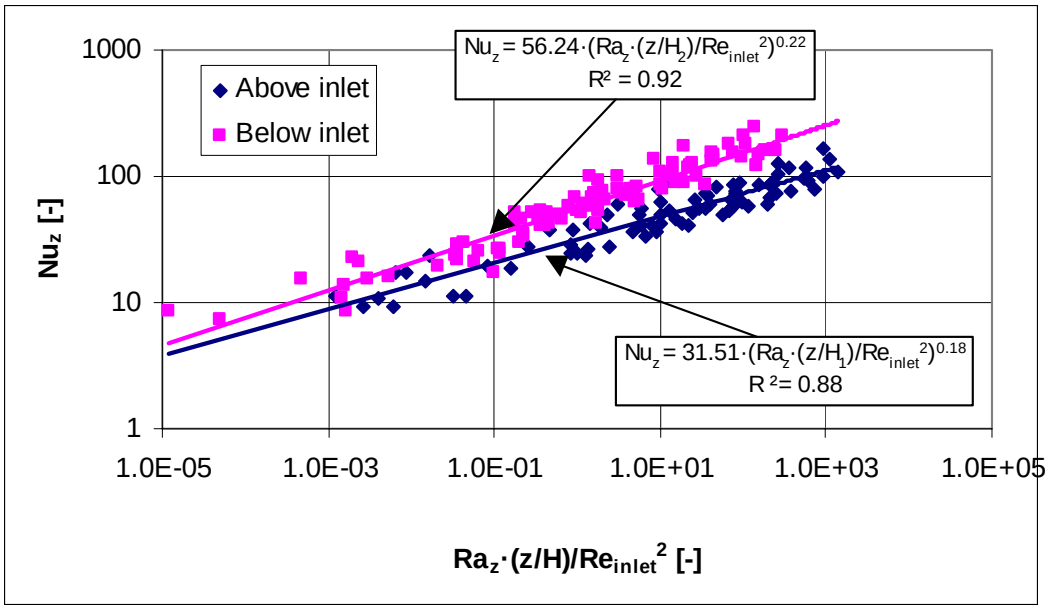

Figure 7-28: The local Nusselt number as a function of the ratio between the local Rayleigh number and the squared inlet Reynolds number multiplied by the dimensionless vertical distance from mantle inlet for the different tank designs and operation conditions. A correlation is given for the part above the mantle inlet and for the part below the mantle inlet.

It appears from Figure 7-28 that the R^2-values for the correlations are lower than for the correlations for the heat transfer from mantle fluid to inner mantle wall, which are shown in Figure 7-3. This means that the data for heat transfer at the inner mantle wall have a better correlation than the data for heat transfer at the outer mantle wall.

Lower half of the mantle:
Figure 7-29 shows the local Nusselt number as a function of the ratio between the horizontal flow area of the mantle gap and the heat transfer area at the outer mantle wall. The correlation in Figure 7-29 is calculated by the least squared fit through the points using the equation $Nu_{w,z} = C_7 \cdot (A_{flow}/A_{heat\ transfer}) + C_8$ where C_7 and C_8 are constants.

Thus, the correlation becomes:

$$Nu_{w,z} = 570.6 \cdot \left(\frac{A_{flow}}{A_{heat\ transfer}} \right) + 5.6 \tag{7.18}$$

where the ratio between the horizontal flow area of the mantle gap and the heat transfer area at the outer mantle wall is defined as:

$$\frac{A_{flow}}{A_{heat\ transfer}} = \frac{\pi \cdot \left(r_o^2 - r_i^2 \right)}{2 \cdot \pi \cdot r_o \cdot H} = \frac{\left(r_o^2 - r_i^2 \right)}{2 \cdot r_o \cdot H} \tag{7.19}$$

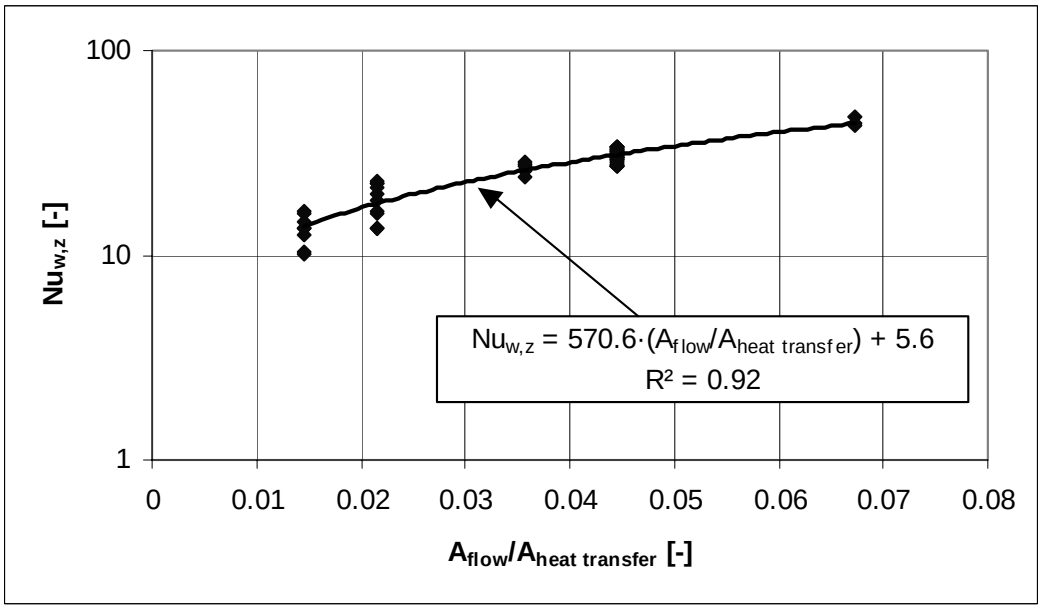

Figure 7-29: Local Nusselt number as a function of the ratio between the horizontal flow area of the mantle gap and the heat transfer area at the outer mantle wall.

It is seen that the local Nusselt number, both in upper half and in lower half, is higher for the heat transfer at the outer mantle wall than for heat transfer at the inner mantle wall.

7.4.1 Comparison of calculated heat flux at outer mantle wall

The heat fluxes calculated by use of the correlations (equations 7.16 - 7.18) are compared to the heat fluxes calculated by CFD to make sure that the correlations behave as expected. If a good agreement is achieved, the correlations are suitable for calculating heat fluxes from the mantle fluid to the outer mantle wall. Table 7-2 gives an overview of the comparisons.

Model	Tank volume [m³]	Inner tank height [m]	Inner diameter [m]	Inner mantle height [m]	Mantle gap [m]	Mantle flow rate [l/min]	Heat fluxes illustrated in:
Ref. tank Lower inlet	0.175	1.440	0.394	0.700	0.0335	0.4	Figure 7-30 – Figure 7-31
Top inlet	0.175	1.440	0.394	0.700	0.0335	0.4	Figure 7-32 – Figure 7-33
Ini. cold tank	0.175	1.440	0.394	0.700	0.0335	0.4	Figure 7-34
1” inlet	0.175	1.440	0.394	0.700	0.0335	0.4	Figure 7-35 – Figure 7-36
Small mantle gap	0.175	1.440	0.394	0.700	0.0105	0.4	Figure 7-37 – Figure 7-38
High flow rate	0.175	1.440	0.394	0.700	0.0335	0.8	Figure 7-39 – Figure 7-40
Stainless steel	0.175	1.440	0.394	0.700	0.0335	0.4	Figure 7-41 – Figure 7-42
40% Glycol	0.175	1.440	0.394	0.700	0.0335	0.4	Figure 7-43 – Figure 7-44
High mantle	0.175	1.440	0.394	1.440	0.0335	0.4	Figure 7-45 – Figure 7-46
Small H/D ratio	0.175	0.959	0.482	0.468	0.0335	0.4	Figure 7-47
Large H/D ratio	0.175	1.778	0.354	0.864	0.0335	0.4	Figure 7-48

Table 7-2: Overview of the comparisons of the heat fluxes from the mantle fluid to the outer mantle wall.

Figure 7-30 – Figure 7-48 show heat fluxes from the mantle fluid to the outer mantle wall calculated by CFD, with the correlations developed in this thesis (equations 7.16 - 7.18) and with the correlation (equation 2.22) developed by Shah (1999, 2000). The temperatures used in the correlations are extracted from the CFD results and all the results are presented after 40 minutes with either the hot or the warm inlet condition. It should be noted that equation 2.22, the correlation developed by Shah (1999, 2000), is developed for mantle heat exchangers with mantle inlet port located at the top of the mantle, and most of the mantle heat exchangers in this comparison have the mantle inlet port at a lower position.

It appears that the heat flux at the outer mantle wall is much lower than the heat flux at the inner mantle wall, which is due to the outer insulation. For the warm inlet condition it is seen that in most cases there is a negative heat flux just below the mantle inlet, meaning that the wall temperature at that level is higher than the mantle fluid temperature because of the vertical heat conduction in the wall. The overall conclusions from the figures are that the correlations developed in this thesis give heat fluxes in good agreement with CFD for both hot and warm inlet conditions. It is also seen that the correlation developed by Shah (1999, 2000) gives a good prediction of the heat flux at the outer mantle wall.

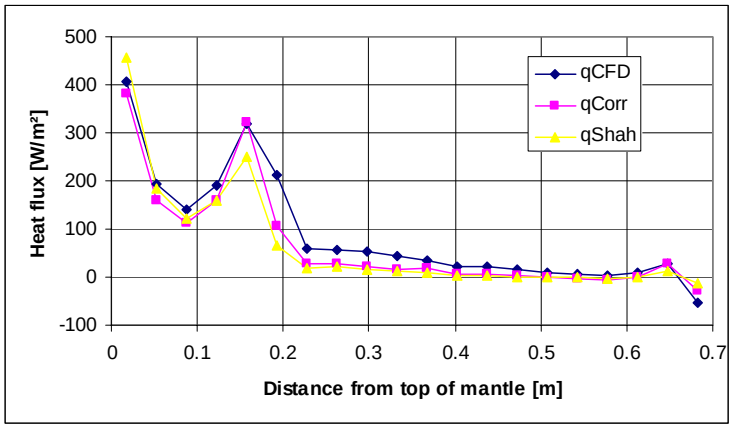

Figure 7-30: Lower inlet configuration (hot inlet condition): Comparison of heat flux from mantle fluid to outer mantle wall after 40 minutes predicted by CFD (qCFD), the correlations developed in this thesis (qCorr) and Shah's correlation (qShah), respectively.

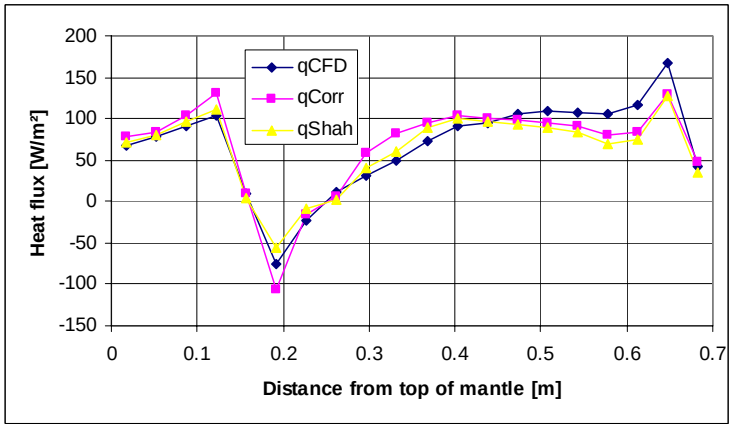

Figure 7-31: Lower inlet configuration (warm inlet condition): Comparison of heat flux from mantle fluid to outer mantle wall after 40 minutes predicted by CFD (qCFD), the correlations developed in this thesis (qCorr) and Shah's correlation (qShah), respectively.

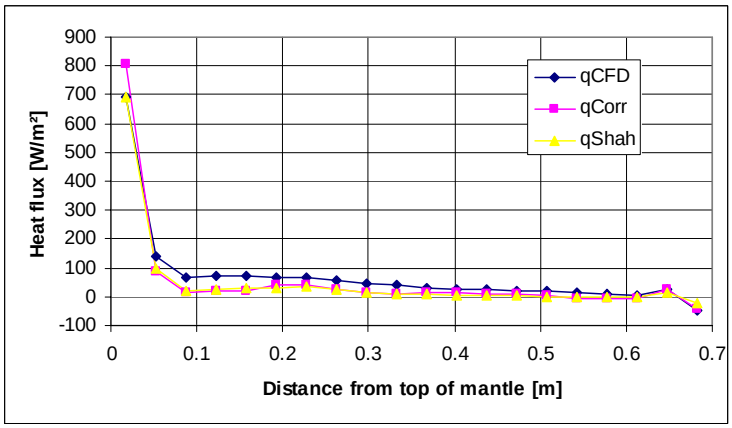

Figure 7-32: Top inlet configuration (hot inlet condition): Comparison of heat flux from mantle fluid to outer mantle wall after 40 minutes predicted by CFD (qCFD), the correlations developed in this thesis (qCorr) and Shah's correlation (qShah), respectively.

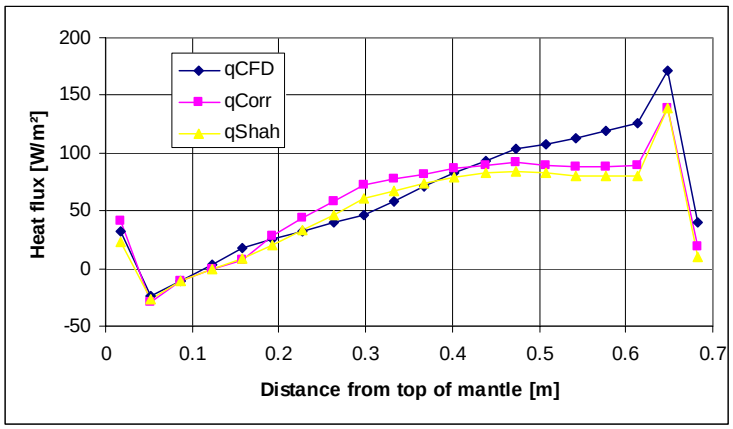

Figure 7-33: Top inlet configuration (warm inlet condition): Comparison of heat flux from mantle fluid to outer mantle wall after 40 minutes predicted by CFD (qCFD), the correlations developed in this thesis (qCorr) and Shah's correlation (qShah), respectively.

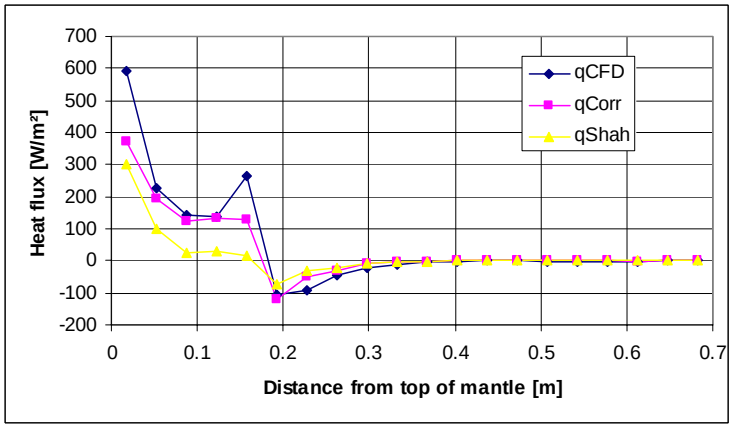

Figure 7-34: Initially cold tank (hot inlet condition): Comparison of heat flux from mantle fluid to outer mantle wall after 40 minutes predicted by CFD (qCFD), the correlations developed in this thesis (qCorr) and Shah's correlation (qShah), respectively.

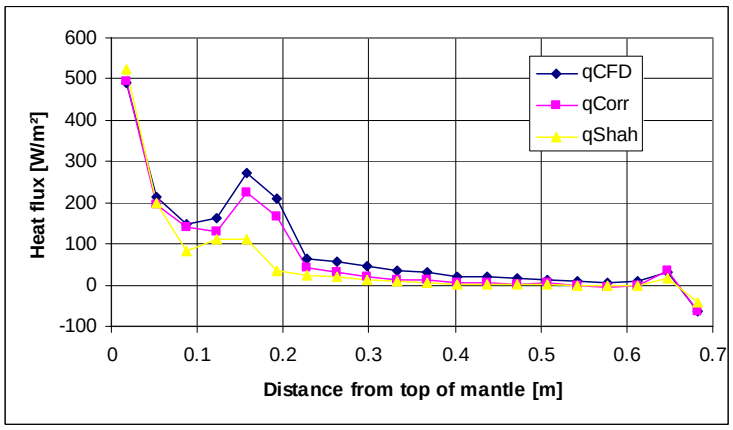

Figure 7-35: 1" inlet configuration (hot inlet condition): Comparison of heat flux from mantle fluid to outer mantle wall after 40 minutes predicted by CFD (qCFD), the correlations developed in this thesis (qCorr) and Shah's correlation (qShah), respectively.

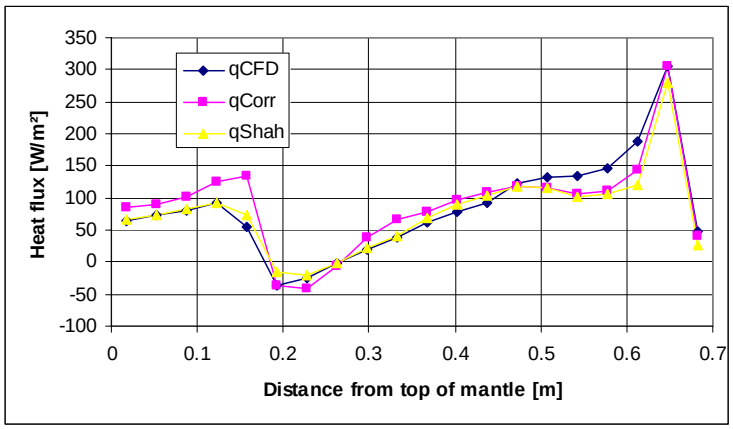

Figure 7-36: 1" inlet configuration (warm inlet condition): Comparison of heat flux from mantle fluid to outer mantle wall after 40 minutes predicted by CFD (qCFD), the correlations developed in this thesis (qCorr) and Shah's correlation (qShah), respectively.

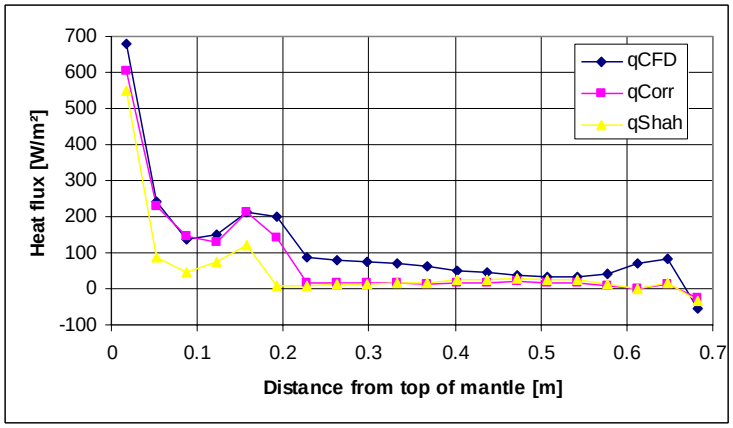

Figure 7-37: Small mantle gap configuration (hot inlet condition): Comparison of heat flux from mantle fluid to outer mantle wall after 40 minutes predicted by CFD (qCFD), the correlations developed in this thesis (qCorr) and Shah's correlation (qShah), respectively.

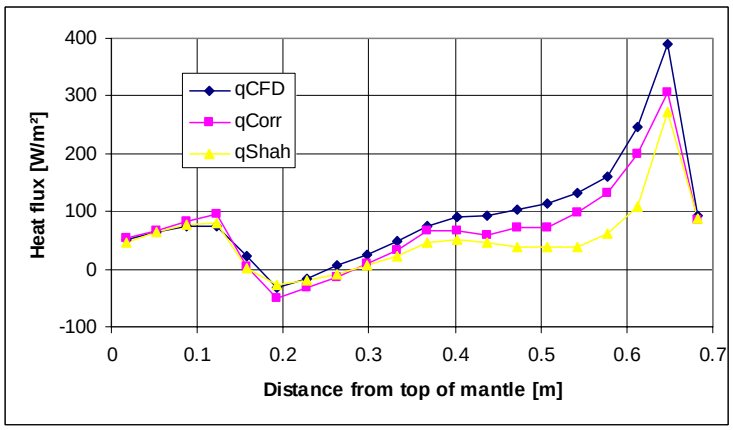

Figure 7-38: Small mantle gap configuration (warm inlet condition): Comparison of heat flux from mantle fluid to outer mantle wall after 40 minutes predicted by CFD (qCFD), the correlations developed in this thesis (qCorr) and Shah's correlation (qShah), respectively.

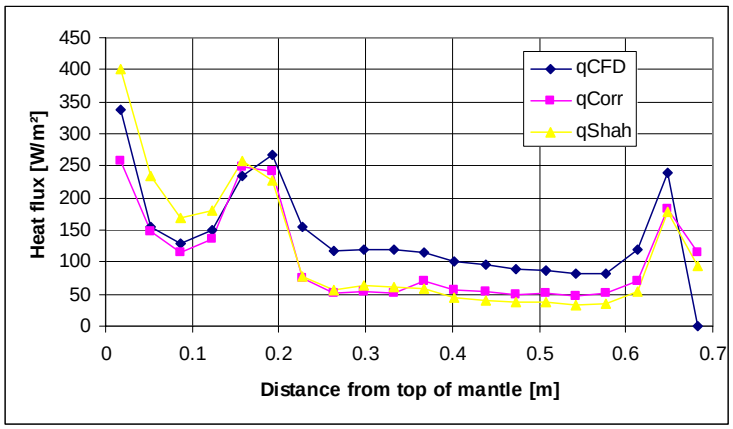

Figure 7-39: High flow rate (hot inlet condition): Comparison of heat flux from mantle fluid to outer mantle wall after 40 minutes predicted by CFD (qCFD), the correlations developed in this thesis (qCorr) and Shah's correlation (qShah), respectively.

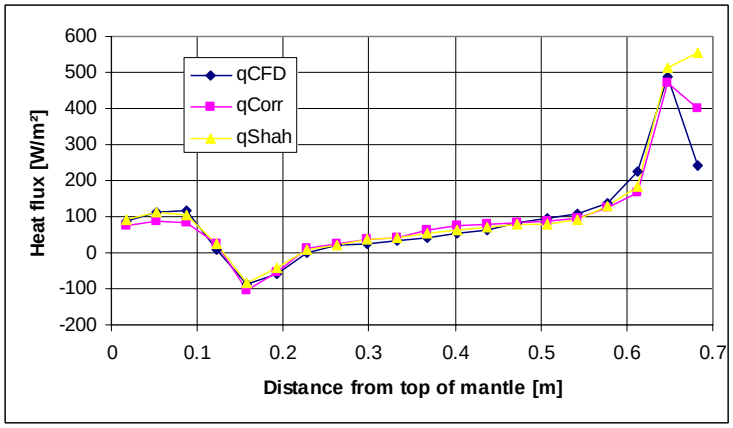

Figure 7-40: High flow rate (warm inlet condition): Comparison of heat flux from mantle fluid to outer mantle wall after 40 minutes predicted by CFD (qCFD), the correlations developed in this thesis (qCorr) and Shah's correlation (qShah), respectively.

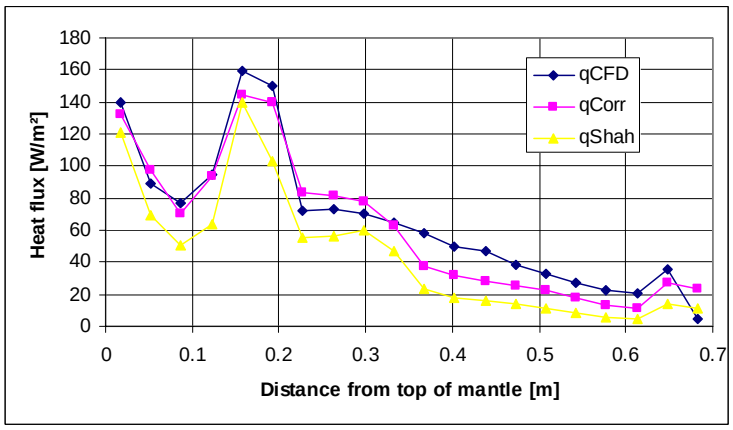

Figure 7-41: Stainless steel tank configuration (hot inlet condition): Comparison of heat flux from mantle fluid to outer mantle wall after 40 minutes predicted by CFD (qCFD), the correlations developed in this thesis (qCorr) and Shah's correlation (qShah), respectively.

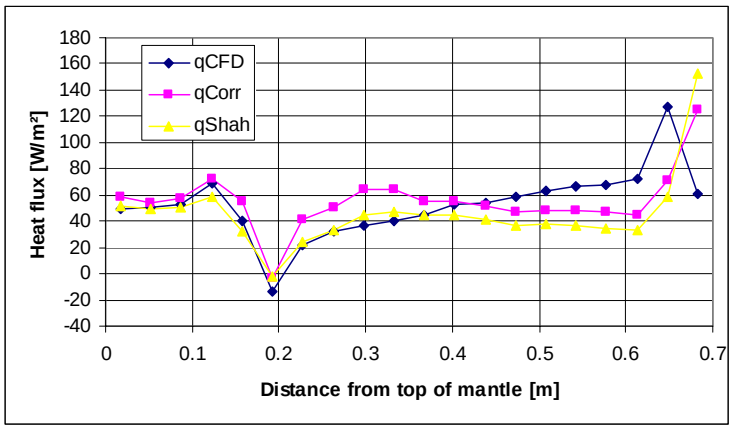

Figure 7-42: Stainless steel tank configuration (warm inlet condition): Comparison of heat flux from mantle fluid to outer mantle wall after 40 minutes predicted by CFD (qCFD), the correlations developed in this thesis (qCorr) and Shah's correlation (qShah), respectively.

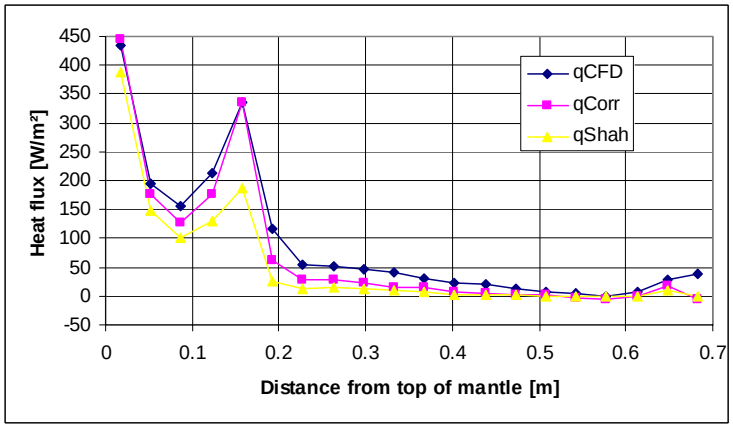

Figure 7-43: 40% Glycol (hot inlet condition): Comparison of heat flux from mantle fluid to outer mantle wall after 40 minutes predicted by CFD (qCFD), the correlations developed in this thesis (qCorr) and Shah's correlation (qShah), respectively.

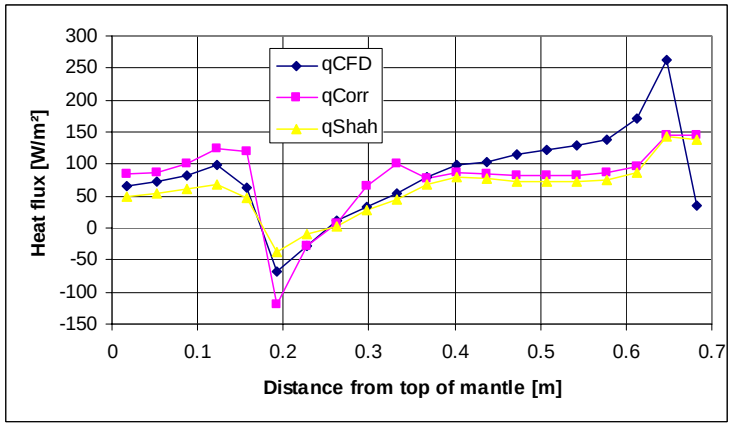

Figure 7-44: 40% Glycol (warm inlet condition): Comparison of heat flux from mantle fluid to outer mantle wall after 40 minutes predicted by CFD (qCFD), the correlations developed in this thesis (qCorr) and Shah's correlation (qShah), respectively.

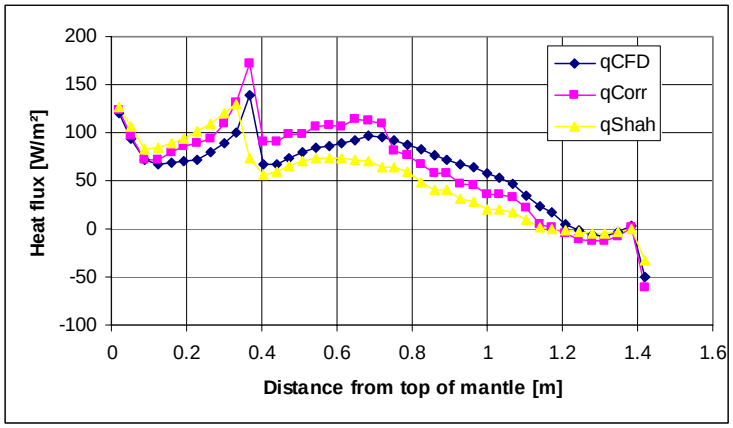

Figure 7-45: High mantle configuration (hot inlet condition): Comparison of heat flux from mantle fluid to outer mantle wall after 40 minutes predicted by CFD (qCFD), the correlations developed in this thesis (qCorr) and Shah's correlation (qShah), respectively.

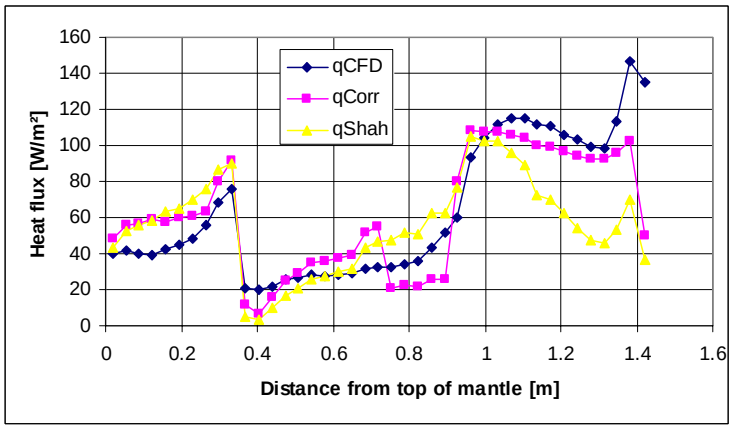

Figure 7-46: High mantle configuration (warm inlet condition): Comparison of heat flux from mantle fluid to outer mantle wall after 40 minutes predicted by CFD (qCFD), the correlations developed in this thesis (qCorr) and Shah's correlation (qShah), respectively.

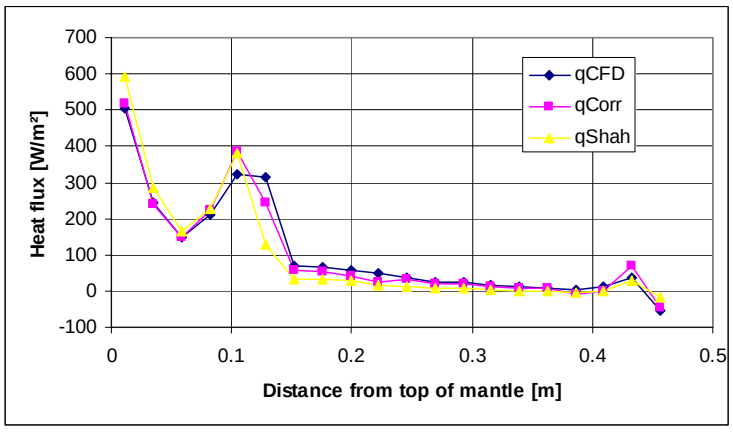

Figure 7-47: Small H/D ratio tank configuration (hot inlet condition): Comparison of heat flux from mantle fluid to outer mantle wall after 40 minutes predicted by CFD (qCFD), the correlations developed in this thesis (qCorr) and Shah's correlation (qShah), respectively.

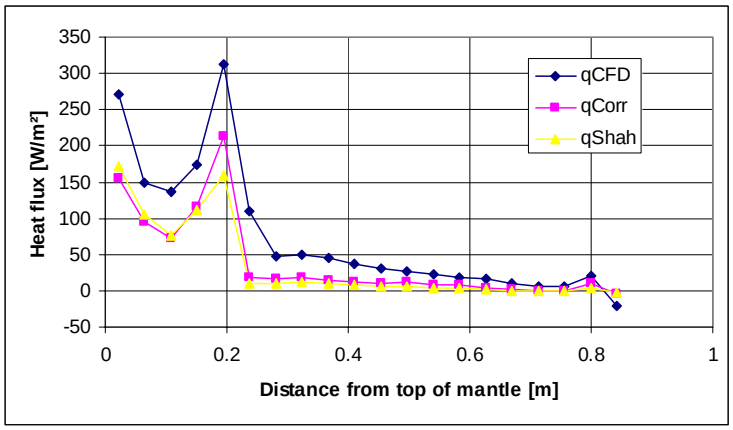

Figure 7-48: Large H/D ratio tank configuration (hot inlet condition): Comparison of heat flux from mantle fluid to outer mantle wall after 40 minutes predicted by CFD (qCFD), the correlations developed in this thesis (qCorr) and Shah's correlation (qShah), respectively.

7.5 Heat transfer from tank wall to domestic water

The flow of the water in the tank and the heat transfer at the tank wall are, when draw-offs are not considered, driven by natural convection only. Therefore, it is the goal, for a given tank, to determine the local Nusselt number as a function of the local Rayleigh number. The characteristic length, z, in the local Rayleigh number is in this case the distance from the bottom of the tank and the temperature difference is the local difference between the tank wall temperature and the temperature of the domestic water in the tank. The temperature of the domestic water is a mean temperature of the control volume at the actual level calculated as in equation 7.3 for the mantle fluid.

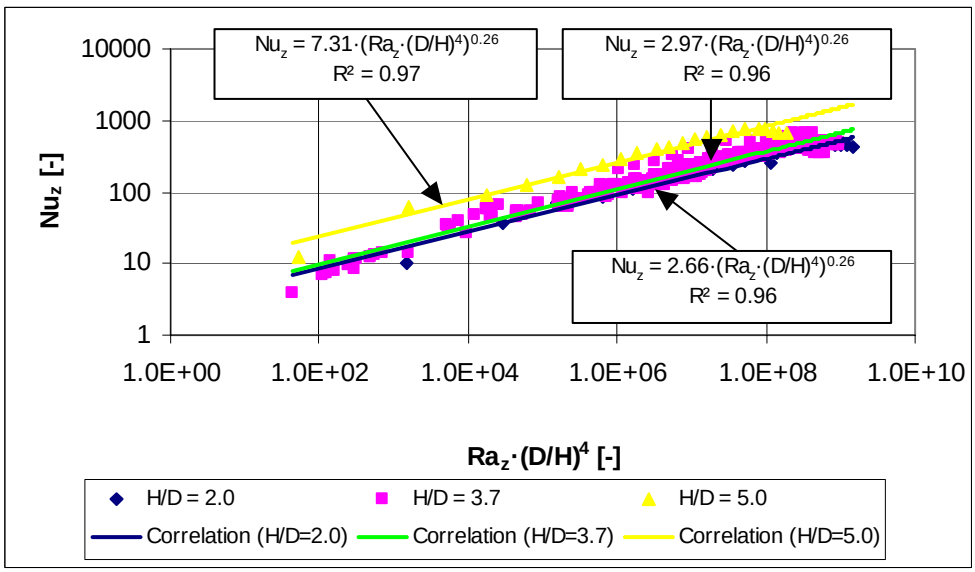

Figure 7-49: Local Nusselt number as a function of local Rayleigh number and as a function of H/D ratio for three different H/D ratios.

Figure 7-49 shows the local Nusselt number as a function of the local Rayleigh number multiplied by (diameter/height)^4 for three different height/diameter ratios. The H/D ratios of 2.0 and 5.0 are only calculated with the hot inlet condition. The points in the graph are the calculated values, whereas the lines are plotted from correlations given in the figure. The correlations are calculated by the least squared fit through the points using the equation $Nu_z=C_1\cdot(Ra_z\cdot(D/H)^4)^{C2}$, where C_1 and C_2 are constants.

From Figure 7-49 it appears that the constant C_1 differs for the different H/D ratios, whereas C_2, which is the slope of the correlation, is the same for the three H/D ratios. Therefore, a new correlation can be found on the following form:

$$Nu_z = f\left(H/D\right)\cdot\left(Ra_z\cdot(D/H)^4\right)^{0.26} \tag{7.20}$$

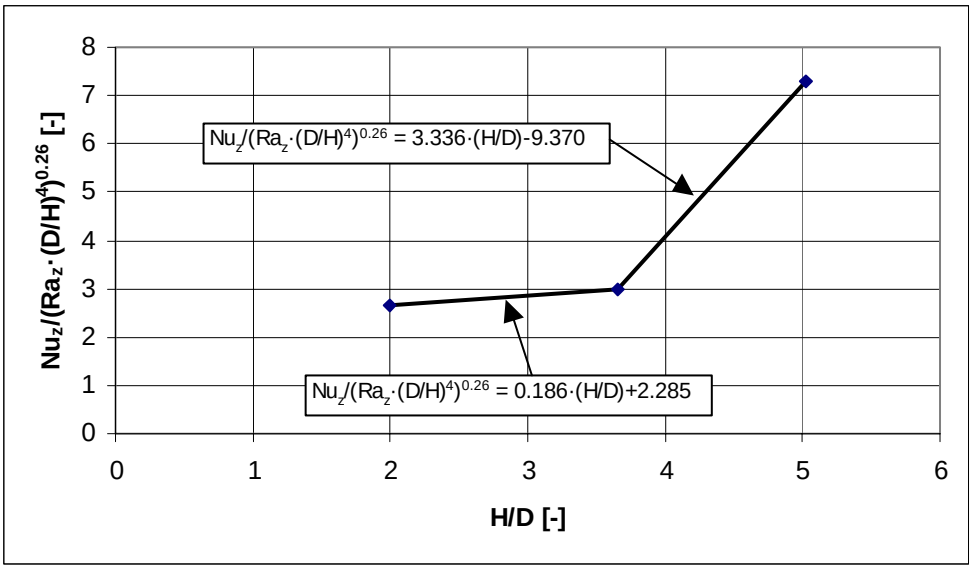

Figure 7-50: $Nu_z/(Ra_z\cdot(D/H)^4)^{0.26}$ as a function the H/D ratio.

Figure 7-50 shows $Nu_z/(Ra_z\cdot(D/H)^4)^{0.26}$ as a function of H/D and it is seen that f(H/D) becomes:

$$f(H/D)=0.186\cdot(H/D)+2.285 \quad \text{for } 2.0 \le H/D \le 3.7 \tag{7.21}$$

and

$$f(H/D)=3.336\cdot(H/D)-9.370 \quad \text{for } 3.7 \le H/D \le 5.0 \tag{7.22}$$

Thus, the final equations are given by:

$$Nu_z=\left(0.186\cdot\left(H/D\right)+2.285\right)\cdot\left(Ra_z\cdot(D/H)^4\right)^{0.26} \quad \text{for } 2.0 \le H/D \le 3.7 \tag{7.23}$$

$$Nu_z=\left(3.336\cdot\left(H/D\right)-9.370\right)\cdot\left(Ra_z\cdot(D/H)^4\right)^{0.26} \quad \text{for } 3.7 \le H/D \le 5.0 \tag{7.24}$$

Equation 7.23 and equation 7.24 are valid for $Ra_z < 10^{11}$.

7.5.1 Comparison of calculated heat flux at tank wall

The heat fluxes calculated by use of the correlations (equations 7.23 - 7.24) are compared to the heat fluxes calculated by CFD to make sure that the correlations behave as expected. If a good agreement is achieved, the correlations are suitable for calculating heat fluxes from the tank wall to the domestic water. Table 7-3 gives an overview of the comparisons.

Model	Tank volume [m³]	Inner tank height [m]	Inner diameter [m]	Inner mantle height [m]	Mantle gap [m]	Mantle flow rate [l/min]	Heat fluxes illustrated in:
Ref. tank Lower inlet	0.175	1.440	0.394	0.700	0.0335	0.4	Figure 7-51 – Figure 7-52
Top inlet	0.175	1.440	0.394	0.700	0.0335	0.4	Figure 7-53 – Figure 7-54
Ini. cold tank	0.175	1.440	0.394	0.700	0.0335	0.4	Figure 7-55
1” inlet	0.175	1.440	0.394	0.700	0.0335	0.4	Figure 7-56 – Figure 7-57
Small mantle gap	0.175	1.440	0.394	0.700	0.0105	0.4	Figure 7-58 – Figure 7-59
High flow rate	0.175	1.440	0.394	0.700	0.0335	0.8	Figure 7-60 – Figure 7-61
Stainless steel	0.175	1.440	0.394	0.700	0.0335	0.4	Figure 7-62 – Figure 7-63
40% Glycol	0.175	1.440	0.394	0.700	0.0335	0.4	Figure 7-64 – Figure 7-65
High mantle	0.175	1.440	0.394	1.440	0.0335	0.4	Figure 7-66 – Figure 7-67
Small H/D ratio	0.175	0.959	0.482	0.468	0.0335	0.4	Figure 7-68
Large H/D ratio	0.175	1.778	0.354	0.864	0.0335	0.4	Figure 7-69

Table 7-3: Overview of the comparisons of the heat fluxes from the tank wall to the domestic water in the tank.

Figure 7-51 – Figure 7-69 show heat fluxes from the tank wall to the domestic water calculated by CFD, with the correlations developed in this thesis (equations 7.23 - 7.24) and with the correlation (equation 2.24) developed by Shah (1999, 2000). The temperatures used in the correlations are extracted from the CFD results and all the results are presented after 40 minutes with either the hot or the warm inlet condition. It should be noted that equation 2.24, the correlation developed by Shah (1999, 2000) is developed for mantle heat exchangers with mantle inlet port located at the top of the mantle, and most of the mantle heat exchangers in this comparison have the mantle inlet port at a lower position.

The overall conclusions from the figures are that the correlations developed in this thesis give heat fluxes in good agreement with CFD for both hot and warm inlet conditions. However, in most of the cases the correlations under-predict the heat flux somewhat at 0.3-0.6 m and over-predict the heat flux somewhat at 0.6-0.8 m from the bottom of the tank for hot inlet condition. 0.6-0.8 m is at the level of the upper part of the mantle above the mantle inlet (for lower inlet position). It is seen that Shah’s correlation also give heat fluxes in good agreement with CFD for both hot and warm inlet condition.

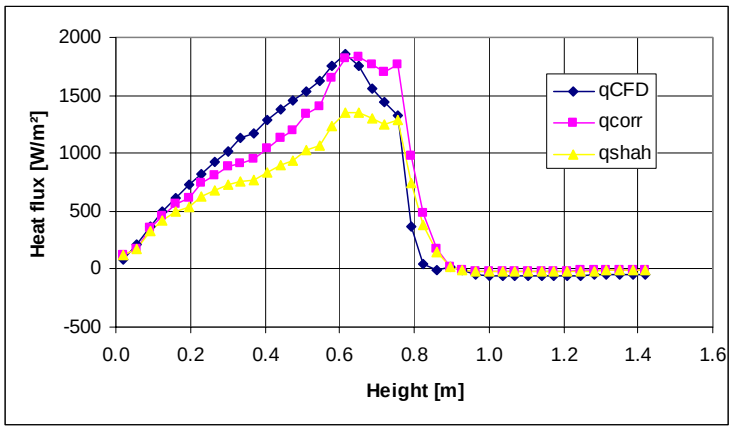

Figure 7-51: Lower inlet configuration (hot inlet condition): Comparison of heat flux from tank wall to domestic water in inner tank after 40 minutes predicted by CFD (qCFD), the correlations developed in this thesis (qcorr) and Shah's correlation (qshah), respectively.

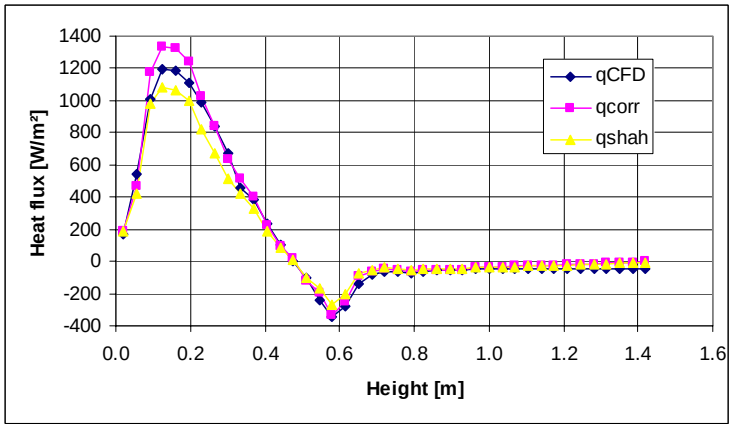

Figure 7-52: Lower inlet configuration (warm inlet condition): Comparison of heat flux from tank wall to domestic water in inner tank after 40 minutes predicted by CFD (qCFD), the correlations developed in this thesis (qcorr) and Shah's correlation (qshah), respectively.

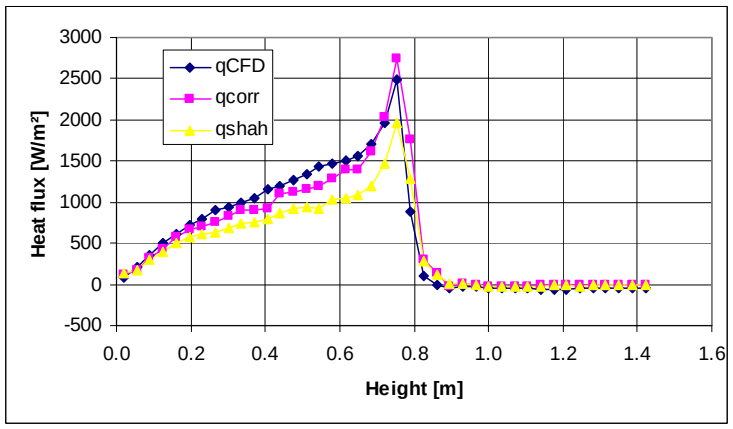

Figure 7-53: Top inlet configuration (hot inlet condition): Comparison of heat flux from tank wall to domestic water in inner tank after 40 minutes predicted by CFD (qCFD), the correlations developed in this thesis (qcorr) and Shah's correlation (qshah), respectively.

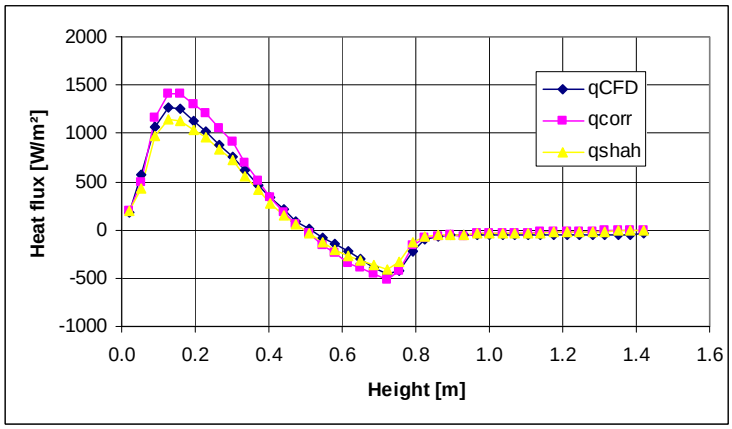

Figure 7-54: Top inlet configuration (warm inlet condition): Comparison of heat flux from tank wall to domestic water in inner tank after 40 minutes predicted by CFD (qCFD), the correlations developed in this thesis (qcorr) and Shah's correlation (qshah), respectively.

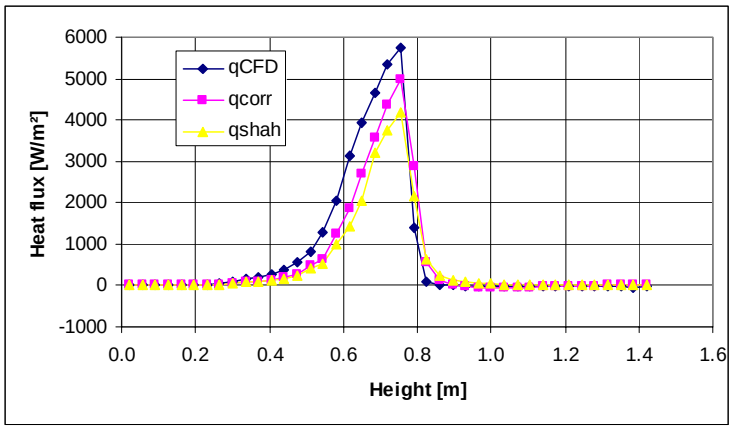

Figure 7-55: Initially cold tank (hot inlet condition): Comparison of heat flux from tank wall to domestic water in inner tank after 40 minutes predicted by CFD (qCFD), the correlations developed in this thesis (qcorr) and Shah's correlation (qshah), respectively.

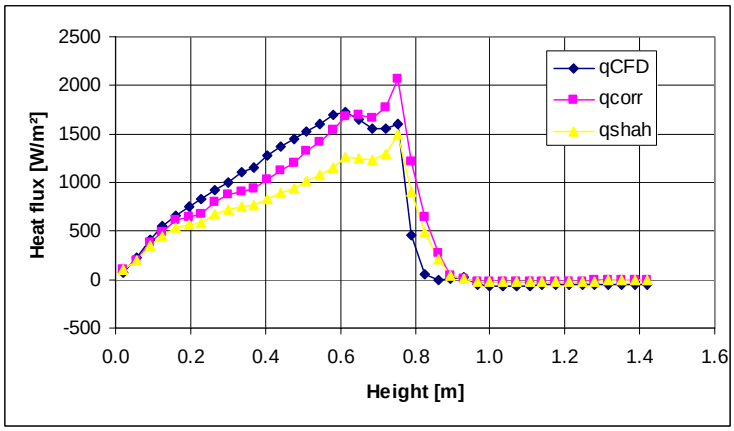

Figure 7-56: 1'' inlet configuration (hot inlet condition): Comparison of heat flux from tank wall to domestic water in inner tank after 40 minutes predicted by CFD (qCFD), the correlations developed in this thesis (qcorr) and Shah's correlation (qshah), respectively.

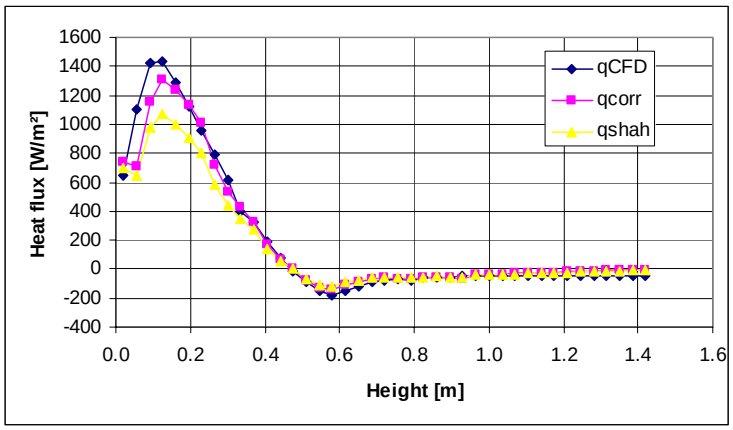

Figure 7-57: 1'' inlet configuration (warm inlet condition): Comparison of heat flux from tank wall to domestic water in inner tank after 40 minutes predicted by CFD (qCFD), the correlations developed in this thesis (qcorr) and Shah's correlation (qshah), respectively.

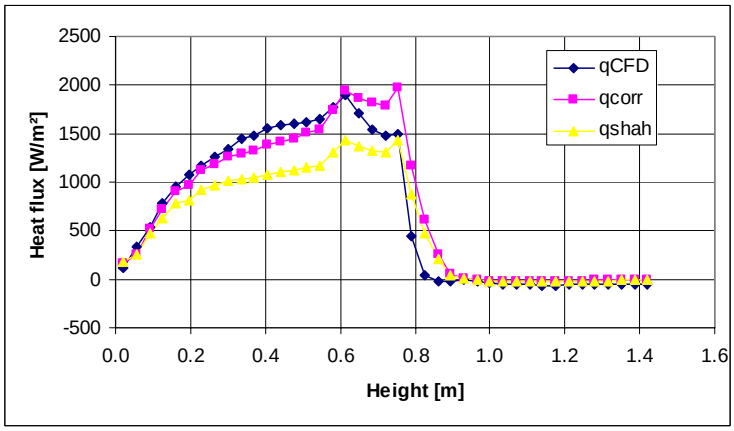

Figure 7-58: Small mantle gap configuration (hot inlet condition): Comparison of heat flux from tank wall to domestic water in inner tank after 40 minutes predicted by CFD (qCFD), the correlations developed in this thesis (qcorr) and Shah's correlation (qshah), respectively.

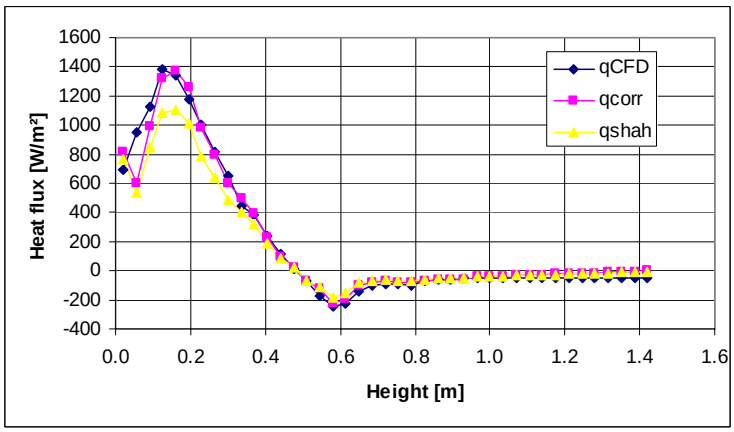

Figure 7-59: Small mantle gap configuration (warm inlet condition): Comparison of heat flux from tank wall to domestic water in inner tank after 40 minutes predicted by CFD (qCFD), the correlations developed in this thesis (qcorr) and Shah's correlation (qshah), respectively.

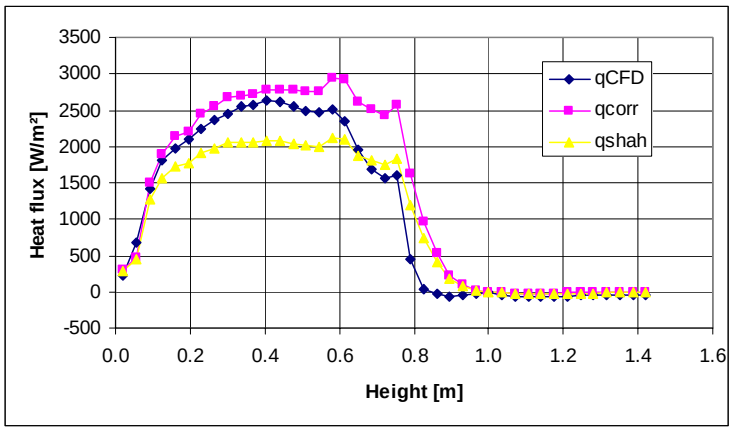

Figure 7-60: High flow rate (hot inlet condition): Comparison of heat flux from tank wall to domestic water in inner tank after 40 minutes predicted by CFD (qCFD), the correlations developed in this thesis (qcorr) and Shah's correlation (qshah), respectively.

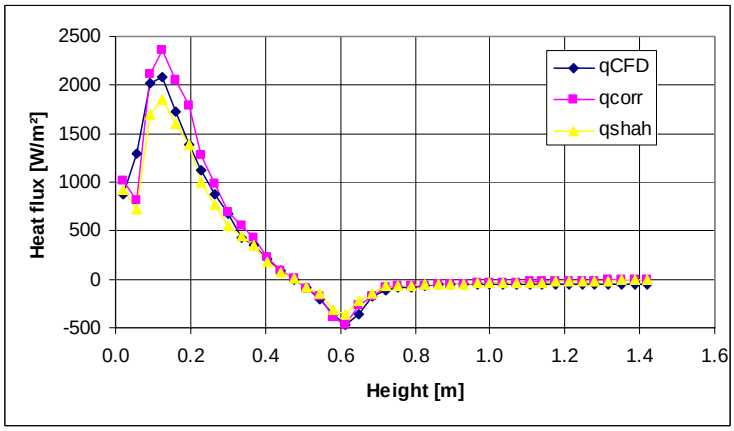

Figure 7-61: High flow rate (warm inlet condition): Comparison of heat flux from tank wall to domestic water in inner tank after 40 minutes predicted by CFD (qCFD), the correlations developed in this thesis (qcorr) and Shah's correlation (qshah), respectively.

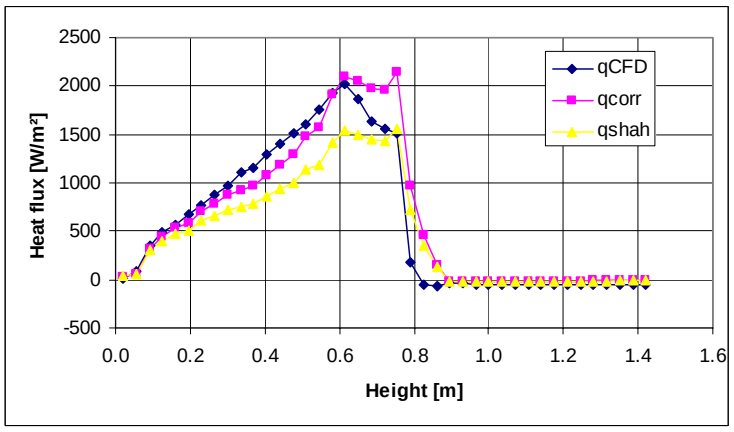

Figure 7-62: Stainless steel tank configuration (hot inlet condition): Comparison of heat flux from tank wall to domestic water in inner tank after 40 minutes predicted by CFD (qCFD), the correlations developed in this thesis (qcorr) and Shah's correlation (qshah), respectively.

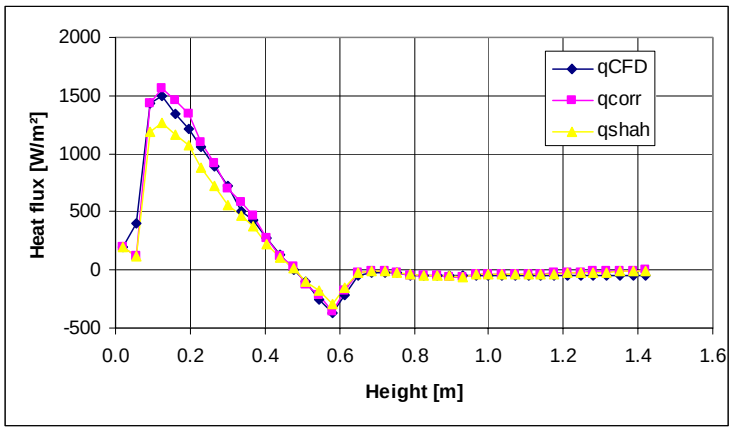

Figure 7-63: Stainless steel tank configuration (warm inlet condition): Comparison of heat flux from tank wall to domestic water in inner tank after 40 minutes predicted by CFD (qCFD), the correlations developed in this thesis (qcorr) and Shah's correlation (qshah), respectively.

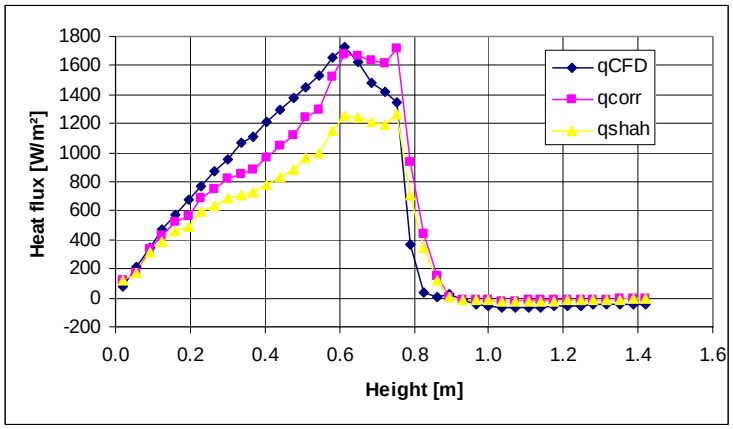

Figure 7-64: 40% Glycol (hot inlet condition): Comparison of heat flux from tank wall to domestic water in inner tank after 40 minutes predicted by CFD (qCFD), the correlations developed in this thesis (qcorr) and Shah's correlation (qshah), respectively.

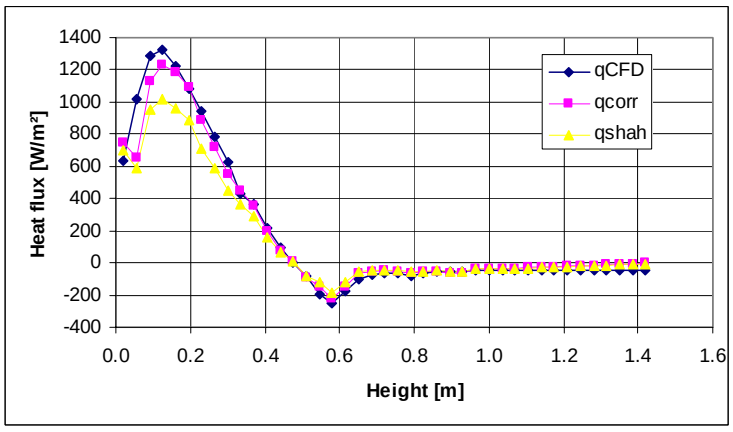

Figure 7-65: 40% Glycol (warm inlet condition): Comparison of heat flux from tank wall to domestic water in inner tank after 40 minutes predicted by CFD (qCFD), the correlations developed in this thesis (qcorr) and Shah's correlation (qshah), respectively.

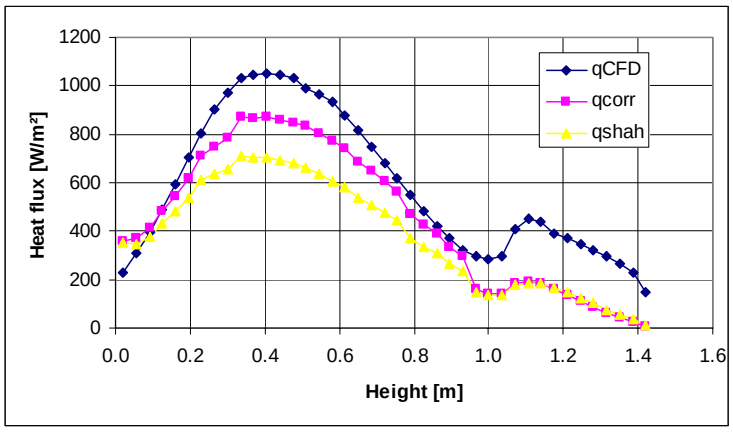

Figure 7-66: High mantle configuration (hot inlet condition): Comparison of heat flux from tank wall to domestic water in inner tank after 40 minutes predicted by CFD (qCFD), the correlations developed in this thesis (qcorr) and Shah's correlation (qshah), respectively.

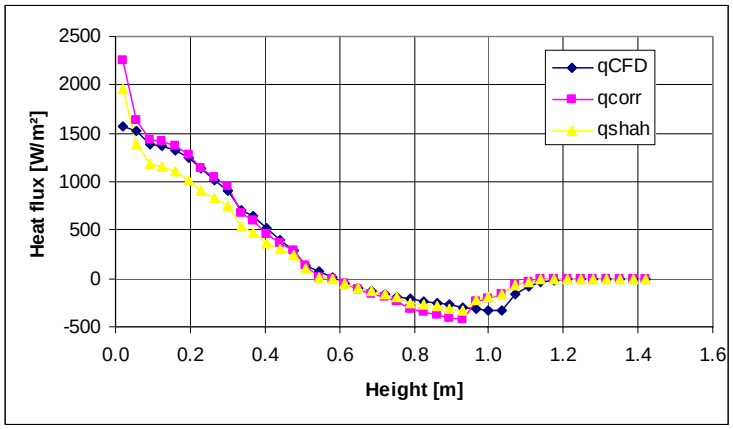

Figure 7-67: High mantle configuration (warm inlet condition): Comparison of heat flux from tank wall to domestic water in inner tank after 40 minutes predicted by CFD (qCFD), the correlations developed in this thesis (qcorr) and Shah's correlation (qshah), respectively.

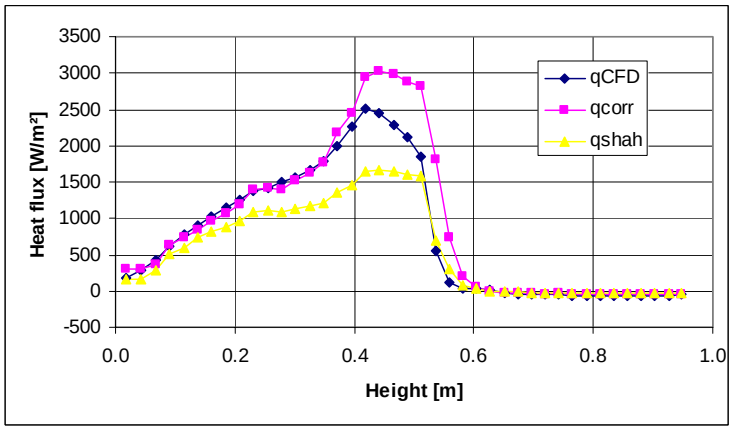

Figure 7-68: Small H/D ratio tank configuration (hot inlet condition): Comparison of heat flux from tank wall to domestic water in inner tank after 40 minutes predicted by CFD (qCFD), the correlations developed in this thesis (qcorr) and Shah's correlation (qshah), respectively.

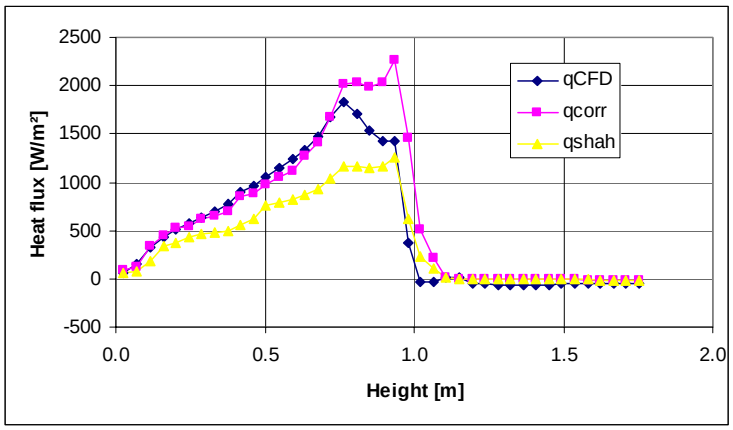

Figure 7-69: Large H/D ratio tank configuration (hot inlet condition): Comparison of heat flux from tank wall to domestic water in inner tank after 40 minutes predicted by CFD (qCFD), the correlations developed in this thesis (qcorr) and Shah's correlation (qshah), respectively.

7.6 Heat transfer from fluid to top and bottom walls

In contrast to the previous heat transfer cases in section 7.3 - 7.5, the convection heat transfer at the mantle and tank top and bottom walls is modelled by a correlation found in the literature. Figure 7-70 illustrates the heat flux from fluid to top and bottom walls. McAdams (1954) recommends:

$$Nu_L = 0.54 \cdot Ra_L^{1/4} \quad \text{for } 10^5 < Ra_L < 2 \cdot 10^7 \tag{7.25}$$

and

$$Nu_L = 0.14 \cdot Ra_L^{1/3} \quad \text{for } 2 \cdot 10^7 < Ra_L < 3 \cdot 10^{10} \tag{7.26}$$

For the top and bottom of the inner tank, L is the inner diameter. For the top and bottom of the mantle gap, L is the gap width.

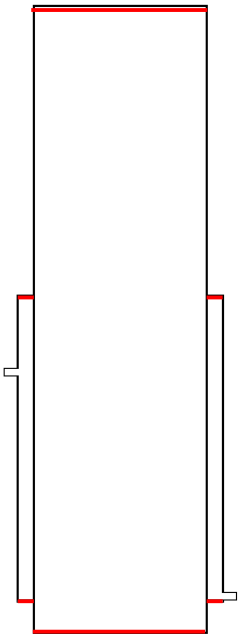

Figure 7-70: Heat flux at top and bottom walls.

7.7 Model for prediction of natural convection flows in tank

In chapter 6 it was revealed that the flow structure inside the inner tank helps to heat up the part of the tank situated above the mantle and then increase the degree of stratification although there might be a negative heat flux at the tank wall above the mantle. Figure 7-71a shows the initial temperature profile and the temperature profiles after 40 minutes of the water in the tank for the initially mixed case, and Figure 7-71b shows the heat flux profile at the tank wall after 40 minutes for the same case. The

effect of the heat flow inside the inner tank is clear from Figure 7-71; there is a negative heat flux at the tank wall above the mantle and the temperature of the domestic water has increased over the period of 40 minutes. Furthermore, the temperatures in the top of the tank have had the largest increase.

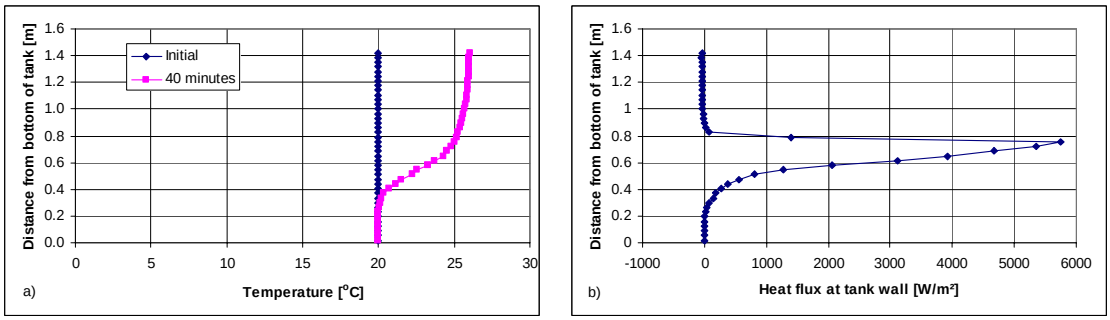

Figure 7-71: Initially mixed case with mantle inlet temperature of 70ºC: a) inner tank temperatures (Initial and after 40 minutes), b) Heat flux from tank wall to water in inner tank after 40 minutes.

Heat transfer correlations for the mantle walls and for the tank wall were developed in section 7-3 – 7-6. In this section a model to predict the heat flows in the inner tank will be developed in order to be able to make a better prediction of the thermal stratification in the tank.

7.7.1 Method of analysis

The heat flow in the inner tank was investigated at 5 levels (three levels at mantle level and at two levels above the mantle). The 5 levels are shown in Figure 7-72. The horizontal grid in the inner tank is shown in Figure 7-73. At each of the five levels the area, the vertical velocity and the temperature of the horizontal faces in the grid were written to a file, and the heat flow at each level was calculated by the equation below:

$$Q_{\text{heat flow,z}} = \rho(T_z) \cdot c_p(T_z) \cdot \sum_{i=1}^{n} A_{i,z} \cdot |v_{i,z}| \cdot (T_{i,z} - T_z) \qquad (7.27)$$

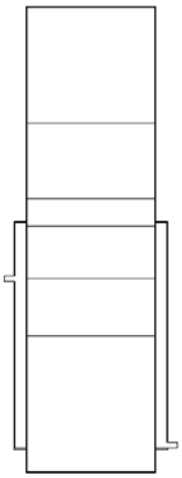

Figure 7-72: The five levels in the inner tank where the heat flow is calculated.

where

$A_{i,z}$	is the area of face number 'i' on the horizontal slice at level z, [z]
c_p	is specific heat capacity of water, [J/kg·K]
n	is the total number of faces on the horizontal slice at level z, [-]
$Q_{\text{heat flow,z}}$	is the heat flow at level z, [W]
$T_{i,z}$	is the temperature of face number 'i' at level z, [K]
T_z	is the average temperature at level z (as calculated by eq. 6.2), [K]

$v_{i,z}$ is the vertical velocity at face number 'i' at level z, [m/s]
z is the distance from bottom of tank, [m]
ρ is the density of water, [kg/m³]

If the temperature difference of $T_{i,z}$ and T_z in equation 7.27 is positive then the heat flow is upward and if the temperature difference is negative then the heat flow is downward. $Q_{heat\ flow,z}$ is the net heat flow at level z.

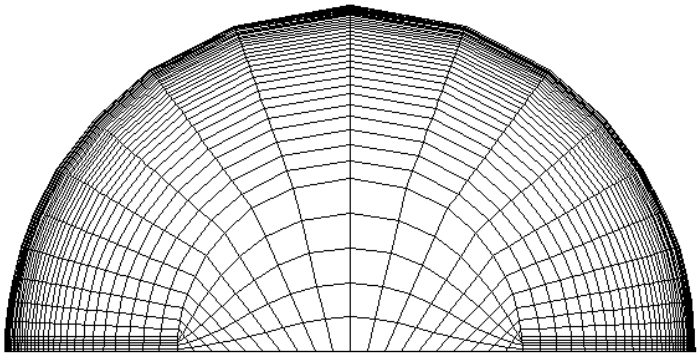

Figure 7-73: The horizontal grid. A face is the white area between four grid points.

The tank wall is divided into 40 small horizontal pieces as shown in Figure 7-74. The sum of the heat transfer at the tank wall (from bottom of tank up to a given level z) is given by:

$$Q_{tank\ wall,z} = \sum_{j=1}^{n} q_j \cdot A_j \qquad (7.28)$$

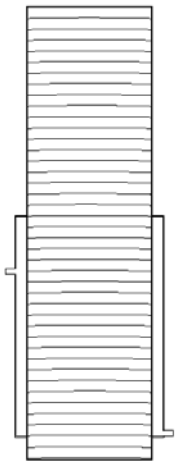

Figure 7-74: The tank wall is divided into 40 small pieces for the analysis of heat transfer

where

A_j is the area of the piece of the tank wall at level 'j', [m²]
q_j is the local heat flux at the tank wall at level 'j', [W/m²]
$Q_{tank\ wall,z}$ is the sum of heat transfer at tank wall up to level z, [W]
n is the number of layers up to level z, [m]

The part of the heat transfer at the wall that flows up in the tank due to the upward flow near the walls is given by:

$$\eta_z = \frac{Q_{\text{heat flow,z}}}{Q_{\text{tank wall,z}}} = \frac{Q_{\text{heat flow,model}}}{Q_{\text{tank wall,z}}} \tag{7.29}$$

where

$Q_{\text{heat flow,model}}$ is the heat flow in the water calculated by the model at level z, [W]

η_z is the part of the heat transfer at the tank wall at level z that flows up in the tank, [-]

The thermal stratification of the domestic water at level z in the tank is given by:

$$Str_j = \frac{T_{j+1} - T_{j-1}}{z_{j+1} - z_{j-1}} \tag{7.30}$$

where

Str_j is the thermal stratification at level 'j', [K/m]

T is the temperature (at level 'j+1' and 'j-1'), [K]

z is the distance from the bottom of tank (at level 'j+1' and 'j-1'), [m]

The resulting heat transfer that heats the domestic water at each level of the tank is then calculated by:

$$Q_{z,\text{model}} = Q_{\text{tank wall,z}} - Q_{\text{heat flow,model}} - \sum_{j=1}^{z-1} Q_{j,\text{model}} \tag{7.31}$$

where

$Q_{z,\text{model}}$ is the net heat transfer to the domestic water at level z , [W]

The resulting heat transfer (after 40 minutes) to the domestic water at each level in the tank calculated by CFD is calculated by:

$$Q_{z,\text{CFD}} = \frac{V_z \cdot \rho \cdot c_p \cdot \left(T_{\text{end,z}} - T_{\text{start,z}}\right)}{\Delta t} \tag{7.32}$$

where

$Q_{z,\text{CFD}}$ is the net heat transfer to the domestic water at level z calculated by CFD, [W]

$T_{\text{end,z}}$ is the average temperature at the end of the time interval Δt, [W]

$T_{\text{start,z}}$ is the average temperature at the beginning of the time interval Δt, [W]

V_z is the total volume of the layer at level z, [m³]

Δt is the time interval (here: Δt = 1 second), [s]

Figure 7-75 shows the sum of heat transfer at tank wall, $Q_{\text{tank wall,z}}$, and the heat flow in water, $Q_{\text{heat flow,z}}$, after 40 minutes as a function of the distance from the bottom of the

tank for the ’Lower inlet’-case where the tank is initially stratified and for the hot inlet condition. Figure 7-76 shows the sum of heat transfer at tank wall and the heat flow in water after 40 minutes as a function of the distance from the bottom of the tank for the ’Ini. cold tank’-case where the tank is initially mixed. It is seen that when the tank is stratified the heat flow in the water is relatively small, and when the tank is initially mixed then the heat flow in the water is relatively large. Thus, a high degree of stratification tends to stop the heat flow in the water. It is also seen that the heat transfer at the tank wall is rather different in the two cases. The slope of the curve shows that in the initially mixed case there is a major heat transfer at 0.4 m to 0.8 m from the bottom while the heat transfer in the initially stratified case is more evenly distributed from the bottom up to 0.8 m from the bottom. Based on Figure 7-75 and Figure 7-76 it is reasonable to expect that the heat flow in the water somehow depends on the heat flux at the tank wall and on the degree of stratification of the water. The heat flux conditions are very different at the level of the mantle and above the mantle. Therefore the results will be split up, and two correlations will be found: one for the level of the mantle and one for the part above the mantle.

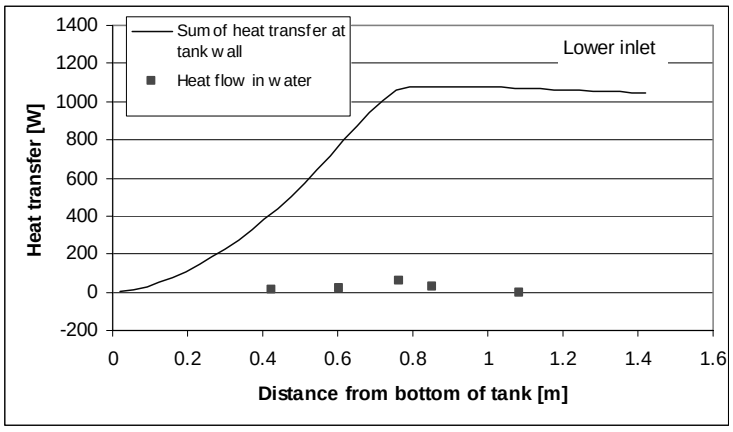

Figure 7-75: The sum of heat transfer at tank wall and heat flow in water as a function of the distance from bottom of tank after 40 minutes for the ‘Lower inlet’ case with hot inlet condition.

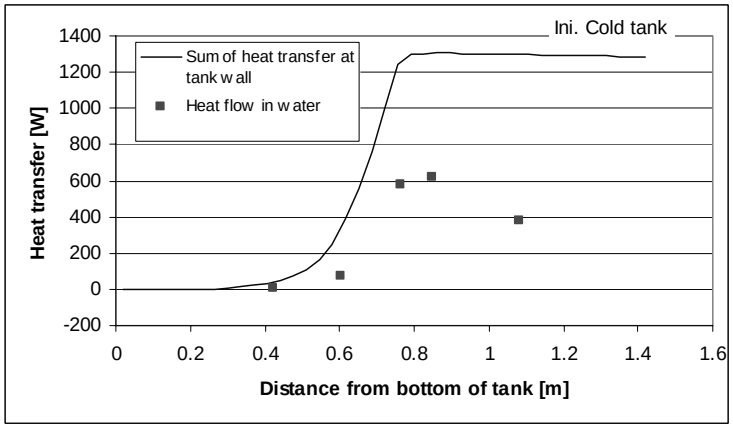

Figure 7-76: The sum of heat transfer at tank wall and heat flow in water as a function of the distance from bottom of tank after 40 minutes for the ‘Ini. cold tank’ case with hot inlet condition.

The aim is to find correlations where η_z can be calculated as a function of known parameters such as heat flux at tank wall and thermal stratification of the water. Then, it is possible to calculate the heat flow in the water, $Q_{heat\ flow,model}$, with equation 7.29 and the net heat transfer, $Q_{z,model}$, at each level by equation 7.31.

Two additional CFD-calculations were carried out for the development of the correlations for the heat flow in the water. The cases of the small H/D-ratio and the large H/D-ratio (see Table 6-3) were simulated with initially mixed tanks (20ºC) and with the hot inlet condition of an inlet temperature of 70ºC. This was done to make the correlation more general by having different H/D-ratios at a low degree of stratification.

7.7.2 Heat flow model at the level of the mantle

To correlate the data concerning the heat flow in tank caused by the heat transfer at the tank wall at the level of the mantle, η_z is plotted as a function of the local heat flux at the tank wall and as a function of the thermal stratification of the domestic water in the tank:

$$\eta_z = f\left(q_z, Str_z\right) \tag{7.33}$$

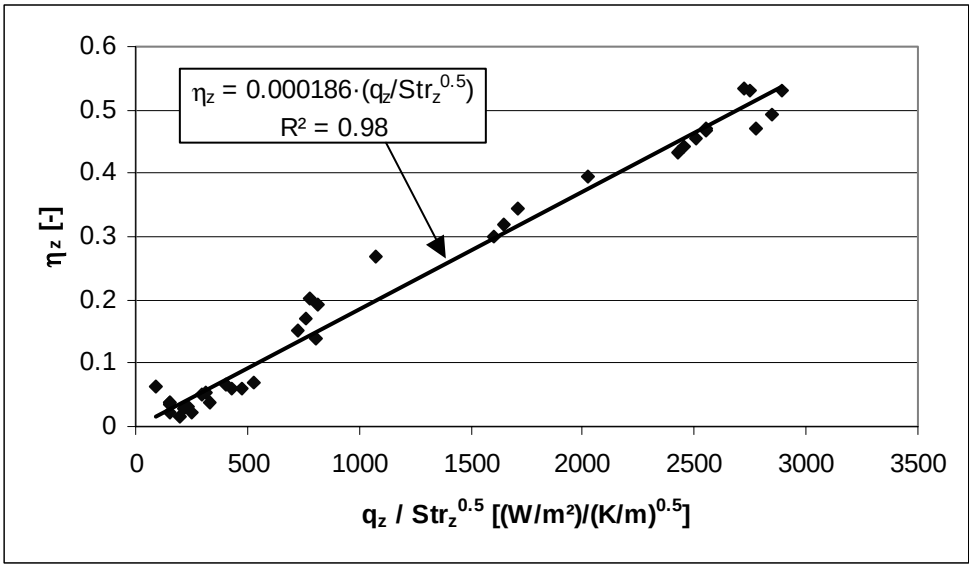

Figure 7-77: η_z as a function of the local heat flux at the tank wall and the thermal stratification of the domestic water in the tank for the different mantle tank designs and operation conditions.

Figure 7-77 shows η_z as a function of the local heat flux at the tank wall and the thermal stratification of the domestic water in the tank for the different mantle tank designs and operation conditions. The points in Figure 7-77 are the calculated values whereas the lines are plotted from the correlation given in the figure. The correlation is calculated by the least squared fit through the points using the equation $\eta_z = C \cdot (q_z / Str_z^{0.5})$ where C is a constant. The usage of the relationship $q_z/Str_z^{0.5}$ gave the highest R^2-value. It appears

from Figure 7-77 that C = 0.000186 and the equation for determination of the heat flow in the tank at the level of the mantle becomes:

$$\eta_z = 0.000186 \cdot \frac{q_z}{Str_z^{0.5}} \quad \text{for} \quad \frac{q_z}{Str_z^{0.5}} < 2900 \ \frac{W/m^2}{(K/m)^{0.5}} \tag{7.34}$$

$$\eta_z = 0.539 \quad \text{for} \quad \frac{q_z}{Str_z^{0.5}} > 2900 \ \frac{W/m^2}{(K/m)^{0.5}} \tag{7.35}$$

The above equations are very sensitive to small values of Str_z, therefore the equations above are developed by setting Str_z = 4 K/m if Str_z < 4 K/m. η_z = 0 for $(q_z/Str_z^{0.5})$ < 0. The local heat flow at the level of the mantle, $Q_{heat\ flow,model}$, based on the model can now be calculated by equations 7.29, 7.34 and 7.35.

7.7.3 Heat flow model for the part above the mantle

To correlate the data concerning the heat flow in the tank above, the mantle caused by the heat transfer at the tank wall, η_z is plotted as a function of the temperature difference between the tank wall and the domestic water, as a function of the thermal stratification of the domestic water in the tank, and as a function of the radius of the tank:

$$\eta_z = f\left(T_{wall,z} - T_{water,z}, Str_z, r\right) \tag{7.36}$$

where

r is the inner radius of the tank, [m]

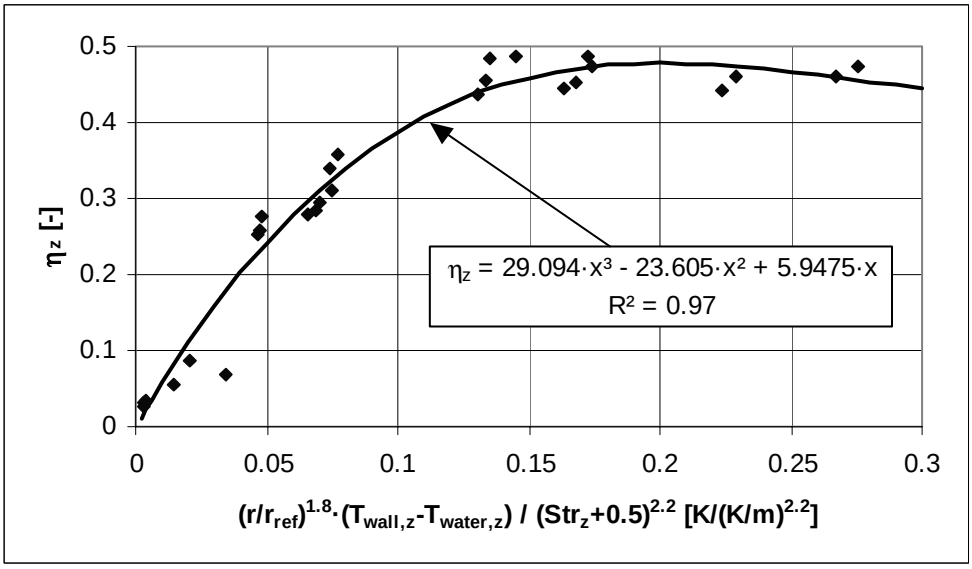

Figure 7-78: η_z as a function of the temperature difference between the tank wall and the domestic water, the thermal stratification of the domestic water and the radius of the tank for the different mantle tank designs and operation condition.

Figure 7-78 shows η_z as a function of the temperature difference between the tank wall and the domestic water, the thermal stratification of the domestic water in the tank and the radius of the tank for the different mantle tank designs and operation conditions. The points in Figure 7-78 are the calculated values whereas the lines are plotted from the correlation given in the figure. The correlation is calculated by the least squared fit through the points using the equation $\eta_z=C_1 \cdot x^3+C_2 \cdot x^2+C_3 \cdot x$ where C_1-C_3 are constants. It appears from Figure 7-78 that C_1 = 29.094, C_2 = -23.605 and C_3 = 5.9475, and the equations for determination of the heat flow in the tank above the level of the mantle become:

$$\eta_z = 29.094 \cdot x^3 - 23.605 \cdot x^2 + 5.9475 \cdot x \quad \text{for } x < 0.3 \tag{7.37}$$

$$\eta_z = 0.445 \quad \text{for } x > 0.3 \tag{7.38}$$

where

$$x = \frac{\left(\frac{r}{r_{ref}}\right)^{1.8} \cdot \left(T_{wall,z} - T_{water,z}\right)}{\left(Str_z + 0.5\right)^{2.2}} \tag{7.39}$$

The above equations are very sensitive to small values of Str_z, therefore the equations above are developed by setting Str_z = 4 K/m if Str_z < 4 K/m. η_z = 0 for x < 0. r_{ref}=0.197 m. The local heat flow above the mantle, $Q_{heat\ flow,model}$, based on the model can now be calculated by equations 7.29, 7.37 and 7.38.

The usage of x, as defined in equation 7.39, and that η_z depend on x as a polynomium of 3rd degree gave the highest R^2-value. The correction of the temperature difference between the tank wall and the domestic water by the factor $(r/r_{ref})^{1.8}$ was introduced because $T_{wall,z}$ is the average temperature of the water at level z. For different radii of the tank there is a relatively large difference in how the boundary layer near the tank wall influences the average temperature, and therefore the factor $(r/r_{ref})^{1.8}$ was introduced.

7.7.4 Summary of heat flow model

The heat flow model was developed in the previous sections and two correlations were found. One correlation to predict the heat flow at the level of the mantle, and one correlation to predict the heat flow above the mantle. The heat flow at the level of the mantle was found to depend on the local heat flux at the tank wall and the thermal stratification of the domestic water in the tank. The heat flow above the mantle was found to depend on the temperature difference between the tank wall and the domestic water, the thermal stratification of the domestic water and the radius of the tank.

The heat flow predicted by the model (equations 7.34, 7.35, 7.37 and 7.38) is compared with the heat flow calculated by CFD (equation 7.27). Furthermore, the resulting heat transfer to each layer in the tank predicted by the model (equation 7.31) and calculated

by CFD (equation 7.32) is compared. The comparisons are made for the following cases: Lower inlet for both hot and warm inlet condition, Ini. cold tank and then both the small H/D ratio and the large H/D ratio with initially mixed tanks (20ºC).

Figure 7-79 - Figure 7-83 show the comparison of the heat flow calculated by the model with the heat flow calculated by CFD for the 5 different cases. Besides the heat flow, the sum of heat transfer at the tank wall, $Q_{tank\ wall,z}$, is also shown in Figure 7-79 to Figure 7-83. It is seen that the heat flow model predicts the heat flow quite well.

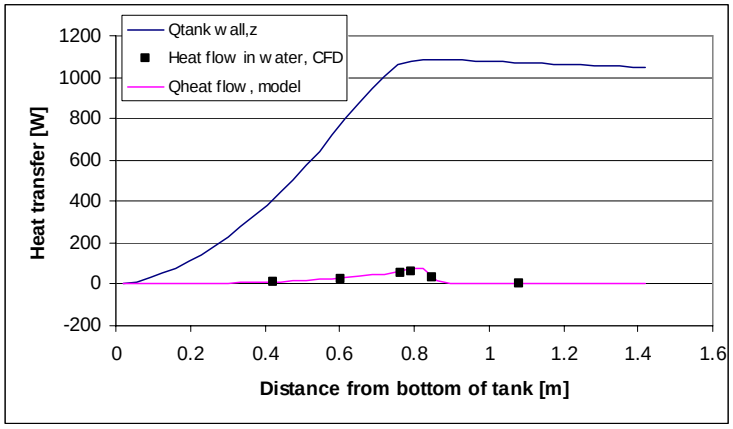

Figure 7-79: Lower inlet case (hot inlet condition): Comparison of heat flow after 40 minutes calculated by CFD and by the model developed in this thesis. The sum of the heat transfer at the tank wall calculated by CFD is also shown.

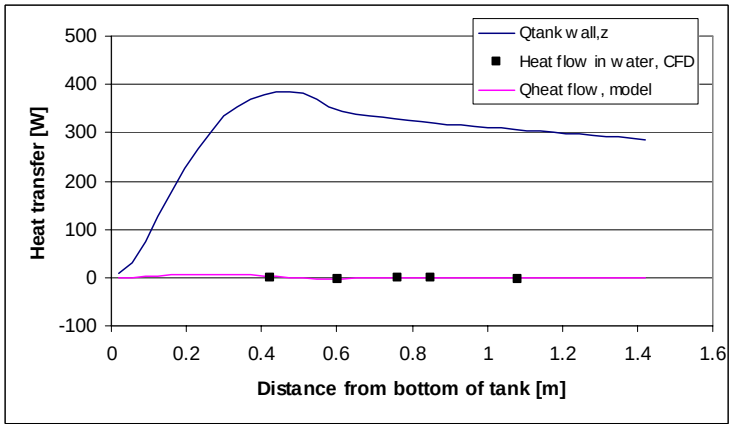

Figure 7-80: Lower inlet case (warm inlet condition): Comparison of heat flow after 40 minutes calculated by CFD and by the model developed in this thesis. The sum of the heat transfer at the tank wall calculated by CFD is also shown.

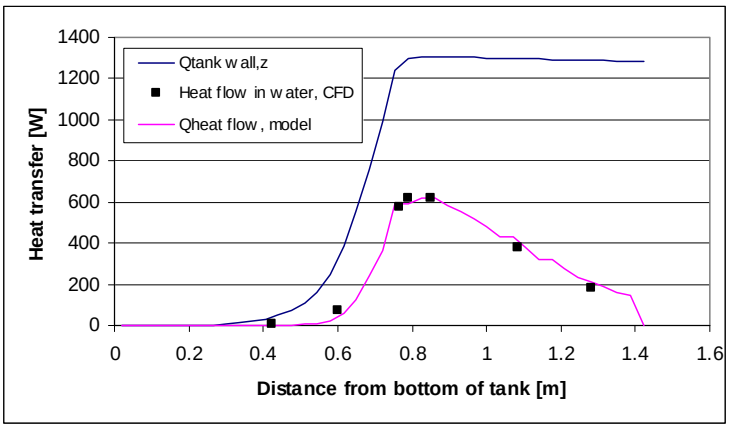

Figure 7-81: Initially cold tank case (hot inlet condition): Comparison of heat flow after 40 minutes calculated by CFD and by the model developed in this thesis. The sum of the heat transfer at the tank wall calculated by CFD is also shown.

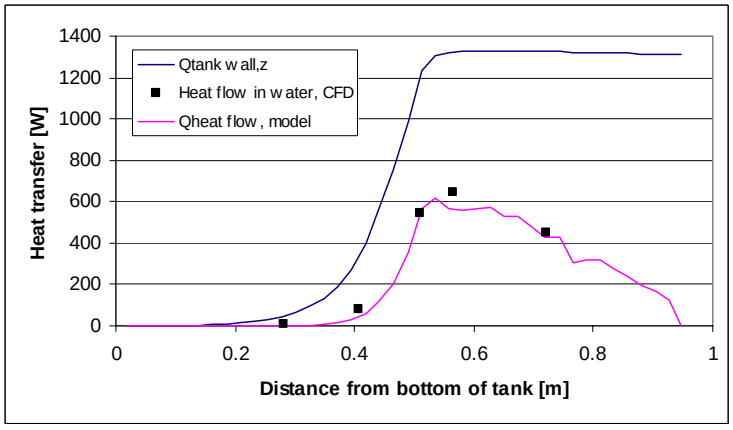

Figure 7-82: Small H/D ratio (hot inlet condition): Comparison of heat flow after 40 minutes calculated by CFD and by the model developed in this thesis. The sum of the heat transfer at the tank wall calculated by CFD is also shown.

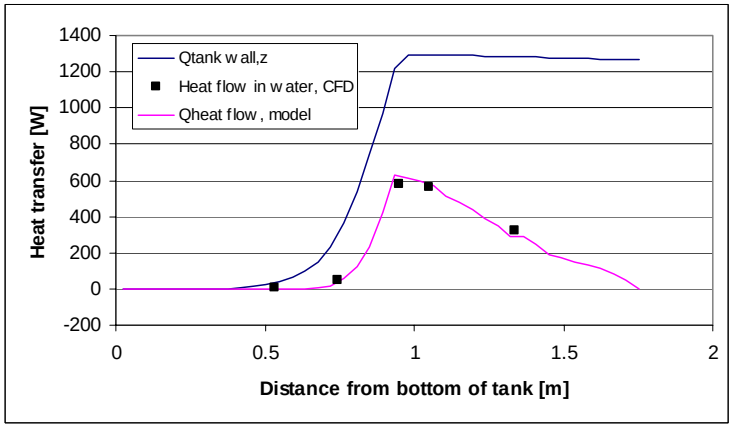

Figure 7-83: Large H/D ratio (hot inlet condition): Comparison of heat flow after 40 minutes calculated by CFD and by the model developed in this thesis. The sum of the heat transfer at the tank wall calculated by CFD is also shown.

Figure 7-84 – Figure 7-88 show the comparison of the resulting heat transfer to each layer in the tank predicted by the model and calculated by CFD ($Q_{z,model}$ and $Q_{z,CFD}$). The heat flow, $Q_{heat\ flow,model}$, calculated by the model is also shown in the figures as well as the heat flux at the wall calculated by CFD ($Q_{z,wall}$), that would have been the resulting heat transfer to each layer if the heat flow model was not introduced. In the cases with initially mixed tank (Figure 7-86 to Figure 7-88) it is seen that the resulting heat transfer predicted by the model is over-predicting at the level of the upper part of the mantle and under-predicting at some levels above the mantle. It is worth noting that with the heat flow model a considerable part of the heat transfer is supplied at the layers above the mantle, that is not the case if the heat transfer at the tank wall were used as resulting heat transfer. There is good agreement between $Q_{z,model}$ and $Q_{z,CFD}$ for the initially stratified case with warm inlet condition (Figure 7-85) where the heat flow is almost non-existing. The resulting heat transfer is for the initially stratified case with hot inlet condition (Figure 7-84) under-predicted by the model at around 0.8 m from the bottom and over-predicted at around 0.9 m from the bottom. The over-prediction is mainly due to the very high $Q_{heat\ flow,\ model}$ at 0.8 m. There is an overall good agreement between the resulting heat transfer predicted by the model and the resulting heat transfer calculated by CFD in the five cases, and the model has a better agreement than if the heat transfer at the tank wall were used as the resulting heat transfer.

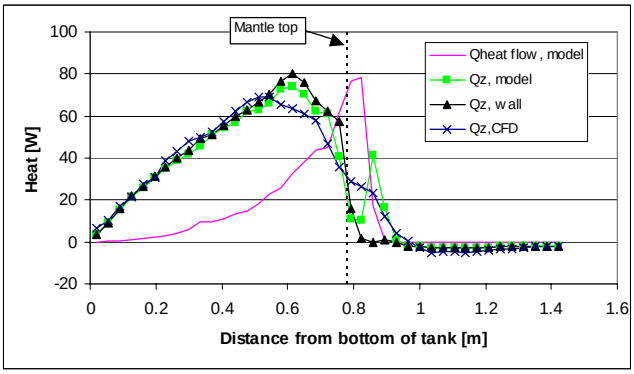

Figure 7-84: Lower inlet case (hot inlet condition): Comparison of the resulting heat transfer to each layer in the tank after 40 minutes predicted by CFD (Qz,CFD) and by the model (Qz,model). The heat flow calculated by the model and the heat transfer at the tank wall (Qz,wall) are also shown.

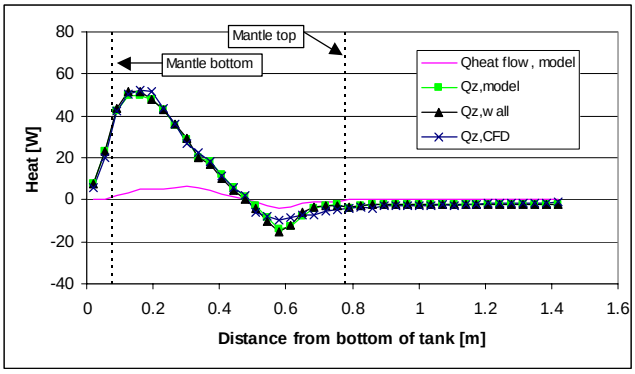

Figure 7-85: Lower inlet (warm inlet condition): Comparison of the resulting heat transfer to each layer in the tank after 40 minutes predicted by CFD (Qz,CFD) and by the model (Qz,model). The heat flow calculated by the model and the heat transfer at the tank wall (Qz,wall) are also shown.

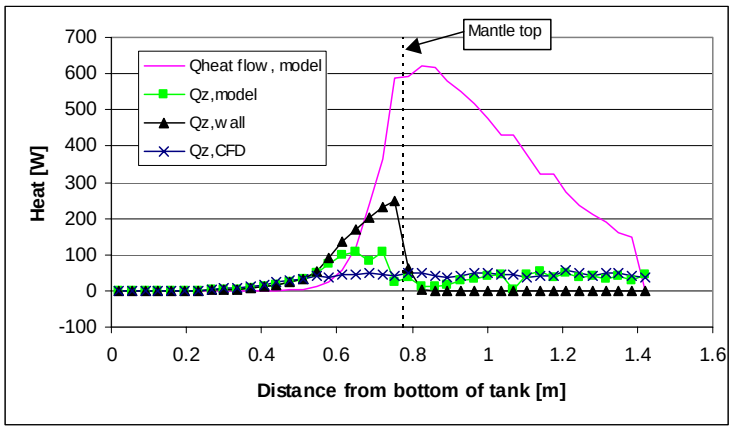

Figure 7-86: Ini. cold tank (hot inlet condition): Comparison of the resulting heat transfer to each layer in the tank after 40 minutes predicted by CFD (Qz,CFD) and by the model (Qz,model). The heat flow calculated by the model and the heat transfer at the tank wall (Qz,wall) are also shown.

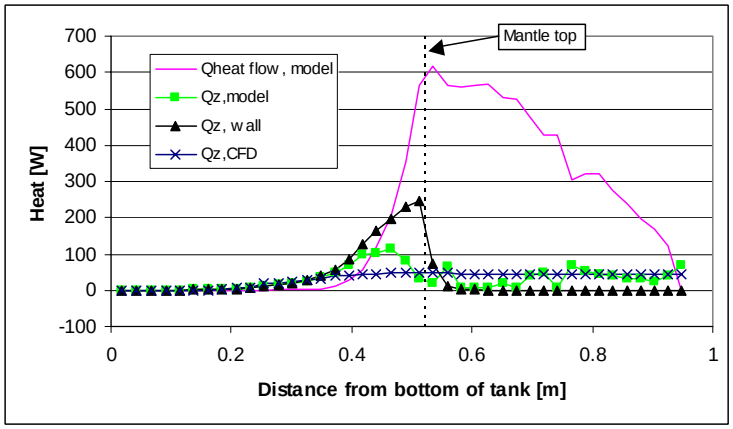

Figure 7-87: Small H/D ratio (hot inlet condition): Comparison of the resulting heat transfer to each layer in the tank after 40 minutes predicted by CFD (Qz,CFD) and by the model (Qz,model). The heat flow calculated by the model and the heat transfer at the tank wall (Qz,wall) are also shown.

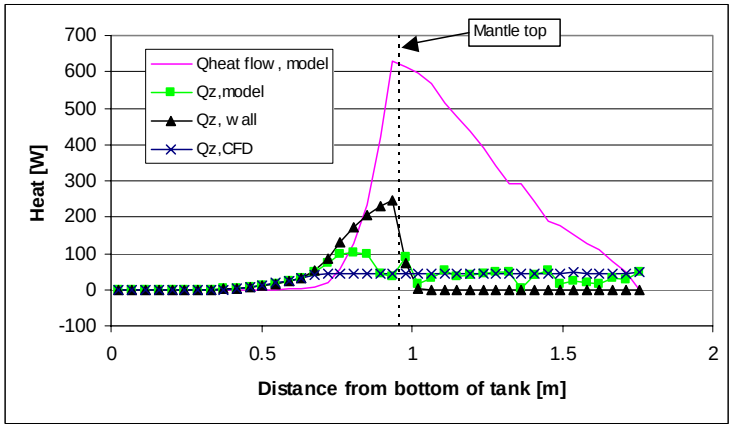

Figure 7-88: Large H/D ratio (hot inlet condition): Comparison of the resulting heat transfer to each layer in the tank after 40 minutes predicted by CFD (Qz,CFD) and by the model (Qz,model). The heat flow calculated by the model and the heat transfer at the tank wall (Qz,wall) are also shown.

7.8 Summary

In this chapter dimensionless heat transfer theory was applied to generalise the results from chapter 6. It was revealed that the heat transfer from the mantle fluid to the inner and outer mantle wall, respectively, was in the mixed convection regime near the mantle inlet. Three heat transfer correlations were developed to describe the heat transfer from the mantle fluid to the inner mantle wall, and three other heat transfer correlations were developed to describe the heat transfer from the mantle fluid to the outer mantle wall. Furthermore, a heat transfer correlation was developed to describe the heat transfer from the tank wall to the domestic water in the inner tank. All the correlations were developed from CFD-results including different mantle tank designs and different operation conditions.

The heat fluxes calculated by the correlations were compared with heat fluxes calculated by CFD, and good agreement was achieved. However, some small inaccuracies were observed. The heat fluxes at the inner mantle wall near the mantle inlet were over-predicted by the correlations for hot inlet condition in some cases. For hot inlet condition, in some cases, the heat fluxes at the tank wall were under-predicted by the correlation at the level just below the mantle inlet and over-predicted at the level just above the mantle inlet.

Two correlations to calculate the natural convection flow inside the inner tank were developed. The two correlations were developed from CFD-results including different mantle tank designs and operation conditions. The heat flows calculated by the correlations were compared with heat flows calculated by CFD and good agreement was achieved.

It should be noted that the correlations developed in this chapter are based on the chosen typical operation conditions and mantle tank designs, and other typical operation conditions and mantle tank designs may result in correlations that are slightly different.

In the next chapter the correlations describing the heat transfer at the walls and the natural convection flows in the inner tank will be implemented into a numerical mantle tank model for simulation of small low-flow SDHW systems with mantle tanks as heat storage.

8. SDHW simulation model

8.1 Introduction

In the previous chapter heat transfer correlations for the heat transfer between the mantle fluid and the inner and outer mantle wall as well as heat transfer correlations for the heat transfer between the tank wall and the domestic water in the tank were developed. Furthermore, correlations describing the natural convection flow in the inner tank were developed.

In this chapter a short introduction to the SDHW simulation program will be given before it is explained how the correlations are implemented in MantlSim and how MantlSim is developed to include the possibility to place the mantle inlet at different levels of the mantle. Finally, the new version of MantlSim is validated against measurement of low-flow SDHW systems; one system with the mantle inlet located at the top of the mantle and one system with the mantle inlet moved down.

8.2 Numerical model

As mentioned in section 3.6, MantlSim was originally developed and validated by Furbo and Berg (1990) and later modified by Shah and Furbo (1996) and Shah (1999, 2000). This section gives a short introduction to the existing version of MantlSim and the changes made in MantlSim are explained in the next section.

The heat storage is in MantlSim modelled with n control volumes along the tank height, z, in order to simulate the thermal stratification in the inner tank. The heat storage model in MantlSim is illustrated in Figure 8-1. The model is divided into NZ3 vertical layers and in order to calculate the horizontal temperature differences each of the NZ3 vertical layers are divided into 2 or 4 control volumes: One volume for the domestic water, one for the tank wall, and at the mantle level further one volume for the mantle fluid and one for the mantle wall. A uniform temperature is assumed in each of these control volumes.

The energy balance for each control volume, (i,j), can be presented as:

$$\Delta E_{i,j} = E_{solar} + E_{conv} + E_{mix} + E_{diff} + E_{aux} - E_{loss} - E_{dhw} \quad (8.1)$$

where

$\Delta E_{i,j}$	is the energy stored in control volume # (i,j)	[J]
E_{solar}	is the solar energy entering control volume # (i,j)	[J]
E_{conv}	is the convective energy entering control volume # (i,j)	[J]
E_{mix}	is the energy entering control volume # (i,j) due to mixing	[J]
E_{diff}	is the diffusive energy entering control volume # (i,j) due to heat conduction between control volumes	[J]
E_{aux}	is the auxiliary energy supplied control volume # (i,j)	[J]
E_{loss}	is the heat loss from control volume # (i,j)	[J]
E_{dhw}	is the energy tapped from control volume # (i,j)	[J]

The mixing energy, E_{mix}, means the energy transport caused by mixing when a lower layer has a higher temperature than a higher layer. The convective energy, E_{conv}, means the energy transport between fluid and wall. The diffusive energy, E_{diff}, means the energy transport due to heat conduction between control volumes (only from fluid to fluid or from wall to wall). For the control volumes with fluid the diffusive energy transport can only be vertical and for control volumes of mantle wall or tank wall the diffusive energy can be both vertical and horizontal.

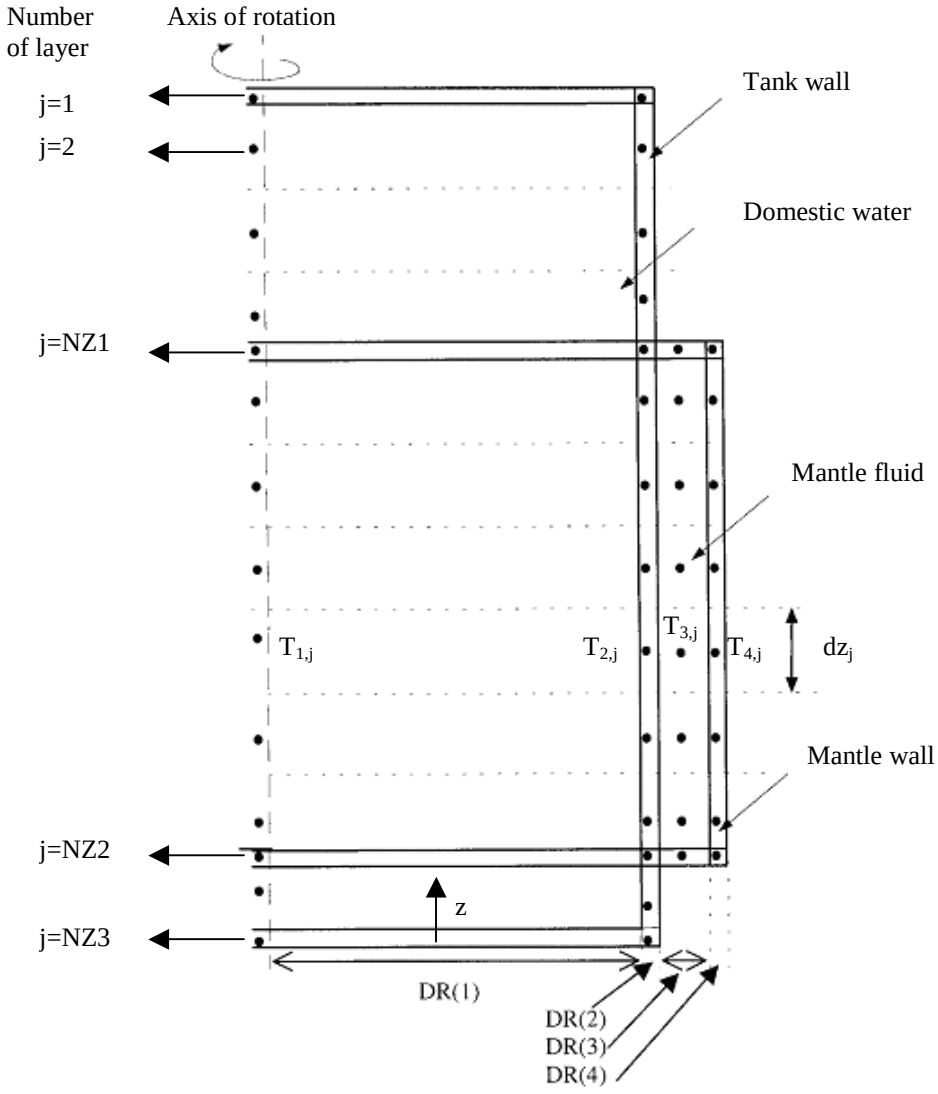

Figure 8-1: Control volumes in the heat storage model in MantlSim.

An auxiliary energy supply system (a heat exchanger connected to an oil or gas burner, or an electrical heating element) is often placed in the upper part of the inner tank above the mantle to keep the domestic water at a certain temperature level. In MantlSim, the auxiliary energy supply system can only be an electric heating element, and the heating element is placed in one layer and it is assumed to heat up the whole control volume.

This control volume is then mixed with the above layers if the temperature is higher than the temperatures of the above layers.

The flow of the fluid in the mantle is based on a plug flow model. The time step, dt, is calculated so that in each time step, the flow shifts the position of all fluid control volumes one layer downwards. Furthermore, it is assumed that the inlet fluid always finds its thermal equilibrium without creating any mixing. Therefore, at the end of each time step, the fluid is scanned from top to bottom and the inlet fluid finds its way to the right layer matching its thermal equilibrium.

The differential equations for the energy balances for all the control volumes are given in appendix A (adapted from Shah (1999)). The energy balances are solved by an implicit method (Berg, 1990).

Besides the heat storage, a SDHW systems also consist of solar collectors, connection piping, control systems and heat transfer medium. It will not be mentioned here how MantlSim treats all these components, but it is very well described in Shah (1999). Thermal properties of water and of the mixture of propylene glycol and water as used in MantlSim are given in appendix B.

8.3 Improvements in MantlSim

The new correlations developed in chapter 7 are implemented in MantlSim. The implementation of the heat transfer correlations was relatively simple. For the calculation of the heat transfer coefficient, $h_{1,j}$, from tank wall to domestic water in the tank the existing correlations were changed to equation 7.23 and equation 7.24. For the calculation of the heat transfer coefficient, $h_{2,j}$, from mantle fluid to inner mantle wall the existing correlations were changed to equation 7.12, equation 7.13 and equation 7.15. For the calculation of the heat transfer coefficient, $h_{3,j}$, from mantle fluid to outer mantle wall the existing correlations were changed to equation 7.16, equation 7.17 and equation 7.18.

The correlations calculating the natural convection flows inside the tank are implemented in the following way in the end of the subroutine where the heat transfer coefficients $h_{1,j}$, $h_{2,j}$ and $h_{3,j}$ are calculated: The heat flow in the water, $Q_{\text{heat flow, model}}$, are calculated based on the equations 7.28-7.30, 7.34, 7.35, 7.37 and 7.38. Then is the resulting heat transfer, $Q_{z,\text{model}}$, to each layer in the inner tank calculated with equation 7.31. Finally, new modified heat transfer coefficients, $h_{1,j}$, from tank wall to domestic water are calculated by equation 7.1 (modified to calculating from tank wall to domestic water) by assuming that the resulting heat transfer, $Q_{z,\text{model}}$, divided by the area of the tank wall in the layer can be used as the heat flux in the equation. Then the modified values of $h_{1,j}$ are used along with the previous calculated values of $h_{2,j}$ and $h_{3,j}$ to the solution of the energy balances described in appendix A in order to find the new temperatures of each control volume in the model. The subroutine calculating the heat transfer coefficients is shown in appendix C.

8.3.1 Mixing in mantle

The flow of the fluid in the mantle in the existing version of MantlSim is, as described in section 8.2, based on a plug flow model where it is assumed that the incoming fluid is not creating any mixing with the fluid already in the mantle. Thus, if it is a hot inlet condition the incoming fluid is placed at the top of the mantle and if it is a warm inlet condition the incoming fluid finds its way to the right layer matching its thermal equilibrium. However, the thermal experiments in chapter 4 and the numerical investigations in chapter 6 showed that the inlet jet at the mantle inlet is subject to mixing in cases with warm inlet condition and also in cases with hot inlet condition for lower inlets. Therefore, the mixing that occurs in the mantle has to be quantified in order to develop MantlSim to model the flow in the mantle in a more correct way. The mixing will in the following be analysed based on CFD-simulations.

For the analysis of the CFD-results, the mantle was in chapter 6 divided into 20 control volumes as shown in Figure 6-3. For the reference tank (Table 6-1) with a mantle flow rate of 0.4 l/min it takes approximately 4 minutes to exchange the fluid in each control volume, for the reference tank with a mantle flow rate of 0.8 l/min it takes approximately 2 minutes to exchange the fluid in each control volume and for the tank with the small mantle gap with a flow rate of 0.4 l/min it takes approximately 1 minute to exchange the fluid in each control volume. Therefore, CFD-calculations of the cases Lower inlet (4 minutes), High flow rate (2 minutes) and Small mantle gap (1 minute) for both hot and warm inlet condition were carried out. Furthermore, a CFD-calculation of 4 minutes with the Top inlet for warm inlet condition was carried out. In all cases the evaluation of the mixing in the mantle were started after 4 minutes of calculation from the initial conditions explained section 6.1 and then the calculations were continued for each case as long as described above. Data for the different CFD-models are shown in Table 6-2 and Table 6-3. The mixing in the mantle is then evaluated in the following way based on the CFD-results.

The change in the energy content of each control volume over the time interval is calculated based on the temperatures at the beginning and at the end of the time interval. The change in the energy content is corrected for the heat transfer in the time interval from the mantle fluid to the inner and outer mantle wall in order to be able to calculate the mixing that would have occurred if the walls were adiabatic. Vertical heat conduction between the control volumes is neglected in this analysis. The equations below describe the method.

The change in energy content over the time interval for each control volume can be calculated by:

$$\Delta E_j = V_j \cdot \rho_j \cdot c_{p,j} \cdot \left(T_{end,j} - T_{start,j} \right) \tag{8.2}$$

where

$c_{p,j}$	specific heat of the fluid in control volume # j, [J/kg·K]
ΔE_j	change in energy content of control volume # j, [J]
$T_{end,j}$	temperature of the control volume # j at the end of time interval, [ºC]
$T_{start,j}$	temperature of the control volume # j at the start of time interval, [ºC]

V_j volume of control volume # j, [m³]
ρ_j density of the fluid in control volume # j, [kg/m³]

The change in energy of control volume # j has to be corrected for the heat transfer in the time interval from the mantle fluid to the inner and outer mantle wall, respectively.

$$E_{1,j} = \left(\frac{q_{1,start,j} + q_{1,end,j}}{2} \right) \cdot A_{1,j} \cdot \Delta t \tag{8.3}$$

$$E_{2,j} = \left(\frac{q_{2,start,j} + q_{2,end,j}}{2} \right) \cdot A_{2,j} \cdot \Delta t \tag{8.4}$$

where
$A_{1,j}$ the area of inner mantle wall at level j, [m²]
$A_{2,j}$ the area of outer mantle wall at level j, [m²]
$E_{1,j}$ the heat transfer from mantle fluid to inner mantle wall, [J]
$E_{2,j}$ the heat transfer from mantle fluid to outer mantle wall, [J]
$q_{1,end,j}$ heat flux at inner mantle wall at the end of the time interval, [W/m²]
$q_{2,end,j}$ heat flux at outer mantle wall at the end of the time interval, [W/m²]
$q_{1,start,j}$ heat flux at inner mantle wall at the start of the time interval, [W/m²]
$q_{2,start,j}$ heat flux at outer mantle wall at the start of the time interval, [W/m²]
Δt time interval, [s]
The heat fluxes in equation 8.3 and equation 8.4 are defined as positive for heat flux from the mantle fluid to the inner and outer mantle wall. The mean values of the heat flux at the inner and outer mantle wall are used in equation 8.3 and equation 8.4 because they are not changing very much due to the relatively short time intervals (1-4 minutes).

Then the change in energy content corrected for the heat transfer at the walls can be calculated:

$$\Delta E_{corr,j} = \Delta E_j + E_1 + E_2 = V_j \cdot \rho_j \cdot c_{p,j} \cdot \left(T_{end,corr,j} - T_{start,j} \right) \tag{8.5}$$

where
$T_{end,corr,j}$ temperature at the end of time interval if the walls had been adiabatic, [ºC]

Based on equation 8.5, $T_{end,corr,j}$ and the mixing rate of the control volume can be calculated:

$$T_{end,corr,j} = \frac{\Delta E_{corr,j}}{V_j \cdot \rho_j \cdot c_{p,j}} + T_{start,j} = Mix_j \cdot T_{start,j} + (1 - Mix_j) \cdot T_{in} \tag{8.6}$$

$$\Downarrow$$

$$Mix_j = \frac{T_{end,corr,j} - T_{in}}{T_{start,j} - T_{in}} \tag{8.7}$$

where

Mix_j is the part of control volume # j that is mixed with the incoming fluid, [-]

T_{in} is the mantle inlet temperature, [ºC]

A value of $Mix_j = 1$ means that no mixing occurs in the control volume. Figure 8-2 shows the mixing rate as a function of the vertical distance below the mantle inlet for the investigated cases for warm inlet condition. It appears, as expected, that most mixing occurs in the cases with high flow rate and small mantle gap. It is also seen that less mixing of the control volumes occurs in the case with top inlet, but there the mixing takes place in a larger part of the mantle. The reason for this is that in the case with the top inlet there is a longer distance from the inlet down to the level, where there is thermal equilibrium between the inlet fluid and the mantle fluid.

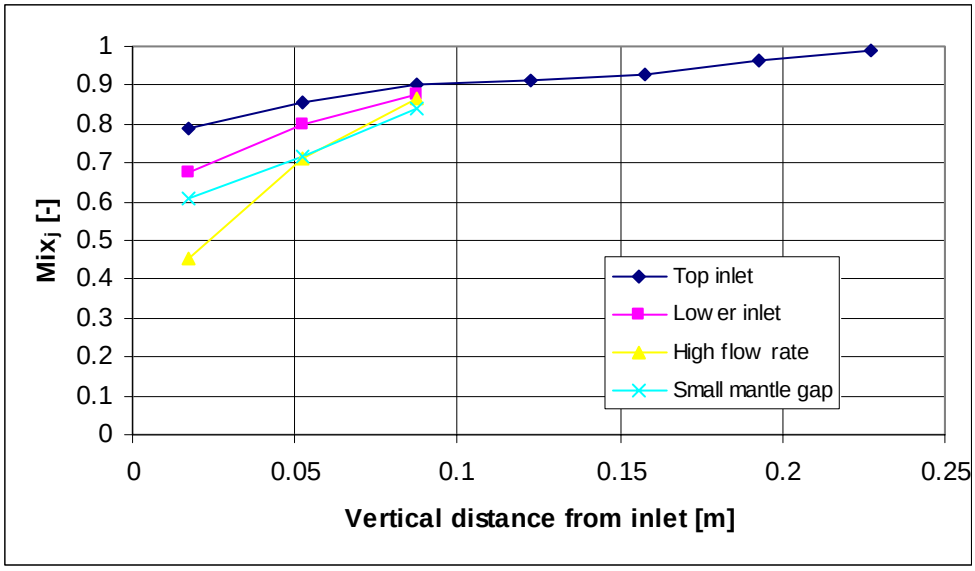

Figure 8-2: The mixing rate as a function of the vertical distance below the mantle inlet for warm inlet condition.

Figure 8-3 shows the mixing rate as a function of the vertical distance above the mantle inlet for the investigated cases for hot inlet condition. It is seen that also for the hot inlet condition most mixing occurs in the cases with high flow rate and small mantle gap.

It was mentioned in the discussion of Figure 8-2 that there was a longer distance from the mantle inlet to the thermal equilibrium in the case with top inlet. Figure 8-4 shows the mixing rate as a function of the relative distance from the mantle inlet to the level where there is thermal equilibrium between inlet fluid and mantle fluid for the investigated cases for warm inlet condition. From Figure 8-4 it appears that the mixing only occurs in 33-56% of the volume between the inlet and the level with thermal equilibrium. The reason for this is that the inlet fluid is heated on its way down through the layers due to the mixing. Therefore, the mantle inlet temperature will in the following analysis be corrected due to the calculated mixing before entering the next control volume, where a new mixing rate is calculated.

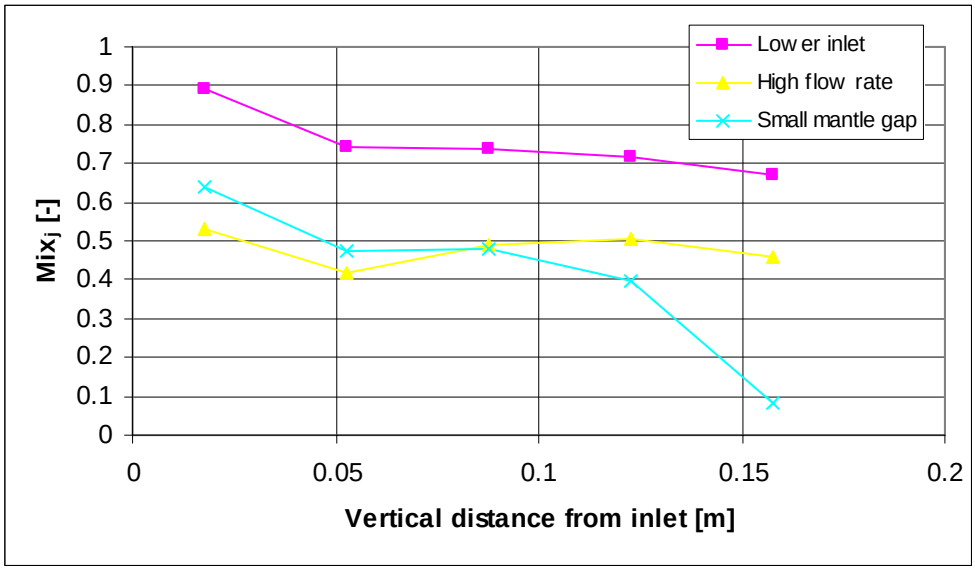

Figure 8-3: The mixing rate as a function of the vertical distance above the mantle inlet for hot inlet condition.

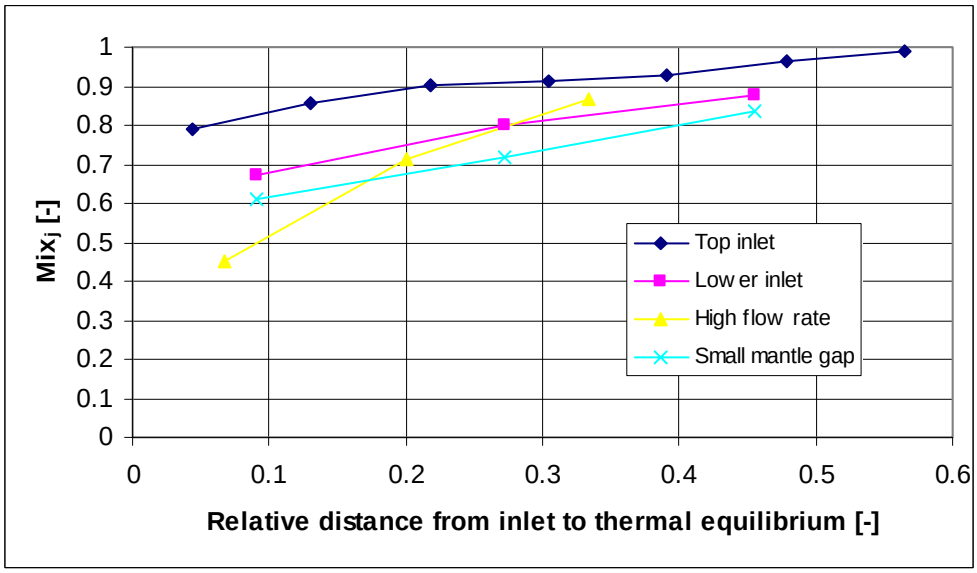

Figure 8-4: The mixing rate as a function of the relative vertical distance from the mantle inlet to the level where there is thermal equilibrium between inlet fluid and mantle fluid for warm inlet condition.

The mixing at the level of the mantle inlet is calculated as described in equations 8-2 - 8-7 and then is a new corrected inlet temperature, that enters the next layer, calculated:

$$T_{in,corr,j+1} = Mix_j \cdot T_{in} + (1-Mix_j) \cdot T_{start,j} \quad \text{for warm inlet condition} \qquad (8.8)$$

$$T_{in,corr,j-1} = Mix_j \cdot T_{in} + (1-Mix_j) \cdot T_{start,j} \quad \text{for hot inlet condition} \qquad (8.9)$$

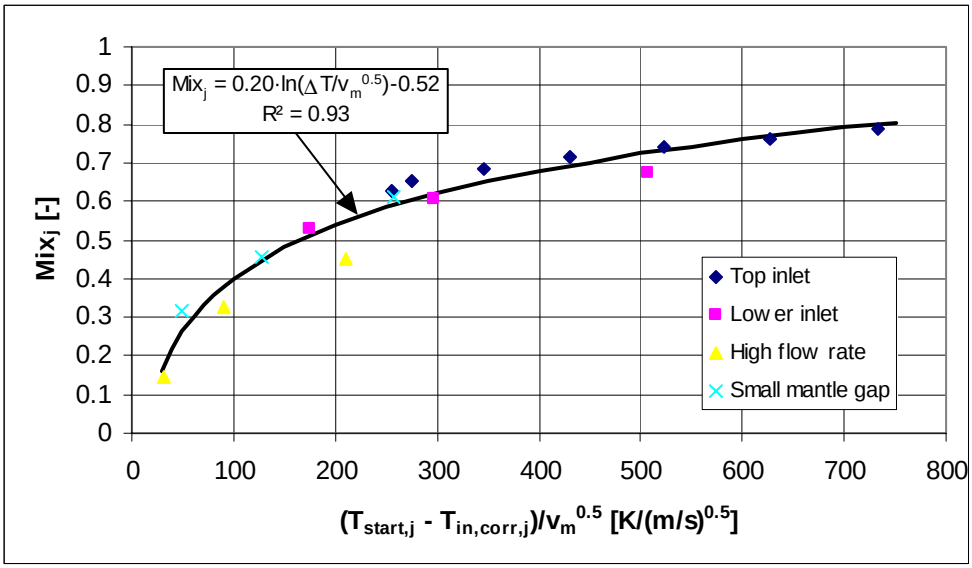

Figure 8-5: The mixing rate as a function of the temperature difference between $T_{start,j}$ and $T_{in,corr,j}$ divided by $v_m^{0.5}$ for warm inlet condition.

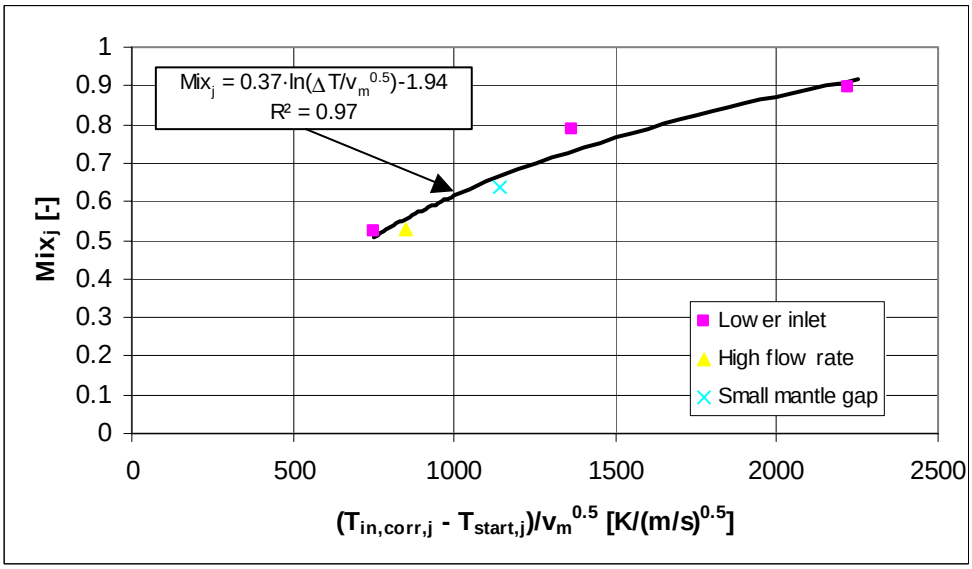

Figure 8-6: The mixing rate as a function of the temperature difference between $T_{in,corr,j}$ and $T_{start,j}$ divided by $v_m^{0.5}$ for hot inlet condition.

Then is the mixing rate calculated in the next control volume based on $T_{in,corr}$ instead of T_{in} and then is a new $T_{in,corr}$ calculated. This procedure continues until $T_{in,corr}$ reaches its thermal equilibrium.

Figure 8-5 shows the mixing rate as a function of the temperature difference between $T_{in,corr,j}$ and $T_{start,j}$ divided by $v_m^{0.5}$ (the square root of the average velocity in the mantle) for warm inlet condition. The average velocity in the mantle is given by equation 8.10:

$$v_m = \frac{\dot{V}_{mantle}}{\pi(r_o^2 - r_i^2)} \tag{8.10}$$

where

r_{inner}	is the inner annuli radius, [m]
r_{outer}	is the outer annuli radius, [m]
v_m	average velocity in mantle, [m/s]
$\dot{V}_{mantle}$	is the mantle flow rate, [m³/s]

The correlation in Figure 8-5 is calculated by the least squared fit through the points. Figure 8-6 shows the mixing rate as a function of the temperature difference between $T_{in,corr,j}$ and $T_{start,j}$ divided by $v_m^{0.5}$ for hot inlet condition. The correlation in Figure 8-6 is calculated by the least squared fit through the points.

Thus the correlations become:

Warm inlet condition:
$$Mix_j = 0.20 \cdot \ln\left(\frac{T_{start,j} - T_{in,corr,j}}{v_m^{0.5}}\right) - 0.52 \tag{8.11}$$

Hot inlet condition:
$$Mix_j = 0.37 \cdot \ln\left(\frac{T_{in,corr,j} - T_{start,j}}{v_m^{0.5}}\right) - 1.94 \tag{8.12}$$

where $Mix_j = 0$ if $Mix_j < 0$ and $Mix_j = 1$ if $Mix_j > 1$.

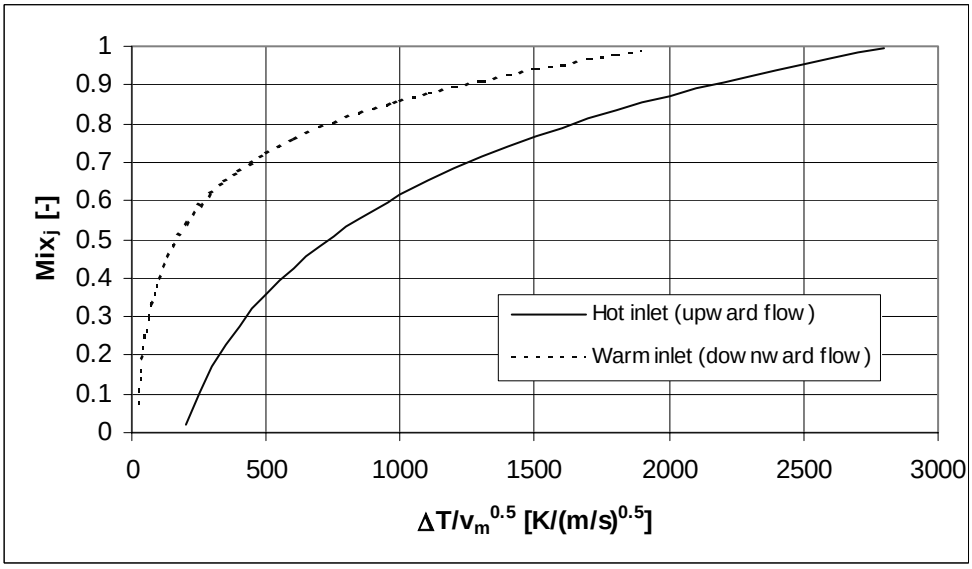

Figure 8-7: The mixing rate correlation for hot and warm inlet condition.

Figure 8-7 shows a comparison of the two correlations in equation 8.11 and equation 8.12 and it is seen that most mixing occurs for the hot inlet condition. The reason for

this is that for a hot inlet condition the mixing occurs for upward flow while the general flow in the mantle is downward and this is creating the higher mixing rate. Furthermore, the change in density between the incoming fluid and the fluid in the mantle is increasing for higher temperatures, which creates larger velocities and thus more mixing.

The correlations in equation 8.11 and equation 8.12 are integrated in the plug flow model for modelling the flow in the mantle. It is assumed for lower mantle inlets that the fluid above the inlet is undisturbed at warm inlet conditions. The subroutine that models the flow in the mantle in MantlSim is shown in appendix D.

The two equations (equation 8.11 and equation 8.12) for determining the mixing in the mantle due to the inlet jet are developed based on limited parameter variations. Only the mantle inlet position, the mantle flow rate and the mantle gap are considered as well as only one warm inlet temperature (50ºC) and only one hot inlet temperature (70ºC). The mixing rate might, among other things, also depend on inlet velocity (inlet size), diameter of tank and type of mantle fluid. This has to be kept in mind when using the new version of MantlSim.

8.4 Model verification

Measurements from the test of the two SDHW systems described in section 4.3 are used for the model verification of the new version of MantlSim. A period of 30 days of the measurements is chosen for validation of the MantlSim models. This period is from 26/9-2003 to 25/10-2003. The total and diffuse solar irradiance in the period is shown in Figure 8-8 and Figure 8-9. It is seen that the solar irradiance has varied during the period, which is desirable to avoid systematic errors in the simulation model. Figure 8-10 shows the indoor, outside and cold-water temperatures in the period.

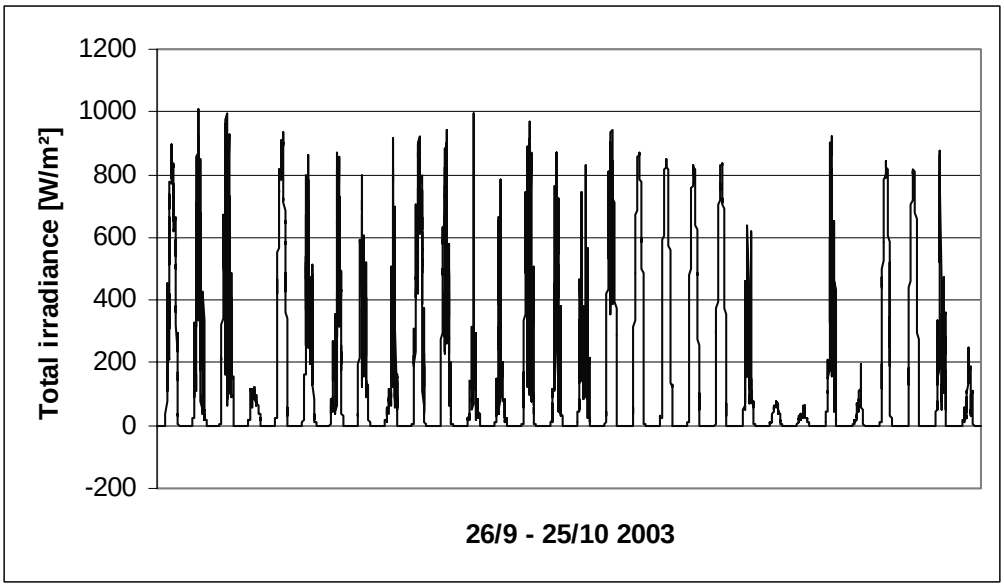

Figure 8-8: Total solar irradiation on the collectors.

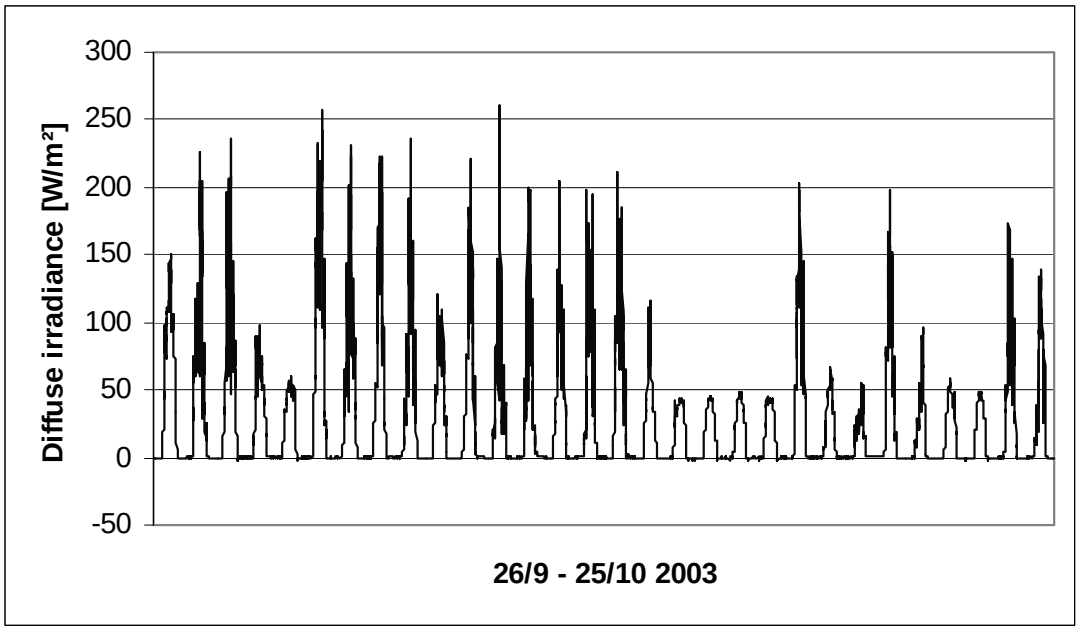

Figure 8-9: Diffuse solar irradiation on the collectors.

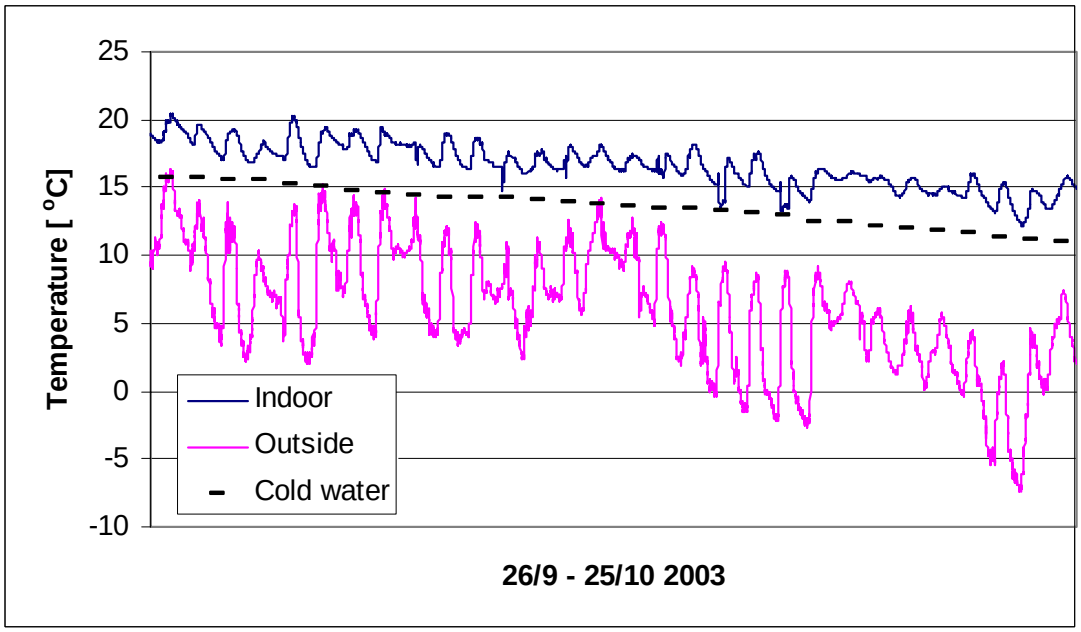

Figure 8-10: Indoor, outside and cold-water temperatures.

All the data from Figure 8-8 to Figure 8-10 are used as input for the simulation model as well as the measured solar collector flow rate and tapped volume of hot water.

For each of the two SDHW systems a simulation with MantlSim is carried out for the test period described above. 5-minute values of the weather data were used in the simulations. The MantlSim models are validated against measured temperatures and energy quantities.

The temperatures are:

- The temperature at the top of the tank (T7)
- The inlet temperature to the collector (T4)
- The outlet temperature from the collector (T1)
- The inlet temperature to the mantle (T2)
- The outlet temperature from the mantle (T3)

The energy quantities are:

- The solar energy transferred to the collector fluid
- The solar energy transferred to the storage
- The auxiliary energy supplied to the storage
- The DHW energy tapped from the storage
- The net utilised solar energy

Figure 8-11 shows a system sketch, which illustrates the principles and measuring points of both of the tested systems. Measuring equipment and measuring accuracy is described in section 3.3.

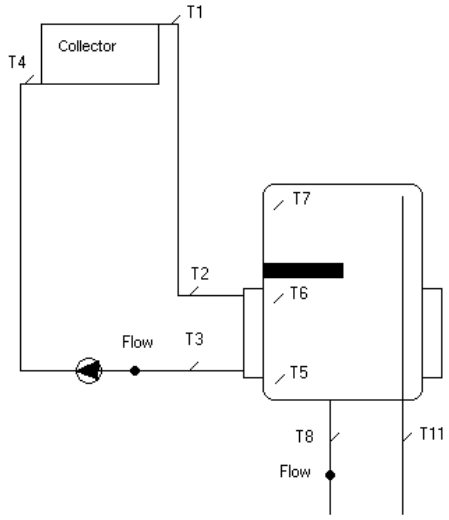

Figure 8-11: System sketch with measuring points.

8.4.1 System with lower mantle inlet

Data for the SDHW system with lower mantle inlet is given in Table 4-5.

Figure 8-12 – Figure 8-16 show measured and calculated solar energy transferred to the fluid in the collector, measured and calculated solar energy transferred to the storage, measured and calculated auxiliary energy supply, measured and calculated DHW energy tapped from the storage and measured and calculated net utilised solar energy. The figures show that a good agreement between measured and calculated energy quantities is achieved. The results are summarised in Table 8-1, and it appears that the differences are small.

Energy quantity:	Calculated [kWh]	Measured [kWh]	Difference [%]
Solar energy to collector fluid	114	113	0.9
Solar energy to storage	97	96	1.1
Auxiliary energy to storage	75	75	0.0
DHW energy tapped from storage	138	138	0.0
Net utilised solar energy	63	63	0.0

Table 8-1: Measured and calculated energy quantities in system with lower inlet in the period 26/9 2003 – 25/10 2003.

Figure 8-17 shows the measured and calculated temperatures at the top of the tank and a good agreement is achieved. However, the set point temperature for the auxiliary heating is not totally constant in the measurements, and the measured T7 is therefore higher than the calculated values during the period in the circle in Figure 8-17. It is also seen in Figure 8-14 that the measured auxiliary energy is higher than the calculated auxiliary energy supply in that period. The reason for the variations in the set point temperature could very well be that some lime in the tank is disturbing the temperature sensor measuring the temperature for the control system of the auxiliary heater.

It is also important that the calculated collector inlet and outlet temperatures and the calculated mantle inlet and outlet temperature fits the measured temperatures to make sure that the collector model and the heat transfer model for the mantle work as expected. Figure 8-18 shows the measured and calculated collector inlet and outlet temperatures for the whole validation period, while Figure 8-19 shows the measured and calculated collector inlet and outlet temperatures for 3 days (10/10-12/10 2003) during the validation period. There is good agreement between the measured and calculated temperatures.

Figure 8-20 shows the measured and calculated mantle inlet and outlet temperatures for the whole validation period, while Figure 8-21 shows the measured and calculated mantle inlet and outlet temperatures for 3 days (10/10-12/10 2003) during the validation period. There is good agreement between the measured and calculated temperatures.

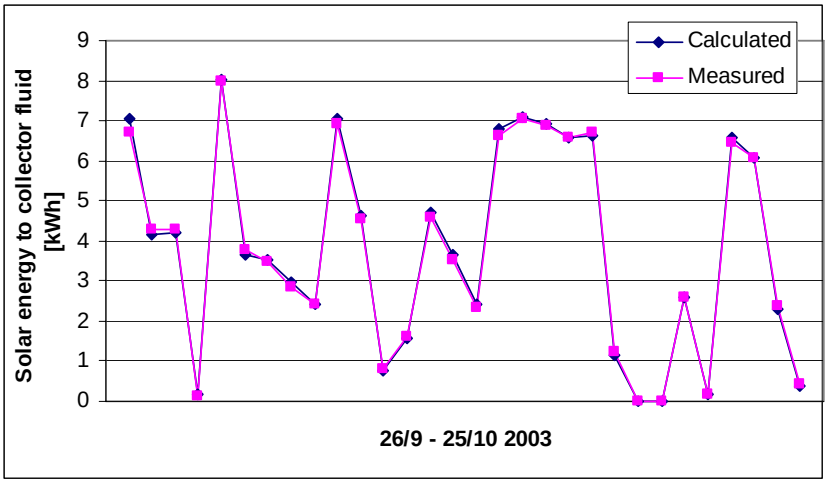

Figure 8-12: Measured and calculated daily solar energy to collector fluid in system with lower inlet.

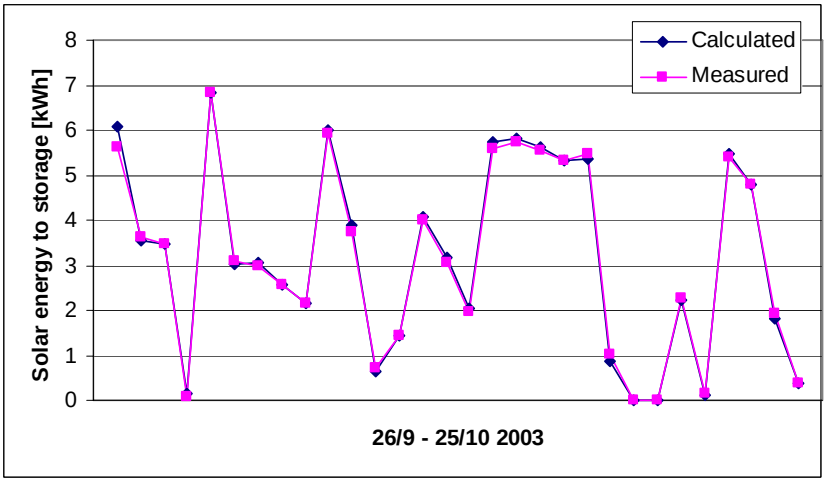

Figure 8-13: Measured and calculated daily solar energy to storage in system with lower inlet.

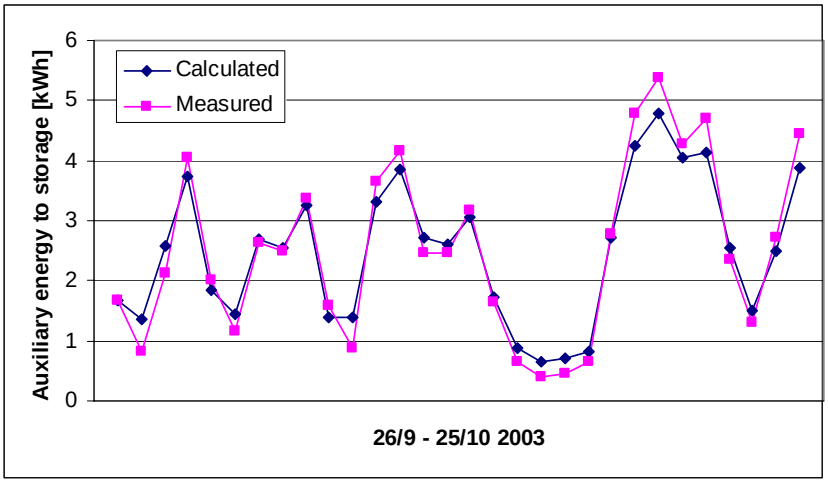

Figure 8-14: Measured and calculated daily auxiliary energy to storage in system with lower inlet.

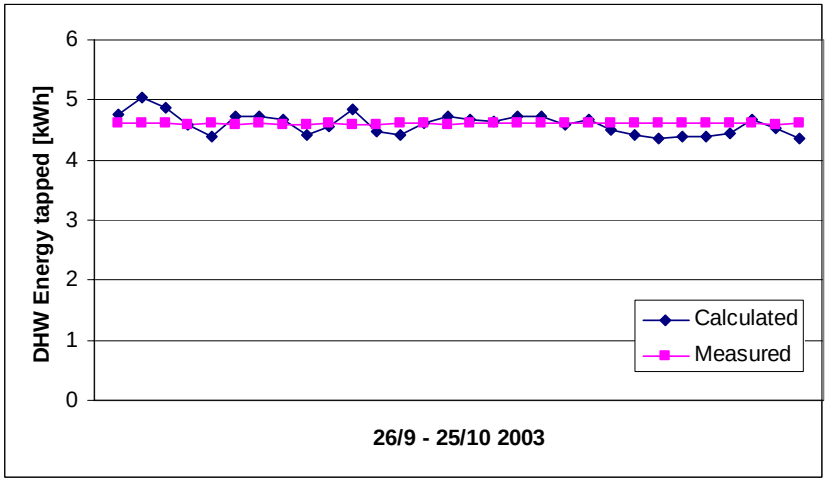

Figure 8-15: Measured and calculated daily DHW energy tapped from the system with lower inlet.

Figure 8-16: Measured and calculated daily net utilised solar energy in system with lower inlet.

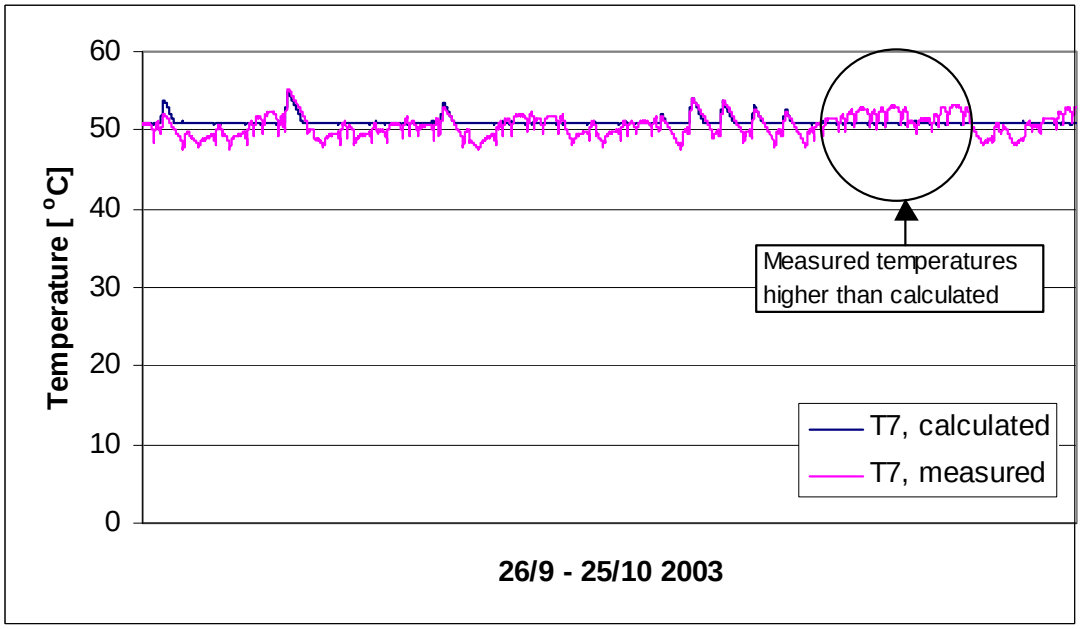

Figure 8-17: Measured and calculated temperatures in the top of the tank in the system with lower inlet.

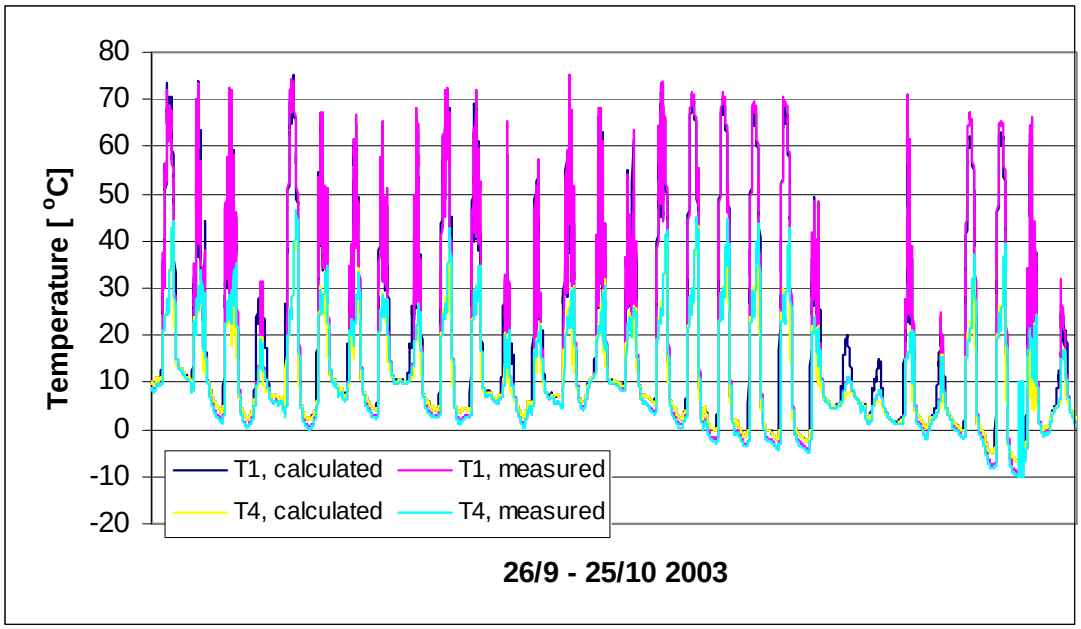

Figure 8-18: Measured and calculated collector inlet and outlet temperatures in the system with lower inlet.

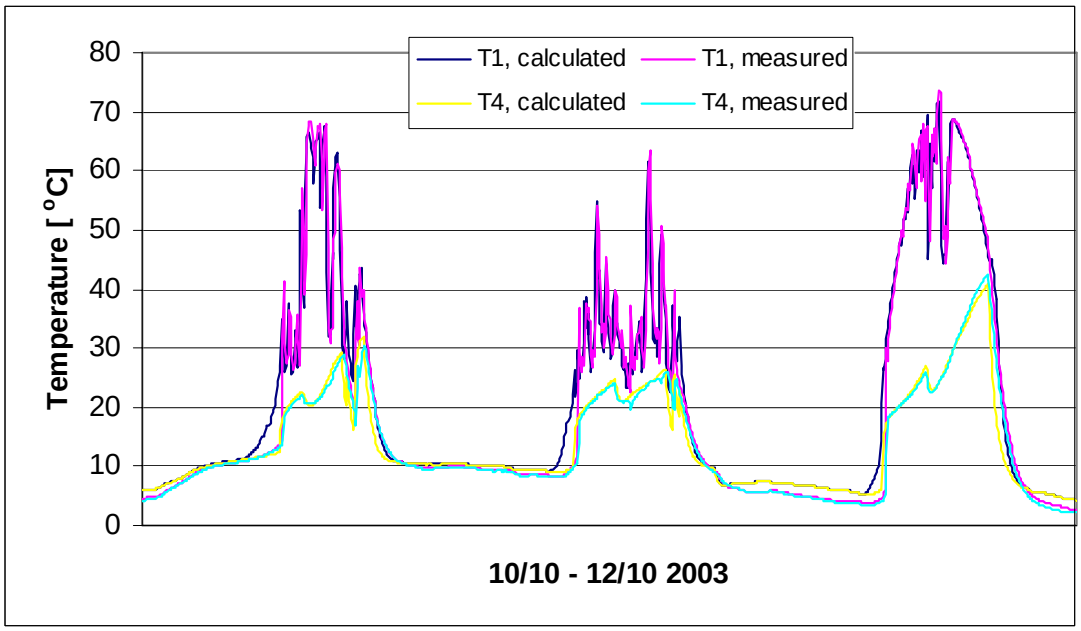

Figure 8-19: Measured and calculated collector inlet and outlet temperatures in the system with lower inlet in the period 10/10 – 12/10 2003.

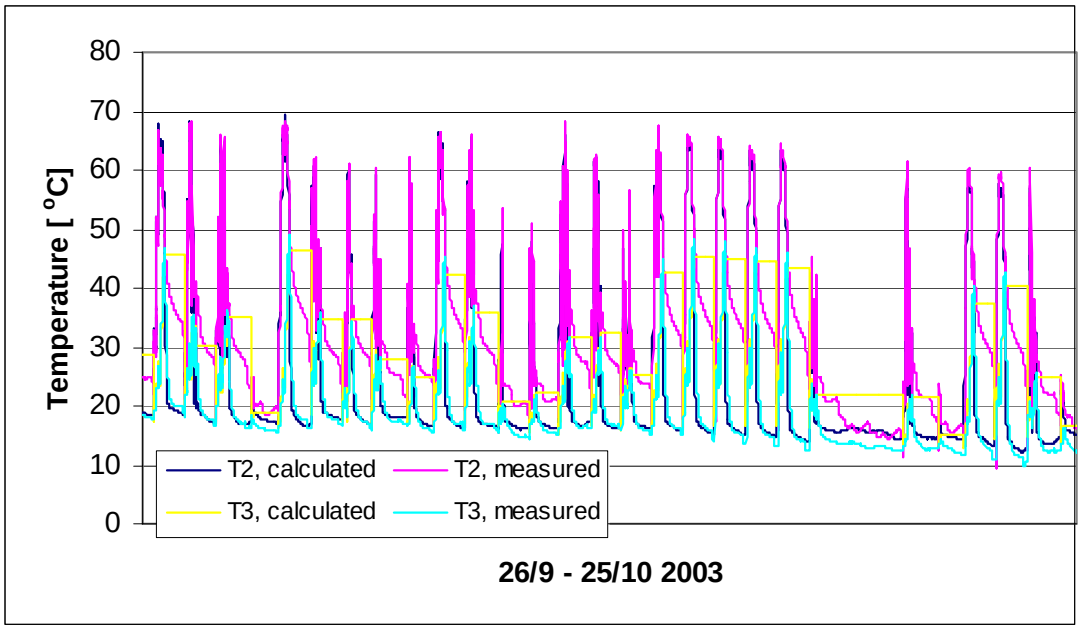

Figure 8-20: Measured and calculated mantle inlet and outlet temperatures in the system with lower inlet.

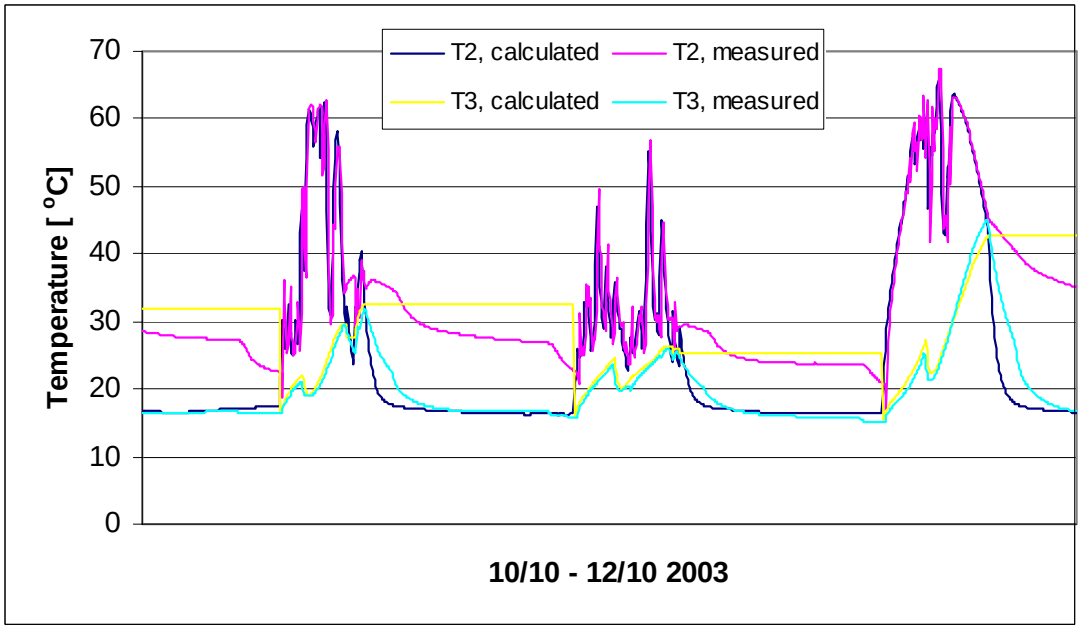

Figure 8-21: Measured and calculated mantle inlet and outlet temperatures in the system with lower inlet in the period 10/10 – 12/10 2003.

8.4.2 System with top mantle inlet

Data for the SDHW system with top mantle inlet is given in Table 4-5.

Figure 8-22 – Figure 8-26 show measured and calculated solar energy transferred to the fluid in the collector, measured and calculated solar energy transferred to the storage,

measured and calculated auxiliary energy supply, measured and calculated DHW energy tapped from the storage and measured and calculated net utilised solar energy. The figures show that a good agreement between measured and calculated energy quantities is achieved. The results are summarised in Table 8-2, and it appears that the differences are small.

Energy quantity:	Calculated [kWh]	Measured [kWh]	Difference [%]
Solar energy to collector fluid	113	112	0.9
Solar energy to storage	92	92	0.0
Auxiliary energy to storage	78	79	-1.3
DHW energy tapped from storage	138	138	0.0
Net utilised solar energy	60	59	1.7

Table 8-2: Measured and calculated energy quantities in system with top inlet in the period 26/9 2003 – 25/10 2003.

Figure 8-27 shows the measured and calculated temperatures at the top of the tank and a good agreement is achieved. However, the set point temperature for the auxiliary heating is not totally constant in the measurements, and the measured T7 is therefore higher than the calculated values during the period in the circle in Figure 8-27. The measuring point for T7 is, for the system with top inlet, located in the lower part of the auxiliary volume and it is therefore the temperatures become lower during draw-offs than in the systems with lower inlet.

Figure 8-28 shows the measured and calculated collector inlet and outlet temperatures for the whole validation period, while Figure 8-29 shows the measured and calculated collector inlet and outlet temperatures for 3 days (10/10-12/10 2003) during the validation period. There is good agreement between the measured and calculated temperatures.

Figure 8-30 shows the measured and calculated mantle inlet and outlet temperatures for the whole validation period, while Figure 8-31 shows the measured and calculated mantle inlet and outlet temperatures for 3 days (10/10-12/10 2003) during the validation period. There is good agreement between the measured and calculated temperatures.

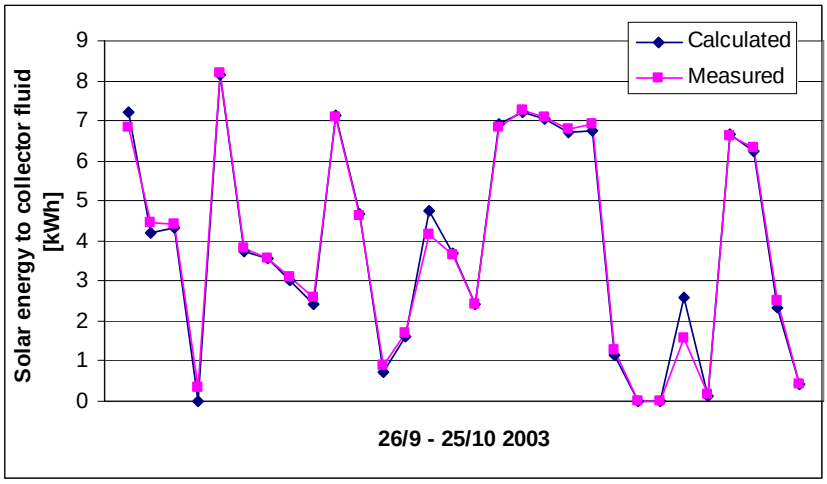

Figure 8-22: Measured and calculated daily solar energy to collector fluid in system with top inlet.

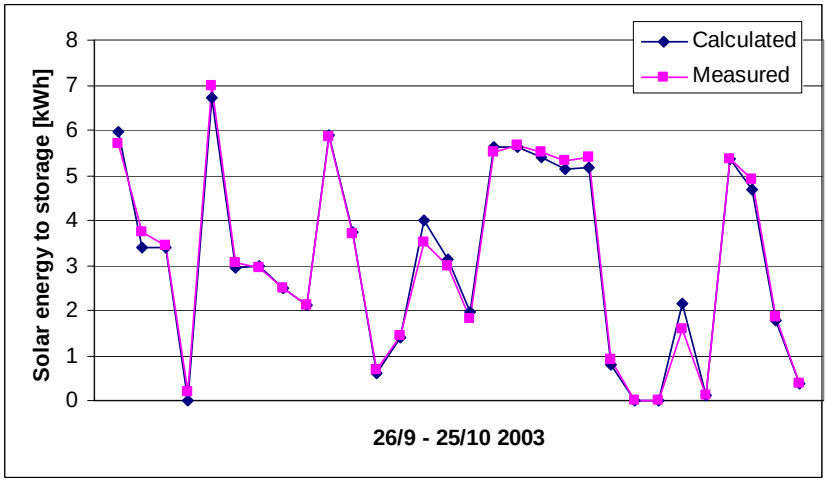

Figure 8-23: Measured and calculated daily solar energy to storage in system with top inlet.

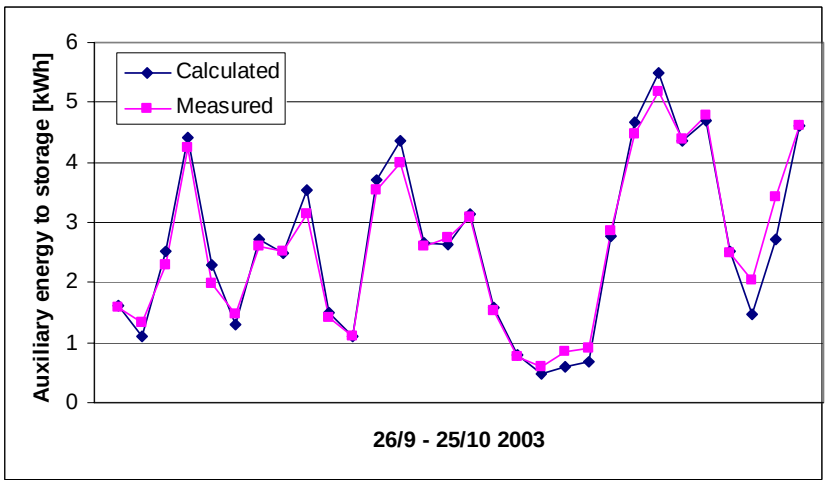

Figure 8-24: Measured and calculated daily auxiliary energy to storage in system with top inlet.

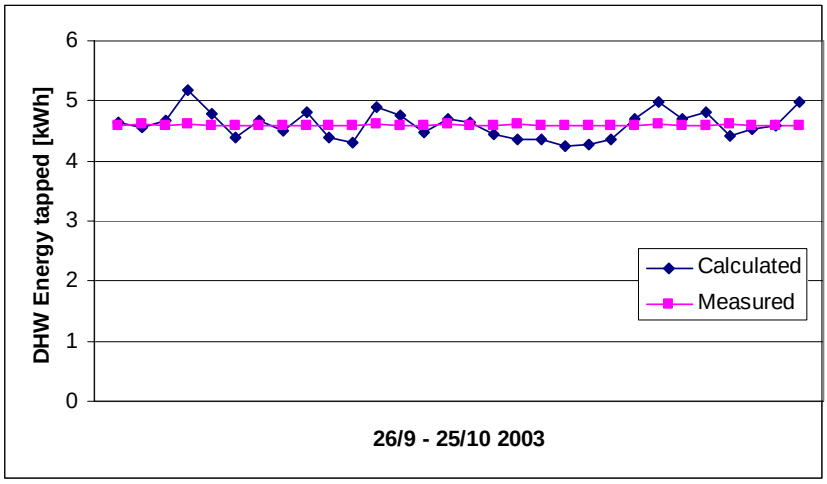

Figure 8-25: Measured and calculated daily DHW energy tapped from the storage in the system with top inlet.

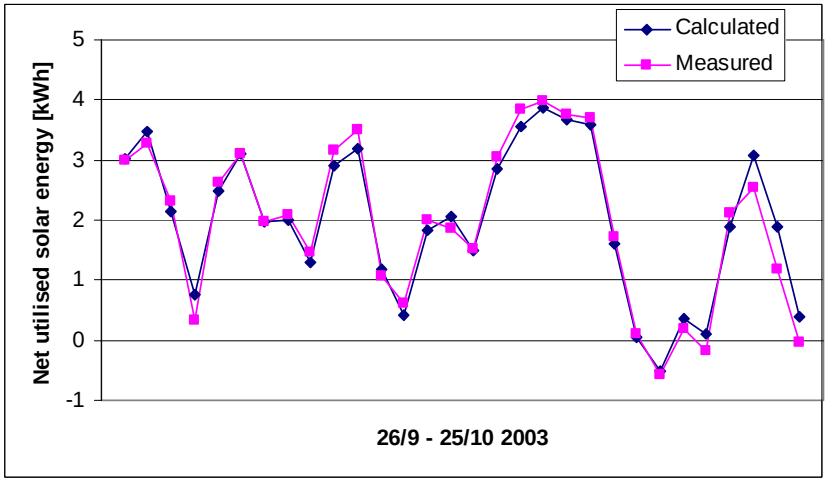

Figure 8-26: Measured and calculated daily net utilised solar energy in system with top inlet.

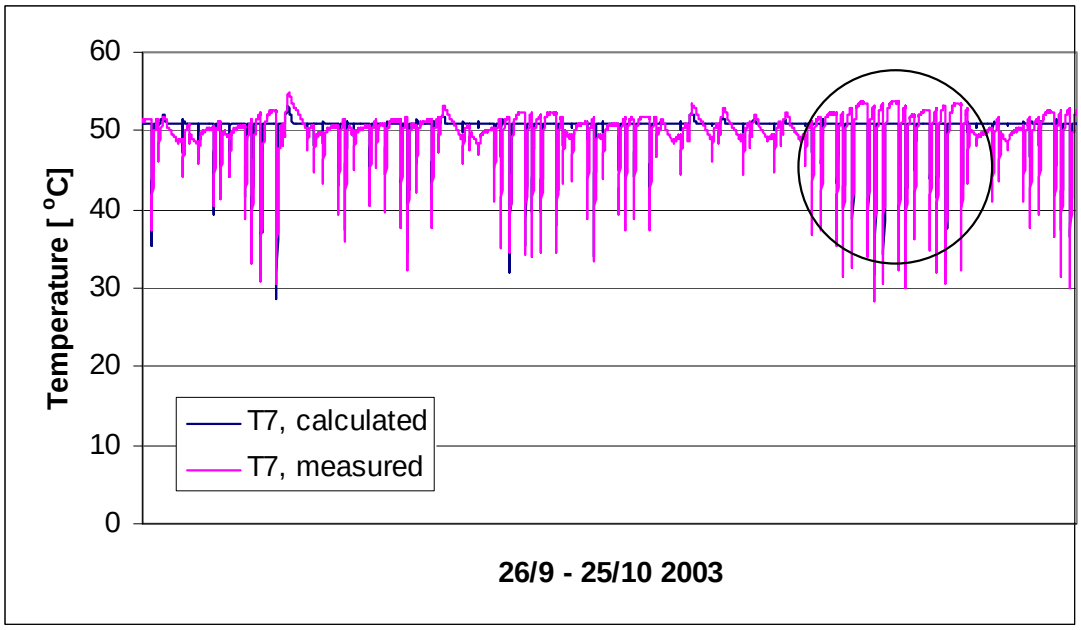

Figure 8-27: Measured and calculated temperatures in the top of the tank in system with top inlet.

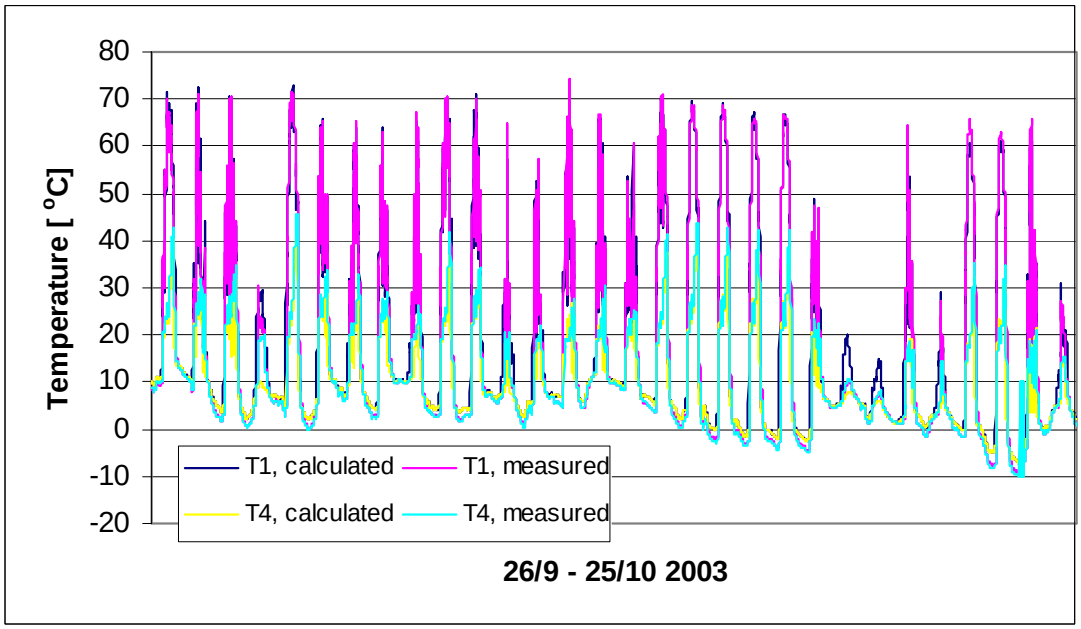

Figure 8-28: Measured and calculated collector inlet and outlet temperatures in system with top inlet.

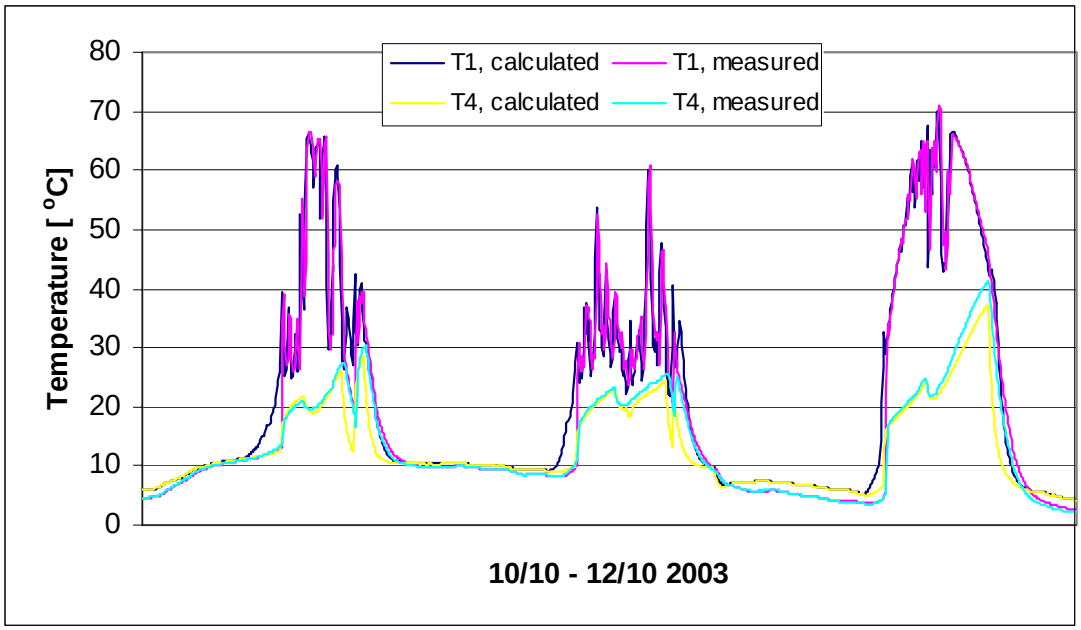

Figure 8-29: Measured and calculated collector inlet and outlet temperatures in system with top inlet in the period 10/10 – 12/10 2003.

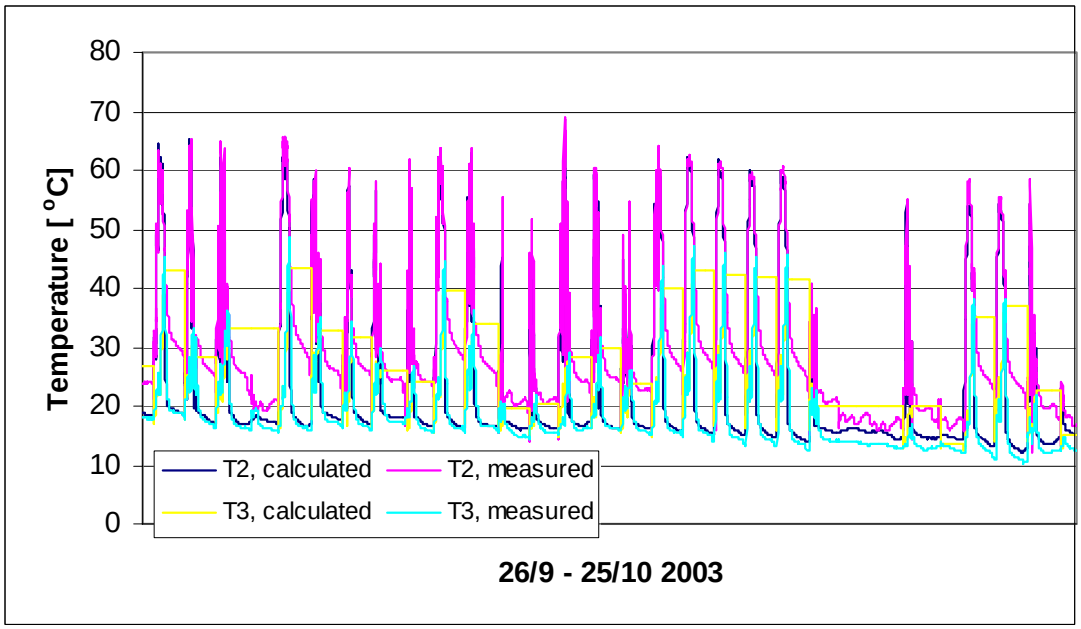

Figure 8-30: Measured and calculated mantle inlet and outlet temperatures in system with top inlet.

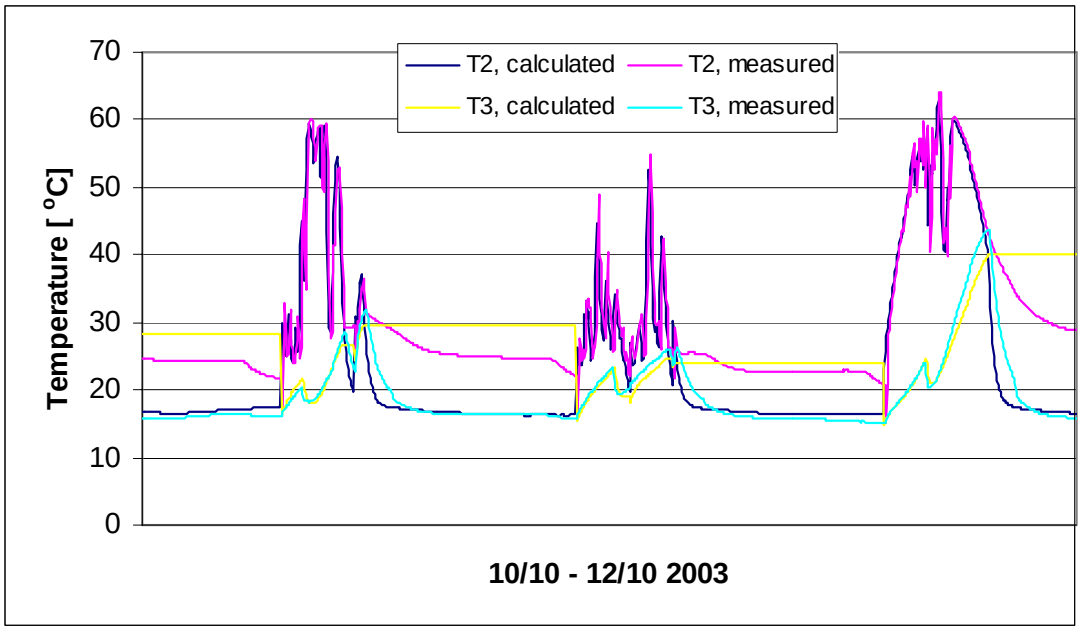

Figure 8-31: Measured and calculated mantle inlet and outlet temperatures in system with top inlet in the period 10/10 – 12/10 2003.

8.5 Summary and discussion

A short introduction to the SDHW simulation program, MantlSim, was given in this chapter. It was also explained how the correlations concerning the heat transfer coefficients and the heat flow in the water inside the tank, that was developed in chapter 7, are implemented in MantlSim.

The mixing in the mantle due to the inlet jet was investigated based on CFD-calculations and two correlations, one for warm inlet condition and one for hot inlet condition, were developed. The two correlations were implemented in MantlSim, and MantlSim was furthermore developed to be able to take different vertical positions of the mantle inlet into account. The two correlations were developed for different mantle inlet positions, mantle flow rates and mantle gaps and for a warm inlet temperature of 50ºC and for a hot inlet temperature of 70ºC. If the inlet velocity, diameter of the tank and the mantle fluid also had been taken into account, then slightly different correlations might have been obtained.

The new version of MantlSim was verified by comparing calculated with measured results. The verification was based on the measurements of the two low-flow systems that were tested in section 4.3, that was one system with the mantle inlet located at the top of the mantle and one system with the mantle inlet located at a lower position. A good agreement between measured and calculated temperatures and energy quantities was found. Thus, the model was assumed to predict thermal performances for low-flow systems based on mantle tanks in good agreement with reality.

In the next chapter MantlSim will be used to perform a heat storage design analysis for vertical mantle heat exchangers.

9. Mantle tank design analysis

9.1 Introduction

In chapter 8, results from the new version of MantlSim were compared to measured results from two systems, and a good agreement between measured and calculated temperatures and energy quantities was found. It is therefore assumed that the model predicts the yearly thermal performances of low-flow SDHW systems with mantle heat exchangers in good agreement with reality. In this chapter a mantle tank design analysis is carried out with MantlSim in order to investigate how the thermal performance of the system is influenced by different tank parameters.

The mantle tank design analysis is carried out with the Danish commercially manufactured mantle tank, Danlager 1000, as the standard reference tank. The design analysis is performed in such a way that only one parameter has been changed at a time in the calculation. Table 9-1 gives data for the standard reference system.

The circulation pump in the system is controlled by a differential thermostat, which measures the temperature difference between the outlet from the solar collector and the bottom of the mantle. The differential thermostat has start/stop set point at 10/2 K.

All the calculations in this chapter are carried out with weather data from the Danish Test Reference Year (Statens Byggeforskningsinstitut, 1982). The daily hot-water consumption is 0.100 m³ heated from 10ºC to 50ºC, which is tapped from the tank in three equally large parts at 7 am, 12 am and 7 pm. The yearly hot-water consumption is 1674 kWh. The auxiliary energy supply system heats the top 0.082 m³ of the tank to 50.5ºC and the indoor air temperature is 20ºC.

The tank parameters that are investigated are the mantle inlet position, mantle inlet size, mantle gap, mantle height, H/D-ratio of tank, auxiliary volume, thermal conductivity of tank material and insulation of tank. Furthermore, it is investigated how the effect of changing the mantle inlet position depends on hot-water consumption, mantle gap, mantle height, H/D-ratio of tank and collector loop flow rate.

In some of the figures in the following sections, the net utilised solar energy and the solar fraction are shown as a function of the parameter in question, and in some figures the performance ratio is shown as a function of the parameter in question. The net utilised solar energy is defined as the energy tapped from the heat storage minus the auxiliary energy supply (equation 4.8). The solar fraction is defined as the net utilised solar energy divided by the energy tapped from the heat storage (equation 4.9). The performance ratio is defined as the net utilised solar energy for the system in question divided by the net utilised solar energy for the reference system. In some of the sections, the performance ratio will be defined in another way, but then it is explained in the section. The standard reference system is marked in the figures.

Tank design	
Inner tank	
Hot-water tank volume, [m³]	0.175
Solar volume, [m³]	0.082
Auxiliary volume, [m³]	0.082
Dead volume, [m³]	0.011
Inner height [m]	0.913
Inner diameter, [m]	0.494
Tank wall thickness, [m]	0.003
Power of auxiliary energy supply, [W]	1200
Mantle	
Mantle volume, [m³]	0.0073
Mantle height, [m]	0.431
Mantle gap, [m]	0.0105
Inside diameter of mantle inlet, [m]	0.0244 (3/4")
Insulation	
Material	PUR-foam
Insulation top, [m]	0.075
Insulation side above/below mantle, [m]	0.050
Insulation side mantle, [m]	0.035
Insulation bottom, [m]	0.030
Thermal bridges, tank top, [W/K]	0
Thermal bridges, tank bottom, [W/K]	0.8
Solar collector	
Area, [m²]	2.5
Start efficiency, [-]	0.801
Heat loss coefficient, [W/m²·K]	3.86
Incident angle modifier (tangens equation)	a = 3.6
Heat capacity, [J/m²·K]	5339
Tilt, [°]	45
Orientation	South
Solar collector loop	
Pipe material	Copper
Outer diameter, [m]	0.015
Inner diameter, [m]	0.013
Insulation thickness (PUR foam), [m]	0.01
Length of pipe from storage to collector, indoor, [m]	1.5
Length of pipe from storage to collector, outdoor, [m]	3.5
Length of pipe from collector to storage, indoor, [m]	1.5
Length of pipe from collector to storage, outdoor, [m]	3.5
Solar collector fluid (propylene glycol / water mixture), [%]	40
Power of circulation pump, [W]	50
Flow rate in collector loop, [l/min]	0.5
Start/stop difference for circulation pump, [K/K]	10/2

Table 9-1: Data for the standard reference system.

9.2 Mantle inlet port position

The side-by-side measurements in section 4.3 of two SDHW systems with different mantle inlet positions showed that for those two systems it was an advantage to use a lower mantle inlet position instead of the normal top inlet position. In this investigation

the inlet position is varied from the top position and down to a position approximately midway between top and bottom.

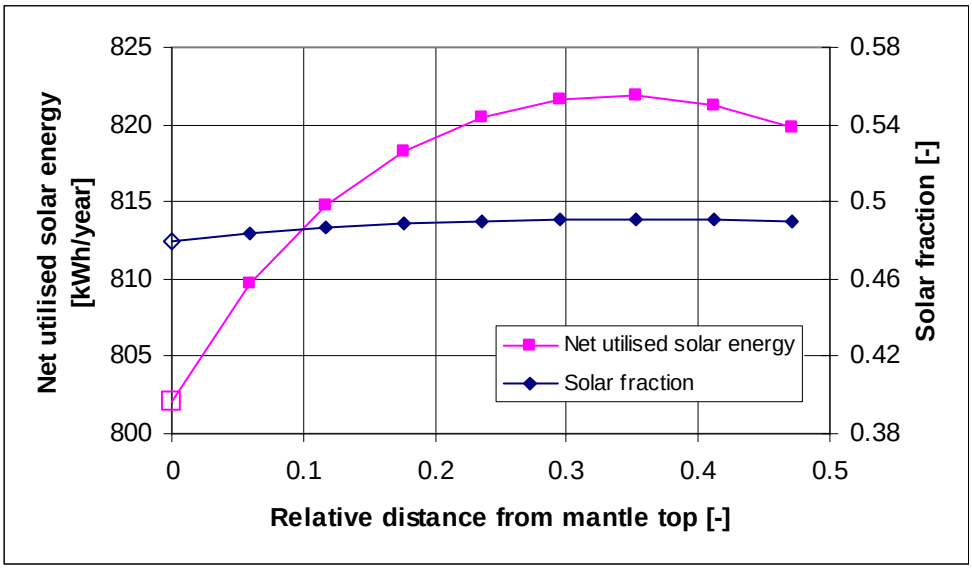

Figure 9-1: Net utilised solar energy and solar fraction as a function of the mantle inlet position.

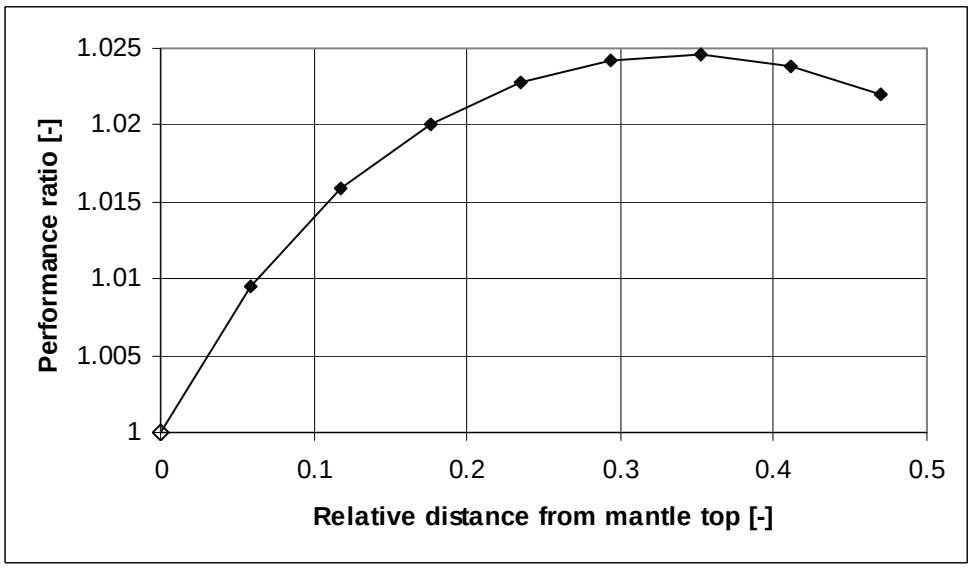

Figure 9-2: Performance ratio as a function of the mantle inlet position.

Figure 9-1 shows the net utilised solar energy and the solar fraction as a function of the different mantle inlet positions (shown as the relative distance from the mantle top). All other system parameters are equal to the parameters of the reference system. The figure shows that the thermal performance of the system increases for inlet positions moved from the top and down to a relative position of 0.35 from the mantle top, and the thermal performance of the system decreases if the inlet position is moved further down. Figure 9-2 shows the performance ratio as a function of the different mantle inlet positions and the system with top inlet position is used as the reference in the

performance ratio. It is seen that the net utilised solar energy of the system can be increased by more than 2% by moving the inlet port down to a relative position of 0.35.

9.3 Size of mantle inlet port

The thermal experiments in section 4.2 showed that the size of the mantle inlet port has a minor effect on the thermal stratification in the mantle and the inner tank, and the CFD-calculations in section 6.5 showed that the size of the mantle inlet port has a small effect on the heat flux profile at the mantle wall and on the flow structure in the mantle. In this investigation the following inlet sizes (inner diameter) are taken into calculation: 0.0189 m (½"), 0.0244 m (3/4"), 0.0306 m (1"), 0.0452 m (1½") and 0.057 m (2"). In all the calculations, the mantle inlet is located at a relative distance of 0.35 from the mantle top.

Figure 9-3 shows the net utilised solar energy and the solar fraction as a function of the different mantle inlet sizes. All other system parameters are equal to the parameters of the reference system. The figure shows that there is a small increase in the thermal performance by increasing the size of the mantle inlet port. Figure 9-4 shows the performance ratio as a function of the inlet size, the system with the inlet size of 0.0244 m is used as the reference. It appears that the effect of changing the mantle inlet size is very small (<0.2%).

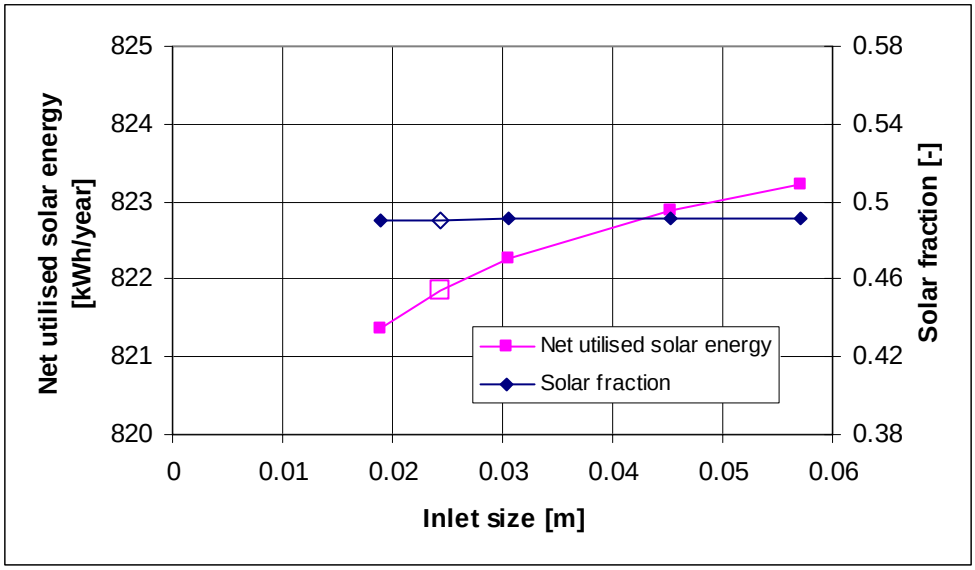

Figure 9-3: Net utilised solar energy and solar fraction as a function of the mantle inlet size.

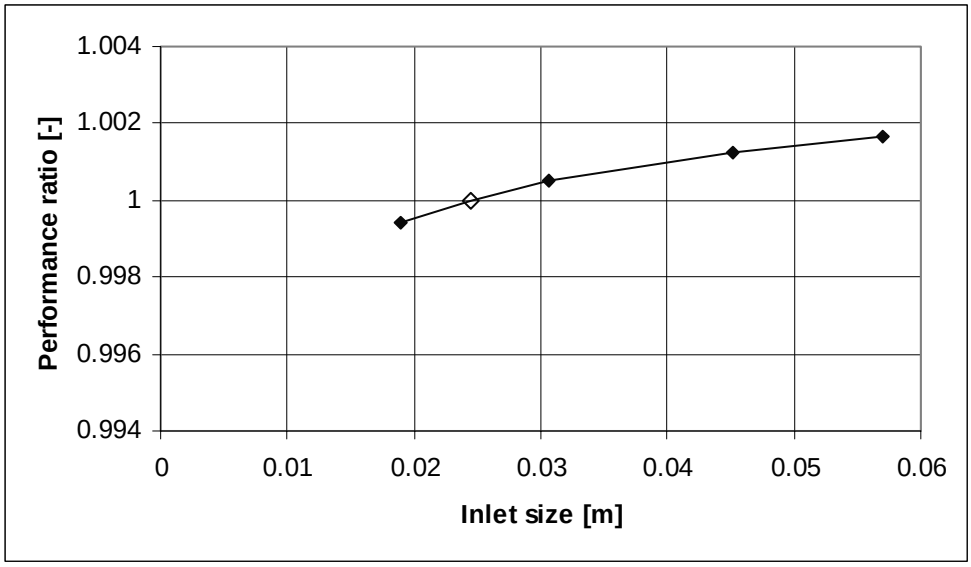

Figure 9-4: Performance ratio as a function of the mantle inlet size.

9.4 Size of mantle gap

The CFD-calculations in section 6.6 showed that the mantle gap has a significant influence on the heat flux profile at the mantle wall and on the flow structure in the mantle. In this section it is investigated how the mantle gap influences the yearly thermal performance of the system. The following mantle gap widths are taken into calculation: 0.0025 m, 0.005 m, 0.0105 m (reference), 0.02 m, 0.03 m, 0.04 m, 0.05 m, 0.06 m and 0.07 m. In all calculations, the mantle inlet is located at the top of the mantle.

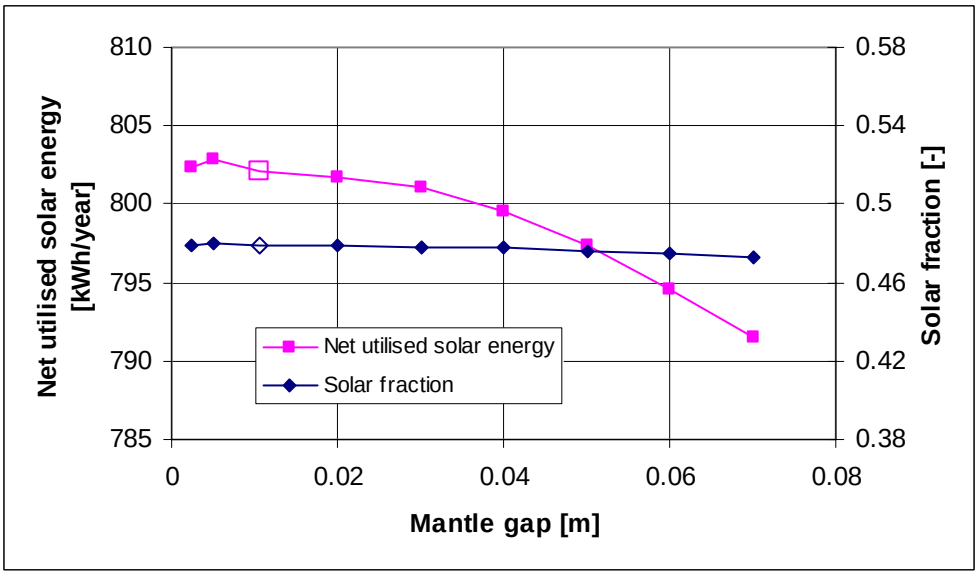

Figure 9-5: Net utilised solar energy and solar fraction as a function of the mantle gap width.

Figure 9-5 shows the net utilised solar energy and the solar fraction as a function of the mantle gap. All other system parameters are equal to the parameters of the reference system. The figure shows that the thermal performance is decreasing with increasing mantle gap widths, and a mantle gap of 0.005 m gives the best thermal performance. Figure 9-6 shows the performance ratio as a function of the mantle gap, and it is seen that the decrease in thermal performance is up to 1.5%.

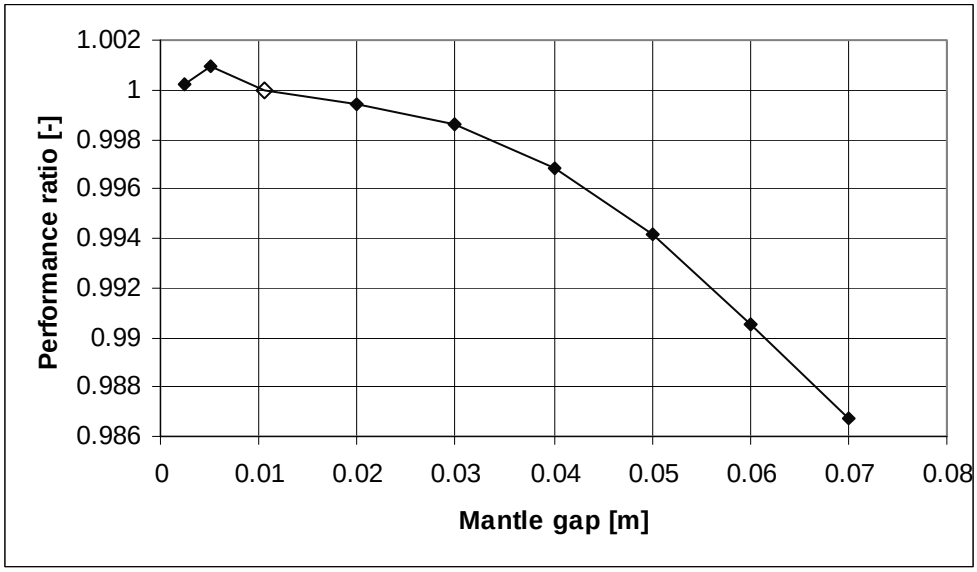

Figure 9-6: Performance ratio as a function of the mantle gap width.

There is inconsistency in previous investigations on the effect of changing the mantle gap width. In theoretical investigations, Furbo and Carlsson (1991) and Furbo and Jensen (1995) found that the mantle gap had a minor effect on the thermal performance of the system, but the numerical model used in both investigations used convective heat transfer coefficients that were independent of the mantle gap. Shah and Furbo (1996) found in a theoretical investigation that the thermal performance of the system increased with increasing mantle gap widths, and in an experimental investigation, Shah (1997) also found that the thermal performance of the system increased with increasing mantle gap widths. Later, by means of MantlSim, Shah (1999) found that the thermal performance of the system decreased with increasing mantle gap widths, and concluded that the results were due to the fact that the old version of MantlSim did not take mixing in the mantle into account. However, in this study MantlSim is developed to take the mixing in the mantle into account. It is a possibility, that there still is some positive effects on the flow field in the mantle by increasing the mantle gap that MantlSim is not able to model, but it could also be that these positive effects are overshadowed by the increased heat loss from the storage due to the wider mantle. The insulation thickness is constant in the investigation, and the overall heat loss coefficient for the heat storage is therefore increasing for increasing mantle gap. Figure 9-7 shows the net utilised solar energy and the heat loss from the storage as a function of the mantle gap. It appears that there is a considerable increase in the heat loss for larger mantle gaps. In fact, when the Danlager 1000 mantle tank is sold to customers, it is mounted inside a cabinet with a cross section area of 0.6x0.6 m², and if the mantle gap is increased there is less space for

insulation. This will further increase the heat loss and reduce the thermal performance more than shown in Figure 9-5 to Figure 9-7. The flow regime in the mantle might change to be more like duct flow for mantle gap widths smaller than 0.01 m (Rosengarten, 2000) and therefore, the heat transfer correlations developed in this thesis might not be valid for the small mantle gap widths.

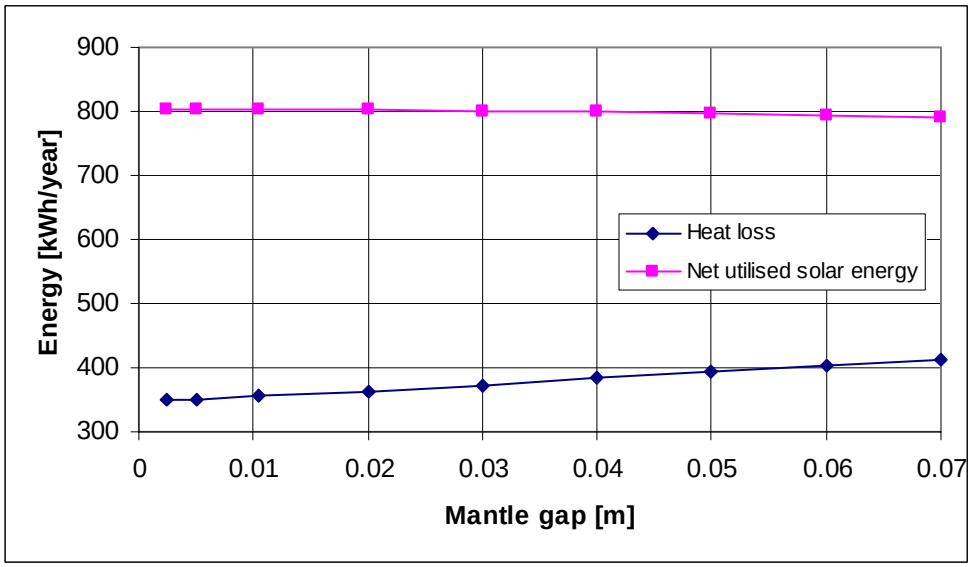

Figure 9-7: Net utilised solar energy and heat loss as a function of the mantle gap width.

9.5 Mantle height

The CFD-calculations in section 6.9 showed that the mantle height has a significant influence on the heat flux profile at the mantle wall and on the flow structure in the mantle. In this section it is investigated how the mantle height influences the yearly thermal performance of the system. In all calculations, the bottom of the mantle is placed at a distance of 0.057 m from the bottom of the tank to maintain the dead volume of 0.011 m^3, and the position of the top of the mantle is then changed to vary the mantle height. The mantle height is varied from 0.15 m to 0.61 m, and when the mantle height is more than 0.45 m then the upper part of the mantle is situated above the level of the auxiliary energy supply system in the inner tank. In all calculations, the mantle inlet is located at the top of the mantle.

Figure 9-8 shows the net utilised solar energy and the solar fraction as a function of the mantle height. All other system parameters are equal to the parameters of the reference system. The figure shows that the highest thermal performance is obtained with a mantle height of 0.25-0.30 m. Figure 9-9 shows the performance ratio as a function of the mantle height, the mantle height of 0.43 m is used as reference. It is seen that the net utilised solar energy can be increased by up to 5% by changing the mantle height from 0.43 m to 0.27 m.

These results are unexpected, or at least not in agreement with earlier results. Both Furbo and Jensen (1995) and Shah (1999) found that the top of the mantle should be

situated just below the level of the auxiliary energy supply system, because that maximises the heat exchange area without the auxiliary energy supply system heating the mantle fluid. If the top of the mantle is located above the level of the auxiliary energy supply system then the auxiliary system will heat up the mantle fluid and the thermal performance will decrease.

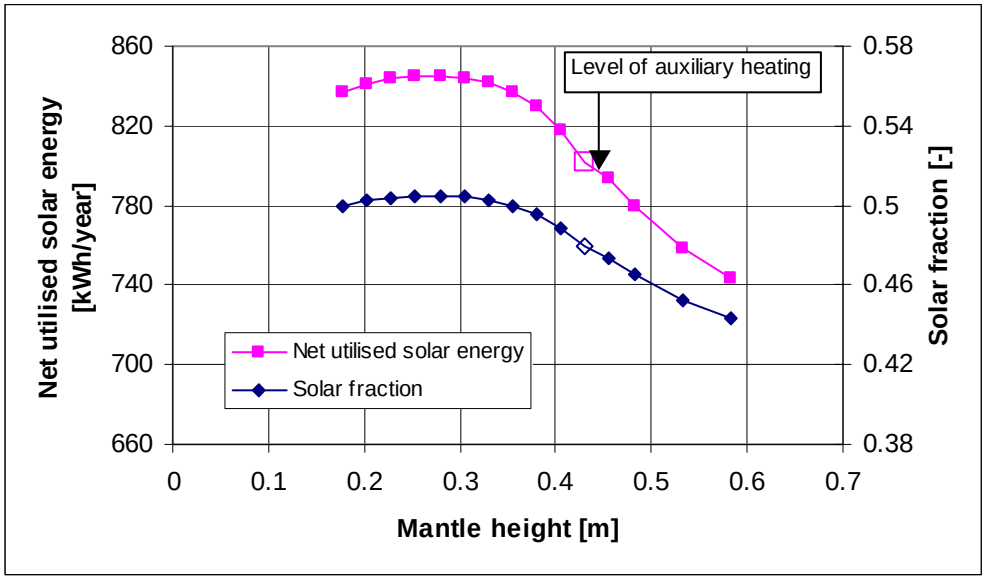

Figure 9-8: Net utilised solar energy and solar fraction as a function of the mantle height.

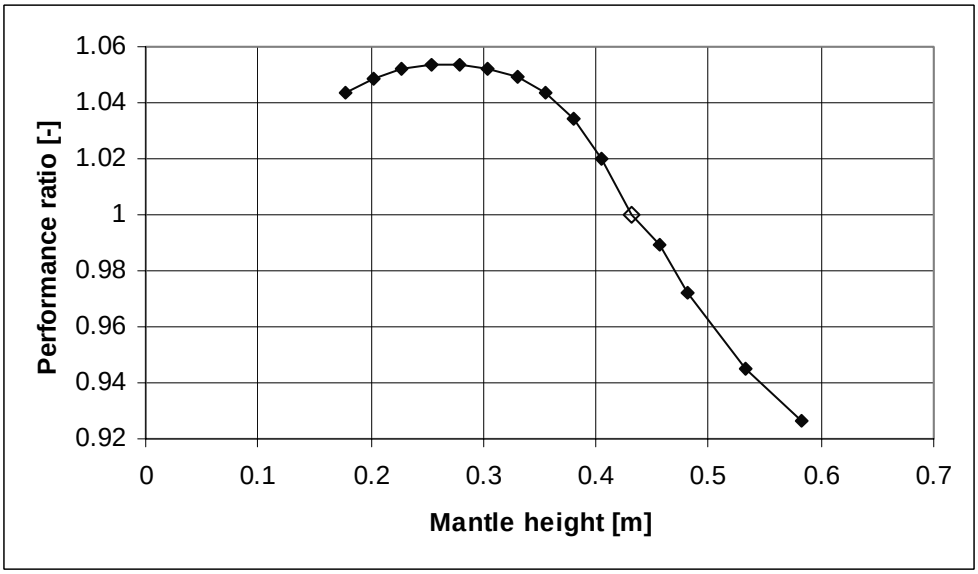

Figure 9-9: Performance ratio as a function of the mantle height.

The results obtained in this study tells that a decrease in the heat exchange area from 0.67 m² (mantle height = 0.43 m) to 0.42 m² (mantle height = 0.27 m) will increase the net utilised solar energy by up to 5%. The reason for these new results is probably that the new version of MantlSim takes the heat flow in the water in the inner tank into

consideration. Therefore, even for small mantle heights the natural convection flow inside the tank creates a high degree of stratification between the top of the mantle and the level of the auxiliary heating, and the heat loss decreases for a smaller mantle height. Furthermore, a smaller mantle height will reduce both the mixing in the mantle and the vertical heat conduction. However, the heat flow model presented in section 7.7 was developed based on CFD-calculations where the mantle covered either the lower half of the tank or all the tank height. The mantle height that gives the highest thermal performance in this study is when the mantle is covering less than one-third of the mantle height. There is a risk that when the mantle gets too small the model is not calculating the natural convection flow correctly and is over-predicting the effect of natural convection.

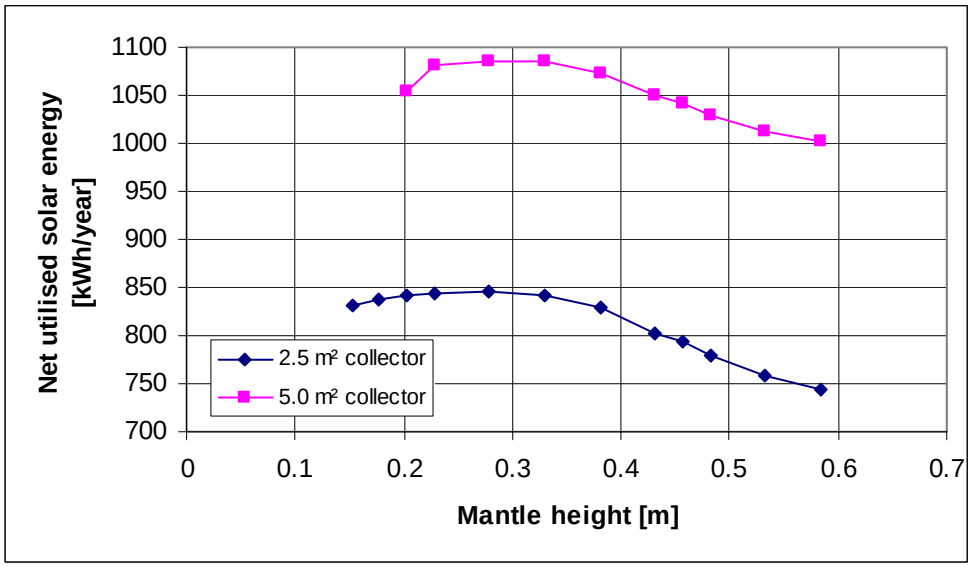

Figure 9-10: Net utilised solar energy as a function of the mantle height for two collector areas.

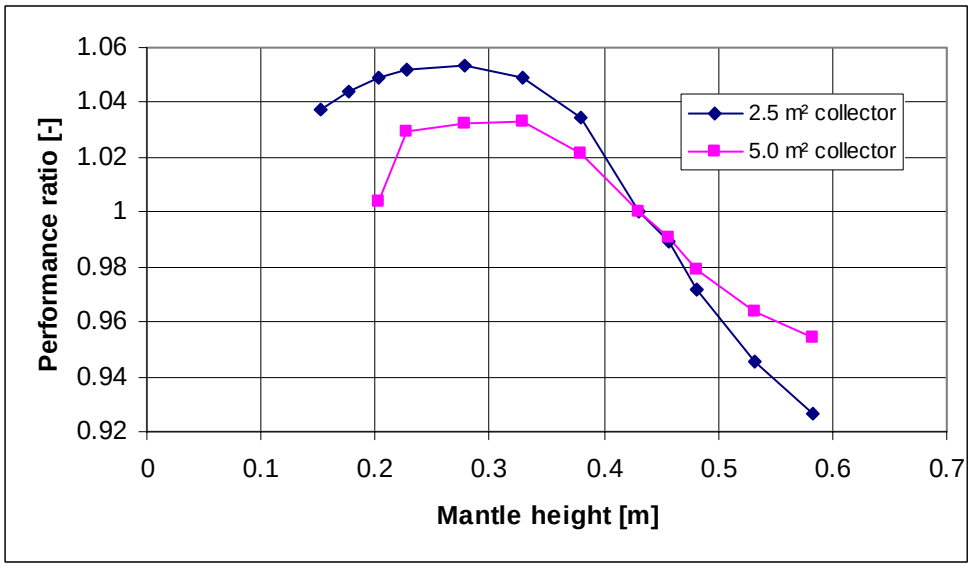

Figure 9-11: Performance ratio as a function of the mantle height for two collector areas.

On the other hand, if these results are true, it opens a new perspective in the mantle tank design because less material can be used (makes the mantle tank cheaper and less heavy) if only the bottom third of the tank should be covered by the mantle. But it needs to be verified by thermal experiments that the small mantle height is able to create a high degree of thermal stratification above the mantle, and the model for natural convection flow developed in section 7.7 should be further developed to be valid for smaller mantle heights.

Another factor that influences the results is that the investigation is carried out with a collector area of 2.5 m². Figure 9-10 shows net utilised solar energy as a function of the mantle height for a collector area of 2.5 m² and 5.0 m², respectively. It is seen that for a collector area of 5.0 m², a larger heat transfer area is needed and a mantle height of 0.33 m gives the best thermal performance. Figure 9-11 shows the performance ratio as a function of the mantle height for a collector area of 2.5 m² and 5.0 m², respectively. A mantle height of 0.43 is used as reference in the performance ratio for the two collector areas. It is seen that, when the collector area is increased, the relative improvement of decreasing the mantle height is smaller.

9.6 H/D ratio of tank

In this section it is investigated how the H/D ratio of the tank influences the yearly thermal performance of the system. The following H/D ratios are taken into calculation: 2 (reference), 3, 4 and 5. The inlet to the mantle is located at the top of the mantle in all calculations, and the mantle height is varied to keep the same fraction between the auxiliary volume and the solar volume.

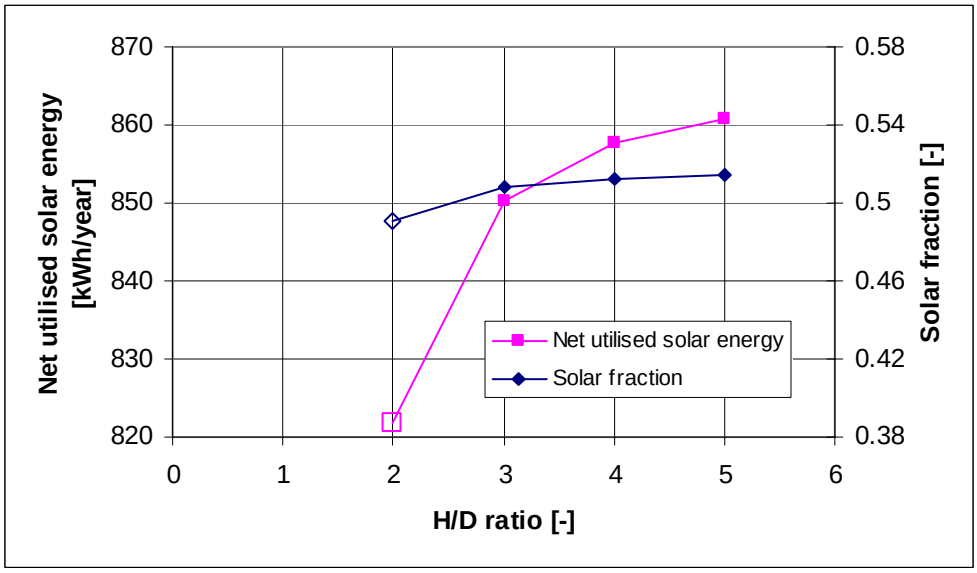

Figure 9-12: Net utilised solar energy and solar fraction as a function of the H/D ratio of the tank.

Figure 9-12 shows the net utilised solar energy and the solar fraction as a function of the H/D ratio of the tank. It appears that the thermal performance increases with increasing H/D ratios. Figure 9-13 shows the performance ratio as a function of the H/D ratio of

the tank and it is seen that the net utilised solar energy increases by about 4% if the H/D ratio is increased from 2 to 5. When the H/D ratio is increased, the thermal stratification in the inner tank will also be increased, as the distance between top and bottom of the tank is increased. Furthermore, the heat transfer area is increased when the H/D ratio is increased. The heat loss from the tank is also increased when the H/D ratio is increased, but this is for H/D ratio between 2 and 5 overshadowed by the increase in heat transfer area and thermal stratification. If larger H/D ratios than 5 were investigated, the net utilised solar energy would at some point start to decrease because the increasing heat loss gets more and more dominating.

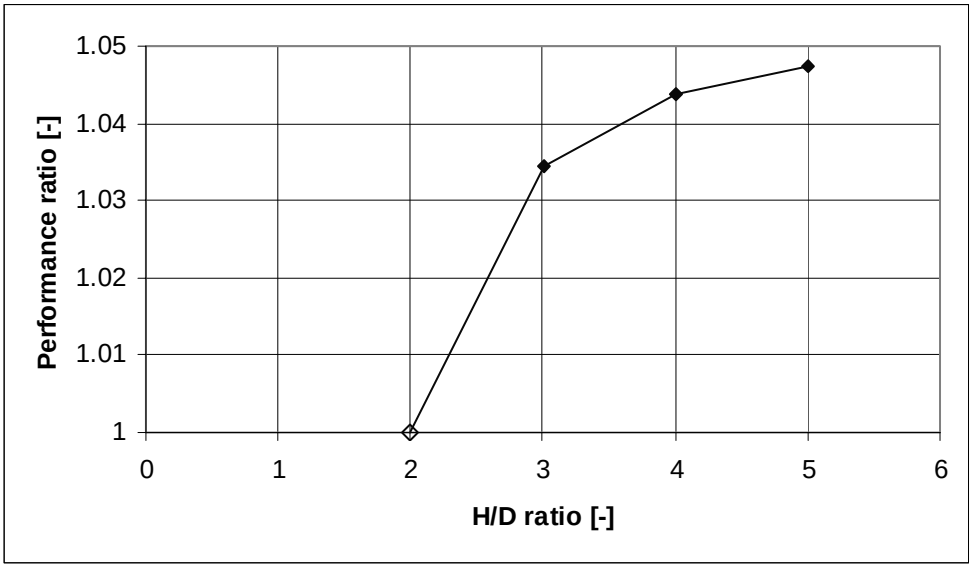

Figure 9-13: Performance ratio as a function of the H/D ratio of the tank.

9.7 Auxiliary volume

In this section it is investigated how the auxiliary volume influences the yearly thermal performance of the system. The auxiliary volume is varied from 39 l to 82 l (reference). The mantle inlet is located at the top of the mantle in all calculations.

Figure 9-14 shows the net utilised solar energy and the solar fraction as a function of the auxiliary volume. It is seen that the thermal performance increases with decreasing auxiliary volumes. This result is expected as a larger auxiliary volume will increase both the auxiliary energy demand and the heat loss, and thus decrease the net utilised solar energy. The storage capacity for the solar energy is increased with decreasing auxiliary volume, and this also influences the result. Figure 9-15 shows the performance ratio as a function of the auxiliary volume, and it is seen that the net utilised solar energy increases about by 19% by decreasing the auxiliary volume from 82 l to 39 l. The auxiliary volume should be as small as possible while still meeting the demand of hot water.

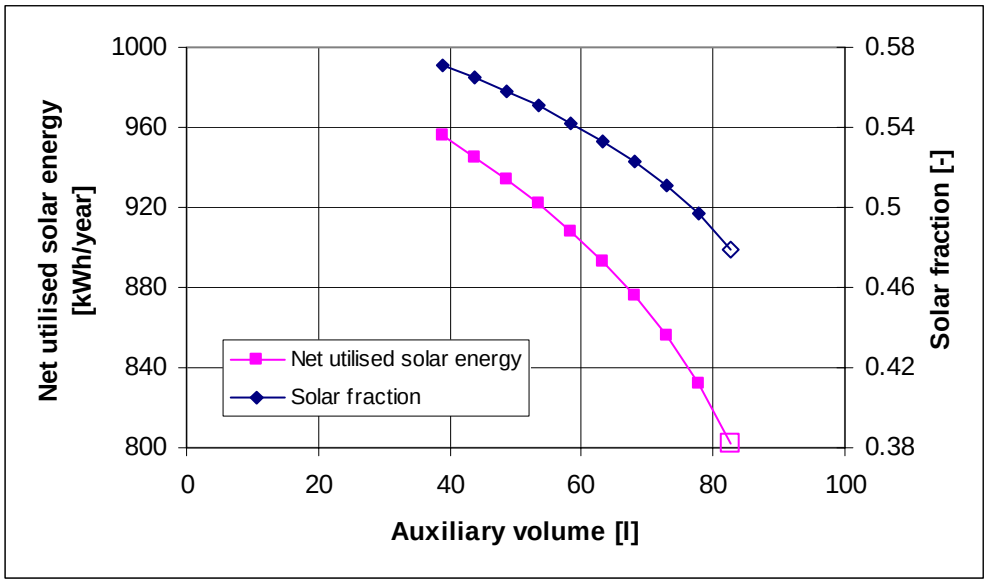

Figure 9-14: Net utilised solar energy and solar fraction as a function of the auxiliary volume.

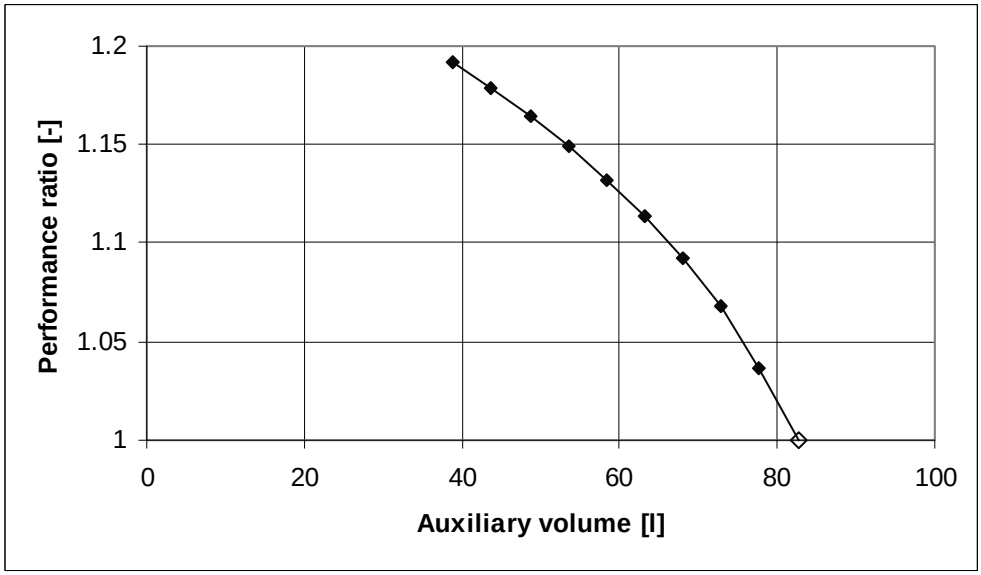

Figure 9-15: Performance ratio as a function of the auxiliary volume.

9.8 Thermal conductivity of tank material

In this section it is investigated how the thermal conductivity of the tank material influences the yearly thermal performance of the system. The thermal conductivity is varied from 15 W/m·K to 60 W/m·K (reference). The mantle inlet is in all the calculations located at a relative distance of 0.35 from the mantle top.

Figure 9-16 shows the net utilised solar energy and the solar fraction as a function of the thermal conductivity. It appears that the thermal performance increases with decreasing

thermal conductivity. This result is expected as the vertical heat conduction in the tank material (decreasing the thermal stratification) is reduced when the thermal conductivity is decreased. Figure 9-17 shows the performance ratio as a function of the thermal conductivity, and it is seen that the net utilised solar energy is increased by about 10% by changing the thermal conductivity from 60 W/m·K to 15 W/m·K. A wall thickness of 2 mm can be used for stainless steel because it is stronger than normal steel. If 2 mm stainless steel with thermal conductivity of 15 W/m·K is used the net utilised solar energy is increased by 12% compared to 3 mm normal steel with thermal conductivity of 60 W/m·K.

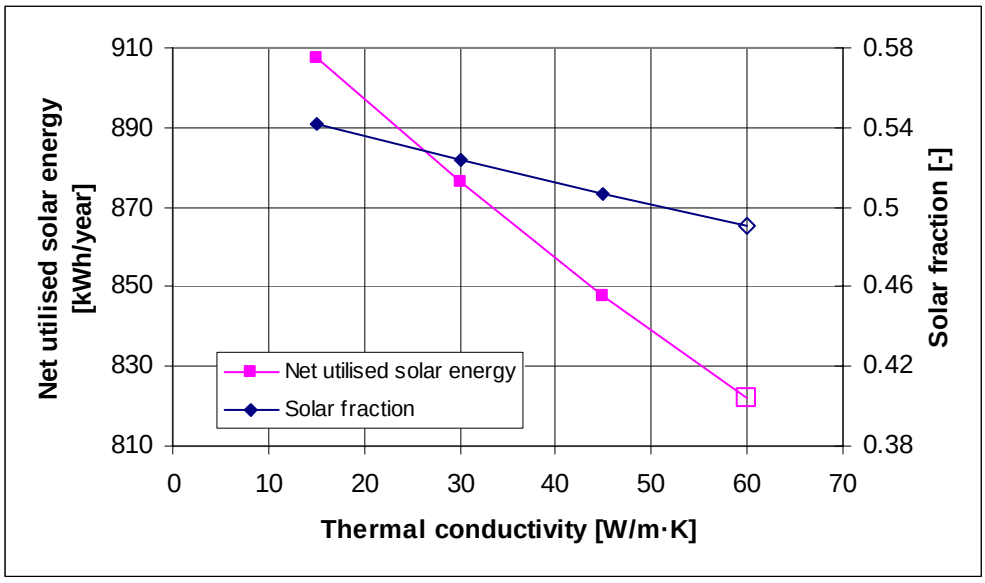

Figure 9-16: Net utilised solar energy and solar fraction as a function of the thermal conductivity of the tank material.

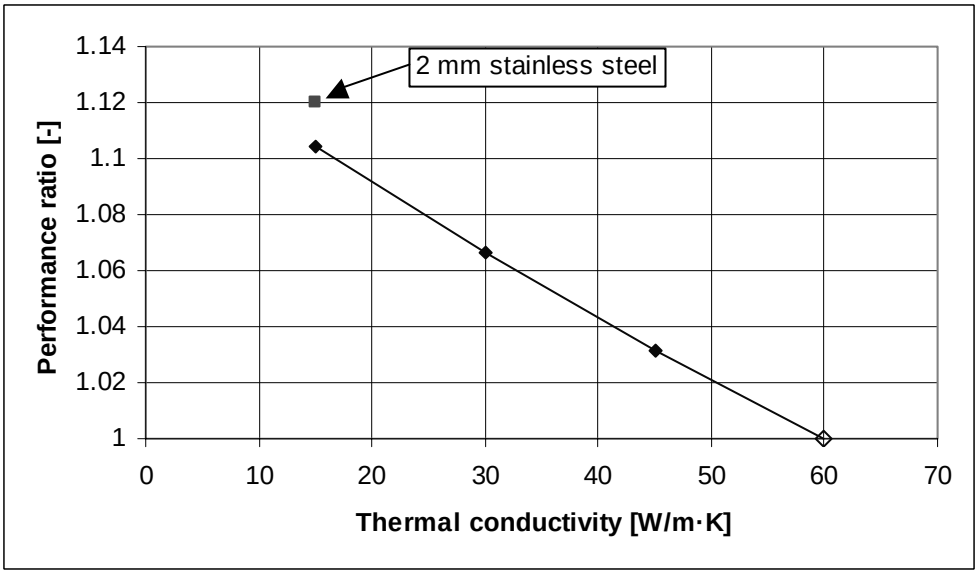

Figure 9-17: Performance ratio as a function of the thermal conductivity of the tank material.

9.9 Insulation of mantle tank

In this section it is investigated how the insulation of the mantle tank influences the thermal performance of the system. In all the calculations in this section, the mantle inlet is located at a relative distance of 0.35 from the mantle top.

Figure 9-18 shows the net utilised solar energy and the solar fraction as a function of the top insulation thickness. The figure shows that the thermal performance of the system increases with increasing insulation thickness at the top.

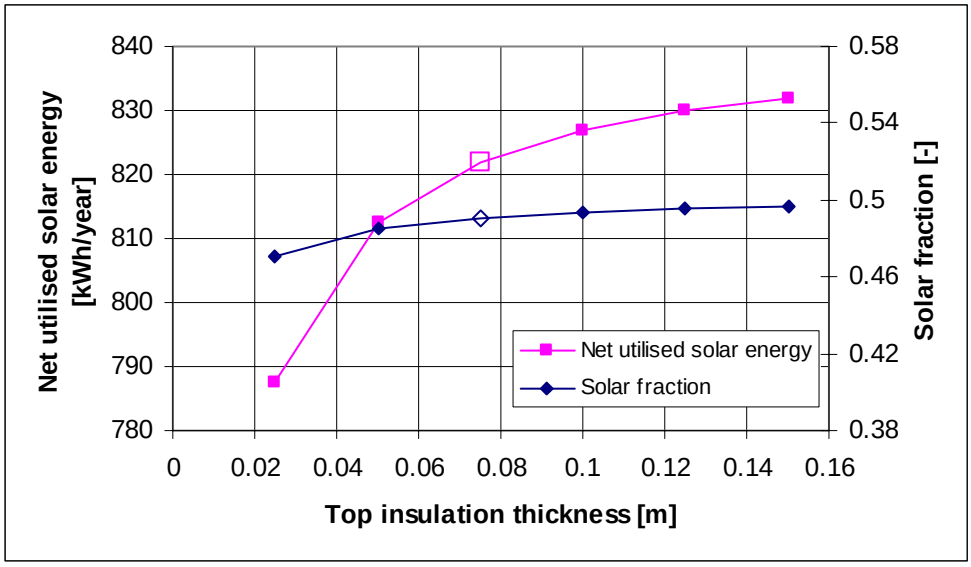

Figure 9-18: Net utilised solar energy and solar fraction as a function of the insulation thickness of the top of the tank.

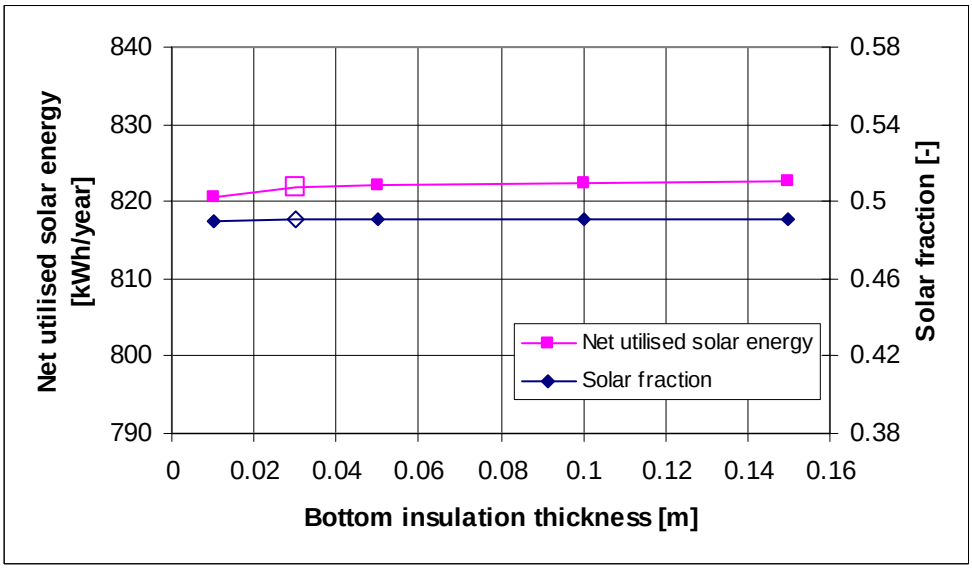

Figure 9-19: Net utilised solar energy and solar fraction as a function of the insulation thickness of the bottom of the tank.

Figure 9-19 shows the net utilised solar energy and the solar fraction as a function of the bottom insulation thickness. It is seen that the thermal performance is almost independent of the bottom insulation thickness because the temperature of the water in the bottom of the tank is normally lower than the ambient temperature.

Figure 9-20 shows the net utilised solar energy and the solar fraction as a function of the insulation thickness of the sides of the tank. The figure shows that the thermal performance of the system increases with increasing insulation thickness at the sides.

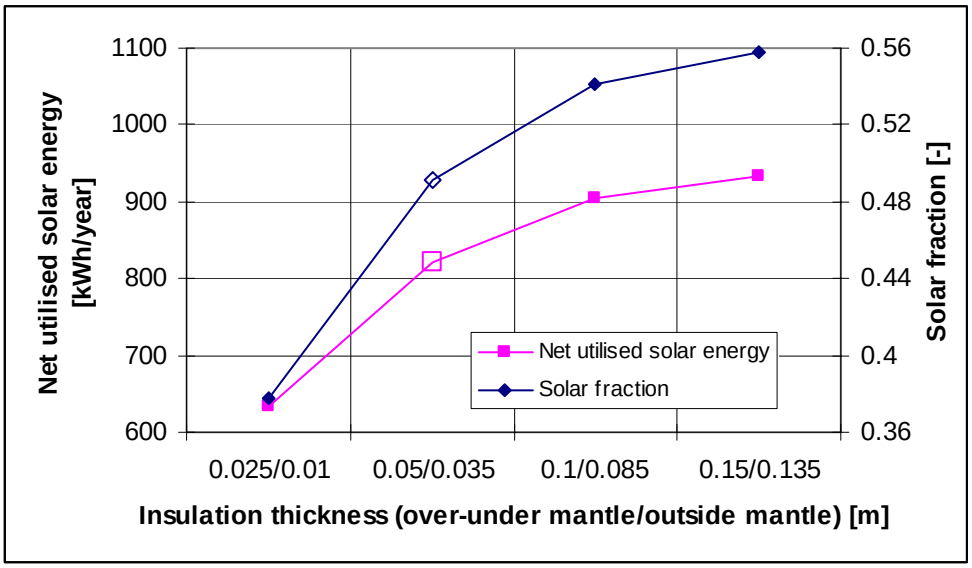

Figure 9-20: Net utilised solar energy and solar fraction as a function of the insulation thickness of the sides of the tank.

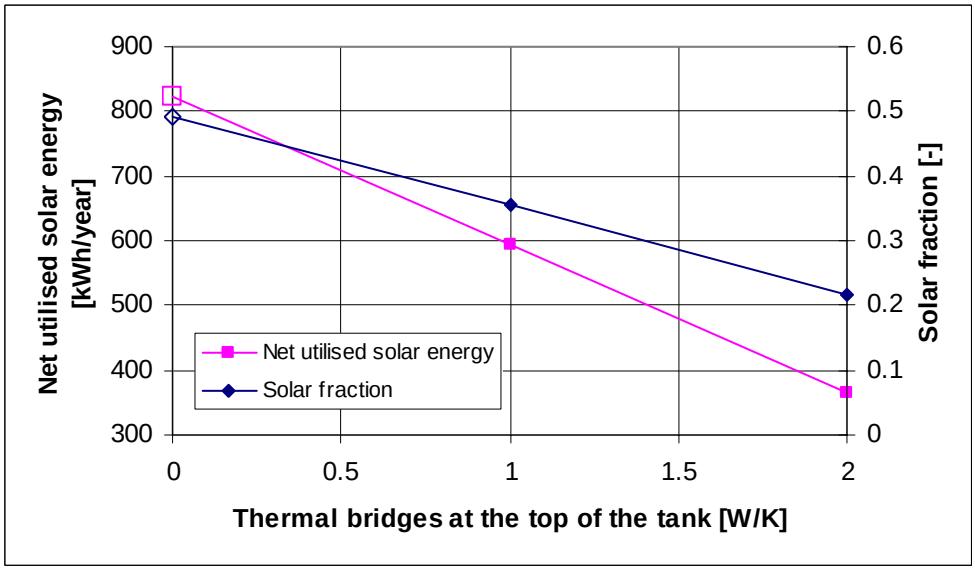

Figure 9-21: Net utilised solar energy and solar fraction as a function of the thermal bridges at the top of the tank.

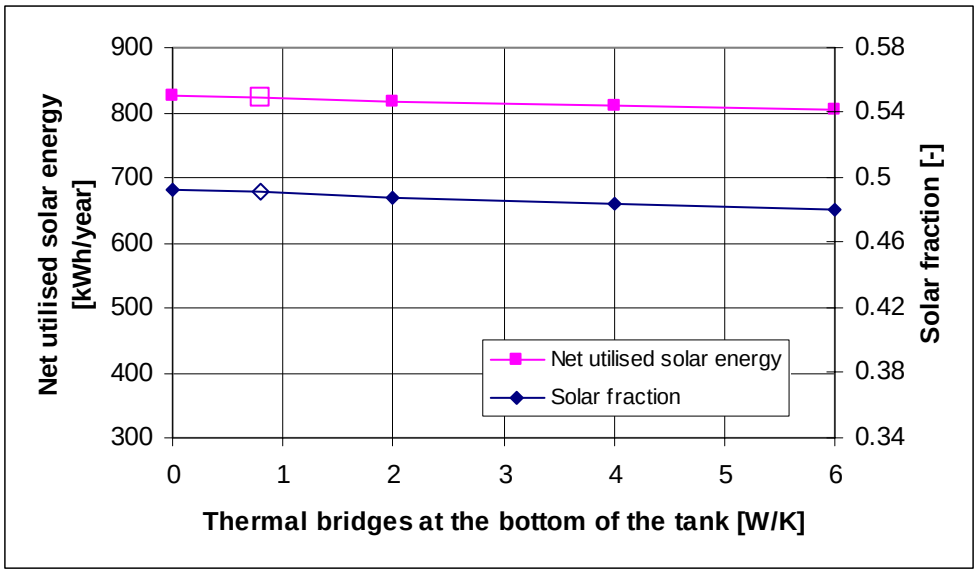

Figure 9-22: Net utilised solar energy and solar fraction as a function of the thermal bridges at the bottom of the tank.

Figure 9-21 shows the net utilised solar energy and the solar fraction as a function of the thermal bridges at the top of the tank. The figure shows that the thermal performance of the system decreases with increasing thermal bridges at the top, and the thermal bridges at the top can have a severe influence on the thermal behaviour of the system.

Figure 9-22 shows the net utilised solar energy and the solar fraction as a function of the thermal bridges at the bottom of the tank. As for the bottom insulation thickness, the thermal performance is almost independent of this parameter.

The investigations in this section concerning the insulation of the mantle tank showed that it is important to avoid thermal bridges at the top of the tank and that the thermal performance of the system is also very dependent on the insulation thickness at the sides and at the top. The thermal performance showed to be almost independent of the bottom insulation and thermal bridges at the bottom of the tank.

9.10 Sensitivity of mantle inlet position

It was shown in section 9.2 that the thermal performance of the system could be improved by moving the mantle inlet position down to a relative distance of 0.35 from the top of the mantle. In this section it is investigated how the effect of changing the mantle inlet position is influenced by hot-water consumption, mantle gap, mantle height, H/D ratio of tank and collector loop flow rate.

9.10.1 Hot-water consumption

The investigation from section 9.2 is here supplied with an identical investigation where the daily hot-water consumption is 0.160 m³/day heated from 10ºC to 50ºC, which is tapped from the tank in three equally large parts at 7 am, 12 am and 7 pm. The yearly hot-water consumption is 2679 kWh.

Figure 9-23 shows the net utilised solar energy as a function of the different mantle inlet positions (shown as the relative distance from the mantle top) for the two hot-water consumptions. All other system parameters are equal to the parameters of the reference system. Figure 9-24 shows the performance ratio as a function of the different mantle inlet positions, and the system with top inlet position for each of the two hot-water consumptions is used as the reference in the performance ratio. It is seen from the figures that the relative improvement of moving the mantle inlet down is smaller for the large hot-water consumption, and that the best inlet position is closer to the mantle top for the large hot-water consumption. The reason for this is that when the hot-water consumption is increased then the temperature of the water in the inner tank at the level of the upper part of the mantle will decrease, and therefore the negative effect of warm mantle inlet temperatures will be reduced.

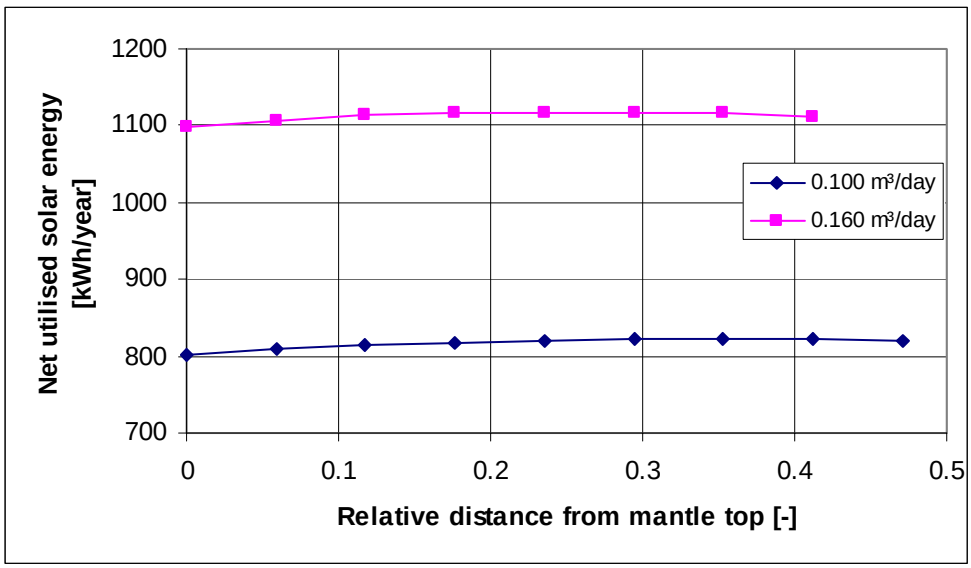

Figure 9-23: Net utilised solar energy as a function of the mantle inlet position for two hot-water consumptions.

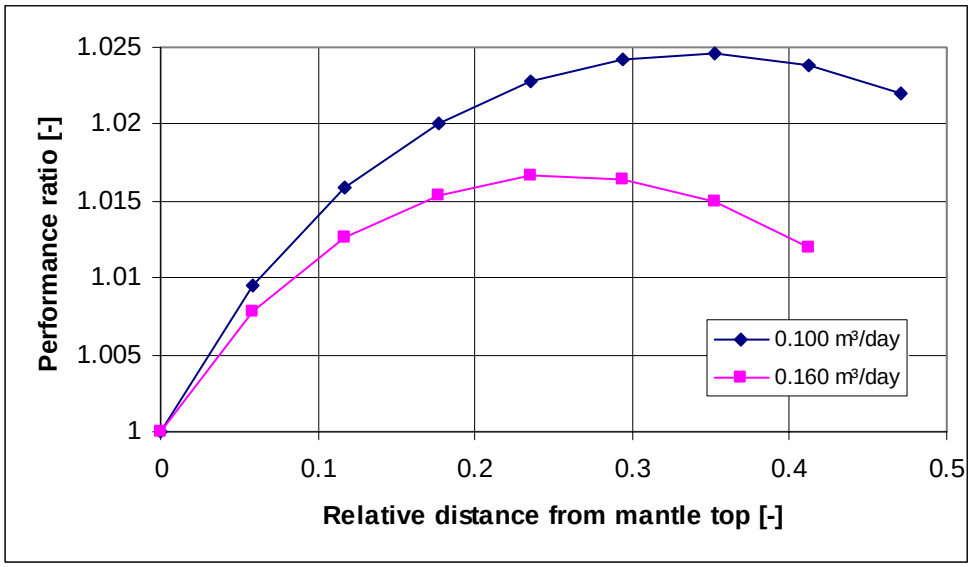

Figure 9-24: Performance ratio as a function of the mantle inlet position for two hot-water consumptions.

9.10.2 Mantle gap

The investigation from section 9.2 is here supplied with two identical investigations where the mantle gap is 0.03 m and 0.05 m, respectively.

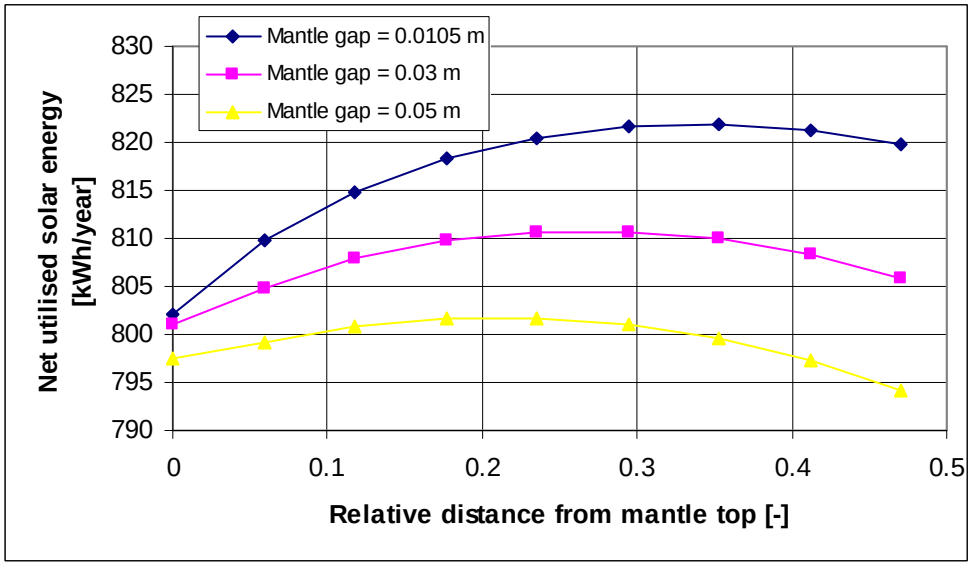

Figure 9-25: Net utilised solar energy as a function of the mantle inlet position for three mantle gap widths.

Figure 9-25 shows the net utilised solar energy as a function of the different mantle inlet positions (shown as the relative distance from the mantle top) for the three mantle gaps.

All other system parameters are equal to the parameters of the reference system. Figure 9-26 shows the performance ratio as a function of the different mantle inlet positions, and the system with top inlet position for each of the mantle gaps is used as the reference in the performance ratio. It is seen from the figures that the relative improvement of moving the mantle inlet down is smaller for increasing mantle gaps. This result is expected, as the negative effect of mixing in the mantle is reduced for increasing mantle gaps.

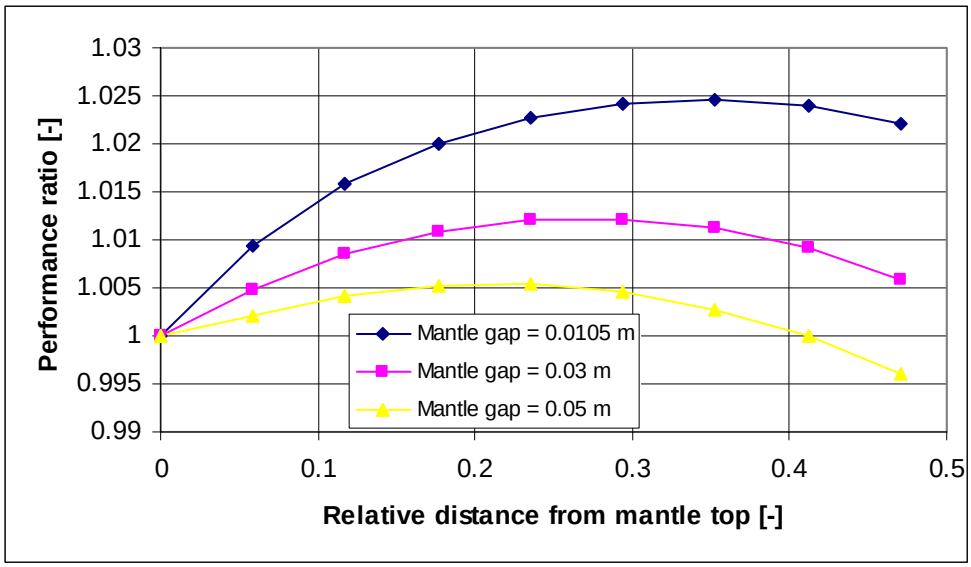

Figure 9-26: Performance ratio as a function of the mantle inlet position for three mantle gaps.

9.10.3 Mantle height

The investigation from section 9.2 is here supplied with nine identical investigations where the mantle height is varied between 0.23 m and 0.53 m.

Figure 9-27 shows the net utilised solar energy as a function of the different mantle inlet positions (shown as the relative distance from the mantle top) for the different mantle heights. All other system parameters are equal to the parameters of the reference system. Figure 9-28 shows the performance ratio as a function of the different mantle inlet positions, and the system with top inlet position for each of the mantle heights is used as the reference in the performance ratio. It is seen from the figures that the relative improvement of moving the mantle inlet down is largest for increasing mantle heights. The improvement in thermal performance is especially large when the top of the mantle is located above the level of the auxiliary energy supply system (H=0.53 m, H=0.48 m and H=0.46 m), because with these designs the temperature in the upper part of the mantle is always high and therefore the part of the operation time with warm mantle inlet temperatures will be increased. For small mantle heights it has little effect to move the mantle inlet position away from the top of the mantle because with these designs the top of the mantle is relatively far away from the level of the auxiliary energy supply system, and the temperature in the inner tank at the level of the upper part of the mantle is therefore lower.

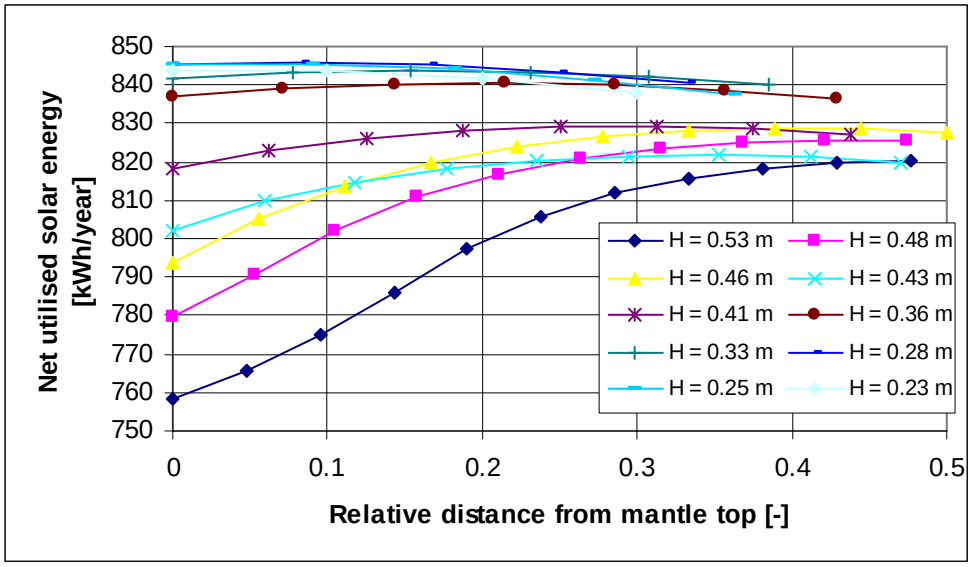

Figure 9-27: Net utilised solar energy as a function of the mantle inlet position for ten mantle heights.

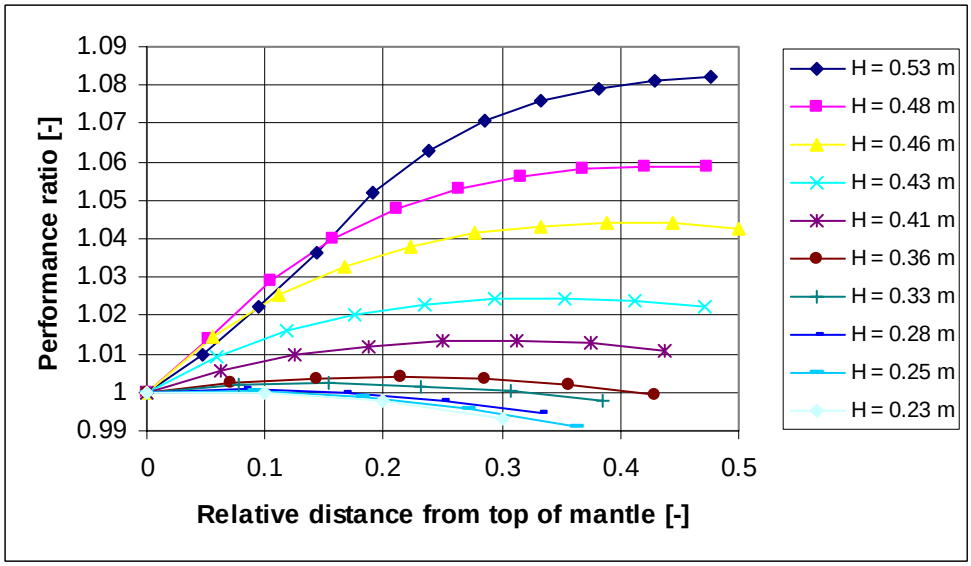

Figure 9-28: Performance ratio as a function of the mantle inlet position for ten mantle heights.

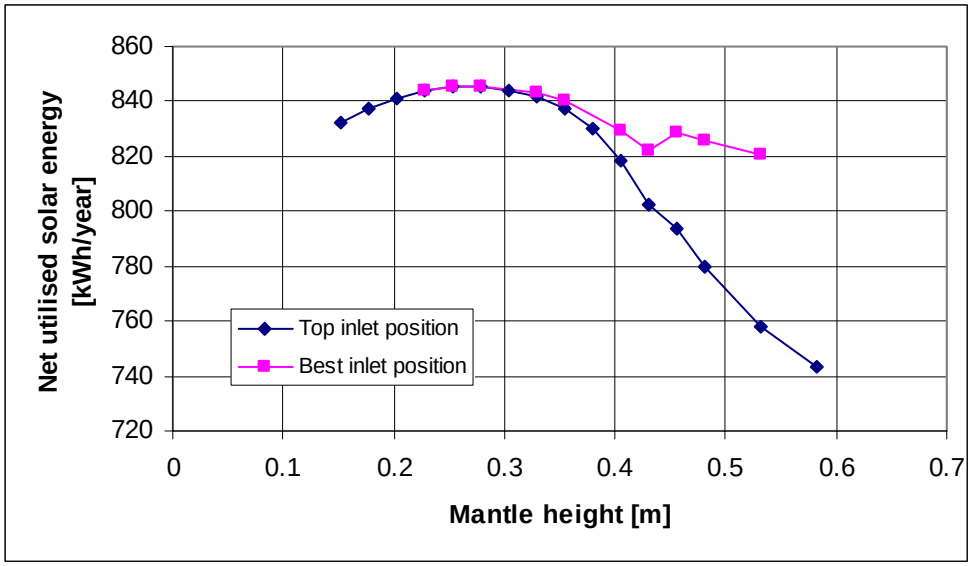

Figure 9-29: Net utilised solar energy as a function of the mantle height.

Figure 9-29 shows the net utilised solar energy as a function of the mantle height for top mantle inlet position and for the optimum mantle inlet position for each mantle height. It appears that the mantle height of 0.27 m gives the best thermal performance both for top inlet position and when using the best inlet position for each mantle height. Furthermore, it is seen (as in Figure 9-27 and Figure 9-28) that for small mantle heights the top mantle inlet position gives the best thermal performance, and for larger mantle heights the thermal performance can be improved significantly by moving the mantle inlet down to a lower position.

9.10.4 H/D ratio of tank

The investigation from section 9.2 is here supplied with three identical investigations where the H/D ratio of the tank is 3,4 and 5, respectively.

Figure 9-30 shows the net utilised solar energy as a function of the different mantle inlet positions (shown as the relative distance from the mantle top) for the four H/D ratios. All other system parameters are equal to the parameters of the reference system. Figure 9-31 shows the performance ratio as a function of the different mantle inlet positions, and the system with top inlet position for each of the H/D ratios is used as the reference in the performance ratio. It is seen from the figures that the relative improvement of moving the mantle inlet down is almost independent of the H/D ratio of the tank. The relative mantle inlet position that gives the highest net utilised solar energy is 0.35 for the H/D ratio of 2 and 0.29 for H/D ratios of 3, 4 and 5.

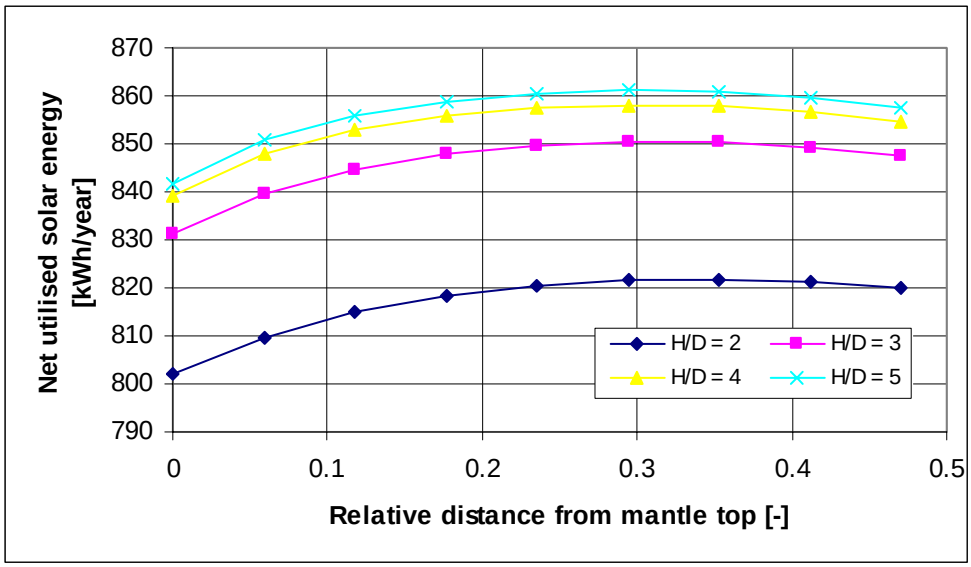

Figure 9-30: Net utilised solar energy as a function the mantle inlet position for four H/D ratios.

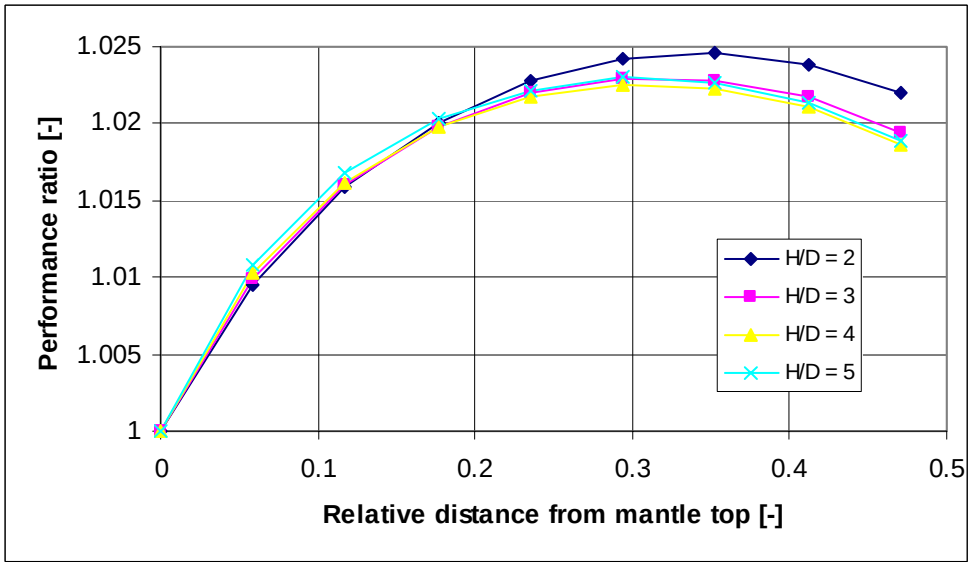

Figure 9-31: Performance ratio of the mantle inlet position for four H/D ratios.

9.10.5 H/D ratio of tank and mantle height

It was shown in section 9.5 that the thermal performance increased if the height of the mantle was reduced from 0.43 m to 0.27 m. The analysis concerning the influence of the H/D ratio on the thermal performance is here supplied with a variation of the mantle height. Figure 9-32 shows the net utilised solar energy as a function of the mantle height for different H/D ratios of the tank. A relative mantle height of 0.47 corresponds to a mantle height of 0.43 m for the reference tank. It is seen from the figure that for increasing H/D ratio of the tank, the thermal performance is also increasing for

decreasing mantle heights, until a certain level where the thermal performance starts to decrease. It is also seen that for mantle tanks with H/D ratios of 3, 4 and 5 a relative mantle height of 0.36 gives the highest thermal performance, while the relative mantle height should be 0.31 for mantle tanks with H/D ratio of 2.

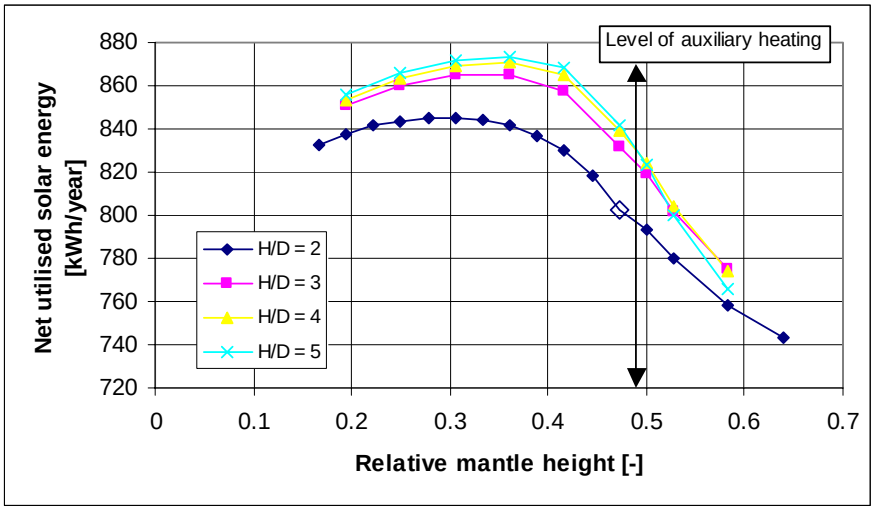

Figure 9-32: Net utilised solar energy as a function of the relative mantle height for different H/D ratios of the tank.

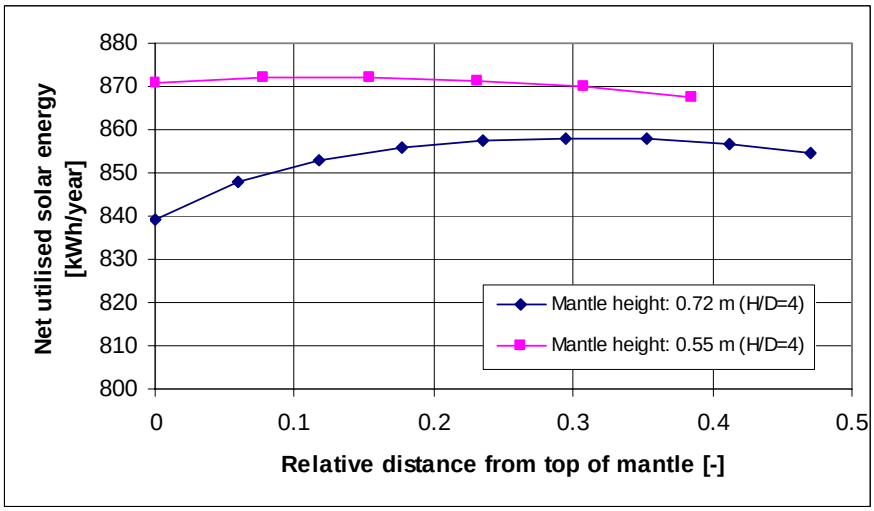

Figure 9-33: Net utilised solar energy as a function of the mantle inlet position for two mantle heights at H/D ratio of 4.

It was shown in section 9.10.3 that for smaller mantle heights it is preferable to locate the mantle inlet at the top of the mantle for a mantle tank with H/D ratio of 2. Figure 9-33 shows the net utilised solar energy as a function of the mantle inlet position for two mantle heights for the mantle tank with H/D ratio of 4. Mantle heights of 0.55 m and 0.72 m at an H/D ratio of 4 correspond to relative mantle heights of 0.36 and 0.47. It is seen that for the small mantle height, the net utilised solar energy is almost independent of the mantle inlet position.

9.10.6 Collector loop flow rate

The investigation from section 9.2 is here supplied with seven identical investigations where the collector loop flow rate is varied between 0.06 l/min/m² to 0.50 l/min/m².

The investigation is carried out in such a way that for each flow rate the stop temperature difference is varied to find the optimum stop temperature difference for each flow rate. Figure 9-34 shows the net utilised solar energy as a function of the stop temperature difference for each of the flow rates. The mantle inlet is located at the top of the mantle in the calculations shown in Figure 9-34. It appears from Figure 9-34 that the stop temperature difference has only a little influence on the net utilised solar energy of the systems. For most of the flow rates a stop temperature difference of 2 K is optimum.

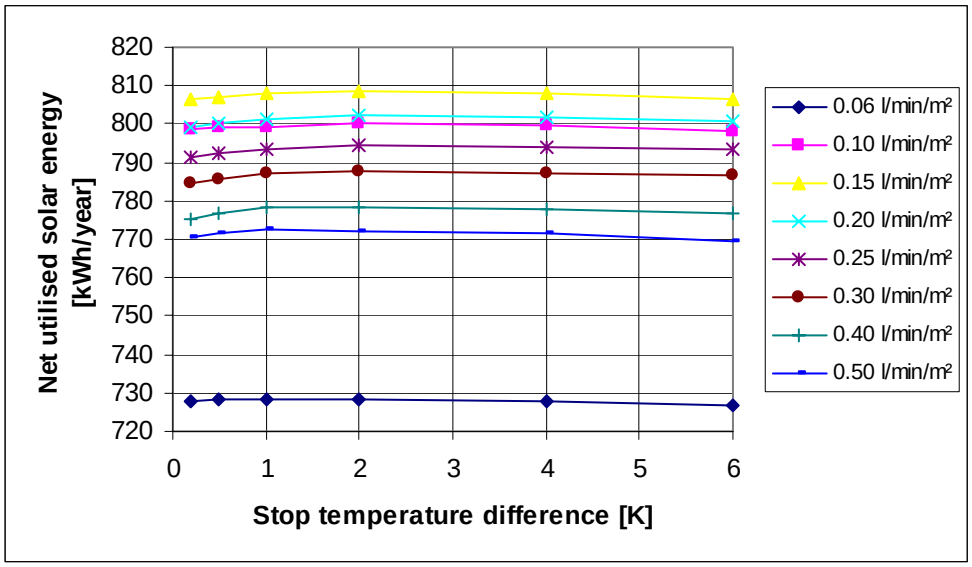

Figure 9-34: Net utilised solar energy as a function of the stop temperature difference for different flow rates.

Figure 9-35 shows the net utilised solar energy as a function of the different mantle inlet positions (shown as the relative distance from the mantle top) for the different flow rates using the optimum combination of flow rate and stop temperature difference. All other system parameters are equal to the parameters of the reference system. Figure 9-36 shows the performance ratio as a function of the different mantle inlet positions, and the system with top inlet position for each of the flow rates is used as the reference in the performance ratio. It is seen from the figures that the relative improvement of moving the mantle inlet down is increasing with increasing flow rates, and that for increasing flow rates the best inlet position is moving further away from the top of the mantle. This is due to the higher degree of mixing in the mantle for higher flow rates and lower return temperatures from the collector.

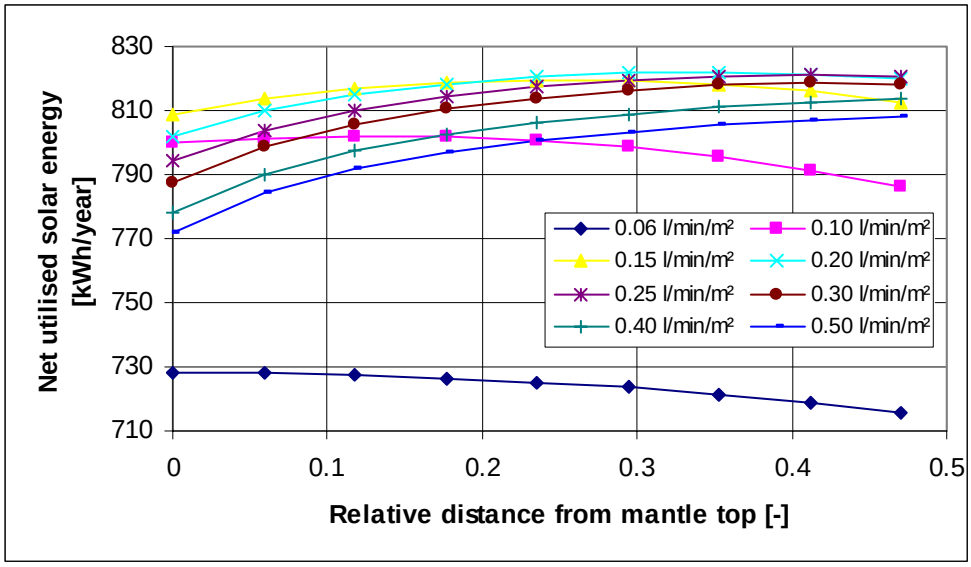

Figure 9-35: Net utilised solar energy as a function the mantle inlet position for different flow rates.

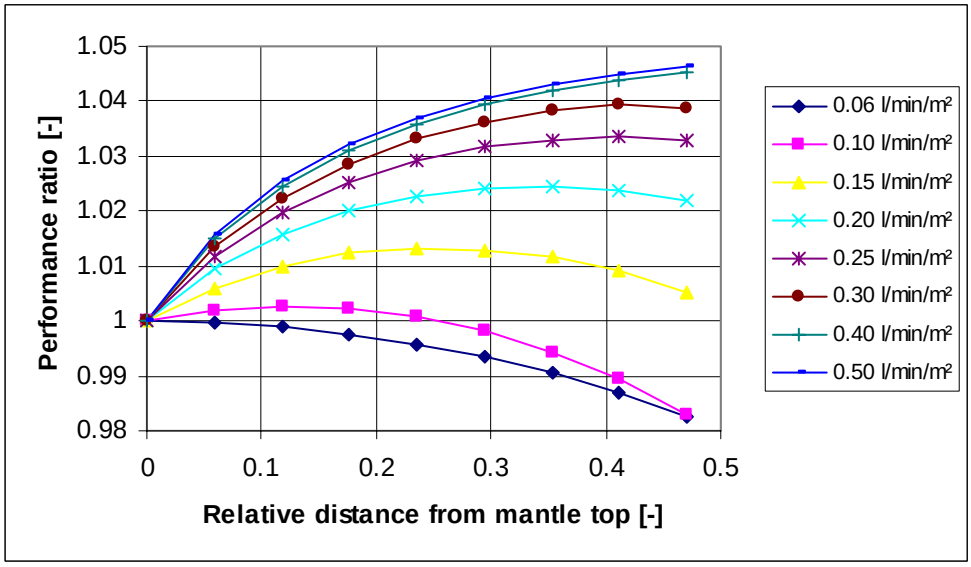

Figure 9-36: Performance ratio as a function of the mantle inlet position for different flow rates.

In Figure 9-37 the net utilised solar energy is shown as a function of the flow rate (using optimum stop temperature difference for each flow rate) for top mantle inlet and for the optimum mantle inlet position at each flow rate. It appears that with top inlet the optimum flow rate of the system is around 0.15 l/min/m², and with optimum mantle inlet position the optimum flow rate is around 0.20 l/min/m². Furthermore, it is seen for the top inlet case that there is a relatively larger decrease in the net utilised solar energy for flow rates above 0.20 l/min/m² than is seen in previous investigations of the flow rate in mantle tank systems (Furbo and Carlsson (1991) and Shah (1999)). The reason for this larger decrease is that the mixing in the mantle is now incorporated in the simulation program, and the mixing is increasing for increasing flow rates.

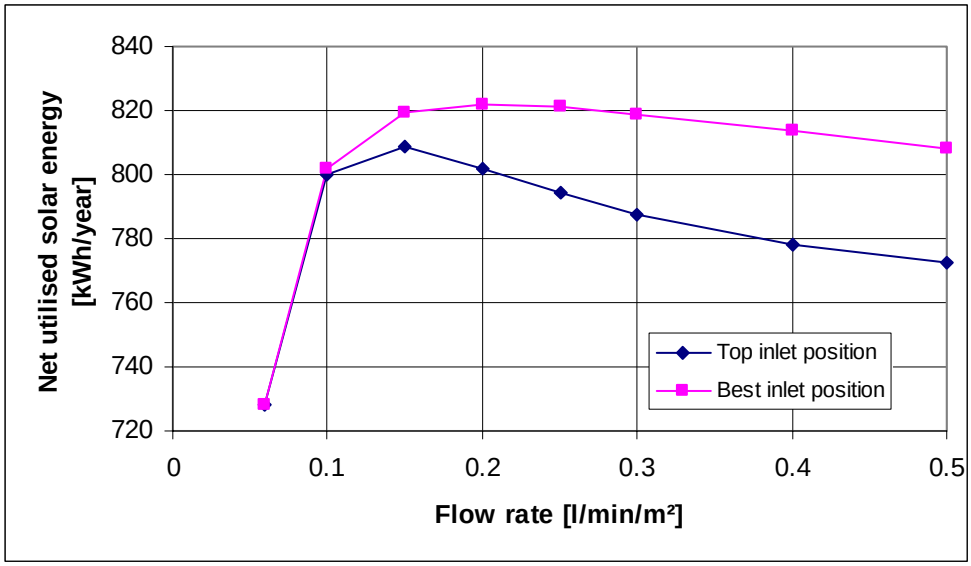

Figure 9-37: Net utilised solar energy as a function of the collector loop flow rate.

Figure 9-38 shows the net utilised solar energy as a function of the flow rate for two mantle heights with top mantle inlet. It is seen that the flow rate giving the highest thermal performance for the system with a mantle height of 0.27 m is 0.2 l/min/m². It is also seen that for the small mantle height the thermal performance is not decreasing as much for high flow rates as for the mantle height of 0.43 m. This shows that the negative effect of mixing in the mantle has a smaller impact for smaller mantle heights.

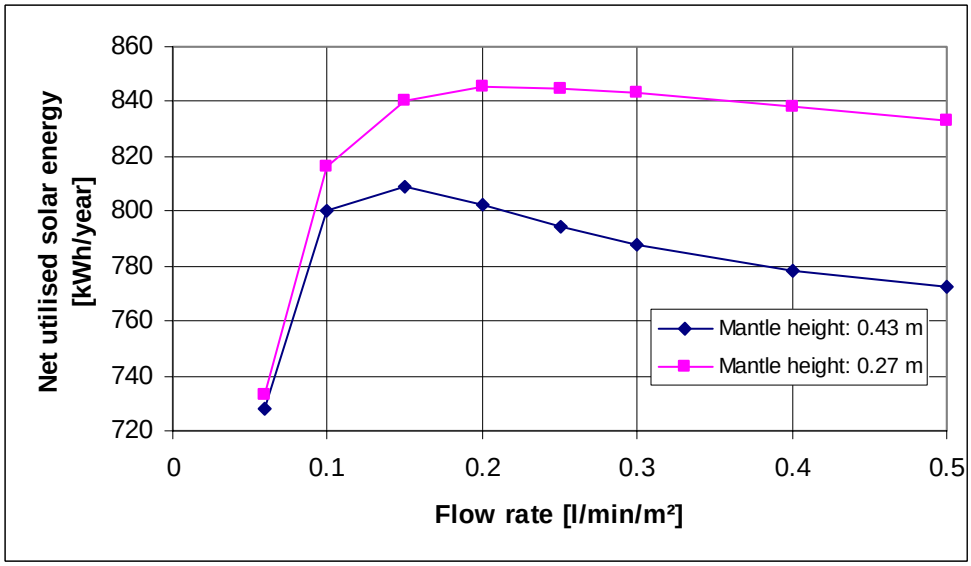

Figure 9-38: Net utilised solar energy as a function of the collector loop flow rate for two mantle heights with top mantle inlet.

9.11 Optimising the Danlager 1000 design

A number of parameter variations have been carried out so far in this chapter to reveal how the different tank parameters influence the thermal performance of low-flow SDHW systems. In this section the findings from the previous section are used to improve the design of the Danlager 1000 mantle heat exchanger by relatively simple geometrical changes. The change of the design is made in such a way that one parameter is changed at a time in the calculations. Table 9-1 gives data for the reference system in the calculations.

All the calculations are carried out with weather data from the Danish Test Reference Year (Statens Byggeforskningsinstitut, 1982). The daily hot-water consumption is 0.100 m³ heated from 10ºC to 50ºC, which is tapped from the tank in three equally large parts at 7 am, 12 am and 7 pm. The yearly hot-water consumption is 1674 kWh.

The following tank parameters are changed: H/D ratio of the tank, mantle height, insulation, thermal conductivity of the tank material and the wall thickness of tank and mantle.

Figure 9-39 shows the net utilised solar energy and the solar fraction as a function of the different changes in the mantle tank design. The first column shows the thermal performance of the system with the Danlager 1000 heat storage with mantle inlet position at the top of the mantle.

The first change is the H/D ratio of the tank, which is changed from a H/D ratio of 2 to a H/D ratio of 4. The total volume and the ratio between the auxiliary volume and the total volume are kept constant. The second change is the mantle height, which is decreased from 0.72 m to 0.55 m. The third change is the insulation of the tank. It is assumed that it should fit into a cabinet with dimensions 0.6x0.6x2.0 m³, and by increasing the H/D ratio the outer diameter is reduced, and the side insulation is increased with further 0.05 m. The fourth change is the tank material, which is changed from normal steel to stainless steel. The fifth, and last, change is the wall thickness of tank and mantle, which is reduced from 3 mm to 2 mm.

The change concerning the insulation gives the most significant improvement, while the change of the wall thickness gives the smallest improvement. The net utilised solar energy is increased from 802 kWh/year to 1009 kWh/year by applying the mentioned changes in the design. It is an improvement of 26% of the net utilised solar energy.

It was shown in section 9.7 that the thermal performance increased for smaller auxiliary volumes. It is chosen in this section not to change the size of the auxiliary volume. The auxiliary volume of 0.082 m³ is relatively large for a hot-water consumption of the 0.100 m³. However, the system would be less flexible for other hot-water consumptions if it were decreased. A possible future solution to the question about the size of the auxiliary volume is briefly discussed in section 9.12.2.

The optimised design found in this section differs a little from the design found by Shah et al. (2000) in a similar study. Shah et al. (2000) found that the mantle should have a

relative height of 0.55 and a gap width of 0.03 m, while the relative mantle height is 0.36 and the mantle gap width is 0.0105 m in the design proposed in this thesis.

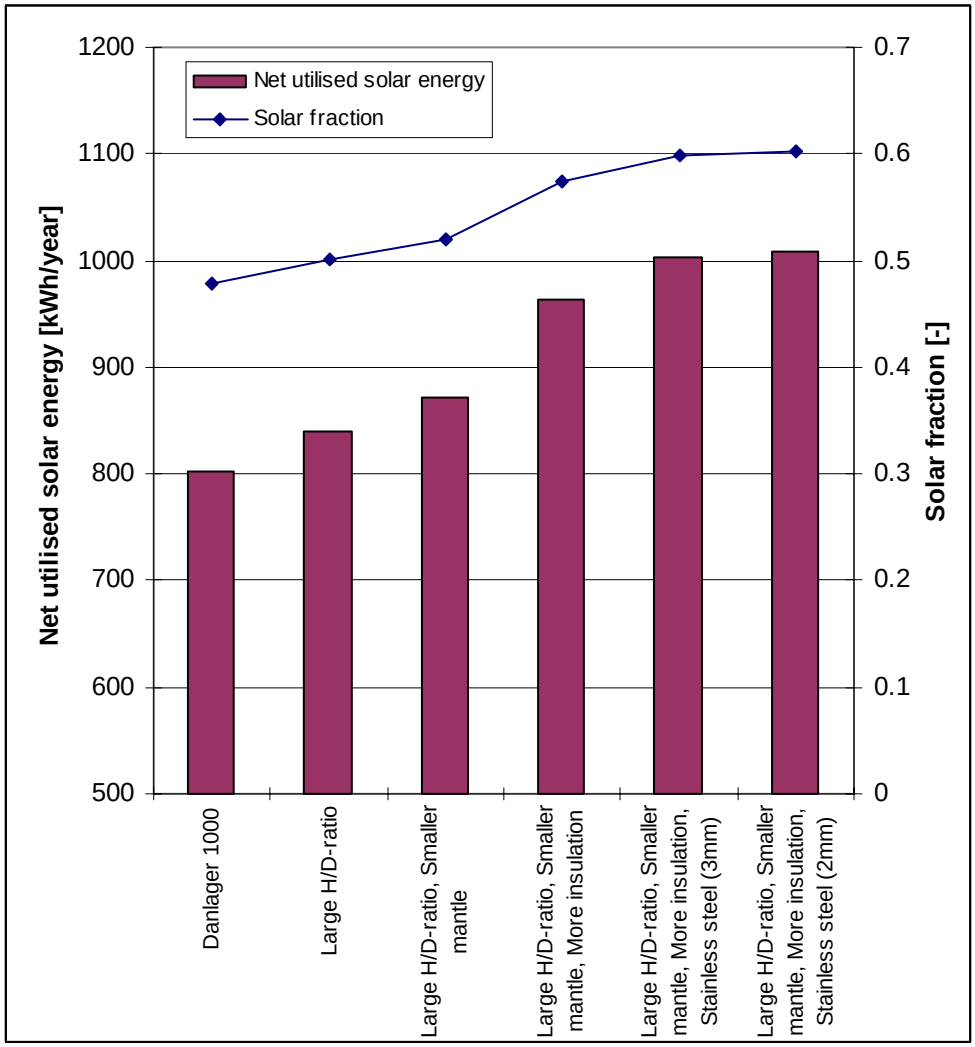

Figure 9-39: Net utilised solar energy and solar fraction as a function of the different changes in the Danlager 1000 system.

9.12 Other aspects of the mantle tank design

In this chapter some of the geometrical parameters of the mantle design have been investigated in order to find out how they influence the thermal performance of the system. However, it is not all parameters that are included in the investigation, and in this section two important parameters, which are not investigated, will be discussed. That is the mixing in the tank due to the cold water inlet, and it is the auxiliary energy supply system.

9.12.1 Cold water inlet

The mixing that occurs in the bottom of the tank during draw-offs is not treated so far in this thesis. However, it is important to design the cold water inlet to minimise the mixing during draw-offs because the mixing degrades the thermal stratification, and a poorly designed cold water inlet can have a large negative impact on the thermal performance of the system.

In a study, presented in Knudsen (2002), it was investigated how the rate of mixing in the inner tank influences the thermal performance of the system. 12 different SDHW systems – 6 based on mantle tanks and 6 based on spiral tanks - were included in the investigation as well as a number of different hot-water consumptions. Two different hot-water load profiles were used in the investigation, one load profile with three draw-offs at equal time, size and duration every day and one more realistic load profile where the hot-water consumption and consumption pattern vary from day to day (Jordan and Vajen, 2000). Figure 9-40 summarises the results and shows the relative reduction in the net utilised solar energy as a function of the mixing rate in the inner tank. The mixing rate is defined as the part of the volume above the cold water inlet that is completely mixed during a draw-off. It is seen from the figure that the net utilised solar energy for the mantle tank systems is reduced by 2% at a mixing rate of 20% and by 10% at a mixing rate of 40%. It is also seen that the mixing has a stronger negative impact on the thermal performance of the spiral tank systems. This is because the temperature in the bottom of a spiral tank is normally higher than the temperature in the bottom of a mantle tank, and therefore the mixing will destroy more of the thermal stratification in the spiral tank than in the mantle tank and consequently reduce the thermal performance more in the spiral tank systems.

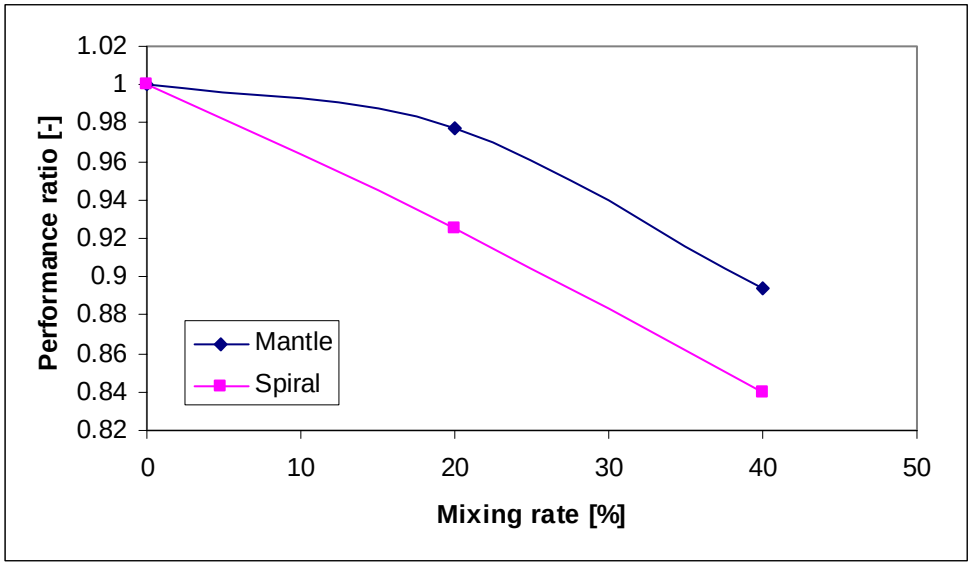

Figure 9-40: Performance ratio as a function of the mixing rate. Adapted from Knudsen (2002).

In Figure 9-40, it is assumed that the mixing is constant during all draw-offs during the year. This is of course not realistic since the mixing depends on cold water inlet design, tank design, flow rate during draw-off, tapped volume, cold water temperature, and the

thermal stratification in the tank. Currently, a study based on CFD-calculations and PIV measurements is carried out in order to characterise the amount of mixing during draw-offs as a function of the mentioned parameters (Jordan and Furbo, 2003). However, the results shown in Figure 9-40 show that it is important to avoid mixing in the tank during draw-offs.

9.12.2 Advanced control strategies for auxiliary energy system

It was shown in section 9.7 that the thermal performance of the system is highly influenced by the size of the auxiliary volume, and the auxiliary volume should be as small as possible while still meeting the hot-water demand. However, it is difficult to choose the size of the auxiliary volume in the right way, because the hot-water consumption is normally not known prior to installation of a SDHW system, and the hot-water consumption and consumption pattern vary strongly from family to family. Therefore, the solar tank is in many cases oversized to be on the safe side, but this results in poorer profitability of the SDHW system due to higher costs and in some cases also lower thermal performance.

Different investigations on advanced control strategies for the auxiliary energy supply system have been carried out (Furbo and Shah (1997), Prud'homme and Gillet (2001), Dennis (2003) and Furbo et al. (2003)) to overcome this problem. The idea behind the advanced control strategy is to heat up the water by the auxiliary energy supply system only when the hot water is needed by the user, instead of having a large volume heated to a constant temperature by the auxiliary energy supply system all the time. This strategy leads to a decrease in auxiliary energy supply, decrease in heat loss and an increase in the solar energy contribution. Furthermore, the auxiliary energy supply system can be designed in such a way that it heats up the water from the top, and the water volume heated by the auxiliary energy supply system is fitted to the hot-water consumption and consumption pattern. In periods with a large hot-water demand, the volume is large; in periods with a small hot-water demand, the volume is small.

Figure 9-41 shows two designs proposed by Furbo et al. (2003). One system with the auxiliary heating element in a side arm and another system with a horizontal heating element and a vertical heating element inside a pipe, both heating elements are inside the tank. Both Prud'homme and Gillet (2001) and Dennis (2003) worked more on control strategies than on the design. In those investigations the user's needs were predicted every day and weather forecast was used to optimise collector flow rate and minimise the auxiliary heating. The investigations showed that the thermal performance could be improved by 5-35% by applying the advanced control strategies for the auxiliary energy supply system depending on hot-water consumption and consumption pattern (Furbo et al. (2003)).

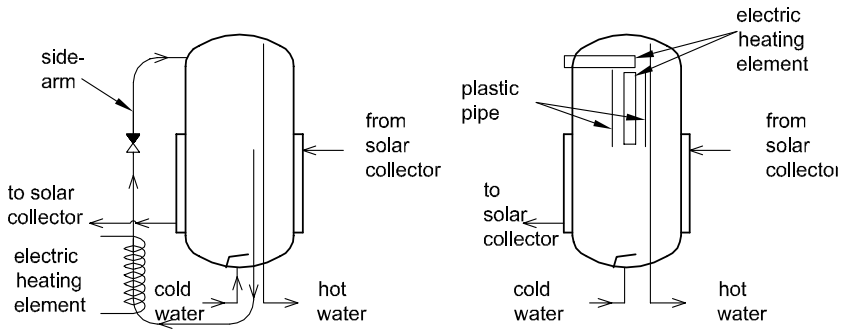

Figure 9-41: Two smart solar tank designs proposed by Furbo et al. (2003).

9.13 Discussion and conclusion

In this chapter a mantle tank design analysis was performed with MantlSim in order to investigate how different tank parameters influence the thermal performance of the system. The design analysis was carried out with the Danish commercially manufactured mantle tank Danlager 1000 as the standard reference tank.

The tank design analysis showed that MantlSim predicted expected tendencies in most of the parameter variations. However, for the mantle height variations unexpected results were found. It was found that a relatively low mantle height gave the highest thermal performance. It was not clarified whether these results could be trusted or MantlSim were over-predicting the effect of natural convection inside the tank for low mantle heights. Therefore, the routine calculating the natural convection inside the tank should be verified for low mantle heights.

The possibility of varying the mantle inlet position is a new feature in MantlSim. It was found that the thermal performance of the reference system could be improved by moving the mantle inlet down to a relative distance of 0.35 from the mantle top. However, the investigations showed that the optimum mantle inlet position is case sensitive and among other things depends on hot-water consumption, mantle gap, mantle height, distance from mantle top to level of auxiliary energy supply system and collector loop flow rate.

It was shown that the net utilised solar energy of the Danlager 1000 system could be improved by up to 26% by relatively simple changes in the design.

10. Conclusion

The aim of this study was to investigate and analyse the heat transfer and flow structure in heat storage tanks for low-flow SDHW systems. The study was concentrated on vertical mantle heat exchangers because it was revealed in chapter 1 that the vertical mantle heat exchanger is one of the most promising heat storage designs for low-flow SDHW systems.

The investigations were made by means of both experimental and numerical methods. To simplify the study of vertical mantle heat exchangers, the thermal conditions at the mantle inlet were divided into two categories: Hot inlet condition, which is when the temperature of the mantle inlet flow is equal or higher than the temperature of the fluid in the top of the mantle, and warm inlet condition, which is when the temperature of the mantle inlet flow lies between the temperature of the fluid in the top and in the bottom of the mantle.

At first, thermal experiments of vertical mantle heat exchangers with different mantle inlet designs were carried out. The investigations were carried out in an indoor heat storage test facility and in a laboratory test facility for solar heating systems. The experiments in the heat storage test facility showed that the size of the mantle inlet port has a minor effect on the thermal conditions in mantle heat exchangers due to the low flow rates, and thereby small inlet velocities, that are typical in low-flow SDHW systems. Furthermore, the thermal experiments in the heat storage test facility showed that the vertical position of the mantle inlet port has an influence on the thermal conditions in mantle heat exchangers. For hot inlet conditions it is preferable to have the mantle inlet located at the top, and for warm inlet conditions it is preferable to have the mantle inlet located at a lower position. A side-by-side laboratory test of two SDHW systems, with mantle heat exchangers where the inlet to the mantle was either located at the top of the mantle or located about one fourth of the mantle height from the mantle top, was carried out to investigate how the mantle inlet position influences the thermal performance of the system. The side-by-side test showed that the thermal performance of the system increased by moving the mantle inlet down to a lower inlet position.

The heat transfer and flow structure in mantle heat exchangers are rather complex, and the thermal experiments were followed by investigations by means of advanced experimental and numerical techniques. Computational Fluid Dynamics (CFD) models were used to model the convection process in mantle heat exchangers. A CFD program solves the Navier-Stokes and energy equations and thus, detailed information of the heat transfer and flow structure can be obtained. The commercial CFD program FLUENT (FLUENT, 2001) was used in this study. The CFD-models were validated by means of thermal experiments and by flow visualisation.

With a steel mantle tank, different thermal experiments with hot and warm inlet conditions were carried out in a heat storage test facility. The measured temperatures were used to evaluate the temperatures calculated by CFD. Measured and calculated temperatures inside the tank and the mantle outlet temperature were compared. Good agreement between measured and calculated temperatures was obtained.

The experimental flow visualisation was carried out with a Particle Image Velocimetry (PIV) system, which combines flow visualisation and digital image processing to measure the fluid velocity over a 2-dimensional cross-section of the flow field. With a transparent glass mantle tank flow structures inside the mantle and inside the tank were visualised and then compared with the flow structures predicted by CFD. For hot inlet conditions, there was a re-circulating flow in the top of the mantle, and below the re-circulating flow the fluid dropped slowly down to the bottom where a return stream along the bottom of the mantle towards the outlet was developed. For warm inlet conditions, the inlet stream dropped down and passed around the middle part of the mantle and induced a reverse flow in the upper part of the mantle, and in the bottom of the mantle there was still suction towards the outlet. Inside the tank at hot inlet conditions, the heat exchange from the hot mantle fluid to the water in the tank induced an upward flow near the tank wall due to natural convection. Meanwhile, there was a very slow downward flow in the middle of the tank. The upward flow near the tank wall helps promoting thermal stratification. For warm inlet conditions, the flow in the tank above the mantle was governed by the heat loss at the walls, and a downward flow near the walls above the mantle was created. There was good agreement between the flow structures measured by PIV and the flow structures calculated by CFD. Based on the validations by means of thermal experiments and PIV measurements along with analysis of grid dependence, effect of turbulence and time dependence, it was concluded that the CFD-models were able to simulate the flow and heat transfer in vertical mantle heat exchangers.

With the verified CFD-models, a parameter analysis was carried out for differently designed mantle heat exchangers for both hot and warm inlet conditions to reveal how the mantle tank parameters influence the flow structure and heat transfer in mantle heat exchangers. Based on the CFD-analysis, dimensionless heat transfer theory was applied to develop heat transfer correlations for the heat transfer between the solar collector in the mantle and the inner and outer mantle walls, and between the tank wall and the domestic water in the inner tank. The heat transfer in the mantle near the mantle inlet port showed to be in the mixed convection regime, and as the distance from the inlet increased, natural convection started to dominate. For both inner and outer mantle wall, two mixed convection Nusselt number correlations ($Nu\text{-}Ra/Re^2$) for the upper half of the mantle were developed: One correlation for the part above the mantle inlet and one correlation for the part below the mantle inlet. Furthermore, for both inner and outer mantle wall, a Nusselt number correlation based on the ratio between the horizontal flow area in the mantle gap and the heat transfer area was developed. The heat transfer between the tank wall and the domestic water in the tank is governed by natural convection, and a natural convection Nusselt number correlation (Nu-Ra) was developed.

The CFD-calculations and PIV measurements revealed that thermal stratification is built up in the inner tank above the mantle due to natural convection flow along the tank wall. By means of the analysis of the CFD-calculations, a method was developed to determine the heat transfer caused by the natural convection flow in the inner tank. The method for determining the natural convection flow consists of two correlations: one for the part of the inner tank at the level of the mantle, and one for the part of the inner tank

above the mantle. Furthermore, a method for determining the mixing inside the mantle, caused by the incoming solar collector fluid, was developed, based on CFD-calculations. The method for determining the mixing inside the mantle consists of two correlations: One for the downward flow at warm inlet condition, and one for the upward flow at hot inlet condition when the mantle inlet port is not located at the top of the mantle.

The developed heat transfer correlations, the method for determining the heat transfer in the inner tank caused by natural convection and the method for determininge the mixing in the mantle were implemented in a simulation program, MantlSim, for low-flow SDHW systems. The SDHW simulation program is simpler than the CFD-models, and can, based on weather data from the Danish Test Reference Year, be used to predict the yearly thermal performance of low-flow SDHW systems based on mantle tanks. MantlSim was verified by comparing calculated results with measurements on two low-flow SDHW systems. The two SDHW systems were identical, except for the mantle inlet position: one system had the mantle inlet located at the top of the mantle, and the other system had the mantle inlet located about one fourth of the mantle height from the top of the mantle. The comparison showed a good agreement between measured and calculated temperatures and energy quantities. Thus, the model was assumed to predict thermal performances for low-flow SDHW systems based on mantle tanks in good agreement with reality.

A heat storage design analysis was performed with MantlSim to elucidate how the thermal performance of low-flow SDHW systems is influenced by the mantle tank design. The Danish commercial manufactured mantle tank, Danlager 1000, was used as the reference tank in the analysis. The heat storage design analysis showed that the thermal performance of the system could be improved by using more insulation, by increasing the H/D-ratio of the tank, by changing the tank material to stainless steel and by decreasing the height of the mantle. The effect of more insulation, increased H/D-ratio, and stainless steel as tank material was expected as previous studies had showed the same. The results, saying that the mantle height should be reduced from covering the bottom half of the tank to cover the bottom third of the tank, were rather unexpected, as it was in poor agreement with previous studies. The new finding was a result of the implementation of the model to determine the natural convection flow inside the tank combined with smaller heat loss, and a reduction of both mixing in mantle and vertical downward heat conduction. However, the natural convection flow model was not verified for these small mantle heights, and there is a risk that the effect of natural convection is over-predicted by the model for small mantle heights. The possibility of varying the mantle inlet position is a new feature in MantlSim. It was found that the thermal performance of the reference system could be improved by moving the mantle inlet down to a relative distance of 0.35 from the mantle top. However, the investigations showed that the optimum mantle inlet position is case sensitive and for the small mantle heights the mantle inlet should be located at the top of the mantle.

10.1 Recommendations for future work

In this study new findings concerning heat transfer in mantle heat exchangers, natural convection flow in inner tank and mixing inside the mantle caused by the incoming

solar collector fluid have been revealed, and the new findings were implemented into the low-flow SDHW system simulation program, MantlSim. The program now forms an improved basis for the future development of SDHW systems. However, there are still possibilities in further improvement and verification of the methods that have been implemented in MantlSim during this study:

The heat transfer correlations have been developed, based on CFD-calculations of mantle heat exchangers with an inner tank volume of 0.175 m^3. The heat transfer correlations would be more general if they were verified for other inner tank volumes, for lower mantle heights and for smaller mantle gap widths (< 0.01 m).

The model for the natural convection flow in the inner tank was developed for mantle heat exchangers where the mantle covered the bottom half of the tank. CFD-calculations of mantle heat exchangers with other mantle heights would be very beneficial to make the model valid for other mantle heights. Furthermore, it is recommended to carry out thermal experiments with mantle heat exchangers with different mantle heights in order to investigate the natural convection effect for small mantle heights, and by that find out whether the results concerning the small mantle heights found in this thesis can be trusted.

The model for the mixing in the mantle due to the incoming jet was developed based on different mantle inlet positions, different mantle flow rates and different mantle gaps. The inlet velocity, the diameter of the tank and the type of mantle fluid are parameters that also are expected to have an influence on the mixing. Therefore, it is recommended to further develop the model for mixing in the mantle to take these parameters into account.

MantlSim is a simulation program developed and used at Department of Civil Engineering at Technical University of Denmark. Therefore, it is recommended to translate the heat storage model in MantlSim into a model type in the simulation program TRNSYS (Klein et al., 1996). TRNSYS is the dominating simulation tool for research in solar water heating systems, and the findings described in this thesis could be used more widespread if such a TRNSYS type model of the heat storage model in MantlSim was made.

Other areas that offer scope for further investigations are the mixing in the inner tank due to the cold-water inlet and the control strategy of the auxiliary energy supply system. These areas were briefly discussed in chapter 9. Mixing in the inner tank can cause a drastic reduction in the thermal performance of SDHW systems, and it is therefore recommended to develop cold-water inlet devices that minimises mixing during draw-offs. Research has shown that advanced designs and advanced control strategies for the auxiliary energy supply system have the potential of being a good improvement in the future. It is recommended to continue research on this and to develop heat storage units with an oil-fired boiler or a natural gas burner as auxiliary energy supply system including complete control systems, so that the control system is included in the unit from the start. This compact design will improve the thermal performance of the systems and makes the heat storage easier to install.

References

Arpaci, V.S. and Larsen, P.S. (1984):
Convection Heat Transfer. Prentice-Hall Inc.

Baur, J.M., Klein, S.A. and Beckman, W.A. (1993):
Simulation of water tanks with mantle heat exchangers. Proceedings ASES Annual Conference, Solar93, pp. 286-291.

Berg, P. (1990):
Højtydende solvarmeanlæg med små volumenstrømme – teoretiske undersøgelser. Technical University of Denmark, Thermal Insulation Laboratory. Report 209. (In Danish).

Churchill, S.W. (1977):
A comprehensive correlating equation for laminar, assisting, forced and free convection. AIChE Journal, Vol. 23, pp. 10-16.

Dahl, S.D. and Davidson, J.H. (1998):
Mixed convection heat transfer and pressure drop correlations for tube-in-shell thermosyphon heat exchangers with uniform heat flux. ASME Journal of Solar Energy Engineering, Vol. 120, pp. 260-269.

Dahm, J., Bales, C., Lorenz, K. and Dahlenbäck, J.O. (1998):
Evaluation of heat storage configurations with internal heat exchangers. Solar Energy, Vol. 62, pp. 407-417.

Danish Energy Agency, (1998):
Solar Energy – Plan of action 1998-2000. Danish Energy Agency, Copenhagen, Denmark.

Dennis, M. (2003):
Optimising energy balance for systems with storage. Proceedings of ISES 2003 Solar World Congress, Göteborg, Sweden.

Dhimdi, S and Bolle, L. (1997):
Natural convection: The effect of geometrical parameters. Proceedings of the 4th National Congress on Theoretical and Applied Mechanics, Leuvren, Belgium, pp. 43-46.

Duffie, J.A. and Beckman, W.A. (1991):
Solar Engineering of Thermal Processes. 2nd edition. John Wiley and Sons Inc. ISBN 0-471-51056-4.

El-Genk, M.S. and Rao, D.V. (1989):
Heat transfer experiments and correlations for low-Reynolds-number flows of water in vertical annuli. Heat Transfer Engineering, Vol. 10, pp. 44-57.

El-Genk, M.S. and Rao, D.V. (1990):
Buoyancy induced instability of laminar flows in vertical annuli – I. Flow visualisation and heat transfer experiments. International Journal of Heat and Mass Transfer, Vol. 33, pp. 2145-2159.

El-Shaarawi, M.A.I. and Sarhan, A. (1980):
Free convection effects on the developing laminar flow in vertical concentric annuli. ASME Journal of Heat Transfer, Vol. 102, pp. 617-622.

El-Shaarawi, M.A.I. and Al-Nimr, M.A. (1990):
Fully developed laminar natural convection in open-ended vertical concentric annuli. International Journal of Heat and Mass Transfer, Vol. 33, pp. 1873-1884.

Ellehauge, K. (1993):
Små markedsførte solvarmeanlæg til brugsvandsopvarmning – funktionsafprøvning og ydelsesmålinger. Opbygning af prøvestand. Technical University of Denmark, Thermal Insulation Laboratory. Report 93-37. (In Danish).

Ferziger, J.H., Perić, M. (2002):
Computational Methods for Fluid Dynamics. Springer. ISBN 3-540-42074-6.

FLUENT (2001):
FLUENT 6.0 User's Guide. Fluent Inc., 10 Cavendish Court, Lebanon, NH03766, USA.

Furbo, S. (1984):
Varmelagring til solvarmeanlæg. Ph.D. thesis. Technical University of Denmark, Thermal Insulation Laboratory. Report 162. (In Danish).

Furbo, S. and Mikkelsen, S.E. (1987):
Is low flow operation an advantage for solar heating systems? Proceedings of ISES Solar World Congress. Hamburg, Germany. Vol. 1, pp. 962-966.

Furbo, S. and Berg, P. (1990):
Calculation of the thermal performance of small hot water solar heating systems using low flow operation. North Sun 90, Reading, UK.

Furbo, S. and Carlsson, P.F. (1991):
The thermal performance of small low flow solar heating systems. Technical University of Denmark, Thermal Insulation Laboratory. Report no. 91-22.

Furbo, S. (1993):
Optimum design of small DHW low flow solar heating systems. Proceedings of ISES Solar World Congress. Budapest, Hungary.

Furbo, S. and Jensen, S.Ø. (1995):
Varmtvandsbeholdere til solvarmeanlæg. Technical University of Denmark, Thermal Insulation Laboratory. Report 276. (In Danish)

Furbo, S. and Shah, L.J. (1997):
Smart Solar Tanks – Heat Storage of the Future? Proceedings of ISES 1997 Solar World Congress, Taejan, Korea.

Furbo, S., Andersen, E., Knudsen, S., Vejen, N.K. and Shah, L.J. (2003):
Smart solar tanks for small solar domestic hot water systems. Proceedings of ISES 2003 Solar World Congress, Göteborg, Sweden.

Gebhart, B., Jaluria, Y., Mahajan, R.L. and Sammakia, B. (1988):
Buoyancy-Induced Flows and Transport: Reference Edition. Hemisphere Publishing Corporation. ISBN 0-89116-402-2.

Hollands, K.G.T. and Lightstone, M.F. (1989):
A review of low-flow, stratified-tank solar water heating systems. Solar Energy, Vol. 43, pp. 97-105.

Iannello, V., Suh, K.Y. and Todreas, N.E. (1988a):
Mixed convection friction factors and Nusselt numbers in vertical annular and subchannel geometries. International Journal of Heat and Mass Transfer, Vol. 31, pp. 2175-2189.

Iannello, V., Suh, K.Y. and Todreas, N.E. (1988b):
Mixed convection friction factors in flow channels. Nuclear Engineering Department, Massachusetts Institute of Technology, Report PNC/MIT-20TR and GE/MIT-2TR, Rev. 2.

IEA, Task 14 (1996) (Editor: Duff, W.):
Advanced Solar Domestic Hot Water Systems. A report of the Task 14 Advanced Solar Domestic Hot Water Systems Working Group. IEA, Solar Heating and Cooling Programme.

ILA (2002): Technische Dokumentation. ILA – Intelligent Laser Applications GmbH. Karl-Hein-Beckurts-Straße 13, D-52428, Jülich, Germany. (In German).

ISO (1992):
ISO/DIS 9806-1.2. Thermal performance tests for solar collectors. International Organization for Standardization.

Jensen, S.Ø. (1984):
Varmeovergang for varmevekslerspiraler neddykket i vand. Technical University of Denmark, Thermal Insulation Laboratory. Report 84-10 (In Danish).

Jordan, U. and Vajen, K. (2000):
Influence of the DHW-load profile on the fractional energy savings: a case study of a solar combi-system with Trnsys simulations. Solar Energy, Vol. 69, pp. 197-208.

Jordan, U. and Furbo, S. (2003):
Investigations of the flow into a storage tank by means of advanced experimental and theoretical methods. Proceedings of ISES 2003 Solar World Congress, Göteborg, Sweden.

Kays, W.M. and Crawford, M.E. (1993):
Convective Heat and Mass Transfer. McGraw-Hill. ISBN 0-07-112516-7.

Keyhani, M., Kulacki, F.A. and Christensen, R.N. (1983):
Free convection in a vertical annulus with constant heat flux on the inner wall. ASME Journal of Heat Transfer, Vol. 105, pp. 454-459.

Khan, J.A. and Kumar, R. (1989):
Natural convection in vertical annuli: A numerical study for constant heat flux on the inner wall. ASME Journal of Heat Transfer, Vol. 111, pp. 909-915.

Klein, S.A. et al. (1996):
TRNSYS 14.1, User Manual. Solar Energy Laboratory, University of Wisconsin.

Knudsen, S. (2002):
Consumers' influence on the thermal performance of small SDHW systems – theoretical investigations. Solar Energy, Vol. 73, pp. 33-42.

Kubair, V.G. and Simha, C.R.V. (1982):
Free convection heat transfer to mercury in vertical annuli. International Journal of Heat and Mass Transfer, Vol. 25, pp. 399-407.

Lin, T.F, Yin, C.P. and Yan, W.M. (1991):
Transient laminar mixed convective heat transfer in a vertical flat duct. ASME Journal of Heat Transfer, Vol. 113, pp. 384-390.

McAdams, W.H. (1954):
Heat Transmission. 3rd edition. McGraw-Hill. New York.

Mercer, W.E., Pearce, W.M. and Hitchcock, J.E. (1967):
Laminar forced convection in the entrance region between parallel flat plates. ASME Journal of Heat Transfer, Vol. 89, pp. 251-257.

Mills, A.F. (1992):
Heat Transfer. International Student Edition. Richard D. Irwing Inc. ISBN 0-256-07642-1.

Morrison, G.L., Nasr, A., Behnia, M. and Rosengarten, G. (1998):
Analysis of horizontal mantle heat exchangers in solar water heating systems. Solar Energy, Vol. 64, pp. 19-31.

Morrison, G.L., Rosengarten, G. and Behnia, M. (1999):
Mantle heat exchangers for horizontal thermosyphon solar water heaters. Solar Energy, Vol. 67, pp. 53-64.

Nagendra, H.R., Tirunarayana, M.A. and Ramachandran, A. (1970):
Free convection heat transfer in vertical annuli. Chemical Engineering Science, Vol. 25, pp. 605-610.

Nielsen, J.E. (2000):
Data sheet for solar collector efficiency D2152 A of ARCON Solvarme A/S ST-NA. Solar Energy Centre Denmark, Danish Technological Institute.

Optical Flow Systems (1999):
VidPIV3.0 Rowan. Optical Flow Systems Ltd., The Bush Research Park, The Technopole Centre, Bush Loan, Penicuik, EH26 OPJ, Scotland.

Patankar, S.V. (1980):
Numerical Heat Transfer and Fluid Flow Hemisphere, Public Corporation.

Prud'homme, T. and Gillet, D. (2001):
Advanced control strategy of a solar domestic hot water system with a segmented auxiliary heater. Energy and Buildings, Vol. 33, pp. 464-475.

Raffel, M., Willert, C. and Kompenhans J. (1998):
Particle Image Velocimetry – A Practical Guide. Springer Berlin. ISBN 3-540-63683-8.

Rogers, B.B. and Yao, L.S. (1990):
The effect of mixed convection instability on heat transfer in a vertical annulus. International Journal of Heat and Mass Transfer, Vol. 33, pp. 79-90.

Rogers, B.B. and Yao, L.S. (1993):
Natural convection in a heated annulus. International Journal of Heat and Mass Transfer, Vol. 36, pp. 35-47.

Rosengarten, G., Behnia, M. and Morrison, G.L. (1999):
Some aspects concerning modelling the flow and heat transfer in horizontal mantle heat exchangers in solar water heaters. International Journal of Energy Research, Vol. 23, pp. 1007-1016.

Rosengarten, G. (2000):
An experimental and numerical study of mantle heat exchangers for solar water heaters. Ph.D. thesis. School of Mechanical and Manufacturing Engineering, University of New South Wales.

Rosengarten, G., Morrison, G.L. and Behnia, M. (2001):
Mixed convection in a narrow rectangular cavity with bottom inlet and outlet. International Journal of Heat and Fluid Flow, Vol. 22, pp. 168-179.

Shah, L.J. and Furbo, S. (1996):
Optimisation of mantle tanks for low flow solar heating systems. Proceedings EuroSun ’96, Vol. I, pp. 369-375. Freiburg, Germany.

Shah, L.J. (1997): Små low flow solvarmeanlæg med kappebeholdere. Technical University of Denmark, Department of Buildings and Energy. Report R-009. (In Danish).

Shah, L.J. and Furbo, S. (1998):
Correlation of experimental and theoretical heat transfer in mantle tanks used in low flow SDHW systems. Solar Energy, Vol. 64, pp. 245-256.

Shah, L.J. (1999):
Investigation and modelling of thermal conditions low flow SDHW systems. Ph.D. thesis. Technical University of Denmark, Department of Buildings and Energy. Report–034. ISBN 87-7877-035-1.

Shah, L.J., Morrison, G.L. and Behnia, M. (1999):
Characteristics of vertical mantle heat exchangers for solar water heaters. Solar Energy, Vol. 67, pp. 79-91.

Shah L.J. (2000):
Heat transfer correlation for vertical mantle heat exchangers. Solar Energy, Vol. 69, pp. 157-171.

Shah, L.J., Larsen, A.M. and Madsen, M.L. (2000):
Ideel solvarmebeholder. Technical University of Denmark, Department of Buildings and Energy. Report SR-0007. (In Danish).

Shah, R.K. and London, A.L. (1978):
Laminar flow forced convection in ducts. A source book for compact heat exchanger analytical data. Academic Press. ISBN 0-12-020051-1.

Statens Byggeforskningsinstitut (1982):
Vejrdata for VVS og energi. Dansk referenceår TRY. Statens Byggeforskningsinstitut. Hørsholm, Denmark. (In Danish).

Tsay, Y.L. (1994):
Transient conjugated mixed-convective heat transfer in a vertical annular passage. International Journal of Heat and Fluid Flow. Vol. 15, pp. 226-232.

van Koppen, C.W.J., Thomas, J.P.S and Veltkamp W.B. (1979):
The actual benefits of thermally stratified storage in a small and medium size solar system. SUN II, Proceedings of ISES Biennial Meeting. Atlanta, USA, pp. 576-580.

Versteeg, H.K. and Malalasekear, W. (1995):
An introduction to computational fluid dynamics. The finite volume method. Prentice Hall.

Wilcox, D.C. (1998):
Turbulence Modeling for CFD. DCW Industries, Inc. Canada. ISBN 0-9636051-5-1.

Wuestling, M.D., Klein, S.A. and Duffie, J.A. (1985):
Promising control alternatives for solar water heating systems. ASME Journal of Solar Energy Engineering, Vol. 107, pp. 215-221.

Zenen, S.R., Collins, M.W. and Simonson, J.R. (1985):
Combined convection in an annulus applied to a thermal storage problem. International Journal for Numerical Methods in Engineering, Vol. 21, pp. 691-711.

Appendix A

Energy balances for control volumes in MantlSim

Inner tank (i = 1):

The temperature gradient along the vertical direction in the inner tank is calculated by modelling the inner tank with NZ3 control volumes. The inner tank contains the domestic water and eventual draw-off is included in the energy balances. Layers including the auxiliary energy supply are described later in this appendix.

Top wall, j = 1:

$$V_{i,j}\cdot\rho_{i,j}\cdot c_{p(i,j)}\cdot\frac{dT_{i,j}}{dt}=A_{t(i,j)}\cdot h_{t,i}\cdot\left(T_{i,j+1}-T_{i,j}\right)-A_{t(i,j)}\cdot U_{t(i)}\cdot\left(T_{i,j}-T_a\right) \\ -2\cdot DR(1)\cdot\pi\cdot dz_{i,j}\cdot k_{i,j}\cdot\frac{T_{i,j}-T_{i+1,j}}{DR(1)+0.5\cdot DR(2)} \qquad (A.1)$$

First fluid layer, j = 2:

$$V_{i,j}\cdot\rho_{i,j}\cdot c_{p(i,j)}\cdot\frac{dT_{i,j}}{dt}=c_{p(i,j)}\cdot\dot{m}_{dhw}\cdot\left(T_{i,j+1}-T_{i,j}\right)-A_{t(i,j)}\cdot\left[k_{i,j}\cdot\left(\frac{T_{i,j}-T_{i,j+1}}{dz_j}\right)+h_{t,i}\cdot\left(T_{i,j}-T_{i,j-1}\right)\right] \\ -2\cdot DR(1)\cdot\pi\cdot dz_{i,j}\cdot h_{1,j}\cdot\left(T_{i,j}-T_{i+1,j}\right) \qquad (A.2)$$

For layer 2<j<NZ3-2:

$$V_{i,j}\cdot\rho_{i,j}\cdot c_{p(i,j)}\cdot\frac{dT_{i,j}}{dt}=c_{p(i,j)}\cdot\dot{m}_{dhw}\cdot\left(T_{i,j+1}-T_{i,j}\right)-A_{t(i,j)}\cdot k_{i,j}\cdot\left[\frac{T_{i,j}-T_{i,j+1}}{dz_j}+\frac{T_{i,j}-T_{i,j-1}}{dz_{j-1}}\right] \\ -2\cdot DR(1)\cdot\pi\cdot dz_{i,j}\cdot h_{1,j}\cdot\left(T_{i,j}-T_{i+1,j}\right) \qquad (A.3)$$

Last fluid layer, j = NZ3-1:

$$V_{i,j}\cdot\rho_{i,j}\cdot c_{p(i,j)}\cdot\frac{dT_{i,j}}{dt}=c_{p(i,j)}\cdot\dot{m}_{dhw}\cdot\left(T_{cold}-T_{i,j}\right)-A_{t(i,j)}\cdot\left[k_{i,j}\cdot\left(\frac{T_{i,j}-T_{i,j-1}}{dz_{j-1}}\right)+h_{b,i}\cdot\left(T_{i,j}-T_{i,j+1}\right)\right] \\ -2\cdot DR(1)\cdot\pi\cdot dz_{i,j}\cdot h_{1,j}\cdot\left(T_{i,j}-T_{i+1,j}\right) \qquad (A.4)$$

Bottom wall, j = NZ3:

$$V_{i,j} \cdot \rho_{i,j} \cdot c_{p(i,j)} \cdot \frac{dT_{i,j}}{dt} = A_{t(i,j)} \cdot h_{b,i} \cdot \left(T_{i,j-1} - T_{i,j}\right) - A_{t(i,j)} \cdot U_{b(i)} \cdot \left(T_{i,j} - T_a\right) - 2 \cdot DR(1) \cdot \pi \cdot dz_{i,j} \cdot k_{i,j} \cdot \frac{T_{i,j} - T_{i+1,j}}{DR(1) + 0.5 \cdot DR(2)} \quad \text{(A.5)}$$

Mixing:

If a lower layer in the inner tank obtains a higher temperature than the above layer, the two layers are mixed so they get the same temperature.

Tank wall (i = 2):

The energy balances are divided into seven parts because the wall of the inner tank is partly covered by the mantle and special boundaries are found at the end walls of both mantle and inner tank:

Tank wall at top of tank, j = 1:

$$V_{i,j} \cdot \rho_{i,j} \cdot c_{p(i,j)} \cdot \frac{dT_{i,j}}{dt} = 2 \cdot DR(1) \cdot \pi \cdot dz_{i,j} \cdot k_{i,j} \cdot \frac{T_{i-1,j} - T_{i,j}}{DR(1) + 0.5 \cdot DR(2)} - 2 \cdot \left(DR(1) + DR(2)\right) \cdot \pi \cdot dz_{i,j} \cdot U_{l(j)} \cdot \left(T_{i,j} - T_a\right) - A_{t(i,j)} \cdot U_{t(i)} \cdot \left(T_{i,j} - T_a\right) + A_{t(i,j)} \cdot k_{i,j} \cdot \frac{T_{i,j+1} - T_{i,j}}{\left(dz_{j+1} + dz_j\right)/2} \quad \text{(A.6)}$$

Tank wall above mantle, 1<j<NZ1:

$$V_{i,j} \cdot \rho_{i,j} \cdot c_{p(i,j)} \cdot \frac{dT_{i,j}}{dt} = 2 \cdot DR(1) \cdot \pi \cdot dz_{i,j} \cdot h_{1,j} \cdot \left(T_{i-1,j} - T_{i,j}\right) - 2 \cdot \left(DR(1) + DR(2)\right) \cdot \pi \cdot dz_{i,j} \cdot U_{l(j)} \cdot \left(T_{i,j} - T_a\right) + A_{t(i,j)} \cdot k_{i,j} \cdot \left[\frac{T_{i,j-1} - T_{i,j}}{\left(dz_{j-1} + dz_j\right)/2} - \frac{T_{i,j} - T_{i,j+1}}{\left(dz_j + dz_{j+1}\right)/2}\right] \quad \text{(A.7)}$$

Tank wall at mantle top, j = NZ1:

$$V_{i,j} \cdot \rho_{i,j} \cdot c_{p(i,j)} \cdot \frac{dT_{i,j}}{dt} = 2 \cdot DR(1) \cdot \pi \cdot dz_{i,j} \cdot h_{1,j} \cdot \left(T_{i-1,j} - T_{i,j}\right) - 2 \cdot \left(DR(1) + DR(2)\right) \cdot \pi \cdot dz_{i,j} \cdot k_{i,j} \cdot \left(\frac{T_{i,j} - T_{i+1,j}}{\left(DR(2) + DR(3)\right)/2}\right) + A_{t(i,j)} \cdot k_{i,j} \cdot \left[\frac{T_{i,j-1} - T_{i,j}}{\left(dz_{j-1} + dz_j\right)/2} - \frac{T_{i,j} - T_{i,j+1}}{\left(dz_j + dz_{j+1}\right)/2}\right] \quad \text{(A.8)}$$

Tank wall inside mantle, NZ1<j<NZ2:

$$V_{i,j} \cdot \rho_{i,j} \cdot c_{p(i,j)} \cdot \frac{dT_{i,j}}{dt} = 2 \cdot DR(1) \cdot \pi \cdot dz_{i,j} \cdot h_{1,j} \cdot \left(T_{i-1,j} - T_{i,j}\right)$$
$$-2 \cdot \left(DR(1)+DR(2)\right) \cdot \pi \cdot dz_{i,j} \cdot h_{2,j} \cdot \left(T_{i,j} - T_{i+1,j}\right) \qquad \text{(A.9)}$$
$$+ A_{t(i,j)} \cdot k_{i,j} \cdot \left[\frac{T_{i,j-1} - T_{i,j}}{\left(dz_{j-1}+dz_j\right)/2} - \frac{T_{i,j} - T_{i,j+1}}{\left(dz_j+dz_{j+1}\right)/2} \right]$$

Tank wall at mantle bottom, j = NZ2:

$$V_{i,j} \cdot \rho_{i,j} \cdot c_{p(i,j)} \cdot \frac{dT_{i,j}}{dt} = 2 \cdot DR(1) \cdot \pi \cdot dz_{i,j} \cdot h_{1,j} \cdot \left(T_{i-1,j} - T_{i,j}\right)$$
$$-2 \cdot \left(DR(1)+DR(2)\right) \cdot \pi \cdot dz_{i,j} \cdot k_{i,j} \cdot \left(\frac{T_{i,j} - T_{i+1,j}}{\left(DR(2)+DR(3)\right)/2} \right) \qquad \text{(A.10)}$$
$$+ A_{t(i,j)} \cdot k_{i,j} \cdot \left[\frac{T_{i,j-1} - T_{i,j}}{\left(dz_{j-1}+dz_j\right)/2} - \frac{T_{i,j} - T_{i,j+1}}{\left(dz_j+dz_{j+1}\right)/2} \right]$$

Tank wall below mantle, NZ2<j<NZ3:

$$V_{i,j} \cdot \rho_{i,j} \cdot c_{p(i,j)} \cdot \frac{dT_{i,j}}{dt} = 2 \cdot DR(1) \cdot \pi \cdot dz_{i,j} \cdot h_{1,j} \cdot \left(T_{i-1,j} - T_{i,j}\right)$$
$$-2 \cdot \left(DR(1)+DR(2)\right) \cdot \pi \cdot dz_{i,j} \cdot U_{l(j)} \cdot \left(T_{i,j} - T_a\right) \qquad \text{(A.11)}$$
$$+ A_{t(i,j)} \cdot k_{i,j} \cdot \left[\frac{T_{i,j-1} - T_{i,j}}{\left(dz_{j-1}+dz_j\right)/2} - \frac{T_{i,j} - T_{i,j+1}}{\left(dz_j+dz_{j+1}\right)/2} \right]$$

Tank wall at bottom of tank, j = NZ3:

$$V_{i,j} \cdot \rho_{i,j} \cdot c_{p(i,j)} \cdot \frac{dT_{i,j}}{dt} = 2 \cdot DR(1) \cdot \pi \cdot dz_{i,j} \cdot k_{i,j} \cdot \frac{T_{i-1,j} - T_{i,j}}{DR(1)+0.5 \cdot DR(2)}$$
$$-2 \cdot \left(DR(1)+DR(2)\right) \cdot \pi \cdot dz_{i,j} \cdot U_{l(i,j)} \cdot \left(T_{i,j} - T_a\right) - A_{t(i,j)} \cdot U_{b(i)} \cdot \left(T_{i,j} - T_a\right) \qquad \text{(A.12)}$$
$$+ A_{t(i,j)} \cdot k_{i,j} \cdot \frac{T_{i,j-1} - T_{i,j}}{\left(dz_{j-1}+dz_j\right)/2}$$

Fluid in the mantle (i = 3):

Top mantle wall, j = NZ1:

$$V_{i,j}\cdot\rho_{i,j}\cdot c_{p(i,j)}\cdot\frac{dT_{i,j}}{dt}=2\cdot\left(DR(1)+DR(2)\right)\cdot\pi\cdot dz_{i,j}\cdot k_{i,j}\cdot\left(\frac{T_{i-1,j}-T_{i,j}}{\left(DR(2)+DR(3)\right)/2}\right)$$
$$-2\cdot\left(DR(1)+DR(2)+DR(3)\right)\cdot\pi\cdot dz_{i,j}\cdot k_{i,j}\cdot\left(\frac{T_{i,j}-T_{i+1,j}}{\left(DR(3)+DR(4)\right)/2}\right) \qquad (A.13)$$
$$-A_{t(i,j)}\cdot\left[U_{t(i,j)}\cdot\left(T_{i,j}-T_a\right)+h_{t,i}\cdot\left(T_{i,j}-T_{i,j+1}\right)\right]$$

First fluid layer, j = NZ1+1:

$$V_{i,j}\cdot\rho_{i,j}\cdot c_{p(i,j)}\cdot\frac{dT_{i,j}}{dt}=2\cdot\left(DR(1)+DR(2)\right)\cdot\pi\cdot dz_{i,j}\cdot h_{2,j}\cdot\left(T_{i-1,j}-T_{i,j}\right)$$
$$-2\cdot\left(DR(1)+DR(2)+DR(3)\right)\cdot\pi\cdot dz_{i,j}\cdot h_{3,j}\cdot\left(T_{i,j}-T_{i+1,j}\right) \qquad (A.14)$$
$$-A_{t(i,j)}\cdot\left[h_{t,i}\cdot\left(T_{i,j}-T_{i,j-1}\right)+k_{i,j}\cdot\frac{T_{i,j}-T_{i,j+1}}{\left(dz_{i,j+1}+dz_{i,j}\right)/2}\right]$$

Fluid layers, NZ1+2<j<NZ2-2:

$$V_{i,j}\cdot\rho_{i,j}\cdot c_{p(i,j)}\cdot\frac{dT_{i,j}}{dt}=2\cdot\left(DR(1)+DR(2)\right)\cdot\pi\cdot dz_{i,j}\cdot h_{2,j}\cdot\left(T_{i-1,j}-T_{i,j}\right)$$
$$-2\cdot\left(DR(1)+DR(2)+DR(3)\right)\cdot\pi\cdot dz_{i,j}\cdot h_{3,j}\cdot\left(T_{i,j}-T_{i+1,j}\right) \qquad (A.15)$$
$$-A_{t(i,j)}\cdot\left[k_{i,j}\cdot\left(\frac{T_{i,j}-T_{i,j-1}}{\left(dz_{i,j-1}+dz_{i,j}\right)/2}\right)+k_{i,j}\cdot\frac{T_{i,j}-T_{i,j+1}}{\left(dz_{i,j+1}+dz_{i,j}\right)/2}\right]$$

Last fluid layer, j = NZ2-1:

$$V_{i,j}\cdot\rho_{i,j}\cdot c_{p(i,j)}\cdot\frac{dT_{i,j}}{dt}=2\cdot\left(DR(1)+DR(2)\right)\cdot\pi\cdot dz_{i,j}\cdot h_{2,j}\cdot\left(T_{i-1,j}-T_{i,j}\right)$$
$$-2\cdot\left(DR(1)+DR(2)+DR(3)\right)\cdot\pi\cdot dz_{i,j}\cdot h_{3,j}\cdot\left(T_{i,j}-T_{i+1,j}\right) \qquad (A.16)$$
$$-A_{t(i,j)}\cdot\left[h_{b,i}\cdot\left(T_{i,j}-T_{i,j+1}\right)+k_{i,j}\cdot\frac{T_{i,j}-T_{i,j-1}}{\left(dz_{i,j-1}+dz_{i,j}\right)/2}\right]$$

Bottom mantle wall, j = NZ2:

$$V_{i,j}\cdot\rho_{i,j}\cdot c_{p(i,j)}\cdot\frac{dT_{i,j}}{dt}=2\cdot\left(DR(1)+DR(2)\right)\cdot\pi\cdot dz_{i,j}\cdot k_{i,j}\cdot\left(\frac{T_{i-1,j}-T_{i,j}}{\left(DR(2)+DR(3)\right)/2}\right)$$
$$-2\cdot\left(DR(1)+DR(2)+DR(3)\right)\cdot\pi\cdot dz_{i,j}\cdot k_{i,j}\cdot\left(\frac{T_{i,j}-T_{i+1,j}}{\left(DR(3)+DR(4)\right)/2}\right) \qquad (A.17)$$
$$-A_{t(i,j)}\cdot\left[U_{b(i,j)}\cdot\left(T_{i,j}-T_a\right)+h_{b,i}\cdot\left(T_{i,j}-T_{i,j-1}\right)\right]$$

Mantle wall (i = 4):

Mantle wall at top of mantle, j = NZ1:

$$V_{i,j}\cdot\rho_{i,j}\cdot c_{p(i,j)}\cdot\frac{dT_{i,j}}{dt}=2\cdot\left(DR(1)+DR(2)+DR(3)\right)\cdot\pi\cdot dz_{i,j}\cdot k_{i,j}\cdot\left(\frac{T_{i-1,j}-T_{i,j}}{\left(DR(3)+DR(4)\right)/2}\right)$$
$$-2\cdot\left(DR(1)+DR(2)+DR(3)+DR(4)\right)\cdot\pi\cdot dz_{i,j}\cdot U_{l(i,j)}\cdot\left(T_{i,j}-T_a\right) \qquad (A.18)$$
$$+A_{t(i,j)}\cdot\left[k_{i,j}\cdot\frac{T_{i,j+1}-T_{i,j}}{\left(dz_{i,j+1}+dz_{i,j}\right)/2}-U_{t(i,j)}\cdot\left(T_{i,j}-T_a\right)\right]$$

Mantle wall, NZ1<j<NZ2:

$$V_{i,j}\cdot\rho_{i,j}\cdot c_{p(i,j)}\cdot\frac{dT_{i,j}}{dt}=2\cdot\left(DR(1)+DR(2)+DR(3)\right)\cdot\pi\cdot dz_{i,j}\cdot h_{3,j}\cdot\left(T_{i-1,j}-T_{i,j}\right)$$
$$-2\cdot\left(DR(1)+DR(2)+DR(3)+DR(4)\right)\cdot\pi\cdot dz_{i,j}\cdot U_{l(i,j)}\cdot\left(T_{i,j}-T_a\right) \qquad (A.19)$$
$$+A_{t(i,j)}\cdot k_{i,j}\cdot\left[\frac{T_{i,j-1}-T_{i,j}}{\left(dz_{i,j-1}+dz_{i,j}\right)/2}-\frac{T_{i,j}-T_{i,j+1}}{\left(dz_{i,j+1}+dz_{i,j}\right)/2}\right]$$

Mantle wall at bottom of mantle, j = NZ2:

$$V_{i,j}\cdot\rho_{i,j}\cdot c_{p(i,j)}\cdot\frac{dT_{i,j}}{dt}=2\cdot\left(DR(1)+DR(2)+DR(3)\right)\cdot\pi\cdot dz_{i,j}\cdot k_{i,j}\cdot\left(\frac{T_{i-1,j}-T_{i,j}}{\left(DR(3)+DR(4)\right)/2}\right)$$
$$-2\cdot\left(DR(1)+DR(2)+DR(3)+DR(4)\right)\cdot\pi\cdot dz_{i,j}\cdot U_{l(i,j)}\cdot\left(T_{i,j}-T_a\right) \qquad (A.20)$$
$$+A_{t(i,j)}\cdot\left[k_{i,j}\cdot\frac{T_{i,j-1}-T_{i,j}}{\left(dz_{i,j-1}+dz_{i,j}\right)/2}-U_{b(i,j)}\cdot\left(T_{i,j}-T_a\right)\right]$$

Auxiliary energy supply (i = 1):

The heating element is placed in one layer and it is assumed to heat up the whole control volume. This control volume is then mixed with the above layers if the temperature is higher than the temperatures of the above layers. The energy balance for this specific layer in the inner tank becomes:

$$V_{i,j} \cdot \rho_{i,j} \cdot c_{p(i,j)} \cdot \frac{dT_{i,j}}{dt} = c_{p(i,j)} \cdot \dot{m}_{dhw} \cdot \left(T_{i,j+1} - T_{i,j}\right) - A_{t(i,j)} \cdot k_{i,j} \cdot \left[\frac{T_{i,j} - T_{i,j+1}}{dz_j} + \frac{T_{i,j} - T_{i,j-1}}{dz_{j-1}}\right] \quad (A.21)$$
$$-2 \cdot DR(1) \cdot \pi \cdot h_{1,j} \cdot \left(T_{i,j} - T_{i+1,j}\right) + Q_{aux}$$

Symbols

The symbols used in equations A.1 – A.21 are given by:

$A_{t(i,j)}$	cross section area of control volume # (i,j), [m²]
$c_{p(i,j)}$	specific heat capacity of control volume # (i,j), [J/(kg·K)]
DR(1)	Inner radius of inner tank, [m]
DR(2)	thickness of tank wall, [m]
DR(3)	mantle gap, [m]
DR(4)	thickness of mantle wall, [m]
i	section number, [-]
j	layer number, [-]
$h_{1,j}$	heat transfer coefficient from tank wall to tank water, [W/m²·K]
$h_{2,j}$	heat transfer coefficient from mantle fluid to inner mantle wall, [W/m²·K]
$h_{3,j}$	heat transfer coefficient from mantle fluid to outer mantle wall, [W/m²·K]
$h_{b,i}$	heat transfer coefficient between fluid and bottom wall, [W/m²·K]
$h_{t,i}$	heat transfer coefficient between fluid and top wall, [W/m²·K]
$k_{i,j}$	thermal conductivity of control volume # (i,j), [W/m·K]
$\dot{m}_{dhw}$	tapping mass flow rate, [kg/s]
Q_{aux}	auxiliary power entering the layer with the auxiliary energy supply, [W]
$T_{i,j}$	temperature of control volume # (i,j), [°C]
$V_{i,j}$	volume of control volume # (i,j), [m³]
$U_{b(i)}$	heat loss coefficient of tank or mantle bottom, [W/m²·K]
$U_{l(i,j)}$	heat loss coefficient of tank or mantle side wall, [W/m²·K]
$U_{t(i)}$	heat loss coefficient of tank or mantle top, [W/m²·K]
$\rho_{i,j}$	density of control volume # (i,j), [kg/m³]

The values of $h_{1,j}$, $h_{2,j}$, $h_{3,j}$, $h_{b,i}$ and $h_{t,i}$ are found from the correlations developed in chapter 7.

Appendix B

Fluid properties

In this appendix the fluid property data that was used in MantlSim and in all the data analysis is presented. The equations are obtained from Jensen (1984).

Water:

Density [kg/m³]:

$$\rho = 1000.5 - 6.9\cdot10^{-2}\cdot T - 36.0\cdot10^{-4}\cdot T^2 \quad \text{(B.1)}$$

Specific heat capacity [J/kg·K]:

$$c_p = 4209.1 - 132.8\cdot10^{-2}\cdot T + 143.2\cdot10^{-4}\cdot T^2 \quad \text{(B.2)}$$

Thermal conductivity [W/m·K]:

$$k = 0.5762 + 10.5\cdot10^{-4}\cdot T \quad \text{(B.3)}$$

Kinematic viscosity [m²/s]:

$$\nu = 1.477\cdot10^{-6}\cdot\exp(-1.747\cdot10^{-2}\cdot T) \quad \text{(B.4)}$$

Prandtl number [-]:

$$Pr = 39.5345\cdot T^{-0.144} - 18.8396 \quad \text{(B.5)}$$

Thermal expansion coefficient [K^{-1}]:

$$\beta = (0.8\cdot T^{0.5348} - 1.9114)\cdot10^{-4} \quad \text{(B.6)}$$

T is the fluid temperature [ºC] in equations B.1 – B.6.

Propylene glycol/water mixture:

Density [kg/m³]:

$$\begin{aligned}\rho = {} & (996.5 + 152.3\cdot10^{-2}\cdot x - 96.6\cdot10^{-4}\cdot x^2) \\ & + (-1.7 - 146.1\cdot10^{-2}\cdot x + 76.7\cdot10^{-4}\cdot x^2)\cdot10^{-2}\cdot T \\ & + (-38.4 + 62.1\cdot10^{-2}\cdot x - 30.8\cdot10^{-4}\cdot x^2)\cdot10^{-4}\cdot T^2\end{aligned} \quad \text{(B.7)}$$

Specific heat capacity [J/kg·K]:

$$\begin{aligned}c_p = {} & (4255.5 - 958.5\cdot10^{-2}\cdot x - 941.7\cdot10^{-4}\cdot x^2) \\ & + (-168.9 + 843.5\cdot10^{-2}\cdot x - 35.0\cdot10^{-4}\cdot x^2)\cdot10^{-2}\cdot T \\ & + (146.5 - 79.3\cdot10^{-2}\cdot x - 85.3\cdot10^{-4}\cdot x^2)\cdot10^{-4}\cdot T^2\end{aligned} \quad \text{(B.8)}$$

Thermal conductivity [W/m·K]:

$$k = (0.571 - 0.42 \cdot 10^{-2} \cdot x + 0.1 \cdot 10^{-4} \cdot x^2) + (12.6 - 31.3 \cdot 10^{-2} \cdot x + 12.2 \cdot 10^{-4} \cdot x^2) \cdot 10^{-4} \cdot T \quad \text{(B.9)}$$

Kinematic viscosity [m²/s]:

$$\nu = (1.293 \cdot \exp(4.388 \cdot 10^{-2} \cdot x)) \cdot 10^{-6} \cdot \exp((-1.709 - 1.921 \cdot 10^{-2} \cdot x - 0.6 \cdot 10^{-4} \cdot x^2) \cdot 10^{-2} \cdot T) \quad \text{(B.10)}$$

Prandtl number [-]:

$$Pr = \frac{\nu \cdot \rho \cdot c_p}{k} \quad \text{(B.11)}$$

Thermal expansion coefficient [K^{-1}]:

$$\beta = 6.346121745 \cdot 10^{-5} + 6.945324481 \cdot 10^{-6} \cdot T + 1.078430353 \cdot 10^{-5} \cdot x + 5.340546887 \cdot 10^{-9} \cdot T^2 - 2.77885339 \cdot 10^{-8} \cdot x^2 - 8.094592481 \cdot 10^{-8} \cdot x \cdot T \quad \text{(B.12)}$$

T is the fluid temperature [ºC] and x [%] is the weight percentage of propylene glycol in equations B.7 – B.12.

Appendix C

Subroutine calculating heat transfer coefficients

```
C ------------------------ UN15:  HBEHOL   ----------------------
      subroutine HBEHOL(TGL,NZ1,NZ2,NZ3,IFLOW,svtyk,xks
     &,H1,H2,H3,IH,HOJKAP,HOJTANK,PROCENT,dr,dz,HTB,HBB,HTK,HBK,GTYPE
     &,FLOW,NZINL,DMI,TKIN)
C
      REAL*8 NY, LAMBDA, BETA, TFILM, DT, HELP, RA, NU, HELP1,ALFA
      REAL*8 LDIMH1, LDIMH2, LDIMH3,HOJTANK, HOJKAP,HD,RE,NYINL,RREF
      DIMENSION TGL(4,50),H1(50),H2(50),H3(50),SUMQW(50),STR(50)
      DIMENSION DR(4),DZ(50),ETA(50),QFLOW(50),QWNY(50),QW(50)
      INTEGER GTYPE

      PI=3.14159265
      G=9.81
      NZ1P1=NZ1+1
      NZ2M1=NZ2-1
      NZINLM1=NZINL-1
      NZM=INT((NZ1P1+NZ2M1)/2)
      NZMP1=NZM+1
      NZ3M1=NZ3-1
      NZ3M2=NZ3-2
C
      IF (GTYPE.EQ.1)THEN
      NYINL=1.293E-6*EXP(4.388E-2*PROCENT)*    !KIN. VISKOSITET  INLET
     &     EXP((-1.709-1.921E-2*PROCENT
     &     -0.6E-4*PROCENT**2)*TKIN*1.0E-2)
      ELSE
      NYINL=2.67E-13*TKIN**4-8.5E-11*TKIN**3     !TYFOCOR LS
     &    +9.96E-9*TKIN**2-5.29E-7*TKIN+1.24E-5
      ENDIF
      RE=(FLOW/(0.25*PI*DMI**2))*DMI/NYINL      !INLET REYNOLDS NUMBER
      IH=1
C     NULSTILLING
      LDIMH1=0
      LDIMH2=0
      LDIMH3=0
      DO 45 J=1,(NZ3)
        H1(J)=0.0                              !H1: INDV I TANK
        H2(J)=0.0                              !H2: INDV I KAPPE
        H3(J)=0.0                              !H3: INDV I KAPPE
   45 CONTINUE
C-----COEFFICIENTS INSIDE TANK--------------------
      DO 50 J=(NZ3-1),2,-1
C       FILM TEMPERATUR
        TFILM=(TGL(1,J)+TGL(2,J))/2          !T_FILM    INDV. I KAPPE
        DT=ABS(TGL(1,J)-TGL(2,J))
        BETA=0.8E-4*TFILM**(.5348)-1.9114E-4    !UDVIDELSESKOEFF. -''-
        PR=39.5345*TFILM**(-.144)-18.8396       !PRANDELS TAL     -''-
        LAMBDA=0.5762+0.00105*EXP(-1.757E-2*TFILM)!VARMELEDN.     -''-
        NY=1.477E-6*EXP(-1.747E-2*TFILM)        !KIN. VISKOSITET  -''-
        LDIMH1=LDIMH1+DZ(J)
        HD=HOJTANK/(2*DR(1))
        HELP=HD
```

```
        RA=G*BETA*LDIMH1**3*DT/(NY**2)*PR
        IF (HELP.LT.3.7) THEN
          IF (HELP.LT.2) HELP=2.0
          NU=(0.186*HELP+2.285)*(ABS(RA)*HD**-4)**0.26
        ELSE
          IF (HELP.GT.5) HELP=5.0
          NU=(3.336*HELP-9.37)*(ABS(RA)*HD**-4)**0.26
        ENDIF
        H1(J)=(NU*LAMBDA/LDIMH1)
   50 CONTINUE
c     Top coefficient_
C     FILM TEMPERATUR
      TFILM=(TGL(1,1)+TGL(1,2))/2             !T_FILM    INDV. I KAPPE
      DT=ABS(TGL(1,1)-TGL(1,2))
      BETA=0.8E-4*TFILM**(.5348)-1.9114E-4    !UDVIDELSESKOEFF. -''-
      PR=39.5345*TFILM**(-.144)-18.8396       !PRANDELS TAL     -''-
      LAMBDA=0.5762+0.00105*EXP(-1.757E-2*TFILM)  !VARMELEDN.   -''-
      NY=1.477E-6*EXP(-1.747E-2*TFILM)        !KIN. VISKOSITET  -''-
      LDIMH1=2*dr(1)
      RA=G*BETA*LDIMH1**3*DT/(NY**2)*PR
      NU=0.54*(ABS(RA))**0.25
      HTB=NU*LAMBDA/LDIMH1

c     Bottom coefficient_
C     FILM TEMPERATUR
      NZ3M1=NZ3-1
      TFILM=(TGL(1,NZ3)+TGL(1,NZ3M1))/2       !T_FILM    INDV. I KAPPE
      DT=ABS(TGL(1,NZ3)-TGL(1,NZ3M1))
      BETA=0.8E-4*TFILM**(.5348)-1.9114E-4    !UDVIDELSESKOEFF. -''-
      PR=39.5345*TFILM**(-.144)-18.8396       !PRANDELS TAL     -''-
      LAMBDA=0.5762+0.00105*EXP(-1.757E-2*TFILM)  !VARMELEDN.   -''-
      NY=1.477E-6*EXP(-1.747E-2*TFILM)        !KIN. VISKOSITET  -''-
      LDIMH1=2*dr(1)
      RA=G*BETA*LDIMH1**3*DT/(NY**2)*PR
      NU=0.54*(ABS(RA))**0.25
      HBB=NU*LAMBDA/LDIMH1

C-----OVERGANGSKOEFFICIENTER INDVENDIGT I KAPPE--------------------
      IF (NZINL.GT.NZ1P1) THEN                    !ABOVE MANTLE INLET
        DO 51 J=(NZ1P1),(NZINLM1)
C         FILM TEMPERATUR
          TFILM=(TGL(2,J)+TGL(3,J))/2         !T_FILM    INDV. I KAPPE
          DT=ABS(TGL(3,J)-TGL(2,J))
          IF (GTYPE.EQ.1)THEN
          RHO=(996.5+152.3E-2*PROCENT-96.6E-4*PROCENT**2)
     &       +(-1.7-146.1E-2*PROCENT+76.7E-4*PROCENT**2)*1E-2*TFILM
     &       +(-38.4+62.1E-2*PROCENT-30.8E-4*PROCENT**2)*1E-4*TFILM**2
          CP=(4255.5-958.2E-2*PROCENT-941.76E-4*PROCENT**2)
     &       +(-168.9+843.5E-2*PROCENT-35.0E-4*PROCENT**2)*1E-2*TFILM
     &       +(146.5-79.3E-2*PROCENT-85.3E-4*PROCENT**2)*1E-4*TFILM**2
           LAMBDA=(0.571-0.42E-2*PROCENT+0.1E-4*PROCENT**2)
     &        +(12.6-31.3E-2*PROCENT+12.2E-4*PROCENT**2)*1.0E-4*TFILM
           NY=1.293E-6*EXP(4.388E-2*PROCENT)*  !KIN. VISKOSITET  -''-
     &        EXP((-1.709-1.921E-2*PROCENT
     &        -0.6E-4*PROCENT**2)*TFILM*1.0E-2)
           BETA=6.346121745E-5
     &        +6.945324481E-6*TFILM
     &        +1.078430353E-5*PROCENT
```

```
     &        +5.340546887E-9*TFILM**2
     &        -2.77885339E-8*PROCENT**2
     &        -8.094592481E-8*PROCENT*TFILM
           ELSE
c*****************************Tyfocor LS*************************
           RHO=1045.2-0.0016*TFILM**2-0.5141*TFILM
           CP=3520+4*TFILM
           LAMBDA=0.3986+0.0007*TFILM
           NY=2.67E-13*TFILM**4-8.5E-11*TFILM**3
     &       +9.96E-9*TFILM**2-5.29E-7*TFILM+1.24E-5
           BETA=0.0005+3E-6*TFILM
c*****************************
           ENDIF
           ALFA=LAMBDA/(RHO*CP)       !TERMISK DIFUSIVITET
           PR=NY/ALFA                 !PRANDTLS TAL
           LDIMH2=(NZINL-J)*DZ(J)-0.5*DZ(J)
           RA=G*BETA*LDIMH2**3*DT/(NY**2)*PR
           HELP=LDIMH2/((NZINL-NZ1P1)*DZ(NZ1P1))
           NU=23.79*(RA*HELP/(RE**2))**0.22
           H2(J)=NU*LAMBDA/LDIMH2
   51    CONTINUE
      ENDIF
      DO 151 J=(NZINL),(NZM)                     !BELOW MANTLE INLET
C       FILM TEMPERATUR
        TFILM=(TGL(2,J)+TGL(3,J))/2         !T_FILM    INDV. I KAPPE
        DT=ABS(TGL(3,J)-TGL(2,J))
        IF (GTYPE.EQ.1)THEN
        RHO=(996.5+152.3E-2*PROCENT-96.6E-4*PROCENT**2)
     &     +(-1.7-146.1E-2*PROCENT+76.7E-4*PROCENT**2)*1E-2*TFILM
     &     +(-38.4+62.1E-2*PROCENT-30.8E-4*PROCENT**2)*1E-4*TFILM**2
        CP=(4255.5-958.2E-2*PROCENT-941.76E-4*PROCENT**2)
     &     +(-168.9+843.5E-2*PROCENT-35.0E-4*PROCENT**2)*1E-2*TFILM
     &     +(146.5-79.3E-2*PROCENT-85.3E-4*PROCENT**2)*1E-4*TFILM**2
        LAMBDA=(0.571-0.42E-2*PROCENT+0.1E-4*PROCENT**2)
     &     +(12.6-31.3E-2*PROCENT+12.2E-4*PROCENT**2)*1.0E-4*TFILM
        NY=1.293E-6*EXP(4.388E-2*PROCENT)*     !KIN. VISKOSITET  -''-
     &     EXP((-1.709-1.921E-2*PROCENT
     &     -0.6E-4*PROCENT**2)*TFILM*1.0E-2)
        BETA=6.346121745E-5
     &     +6.945324481E-6*TFILM
     &     +1.078430353E-5*PROCENT
     &     +5.340546887E-9*TFILM**2
     &     -2.77885339E-8*PROCENT**2
     &     -8.094592481E-8*PROCENT*TFILM
        ELSE
c*****************************Tyfocor LS*************************
        RHO=1045.2-0.0016*TFILM**2-0.5141*TFILM
        CP=3520+4*TFILM
        LAMBDA=0.3986+0.0007*TFILM
        NY=2.67E-13*TFILM**4-8.5E-11*TFILM**3
     &    +9.96E-9*TFILM**2-5.29E-7*TFILM+1.24E-5
        BETA=0.0005+3E-6*TFILM
c*****************************
        ENDIF
        ALFA=LAMBDA/(RHO*CP)                  !TERMISK DIFUSIVITET
        PR=NY/ALFA                            !PRANDTLS TAL
        LDIMH2=(J-NZINL)*DZ(J)+0.5*DZ(J)
        RA=G*BETA*LDIMH2**3*DT/(NY**2)*PR
        HELP=LDIMH2/((NZ2M1-NZINL+1)*DZ(NZ1P1))
```

```
        NU=33.37*(RA*HELP/(RE**2))**0.25
        H2(J)=NU*LAMBDA/LDIMH2
  151 CONTINUE
C
      DO 152 J=(NZMP1),(NZ2M1)             !LOWER HALF OF MANTLE
C       FILM TEMPERATUR
        TFILM=(TGL(2,J)+TGL(3,J))/2          !T_FILM    INDV. I KAPPE
        DT=ABS(TGL(3,J)-TGL(2,J))
        IF (GTYPE.EQ.1)THEN
           RHO=(996.5+152.3E-2*PROCENT-96.6E-4*PROCENT**2)
     &       +(-1.7-146.1E-2*PROCENT+76.7E-4*PROCENT**2)*1E-2*TFILM
     &       +(-38.4+62.1E-2*PROCENT-30.8E-4*PROCENT**2)*1E-4*TFILM**2
           CP=(4255.5-958.2E-2*PROCENT-941.76E-4*PROCENT**2)
     &       +(-168.9+843.5E-2*PROCENT-35.0E-4*PROCENT**2)*1E-2*TFILM
     &       +(146.5-79.3E-2*PROCENT-85.3E-4*PROCENT**2)*1E-4*TFILM**2
           LAMBDA=(0.571-0.42E-2*PROCENT+0.1E-4*PROCENT**2)
     &       +(12.6-31.3E-2*PROCENT+12.2E-4*PROCENT**2)*1.0E-4*TFILM
           NY=1.293E-6*EXP(4.388E-2*PROCENT)*   !KIN. VISKOSITET  -''-
     &       EXP((-1.709-1.921E-2*PROCENT
     &       -0.6E-4*PROCENT**2)*TFILM*1.0E-2)
           BETA=6.346121745E-5
     &       +6.945324481E-6*TFILM
     &       +1.078430353E-5*PROCENT
     &       +5.340546887E-9*TFILM**2
     &       -2.77885339E-8*PROCENT**2
     &       -8.094592481E-8*PROCENT*TFILM
        ELSE
c*****************************Tyfocor LS*************************
           RHO=1045.2-0.0016*TFILM**2-0.5141*TFILM
           CP=3520+4*TFILM
           LAMBDA=0.3986+0.0007*TFILM
           NY=2.67E-13*TFILM**4-8.5E-11*TFILM**3
     &       +9.96E-9*TFILM**2-5.29E-7*TFILM+1.24E-5
           BETA=0.0005+3E-6*TFILM

c*****************************
        ENDIF
        ALFA=LAMBDA/(RHO*CP)                 !TERMISK DIFUSIVITET
        PR=NY/ALFA                           !PRANDTLS TAL
        HELP=((DR(1)+DR(2)+DR(3))**2-DR(1)+DR(2))**2)/(2*(DR(1)+DR(2))
     &    *HOJKAP)
        NU=403.9*HELP+0.98
        H2(J)=NU*LAMBDA/DR(3)
  152 CONTINUE
C-----OVERGANGSKOEFFICIENTER UDVENDIGT I KAPPE--------------------
      IF (NZINL.GT.NZ1P1) THEN                !ABOVE MANTLE INLET
        DO 52 J=(NZ1P1),(NZINLM1)


C         FILM TEMPERATUR
          TFILM=(TGL(4,J)+TGL(3,J))/2         !T_FILM    INDV. I KAPPE
          DT=ABS(TGL(3,J)-TGL(4,J))
          IF (GTYPE.EQ.1)THEN
          RHO=(996.5+152.3E-2*PROCENT-96.6E-4*PROCENT**2)
     &      +(-1.7-146.1E-2*PROCENT+76.7E-4*PROCENT**2)*1E-2*TFILM
     &      +(-38.4+62.1E-2*PROCENT-30.8E-4*PROCENT**2)*1E-4*TFILM**2
          CP=(4255.5-958.2E-2*PROCENT-941.76E-4*PROCENT**2)
     &      +(-168.9+843.5E-2*PROCENT-35.0E-4*PROCENT**2)*1E-2*TFILM
     &      +(146.5-79.3E-2*PROCENT-85.3E-4*PROCENT**2)*1E-4*TFILM**2
```

```
          LAMBDA=(0.571-0.42E-2*PROCENT+0.1E-4*PROCENT**2)
     &      +(12.6-31.3E-2*PROCENT+12.2E-4*PROCENT**2)*1.0E-4*TFILM
          NY=1.293E-6*EXP(4.388E-2*PROCENT)*    !KIN. VISKOSITET  -''-
     &      EXP((-1.709-1.921E-2*PROCENT
     &      -0.6E-4*PROCENT**2)*TFILM*1.0E-2)
          BETA=6.346121745E-5
     &      +6.945324481E-6*TFILM
     &      +1.078430353E-5*PROCENT
     &      +5.340546887E-9*TFILM**2
     &      -2.77885339E-8*PROCENT**2
     &      -8.094592481E-8*PROCENT*TFILM
          ELSE
c*****************************Tyfocor LS*************************
          RHO=1045.2-0.0016*TFILM**2-0.5141*TFILM
          CP=3520+4*TFILM
          LAMBDA=0.3986+0.0007*TFILM
          NY=2.67E-13*TFILM**4-8.5E-11*TFILM**3
     &      +9.96E-9*TFILM**2-5.29E-7*TFILM+1.24E-5
          BETA=0.0005+3E-6*TFILM
c*****************************
          ENDIF
          ALFA=LAMBDA/(RHO*CP)              !TERMISK DIFUSIVITET
          PR=NY/ALFA                        !PRANDTLS TAL
          LDIMH3=(NZINL-J)*DZ(J)-0.5*DZ(J)
          RA=G*BETA*LDIMH3**3*DT/(NY**2)*PR
          HELP=LDIMH3/((NZINL-NZ1P1)*DZ(NZ1P1))
          NU=31.51*(RA*HELP/(RE**2))**0.18
          H3(J)=NU*LAMBDA/LDIMH3
   52   CONTINUE
        ENDIF
        DO 153 J=(NZINL),(NZM)                  !BELOW MANTLE INLET
C         FILM TEMPERATUR
          TFILM=(TGL(4,J)+TGL(3,J))/2          !T_FILM    INDV. I KAPPE
          DT=ABS(TGL(3,J)-TGL(4,J))
          IF (GTYPE.EQ.1)THEN
            RHO=(996.5+152.3E-2*PROCENT-96.6E-4*PROCENT**2)
     &        +(-1.7-146.1E-2*PROCENT+76.7E-4*PROCENT**2)*1E-2*TFILM
     &        +(-38.4+62.1E-2*PROCENT-30.8E-4*PROCENT**2)*1E-4*TFILM**2
            CP=(4255.5-958.2E-2*PROCENT-941.76E-4*PROCENT**2)
     &        +(-168.9+843.5E-2*PROCENT-35.0E-4*PROCENT**2)*1E-2*TFILM
     &        +(146.5-79.3E-2*PROCENT-85.3E-4*PROCENT**2)*1E-4*TFILM**2
            LAMBDA=(0.571-0.42E-2*PROCENT+0.1E-4*PROCENT**2)
     &        +(12.6-31.3E-2*PROCENT+12.2E-4*PROCENT**2)*1.0E-4*TFILM
            NY=1.293E-6*EXP(4.388E-2*PROCENT)*   !KIN. VISKOSITET  -''-
     &        EXP((-1.709-1.921E-2*PROCENT
     &        -0.6E-4*PROCENT**2)*TFILM*1.0E-2)

            BETA=6.346121745E-5
     &        +6.945324481E-6*TFILM
     &        +1.078430353E-5*PROCENT
     &        +5.340546887E-9*TFILM**2
     &        -2.77885339E-8*PROCENT**2
     &        -8.094592481E-8*PROCENT*TFILM
          ELSE
c*****************************Tyfocor LS*************************
            RHO=1045.2-0.0016*TFILM**2-0.5141*TFILM
            CP=3520+4*TFILM
            LAMBDA=0.3986+0.0007*TFILM
            NY=2.67E-13*TFILM**4-8.5E-11*TFILM**3
```

```
     &      +9.96E-9*TFILM**2-5.29E-7*TFILM+1.24E-5
            BETA=0.0005+3E-6*TFILM
c*****************************
          ENDIF
          ALFA=LAMBDA/(RHO*CP)                        !TERMISK DIFUSIVITET
          PR=NY/ALFA                                  !PRANDTLS TAL
          LDIMH3=(J-NZINL)*DZ(J)+0.5*DZ(J)
          RA=G*BETA*LDIMH3**3*DT/(NY**2)*PR
          HELP=LDIMH3/((NZ2M1-NZINL+1)*DZ(NZ1P1))
          NU=56.24*(RA*HELP/(RE**2))**0.22
          H3(J)=NU*LAMBDA/LDIMH3
  153 CONTINUE
C
       DO 154 J=(NZMP1),(NZ2M1)                    !LOWER HALF OF MANTLE
C         FILM TEMPERATUR
          TFILM=(TGL(4,J)+TGL(3,J))/2          !T_FILM    INDV. I KAPPE
          DT=ABS(TGL(3,J)-TGL(4,J))
          IF (GTYPE.EQ.1)THEN
            RHO=(996.5+152.3E-2*PROCENT-96.6E-4*PROCENT**2)
     &        +(-1.7-146.1E-2*PROCENT+76.7E-4*PROCENT**2)*1E-2*TFILM
     &        +(-38.4+62.1E-2*PROCENT-30.8E-4*PROCENT**2)*1E-4*TFILM**2
            CP=(4255.5-958.2E-2*PROCENT-941.76E-4*PROCENT**2)
     &        +(-168.9+843.5E-2*PROCENT-35.0E-4*PROCENT**2)*1E-2*TFILM
     &        +(146.5-79.3E-2*PROCENT-85.3E-4*PROCENT**2)*1E-4*TFILM**2
            LAMBDA=(0.571-0.42E-2*PROCENT+0.1E-4*PROCENT**2)
     &        +(12.6-31.3E-2*PROCENT+12.2E-4*PROCENT**2)*1.0E-4*TFILM
            NY=1.293E-6*EXP(4.388E-2*PROCENT)*  !KIN. VISKOSITET  -''-
     &        EXP((-1.709-1.921E-2*PROCENT
     &        -0.6E-4*PROCENT**2)*TFILM*1.0E-2)
            BETA=6.346121745E-5
     &        +6.945324481E-6*TFILM
     &        +1.078430353E-5*PROCENT
     &        +5.340546887E-9*TFILM**2
     &        -2.77885339E-8*PROCENT**2
     &        -8.094592481E-8*PROCENT*TFILM
          ELSE
c*************************Tyfocor LS************************
            RHO=1045.2-0.0016*TFILM**2-0.5141*TFILM
            CP=3520+4*TFILM
            LAMBDA=0.3986+0.0007*TFILM
            NY=2.67E-13*TFILM**4-8.5E-11*TFILM**3
     &        +9.96E-9*TFILM**2-5.29E-7*TFILM+1.24E-5
            BETA=0.0005+3E-6*TFILM
c*****************************
          ENDIF
          ALFA=LAMBDA/(RHO*CP)              !TERMISK DIFUSIVITET
          PR=NY/ALFA                        !PRANDTLS TAL
          HELP=((DR(1)+DR(2)+DR(3))**2-(DR(1)+DR(2))**2)/
     &         (2*(DR(1)+DR(2)+DR(3))*HOJKAP)
          NU=570.6*HELP+5.6
          H3(J)=NU*LAMBDA/DR(3)
  154 CONTINUE
c         Top MANTLE coefficient************************************
          NZ1P1=NZ1+1
C         FILM TEMPERATUR
          TFILM=(TGL(3,NZ1)+TGL(3,NZ1P1))/2   !T_FILM    INDV. I KAPPE
          DT=ABS(TGL(3,NZ1)-TGL(3,NZ1P1))
          BETA=0.8E-4*TFILM**(.5348)-1.9114E-4   !UDVIDELSESKOEFF. -''-
          PR=39.5345*TFILM**(-.144)-18.8396      !PRANDELS TAL     -''-
```

```
        LAMBDA=0.5762+0.00105*EXP(-1.757E-2*TFILM)!VARMELEDN.    -''-
        NY=1.477E-6*EXP(-1.747E-2*TFILM)       !KIN. VISKOSITET  -''-
        LDIMH1=dr(3)
        RA=G*BETA*LDIMH1**3*DT/(NY**2)*PR
        NU=0.54*(ABS(RA))**0.25
        HTK=NU*LAMBDA/LDIMH1
c       Bottom coefficient_
C       FILM TEMPERATUR
        NZ2M1=NZ2-1
        TFILM=(TGL(3,NZ2)+TGL(3,NZ2M1))/2     !T_FILM    INDV. I KAPPE
        DT=ABS(TGL(3,NZ2)-TGL(3,NZ2M1))
        BETA=0.8E-4*TFILM**(.5348)-1.9114E-4    !UDVIDELSESKOEFF. -''-
        PR=39.5345*TFILM**(-.144)-18.8396       !PRANDELS TAL     -''-
        LAMBDA=0.5762+0.00105*EXP(-1.757E-2*TFILM) !VARMELEDN.    -''-
        NY=1.477E-6*EXP(-1.747E-2*TFILM)        !KIN. VISKOSITET  -''-
        LDIMH1=dr(3)
        RA=G*BETA*LDIMH1**3*DT/(NY**2)*PR
        NU=0.54*(ABS(RA))**0.25
        HBK=NU*LAMBDA/LDIMH1
C
   10 CONTINUE
C******************STRATIFICATION MODEL*****************************
       SUMQW(NZ3)=0
       DO J=NZ3M1,2,-1                          !Heat flux tank wall
       QW(J)=H1(J)*2*PI*DR(1)*DZ(J)*(TGL(2,J)-TGL(1,J))
       SUMQW(J)=SUMQW(J+1)+QW(J)      !Sum of heat flux at tank wall
       STR(J)=MAX(4.0,((TGL(1,J-1)-TGL(1,J+1))/(0.5*DZ(J-1)+DZ(J)+
     &    0.5*DZ(J+1))))                    !Stratification in tank
       ENDDO
       STR(2)=MAX(4.0,(TGL(1,2)-TGL(1,3)/DZ(2)))
       STR(NZ3M1)=MAX(4.0,(TGL(1,NZ3M2)-TGL(1,NZ3M1)/DZ(NZ3M1)))
       DO J=NZ3M1,NZ1P1,-1                  !Mantle level
         HELP1=QW(J)/SQRT(STR(J))
         ETA(J)=0.000186*HELP1
         IF (HELP1.GE.2900) ETA(J)=0.539
         IF (HELP1.LT.0) ETA(J)=0
         QFLOW(J)=ETA(J)*SUMQW(J)           !Heat flow in water
       ENDDO
       RREF=0.197
       DO J=NZ1,2,-1                        !Above mantle
       HELP1=(DR(1)/RREF)**1.8*(TGL(2,J)-TGL(1,J))/(STR(J)+0.5)**2.2
     &   ETA(J)=29.094*HELP1**3-23.605*HELP1**2+5.9475*HELP1
       IF (HELP1.GE.0.3) ETA(J)=0.445
       IF (HELP1.LT.0) ETA(J)=0
       QFLOW(J)=ETA(J)*SUMQW(J)             !Heat flow in water
       ENDDO
       QFLOW(2)=0
       HELP1=0
       DO J=NZ3M1,2,-1
       QWNY(J)=SUMQW(J)-QFLOW(J)-HELP1      !Resulting heat transfer
       IF (QWNY(J).LT.0) THEN
         IF (QFLOW(J).GT.0) THEN
           QFLOW(J)=QFLOW(J)+QWNY(J)
           QWNY(J)=SUMQW(J)-QFLOW(J)-HELP1
         ENDIF
       ENDIF
       HELP1=HELP1+QWNY(J)
       IF ((TGL(2,J)-TGL(1,J)).LE.0) THEN
         H1(J)=H1(J)
```

```
 ELSE
 !New heat transfer coefficient based on resulting heat transfer
   H1(J)=ABS(QWNY(J)/(2*PI*DR(1)*DZ(J)*(TGL(2,J)-TGL(1,J))))
ENDIF
ENDDO
RETURN
END
```

Appendix D

Subroutine for modelling flow in mantle

```
C -------------------------  UN13:  TAPKAP   --------------------
      SUBROUTINE TAPKAP(NZ1,NZ2,TGL,VOL,ROCP,TKIN
     &,TKUD,QKAP,NZINL,FLOW,DR)
C
      DIMENSION TGL(4,50),VOL(4,50),ROCP(4,50),DR(4)
      REAL*8 TKINNEW,DT,OPBL,THELP,PI,VMANTLE,THELP1
      NZ1P1=NZ1+1
      NZ1P2=NZ1+2
      NZ1P3=NZ1+3
      NZ2M1=NZ2-1
      NZINLP1=NZINL+1
      NZINLM1=NZINL-1
      TKINNEW=TKIN
      TKUD=TGL(3,NZ2M1)
      PI=3.14159265
      !AVERAGE VELOCITY IN MANTLE
      VMANTLE=FLOW/(PI*((DR(1)+DR(2)+DR(3))**2-(DR(1)+DR(2))**2))
      IF (TKIN.LE.TGL(3,NZINL)) THEN        !WARM INLET - DOWNFLOW
        DO J=NZINL,NZ2M1
          DT=TGL(3,J)-TKINNEW
          IF (DT.LT.0) THEN
            I=J
            GO TO 20
          ELSEIF (DT.EQ.0) THEN
            OPBL=0
          ELSE
            OPBL=0.21*LOG(DT/VMANTLE**0.5)-0.52 !MIX. FACTOR
            IF (OPBL.LT.0) OPBL=0
            IF (OPBL.GT.1) OPBL=1
          ENDIF
          THELP=TGL(3,J)
          TGL(3,J)=OPBL*TGL(3,J)+(1-OPBL)*TKINNEW
          TKINNEW=OPBL*TKINNEW+(1-OPBL)*THELP !MOD. TKIN IN NEXT LAYER
        ENDDO
        TKUD=OPBL*TKINNEW+(1-OPBL)*THELP
        GO TO 30
   20   CONTINUE
        DO JJ=NZ2M1,I,-1
          TGL(3,JJ)=TGL(3,JJ-1)
        ENDDO
        TGL(3,I)=TKINNEW
   30   CONTINUE
      ELSE                                  !HOT INLET - UPFLOW
        DO J=NZINL,NZ1P1,-1
          DT=TKINNEW-TGL(3,J)
          IF (DT.LT.0) THEN
            I=J
            GO TO 40
          ELSEIF (DT.EQ.0) THEN
            OPBL=0
          ELSE
            OPBL=0.37*LOG(DT/VMANTLE**0.5)-1.94 !MIX. FACTOR
```

```
            IF (OPBL.LT.0) OPBL=0
            IF (OPBL.GT.1) OPBL=1
          ENDIF
          THELP=TGL(3,J)
          TGL(3,J)=OPBL*TGL(3,J)+(1-OPBL)*TKINNEW
          TKINNEW=OPBL*TKINNEW+(1-OPBL)*THELP !MOD. TKIN IN NEXT LAYER
        ENDDO
        THELP=TGL(3,NZ1P1)
        THELP1=TGL(3,NZ1P2)
        TGL(3,NZ1P1)=TKINNEW
        TGL(3,NZ1P2)=THELP
        DO J=NZ2M1,NZ1P3,-1
          TGL(3,J)=TGL(3,J-1)
        ENDDO
        TGL(3,NZ1P3)=THELP1
        GO TO 50
   40   CONTINUE
        DO JJ=NZ2M1,I,-1
          TGL(3,JJ)=TGL(3,JJ-1)
        ENDDO
        TGL(3,I)=TKINNEW
   50   CONTINUE
      ENDIF
C---->OPBLANDNING I KAPPE-----------------------------------:
      DO 101 J=NZ1p1,NZ2M1
        DO 102 JJ=NZ1p1,NZ2M1
          if (tgl(3,jj+1).gt.tgl(3,jj)) then
            thelp=tgl(3,jj)
            tgl(3,jj)=tgl(3,jj+1)
            tgl(3,jj+1)=thelp
          endif
  102   continue
  101 continue
      QKAP=VOL(3,NZ1P1)*ROCP(3,NZ1P1)*(TKIN-TKUD)
      RETURN
      END
```